School of Physics and Astronomy
Queen Mary University of London

Measurements of the Differential Charged-Current Drell-Yan Cross-Section and Muon Charge Asymmetry at High Transverse Masses with the ATLAS Detector

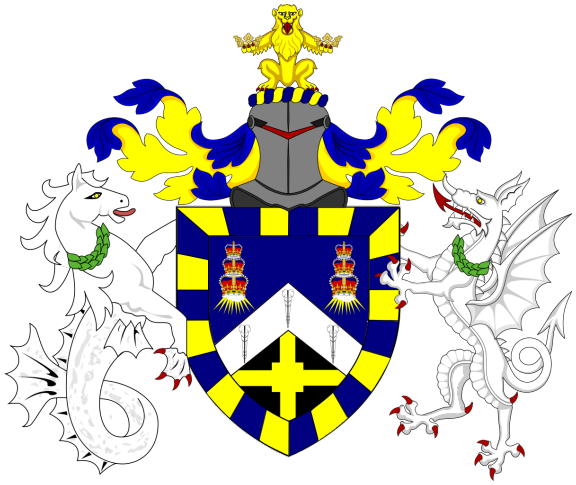

Jesal Mandalia

March 2023

Submitted in partial fulfillment of the requirements of the Degree of Doctor of Philosophy from Queen Mary University of London

Statement of Originality

I, Jesal Mandalia, confirm that the research included within this thesis is my own work or that where it has been carried out in collaboration with, or supported by others, that this is duly acknowledged below and my contribution indicated. Previously published material is also acknowledged below.

I attest that I have exercised reasonable care to ensure that the work is original, and does not to the best of my knowledge break any UK law, infringe any third party's copyright or other Intellectual Property Right, or contain any confidential material.

I accept that the College has the right to use plagiarism detection software to check the electronic version of the thesis.

I confirm that this thesis has not been previously submitted for the award of a degree by this or any other university.

Signature: Jesal Mandalia

Date: 23/03/2023

Acknowledgements

I extend my heartfelt gratitude to my family for their unwavering support throughout my life/academic journey and my friends for their encouragement and motivation. I am immensely grateful to the brilliant Dr. Alison Elliot for sharing her intelligence, invaluable technical assistance, wise mentorship and being a true inspiration especially in the hard times. My deepest appreciation goes to the staff and students at QMUL, ATLAS and CERN, whose assistance and insights have contributed greatly to the completion of this research. I am also thankful to the DISCnet STFC for their funding, which made this work possible. Lastly, I would like to express my thanks to you, dear reader.

Jesal Mandalia ★

Abstract

This thesis presents the measurements of the $W \to \mu\nu$ charged-current Drell-Yan process, utilising the experimental data recorded by the ATLAS experiment during the Run – 2 period of pp collisions at the LHC at 13 TeV, corresponding to a total integrated luminosity of 139 fb^{-1}. The measurements are performed differentially in the transverse mass of the W boson, m_{T}^{W}, focusing on the high mass tail ranging from 200 GeV to 2000 GeV. In this region, the statistical uncertainty dominates, with the systematic uncertainty originating from the muon sagitta bias correction being a significant contributor. Specifically, for W^+ bosons, the muon sagitta bias correction reaches up to around 8%, while for W^- bosons, it reaches up to around 15%, with a maximum of around 33% for the muon charge asymmetry. Notably, in the highest m_{T}^{W} bin, the statistical uncertainty exceeds the systematic uncertainty, reaching up to around 40% for the muon charge asymmetry. When compared to the theoretical predictions of POWHEG-BOX and PYTHIA8 at the born level of the signal, the results show a good agreement between the theory and measurements.

Contents

Statement of Originality ii
Acknowledgements iii
Abstract iv

1. Introduction **1**

2. Theory **3**
2.1. Standard Model 3
2.1.1. Electro-Weak Theory 5
Experimental Evidence 7
Renormalisation and Running Coupling 7
2.1.2. Quantum Chromodynamics 8
2.2. Parton Distribution Functions 10
2.3. Drell-Yan Process 12
2.3.1. Higher Order Corrections 15
2.4. Effective Field Theory 16
2.5. Measurement Overview 17

3. The LHC & ATLAS Detector **19**
3.1. The LHC 19
3.2. Luminosity 19
3.3. Pileup 21
3.4. ATLAS Detector 21
3.5. Coordinate System 22
3.6. Magnets 24
3.7. Inner Detector 25
3.7.1. Silicon Pixel Detector 26
3.7.2. Semi-Conductor Tracker 27
3.7.3. TRT Detector 27
3.7.4. Insertable B-Layer 28
3.8. Calorimeters 28
3.8.1. ECAL 29
3.8.2. HCAL 30
TileCal 31

HEC . . . 31
FCAL . . . 31
3.9. Muon Spectrometer . . . 31
3.9.1. MDT . . . 32
3.9.2. CSC . . . 33
3.9.3. RPC . . . 33
3.9.4. TGC . . . 33
3.10. Trigger System . . . 35
3.10.1. Level 1 Trigger . . . 35
3.10.2. High Level Trigger . . . 36
3.11. Muon Reconstruction . . . 37
3.11.1. CB . . . 38
3.11.2. ST . . . 38
3.11.3. CT . . . 38
3.11.4. ME . . . 39
3.11.5. Reconstruction Algorithms . . . 39
Chain 1 . . . 39
Chain 2 . . . 39
Chain 3 . . . 39
3.11.6. Momentum Measurement . . . 40
3.11.7. The Tag and Probe Method . . . 41
3.11.8. Reconstruction and Identification Efficiency . . . 41
3.12. Electron Reconstruction . . . 42
3.13. Jet Reconstruction . . . 44
3.14. Missing Transverse Energy Reconstruction . . . 45

4. Level 1 Calorimeter Validation Code Study **46**
4.1. The L1Calo Phase 1 Upgrade . . . 46
4.2. Samples and Objects . . . 47
4.2.1. Electron and Dijet Selections . . . 48
4.3. Analysis Results . . . 51
4.3.1. Trigger Efficiency . . . 51
4.3.2. Isolation Variables . . . 54
4.3.3. Total Shower Width (w_{stot}) . . . 54
4.3.4. f_3 . . . 56
4.4. Next steps . . . 57

5. Data and Monte Carlo Samples **59**
5.1. Data Samples . . . 59
5.2. Monte Carlo Samples . . . 61
5.2.1. Motivation For Monte Carlo Use . . . 61

5.2.2. Monte Carlo Generators . . . 63
5.2.3. Signal and Background Monte Carlo . . . 64
Monte Carlo Signal . . . 65
Background Samples . . . 70
$t\bar{t}$ . . . 70
t . . . 70
$Z \to \mu\mu$ . . . 70
Diboson . . . 71
$W \to \tau\nu$ and $Z \to \tau\tau$ . . . 71

6. Event Selections **72**
6.1. Event Selection Criteria . . . 72
6.1.1. Good Runs List . . . 73
6.1.2. LAr Error . . . 73
6.1.3. Primary Vertex . . . 73
Impact Parameter . . . 74
6.1.4. Trigger Selection . . . 74
6.1.5. Jet Cleaning . . . 76
6.1.6. Overlap Removal . . . 76
6.1.7. Muon Isolation . . . 76
6.1.8. Muon Kinematics . . . 78
6.1.9. Missing Transverse Energy . . . 78
6.1.10. Transverse Mass . . . 80
6.1.11. Truth Level . . . 80

7. Multijet Background Estimate **81**
7.1. Introduction . . . 81
7.2. Matrix Method . . . 82
Overlap Removal . . . 83
7.2.1. Matrix Method Strategy . . . 83
7.3. Multijet Estimate . . . 85
7.3.1. Real Efficiency . . . 85
7.3.2. Fake Efficiency . . . 86
7.4. Multijet Results . . . 88
7.5. Multijet Systematic Uncertainties . . . 94

8. Systematic Uncertainties **98**
8.1. Systematic Uncertainty Definition . . . 98
8.2. Experimental Systematic Uncertainties . . . 100
8.2.1. Muon Uncertainties . . . 100
Muon Momentum and Scale Resolution . . . 100

Muon Scale Factors . . . 101
Muon Sagitta . . . 102
8.2.2. Muon Charge Misidentification . . . 102
8.2.3. Missing Energy Uncertainties . . . 103
8.2.4. Jet Uncertainties . . . 103
8.2.5. Pileup Reweighting . . . 106
8.2.6. Luminosity . . . 106
8.3. Fake Muon Background Systematic Uncertainties . . . 106
8.4. Theoretical Systematic Uncertainties . . . 106

9. Control Distributions **114**
9.1. Monte Carlo to Data Comparison . . . 114
9.2. Cutflows . . . 117
9.2.1. Event Selection Efficiency and Pileup . . . 124

10. Cross-Section and Charge Asymmetry **126**
10.1. Extraction of Cross-Section and Asymmetry . . . 126
10.1.1. Cross-Section Calculation . . . 126
10.1.2. Asymmetry Calculation . . . 126
10.2. Stability, Purity and Acceptance . . . 127
10.3. Truth Level Definition . . . 132
10.4. Optimisation of Binning . . . 132
10.4.1. Migration . . . 134
10.5. Iterative Bayesian Unfolding . . . 137
10.6. Response Matrix for the Iterative Bayesian Unfolding . . . 138
10.7. Shadow Bin . . . 138
10.8. Technical Closure Test . . . 139
10.9. Results . . . 141
10.9.1. Unfolded Differential Cross-Section . . . 141
10.9.2. Muon Charge Asymmetry . . . 142
10.9.3. Summary . . . 142
10.9.4. Measurement Conclusions . . . 144

11. Conclusion **151**

A. Appendix: Samples **154**
A.1. Data samples . . . 154
A.1.1. 2015 . . . 154
A.1.2. 2016 . . . 154
A.1.3. 2017 . . . 154
A.1.4. 2018 . . . 155

A.2. Signal samples . . . 155
A.2.1. $W \to \mu\nu$ . . . 155
A.3. Background samples . . . 159
A.3.1. $t\bar{t}$ . . . 159
A.3.2. Single Top . . . 159
A.3.3. Z+Jets . . . 160
A.3.4. Diboson . . . 163
A.3.5. $W \to \tau\nu$ . . . 164

B. Appendix: Scale Factors **168**

C. Appendix: Multijet Background Estimation **177**
C.1. Real Efficiency . . . 178
C.2. Fake Efficiency . . . 180

D. Appendix: Systematic Uncertainties **182**
D.1. Individual Cross-Section Systematic Uncertainties . . . 182
D.2. Individual Asymmetry Systematic Uncertainties . . . 189
D.3. Systematic Uncertainties For Individual Monte Carlo Campaigns . . . 193
D.4. Cross-Section Systematic Uncertainties For Individual Monte Carlo Campaigns . . . 212
D.5. Asymmetry Systematic Uncertainties For Individual Monte Carlo Campaigns . . . 231

E. Appendix: Control Distributions **241**
E.1. MC16a . . . 241
E.2. MC16d . . . 251
E.3. MC16e . . . 261
E.4. Run-2 Combined Charge Plots . . . 271
E.5. Event Selection Efficiency for Individual MC Campaigns . . . 274

F. Appendix: Results **276**
F.1. Stability, Purity and Acceptance Correction Factors . . . 276
F.2. Migrations . . . 298
F.3. Results . . . 304
F.3.1. Individual Systematic Uncertainty Tables . . . 304

References **317**

List of Figures

2.1. Deep inelastic scattering Feynman diagram with kinematics. 10
2.2. MSHT20 NNLO PDFs at $Q^2 = 10\ GeV^2$ and $Q^2 = 10^4\ GeV^2$. 11
2.3. Feynman diagram of the neutral current Drell-Yan process. 13
2.4. Feynman diagram of the positively charged current Drell-Yan process. . . 13
2.5. Feynman diagram of the negatively charged current Drell-Yan process. . . 14
2.6. Drell-Yan cross-sections as a function of invariant mass at NLO. 15
2.7. Projected 95% CL exclusions in the W–Y (oblique parameters) plane. 17

3.1. CERN Accelerator Complex 20
3.2. ATLAS Detector with labelled subsystems. 22
3.3. Schematic of the ATLAS magnet systems. 25
3.4. ATLAS magnetic field. 25
3.5. Schematic of the ATLAS inner detector subsystem. 26
3.6. Schematic of the ATLAS 4-Layer pixel detector for Run-2. 28
3.7. Schematic of the ATLAS electromagnetic and hadronic calorimeters. 29
3.8. Schematic of the ATLAS LAr calorimeter. 30
3.9. Schematic of the ATLAS forward calorimeter. 32
3.10. ATLAS cross and side view of the Muon System. 34
3.11. ATLAS TDAQ system in Run-2. 35
3.12. Diagram of the radius of curvature r, length L and sagitta s. 40
3.13. Muon reconstruction and identification efficiencies. 42
3.14. Measured LH electron-identification efficiencies in $Z \rightarrow ee$ events. 43

4.1. Upgraded SuperCell configuration in a LAr trigger tower for Run-3. 48
4.2. Schematic of L1Calo in Run-3. 49
4.3. An electron seen passing through the L1Calo trigger electronics. 52
4.4. Truth and Matched electron p_T distributions. 53
4.5. Efficiency of electron sample in p_T. 53
4.6. Efficiency of electron sample in η. 54
4.7. Normalised distribution of w_{stot} in Layer 1. 56
4.8. Normalised distribution of w_{stot} in Layer 2. 57
4.9. Normalised distributions of f_3. 58

5.1. Total integrated luminosity and data quality in 2015-2018. 60

5.2. Luminosity weighted distribution of the mean number of interactions per crossing for 13 TeV data from 2015-2018. 61
5.3. Feynman diagram showing $W \rightarrow \mu\nu$ process. 65
5.4. Average k-Factor efficiency scale factors for $W^+ \rightarrow \mu^+\nu$. 67
5.5. Born level invariant mass slices distribution for $W \rightarrow \mu\nu$ events in MC16a. . 68
5.6. Feynman diagram showing $t\bar{t}$ background process. 70
5.7. Feynman diagram showing $Z \rightarrow \mu\mu$ background. 71
5.8. Feynman diagram showing $W \rightarrow \tau\nu$ background. 71
5.9. Feynman diagram showing $Z \rightarrow \tau\tau$ background. 71

6.1. Diagram of impact parameter d_0 and z_0. 75
6.2. Average trigger cut efficiency scale factors for $W^+ \rightarrow \mu\nu$. 77
6.3. Average isolation selection efficiency scale factors for $W^+ \rightarrow \mu\nu$. 79

7.1. Real muon efficiency for MC16e. 87
7.2. Fake muon efficiency for MC16e. 89
7.3. Multijet background for $W^+ \rightarrow \mu^+\nu$ in p_T^μ, $|\Delta\phi|$, E_T^{miss}, m_T, η^μ and ϕ^μ 90
7.4. Multijet background for $W^+ \rightarrow \mu^+\nu$ in $<\mu>$, $d0^{sig}$, $TrackE_T20/p_T^\mu$ and $\phi^{E_T^{miss}}$. 91
7.5. Multijet background for $W^- \rightarrow \mu^-\bar{\nu}$ in p_T^μ, $|\Delta\phi|$, E_T^{miss}, m_T, η^μ and ϕ^μ. 92
7.6. Multijet background for $W^- \rightarrow \mu^-\bar{\nu}$ in $<\mu>$, $d0^{sig}$, $TrackE_T20/p_T^\mu$ and $\phi^{E_T^{miss}}$. 93
7.7. Systematic uncertainties for the multijet background. 95
7.8. Systematic uncertainties for the multijet background calculated for the cross-section. 96
7.9. Systematic uncertainties for the multijet background calculated for the asymmetry. 97

8.1. Individual contributions to the systematic variations for the muon, sagitta and missing energy uncertainties for $W^+ \rightarrow \mu^+\nu$ 108
8.2. Individual contributions to the systematic variations for the scale factor and jet uncertainties for $W^+ \rightarrow \mu^+\nu$. 109
8.3. Individual contributions to the systematic variations for the jet uncertainties for $W^+ \rightarrow \mu^+\nu$. 110
8.4. Individual contributions to the systematic variations for the muon, sagitta and missing energy uncertainties for $W^- \rightarrow \mu^-\bar{\nu}$. 111
8.5. Individual contributions to the systematic variations for the scale factor and jet uncertainties for $W^- \rightarrow \mu^-\bar{\nu}$. 112
8.6. Individual contributions to the systematic variations for the jet uncertainties for $W^- \rightarrow \mu^-\bar{\nu}$. 113

9.1. Chart showing relative contributions of all Monte Carlo in the signal region. 115
9.2. Control distributions for $W^+ \rightarrow \mu^+\nu$ for p_T^μ, $|\Delta\phi|$, E_T^{miss}, m_T, η^μ and ϕ^μ. . . . 118

9.3. Control distributions for $W^+ \to \mu^+\nu$ for $< \mu >$, $d0^{sig}$, $TrackE_T20/p_T^\mu$ and $\phi^{E_T^{miss}}$ . . . 119
9.4. Control distributions for $W^- \to \mu^-\bar{\nu}$ for p_T^μ, $|\Delta\phi|$, E_T^{miss}, m_T, η^μ and ϕ^μ. . . . 120
9.5. Control distributions for $W^- \to \mu^-\bar{\nu}$ for $< \mu >$, $d0^{sig}$, $TrackE_T20/p_T^\mu$ and $\phi^{E_T^{miss}}$ . . . 121
9.6. Event selection efficiency as a function of the average $< \mu >$. . . . 125

10.1. Stability for the $W^+ \to \mu^+\nu$ signal process. . . . 129
10.2. Purity for the $W^+ \to \mu^+\nu$ signal process. . . . 130
10.3. Acceptance for the $W^+ \to \mu^+\nu$ signal process. . . . 131
10.4. Truth invariant mass distributions for the W boson for both charges using the bare, born or dressed level truth level definitions. . . . 133
10.5. Migration matrix $M_{\text{reco,truth}}$ for the $W^+ \to \mu^+\nu$ signal process. . . . 135
10.6. Migration matrix $M_{\text{reco,truth}}$ for the $W^- \to \mu^-\bar{\nu}$ signal process. . . . 136
10.7. Closure test for unfolding. . . . 140
10.8. Unfolded 1D cross sections. . . . 143
10.9. Muon charge aymmetry. . . . 148

B.1. Average trigger cut efficiency scale factors for $W^- \to \mu^-\bar{\nu}$ . . . 168
B.2. Average isolation selection efficiency scale factors for $W^- \to \mu^-\bar{\nu}$ . . . 169
B.3. Average muon identification selection efficiency scale factors for $W^- \to \mu^-\bar{\nu}$ 170
B.4. Average TTVA selection efficiency scale factors for $W^- \to \mu^-\bar{\nu}$ . . . 171
B.5. Average k-Factor efficiency scale factors for $W^- \to \mu^-\bar{\nu}$ . . . 172
B.6. Average pileup weight for $W^- \to \mu^-\bar{\nu}$ . . . 173
B.7. Average muon identification selection efficiency scale factors for $W^+ \to \mu^+\nu$ 174
B.8. Average TTVA selection efficiency scale factors for $W^+ \to \mu^+\nu$ . . . 175
B.9. Average pileup weight for $W^+ \to \mu^+\nu$ . . . 176

C.1. Real muon efficiency for MC16a. . . . 178
C.2. Real muon efficiency for MC16d. . . . 179
C.3. Fake muon efficiency for MC16a. . . . 180
C.4. Fake muon efficiency for MC16d. . . . 181

D.1. Individual contributions to the cross-section systematic variations for the muon, sagitta and missing energy uncertainties for $W^+ \to \mu^+\nu$. . . . 183
D.2. Individual contributions to the cross-section systematic variations for the scale factor and jet uncertainties for $W^+ \to \mu^+\nu$. . . . 184
D.3. Individual contributions to the cross-section systematic variations for the jet uncertainties for $W^+ \to \mu^+\nu$. . . . 185
D.4. Individual contributions to the cross-section systematic variations for muon, sagitta and missing energy uncertainties for $W^- \to \mu^-\bar{\nu}$. . . . 186

D.5. Individual contributions to the cross-section systematic variations for the scale factor and jet uncertainties for $W^- \to \mu^- \bar{\nu}$. 187
D.6. Individual contributions to the cross-section systematic variation for the jet uncertainties for $W^- \to \mu^- \bar{\nu}$. 188
D.7. Individual contributions to the muon asymmetry systematic variations for the muon, sagitta and missing energy uncertainties for $W \to \mu\nu$ 190
D.8. Individual contributions to the asymmetry systematic variations for the scale factor and jet uncertainties for $W \to \mu\nu$. 191
D.9. Individual contributions to the muon asymmetry systematic variations for the jet uncertainties for $W \to \mu\nu$. 192
D.10. Individual contributions to the systematic variations in MC16a for the muon, sagitta and missing energy uncertainties for $W^+ \to \mu^+ \nu$ 194
D.11. Individual contributions to the systematic variations in MC16a for the scale factor and jet uncertainties for $W^+ \to \mu^+ \nu$. 195
D.12. Individual contributions to the systematic variations in MC16a for the jet uncertainties for $W^+ \to \mu^+ \nu$. 196
D.13. Individual contributions to the systematic variations in MC16a for the muon, sagitta and missing energy uncertainties for $W^- \to \mu^- \bar{\nu}$. 197
D.14. Individual contributions to the systematic variations in MC16a for the scale factor and jet uncertainties for $W^- \to \mu^- \bar{\nu}$. 198
D.15. Individual contributions to the systematic variations in MC16a for the jet uncertainties for $W^- \to \mu^- \bar{\nu}$. 199
D.16. Individual contributions to the systematic variations in MC16d for the muon, sagitta and missing energy uncertainties for $W^+ \to \mu^+ \nu$ 200
D.17. Individual contributions to the systematic variations in MC16d for the scale factor and jet uncertainties for $W^+ \to \mu^+ \nu$. 201
D.18. Individual contributions to the systematic variations in MC16d for the jet uncertainties for $W^+ \to \mu^+ \nu$. 202
D.19. Individual contributions to the systematic variations in MC16d for the muon, sagitta and missing energy uncertainties for $W^- \to \mu^- \bar{\nu}$. 203
D.20. Individual contributions to the systematic variations in MC16d for the scale factor and jet uncertainties for $W^- \to \mu^- \bar{\nu}$. 204
D.21. Individual contributions to the systematic variations in MC16d for the jet uncertainties for $W^- \to \mu^- \bar{\nu}$. 205
D.22. Individual contributions to the systematic variations in MC16e for the muon, sagitta and missing energy uncertainties for $W^+ \to \mu^+ \nu$ 206
D.23. Individual contributions to the systematic variations in MC16e for the scale factor and jet uncertainties for $W^+ \to \mu^+ \nu$. 207
D.24. Individual contributions to the systematic variations in MC16e for the jet uncertainties for $W^+ \to \mu^+ \nu$. 208

D.25.Individual contributions to the systematic variations in MC16e for the muon, sagitta and missing energy uncertainties for $W^- \to \mu^- \bar{\nu}$. 209
D.26.Individual contributions to the systematic variations in MC16e for the scale factor and jet uncertainties for $W^- \to \mu^- \bar{\nu}$. 210
D.27.Individual contributions to the systematic variations in MC16e for the jet uncertainties for $W^- \to \mu^- \bar{\nu}$. 211
D.28.Individual contributions to the cross-section systematic variations in MC16a for the muon, sagitta and missing energy uncertainties for $W^+ \to \mu^+ \nu$. . . . 213
D.29.Individual contributions to the cross-section systematic variations in MC16a for the scale factor and jet uncertainties for $W^+ \to \mu^+ \nu$. 214
D.30.Individual contributions to the cross-section systematic variations in MC16a for the jet uncertainties for $W^+ \to \mu^+ \nu$. 215
D.31.Individual contributions to the cross-section systematic variations in MC16a for muon, sagitta and missing energy uncertainties for $W^- \to \mu^- \bar{\nu}$. 216
D.32.Individual contributions to the cross-section systematic variations in MC16a for the scale factor and jet uncertainties for $W^- \to \mu^- \bar{\nu}$. 217
D.33.Individual contributions to the cross-section systematic variation in MC16a for the jet uncertainties for $W^- \to \mu^- \bar{\nu}$. 218
D.34.Individual contributions to the cross-section systematic variations in MC16d for the muon, sagitta and missing energy uncertainties for $W^+ \to \mu^+ \nu$. . . . 219
D.35.Individual contributions to the cross-section systematic variations in MC16d for the scale factor and jet uncertainties for $W^+ \to \mu^+ \nu$. 220
D.40.Individual contributions to the cross-section systematic variations in MC16e for the muon, sagitta and missing energy uncertainties for $W^+ \to \mu^+ \nu$. . . . 221
D.36.Individual contributions to the cross-section systematic variations in MC16d for the jet uncertainties for $W^+ \to \mu^+ \nu$. 222
D.37.Individual contributions to the cross-section systematic variations in MC16d for muon, sagitta and missing energy uncertainties for $W^- \to \mu^- \bar{\nu}$. 223
D.38.Individual contributions to the cross-section systematic variations in MC16d for the scale factor and jet uncertainties for $W^- \to \mu^- \bar{\nu}$. 224
D.39.Individual contributions to the cross-section systematic variation in MC16d for the jet uncertainties for $W^- \to \mu^- \bar{\nu}$. 225
D.41.Individual contributions to the cross-section systematic variations in MC16e for the scale factor and jet uncertainties for $W^+ \to \mu^+ \nu$. 226
D.42.Individual contributions to the cross-section systematic variations in MC16e for the jet uncertainties for $W^+ \to \mu^+ \nu$. 227
D.43.Individual contributions to the cross-section systematic variations in MC16e for muon, sagitta and missing energy uncertainties for $W^- \to \mu^- \bar{\nu}$. 228
D.44.Individual contributions to the cross-section systematic variations in MC16e for the scale factor and jet uncertainties for $W^- \to \mu^- \bar{\nu}$. 229

D.45. Individual contributions to the cross-section systematic variation in MC16e for the jet uncertainties for $W^- \to \mu^- \bar{\nu}$. 230
D.46. Individual contributions to the muon asymmetry systematic variations in MC16a for the muon, sagitta and missing energy uncertainties for $W \to \mu\nu$ 232
D.47. Individual contributions to the asymmetry systematic variations in MC16a for the scale factor and jet uncertainties for $W \to \mu\nu$. 233
D.48. Individual contributions to the muon asymmetry systematic variations in MC16a for the jet uncertainties for $W \to \mu\nu$. 234
D.49. Individual contributions to the muon asymmetry systematic variations in MC16d for the muon, sagitta and missing energy uncertainties for $W \to \mu\nu$ 235
D.50. Individual contributions to the asymmetry systematic variations in MC16d for the scale factor and jet uncertainties for $W \to \mu\nu$. 236
D.51. Individual contributions to the muon asymmetry systematic variations in MC16d for the jet uncertainties for $W \to \mu\nu$. 237
D.52. Individual contributions to the muon asymmetry systematic variations in MC16e for the muon, sagitta and missing energy uncertainties for $W \to \mu\nu$ 238
D.53. Individual contributions to the asymmetry systematic variations in MC16e for the scale factor and jet uncertainties for $W \to \mu\nu$. 239
D.54. Individual contributions to the muon asymmetry systematic variations in MC16e for the jet uncertainties for $W \to \mu\nu$. 240

E.1. Chart showing relative contributions of all Monte Carlo in the signal region for MC16a, for muon charge (a) W^+ and (b) W^-. 241
E.2. Control distributions in MC16a for $W^+ \to \mu^+\nu$ for p_T^μ, $|\Delta\phi|$, E_T^{miss}, m_T, η^μ and ϕ^μ 242
E.3. Control distributions in MC16a for $W^+ \to \mu^+\nu$ for $<\mu>$, $d0^{sig}$, $TrackE_T20/p_T^\mu$ and $\phi^{E_T^{miss}}$ 243
E.4. Control distributions in MC16a for $W^- \to \mu^-\nu$ for p_T^μ, $|\Delta\phi|$, E_T^{miss}, m_T, η^μ and ϕ^μ 244
E.5. Control distributions in MC16a for $W^- \to \mu^-\nu$ for $<\mu>$, $d0^{sig}$, $TrackE_T20/p_T^\mu$ and $\phi^{E_T^{miss}}$ 245
E.6. Control distributions in MC16a for $W^\pm \to \mu\nu$ for p_T^μ, $|\Delta\phi|$, E_T^{miss}, m_T, η^μ and ϕ^μ 246
E.7. Control distributions in MC16a for $W^\pm \to \mu\nu$ for $<\mu>$, $d0^{sig}$, $TrackE_T20/p_T^\mu$ and $\phi^{E_T^{miss}}$ 247
E.8. Chart showing relative contributions of all Monte Carlo in the signal region for MC16d, for muon charge (a) W^+ and (b) W^-. 251
E.9. Control distributions in MC16d for $W^+ \to \mu^+\nu$ for p_T^μ, $|\Delta\phi|$, E_T^{miss}, m_T, η^μ and ϕ^μ. 252

E.10. Control distributions in MC16d for $W^+ \to \mu^+\nu$ for $<\mu>$, $d0^{sig}$, $TrackE_T20/p_T^\mu$ and $\phi^{E_T^{miss}}$ . . . 253
E.11. Control distributions in MC16d for $W^- \to \mu^-\nu$ for p_T^μ, $|\Delta\phi|$, E_T^{miss}, m_T, η^μ and ϕ^μ. . . . 254
E.12. Control distributions in MC16d for $W^- \to \mu^-\nu$ for $<\mu>$, $d0^{sig}$, $TrackE_T20/p_T^\mu$ and $\phi^{E_T^{miss}}$ . . . 255
E.13. Control distributions in MC16d for $W^\pm \to \mu\nu$ for p_T^μ, $|\Delta\phi|$, E_T^{miss}, m_T, η^μ and ϕ^μ. . . . 256
E.14. Control distributions in MC16d for $W^\pm \to \mu\nu$ for $<\mu>$, $d0^{sig}$, $TrackE_T20/p_T^\mu$ and $\phi^{E_T^{miss}}$ . . . 257
E.15. Chart showing relative contributions of all Monte Carlo in the signal region for MC16e, for muon charge (a) W^+ and (b) W^-. . . . 261
E.16. Control distributions in MC16e for $W^+ \to \mu^+\nu$ for p_T^μ, $|\Delta\phi|$, E_T^{miss}, m_T, η^μ and ϕ^μ. . . . 262
E.17. Control distributions in MC16e for $W^+ \to \mu^+\nu$ for $<\mu>$, $d0^{sig}$, $TrackE_T20/p_T^\mu$ and $\phi^{E_T^{miss}}$ . . . 263
E.18. Control distributions in MC16e for $W^- \to \mu^-\nu$ for p_T^μ, $|\Delta\phi|$, E_T^{miss}, m_T, η^μ and ϕ^μ. . . . 264
E.19. Control distributions in MC16e for $W^- \to \mu^-\nu$ for $<\mu>$, $d0^{sig}$, $TrackE_T20/p_T^\mu$ and $\phi^{E_T^{miss}}$ . . . 265
E.20. Control distributions in MC16e for $W^\pm \to \mu\nu$ for p_T^μ, $|\Delta\phi|$, E_T^{miss}, m_T, η^μ and ϕ^μ. . . . 266
E.21. Control distributions in MC16e for $W^\pm \to \mu\nu$ for $<\mu>$, $d0^{sig}$, $TrackE_T20/p_T^\mu$ and $\phi^{E_T^{miss}}$ . . . 267
E.22. Control distributions for Run-2 $W^\pm \to \mu\nu$ for p_T^μ, $|\Delta\phi|$, E_T^{miss}, m_T, η^μ and ϕ^μ. 271
E.23. Control distributions for Run-2 for $W^\pm \to \mu\nu$ for $<\mu>$, $d0^{sig}$, $TrackE_T20/p_T^\mu$ and $\phi^{E_T^{miss}}$ . . . 272
E.24. Event selection efficiency as a function of the pileup $<\mu>$ for MC16a (36.2^{-1}), MC16d (44.3^{-1}) and MC16e (58.5^{-1}). . . . 275

F.1. Stability for the $W^+ \to \mu^+\nu$ MC16a signal process. . . . 277
F.2. Purity for the $W^+ \to \mu^+\nu$ MC16a signal process. . . . 278
F.3. Acceptance for the $W^+ \to \mu^+\nu$ MC16a signal process. . . . 279
F.4. Stability for the $W^- \to \mu^-\bar{\nu}$ MC16a signal process. . . . 280
F.5. Purity for the $W^- \to \mu^-\bar{\nu}$ MC16a signal process. . . . 281
F.6. Acceptance for the $W^- \to \mu^-\bar{\nu}$ MC16a signal process. . . . 282
F.7. Stability for the $W^+ \to \mu^+\nu$ MC16d signal process. . . . 283
F.8. Purity for the $W^+ \to \mu^+\nu$ MC16d signal process. . . . 284
F.9. Acceptance for the $W^+ \to \mu^+\nu$ MC16d signal process. . . . 285
F.10. Stability for the $W^- \to \mu^-\bar{\nu}$ MC16d signal process. . . . 286

F.11. Purity for the $W^- \to \mu^- \bar{\nu}$ MC16d signal process. 287
F.12. Acceptance for the $W^- \to \mu^- \bar{\nu}$ MC16d signal process. 288
F.13. Stability for the $W^+ \to \mu^+ \nu$ MC16e signal process. 289
F.14. Purity for the $W^+ \to \mu^+ \nu$ MC16e signal process. 290
F.15. Acceptance for the $W^+ \to \mu^+ \nu$ MC16e signal process. 291
F.16. Stability for the $W^- \to \mu^- \bar{\nu}$ MC16e signal process. 292
F.17. Purity for the $W^- \to \mu^- \bar{\nu}$ MC16e signal process. 293
F.18. Acceptance for the $W^- \to \mu^- \bar{\nu}$ MC16e signal process. 294
F.19. Stability for the $W^- \to \mu^- \bar{\nu}$ Run-2 signal process. 295
F.20. Purity for the $W^- \to \mu^- \bar{\nu}$ Run-2 signal process. 296
F.21. Acceptance for the $W^- \to \mu^- \bar{\nu}$ Run-2 signal process. 297
F.22. Migration matrix $M_{\text{reco,truth}}$ for the $W^+ \to \mu^+ \nu$ MC16a signal process. 298
F.23. Migration matrix $M_{\text{reco,truth}}$ for the $W^- \to \mu^- \nu$ MC16a signal process. 299
F.24. Migration matrix $M_{\text{reco,truth}}$ for the $W^+ \to \mu^+ \nu$ MC16d signal process. 300
F.25. Migration matrix $M_{\text{reco,truth}}$ for the $W^- \to \mu^- \nu$ MC16d signal process. 301
F.26. Migration matrix $M_{\text{reco,truth}}$ for the $W^+ \to \mu^+ \nu$ MC16e signal process. 302
F.27. Migration matrix $M_{\text{reco,truth}}$ for the $W^- \to \mu^- \nu$ MC16e signal process. 303
F.28. Unfolded 1D cross sections for 2015/2016 data and MC16a. 305
F.29. Muon charge aymmetry for 2015/2016 data and MC16a. 306
F.30. Unfolded 1D cross sections for 2017 data and MC16d. 307
F.31. Muon charge aymmetry for 2017 data and MC16d. 308
F.32. Unfolded 1D cross sections for 2018 data and MC16e. 309
F.33. Muon charge aymmetry for 2018 data and MC16e. 310

List of Tables

2.1. Standard Model of Elementary Particles. 4

3.1. LHC parameters for pp collisions at $\sqrt{s} = 13$ TeV in 2015-2018. 21
3.2. Summary of the jet reconstruction criteria and requirements. 44
3.3. Summary of the E_T^{miss} reconstruction criteria. 45

4.1. Table of samples used for L1Calo study. 48
4.2. Truth Electron Selections. 49
4.3. Truth Dijet Selections. 50
4.4. Trigger Object (TOB) selections. 50
4.5. Electron selection for the $Z \rightarrow ee$ sample. 50
4.6. Dijet sample selections. 51

5.1. Table for data years 2015-2018 showing run numbers, average pileup, and ATLAS recorded luminosity. 60
5.2. Table for 2015-2018 data showing run numbers, triggers and ATLAS recorded luminosity. 61
5.3. Event Generation for each MC process used. 64
5.4. Table for MC16a $W \rightarrow \mu\nu$ mass slices showing DSID, cross-section, N_{evt} and k-Factor. 69

6.1. Overlap removal criteria. 76

7.1. Loose and tight selections for the multijet estimation. 83

8.1. List of the experimental systematic uncertainties on the muons. 100
8.2. List of experimental systematic uncertainties on the $E_{\text{T}}^{\text{miss}}$ soft term. 104
8.3. List of experimental systematic uncertainties for the jet energy scale and jet energy resolution. 105

9.1. Cutflow table for Run-2 data for the W^+ selection. 122
9.2. Cutflow table for Run-2 data for the W^- selection. 123

10.1. Cross-section values for $W^+ \rightarrow \mu^+\nu$. 145
10.2. Cross-section values for $W^- \rightarrow \mu^-\nu$. 146
10.3. Grouped experimental systematic uncertainties for the $W^+ \rightarrow \mu^+\nu$. 147

10.4. Grouped experimental systematic uncertainties in each bin for $W^- \to \mu^- \nu$. 147
10.5. Muon charge asymmetry values. 148
10.6. Grouped systematic uncertainty values for the asymmetry. 149
10.7. Summary of the charged current Drell-Yan cross-sections and the muon charge asymmetry measurements. 150

E.1. Cutflow table for 2015 and 2016 data for the W^+ selection. 248
E.2. Cutflow table for 2015 and 2016 data for the W^- selection. 249
E.3. Cutflow table for 2015 and 2016 data for the $W^\pm$ selection. 250
E.4. Cutflow table for 2017 data for the W^+ selection. 258
E.5. Cutflow table for 2017 data for the W^- selection. 259
E.6. Cutflow table for 2017 data for the $W^\pm$ selection. 260
E.7. Cutflow table for 2018 data for the W^+ selection. 268
E.8. Cutflow table for 2018 data for the W^- selection. 269
E.9. Cutflow table for 2018 data for the $W^\pm$ selection. 270
E.10. Cutflow table for Run-2 data for the $W^\pm$ selection. 273

F.1. Individual experimental systematic uncertainties for $W^+ \to \mu^+ \nu$. 312
F.2. Individual experimental systematic uncertainties for $W^- \to \mu^- \bar{\nu}$. 314
F.3. Individual experimental systematic uncertainties for the charge asymmetry. 316

1. Introduction

Scientists have long sought to understand the fundamental levels of nature. Fundamental particle physics can address this problem as it describes the interaction of fundamental particles at the smallest scales. These fundamental particles' theoretical descriptions are based on quantum field theories (QFTs), which yield unprecedented insight into these interactions. The Standard Model (SM) of Fundamental Particle Physics combines two QFTs, Electroweak Interaction (EW) and Quantum Chromodynamics (QCD), to describe particle behaviour at a subatomic level [1].

High-energy experiments are used to test the SM. The Large Hadron Collider (LHC) is the highest-energy particle accelerator currently operating at CERN near Geneva, Switzerland. With a centre of mass energy for proton-proton (pp) collisions at 13 TeV corresponding to an integrated luminosity of 139 fb^{-1} it can access a kinematic phase space never previously studied experimentally. The successful running from 2015 to 2018 provides data for the scientific community to test the SM more precisely than ever before [2, 3].

In this thesis the author measured the Drell-Yan process's unfolded differential cross section and muon charge asymmetry at high transverse masses. This measurement was carried out using data collected by ATLAS [4] in the Run-2 period. The inclusive cross-section has been previously well studied [5, 6]. However, the measurement at the high mass region will be done for the first time. The high mass region has been inaccessible in previous experiments.

A complete and precise understanding of the proton's structure is essential for further measurements and searches at the LHC. Precise measurements will provide important insights into the proton's structure by constraining parton distribution functions. Furthermore, the results of this measurement provide sensitivity to the electroweak parameter, which allows effective field theory interpretations.

This thesis is structured as follows. Firstly, an overview of the Standard Model and the theoretical context needed to appreciate the charged-current Drell-Yan theory and guide measurement is presented in Chapter 2. A summary of the LHC and ATLAS detector follows in Chapter 3. Chapter 4 contains a validation code study for the Level 1 Calorimeter in the ATLAS detector. An overview of the data and Monte Carlo samples of the signal and background processes that contribute are discussed in Chapter 5. Chapter 6 describes the event selection for this analysis. The strategy for estimating multijet background via the Matrix Method is described in Chapter 7. Chapter 8 summarises

the systematic uncertainties considered. In Chapter 9, the comparison between data, predicted signal and backgrounds of key kinematic distributions are displayed, helping to validate the selection criteria and events weights considered. In Chapter 10, the results of the measurement of the unfolded differential cross-section and muon charge asymmetry, along with the unfolding procedure via Iterative Bayesian Unfolding, are presented. Finally, a summary of the analysis and conclusions are given in Chapter 11.

Several inputs were utilised to complete the analysis presented here. The ATLAS Physics Modelling Group (PMG) centrally produced the samples required for the data and Monte Carlo simulation used [7]. The samples required for the charged-current Drell-Yan phase space were requested (by the author and the analysis team) as derived samples. Derived samples have already passed several kinematic cuts, which is convenient as it reduces the size of the samples but keeps the events of interest for this physics analysis. Next, the author customised an official ATLAS software called AnalysisTop [8]. This software was chosen as it is flexible and under constant development. The version used for this analysis is AnalysisTop.21.2.198. AnalysisTop can perform all centrally produced corrections and calibrations to physics objects provided by the ATLAS physics groups (Jet and Etmiss Combined Performance, Muon Combined Performance, Pileup). AnalysisTop also handles most of the systematics used. The customisation included adding different variables, corrections, and truth information from W bosons. Finally, the customised output from AnalysisTop is taken and processed using the author's framework. The figures and tables shown in this thesis are the outputs of this framework.

The ATLAS collaboration comprises over 3000 members; therefore, all analyses are produced as part of a team effort. The work contained in this thesis was conducted as part of a broader analysis group in ATLAS for Standard Model measurements in the W/Z physics group for high m_T^W. The author is grateful for the contributions of members of the analysis team.

2. Theory

This chapter includes relevant theoretical background which motivates this measurement. It begins with a brief overview of the Standard Model followed by Parton Distribution Functions (PDFs). The Drell-Yan process is discussed in detail as this is the production mechanism used to detect W bosons. Finally, an explanation of effective field theory and its relevance to measuring high-mass W bosons is given.

2.1. Standard Model

The Standard Model is a relativistic Quantum Field Theory (QFT) and describes elementary particles as excitations of fields. The success of the Standard Model is based on its predictive power and description of most experimental results. Table 2.1 lists the basic properties of the elementary particles that constitute the Standard Model.

The Standard Model does not describe gravitational interactions. This is due to the difficulty in representing them as a QFT and the weakness of gravity at a small scale (<1mm). Although attempts to describe quantum gravity have been made, evidence has yet to be found to support these attempts [9].

The Standard Model can be written as a Lagrangian, which describes the system's dynamics. The Lagrangian $\mathscr{L}$ contains information on how fields, usually represented using ϕ (a scalar field), ψ (a fermionic spin $\frac{1}{2}$ field) or A_μ (a vector/gauge field), behave. Fundamental interactions can be explained using different terms of the Lagrangian. When using the principle of least action, the field's equations of motion (EOM) can be derived [1].

$$S = \int \mathscr{L}(\phi, \partial_\mu \phi) d^4x \rightarrow EOM \equiv \delta S = 0 \tag{2.1}$$

All fundamental interactions derive from one general principle; local gauge invariance. A gauge transformation is a transformation which does not change any measurable, physically meaningful magnitudes but alters non-observables. When applying a gauge transformation on the EOM, the physics remains unchanged, referred to as the principle of gauge invariance. The Standard Model can be mathematically constructed by requiring local gauge invariance for the Lagrangian and using group theory.

Symmetries in the Standard Model play a fundamental role. Noether's theorem states that a conserved quantity can be derived when an action has a symmetry [10]. When

requiring the Standard Model Lagrangian to be invariant under local-gauge transformations, this leads to the different conserved currents of the theory [11].

Table 2.1.: Standard Model of Elementary Particles [1].

	symbol	name	mass (MeV)	charge (e)
Quarks (Spin $\frac{1}{2}$)	u	up	$2.16^{+0.49}_{-0.26}$	+2/3
	d	down	$4.67^{+0.48}_{-0.17}$	−1/3
	c	charm	1270 ± 20	+2/3
	s	strange	93^{+11}_{-5}	−1/3
	t	top	172900 ± 400	+2/3
	b	bottom	4180^{+30}_{-20}	−1/3
Leptons (Spin $\frac{1}{2}$)	e	electron	0.511 [1]	-1
	μ	muon	105.7 [2]	-1
	τ	tau	1777 [3]	-1
	ν_e	electron neutrino	$< 1.10 \cdot 10^{-5}$	0
	ν_μ	muon neutrino	< 0.17	0
	ν_τ	tau neutrino	< 18.2	0
Gauge bosons (Spin 1)	γ	photon	0	0
	W	W	80377 [4]	± 1
	Z	Z	91200 [5]	0
	g	gluon	0	0
Scalar bosons (Spin 0)	H	Higgs	125250 [6]	0

[1] $m_e = 0.51099895000 \pm 0.00000000015$ MeV
[2] $m_\mu = 105.6583755 \pm 0.0000023$ MeV
[3] $m_\tau = 1776.86 \pm 0.12$ MeV
[4] $m_W = 80.377 \pm 0.012$ GeV
[5] $m_Z = 91.1876 \pm 0.0021$ GeV
[6] $m_H = 125.25 \pm 0.17$ GeV

2.1.1. Electro-Weak Theory

Electromagnetic and weak nuclear interactions are described by Electroweak Theory (EW). Their gauge group is $U(1)_Y$ x $SU(2)_L$. One of the simplest interactions described by the Standard Model is Quantum Electrodynamics (QED), which describes the electromagnetic interaction between charged leptons and photons. For the Lagrangian for QED, begin with a Dirac fermion field $\psi(x \equiv \vec{x}, t)$ of charge e, for a free Dirac fermion of mass m, the Lagrangian density has a kinetic term and a mass term given by:

$$\mathscr{L}_f = i\bar{\psi}\gamma^\mu\partial_\mu\psi - m\bar{\psi}\psi \tag{2.2}$$

where γ^μ are the Dirac matrices and m is the mass of the gauge boson.

This Lagrangian density, however, is not invariant under a local $U(1)$ gauge transformation:

$$\psi(x) \rightarrow e^{i\alpha}\psi(x), \text{ with } \alpha = \alpha(x) \tag{2.3}$$

where $\alpha(x)$ is a real number with a space-time dependence.

The importance of gauge invariance is that it leads to conserved currents that describe observations, and gauge invariance leads to a renormalisable theory. To preseve the local gauge invariance on the Lagrangian density, the derivative ∂_μ is replaced with the covariant derivative: $D_\mu\psi(x) \rightarrow D_\mu\psi(x)e^{i\alpha(x)}$. A vector field A_μ, called the gauge field, is introduced. Thus the covariant derivative is:

$$D_\mu = \partial_\mu - ieA_\mu \tag{2.4}$$

Where e is the electron charge. The gauge transformation of the A_μ field generates a term which cancels the spurious term from the local U(1) transformation of the fermion field. The gauge field, A_μ, using the gauge freedom of A_μ transforms as:

$$A_\mu \rightarrow A_\mu + \frac{1}{e}\partial_\mu\alpha(x) \tag{2.5}$$

Introducing a combination of the kinetic term for the fermion, which is also gauge invariant, and the gauge transformation of a vector field gives:

$$\left(\partial_\mu - ieA_\mu\right)\psi \rightarrow e^{i\alpha(x)}\left(\partial_\mu - ieA_\mu\right)\psi \tag{2.6}$$

Under the gauge transformation of the fermion field, the vector field will also transform with the same transformation parameter $\alpha(x)$. The gauge invariant electromagnetic field tensor $F_{\mu\nu}$ is needed to provide a kinematic term for the A_μ field.

$$F_{\mu\nu} = \partial_\mu A_\nu - \partial_\nu A_\mu \tag{2.7}$$

This gives the following Lagrangian density for QED:

$$\mathscr{L}_{QED} = i\bar{\psi}\gamma^{\mu}D_{\mu}\psi - m\bar{\psi}\psi - \frac{1}{4}F_{\mu\nu}F^{\mu\nu} \tag{2.8}$$

$$= i\bar{\psi}\gamma^{\mu}\left(\partial_{\mu} - ieA_{\mu}\right)\psi - m\bar{\psi}\psi - \frac{1}{4}F_{\mu\nu}F^{\mu\nu} \tag{2.9}$$

$$= i\bar{\psi}\gamma^{\mu}\partial_{\mu}\psi - m\bar{\psi}\psi - \frac{1}{4}F_{\mu\nu}F^{\mu\nu} + e\bar{\psi}\gamma^{\mu}\psi A_{\mu} \tag{2.10}$$

$$= \mathscr{L}_{f} + \mathscr{L}_{gauge} + \mathscr{L}_{int} \tag{2.11}$$

with $\mathscr{L}_f$ being the Lagrangian for the free fermion field ψ of mass m, $\mathscr{L}_{\text{gauge}}$ being the Lagrangian for the free massless gauge field A_μ and the Lagrangian for the interaction term $\mathscr{L}_{\text{int}}$. The QED Lagrangian is invariant under gauge transformations with the condition that the term, including the gauge boson mass m, is zero. Therefore, the electromagnetic interaction must have a massless gauge boson. This massless gauge boson is the photon (γ), which mediates the electromagnetic interaction [12].

When combining both electromagnetic interactions and weak interactions into an electroweak theory, a problem arises. If a similar gauge transformation is applied to the electroweak interactions, the massive W and Z bosons result in the Lagrangian no longer being gauge invariant. $SU(2)$ x $SU(3)$ gauge invariance only works for massless gauge bosons. However, if spontaneous symmetry breaking is added to the Standard Model, the masses of the W and Z can be included.

Therefore, a scalar field, known as the Higgs field, is introduced into the Lagrangian to uphold local gauge invariance. However, the purpose of the Higgs field potential extends beyond preserving gauge invariance; it aims to spontaneously break this symmetry through the establishment of a non-zero vacuum expectation value. The Higgs field potential is represented by the equation:

$$V(\phi) = \frac{1}{2}\mu^2\phi^2 + \frac{1}{4}\lambda\phi^4 \tag{2.12}$$

The potential when $\mu^2 > 0$ describes a scalar field with mass μ with a vacuum expectation value of $\phi = 0$. If $\mu^2 < 0$ the potential has a minima of $\phi^2 = -\mu^2/\lambda$ resulting in a non zero vacuum expectation value. This departure from a zero vacuum expectation value marks the onset of spontaneous symmetry breaking within the Higgs potential. Here v is the value of the field at the minimum of the Higgs potential. The vacuum state is not gauge invariant under local gauge transformations, which leads to gauge boson mass terms; the masses of the $W^{\pm}$ and Z now have been included. The mass terms arise from the covariant derivative in the kinematic term of the Higgs field, which are:

$$m_Z = \frac{v}{2}\sqrt{g^2 + g'^2}, \quad m_W = \frac{v}{2}g, \tag{2.13}$$

the Z and W boson masses. Finally, the v value gives a gauge boson coupled to mass, the Higgs (H) boson [13, 14].

Experimental Evidence

The Standard Model has been verified by experimental evidence of the W, Z and Higgs bosons. The existence of the W and Z bosons was first verified at CERN in 1983 through the UA1 and UA2 experiments, providing evidence for the electroweak theory. Carlo Rubbia and Simon van der Meer received the 1984 Nobel prize in physics for this discovery [15, 16]. Further evidence of the Standard Model was obtained by the ATLAS and CMS experiments at the LHC in 2012. This confirmed the discovery of the Higgs boson, validating the mechanism of electroweak symmetry breaking and providing insight into the origin of particle masses. The discovery of the Higgs boson was awarded the 2013 Nobel prize in physics to François Englert and Peter Higgs [17].

Renormalisation and Running Coupling

The fine structure constant describes the strength of electromagnetic interactions:

$$\alpha = \frac{e^2}{4\pi} \tag{2.14}$$

Here e signifies the charge. Electromagnetic interactions have an energy scale dependence. At low energies and large distances, the interactions decrease in strength, known as the "running" of the coupling. In this context, virtual fermion-antifermion pairs emerge spontaneously within the quantum vacuum, influencing the behaviour described by the photon propagator. The additional loop processes create a polarisation in the vacuum between particles, becoming a screen of charge. When the distance between the particles decreases, polarisation decreases, increasing the effective interaction strength.

This leads to an effective coupling constant proportional to Q between the particles. Q is the four momenta exchange and larger Q means smaller distance. Perturbation theory is required to include additional loop processes that occur in the interaction. To define the coupling constant, begin with the leading order interaction and add the higher-order loop processes as part of a geometric series. There are an infinite number of higher-order corrections. Therefore, an arbitrary limit is introduced to stop divergences to infinity called renormalisation. The coupling constant can therefore be defined as:

$$\alpha(Q^2) = \frac{\alpha(\mu_R^2)}{1 - \frac{\alpha(\mu_R^2)}{3\pi}\log(\frac{Q^2}{\mu_R 2})} \tag{2.15}$$

With μ_R as the renormalisation momentum, which is chosen to be on the scale of the

measured physics. Renormalisation in QED provides accurate theoretical descriptions of electromagnetic interaction as seen from the logarithmic dependence of Q, which cause higher-order corrections to contribute less to the interaction [18].

2.1.2. Quantum Chromodynamics

Quantum Chromodynamics (QCD) is the quantum field theory describing the strong interactions of coloured quarks and gluons. QCD is represented by the gauge group $SU(3)_C$, which describes interactions between quarks and gluons via colour charge. Eight gluon fields must be introduced to preserve the invariance of the Lagrangian under local $SU(3)_C$ transformations. The adjoint representation of $SU(3)_C$ describes eight colour states (colour octet) which form combinations of colour and anti-colour. Gluons (g) carry components of colour charge and, therefore, not only mediate but participate in QCD interactions.

The Standard Model can be represented as a product of these groups $SU(3)_C$ x $SU(2)_L$ x $U(1)_Y$. The group is non-commutative (non-abelian) except for U(1) which is abelian. The Lagrangian for QCD is given by:

$$\mathscr{L}_{QCD} = \sum_q \bar{\psi}_{q,a}\left(i\gamma^\mu D_\mu - m_q\delta_{ab}\right)\psi_{q,b} - \frac{1}{4}F^A_{\mu\nu}F^{A\mu\nu} \tag{2.16}$$

Where repeated indices are summed over. Where D_μ is the covariant derivative:

$$D_\mu = \partial_\mu - ig_s t^C_{ab}\mathscr{A}^A_\mu \tag{2.17}$$

and is summed over q, the different quark flavours. Rewriting Equation 2.16 gives:

$$\mathscr{L}_{QCD} = \sum_q \bar{\psi}_{q,a}\left(i\gamma^\mu\partial_\mu\delta_{ab} - g_s\gamma^\mu t^C_{ab}\mathscr{A}^C_\mu - m_q\delta_{ab}\right)\psi_{q,b} - \frac{1}{4}F^A_{\mu\nu}F^{A\mu\nu} \tag{2.18}$$

$\psi_{q,a}$ and $\bar{\psi}_{q,a}$ are the quark fields for a quark of flavor q and mass m_q. The colour index a sums over $a = 1$ to $N_c = 3$, representing that quarks come in three colours. $\mathscr{A}^C_\mu$ are the gluon fields. Here C sums over 1 to $N_c^2 - 1 = 8$, representing eight kinds of gluons. Quarks and gluons can have six types of colour charge: red, green, blue, anti-red, anti-green and anti-blue ($r, g, b, \bar{r}, \bar{g}, \bar{b}$). The Dirac γ-matrices are γ^μ. The QCD coupling constant is g_s (or $\alpha_s = g_s^2/4\pi$). The t^C_{ab} corresponds to eight 3×3 matrices that are the generators of the SU(3) group. An explicit representation of these is $t^C_{ab} \equiv \lambda^C_{ab}/2$, where λ are the Gell-Mann matrices. They describe how a gluon's interaction with a quark rotates its colour. $F^A_{\mu\nu}$ is the field tensor given by:

$$F^A_{\mu\nu} = \partial_\mu\mathscr{A}^A_\nu - \partial_\nu\mathscr{A}^A_\mu - g_s f_{ABC}\mathscr{A}^B_\mu\mathscr{A}^C_\nu \tag{2.19}$$

where the f_{ABC} are the structure constants of the SU(3) group. The indices of the field strength tensor run over the three colour indices A, B and C, which are the eight

colour combinations of the gluon field. Neither quarks nor gluons are observed as free particles. Hadrons are colour-neutral or colour-singlet combinations of quarks, anti-quarks, and gluons [19].

The last term in Equation 2.19 gives rise to triple and quartic gluon self-interactions. Gluon self-interaction leads to a property of strong interaction called asymptotic freedom. Like in QED, particle and antiparticle pairs can be spontaneously produced and annihilated by their propagating boson. However, the gluon can produce additional gluons through triple and quartic self-interactions, unlike in photons.

In QED, charge screening is when the coupling becomes large at a very short distance Q, but its effect is small. For QCD, however, the antiscreening effect causes the strong coupling to become small at a short distance Q (large momentum transfer). The screening effect also occurs through quark loops; however, the antiscreening effect through gluon loops is larger. This leads to the concept called asymptotic freedom, when QCD interactions occur at a short distance, e.g. width of a hadron, high four momenta Q transfer perturbative calculations of cross sections are possible.

Quarks unable to escape the strong interaction lead to quarks clustering into a colourless state called colour confinement. This effect is the reason that no individual quark has been experimentally observed. When the distance between two quarks is large enough, the colour field will have enough energy to produce quark and anti-quark pairs. The process between quark and anti-quark pairs will repeat to form more quarks until the quarks hadronise into colourless hadrons. At proton-proton colliders, the energy is high enough to separate partons to form jets of multiple hadrons.

When adding higher-order loop corrections in QED, the strength of the strong interaction changes. This is similar to the case in QCD; however, in Equation 2.15 with the additional gluon self-coupling terms $\log(Q^2/\mu_R^2)$ the strong running coupling constant changes sign. The effective strong coupling constant is:

$$\alpha_s(Q^2) = \frac{\alpha_s(\mu_R^2)}{1 + \frac{\alpha_s(\mu_R^2)}{12\pi}(33-2q)\log(\frac{Q^2}{\mu_{R^2}})} \tag{2.20}$$

Where q is the number of quark flavours. If q were 17, the log term in the denominator of the equation, specifically $(33-2q)$, would cause a change in sign and the effects of QCD would be similar to QED. There are 6 quark flavours. When Q^2 is low, the perturbation will break down as the coupling strength is too large. Equation 2.20 can then be rewritten as:

$$\alpha_s(Q^2) = \frac{12\pi}{(33-2q)\log(\frac{Q^2}{\Lambda^2})} \tag{2.21}$$

Where Λ^2 gives the energy limit on perturbation theory in QCD. When there are energies of $Q^2 > \Lambda^2$, the strong interaction can be described using perturbation theory. If the energy is $Q^2 < \Lambda^2$, then a non-perturbative approach is used [18].

2.2. Parton Distribution Functions

Parton Distribution Functions (PDFs) are essential for making predictions for the Standard Model and Beyond the Standard Model (BSM) physics in hadron colliders. The proton is not a fundamental particle but is composed of quarks and gluons. Understanding the proton's structure began with Deeply Inelastic Scattering (DIS) experiments [20]. To study the structure of the composite system in protons, experiments can use a probe to study the distribution of energy/momentum of the fundamental constituents. DIS experiments use a lepton to probe the proton by exchanging an electroweak boson γ/Z or $W^{\pm}$. The following diagram depicts this Figure 2.1 [21].

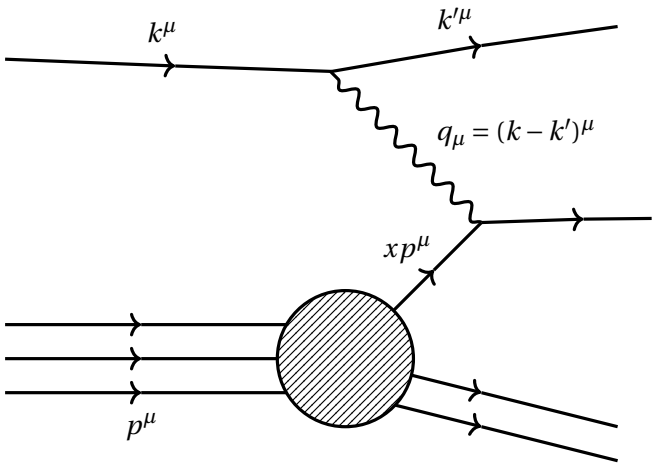

Figure 2.1.: Deep inelastic scattering Feynman diagram with kinematics.

Using data from the SLAC experiment, Feynman observed that scaling behaviour could be explained by the proton's point-like scattering of free particles [22]. These free particles were called partons. This model proved successful, and partons were later identified as quarks and gluons. In the Quark Parton Model (QPM), nucleons have massless, point-like, spin 1/2 quarks which are free within the nucleon. This model could be better, as it does not include gluons, but it is still successful as a conceptual model. The mass of nucleons and quarks is also neglected. However, this approximation is valid when looking at a large enough momentum scale of the scattering process Q.

PDFs do include gluon interactions unlike the QPM. The PDF $f_i(x, Q^2)$ gives the probability of finding in the proton a parton of flavour i (quark or gluon) carrying a fraction x of the proton momentum with Q being the energy scale of the hard interaction. The momentum weighted $x_i f(x)$ is often used so that the area under the curve when plotting is the momentum fraction carried by partons of species i. In standard notation the antiquark PDFs are denoted $x_i \bar{f}(x)$ and PDFs for each quark flavour u, d, s, c, b [23].

Cross sections are calculated by convoluting the parton level cross-section with the PDFs. The hadronic cross section for a process of two hadrons A and B interacting,

$A+B \to X$, with X being any final state is shown in Equation 2.22. The $\hat{\sigma}_{i,j\to X}$ represents the partonic cross section for interactions between two partons with flavour i and j.

$$\sigma_{A,B\to X} = \sum_{i,j} \iint \mathrm{d}x_1 \mathrm{d}x_2 f_i^A(x_1) f_j^B(x_2) \cdot \hat{\sigma}_{i,j\to X} + [x_1 \leftrightarrow x_2] \tag{2.22}$$

The PDFs in this equation are universal and factorise. This factorisation allows PDFs extracted from an analysis of inclusive DIS measurements to calculate cross-sections of other processes in lepton-hadron or hadron-hadron interactions. Since perturbative QCD does not predict the parton content of the proton, the shapes of the PDFs are determined by a fit to data from experimental observables in various processes using the DGLAP evolution equation.

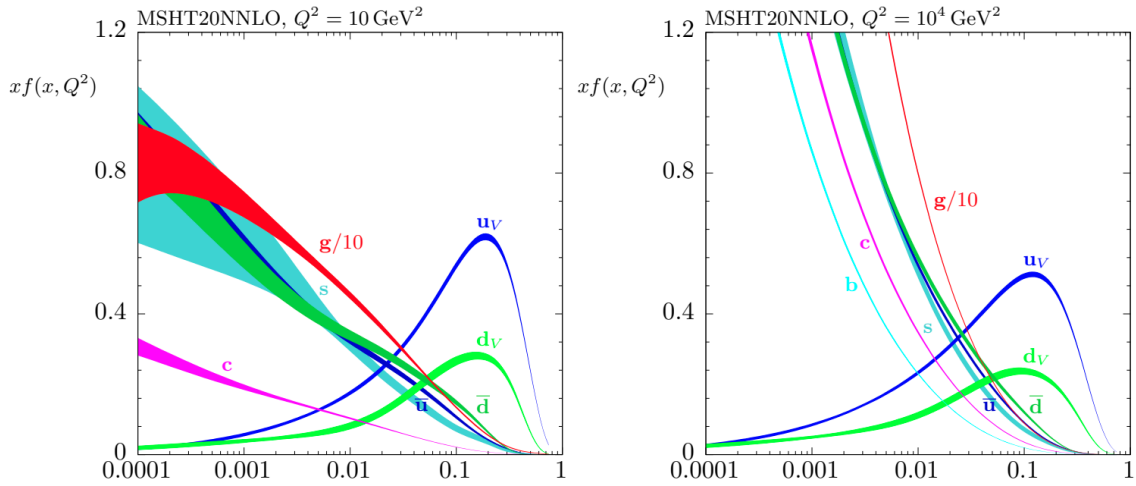

Figure 2.2.: MSHT20 NNLO PDFs at $Q^2 = 10\ GeV^2$ and $Q^2 = 10^4\ GeV^2$ with associated 68% confidence level uncertainty bands [24].

Equation 2.22 cannot describe processes with the emission of real and virtual gluons. For gluons emitted collinear with quarks and anti-quarks, there are large logarithmic contributions in the perturbative expansion that result in divergences in the calculation. PDFs are redefined to an appropriate scale, called the factorisation scale μ_F, to remove these divergences which separate the short and long-distance physics. Generally, this scale equals the hard scattering process's momentum transfer Q^2. This is similar to the renormalisation scale μ_R which is also usually taken to be Q^2 and typically $\mu_F = \mu_R = Q^2$.

The PDFs will be dependent on the factorisation scale. When the perturbative expansion is calculated to all orders, the scale dependence is required to vanish. It is this requirement that results in a set of evolution equations which are derived from relating PDFs at different scales. These are the DGLAP equations which for the quarks q_i and

gluon g are:

$$\frac{\partial q_i\left(x,\mu^2\right)}{\partial \log \mu^2} = \frac{\alpha_s}{2\pi}\int_x^1 \frac{dz}{z}\left[P_{q_i q_j}\left(z,\alpha_s\right) q_j\left(\frac{x}{z},\mu^2\right) + P_{q_i g}\left(z,\alpha_s\right) g\left(\frac{x}{z},\mu^2\right)\right] \tag{2.23}$$

$$\frac{\partial g\left(x,\mu^2\right)}{\partial \log \mu^2} = \frac{\alpha_s}{2\pi}\int_x^1 \frac{dz}{z}\left[P_{g q_i}\left(z,\alpha_s\right) q_j\left(\frac{x}{z},\mu^2\right) + P_{g g}\left(z,\alpha_s\right) g\left(\frac{x}{z},\mu^2\right)\right] \tag{2.24}$$

The P_{xy} terms are the splitting functions which give the probability of parton x producing a parton y with a momentum fraction z. Splitting functions are calculated to next-to-leading order (NLO) and next-to-next-to-leading order (NNLO) for perturbative expansions in the order of $\left(\alpha_s \log \mu_F^2\right)^n$. The dependence on Q^2 in the DGLAP equations results in the dependence of Q^2 in the PDFs. This allows PDFs to be recalculated at different energy scales. An example of PDFs calculated at two different energy scales is shown in Figure 2.2. The dependence on the momentum fraction z in the PDFs is determined through experiment [21, 23, 25].

2.3. Drell-Yan Process

The Drell-Yan (DY) process is named after physicists Sidney Drell and Tung-Mow Yan, who predicted dilepton production in hadron-hadron colliders [26]. This dilepton production involves a neutral and a charged current process known as the neutral-current Drell-Yan (NCDY) process and the charged current Drell-Yan (CCDY) process. The NCDY is the lepton and its anti-lepton pair production in a hadron-hadron collision. Figure 2.3 shows the Feynman diagram of this process at leading order from s-channel production from two incoming hadrons to a virtual gauge boson decaying to two leptons in the final state. A photon γ and a Z are the bosons that mediate this process. Similarly, a Feynman diagram of the CCDY process is shown in Figure 2.4 and Figure 2.5 with a quark and anti-quark interaction to result in a W boson.

To calculate the cross section for the CCDY process in a hadron-hadron collision, the dynamics of hadrons and partons are related to each other with an on-shell or off-shell centre-of-mass energy of a hadron-hadron collision $\sqrt{s}$, in terms of the four-momenta of the incoming partons p_1^μ and p_2^μ:

$$p_1^\mu = \frac{\sqrt{s}}{2}\left(x_1,0,0,x_1\right), \quad p_2^\mu = \frac{\sqrt{s}}{2}\left(x_2,0,0,-x_2\right) \tag{2.25}$$

where x_1 and x_2 are the partons momentum fractions. The partonic cross section $\hat{\sigma}^{\bar{q}q'}$ for W boson production is:

$$\hat{\sigma}^{\bar{q}q'} = \frac{\pi}{3}\sqrt{2} G_F m_W^2 \left|V_{qq'}\right|^2 \delta\left(\hat{s} - m_W^2\right) \tag{2.26}$$

Here G_F is the Fermi constant, m_W is the invariant mass of the W boson, $V_{qq'}$ is the

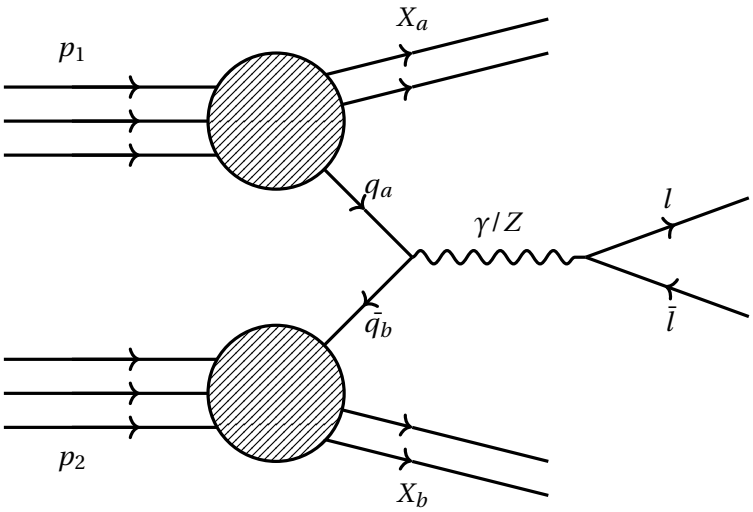

Figure 2.3.: Feynman diagram of the neutral current Drell-Yan process.

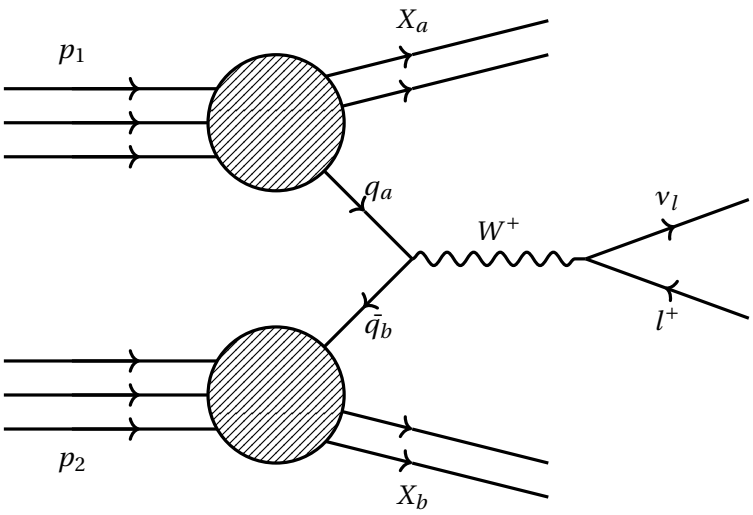

Figure 2.4.: Feynman diagram of the positively charged current Drell-Yan process.

Cabibbo-Kobayashi-Maskawa (CKM) matrix element for qq', and δ is the Dirac delta function.

By combining Equation 2.22 and Equation 2.25 with the cross section for W boson production Equation 2.26. The hadron-hadron CCDY cross-section is obtained at leading order:

$$\frac{\mathrm{d}\sigma}{\mathrm{d}m_W^2} = \frac{\pi}{3}\sqrt{2}G_F m_W^2 \int_0^1 \mathrm{d}x_1 \mathrm{d}x_2 \delta\left(x_1 x_2 s - m_W^2\right) \times \left[\sum_{k,k'} \left|V_{q_k q'_k}\right|^2 \left(q_k\left(x_1, m_W^2\right)\overline{q}_{k'}\left(x_2, m_W^2\right) + [1 \leftrightarrow 2]\right)\right] \tag{2.27}$$

The cross-section can be multiplied by the branching ratios for whichever hadronic or leptonic final state is of interest. Figure 2.6 shows cross-sections for Drell-Yan pro-

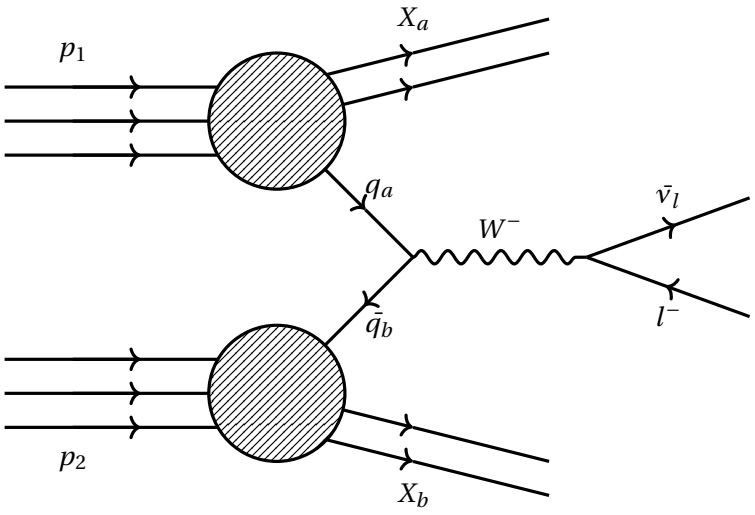

Figure 2.5.: Feynman diagram of the negatively charged current Drell-Yan process.

cesses, including the $W^{\pm}$ cross-sections for this measurement.

Drell-Yan processes are used as a benchmark in LHC physics because the production cross-sections of weak vector bosons (CCDY) are relatively large for the range of energies the LHC operates at. The Drell-Yan process is very well understood theoretically, with clear signatures in the detector, giving insight into the performance of the accelerator and detector. The final state of CCDY provides an easily identifiable and clean experimental signature, a single lepton and large missing E_T (see Section 3.5), which can be measured to high precision.

The cross-sections depend on parton distribution functions (PDFs) and, therefore, will be dependent on the dynamics of strongly interacting particles (QCD) and initial state radiation (higher order QCD). The $W^{\pm}$ bosons produced will decay into a muon/anti-muon and anti-neutrino/neutrino. The final state is used to give information on pairs of parton (quark) flavour distributions in the intial state. These are $u\bar{d}$, $u\bar{s}$, $u\bar{b}$, $c\bar{d}$, $c\bar{s}$, $c\bar{b}$ for the W^+ boson and $d\bar{u}$, $d\bar{c}$, $s\bar{u}$, $s\bar{c}$, $b\bar{u}$, $b\bar{c}$ for the W^-boson. This offers an opportunity to test current models of parton dynamics with the LHC.

From Equation 2.25, the rapidity of the system relative to the beam axis or the z component of the momentum p_Z can be derived:

$$y = \frac{1}{2}\log\frac{E+p_z}{E-p_z} = \frac{1}{2}\log\frac{x_1}{x_2} \tag{2.28}$$

E is incoming parton energy. The parton momentum fractions for W/Z boson production are then:

$$x_1 = \frac{m_{W,Z}}{\sqrt{s}}e^{y}, x_2 = \frac{m_{W,Z}}{\sqrt{s}}e^{-y} \tag{2.29}$$

where x_1 and x_2 are the partons momentum fractions and $m_{W,Z}$ is the mass of the

W/Z boson where $m_{W,Z} = sx_1x_2$. The ATLAS detector will limit the rapidity region accessible with rapidity constraints of $|y| < 2.5$ (for precision analyses) [24].

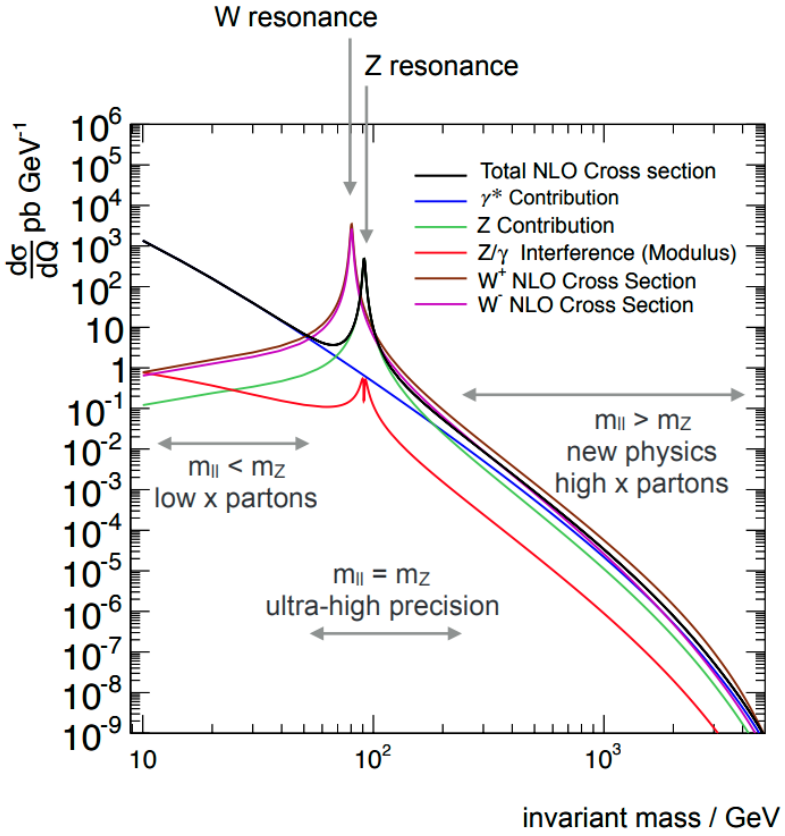

Figure 2.6.: Drell-Yan differential cross-sections as a function of invariant mass at next-to-leading order. Resonances for W and Z bosons are labelled with the ranges for certain characteristic scales and the expected range for which new physics could be found. The W^+ cross-section is consistently higher than W^- by around 60% due to the LHC colliding positively charged protons [27].

2.3.1. Higher Order Corrections

k-Factors are the ratio of cross-sections at different orders of perturbative expansion and are used to evaluate the significance of higher-order corrections in theoretical predictions. In Drell-Yan production the k-Factor is used to assess the impact of next-to-leading-order (NLO) and next-to-next-to-leading-order (NNLO) corrections in comparison to leading-order (LO) predictions. In the high invariant mass region, a challenge arises because it's a kinematic space where NNLO QCD corrections $\mathcal{O}(\alpha_s^2)$ and NLO electroweak corrections $\mathcal{O}(\alpha)$ become a similar size. The calculations of k-Factors for Drell-Yan production involved the use of the programs `FEWZ` [28, 29, 30], `DYNNLO` [31, 32], `ZWPROD` [33] and `VRAP` [34] to compute the cross-sections. These programs utilised PDFs like the CT10 at NLO QCD and MSTW2008nnlo at NNLO QCD. By comparing the results obtained at different orders of perturbation the k-Factors are derived [35]. More information on the k-Factors used in this analysis can be found in Section 5.

2.4. Effective Field Theory

Whilst doing a global analysis of the proton, which is useful for constraints on PDFs, Beyond the Standard Model Physics (BSM) can also be investigated. New physics can be searched for directly and indirectly in a high-energy collider. A direct search involves looking for new heavy particles. However, an indirect search looks for subtle deviations in the cross-section at LHC energies due to the effect of new particles with higher masses than the reach of the LHC. The Lagrangian, when looking for BSM physics in Standard Model Effective Field Theory (SMEFT), contains the renormalisable Standard Model Lagrangian ($\mathscr{L}_{SM}$) with additional higher-dimension interactions ($\mathscr{L}^d$). Therefore, looking for a Lagrangian when taking dimension six will include many more terms taking the form:

$$\mathscr{L}_{SMEFT} = \mathscr{L}_{SM} + \mathscr{L}^d \tag{2.30}$$

SMEFT represents a model-independent way to identify, interpret, and calculate BSM effects from precision measurements. These precision measurements should be taken assuming that the energies examined by experimental data are well below that of the new physics scale (Λ). This new scale might be the mass of a new particle. In this way, SMEFT can connect experimental observables with new physics [36].

The Lagrangian for dimension 6 SMEFT is:

$$\mathscr{L}_{\text{SMEFT}} = \mathscr{L}_{\text{SM}} + \sum_{i=1}^{N} \frac{a_i}{\Lambda^2} \mathscr{O}_i \tag{2.31}$$

The sum over N represents the sum over the number of non-redundant operators. The cut-off scale of EFT is Λ^{d_i-4}, so taking dimension $d = 6$, the new physics scale becomes Λ^2. a_i are the Wilson coefficients (coupling constants) constrained by taking observables' measurements. The dimension six operators are O_i. [36]

The high-energy processes in the LHC (such as the Drell-Yan process), which have energy-growing BSM effects, increase sensitivity to the SMEFT. For Run-2 of the LHC, in particular, the observables will be in the few TeV region, making them more sensitive to PDFs. Therefore, there is a danger that the BSM effects can be fitted away into the PDFs in high-energy tails [37]. The dimension-6 operators alter the high energy behaviour of electroweak gauge boson propagators. This is included in the "oblique parameters" $\hat{S}$, $\hat{T}$, W and Y which modify the bosons γ, W and Z. Oblique parameters are derived from the Taylor expansion coefficients from the new physics contributions to the transverse part of vector boson self-energies [38]. The W and Y parameters have effects that grow with energy meaning that the LHC can have better sensitivity than previous measurements by the previous collider LEP.

Figure 2.7 shows the 95% CL exclusion for neutral Drell-Yan sensitivity to W and Y at LEP at 8 TeV in grey. The neutral Drell-Yan shown in purple and charged Drell-Yan

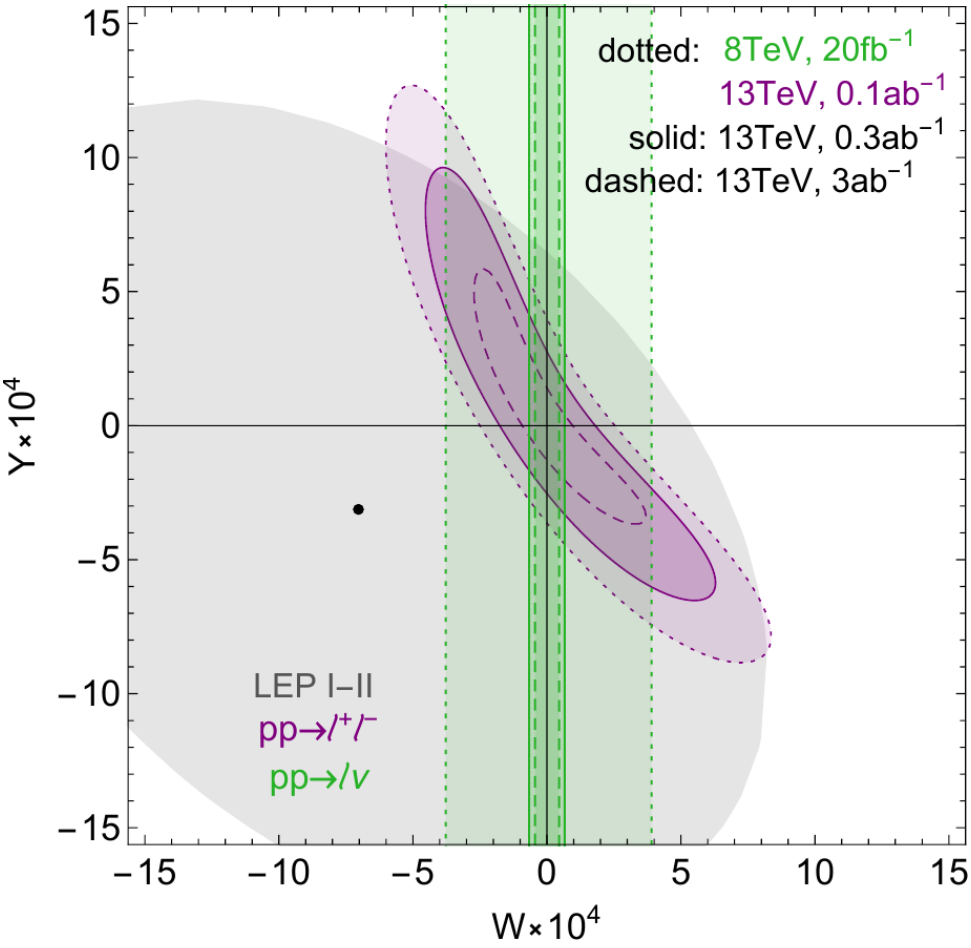

Figure 2.7.: Projected 95% CL exclusions in the W–Y plane [36].

in green from LHC measurements are shown at two different luminosities. Therefore, using the LHC centre of mass energy 13 TeV will allow more precision measurements for electroweak tests, such as measuring high mass W bosons and allowing model-independent EFT coefficients to be extracted, indicating BSM physics [36].

2.5. Measurement Overview

The cross-section and charge asymmetry of W boson production in pp collisions have previously been measured. Charge asymmetry occurs when the cross-section of the produced W boson depends on its charge. This arises as the positively charged valence quarks are slightly more dominant inside the positively charged proton. The ATLAS [4] and CMS [39] experiments provide the latest results for cross-section and charge asymmetry measurements. The ATLAS collaboration published results for the cross-sections and the associated charge asymmetry as a function of the absolute pseudorapidity of the decay muon for W boson production. The results use $\sqrt{s} = 8$ TeV data corresponding to 20.2 fb^{-1} for pp collision data with the ATLAS experiment at the LHC. The pre-

cision of the cross-section measurements varies between 0.8% to 1.5% as a function of the pseudorapidity. The charge asymmetry is measured with an uncertainty between 0.002 and 0.003. The measurement's PDF precision was better than both the uncertainties, and the spread between different PDF sets of the data shows sensitivity to serve as input to improve the knowledge of the proton structure [5]. The latest published results were performed by the CMS collaboration in 2020, the differential cross section and charge asymmetry for inclusive W boson production at the LHC in 2016 corresponding to an integrated luminosity of 35.9 fb^{-1} at the centre of mass energy of $\sqrt{s}$ = 13 TeV is measured for two transverse polarisation states as a function of the W boson absolute rapidity. The precision of the measurements was used to constrain the parton distribution functions of the proton using the next-to-leading order NNPDF3.0 set [6]. The measurement presented in this thesis aims to extend these analyses into the high-mass region using the full Run-2 (2015-2018) dataset provided by the LHC to the ATLAS detector.

3. The LHC & ATLAS Detector

3.1. The LHC

The LHC (Large Hadron Collider) [2] is near Geneva, at CERN (European Organization for Nuclear Research) [40]. The LHC consists of a 26.7 km ring underground in a tunnel with superconducting magnets to accelerate particles around the ring shown in Figure 3.1. There are two beam pipes consisting of high-energy particles in the ring. These beams of particles counter-rotate and collide at 4 locations. At these four locations are the particle detectors ATLAS, ALICE, CMS and LHCb [2].

The beams of particles used at CERN start from hydrogen atoms in a bottle. Protons are produced from hydrogen gas using a strong electric field to strip away the electrons. This leaves bare protons that are then rapidly accelerated through a metallic chamber containing an electric field called a radio frequency cavity. There is a series of accelerators, and at each stage of the acceleration process in the accelerator complex, the energy of the particle beam will increase. The particle beam can be guided around the path of the accelerator complex with dipole magnets that bend the beams, quadrupole magnets that focus the beams and collimators that collimate the beams [2].

The protons are first injected into the Proton Synchrotron Booster (PSB) at the energy of 50 MeV from Linac2. The PSB accelerates them to 1.4 GeV. The protons are sent into the Proton Synchrotron (PS) and accelerated to 25 GeV and then to the Super Proton Synchrotron (SPS), which accelerates them to 450 GeV. Finally, they are injected into the LHC in a clockwise and counter-clockwise direction. In the last element of this accelerator chain, each particle beam is accelerated for about 30 minutes up to the energy of 6.5 TeV. The protons arrive in bunches and circulate in the LHC beam pipes for many hours. The LHC collides these particles resulting in the centre of mass energy $\sqrt{s} = 13$ TeV. The centre of mass energy increased from Run-1 $\sqrt{s} = 8$ TeV [41].

3.2. Luminosity

The measure of a particle accelerator's ability to produce the required interaction rate is called the luminosity $\mathscr{L}$. It is defined as:

$$\sigma \int \mathscr{L}\, dt = N \tag{3.1}$$

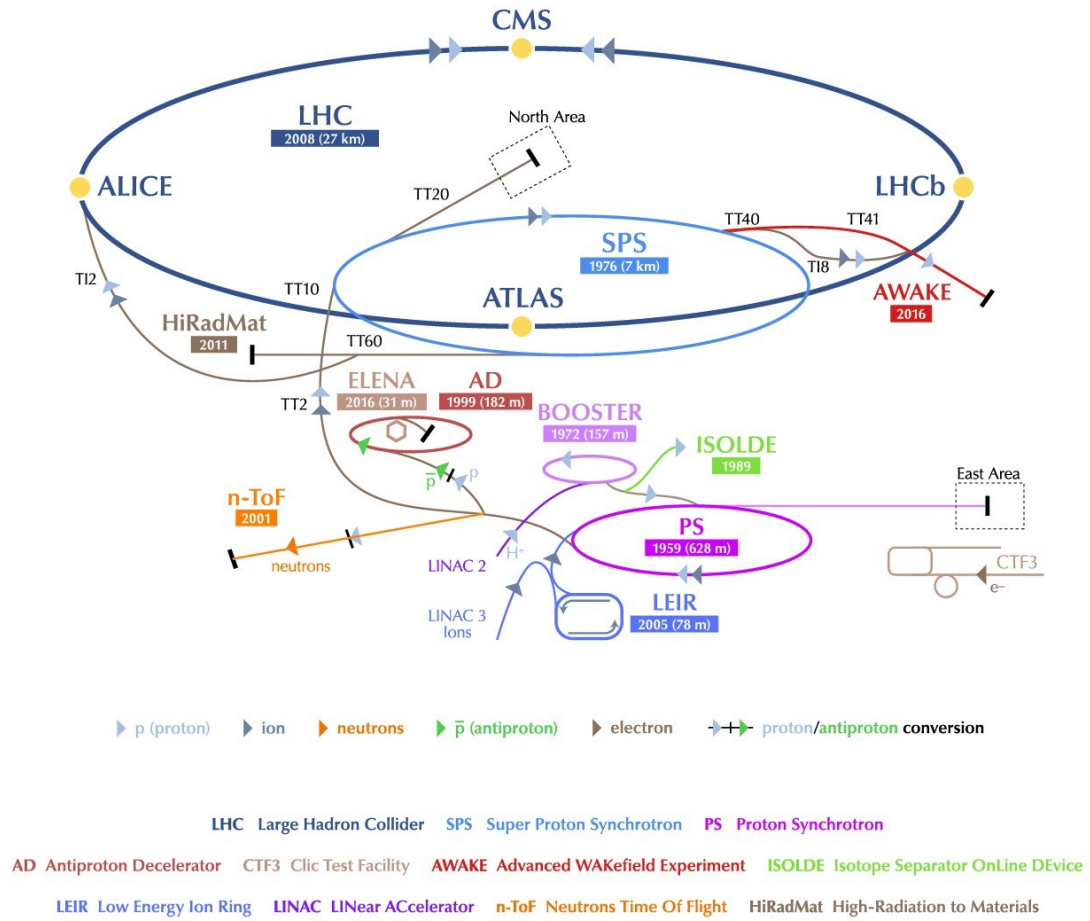

Figure 3.1.: CERN Accelerator Complex [42].

Here σ is the cross-section, N is the number of events, and t is time [41]. The luminosity of a beam of particles is the number of particles passing through the beamline per unit time per unit area: [43]

$$\mathscr{L} = f n_b \frac{n_p^2}{A} \tag{3.2}$$

f is the rotation frequency of the beams, n_b is the number of particle bunches per beam, n_p is the number of protons in the beam, and A is the beam's transverse colliding area.

Table 3.1 shows a selection of LHC parameters for pp collisions at $\sqrt{s} = 13$ TeV in 2015-2018 for best accelerator performance. The LHC design instantaneous luminosity at $\sqrt{s} = 14$ TeV is 10^{34} cm^{-2} s^{-1}. The proton beams have about 10^{11} protons, each containing 2808 bunches. Each of the bunches in the LHC has a bunch spacing of 25 ns (or 7.5 m), with the proton bunches colliding 40 MHz. If the number of bunches increases, the luminosity also increases. In various parts of the LHC, bunches are focused. At the interaction point (IP), the bunches will be squeezed to increase the probability of a

collision or reduce the transverse colliding area of the beam A in Equation 3.2 [2, 44].

Parameter	2015	2016	2017	2018
Maximum number of colliding bunch pairs (n_b)	2232	2208	2544/1909	2544
Bunch spacing (ns)	25	25	25/8 b4e	25
Typical bunch population $\left(10^{11}\text{ protons}\right)$	1.1	1.1	1.1/1.2	1.1
Beta function value at Interaction Point β^* (m)	0.8	0.4	0.3	0.3 – 0.25
Peak luminosity $\mathscr{L}_{\text{peak}}$ $\left(10^{33}\text{ cm}^{-2}\text{ s}^{-1}\right)$	5	13	16	19
Peak number of inelastic interactions/crossing ($\langle\mu\rangle$)	~ 16	~ 41	~ 45/60	~ 55
Luminosity-weighted mean inelastic interactions/crossing	13	25	38	36
Total delivered integrated luminosity (fb $^{-1}$)	4.0	38.5	50.2	63.4

Table 3.1.: LHC parameters for pp collisions at $\sqrt{s}$ = 13 TeV in 2015-2018. The values shown represent the best accelerator performance during normal physics operation. For 2017, the LHC ran in two modes: the standard 25 ns bunch train operation with long trains and 8 b4e, for a pattern of eight bunches separated by 25 ns then followed by a four bunch-slot gap [45].

3.3. Pileup

In order to maximise the potential for measurement and discoveries, the LHC delivers the highest possible collision rates. Therefore, when two bunches cross at the interaction point, multiple overlapping pp collisions will occur.These additional interactions are referred to as pileup. The pileup must be carefully considered as it affects the detector response when an interesting collision occurs and can distort measurements of the high-energy interaction of interest. Therefore, this additional "ambient" energy or particles must be subtracted or accounted for. In the same bunch crossing, the detector can observe the final state of the interaction with additional pileup and zero bias interactions (inelastic hadron-hadron collisions dominated by low momentum). Pileup affects most of the objects reconstructed in the final state. Objects reconstructed with pileup have compromised precision because of miscalculation of energy, momentum and topology from the potential overlap of pileup decay products and overlap with interesting objects. Most pileup contributions are from hadrons. Therefore, hadrons are the most affected final objects. However, lepton and photon isolation criteria will also be affected [46].

3.4. ATLAS Detector

ATLAS (A Toroidal LHC ApparatuS) is a general-purpose detector at the LHC. It resides in an experimental cavern at point 2 at CERN. ATLAS aims to exploit the high energy and collision rate the LHC provides. As ATLAS is a general-purpose detector, it is designed to be sensitive to a range of particle signatures over a wide span of energy and momenta.

The particle signatures are then reconstructed, identified and calibrated. This is used to test the Standard Model's predictions and probe new physics processes [4].

ATLAS has a diameter of 25 m, length of 46 m and overall weight of 7,000 tonnes [47]. It is the largest detector to be built at a particle collider. ATLAS uses a series of subsystems shown in Figure 3.2 to identify the final state of interactions. After a pp collision, each particle produced will interact with different parts of the subsystems in the detector, allowing the particle tracks to be reconstructed, thus identifying the particle. Particles directly detected are protons, neutrons, photons, electrons, muons, pions, and kaons. Neutrinos interact weakly with matter however can be inferred through the missing energy within a particle decay. The b-meson particles have relatively long lifetimes and therefore are a small distance from the beamline but can be detected due to the displaced vertices of the decay products [48].

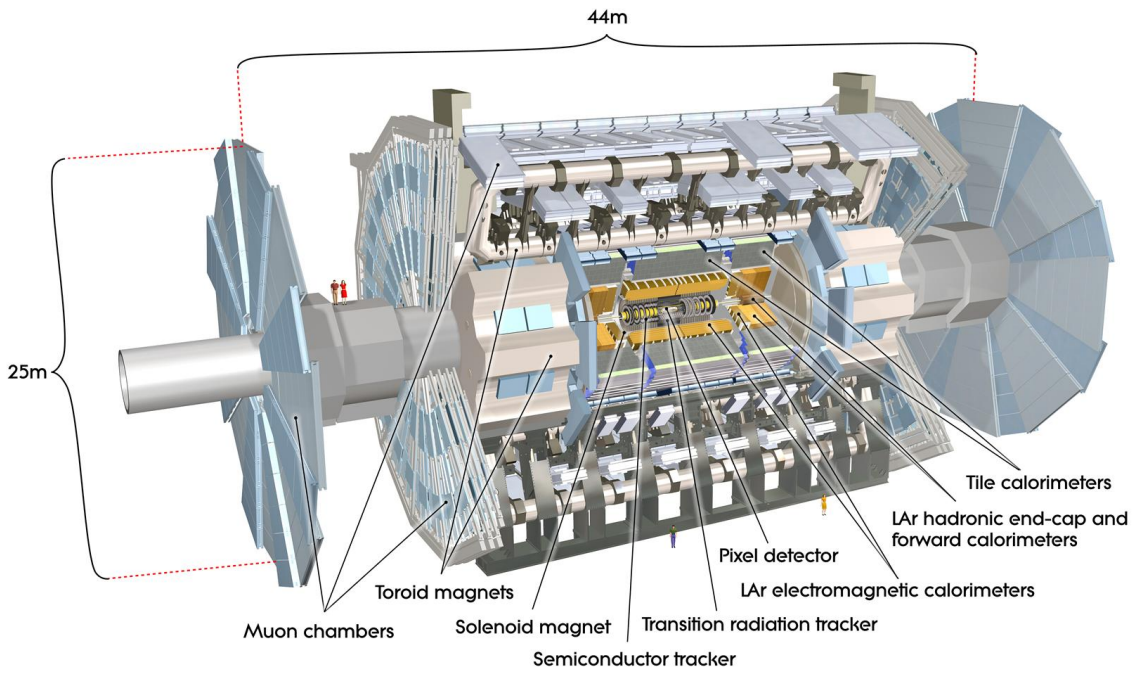

Figure 3.2.: ATLAS Detector with labelled subsystems [49].

3.5. Coordinate System

The interaction point is located in the centre of ATLAS and is the origin of the coordinate system. The beam direction is the z-axis with the x-y plane transverse to this. The x-axis is positive in the direction from the interaction point to the centre of the LHC ring. The y-axis is defined as positive when pointing upwards. The polar angle (θ) is the angle from the beam direction and the azimuthal angle (ϕ) is defined as the angle around the beam in the x-y plane. The rapidity is defined as:

$$y = \frac{1}{2}\ln[\frac{(E+p_z)}{(E-p_z)}] \tag{3.3}$$

The rapidity is difficult to precisely measure for highly relativistic particles due to the difficulty in measuring the total momentum vector where the z component is significant. However, the quantity pseudo-rapidity can be defined:

$$\eta = -\ln\tan(\frac{\theta}{2}) \tag{3.4}$$

where $y \approx \eta$ for highly relativistic particles where the mass is negligible. The distance in ϕ and η, in the pseudorapidity-azimuthal angle space is defined as:

$$\Delta R = \sqrt{\Delta\eta^2 + \Delta\phi^2} \tag{3.5}$$

Defining variables in the transverse plane to the beam pipe (x-y plane) is helpful. In the LHC, protons are accelerated and collide head-on. When collisions occur, both protons dissociate into streams of quarks and gluons which hadronise and a significant amount of the collision energy escapes through the beam pipe ($\pm z$-direction). An example is an interesting physics collision or hard collision, where only one parton could participate in the process and the other does not significantly change. In the transverse plane before the collision, the initial momentum is zero. Considering the conservation of energy and momentum, the quantity in the transverse plane after the collision must also be zero. The transverse momentum, p_T, is the magnitude of the momentum vector projected on the x-y plane.

The missing transverse energy, E_T^{miss}, is inferred from the transverse momentum of invisible particles and detected particles in a hard collision. In the $W \rightarrow \mu\nu$ process missing energy is attributed to the neutrino. The transverse energy of the neutrino is obtained by taking the absolute value of the negative vector sum of the high p_T particles in the final state plus soft tracks (low p_T) not associated with the former particles. This is given by Equation 3.6 [50].

$$E_{x(y)}^{miss} = -\sum_{i\in\{\text{ hardobjects }\}} p_{x(y),i} - \sum_{j\in\{\text{ softsignals }\}} p_{x(y),j} \tag{3.6}$$

The first term in Equation 3.6 reresents the transverse momentum of all the hard objects. The second term in Equation 3.6 represents the tracks associated with the hard vertex but not the selected hard objects. This includes signals or signal traces from scattered soft particles from the underlying event accompanying the hard-scatter interaction or from statistically completely independent pileup interactions. It also could include the tracks from particles and jets which do not satisfy the hard object quality criteria or are below the kinematic threshold. The following Equation 3.7 is the missing

energy vector:

$$\mathbf{E}_T^{\text{miss}} = \left(E_x^{\text{miss}}, E_y^{\text{miss}}\right) \tag{3.7}$$

The magnitude is given by Equation 3.8:

$$E_T^{miss} = \left|\mathbf{E}_T^{miss}\right| = \sqrt{\left(E_x^{miss}\right)^2 + \left(E_y^{miss}\right)^2} \tag{3.8}$$

The direction in the transverse plane is given by the following Equation 3.9:

$$\phi^{E_T^{miss}} = \tan^{-1}\left(\frac{E_y^{\text{miss}}}{E_x^{miss}}\right) \tag{3.9}$$

These equations define the missing energy transverse momentum vector [50]. Reconstruction of the E_T^{miss} is discussed further in Section 3.14.

The quantity transverse mass can be defined as: [4]

$$M_T = \sqrt{2p_T^{\mu}E_T^{miss}(1-\cos(\Delta(\phi))} \tag{3.10}$$

In cases with an unseen neutrino in the final state, the invariant mass cannot be determined from the final state. The M_T is an analogue of the invariant mass. For a 2-body final state where one particle is a neutrino, the M_T is identical to the invariant mass if the neutrino has purely transverse momentum. M_T is a useful observable for the DY processes where only the charged lepton is measured.

3.6. Magnets

A strong magnetic field is required to measure a charged particle's momentum. The ATLAS magnet system comprises four superconducting magnets, three toroids (two end caps and one barrel) and one solenoid. A schematic of this is shown in Figure 3.3. This magnet system is 26 m long and 22 m in diameter and has a stored energy of 1.6 GJ. The magnets are responsible for bending charged particle tracks in a plane perpendicular to B-field and the velocity of the particle in the inner detector and muon detector to measure the particle's momentum. The Lorentz force vector equation, defined in Equation 3.11, gives the force on a charged particle due to magnetic and electric fields.

$$\vec{F} = q\vec{v} \times \vec{B} \tag{3.11}$$

The solenoid is aligned along the beam axis, providing the inner detector with a 2 T axial magnetic field. It has an outer diameter of 2.56 m and is 5.8 m long. The toroids provide a magnetic field for the muon detectors in the end caps and the central regions. The barrel toroid is constructed from 8 coils. It spans the entire length of the muon subsystem and provides the central muon detector with a 0.5 T magnetic field. The

two endcap toroids, each constructed from 8 coils, produce a magnetic field of 1 T. Figure 3.4 is included to demonstrate what the magnetic field looks like in the transverse and longitudinal cross-section [51].

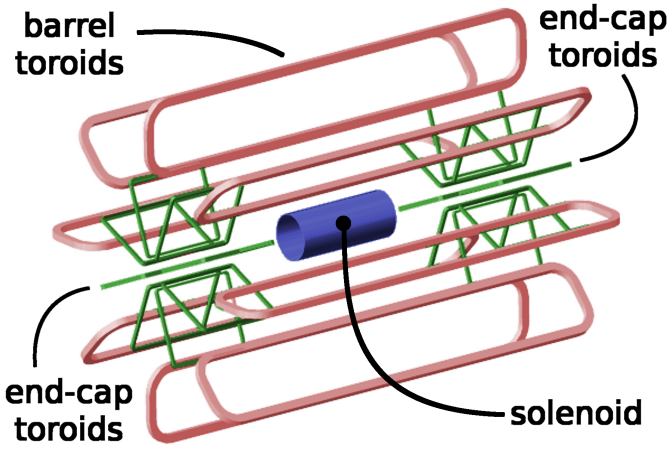

Figure 3.3.: Schematic of the ATLAS magnet systems [52]

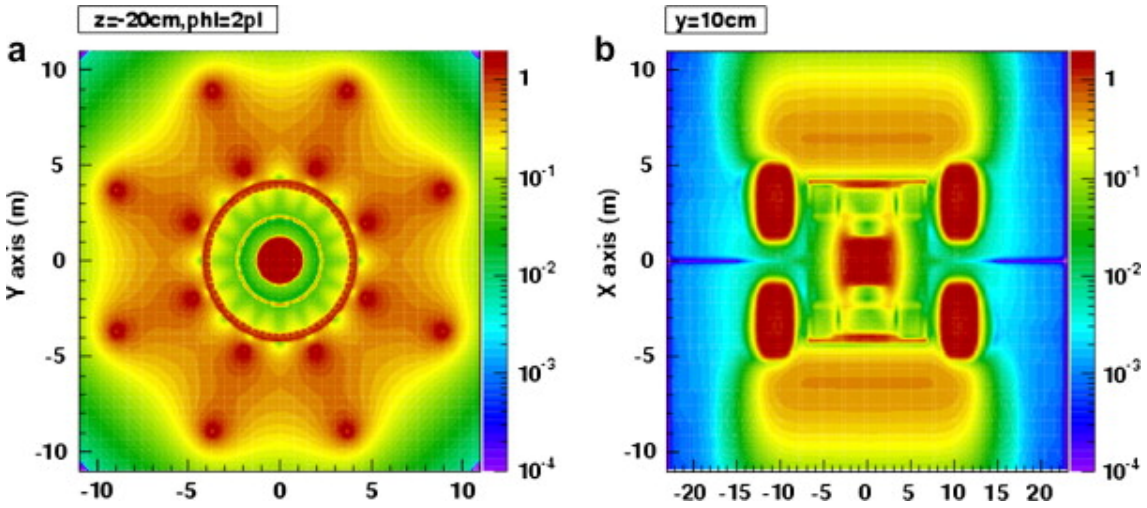

Figure 3.4.: ATLAS magnetic field shown in a) transverse cross-section of the magnetic field in the centre of the magnet system (not including endcap toroids) b) longitudinal cross-section showing central solenoid, end cap toroids and barrel toroids [51].

3.7. Inner Detector

The inner detector shown in Figure 3.5 is the central component of ATLAS. It is the nearest detector to the interaction point and is the first part of ATLAS to detect decay products from a collision. The inner detector can, with high efficiency, reconstruct the tracks and vertices in an event. This together with the other subsystems in ATLAS, is used to identify different particles and can also provide an extra signature for short-lived particle decays [53]. For particles coming from the interaction point, the accep-

tance in pseudo-rapidity is $|\eta| < 2.5$ and full coverage in ϕ to match the rest of the ATLAS subsystems. In the plane perpendicular to the beam, the transverse momentum resolution is given by $\sigma_{p_T}/p_T = 0.05\% p_T$ GeV. The inner detector utilises separate but complementary sub-detectors: the Pixel Detector, the Semi-Conductor Tracker, the Transition Radiation Tracker and the Insertable B-Layer [54].

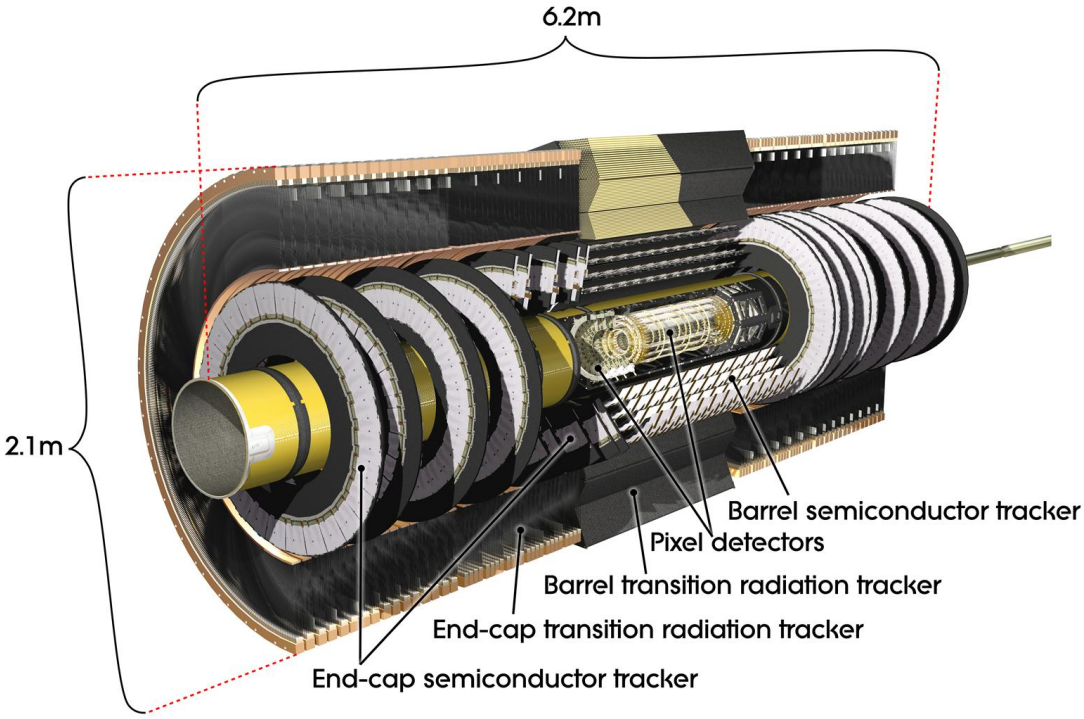

Figure 3.5.: Schematic of the ATLAS inner detector subsystem [55].

3.7.1. Silicon Pixel Detector

The pixel detector consists of 1744 silicon pixel modules positioned into three concentric layers in the barrel and the two endcaps each have three disks. This can typically provide three measurement points for particles from the interaction point. Each module can actively cover an area of 16.4 mm x 60.8 mm with 47,232 pixels of size 50 μm x 400 μm [54].

From the interaction point in ATLAS, a particle will travel and hit the silicon layer from the pixel detector. The charged particle interacts with the doped silicon (which is reverse-biased), which can liberate an electron from the valence band into the conduction band, creating a hole. The doping and the reverse bias create an electric field which sweeps the election-hole pair towards the anode/cathode generating a current pulse. An electric current is used in each pixel to collect these charges as a small electric signal. The readout for each module is provided by attaching a radiation-hard front-end chip to the silicon sensor, which collects the signal. The particles will travel through

three layers of silicon. As the particle travels through the silicon pixel detector, many electron-hole pairs will be created without stopping the particle. A particle's trajectory can be deduced by gathering information on pixels that have been hit. Each pixel provides a 3D space point from which trajectories can be reconstructed [54, 56].

3.7.2. Semi-Conductor Tracker

The Semi-Conductor Tracker (SCT) is used to help in the measurement of the vertex position, momentum and impact parameter (defined in Section 6.1.3) by providing four precision measurements for each track [53]. The SCT encompasses the pixel detector with 4,088 modules of silicon strips. These are arranged concentrically in the barrel region with four layers of silicon micro-strip ($|\eta| < 1.4$) and in each of the two endcaps there are nine disks ($1.4 < |\eta| < 2.5$). This provides four space points from eight strip measurements for particles originating from the beam. Similar to the pixel detector, the SCT uses charged-track-ionisation for detection. [54]

3.7.3. TRT Detector

The Transition Radiation Tracker (TRT) is designed like a straw detector (a detector that has many straw chambers to determine the particle's track). Due to the small diameter and the isolation of the sense wire within each separate tube, they can operate at very high rates [53]. The TRT surrounds the SCT. In the barrel region, the TRT consists of 300,000 drift tubes (straws) of 4mm diameter. The readout for the barrel region is at both ends of the straw. The endcaps have 0.4 m long straws perpendicular to the beam axis, each with 122,880 straws. At the outer end, there is the readout for the endcaps.

The cylinders were initially each filled with a mixture of 70% Xe, 27% CO_2 and 3% O_2. The xenon gas allows for electron identification, the CO_2 stabilises the mixture, and the O_2 increases the drift velocity. The xenon gas detects transition-radiation photons which are created in between the straws. Transition radiation is emitted when a charged particle crosses the boundary between two materials with different electrical properties. Transition radiation can be formed by the propylene added between the tubes, which changes the refractive index when a charged particle passes through it along with the resultant pair production. The lower energy-charged particles ionise the gas mixture in the straws. This allows for particle identification because the particle's mass will increase the amount of transition radiation [57].

During 2012 data-taking period, the TRT experienced issues due to leaks in the gas pipes which delivered the active gas to cleaning and mixing stations. These leaks predominantly occurred in inaccessible areas, rendering direct repairs unfeasible. Accordingly, the expensive Xenon-based gas mixture was replaced with the more affordable Argon-based alternative. Since the start of Run-2 in 2015, the TRT modules with large amounts of leakage were operated with te Argon gas mixture which has allowed

for the continued functionality of the affected modules and sustained detector performance [58].

3.7.4. Insertable B-Layer

The performance of the B-layer is essential for the full physics capabilities of the ATLAS dectector. This layer should ensure there is good vertexing and B-tagging despite the increase in pileup, possible radiation damage effects or other eventual problems in the pixel dectector. The Insertable B-Layer (IBL) is an additional layer integrated into the present pixel detector between the new beryllium beam pipe and the then innermost pixel layer (B-layer) shown in Figure 3.6. The IBL was added into the ATLAS detector in 2014 during the long shutdown. The motivation behind the installation of the IBL was to maintain or to improve the tracking capabilities of the inner region by allowing for a finer resolution and improved efficiency in the reconstruction of particle tracks. It also provides an increased bandwidth requirement for the expected LHC peak luminosity [59, 60].

The IBL integrated two sensor technologies: planar and 3D sensors. Planar sensors, constructed from $n^+ - on - n$ silicon have a thickness of 200 μm, while 3D sensors are 230 μm in thickness. Both sensor types feature pixels sized at 50 $\times$ 250 μm^2, which is 60% of the Pixel Detector's pixel size, with approximately 12 million pixels in total. These sensors are designed to endure radiation levels of up to 5×10^{15} 1MeVn$_{eq}$, corresponding to the expected fluence at the end of LHC Phase-1 operations [61].

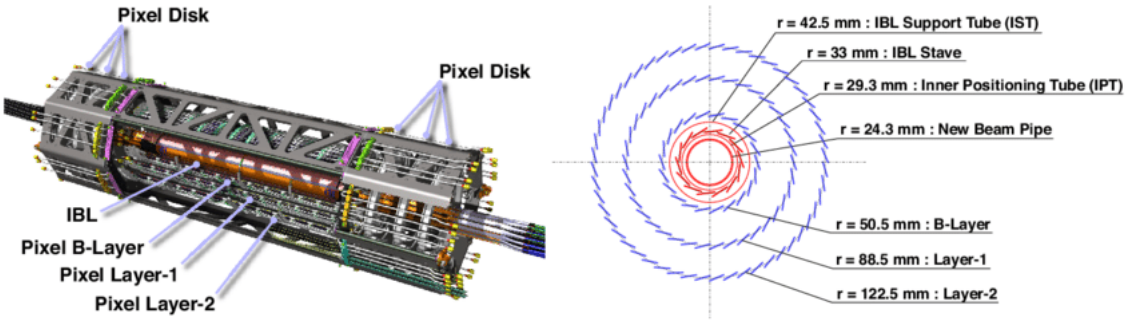

Figure 3.6.: Schematic of the ATLAS 4-Layer pixel detector for Run-2 [62].

3.8. Calorimeters

Next in the ATLAS detector is the calorimetry system which surrounds the ID. The purpose of calorimeters is to measure the energy a particle loses as it travels through the detector. Calorimeters absorb all known particles, except muons and neutrinos, from a collision. ATLAS hosts two calorimeters: the Liquid Argon (LAr) Calorimeters and the Tile Hadronic Calorimeters. A schematic of the calorimeters in ATLAS can be found in Figure 3.7.

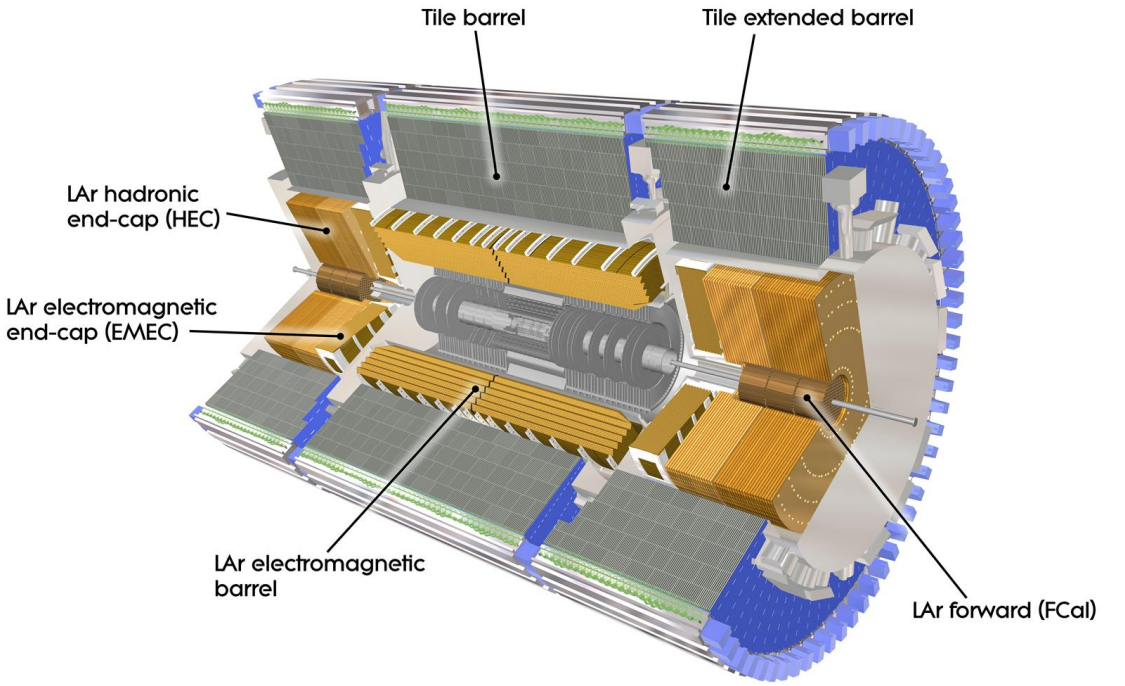

Figure 3.7.: Schematic of the ATLAS electromagnetic and hadronic calorimeter subsystems surrounding the inner detector [63].

Calorimeters usually contain layers of alternating passive or absorbing material and active material in a so-called accordion geometry shown in Figure 3.8. The absorbing material is dense and provides material for the EM and hadronic showers, the low energy particles produced in the showers then ionise the detector material. Whereas, the active material is used to produce an output signal proportional to the energy input. The calorimeters in ATLAS have full coverage $|\eta| < 4.9$ and ϕ-symmetry around the beam axis. The design of the calorimeter system must have enough depth so that the electromagnetic and hadronic showers are contained to limit any propagation into the muon detectors. The ATLAS calorimetry system components are the high granularity liquid argon (LAr) electromagnetic sampling calorimeters (ECAL) and the hadronic calorimetry (HCAL).

3.8.1. ECAL

The electromagnetic calorimeter is used to absorb the energy from electromagnetic showers. The absorbing material in the electromagnetic calorimeter is lead and the active material is liquid argon. The electromagnetic calorimeter has three parts, a barrel component spanning $0 < |\eta| < 1.475$ and two endcaps spanning $1.375 < |\eta| < 3.2$. The electromagnetic calorimeter has a thickness of $> 22X_0$ (radiation lengths) in the barrel and a thickness of $> 24X_0$ in the end caps. The radiation length of a material is the

mean length for an electron to reduce its energy by the factor $\frac{1}{e}$. In the barrel, the active calorimeters have a total thickness of approximately 9.7 λ (interaction lengths, the average distance a hadron travels in a medium before interacting). This gives a good resolution for high-energy jets and can contain the showers enough to limit the amount propagating into the muon system.

3.8.2. HCAL

The hadronic calorimeter absorbs any hadronic showers that are produced. The hadronic calorimeters use steel as the absorbing material and scintillators as the active material. The hadronic calorimeter has three parts: the hadronic tile calorimeter (TileCal), the liquid argon hadronic endcaps (HEC) and the liquid argon forward calorimeter (FCal).

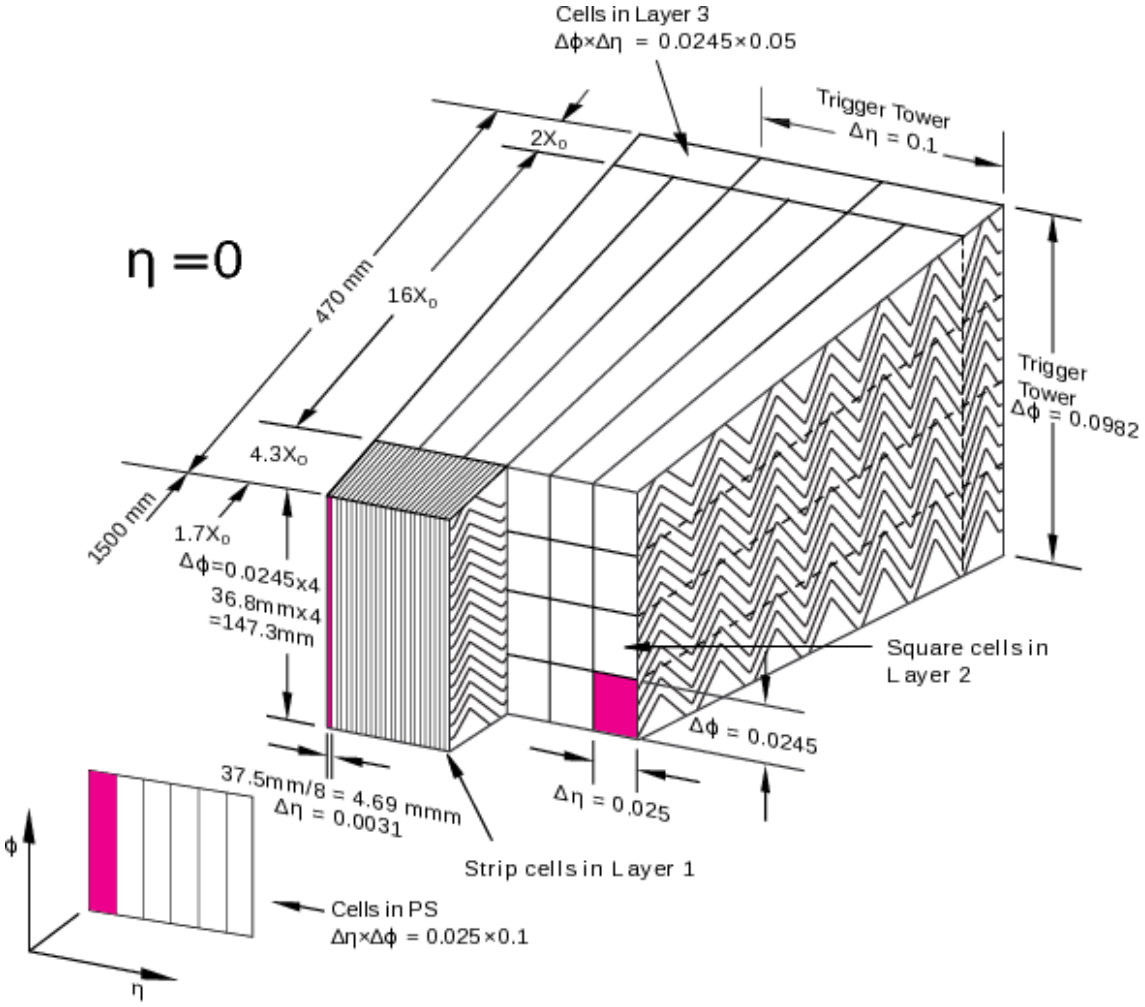

Figure 3.8.: Schematic of the ATLAS LAr calorimeter. This shows an electromagnetic barrel (EMB) module where the different layers are visible. The granularity in eta and phi of the cells for each of the three layers and trigger towers is also shown [4].

TileCal

The hadronic tile calorimeter (TileCal) is located in the barrel and uses plastic tile scintillator plates as the active material and steel as the absorbing material. It consists of a central barrel 5.8 m in length and two extended barrels 2.6 m long. The TileCal covers a region $|\eta| < 1.7$ behind the liquid argon electromagnetic calorimeter. The tile calorimeter is $7.4\ \lambda$. In the electromagnetic and hadronic calorimeters, hadron-nucleon interactions occur within the absorbing material (lead and steel) and TileCal then detects these showers. The scintillators produce photons when they detect these interactions. The resultant photons from the scintillating material are then collected by wavelength-shifting fibres that connect to the tile edges and convert them into a longer wavelength. The photons are then transmitted to photomultipliers outside the calorimeter [4].

HEC

The hadronic endcap calorimeters (HEC) are liquid argon and copper sampling calorimeters. The HEC is located behind the electromagnetic endcap calorimeters. The HEC is important as it can detect muons and measure radiative energy loss. The HEC comprises two-wheel units, a front wheel and a rear wheel. The wheels are each made up of 32 wedge-shaped modules. The HEC can cover a range of $1.5 < |\eta| < 3.2$. This range reduces the drop in material density at the transition regions between the HEC/forward calorimeter and the HEC/tile calorimeter [4].

FCAL

The forward calorimeter (FCAL) consists of three layers of liquid argon and a metal. The electromagnetic layer (FCAL1) uses copper and is closest to the interaction point. The two hadronic layers (FCAL2, FCAL3) are made of tungsten. There is an additional passive layer made of brass which absorbs hadronic shower remnants that punch through called Plug3. This arrangement is shown in Figure 3.9. FCal is positioned in the forward and backward detection regions $3.1 < |\eta| < 4.9$. FCal covers a total depth of 10 λ. Overlap between the tile calorimeter, HEC and FCal makes it possible to cover the range of $0 < |\eta| < 4.9$. The FCal is integrated into the endcap, improving coverage and reducing radiation backgrounds from the passage to the muon spectrometer [4, 64].

3.9. Muon Spectrometer

The next sub-detector in ATLAS is the muon spectrometer (MS) [4]. High-energy muons provide a signature for interesting physics when performing measurements, such as those for W boson leptonic decays. The muon spectrometer in ATLAS must therefore be able to provide muon reconstruction and a momentum-dependent trigger. This

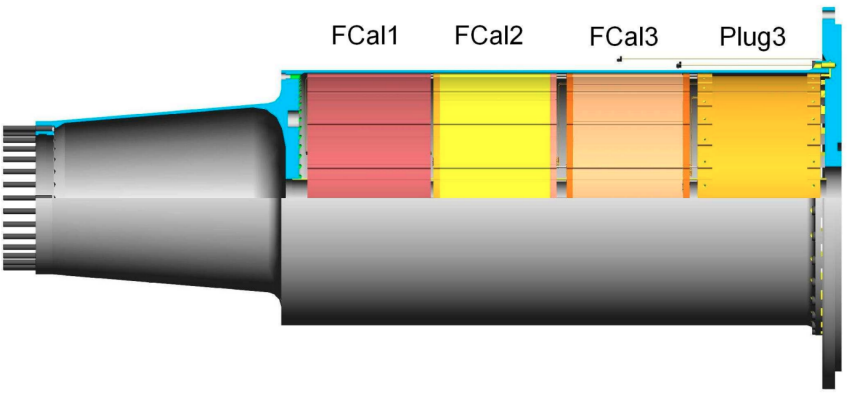

Figure 3.9.: Schematic of the ATLAS forward calorimeter. The electromagnetic layer (FCAL1) is closest to the interaction point. The two hadronic layers (FCAL2, FCAL3) are next. There is an additional passive layer called Plug3 [64].

is achieved through a distinct set of sub-detectors. Muon momentum is determined by measuring position in three points in space. Due to the magnetic fields, there is a solenoid field in the ID and a toroidal field in MS. The particle bends in two different planes and the muon trajectory is curved. The trajectory has a greater curvature for muons with less momentum. The curvature can be measured by fitting the track. A good approximation can also be made using sagitta. Sagitta is the height of an arc. The relationship between sagitta s and the transverse muon momentum is:

$$p_T = \frac{L^2 B}{8s} \tag{3.12}$$

L is the path length and B is the magnetic field [65].

A transverse and side view of the Muon Spectrometer can be found in Figure 3.10. The muon spectrometer is the outer part of ATLAS. The design of the muon spectrometer allows it to detect charged particles from the barrel and end cap calorimeters in the range $|\eta| < 2.7$ and measure their momentum. The main systems in the muon spectrometer are the Monitored Drift Tubes (MDT), Cathode Strip Chambers (CSC), Resistive Plate Chambers (RPG) and Thin Gap Chambers (TGC). Tracks are measured within the barrel region in chambers in three cylindrical layers oriented around the beam axis. In the end cap and transition regions, three layers of chambers are also oriented perpendicular to the beam. The muon spectrometers aim to give a stand-alone muon transverse momentum resolution of 10% for 1 TeV tracks which is approximately a sagitta of about 500 μm with a resolution of ≤ 50 μm along the beam axis [4].

3.9.1. MDT

Monitored Drift Tube (MDT) chambers precisely determine the muon momentum. MDT chambers span an area of 5500 m^2 and in the barrel cover $|\eta| < 1$ and in the endcaps $1 < |\eta| < 2.7$. An MDT is composed mostly of cylindrical aluminium tubes and filled

with Ar (93%), and $C0_2$ (7%). Each MDT has a support frame with three parallel layers of these tubes on either side (6 layers total). They register the drift times of ionised electrons from muons traversing the gas tubes and creating electron-ion pairs. From a typical track, six coordinates can be measured, giving the position of the track in the layer and the direction it travels across the tubes. This gives a measurement with 40 μm precision and an angle with precision 3 x 10^{-4} rad [4].

3.9.2. CSC

Cathode Strip Chambers (CSC) are found in the high pseudo-rapidity regions $2.0 < |\eta| < 2.7$ in the end cap disks with high particle rates. CSC's have an array of cathode strips made from copper crossing with positively charged anode within some gas. They contain a gas mixture of Ar (80%) and CO_2 (20%). When muons pass through the gas, electron-ion pairs are created. The electrons drift with constant velocity to the anode wire, creating an avalanche of electrons. The wires and strips are perpendicular, giving two position coordinates for each particle. The positive ions will move towards the copper cathode. CSC's have a spatial resolution of 50 μm [4].

3.9.3. RPC

Resistive Plate Chambers (RPC) act as trigger instrumentation in the barrel region. RPCs are gaseous detectors that can provide a muon trigger. Like the CSC, they consist of two parallel plates, an anode (positive) and a cathode (negative). They are made of a resistive material, Bakelite, and are separated by an active gas volume of 94.7% tetrafluoroethane ($C_2H_2F_4$),5% isobutane (C_4H_10) and 0.3% sulfur hexafluoride (SF_6). External metallic strips in each plate pick up the signal from the electrons. The drifted charge gives a 2D space coordinate. The strips are aligned in a pattern designed to quickly measure muon momentum and then trigger to decide whether to keep the data. RPCs have a good spatial resolution of 5 ns with a time resolution of 1.5 ns [4].

3.9.4. TGC

Thin Gap Chambers (TGC) are multi-wire proportional chambers found in the end cap chambers. They use anode wires, graphite cathodes and G-10 fibreglass. The gas mixture used 55% CO_2 and 45% n-pentane (n-C_5H_{12}) is high quenching. They provide a fast trigger and high precision tracking with a time resolution > 99% efficiency for a 25 ns gate [65].

By combining the RPC and TGC systems, fast trigger information is provided for muon tracks. The RPC covers the barrel region $|\eta| < 1.05$ and the TGC the end cap region $1.4 < |\eta| < 2.4$. The trigger chambers measure both coordinates, one in the bending

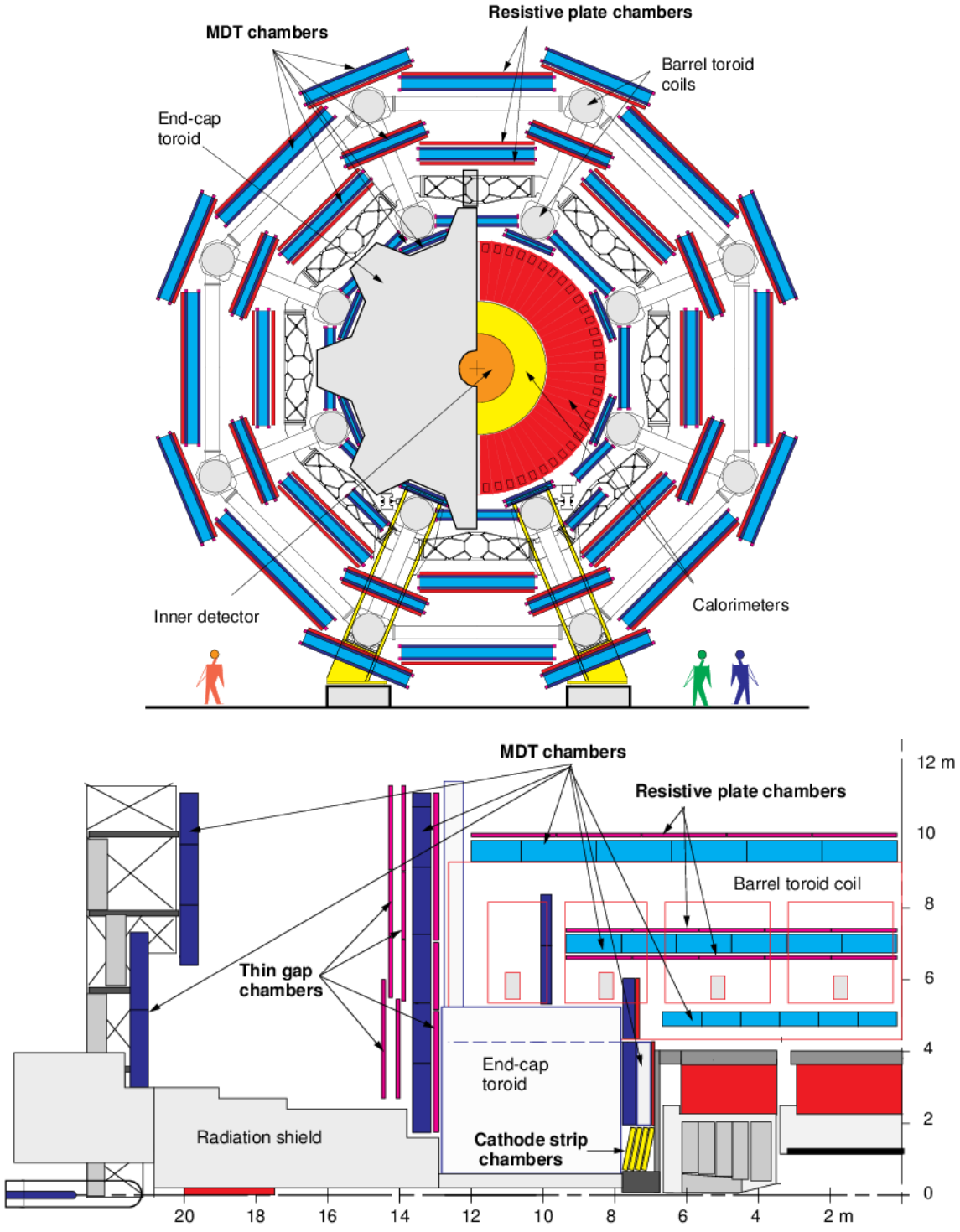

Figure 3.10.: ATLAS cross and side view of the Muon System [66].

η plane and one in the non-bending ϕ plane. The precision tracking chambers determine the coordinate in the bending plane for the track. If there is a match between the MDT and trigger chambers hits in the bending plane, the trigger chambers coordinate in the non-bending plane is used at the second coordinate of the MDT measurement.

3.10. Trigger System

A high proton-proton collision rate is crucial at the LHC due to the rare occurrence of the interesting phenomena. Therefore, a high collision rate is necessary increase the likelihood of observing these events. Among the large number of events generated, many are not of interest for analysis. Hence, a trigger system within the ATLAS Trigger and Data Acquisition (TDAQ) setup is necessary to efficiently differentiate between events for in-depth analysis.

ATLAS utilises a two-tiered trigger system, Level-1 (L1) and High-Level Trigger (HLT). This has been shown diagrammatically in Figure 3.11. These levels refine the selection process applied to the collected data. L1, a hardware-based trigger, and the HLT, a software-based system, work together to identify events of interest [67].

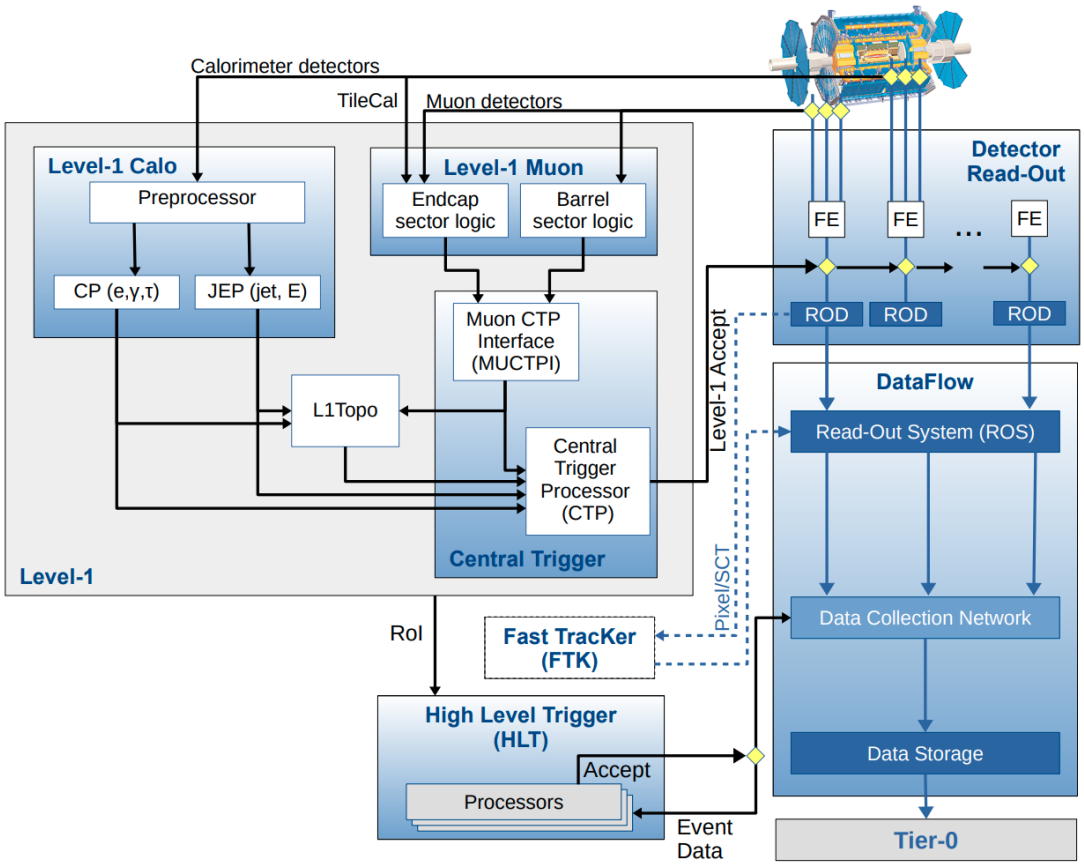

Figure 3.11.: The ATLAS TDAQ system in Run-2 showing the components for triggering and the detector read-out and data flow. [67].

3.10.1. Level 1 Trigger

The L1 trigger has custom electronics used to determine Regions-of-Interest (RoIs), such as the η and ϕ coordinates of regions with interesting objects such as electrons, muons, taus, jets etc. in the detector. This is achieved using input from coarse granu-

larity calorimeter and muon detector information. The L1 triggering system consists of the L1 Calorimeter trigger (L1Calo), L1 Muon trigger (L1Muon), L1 Topological trigger (L1Topo) and Central Trigger Processor (CTP). Accepted events are limited to a maximum read-out rate of 100 kHz, significantly reduced from the bunch crossing rate of 40 MHz. The decision time for the L1 accept is 2.5 μs.

The L1Calo trigger is used for the electromagnetic, hadronic, barrel, endcap and forward calorimeters, utilising analogue signals which undergo digitisation and calibration. The signals are then sent in parallel to the Cluster Processor (CP) and the Jet/Energy – Sum Processor (JEP). The CP system identifies electron, photon and tau candidates which surpass set thresholds. The JEP system identifies jet candidates and computes global energy sums, including total and missing transverse energy ($E_{\mathrm{T}}^{\mathrm{miss}}$).

The L1Muon works along with the calorimeters by assessing the hits in the muon trigger chambers, the RPCs (Resistive Plate Chambers) in the barrel and TGCs (Thin Gap Chambers) in the end caps. This trigger identifies high p_T muons which originate from the interaction point and looks for differences in the hit pattern from a muon with infinite momentum. L1Muon trigger applies coincidence requirements between the outer and inner TGC stations and between the TGCs and the inner detector to minimise the rate of non-interaction point particles in the endcap regions [67].

Introduced in Run-2, the L1Topo takes the L1 trigger objects from the upgraded output merger modules of the L1Calo trigger (CMX) and the L1Muon trigger (MuCTPi). This system is able to apply topological selections at the L1 trigger stage by combining kinematic information from multiple calorimeter and muon trigger objects. The use of L1Topo suppresses backgrounds for many trigger selections, in many cases by more than a factor of two [68].

The CTP makes the overall decision to keep an event at L1 by combining information from different L1Calo, L1Muon, and L1Topo triggers and with signals from various detector subsystems. The CTP implements a trigger menu that is made up of trigger selections. It also applies $dead\ time$, a mechanism preventing excessive L1 accepts that could overload detector read-out capabilities.

The L1 trigger is capable of selecting events based on multiple criteria: event-level quantities, object multiplicities above thresholds or specific topological requirements. When an event is L1-accepted, the Front-End (FE) detector electronics read out the data for all detectors. The event data is then processed through the ReadOut Drivers (RODs) and the ReadOut System (ROS) before being forwarded to the second trigger stage, the High-Level Trigger (HLT) [67].

3.10.2. High Level Trigger

The HLT is a software-based trigger and underwent significant upgrades during the LHC's long shutdown. In Run-1 it consisted of two stages, the Level-2 trigger and the

Event Filter. However, in Run-2, these stages were merged into a HLT stage. This allowed computing operations to be streamlined which reduced data duplication and increased flexibility.

Various algorithms are used by the HLT on a dedicated computing farm to refine event selection. The algorithms utilise the information about the ROIs provided by the L1 trigger. The HLT initially uses fast algorithms which provide early rejection, followed by precise and resource-intensive algorithms, similar to offline reconstruction for the final selection.

Approximately 40,000 Processing Units (PUs) execute event reconstruction algorithms, making decisions within milliseconds. The HLT is capable of reducing the event rate to 1 kHz, which is the maximum rate that can be written to permanent storage and has a decision time of 200 ms. The data is written to data tape storage at the CERN Tier-0 computing centre. Regular hardware updates enhance the computing farm's power and improve the trigger system's efficiency.

Additionally, during Run-2 the Fast TracKer (FTK), a hardware-based system meant for reconstructing inner-detector tracks at the L1 accept rate, was being commissioned. However, it wasn't utilised by the HLT for trigger decisions but was made ready for integration into the HLT tracking algorithms [67, 68].

3.11. Muon Reconstruction

The ATLAS detector records energy deposits and hit information which is reconstructed into physics objects (muons, electrons, etc.) in offline processing. Different reconstruction algorithms taking different approaches can be applied to the data and Monte Carlo simulations. Corrections to the Monte Carlo simulation are applied following the recommendations of the ATLAS combined performance groups [69]. Reconstruction algorithms are used in the HLT during data taking and after data is recorded using more accurate calibration and alignment information with full access to the granularity subdetector readout information across the ATLAS detector.

This section describes event reconstruction for the muon, which is the most relevant object for the charged current Drell-Yan process in the muon channel. Muons in the ATLAS detector interact with matter through several mechanisms: ionisation, bremsstrahlung and pair-production. Ionisation occurs as muons traverse through materials they collide with atomic electrons resulting in the creation of ion pairs. These ion pairs consist of positively charged ions and free electrons within the material. Additionally, muon interactions with matter can result in the excitation of atoms, where electrons are raised to higher energy states. These excited electrons can emit photons when they return to their original energy levels. This process is one of the mechanisms through which muons deposit energy in the detector.

At sufficiently high energies, radiative processes become more important than ion-

isation for charged particles. For muons in materials such as iron, the "critical energy" where these processes dominate occurs at several hundred GeV. The processes that dominate at this energy are bremsstrahlung and pair production. Pair production is the creation of a muon-antimuon pair by a photon in the vicinity of a nucleus. Bremsstrahlung is the emission of photons by charged particles as they are deflected by the electric fields of atomic nuclei [19].

The tracking systems in the muon spectrometer utilise deviations in muon trajectories caused by interactions with atomic nuclei. This information is used to determine the path and momentum of muons. By analysing these trajectories and momenta, the muon spectrometer aids in the reconstruction of data from ionisation and scattering. Specific requirements are placed on muons at the reconstruction level, detailed in Section 6.1.

Muon reconstruction is initially performed independently in the ID and MS. The information from individual subdetectors is then combined to form the muon tracks used for physics analysis. For combined ID-MS muon reconstruction, the information provided by the ID, MS and calorimeters are used. Depending on which subdetector is used in reconstruction, four muon types can be defined: Combined Muon (CB), Segment-Tagged (ST), Calorimeter-Tagged (CT) and Extrapolated Muons (ME) [70].

3.11.1. CB

Combined (CB) muon track reconstruction is performed independently in the ID and MS. Using a fit that takes hits from the ID and the MS, a combined track can be formed that spans the ID and MS and can be used for determining object kinematics. CB muons are the most commonly used type because of their high purity.

3.11.2. ST

Segment-Tagged (ST) muons start with a track in the ID, which is classified as a muon. Once extrapolated to the MS, this track must be associated with at least one track segment in an MDT or CSC chamber. ST muons are used with low p_T muons or in regions of limited MS coverage with coverage up to $|\eta| < 2.7$, where muons only cross one layer of the MS chambers.

3.11.3. CT

Calorimeter-tagged (CT) are muons where a track in the ID matches the energy deposits in the calorimeters compatible with a minimally-ionising particle. CT muons have the lowest purity of all muon types but provide additional acceptance for MS regions without instrumentation such as $|\eta| < 0.1$.

3.11.4. ME

Extrapolated (ME) muons are reconstructed using only the MS track and a loose requirement on compatibility with the origin being the interaction point (IP). ME muons cover areas not covered by the ID, such as in the region $2.5 < |\eta| < 2.7$. In general, the muon must traverse two layers of the MS chambers or three layers in the forward region.

3.11.5. Reconstruction Algorithms

Muon reconstruction algorithms use different "chains", which depend on the muon object that has been identified. Each chain contains a sub-structure of reconstruction algorithms used to reconstruct CB, ST, CT and ME muon object definitions.

Chain 1

"Chain 1" is for the statistical combination of the tracks of muons using the ID and MS track vector's covariance matrices and extrapolates iteratively, adding track segments in the direction of the extrapolation.

Chain 2

The second chain, "Chain 2", or muon identification (MuID), performs a global refit of muons using hits from the ID and MS subdetectors and extrapolates using weighted track covariance matrices. Another strategy the MuID implements is for extrapolating ID hits outward towards MDT and CSC segments via a Hough transform.

Chain 3

"Chain 3" is a unified muon reconstruction chain to incorporate the best features of "Chain 1" and "Chain 2". "Chain 3" ranks the quality of the authored muons from all other chains and records the highest available quality muon candidates.

The muon reconstruction used in this analysis evolved from the "Chain 3" algorithms with additional muon quality requirements as recommended by the ATLAS Muon Combined Performance (MCP) group. The "Chain 3" was improved by using a Hough transform to identify hit patterns for the seeding of the segment-finding algorithm. This makes the reconstruction faster and provides better background rejection by being more robust against misidentified hadrons. Another improvement was calculating energy loss in the calorimeter, where an analytic parameterisation of average energy loss is derived from the detector geometry. The analytic parameterisation and the energy

measured in the calorimeter are combined to obtain the final estimate of the energy loss [71].

3.11.6. Momentum Measurement

Due to the muon charge, the path it traverses through the ATLAS detector will be bent according to the magnetic field vectors passing through it. The curvature of the tracks in ATLAS can be used to determine muon momentum experimentally. The degree of curvature is dependent on the momentum vector of the muon and is described by the Lorentz force, $\vec{F} = Q\vec{v} \times \vec{B}$.

Taking a simplified case of a homogeneous magnetic field, B, traversed by a charged particle with versine angle, 2θ, the momentum can be calculated by measurement of the sagitta of the particle's arc through the magnetic field. The sagitta of the arc is related to the radius by $s = r(1 - \cos\theta)$, as shown in Figure 3.12.

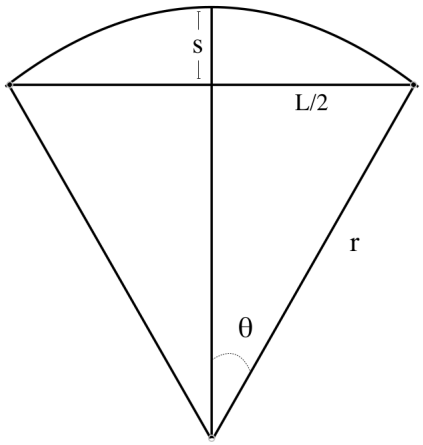

Figure 3.12.: Diagram of the radius of curvature r, length L and sagitta s.

Next, equating the centripetal acceleration and the acceleration of the Lorentz force, the helical radius, r, is given by:

$$r = \frac{p_T}{QB} \tag{3.13}$$

High momentum particles with large arcs relative to the detector will have a small sagitta. The muon trajectory is less curved by the ATLAS detector's magnetic field, and the sagitta measurement, used to calculate p_T, is less precise. The momentum can be determined by assuming a large value r and a small θ, through geometric relationships,

$$p_T = \frac{L^2 QB}{8s} \tag{3.14}$$

The fractional uncertainty on the momentum is proportional to the momentum itself due to the inverse dependence on the sagitta measurement. The arc's curvature is

calculated by reconstructing hits and track segments described earlier. Muon reconstruction algorithms consider the different magnetic field profiles and bending planes acting in the ID and MS subdetectors.

3.11.7. The Tag and Probe Method

The tag and probe method is a data-driven technique used to measure the efficiencies of a selection. Simulations need to be calibrated with data and the tag and probe method provides a way to extract efficiencies from the data. Taking two muons originating from the decay of the same particle have high levels of correlation and allows properties to be inferred from each other. These muons typically are from a Z boson, but other processes, such as J/ψ meson decays, can be used. The decay muons are labelled "tag" and "probe". A tag muon is defined using a series of tight selections ensuring the purity of the $Z \to \mu\mu$ events. The probe muon has very loose selection criteria and is used to measure efficiency [72]. By comparing the efficiencies of data and MC samples, correction scale factors can be determined, which can be applied to the MC to correct mismodelling. The ATLAS Muon Combined Performance group uses the tag and probe method to provide scale factors for the trigger and muon reconstruction efficiencies [69]. The tag and probe method is also used to calculate dedicated scale factors for trigger, isolation and TTVA efficiencies in this analysis, detailed in Section 8.

3.11.8. Reconstruction and Identification Efficiency

After the reconstruction process, high-quality muon candidates for physics analyses are selected based on specific requirements. These requirements include the number of hits in the Inner Detector and the Muon Spectrometer, track fit properties and compatibility of measurements in the two detector systems. Each set of requirements for each muon type is referred to as a selection working point (WP) with multiple WPs are defined to cater to the diverse needs of physics analyses involving muons. These are provied by the ATLAS MCP group [69].

In this analysis, there are two working points defined: "loose" and "tight". For a muon to be considered a loose muon, it must pass the `Medium` selection and have a p_{T} of at least 20 GeV. The lower `Medium` quality is only used for the definition of loose muons that are vetoed. On the other hand, a tight muon must have $p_{\mathrm{T}} > 30$ GeV, be isolated and meet the `HighPt` quality criteria, with the `FCTightTrackOnly_FixedRad` isolation being used. Figure 3.13 displays the reconstruction and identification efficiencies for the `Loose`, `Medium` and `Tight` working points as a function of p_{T}.

The `HighPt` working point is specifically designed for analyses where the muon's transverse momentum is large, typically above a few hundred GeV. It requires a minimum of three hits in three stations of the Muon Spectrometer, which improves the sagitta measurement and enhances the momentum resolution, especially in regions with high p_{T}.

However, there are certain regions in the MS, such as the transition region between the barrel and end-cap with $1.01 < |\eta| < 1.1$, where optimal reconstruction is not possible and muons in this region are vetoed [73].

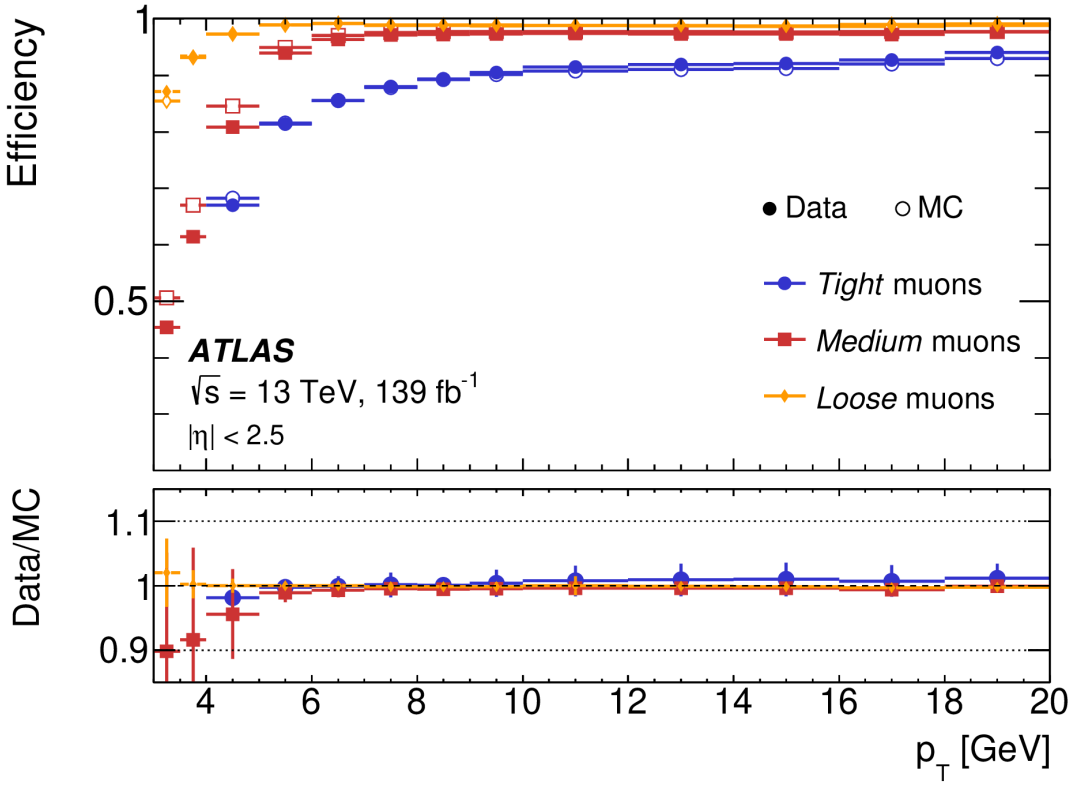

Figure 3.13.: Muon reconstruction and identification efficiencies for the `Loose`, `Medium` and `Tight` criteria. This plot illustrates the efficiencies observed in $J/\psi \to \mu\mu$ events as a function of p_T. Predicted efficiencies are represented by open markers, while the filled markers depict the measurement results obtained from collision data. In cases where the statistical uncertainty in the efficiency measurement is non-negligible, error bars are included. The panel at the bottom presents the ratio of the measured efficiencies to the predicted ones, including statistical and systematic uncertainties [73].

3.12. Electron Reconstruction

Electrons in the ATLAS detector are reconstructed based on their curved tracks, similar to muons. The reconstruction process relies on information from the inner detector, as electrons do not travel beyond the electromagnetic calorimeter. When a relativistic electron passes through matter, it predominantly loses energy through bremsstrahlung. Bremsstrahlung occurs when an electron emits a photon in the presence of the electric field of a nucleus ($e \to \gamma e$). The radiated photon could convert into an electron–positron pair which can then interact with the detector material.

The reconstruction of electrons involves analysing the shape of the energy cluster in the calorimeter and the characteristics of the track in the inner detector, ensuring their

alignment. The process begins by scanning the calorimeter for energy clusters that resemble electrons and then searching for tracks in the inner detector that approximately match the position of the selected cluster in η and ϕ space. A selected track undergoes a secondary fit to the inner detector hits which forms an electron candidate. However, some reconstructed objects labelled as electrons are fakes due to certain physics backgrounds that can mimic similar signals. To improve the purity of the electron sample, identification criteria based on various inner detector track and electromagnetic shower parameters are applied [19, 74].

In Figure 3.14 the electron identification efficiencies for the `Loose`, `Medium` and `Tight` working points are shown as a function of E_T^{miss}. In this analysis electrons were vetoed and therefore not included in the final selection.

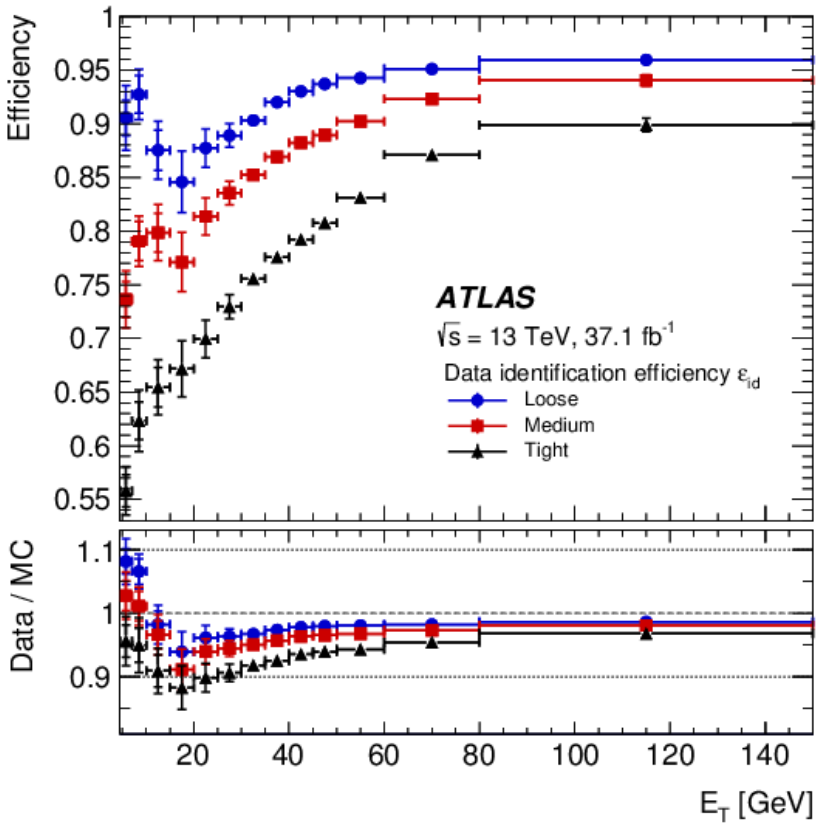

Figure 3.14.: Measured LH electron-identification efficiencies in $Z \to ee$ events for the `Loose`, `Medium` and `Tight` working points are depicted as a function of E_T^{miss}. Vertical bars represent the statistical uncertainties (inner bars) and total uncertainties (outer bars). These data efficiencies are derived by taking ratios between data and simulation efficiencies in $J/\psi \to ee$ and $Z \to ee$ events relative to the $Z \to ee$ simulation. The lower panel displays the data to simulation ratios [74].

Feature	Criterion
Algorithm	Anti- k_t
R-parameter	0.4
Input constituent	EMPFlow
CalibArea tag	00-04-82
Calibration configuration	`JES_MC16Recommendation_Consolidated_PFlow_Apr2019_Rel21.config`
Calibration sequence (Data)	`JetArea_Residual_EtaJES_GSC_Insitu`
Calibration sequence (MC)	`JetArea_Residual_EtaJES_GSC_Smear`
	Selection requirements
Observable	Requirement
Jet cleaning	`LooseBad`
BatMan cleaning	No
p_{T}	> 25GeV
$\lvert\eta\rvert$	< 2.5
JVT	> 0.5 if $p_T(j) \in [20,60]$GeV and $\lvert\eta(j)\rvert < 2.4$ (Tight WP)

Table 3.2.: Summary of the jet reconstruction criteria and requirements.

3.13. Jet Reconstruction

The majority of inelastic proton-proton collisions at the LHC result in the production of quarks and gluons. These collisions do not exist in isolation due to color confinement and the quarks and gluons undergo hadronisation. The results of this are observed as collimated streams of particles that deposit energy in the calorimeters. These energy deposits are reconstructed as jets and provide a representation of the hadronic energy in a collision.

Different use cases require different jet definitions with the resultant jets being calibrated to provide an accurate representation of the event and tagged to understand the jet's likely originating particle. In this analysis, small-R jets for physics results involving quarks and gluons are used. The jet reconstruction process involves defining the input four-vectors and specifying the jet algorithm and parameters.

For the jet reconstruction inputs, ATLAS uses topo-clusters. Topo-clusters are noise-suppressed clusters of calorimeter cells that are grouped topologically. The anti-k_t algorithm [75] is the algorithm typically used for jet reconstruction. Two different distance parameters, R, are used for different purposes. Small-R jets, which represent quarks and gluons, are reconstructed with R= 0.4.

After jet reconstruction, the jets need to be calibrated to account for various effects. The calibration procedure involves suppressing pile-up contributions at the jet level, calibrating the jet to the Monte Carlo truth scale and accounting for differences between MC and data.

Once the jets have been calibrated, their substructure is examined to identify the origin of the jet. This means looking at the angular distribution of energy within the jet, which is useful for distinguishing boosted massive hadronic particle decays from QCD

Parameter	Value
Algorithm	Calo-based
Soft term	Track-based (TST)
MET working point	`Tight`
Calibration tag	`METUtilities/data17_13TeV/prerec_Jan16/`

Table 3.3.: Summary of the E_T^{miss} reconstruction criteria.

dijet/multijet production [76]. The overview of the jets reconstruction criteria and all further requirements are summarised in Table 3.2. These recommendations are set by the ATLAS Jet and Etmiss Combined Performance Group [77].

3.14. Missing Transverse Energy Reconstruction

E_T^{miss} is a important observable as it serves as an experimental proxy for the p_T carried by undetected particles produced in proton-proton (pp) collisions. In order to reconstruct E_T^{miss}, signals from detected particles in the final state are analysed. If a non-zero value is observed, this could be an indicator of neutrinos or new particles predicted by theories beyond the Standard Model. The processs of E_T^{miss} reconstruction relies on all detector subsystems and requires a comprehensive and unambiguous representation of the primary interaction. This is a challenging task due to the limits on detector acceptance and the presence of pileup.

The E_T^{miss} reconstruction involves two contributions shown in Equation 3.6. The first is from hard-event signals which are fully reconstructed and calibrated particles (e.g. electrons, photons, tau-leptons, muons) and jets (the hard objects). Muons are reconstructed from the ID and MS tracks, while electrons and tau-leptons are identified using a combination of calorimeter signals and tracking information. Photons and jets are primarily reconstructed from calorimeter signals, with potential refinements from reconstructed tracks. The second contribution is from soft-event signals. These are reconstructed charged-particle tracks (soft signals) associated with the hard-scatter vertex but not with the hard objects [50].The overview of the E_T^{miss} reconstruction settings used in this analysis are presented in Table 3.3. The `Tight` working point requires that forward jets should satisfy the $p_T > 30$ GeV requirement. These recommendations are set by the ATLAS Jet and Etmiss Combined Performance group [77].

4. Level 1 Calorimeter Validation Code Study

Due to the upgrade of the Level 1 Calorimeter (L1Calo) Trigger of the ATLAS detector, studies need to be undertaken to ensure that a correct simulation is provided for commissioning, monitoring, data quality and reprocessing. This section presents a study on the Level 1 Calorimeter, which was undertaken as part of the ATLAS authorship qualification task. This section uses performance studies of an upgraded L1Calo trigger to create a validation code for the future bitwise simulation of L1Calo. Variables for finding and identifying electrons and photons that take advantage of the upgraded system's higher granularity have been implemented and tested. The results showing the comparison of the different distributions for the samples for the isolation variables investigated have been included in this study.This validation code setup is an essential step towards producing a full bitwise software framework to simulate the upgraded L1Calo system that will go online in Run-3 of the LHC.

4.1. The L1Calo Phase 1 Upgrade

For the upcoming Run-3 at the LHC, components in the ATLAS detector are being upgraded. The instantaneous luminosity delivered by the LHC will increase in the next run. During Run-2 of the LHC, the instantaneous luminosity reached up to $1\text{x}10^{34}$ $\text{cm}^{-2}\text{s}^{-1}$. Run-3 instantaneous luminosity is expected to reach $2\text{x}10^{34}$ $\text{cm}^{-2}\text{s}^{-1}$ and higher [78]. L1Calo in ATLAS is responsible for reducing the trigger rate in custom-built hardware using sophisticated algorithms. The trigger system in ATLAS is being upgraded to cope with the challenges that arise from higher luminosity, such as the increase in the pileup. The upgraded L1Calo trigger system will process digital information from the Liquid-Argon (LAr) Calorimeters and the Tile Hadronic Calorimeter (TileCal) to provide higher granularity, higher resolution and longitudinal shower information from the calorimeter to the trigger processors. The trigger algorithms used in the improved L1Calo will perform better, allowing for improved ATLAS data-taking [79].

ATLAS calorimeters provide the L1Calo trigger with analogue trigger signals independent of those signals provided and used by offline reconstruction software. The calorimeters measure energy deposited in small cells of various sizes down to granularity in $\Delta\eta$ x $\Delta\phi$ of 0.025×0.025. L1Calo uses information from analogue sums in regions

of granularity ranging from 0.1 × 0.1 (central regions) up to 0.4 × 0.4 (forward regions) to form 7168 trigger towers [80]. During the Phase 1 upgrade, the L1Calo system will be provided with inputs with a finer granularity of the calorimeter. The system previously used 7168 towers; however, ~30,000 SuperCells will be used in the upgrade. A SuperCell is a LAr calorimeter region formed by combining E_T from many cells adjacent in η and ϕ. The granularity of the LAr Trigger Tower will increase to ten SuperCells per trigger tower. The segmentation of the SuperCells in the Electromagnetic (EM) calorimeter is shown in Figure 4.1. There will be one SuperCell in Layer 0 and one SuperCell in Layer 3. In Layer 1 and Layer 2, there will be 4 SuperCells in each layer [78].

The upgrade of L1Calo will include three new feature extractors (FEX) subsystems. These are the so-called: Global Feature Extractor (gFEX), Jet Feature Extractor (jFEX) and Electron Feature Extractor (eFEX). This new system architecture has been depicted in Figure 4.2 with new components highlighted in yellow/orange. Each subsystem will use custom-built algorithms to determine physics objects. The eFEX subsystem is designed to identify isolated energy deposits to find electrons, photons and taus. The jFEX performs jet, large-area tau, E_T^{miss} and total-E_T trigger algorithms. The gFEX will be used to identify large-area jets and use global E_T algorithms [78].

In this study, the eFEX subsystem's new output will be used. The eFEX can distinguish electrons from background jets by using the higher granularity discussed previously. An example of a 70 GeV electron, as seen by the existing and upgraded trigger towers, can be found in Figure 4.3. The eFEX has algorithms designed for the longitudinal shower information from an electron shower. An electron will deposit most of its energy in a much narrower area than a jet will and will not have much energy around it, which leads to an isolated energy deposit. The isolated energy deposits can be used to determine an electron. Using algorithms with the new SuperCells designed to determine the isolation and shower shape of the electron for better identification, therefore, allows better reconstruction of objects in the ATLAS trigger and improved physics results. Therefore, different isolation variables must be tested for the best results. These studies contribute to finding the best isolation variable by providing a validation code for the bitwise framework currently under development, which will also test these variables.

4.2. Samples and Objects

Samples with collections of simulated SuperCells from the LAr were used to do studies with the new eFEX algorithm.

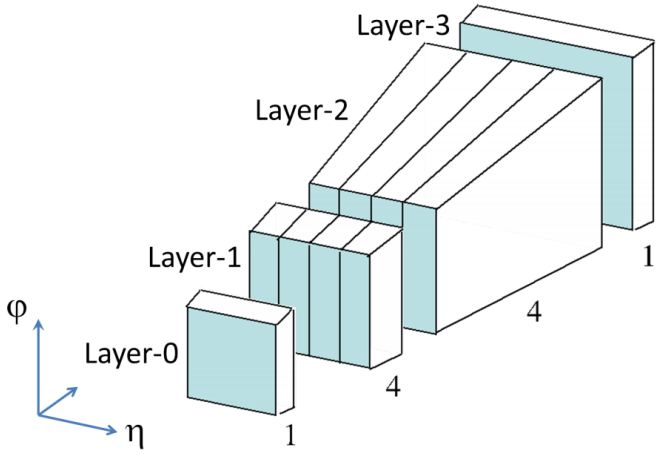

Figure 4.1.: SuperCell configuration in a LAr trigger tower for Run-3 after upgrading the LAr Calorimeter readout/trigger. The dimension of the object depicted in the sketch is 0.1x0.1 in η and ϕ in all layers. Ten E_T values are provided from the ""1-4-4-1"" structure. Layer-0 here corresponds to the pre-scaler [78].

4.2.1. Electron and Dijet Selections

The framework used for writing the validation code for the L1Calo upgrade studies was developed by Will Buttinger.[1]

The Monte Carlo (MC) samples for $Z \rightarrow ee$ were generated using `POWHEG` [81] and `PYTHIA8` [82]. `PYTHIA` is a General Purpose Monte Carlo generator and is a standard tool for high-energy collisions. It provides detailed physics models for the evolution of few-body hard processes to a more complex final state. It is capable of generating hard processes and models for beam remnants, particle decay, initial-and final-state parton showers, multiple parton-parton interactions and string fragmentation [82]. `POWHEG` is a general computational framework. It is used to implement NLO calculations in shower MC algorithms [81]. The MC dijet sample is generated with `PYTHIA8`. The samples are generated in slices of leading jet p_T. The slice used for this analysis corresponds to the events with the lowest leading jet p_T labelled JZ0W. All samples generated contain the old trigger towers and the new trigger towers with SuperCells.

The following Table 4.1 shows the samples used in this study.

Z and Dijet MC Samples	
Process	Sample
$Z \rightarrow ee$	mc15_13TeV.361106.PowhegPythia8EvtGen_AZNLOCTEQ6L1_Zee.recon.AOD.e3601_s2576_s2132_r7380
Dijet	mc15_14TeV.147910.Pythia8_AU2CT10_jetjet_JZ0W.recon.AOD.e2403_s3142_s3143_r10023

Table 4.1.: Table of samples used for L1Calo study.

The following selections have been applied to the electron sample ($Z \rightarrow ee$) and can be seen in Table 4.2. The status code is equal to 1, meaning that stable particles are

[1] This can be found on `GITLAB` at
https://gitlab.cern.ch/l1calo-run3-simulation/validation/L1CaloUpgrade/.

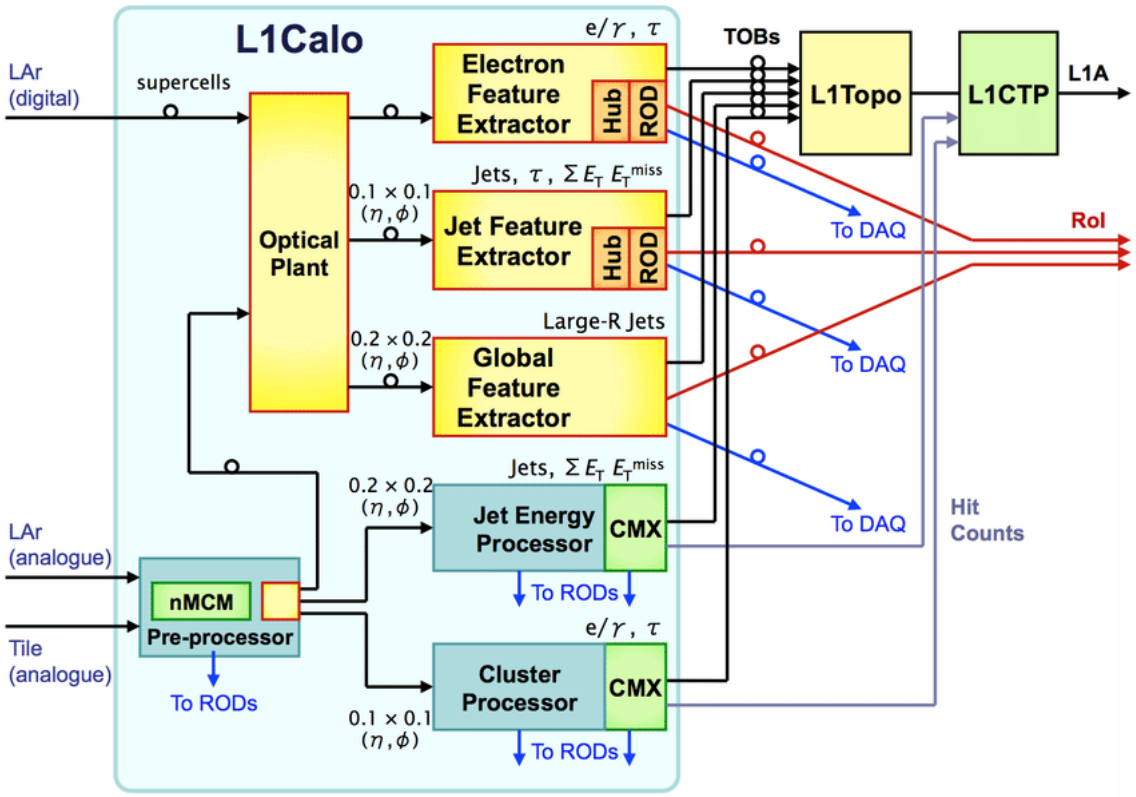

Figure 4.2.: Schematic of L1Calo in Run-3. The new components have been coloured yellow/orange. The old components are shown in green [78].

selected, more specifically it means that particle has long lifetime enough to enter to the detector (interact with material). The PDG ID (Particle Data Group ID) of 11 corresponds to the electron. Kinematic cuts on $p_T > 10$ GeV and $|\eta| < 2.5$ are taken. The electron must also originate from a parent Z particle.

Selection	Requirement
status	1
PDG ID	11
p_T	> 10 GeV
$\|\eta\|$	< 2.5
From Z	True

Table 4.2.: Truth Electron Selections.

A kinematic cut of $p_T > 10$ GeV has been applied to the dijet sample and can be seen in Table 4.3.

The following selections have been applied in the $Z \rightarrow ee$ sample to the Trigger Objects (TOBs) and can be seen in Table 4.4. A trigger object refers to an unspecified particle the trigger has detected. Digitisation allows analogue signals from the calorimeter to be converted into digital signals. The analogue signals come from the trigger towers

Selection	Requirement
p_T	> 10 GeV

Table 4.3.: Truth Dijet Selections.

in the calorimeter. The digitised energies can then be processed into electron, photon, and tau candidates. In Run-2, the preprocessor digitises the energies, allowing the boards to process and store the information efficiently. A 25 MeV cut is taken to match the internal digitisation scale on the hardware. This precision is chosen in the electronics as candidates with energy lower are likely to be fluctuations and uninteresting for physics in ATLAS [83].

Selection	Requirement
digitisation	25 MeV
noise cut per layer	100 MeV

Table 4.4.: Trigger Object (TOB) selections.

Further selections depend on whether the electron or dijet sample is used. For the electron sample, only the electrons which can be matched to the trigger have been included in this study. The L1Calo tower must also have non-zero energy. This cut ensures that only relevant towers with electron energy deposits are included in the study. The momentum of an object in the transverse plane is labelled as p_T and E_T is the transverse energy. A quantity related to the angle of a particle relative to the beam axis is called pseudorapidity η. The selected electrons are required to have kinematic constraints on transverse momentum and pseudorapidity: p_{T} greater than 10 GeV and a detector region with $|\eta| < 2.3$. The transition region between the barrel and end-caps of the electromagnetic calorimeters, $1.375 < |\eta| < 1.52$, is also excluded due to its reduced resolution. Electromagnetic energy deposit found in a cluster of cells in layer 1, layer 2 and η is defined as $E_{\mathrm{T}}^{\mathrm{Clus}}$. A cut on $E_{\mathrm{T}}^{\mathrm{Clus}} > 10$ GeV is included in the selection too.

Selection	Requirement
Trigger Matching	Required
Tower Energy	> 0
p_{T}	$p_{\mathrm{T}} > 10$ GeV
$\|\eta\|$	$\|\eta\| < 2.3$
	($1.375 < \|\eta\| < 1.52$ excluded)
$E_{\mathrm{T}}^{\mathrm{Clus}}$	$E_{\mathrm{T}}^{\mathrm{Clus}} > 10$ GeV

Table 4.5.: Electron selection for the $Z \rightarrow ee$ sample.

The selection of the dijet sample is shown in Table 4.6. The only requirement is to include events in a tower with non-zero energy. This ensures that plots will not contain trigger towers with no trigger objects.

Selection	Requirement
Trigger Matching	Not Required
Tower Energy	> 0
p_T	> 10 GeV

Table 4.6.: Dijet sample selections.

4.3. Analysis Results

4.3.1. Trigger Efficiency

The trigger determines whether to read out or discard the measurements corresponding to each observed interaction for offline analysis. Creating trigger efficiency distributions enables us to find the per electron trigger efficiency for truth and matched electrons. Efficiency, shown in Equation 4.1, denotes the fraction of truth electrons matched to a trigger. The term in the numerator, $N_{p_T^{TOB}}$ represented the number of transverse momentum events matched to a TOB. The term $N_{p_T^{Truth\ Electron}}$ is the number of transverse momentum events matched to a truth election. Here the efficiency being tested is between the truth electrons and between the matched TOBs.

$$\epsilon = \frac{N_{p_T^{TOB}}}{N_{p_T^{Truth\ Electron}}} \tag{4.1}$$

The electron sample also includes a ΔR cut seen in Equation 6.3 for the following Figure 4.4, Figure 4.5 and Figure 4.6. A ΔR cut is no longer included later when looking at the isolation variables, as no cuts on shower width should be included for the latter studies. Multiple values of ΔR were tested to determine which gave the best trigger efficiency distributions and a value of $\Delta R < 0.12$ was determined.

$$\Delta R = \sqrt{\Delta\eta^2 + \Delta\phi^2} \tag{4.2}$$

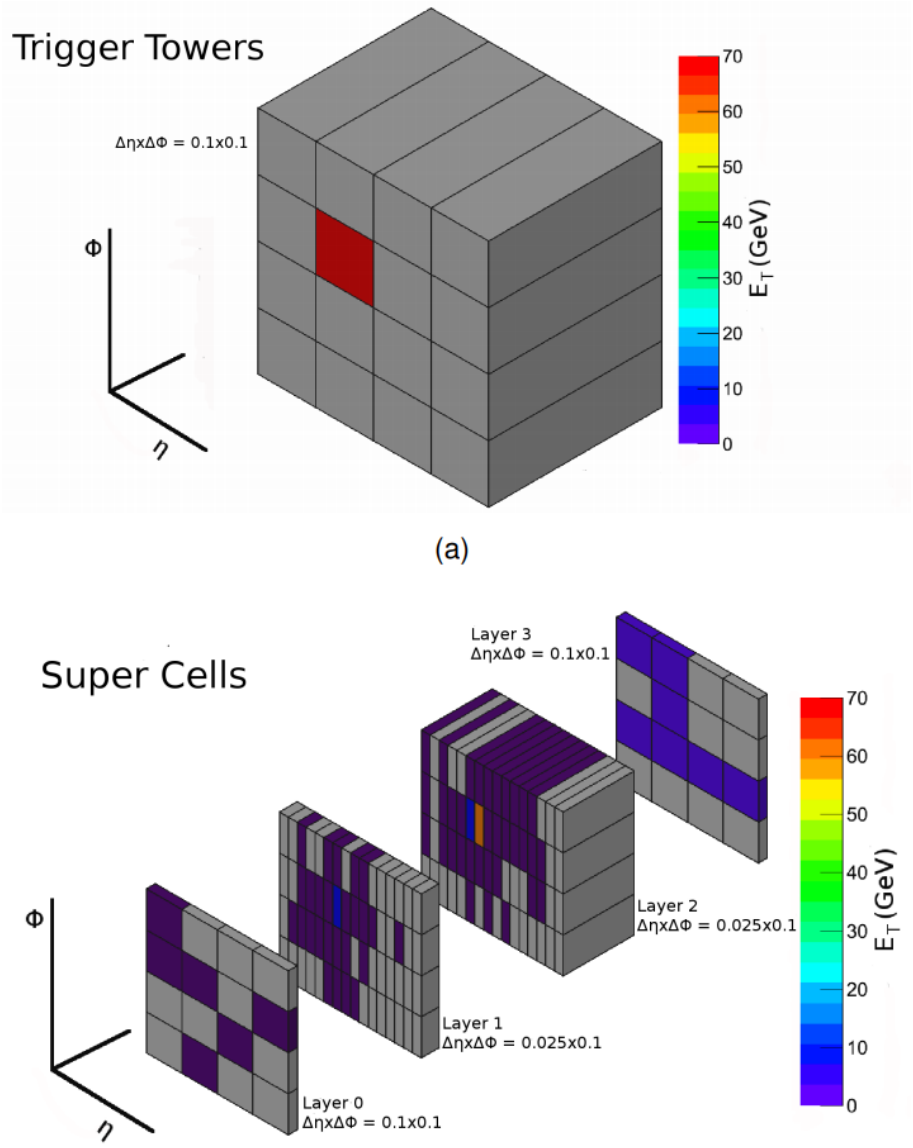

Figure 4.3.: An electron with 70 GeV of transverse energy seen passing through the existing Level-1 Calorimeter trigger electronics (a) and by the upgraded trigger electronics (b) [79].

Figure 4.4 shows the p_T distributions of truth electrons in green and the TOB-matched electrons in red. There is good agreement between the truth and matched TOBs from around $p_T > 40$ GeV shown by the overlapping distributions. Below 40 GeV, there is a separation between the values of p_T.

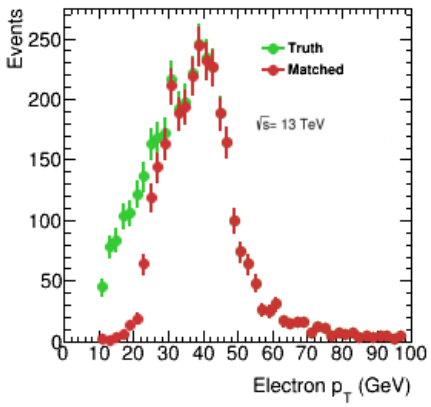

Figure 4.4.: Truth and Matched electron p_T distributions. Truth electrons are in green and the TOB-matched electrons are in red

The trigger efficiency for electron p_T is shown below in Figure 4.5. This takes the two distributions in Figure 4.4 and finds the ratio between them. An efficiency of 50% is reached at ≈20 GeV. An efficiency of ≈100% is reached at $p_T > 40$ GeV. This is also where the efficiency plateau is reached. Therefore, there is a good agreement between truth and matched electrons above this threshold.

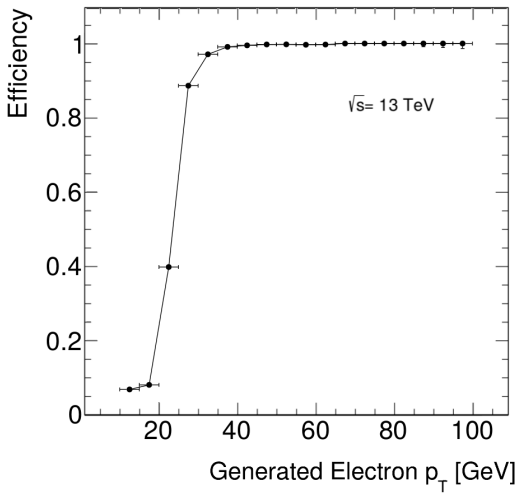

Figure 4.5.: Efficiency of electron sample using the cuts shown in Table 4.5 and $\Delta R < 0.12$. The efficiency is calculated by taking the ratio between the p_T of truth electrons and matched TOBS. Errors have been calculated using the Bayesian Error approach implemented in TGraphAsymmErrors [84].

The trigger efficiency for η is shown below in Figure 4.6. This efficiency is similarly calculated using Equation 4.3. Most points in this distribution are close to 90% effi-

ciency. Therefore, the selection is accurately selecting TOBs which are electrons.

$$\epsilon = \frac{\eta^{TOB}}{\eta^{Truth\ Electron}} \tag{4.3}$$

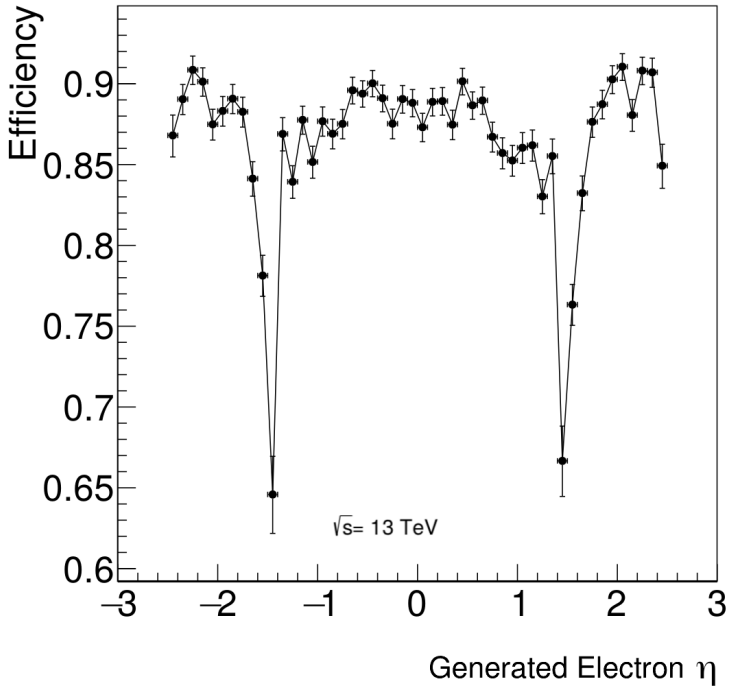

Figure 4.6.: Efficiency of electron sample using the cuts shown in Table 4.5 and $\Delta R < 0.12$. The efficiency is calculated by taking the ratio between the η of truth electrons and matched TOBS.

4.3.2. Isolation Variables

The Phase 1 upgrade L1Calo will result in the trigger tower for Run-3 containing finer granularity due to the Super Cells as shown in Figure 4.1. This enables better shower shape identification. The eFEX module will distinguish between an isolated energy deposit belonging to electrons/photons and other particles. The signature for an electron in the eFEX module is an isolated energy deposit in a narrow shower. Therefore, anything which matches this shape can help to identify it as an electron. In the following sections, two discriminating variables have been used to study their ability to identify electrons. The motivation for studying their performance is their importance in offline electron identification.

4.3.3. Total Shower Width (w_{stot})

The first variable which has been studied is the Total Shower Width (w_{stot}) shown in Equation 4.4.

$$\mathrm{w_{stot}} = \sqrt{\frac{\sum E_{\mathrm{T},i}\left(\eta_i - \eta_{\mathrm{max}}\right)^2}{\sum E_{\mathrm{T},i}}}, \eta_{\mathrm{max}} \rightarrow most\ energetic\ SC\ in\ Layer1 \tag{4.4}$$

The w_{stot} distribution is calculated in the first layer of the EM calorimeter, which can be seen in Figure 4.1. A window uses 15 Super Cells in a 5x3 Super Cell configuration. This window is seeded by taking the Super Cell with the most energy in Layer-1 and making it the central cell. w_{stot} is the energy-weighted average eta distance of the cells in the window from the seed cell. In the denominator of this equation, the sum of the transverse energy (E_T) is taken over 5 Super Cells in η. A sum over the ϕ index is also taken, taking the 5 Super Cells in ϕ + 1 and 5 Super Cells in ϕ - 1. The η of the Super Cell with the most significant energy deposit is called η_{max}. The numerator uses η_{max} by weighting the E_T with the difference between the η_{max} value and the η_i that is currently being summed over. A small value of w_{stot} will indicate a smaller shower width and vice versa. As the electron produces a narrow shower, w_{stot} will be expected to be small.

Using the samples and cuts listed in Section 4.2, the plot in Figure 4.7 shows a normalised histogram with the values of w_{stot} in the $Z \rightarrow ee$ sample and compares it to w_{stot} in a dijet sample. The peak of the electron sample (≈0.01) is lower than that of the dijets (≈0.02). The width of each histogram also shows that the dijets sample has a greater range of w_{stot} values. Therefore, as expected, w_{stot} for electrons will be smaller than for jets, so w_{stot} may improve the separation between electrons and hadronic jets.

The electron curve in Figure 4.7 has an increase in events around the 0.025 regions. This is an artefact of the area used to calculate w_{stot} as the width of a SuperCell is 0.025. Therefore, this is a boundary artefact but should still be studied further. Another bump is visible at 0.05, which is also indicative of a boundary effect as it correlates to the combined width of two supercells.

To see how the w_{stot} distribution changes and how well Layer 2 can be used to identify electrons, distributions of a modified w_{stot} variable calculated from Super Cells in Layer 2 have also been included. Electrons deposit energy in a narrower shape than jets. This will be different in Layer 1 and Layer 2. The comparison between w_{stot} in Layer 1 and Layer 2 will indicate how much a shower changes via depth. This histogram has been plotted in Figure 4.8. Compared to Layer 1, the peaks in the distribution for both electrons and jets have moved to larger values representing an increase in shower widths in Layer 2. The shape of each distribution is similar to Layer 1, and as expected, the electrons have smaller shower widths compared to jets.

To create these plots, three new methods have been added to the validation framework code: getCentralL1Cell(), wstotL1() and wstotL2(). The first method, GetCentralL1Cell(), is used for seeding the w_{stot} equation and returns the index of the strip with the greatest E_T when looking in a window of 5x5 Super Cells. The methods wstotL1() and wstotL2() each return the value of w_{stot} using getCentralL1Cell() or getCentralL2Cell() respectively.

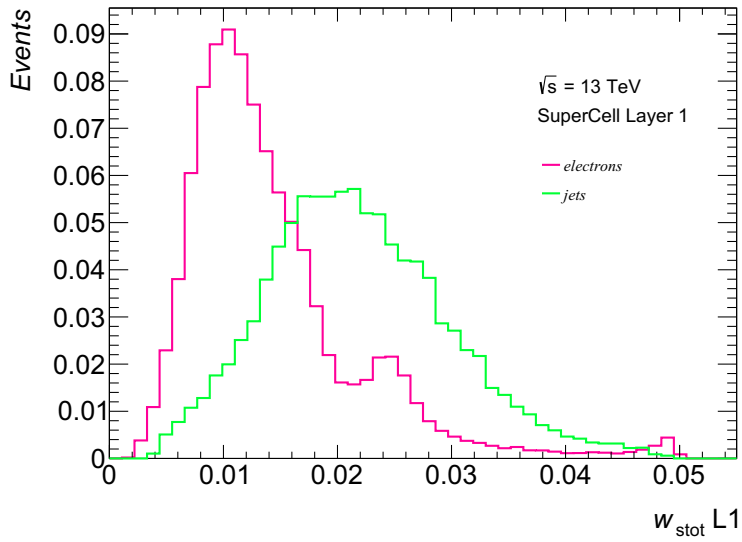

Figure 4.7.: Normalised distribution of w_{stot} in Layer 1. The $Z \rightarrow ee$ sample is shown in pink and the Dijet sample in green.

A minor adjustment was needed in the function used to obtain the central cell. When no energy was found in the cells, it would set the index of the central Super Cell as 0. However, these should be excluded from the w_{stot} calculation. This was fixed by setting the initial index as a negative number and then excluding any events with a negative index in w_{stot}.[2]

4.3.4. f_3

EM showers are typically shorter than hadronic showers, which can be observed in the calorimeters by the different shower shapes. The second isolation variable studied is f_3 which measures the longitudinal shower leakage. It takes the ratio of E_T measured in Layer 3 to the E_T measured in all layers, see Equation 4.5. The peak of the energy deposition for EM showers is earlier, typically in the fine-granulated layers (1,2). For EM showers, f_3 is expected to be closer to 0 than for hadronic distributions.

$$f_3 = \frac{E^{(3)}_{\mathrm{T},\Delta\eta\times\Delta\phi=0.1\times0.2}}{E^{(0)}_{\mathrm{T},\Delta\eta\times\Delta\phi=0.1\times0.2} + E^{(1)}_{\mathrm{T},\Delta\eta\times\Delta\phi=0.075\times0.2} + E^{(2)}_{\mathrm{T},\Delta\eta\times\Delta\phi=0.075\times0.2} + E^{(3)}_{\mathrm{T},\Delta\eta\times\Delta\phi=0.1\times0.2}} \tag{4.5}$$

The E_T in the front and back EM layers (Layer 0 and Layer 3) is measured in an area of size $\Delta\eta \times \Delta\phi = 0.1 \times 0.2$. The E_T in the middle EM layers (Layer 1 and Layer 2) is measured in an area of size $\Delta\eta \times \Delta\phi = 0.075 \times 0.2$. For electrons, as their signature has a smaller shower length, there is expected to be little shower leakage, so compared to jets should have a typically narrower distribution and peak at lower values.

[2]This fix can be found at https://gitlab.cern.ch/l1calo-run3-simulation/validation/L1CaloUpgrade/tree/jesal-dev-branch.

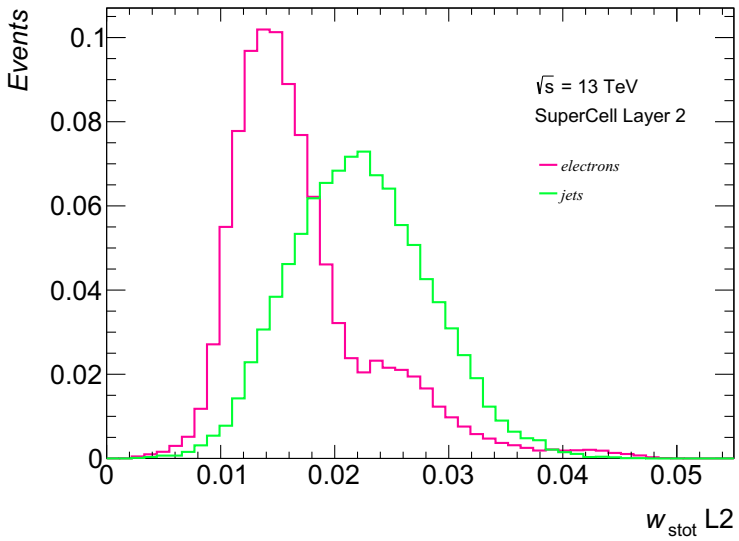

Figure 4.8.: Normalised distribution of w_{stot} in Layer 2. The $Z \rightarrow ee$ sample is shown in pink and the dijet sample in green.

Using the samples and cuts listed in Section 4.2, the following plot in Figure 4.9 shows a normalised distribution of f_3 in a $Z \rightarrow ee$ sample and compares it to f_3 in a dijet sample. The peak of the electron sample is lower than for jets and the distribution of the events is also narrower as expected. Therefore, by taking a cut at small f_3, this isolation variable can improve the separation between electrons and hadronic jets.

This plot has a strange shape in the distribution of the jet, specifically the lack of events around 0 and the peak at around 0.5. A possible explanation raised for further study is that the dijet and Z samples could have a different pileup profile. This can be easily checked but was only noticed once plots were produced and the study completed.

Again a new method has been added in the validation code framework, in this case, $f3()$. The function $f3()$ will return the value of f_3. It utilises the methods already included, emClus1331() and getEnergy(). It was essential to take note of the window being looked at and ensure the correct cells were used. In f_3, Layer 2 is used to determine the seeding and GetCentralL2Cell() is used to find which strip will be used as the centre of the window. In order to get the correct ϕ value, this central strip is used. The E_T directly above and below the central ϕ is checked and whichever is largest is taken to form the window, which will be used to calculate f_3.

4.4. Next steps

The work presented here will be used as validation for the offline bitwise framework. Therefore, the following steps will be to implement the isolation variables detailed in this study into the offline bitwise framework. This will begin by creating an algorithm

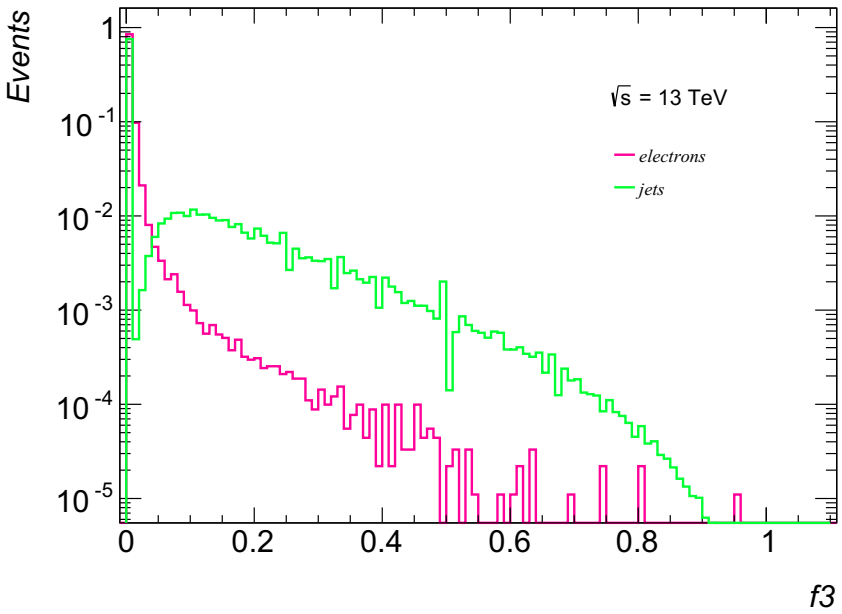

Figure 4.9.: Normalised distributions of f_3. The $Z \rightarrow ee$ sample has been shown in pink and the dijet sample in green.

with the correct seeding for the variables needed. Once this is complete, the isolation variables will also be implemented into the code. The results from here and the future offline bitwise simulation will then be used for comparison and further studies.

5. Data and Monte Carlo Samples

The following chapter describes the Data and Monte Carlo (MC) samples used. First, the data samples chosen are given. The second part lists the MC samples, explains why Monte Carlo is used for the study in the up-coming chapters, the event generators, signal and backgrounds and how different kinematic regions have been combined. Data and Monte Carlo samples were both reconstructed using the ATLAS Athena software [85]. A list of all samples for Data can be found in Appendix A.1 and Monte Carlo in Appendix A.2 and Appendix A.3.

5.1. Data Samples

The datasets used for this thesis are from LHC Run-2 collected between 2015 and 2018. ATLAS collected 139 fb^{-1} of luminosity for pp collisions at 13 TeV centre-of-mass energy with 25 ns bunch spacing. The data used correspond to head-on proton-proton collisions. The time unit in which ATLAS luminosity data is recorded is called a Luminosity Block (LB). It is a 30-second interval where the instantaneous luminosity and detector conditions should remain constant. Data for physics measurements will not be selected for analysis if the LHC is not in stable beam mode, magnets are off or ramping, sub-detectors are switched off/other problems or if there are too many noisy cells. The Good Runs List (GRL) specifies which sets of "good" luminosity blocks should be used. The ATLAS data quality group provides this information via the Good Run Lists [86]. This ensures the data had stable LHC collisions and ATLAS component operations.

Figure 5.1 shows the total integrated luminosity and data quality for 2015-2018. The figure shows LHC delivered luminosity in green. Luminosity recorded by ATLAS is shown in yellow. The luminosity certified to be all good data quality is in blue. When instantaneous luminosity increases, the mean number of particle interactions per bunch-crossing increases, called pileup. Table 5.1 and Figure 5.2 show the pileup for each data-taking year. The pileup corresponds to the Poisson distribution of the number of interactions per crossing calculated for each bunch. The following equation shows the calculation of pileup from instantaneous luminosity per bunch:

$$\mu = \frac{\mathscr{L}_{bunch} \cdot \sigma_{inel}}{f_r} \tag{5.1}$$

$\mathscr{L}_{bunch}$ is the instantaneous luminosity per bunch, σ_{inel} is the total inelastic pp cross

section at $\sqrt{s}$ = 13 TeV, taken to be 80 mb and f_r is the LHC revolution frequency [87].

During the different data-taking years, there were changes in the detector and the beam conditions. These changes were due to differences in the pileup and instantaneous luminosity delivered during a run. The backgrounds and trigger rates increased with these changes. Therefore, different triggers were necessary to ensure good data taking and account for the increase in instantaneous luminosity in different years due to the changes in conditions. Table 5.2 shows the different muon triggers used. More details on the triggers are in Section 6.1.4.

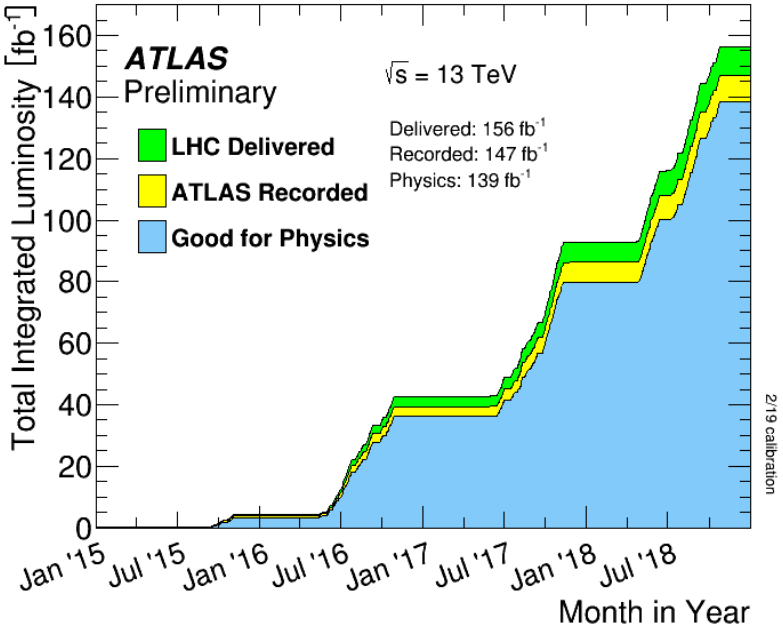

Figure 5.1.: Total integrated luminosity and data quality in 2015-2018. Cumulative luminosity versus time delivered to ATLAS (green), recorded by ATLAS (yellow), and certified to be good quality data (blue) during stable beams for pp collisions at 13 TeV centre-of-mass energy in 2015-2018 [87].

Pileup for Data Years			
Year	Runs	$<\mu>$	Peak $\mathscr{L}_{inst}$ cm^{-2}s^{-1}
2015	266904-284484	13.4	$5 \cdot 10^{-33}$
2016	296939-310216	25.1	$13.80 \cdot 10^{-33}$
2017	324839-341649	37.8	$20.90 \cdot 10^{-33}$
2018	348885-364292	36.1	$21.00 \cdot 10^{-33}$

Table 5.1.: Table for data years 2015-2018 showing run numbers, average pileup, and ATLAS recorded luminosity. The first column indicates the data-taking year. The second column corresponds to the run numbers for each year. The third column gives the mean number of pileup interactions. The fourth column gives the total integrated luminosity collected in each year.

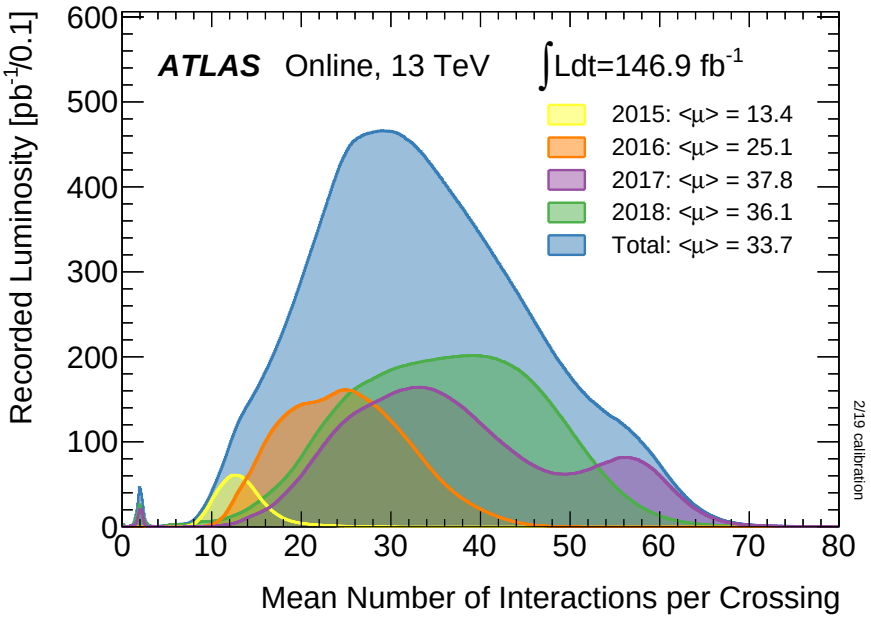

Figure 5.2.: Luminosity weighted distribution of the mean number of interactions per crossing for 13 TeV data from 2015-2018. Only ATLAS data recorded during stable beams are shown. The integrated luminosity and the mean $< \mu >$ value are also shown [87].

Triggers for Data Years			
Year	Runs	Trigger	$\mathscr{L}_{int}$ fb^{-1}
2015	266904-284484	`mu_20iloose` or `mu_50`	3.2
2016	296939-310216	`mu_26ivarmedium` or `mu_50`	36.1
2017	324839-341649	`mu_26ivarmedium` or `mu_50`	46.9
2018	348885-364292	`mu_26ivarmedium` or `mu_50`	60.6

Table 5.2.: Table for 2015-2018 data showing run numbers, triggers and ATLAS recorded luminosity. The first column indicates the data-taking year. The second column corresponds to the run numbers for each year. The third column gives the high-level trigger chain used for trigger algorithms to record the events used in this analysis. The fourth column gives the total integrated luminosity collected in each year.

5.2. Monte Carlo Samples

5.2.1. Motivation For Monte Carlo Use

In high-energy physics, data collected from experiments is distorted by the experiment itself, so extracting the underlying physics from this distortion is essential. From the detector standpoint, all known detector effects, such as detector acceptance from the construction and physical properties of the detector, must be distinguished and well-controlled. These effects are considered the "folded" reconstructed distribution and need to be "unfolded" to provide MC at the generator level with none of these effects to give a generalised result. Therefore, once these effects have been included in the simulation, the MC can predict backgrounds and unfold the data. From the theoretical

standpoint, all known physics effects must be included in predictions. These physics effects are the best perturbative predictions, underlying event models, FSR and ISR effects, and hadronisation effects etc. Additionally, unfolded data and theory can be compared to determine the effects of new physics [88].

The ATLAS experiment distorts and biases the data recorded. Acceptance describes the coverage of the detector kinematically and geometrically. The detector has gaps and holes where acceptance is low. Imperfect resolution smears measured particles momenta. Detector misalignments can translate into momentum mismeasurements etc. A simulation is used to model these effects. Further refinements of the distortions are provided by offline corrections known as "Scale Factors", which fine-tune the efficiencies and resolutions of reconstructed MC into an agreement with data. This is the "distortion model" of ATLAS. Once known, it is used to unfold the data or perform background subtractions.Therefore, it is important to have a simulation that combines the physics of proton-proton collisions and the detailed detector response of ATLAS to the collision products as they propagate through the detector to record these collisions.

The Monte Carlo method is used to generate theoretical event-level simulations. Monte Carlo methods are a practical way to evaluate multi-dimensional phase-space using random sampling techniques integrals or to simulate on an event-by-event basis. Monte Carlo simulation uses a random number generator that takes individual events and determines their kinematic properties according to normalised multi-differential kinematic cross-sections. After the kinematics of an event have been determined, the final states are "convolved" with the ATLAS detector through hit simulation using responses from multiple scattering probabilities and cell/pixel/drift tube. This process is repeated many times to create a Monte Carlo sample that is statistically significant [89].

The Monte Carlo generator combined with a simulation of the particle detector creates predictions for particle physics experiments. However, the detector simulation will not account for all detector effects, e.g. some dead channels in a subdetector mid-way through the run will not be simulated directly and could lead to unsimulated loss of efficiency or deteriorated resolution. Scale factors can be used to correct some mismodelling through smearing and reweighting. Therefore, Monte Carlo simulation can predict LHC collisions at the ATLAS detector. Monte Carlo samples were used here to model the signal and background yields expected, calibrate the detectors and search for new physics.

An alternative to using Monte Carlo simulation to determine background yields is data-driven background estimates. Data-driven backgrounds are used as a cross-check where the simulation is thought to be unreliable or if the event selection selects a small contribution of a much larger background process cross-section, e.g. for multijet production.

5.2.2. Monte Carlo Generators

The event generator used in this analysis is POWHEG [81], PYTHIA [82] is used as a shower/hadronisation generator and a precision tool for photon corrections is PHOTOS [90].

POWHEG (Positive Weight Hardest Emission Generator) interfaces parton-shower Monte Carlo generators to calculate next-to-leading order (NLO) matrix elements for QCD computations. In the POWHEG method, the hardest radiation is first generated in a technique that yields only positive weighted events using exact NLO matrix elements. The POWHEG output is then interfaced to any shower Monte Carlo program, which is p_T-ordered (highest to lowest p_T) or has a p_T veto. The samples generated in this analysis use PYTHIA8 for the shower and hadronisation process [81, 91].

PYTHIA8 is a general-purpose Monte Carlo generator capable of modelling hadron-hadron, hadron-lepton and lepton-lepton events and is a standard tool for high-energy collisions. PYTHIA8 provides detailed physics models for an evolution of a few-body hard processes to a more complex final state. It can generate hard processes and models for beam remnants, particle decay, initial and final-state parton showers, multiple parton-parton interactions, and string fragmentation. Generation starts with a hard scattering process calculated to the lowest order in QCD. Additional QCD and QED radiation are added in a shower approximation. PHOTOS is commonly used with PYTHIA to generate QED radiative effects in W decay events. This analysis uses PYTHIA8 only for the underlying event and hadronisation. The underlying event is any particle production not associated with the leading hardest parton-parton process [82].

PHOTOS generates precision QED radiative corrections for final-state charged leptons. Bremsstrahlung radiation is included in the output events from a Monte Carlo generator. For this analysis, POWHEG handles the matrix element and parton shower, then PYTHIA8 dresses the event with the underlying events, and finally, PHOTOS handles QED ISR/FSR. PHOTOS takes the output from POWHEG and PYTHIA8 and includes photon radiation by reshuffling momenta of particles, ensuring that momentum is conserved and that the cross-section is preserved. The output constitutes the full generator-level information where all particles and their parent/child decay chains are known. This can be used to provide theoretical fiducial predictions for signal processes [90].

The next step in the Monte Carlo generation is to ensure an accurate simulation of the ATLAS detector. This is provided by GEANT4, a tool for the simulation of the passage of particles through matter. This includes a detailed description of all detector volumes, materials and geometry. GEANT4 uses this to trace particles from the generator level and model their interactions with the detector material. All Monte Carlo sample production was processed using the full simulation of ATLAS in GEANT4 [92].

The conditions for data collection varied between 2015-2018 because of changes in the detector and beam conditions. The MC simulation needs to account for changes, so different production campaigns are needed. For 2015 and 2016, campaign *a* is used,

Process	Matrix Element	Parton Shower/ Hadronisation	Event Tune
$W \to \mu\nu$	POWHEG-BOX	PYTHIA8	AZNLOCTEQ6L1
$t\bar{t}$	POWHEG-BOX	PYTHIA8	A14
single top	POWHEG-BOX	PYTHIA8	A14
$Z \to \mu\mu$	POWHEG-BOX	PYTHIA8	AZNLOCTEQ6L1
$Z \to \tau\tau$	POWHEG-BOX	PYTHIA8	AZNLOCTEQ6L1
Diboson	SHERPA	SHERPA	-
$W \to \tau\nu$	POWHEG-BOX	PYTHIA8	AZNLOCTEQ6L1

Table 5.3.: Event Generation for each MC process used. The first column shows the process. The second column depicts the matrix element used. The next two columns show the parton shower or hadronisation used and the corresponding event tune.

2017 campaign *d* and 2018 campaign *e*. These campaigns will be referred to as MC16a, MC16d and MC16e. When complete, the output of the MC is in the same format as data from the real detector, in addition to the truth info and relations between the simulated and truth particles.

A generator-level or particle-level simulation refers to a simulation without detector effects. There are three truth level definitions: Born level, Bare level, and Dressed level. Born-level leptons are leptons before QED Final State Radiation (FSR). Bare-level leptons are leptons after QED FSR. Dressed-level leptons involve a cone or a jet algorithm to cluster photons around the direction of the bare lepton. This creates a lepton after partial QED radiation. Dressed leptons are used for complex topologies which involve multiple objects in the final state, e.g. leptons and jets. The Born and Dressed levels provide observables appropriate for intermediate states like single W or Z and are used for comparison with theory predictions [93].

Event generators when dealing with soft, non-perturbative QCD effects are at their least predictive when their modelling deals with asymptotic behaviours. When extrapolating to more typical conditions parameters are introduced whose values are determined by comparison to data. The process of parameter optimisation is referred to as "tuning" and is based on experimental data from previous colliders which have now been tuned to ATLAS data. The tunes are parameters adjustments that describe multiple parton interactions of the underlying event for the LHC. Different sets of them try to do this in different ways [94].

The detector and physics simulation are combined to give a prediction of the signal $W \to \mu\nu$ and background events in ATLAS.

5.2.3. Signal and Background Monte Carlo

The experimental signature for W production is one muon with missing energy from the neutrino shown in Figure 5.3. However, various processes may mimic a W boson and must be accounted for. These backgrounds are $t\bar{t}$, single top, diboson, $W \to \tau\nu$,

$Z \to \mu\mu$ and $Z \to \tau\tau$. The event generation used is listed in Table 5.3. The signal sample $W \to \mu\nu$ was simulated using POWHEG with the CT10 PDF set and PYTHIA 8.2 for parton shower, hadronisation and the AZNLOCTEQ6L1 tune to include models for simulating the underlying event. For QED final state radiation (FSR) PHOTOS is used to simulate photon radiation after collisions. Background processes also use POWHEG and SHERPA for generating the hard scatter and PYTHIA and SHERPA for the hadronisation.

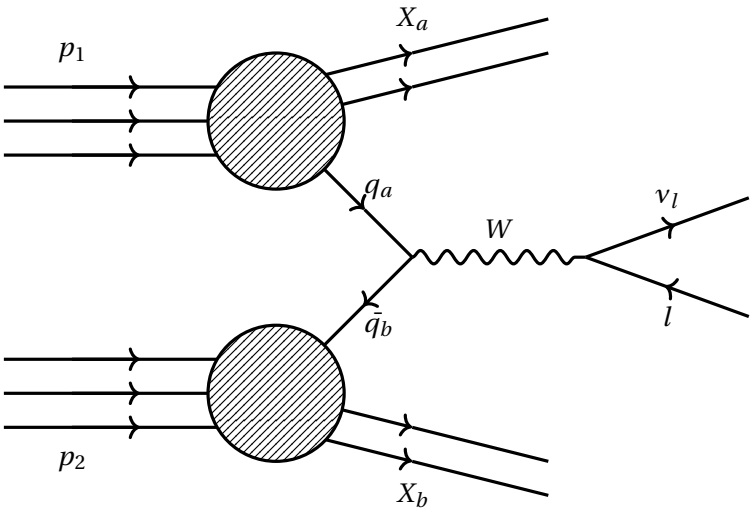

Figure 5.3.: Feynman diagram showing $W \to \mu\nu$ process.

Monte Carlo Signal

The Monte Carlo was generated using 19 mass thresholds (120 GeV, 180 GeV, 250 GeV, 400 GeV, 600 GeV, 800 GeV, 1000 GeV, 1250 GeV, 1500 GeV, 1750 GeV, 2000 GeV, 2250 GeV, 2500 GeV, 2750 GeV, 3000 GeV, 3500 GeV, 4000 GeV, 4500 GeV, 5000 GeV). An inclusive sample was also generated, including the resonant peak region. These will be referred to as the mass slices and the peak sample. Mass slices at the invariant dilepton mass at Born level for W production give better statistical precision and modelling in high invariant mass regions. Mass slices are all generated under identical settings for hadronisation, parton showers, underlying event and QED FSR.

A cut is taken on the peak sample for $M_W < 120$ to avoid double counting the cross-section between the peak and high mass slices. A smooth continuous distribution can be recovered after the luminosity weighting is performed. The equation used for the luminosity weighting follows in Equation 5.2:

$$LumiWeight = \frac{MCWeight \cdot \mathscr{L}_{Data} \cdot \sigma_{MC}}{SumofWeights} \tag{5.2}$$

$$
\begin{aligned}
TotalEventWeight &= LumiWeight \cdot TruthWeight \cdot RecoWeight \\
TruthWeight &= k-Factor \cdot Pileup \\
RecoWeight &= ScaleFactors
\end{aligned}
\tag{5.3}
$$

$MCWeight$ is the Monte Carlo event weight given by the event generator, which has a value of ± 1. This weight avoids double counting QCD ISR in the NLO matrix element and the NLO parton shower since any gluon emission at NLO could arise from either part of the calculation [95].

$\mathscr{L}_{Data}$ is the integrated luminosity of the data year/s and is used to scale the Monte Carlo events to represent the number of events expected in data.

σ_{MC} is the cross-section of the Monte Carlo sample. The cross-section σ is taken from ATLAS Metadata Interface (AMI) [96].

$SumofWeights$ is given by the event generator. A different number of weighted events are used to generate each sample. The number of events generated gives the statistics of the sample or how much fluctuation is seen in each bin due to the random Monte Carlo generation. However, a weight is needed to scale the samples to compare the actual size of the Monte Carlo sample to other samples. Therefore, the sum of event weights for all events produced by the generator is used to normalise the events [97].

The $TruthWeight$ includes the $k-Factor$ weight and the $Pileup$ weights. Often higher-order perturbative calculations have better theoretical accuracy than those used in the Monte Carlo generation. To include the best theoretical knowledge in Monte Carlo, a $k-Factor$ weight from higher-order calculations is used. This is defined in Equation 5.4. The $k-Factor$ corrects for the ratio of the NNLO to NLO or, in some cases, the NLO to LO cross-section for a given sample.

$$
k_{\text{Factor}}\,(m) = k_{QCD} \cdot k_{EW} \tag{5.4}
$$

k_{QCD} is the QCD correction and is the ratio of the NNLO to the NLO or LO cross-section. k_{EW} is the electroweak correction which is the LO electroweak correction matched with NLO corrections. The k-Factor is mass dependent and varies with the mass of W and Z bosons. The `LPXKfactorTool` [98] is used for the k-Factor calculations. The CT10 NLO PDF is corrected to the prediction from the CT14 NNLO PDF and NLO EW corrections are applied. The average k-Factor values for each sample are shown in Table 5.4. For the diboson and top process, the k-Factor value is fixed. Figure 5.4 also shows the average k-Factor values as a function of transverse mass m_T^W, transverse momentum p_T^μ and pseudorapidity η^μ.

The $Pileup$ is the weight that shifts the MC distribution to match the different pileup conditions in each data-taking year shown in Figure 5.1. $ScaleFactors$ are used to correct the MC to describe all relevant efficiencies as measured from the data. This in-

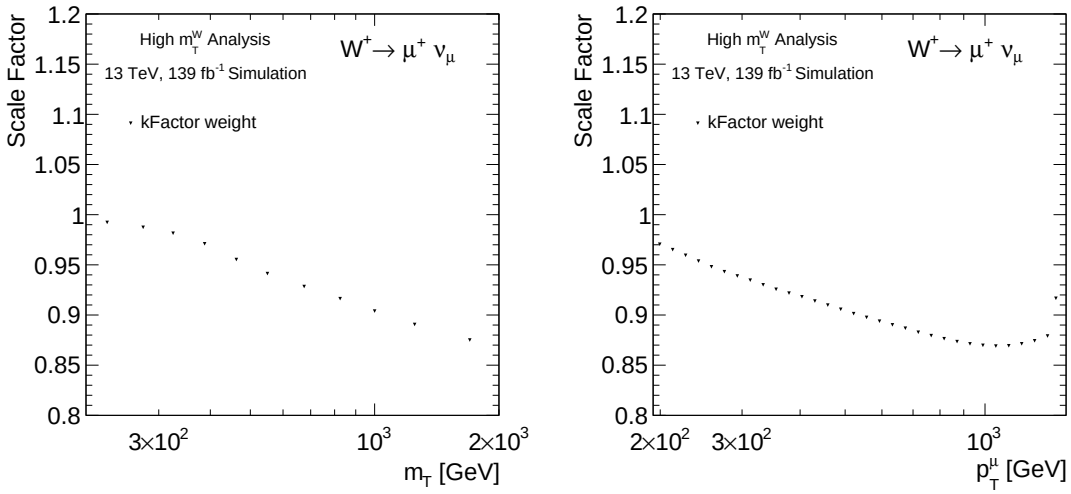

(a) (b)

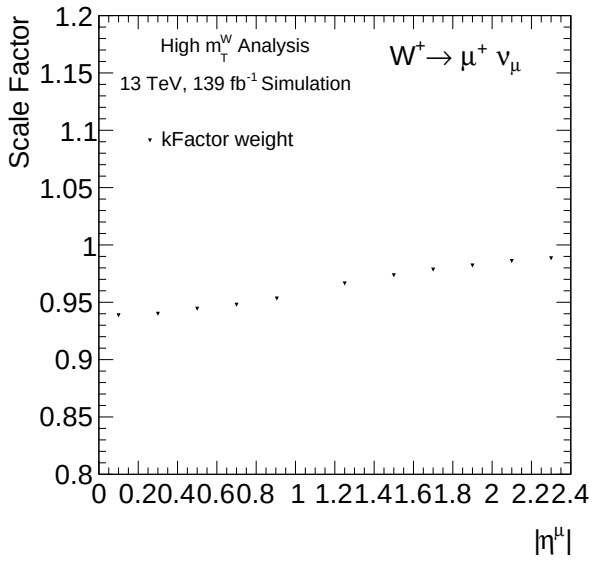

(c)

Figure 5.4.: Scale factor plots for average k-Factor efficiency. These plots are for $W^+ \rightarrow \mu^+ \nu$ for the combination of Monte Carlo campaigns, MC16a, MC16d, and MC16e. The plots show average k-Factor as a function of transverse mass m_T^W (a), transverse momentum p_T^μ (b) and pseudorapidity $|\eta^\mu|$ (c).

cludes a correction to the trigger, isolation, identification and reconstruction. More discussion on the scale factors is in Chapter 6. Table 5.4 lists the individual mass slice MC samples for W^+ and W^- with relevant information for the normalisation process [99].

Figure 5.5 shows the truth invariant mass distribution for $W \rightarrow \mu\nu$ at the Born level after the $TotalEventWeight$ has been applied to all samples. The smooth shape of the distribution shows that the different mass slices have been normalised correctly.

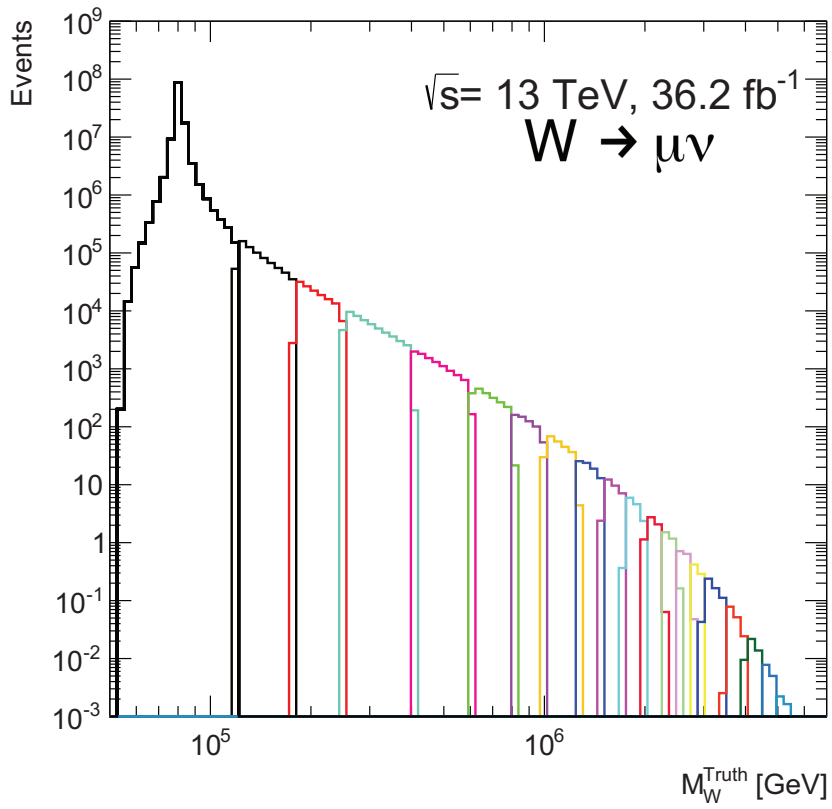

Figure 5.5.: Born generator level invariant mass distribution for MC16a showing each mass slice for $W \rightarrow \mu\nu$. The coloured lines represent the different mass slices. Black represents the peak region. The plot below gives the ratio between the sum of the inclusive peak region and the high mass slices.

DSID	Process & Mass Threshold [GeV]	σ [pb]	N_{evt}	k-Factor
361101	$W^+ \to \mu^+\nu$	11306	39962000	1.02
301100	$W^+(120,180) \to \mu^+\nu$	32.06	500000	1.01
301101	$W^+(180,250) \to \mu^+\nu$	5.0034	250000	$9.97 \cdot 10^{-1}$
301102	$W^+(250,400) \to \mu^+\nu$	1.7546	150000	$9.90 \cdot 10^{-1}$
301103	$W^+(400,600) \to \mu^+\nu$	0.3124	100000	$9.79 \cdot 10^{-1}$
301104	$W^+(600,800) \to \mu^+\nu$	0.0608	50000	$9.64 \cdot 10^{-1}$
301105	$W^+(800,1000) \to \mu^+\nu$	0.0177	50000	$9.49 \cdot 10^{-1}$
301106	$W^+(1000,1250) \to \mu^+\nu$	0.0073	50000	$9.32 \cdot 10^{-1}$
301107	$W^+(1250,1500) \to \mu^+\nu$	0.0025	50000	$9.13 \cdot 10^{-1}$
301108	$W^+(1500,1750) \to \mu^+\nu$	0.0010	50000	$8.96 \cdot 10^{-1}$
301109	$W^+(1750,2000) \to \mu^+\nu$	0.0004	50000	$8.81 \cdot 10^{-1}$
301110	$W^+(2000,2250) \to \mu^+\nu$	0.0002	50000	$8.68 \cdot 10^{-1}$
301111	$W^+(2250,2500) \to \mu^+\nu$	$9.3300 \cdot 10^{-5}$	50000	$8.58 \cdot 10^{-1}$
301112	$W^+(2500,2750) \to \mu^+\nu$	$4.6256 \cdot 10^{-5}$	50000	$8.51 \cdot 10^{-1}$
301113	$W^+(2750,3000) \to \mu^+\nu$	$2.3473 \cdot 10^{-5}$	50000	$8.47 \cdot 10^{-1}$
301114	$W^+(3000,3500) \to \mu^+\nu$	$1.8447 \cdot 10^{-5}$	50000	$8.48 \cdot 10^{-1}$
301115	$W^+(3500,4000) \to \mu^+\nu$	$5.0963 \cdot 10^{-6}$	50000	$8.63 \cdot 10^{-1}$
301116	$W^+(4000,4500) \to \mu^+\nu$	$1.4305 \cdot 10^{-6}$	50000	$8.95 \cdot 10^{-1}$
301117	$W^+(4500,5000) \to \mu^+\nu$	$4.0124 \cdot 10^{-7}$	50000	$9.43 \cdot 10^{-1}$
301118	$W^+(>5000) \to \mu^+\nu$	$1.5341 \cdot 10^{-7}$	50000	1.02
361104	$W^- \to \mu^-\bar{\nu}$	8282.9000	31973000	1.04
301120	$W^-(120,180) \to \mu^-\bar{\nu}$	22.1940	500000	1.02
301121	$W^-(180,250) \to \mu^-\bar{\nu}$	3.2849	250000	1.01
301122	$W^-(250,400) \to \mu^-\bar{\nu}$	1.0831	150000	1.01
301123	$W^-(400,600) \to \mu^-\bar{\nu}$	0.1754	100000	$9.95 \cdot 10^{-1}$
301124	$W^-(600,800) \to \mu^-\bar{\nu}$	0.0310	50000	$9.77 \cdot 10^{-1}$
301125	$W^-(800,1000) \to \mu^-\bar{\nu}$	0.0083	50000	$9.59 \cdot 10^{-1}$
301126	$W^-(1000,1250) \to \mu^-\bar{\nu}$	0.0032	50000	$9.39 \cdot 10^{-1}$
301127	$W^-(1250,1500) \to \mu^-\bar{\nu}$	0.0010	50000	$9.17 \cdot 10^{-1}$
301128	$W^-(1500,1750) \to \mu^-\bar{\nu}$	0.0004	50000	$8.96 \cdot 10^{-1}$
301129	$W^-(1750,2000) \to \mu^-\bar{\nu}$	0.0001	50000	$8.75 \cdot 10^{-1}$
301130	$W^-(2000,2250) \to \mu^-\bar{\nu}$	$6.5000 \cdot 10^{-5}$	50000	$8.54 \cdot 10^{-1}$
301131	$W^-(2250,2500) \to \mu^-\bar{\nu}$	$3.0000 \cdot 10^{-5}$	50000	$8.34 \cdot 10^{-1}$
301132	$W^-(2500,2750) \to \mu^-\bar{\nu}$	$1.4549 \cdot 10^{-5}$	50000	$8.15 \cdot 10^{-1}$
301133	$W^-(2750,3000) \to \mu^-\bar{\nu}$	$7.0000 \cdot 10^{-6}$	50000	$7.95 \cdot 10^{-1}$
301134	$W^-(3000,3500) \to \mu^-\bar{\nu}$	$6.0000 \cdot 10^{-6}$	50000	$7.67 \cdot 10^{-1}$
301135	$W^-(3500,4000) \to \mu^-\bar{\nu}$	$1.5975 \cdot 10^{-6}$	50000	$7.26 \cdot 10^{-1}$
301136	$W^-(4000,4500) \to \mu^-\bar{\nu}$	$4.7210 \cdot 10^{-7}$	50000	$6.83 \cdot 10^{-1}$
301137	$W^-(4500,5000) \to \mu^-\bar{\nu}$	$1.4279 \cdot 10^{-7}$	50000	$6.41 \cdot 10^{-1}$
301138	$W^-(>5000) \to \mu^-\bar{\nu}$	$6.1624 \cdot 10^{-8}$	50000	$5.82 \cdot 10^{-1}$

Table 5.4.: MC16a $W \to \mu\nu$ samples. The first column shows the DSID, which is the dataset identification for each mass slice. The second column shows the sample process and the mass thresholds. The third column σ gives the cross-section. The fourth column N_{evt} is the number of events. The fifth column shows the k-Factor.

Background Samples

The signature for this measurement is a muon and missing transverse energy from the neutrino. Backgrounds to this measurement arise from mismodelling in the ATLAS detector and processes that mimic the signal signature. Missing energy in an event is not a simple quantity. It requires understanding all other objects in the event, e.g. muons and jets. There are many ways missing energy can be "faked". Mismeasurements of the jet's energies can lead to fake MET. Issues with dead parts of the ATLAS detector or not working correctly can also lead to fake MET. Noise with the beams can also lead to fake MET, e.g. from the pileup.

$t\bar{t}$ The most significant background process is the $t\bar{t}$. An example has been depicted in the Feynman diagram found in Figure 5.6. A pair of top quarks produced through gluon interaction will decay into a b quark, muon and neutrino. Therefore, if ATLAS does not detect the b quark, it will mimic the same signature as W production. The two W bosons can also decay leptonically and hadronically. Any leptonic decay will include a real MET (not fake) from a neutrino and a e, μ or τ. Hadronic decays to $c/\bar{c}$ could also lead to fake (i.e. non-prompt) muons. The $b/\bar{b}$ decay is forbidden due to large t mass.

t The single top quark background process also involves a W boson decaying into a neutrino and muon. The second W could also decay to electron, muon, tau leptons or hadronically to 2 jets. Only one muon and MET from a neutrino/neutrinos are needed to mimic W production.

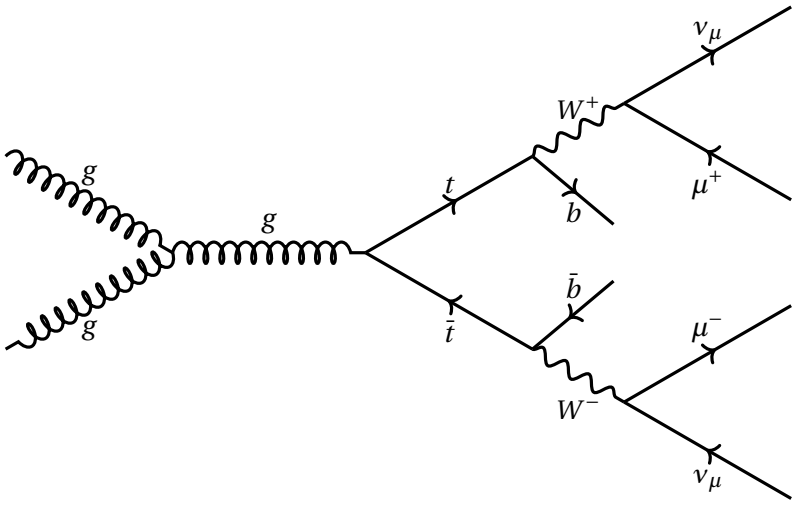

Figure 5.6.: Feynman diagram showing $t\bar{t}$ background process.

$Z \to \mu\mu$ The $Z \to \mu\mu$ is a large background for this measurement. This has been shown in the Feynman diagram found in Figure 5.7. In this process, the two quarks from the

proton will decay via a Z boson to two muons. One muon may not be correctly reconstructed/identified by ATLAS or can be lost in the beampipe, which will mimic W production for this background.

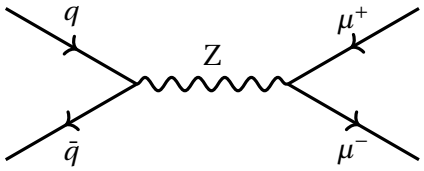

Figure 5.7.: Feynman diagram showing $Z \to \mu\mu$ background.

Diboson Diboson processes are an additional background. In these processes, two quarks scatter leading to EW diboson production or annihilation from two bosons, e.g. ZZ, WZ or WW and produce the final state of particles that mimic the signal process. Nine diboson processes have been included in this analysis. These are $ZZ \to llll$, $ZZ \to qqll$, $ZZ \to llvv$, $WZ \to lvll$, $WZ \to qqll$, $WZ \to lvqq$, $WZ \to lvvv$, $WW \to qqllv$ and $WW \to lvqq$.

$W \to \tau\nu$ and $Z \to \tau\tau$ Some smaller backgrounds include the $W \to \tau\nu$ shown in Figure 5.8 and $Z \to \tau\tau$ shown in Figure 5.9 process. Each has a tau incorrectly identified as a muon or MET. For $W \to \tau\nu$, the tau could decay into a real muon which is also non-prompt. Although $W \to \tau\nu$ is a Drell-Yan process, it will contaminate the muon channel measurement and is considered a background. In $Z \to \tau\tau$, one tau could decay into a muon and the second lepton is not identified or reconstructed correctly or decays hadronically.

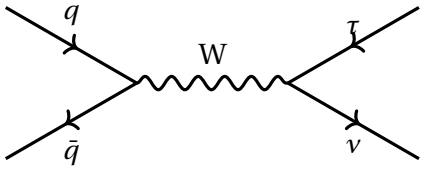

Figure 5.8.: Feynman diagram showing $W \to \tau\nu$ background.

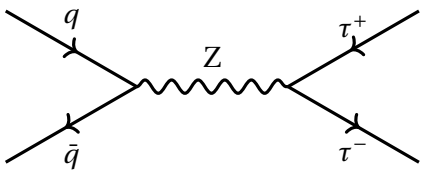

Figure 5.9.: Feynman diagram showing $Z \to \tau\tau$ background.

6. Event Selections

After the real-time selection of physics events during data taking by ATLAS, further selections must be taken at the analysis stage to select the physics signature of the processes being studied. The following chapter details the selections applied to select charged current Drell-Yan events and suppress background processes efficiently. Background processes are discriminated from Drell-Yan signal events by requiring kinematic constraints and detector observables. Further requirements are placed to reject non-prompt, fake or poorly reconstructed muons. Prompt muons originate from the hard scatter of an interaction and non-prompt muons originate from secondary decays. "Fake" muons are particles that have incorrectly been reconstructed as muons.

6.1. Event Selection Criteria

The selection criteria for $W \to \mu\nu$ candidates are listed below. Details of each criterion are provided in the following subsections.

Event Level Cuts

- The event must be in the ATLAS data quality good runs list (GRL).
- The event must pass the LAr quality check.
- Primary vertex cut.
- Trigger selection to be triggered by a muon in the event. For 2015 data is `HLT_mu20_iloose` and `HLT_mu50` triggers. For 2016, 2017 and 2018, triggers are `HLT_mu26_ivarmedium` and `HLT_mu50` triggers.
- Only one muon no other leptons) in the event.
- The selected muon is matched with the trigger (trigger matching).
- Jet cleaning (Loose bad).
- No overlap removal between jet and muon.

Object (Muon) Level Cuts

- The quality of the muon is `HighPt`.

- The muon passes the `FCTightTrackOnly_FixedRad` isolation criteria.
- The muon is well associated with the hard scattering vertex with Track-to-Track Vertex Association (TTVA) cut $d_0^{sig} < 3$ and $|z_0 \sin\theta| < 0.5$ mm.
- The muon must be in the $|\eta_\mu| < 2.4$ region.
- The muon transverse momentum should be $p_\mu > 65$ GeV.
- The missing energy of the event should be $E_T^{miss} > 85$ GeV.
- The transverse mass of the event should be $m_T^W > 200$ GeV.

6.1.1. Good Runs List

The data quality (DQ) group provides information from the DQ monitoring and assessment of data collected by ATLAS in the Good Runs List (GRL). The GRL is a set of XML files containing a list of Luminosity Blocks (LBs) for given runs over a period that has been certified for use in physics analyses. LBs are recorded approximately every 30s during data-taking and record the operational status of all ATLAS detector components. The files filter out recorded data without optimal conditions, e.g. the detector or LHC conditions were compromised. The integrated luminosity of a dataset (good for physics data) is calculated from the LBs in the GRL for a specific trigger [100].

6.1.2. LAr Error

The LAr calorimeter will identify events that do not satisfy certain data-taking conditions. The LAr performs data integrity checks to ensure meaningful data is propagated through its online systems, trigger decisions and event recording. Calorimeter noise is also monitored to reduce the rate of fake calorimeter clusters. Calorimeter noise is split into two main classes, large-scale coherent noise (bursts) and per-channel noise. Bursts affect whole events and occur when there is sudden noise in several thousand calorimeter cells beyond the expected electronic noise. Per-channel noise is from small detector regions, e.g. individual cells. Cells that persistently see an unusually high proportion of events or cells which are systematically recurring or skipped are identified, and the information from neighbouring cells is used for cluster reconstruction instead [101].

6.1.3. Primary Vertex

A primary vertex is a point in space where a pp collision has occurred. Events that do not contain a minimum of 1 primary vertex with 3 or greater tracks associated with it are vetoed. The primary vertex is calculated using measurements taken in different layers of the pixel detector and SCT [102].

Impact Parameter

Due to the high sensitivity in ATLAS, primary cosmic rays that reach the atmosphere and create a cascade of secondary cosmic rays which contain muons can be reconstructed as Drell-Yan events. To remove these events, an impact parameter cut is taken to select events produced close to the primary z vertex position.

In ATLAS measurements, two commonly used impact parameters are d_0 and z_0 as shown in Figure 6.1. These variables give the distance between the closest approach of the muon track and the primary vertex position. d_0 is the transverse impact parameter and z_0 is the longitudinal impact parameter. An additional variable is also defined as d_0^{sig} in Equation 6.1:

$$d_0^{sig} = \frac{d_0}{\sigma(d_0)} \tag{6.1}$$

Here $\sigma(d_0)$ is the measurement uncertainty on d_0, originating from determining the track and primary z vertex position.

The tracks are selected using the following criteria:

- $p_T > 400\text{MeV}; |d_0| < 4$ mm; $\sigma(d_0) < 5$ mm; $\sigma(z_0) < 10$ mm;
- SCT detector hits ≥ 4; silicon (SCT or pixel) hits ≥ 9; no pixel holes;
- if $|\eta| \geq 1.65$, silicon hits ≥ 11; No more than one SCT hole (Run 2);
- Insertable B-Layer (IBL) hits + B-layer (closest pixel layer) hits ≥ 1(Run 2);
- A maximum of 1 shared pixel hit or 2 shared SCT hits (Run 2).

d_0 and z_0 are the transverse and longitudinal impact parameters of tracks with respect to the centre of the luminous region and $\sigma(d_0)$ and $\sigma(z_0)$ are their uncertainties. A hole is a measurement on a detector surface that is not observed but was predicted with the given trajectory [103].

6.1.4. Trigger Selection

Triggers aim to select muons arising from physics processes of interest and are well reconstructed. A trigger chain consists of a Level-1 (L1) trigger item followed by a series of High-Level Trigger (HLT) algorithms that reconstruct and apply kinematic selections to objects. This trigger chain is used to select events, with each chain specifically designed to select different physics signatures, e.g. leptons, jets, photons, total energy, and missing transverse energy [104].

As described previously in Table 5.2, three different muon triggers were used. This analysis uses `HLT_mu20_iloose`, `HLT_mu26_ivarmedium` and `HLT_mu50` triggers. The "HLT"

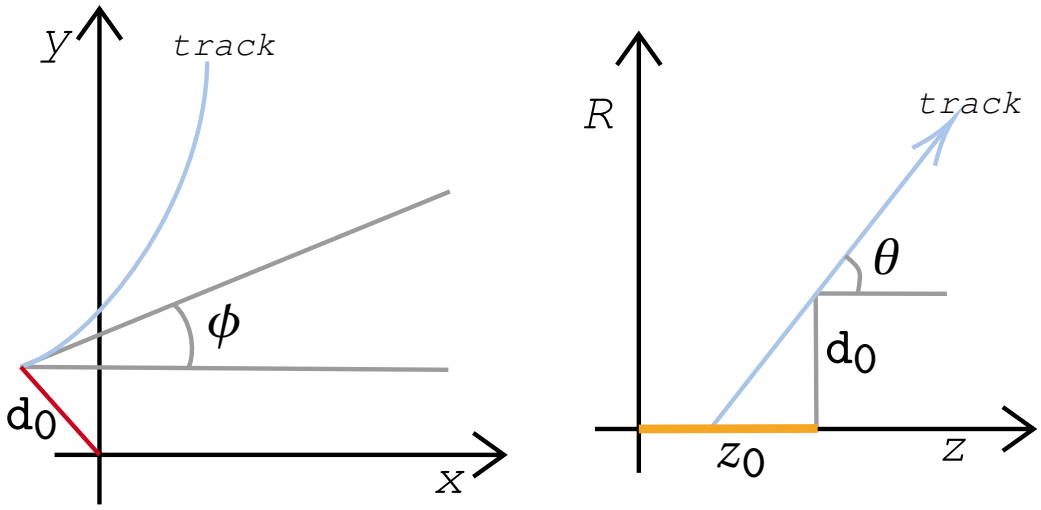

Figure 6.1.: Left: Diagram of impact parameter d_0.The blue line represents the particle track. The primary vertex here is at the origin of the x-y coordinates. The d_0 is the distance of closest approach of the particle track in the transverse plane and is represented by the red line. The conventional ATLAS frame of reference is used in the diagram. Right: Diagram of impact parameter z_0. The blue line represents the particle track. The primary vertex here is at the origin of the R-Z coordinates. The z_0 is the distance of the closest approach of the particle track in the longitudinal plane and is represented by the orange line. The conventional ATLAS frame of reference is used in the diagram.

means High-Level Trigger, the "mu" means triggers are applied to muons, the number after "mu" is the transverse momentum threshold in GeV and "iloose" and "ivarmedium" defines the isolation cut taken on the object. "ivarmedium" requires a candidate passes a medium isolation selection calculated using inner detector tracks reconstructed online by the HLT within a variable cone size which depends on the p_T of the muon. Similarly, the "iloose" requires candidates to pass loose isolation selection computed using inner detector tracks reconstructed online by the HLT; more details are in Section 6.1.7. Triggers with different p_T threshold e.g. $p_T > 26$ GeV and $p_T > 50$ GeV are used for higher efficiency at high p_T.

In this analysis, the lowest un-prescaled single muon trigger is used. The `HLT_mu20_iloose` was only available in 2015-16 data taking and had the lowest isolation and p_T threshold conditions. Therefore, it has the highest rate and could only run when the instantaneous luminosity was relatively low. As instantaneous luminosity increased in 2017 and 2018, more restrictive triggers were needed to maintain a reasonable rate. The `HLT_mu50` trigger has a sufficiently low rate that no isolation condition is needed.

For a muon to be "trigger matched", the object that passes the trigger must correspond to at least one event-level reconstructed muon. The selected muon should have fired the trigger with $\Delta R < 0.1$.

Trigger efficiency scale factors correct for the difference in efficiencies between simulation and data once trigger selections are applied. These values are provided by the Muon Combined Performance (MCP) group. Figure 6.2 shows the average muon trig-

Reject	Against	Criteria
Electron	Electron	shared track, $p_{\mathrm{T},1} < p_{\mathrm{T},2}$
Muon	Electron	is Calo-Muon and shared ID track
Electron	Muon	shared ID track
Jet	Electron	$\Delta R < 0.2$
Electron	Jet	$\Delta R < 0.4$
Jet	Muon	NumTrack < 3 and (ghost-associated or $\Delta R < 0.2$)

Table 6.1.: Overlap removal criteria.

ger scale factor with respect to transverse mass m_T^W, muon p_T and muon η. The scale factor is a ratio between the data and Monte Carlo efficiency. A strong dependence on η_μ in the barrel region is shown because the barrel region has low detector efficiency and modelling simulation is more difficult because of the geometry of the MDT trigger chambers in the barrel region of the MS. There is small dependence on p_T^μ and m_T^W.

6.1.5. Jet Cleaning

Jets produced in pp collisions must be distinguished from jets of non-collision origin. Jet selection criteria should keep the highest efficiency selection for jets produced in proton-proton collisions and efficiently reject "fake/bad jets" from backgrounds either from collisions (calorimeter noise) or non-collision origin (beam-induced backgrounds and cosmic ray showers). Jet candidates are either "good jets" from high-energy objects produced in a collision or "fake/bad jets" from background processes. A Loose selection is also designed for the efficiency of selecting jets from pp collisions above 99.5% (99.9%) for $p_T > 20(100)$ GeV. This analysis used Loose bad jets; therefore, it rejects the bad jets and selects jets that meet the Loose criteria [105].

6.1.6. Overlap Removal

Table 6.1 lists the standard overlap removal used. Overlap between a muon and a jet has been omitted, which is crucial for the multijet estimation described in Section 7. The number of potentially "fake" muons, aka non-prompt muons, is essential for the multijet estimation. Therefore, overlap removal between muons and jets has not been applied to increase the number of muons that could be fake.

6.1.7. Muon Isolation

Isolation is a discriminating variable that helps separate prompt and non-prompt muons. It provides a way to reduce muons arising from the multijet background in semileptonic decays of heavy quarks. Multijet background events with a lepton in the final state arising from the decay of a heavy flavour b or c quark could pass signal selection requirements. However, their tracks will be surrounded by additional energy

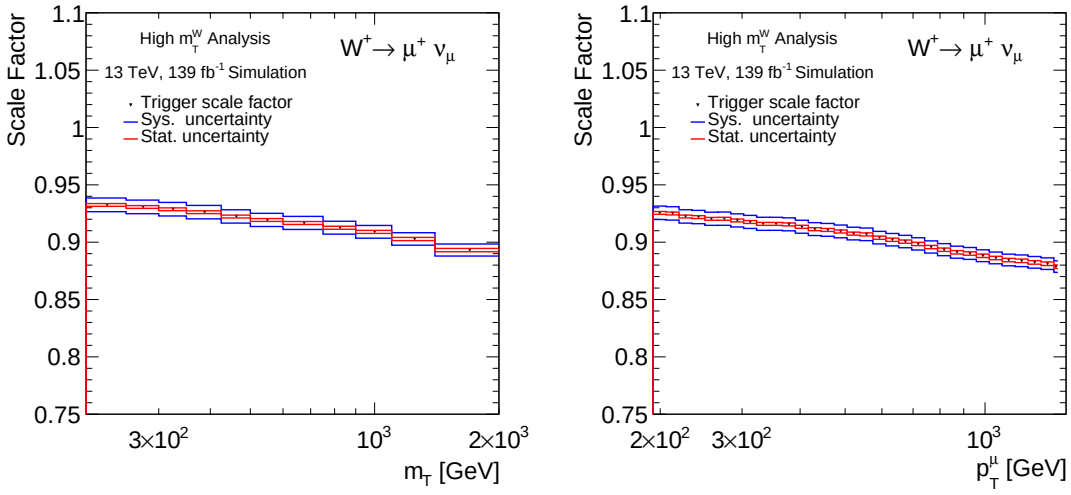

(a) (b)

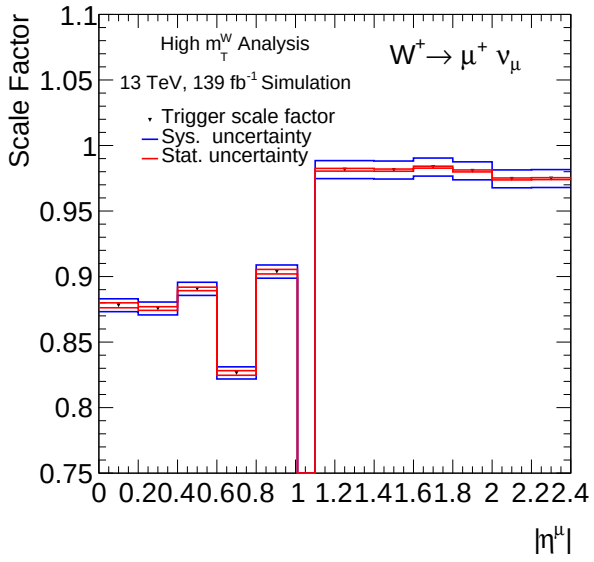

(c)

Figure 6.2.: Average trigger cut efficiency scale factors as a function of transverse mass m_T^W (a), p_T^μ (b) and $|\eta^\mu|$ (c). These plots are for $W^+ \rightarrow \mu\nu$ for the combined Monte Carlo campaigns MC16a, MC16d and MC16e. The same behaviour is seen for $W^- \rightarrow \mu\nu$. The individual systematics and statistical uncertainty for one standard deviation are shown in blue and red. The drop in scale factor as p_T^μ or m_T^W increases shows that the MC overestimates the efficiency in the data.

deposits from additional particles in the surrounding hadronic jet. This differs from single leptons, isolated with a singular track where most energy is deposited.

Isolation for muons is defined as the scalar sum of transverse momenta, $\sum p_{\mathrm{T}}$, of additional tracks inside a cone centred around the muon track direction, ΔR, excluding p_T^{μ}, the transverse momentum of the muon, divided by p_{T}^{μ} [106].

The Muon Combined Performance (MCP) group [69] defines several working points for isolation. The working point for the isolation implemented here is called the `FCTightTrackOnly_FixedRad`. "FC" stands for Fixed Cut. Only tracking information is used to calculate the isolation (no calorimeter information). In ATLAS, the muon ID and MS provide the tracking information to define the energy deposited. In this working point, the upper trigger threshold is taken for $p_T > 50$ GeV and is required to satisfy Equation 6.2:

$$I^{\mu} = \frac{\sum p_{\mathrm{T}}^{(\Delta R=0.2)}}{p_{\mathrm{T}}^{\mu}} < 0.06 \tag{6.2}$$

The cone size ΔR used is defined in Equation 6.3:

$$\Delta R = \min\left(\frac{10\ \mathrm{GeV}}{p_{\mathrm{T}}^{\mu}}, \Delta R_{\mathrm{max}}\right) \tag{6.3}$$

The `FCTightTrackOnly_FixedRad` working point uses p_{T}^{μ} fixed cone isolation for transverse momenta above 50 GeV. Below 50 GeV, the cone size is dependent on p_{T}^{μ} to improve performance for muons [107]. The following Figure 6.3 shows the average muon isolation scale factors.

6.1.8. Muon Kinematics

For this analysis cuts have been taken on p_T^{μ} and $|\eta|$. A cut on $p_T^{\mu} > 65$ GeV is taken, ensuring that the muons from the W boson decay are energetic and efficiently remove background events. The triggers used in this analysis accept events with transverse momentum greater than 20 GeV or 26 GeV or 50 GeV. Therefore, a p_T^{μ} cut above these values ensures good efficiency in event selection. It also efficiently reduces the multijet background contribution; more details are in Chapter 7.

A cut on the muons is applied for $|\eta| < 2.4$ due to the acceptance of ATLAS defined by the muon trigger chambers (MDTs), the ID and MS being $|\eta| = 2.5$ and $|\eta| = 2.7$. The MCP group also provides efficiencies in the region $|\eta| < 2.5$; therefore, a cut lower than this gives access to the provided muon reconstruction efficiencies.

6.1.9. Missing Transverse Energy

The missing transverse energy or E_T^{miss} arises from the neutrino in charged current Drell-Yan processes. The assumption is that in pp collisions, transverse momentum is

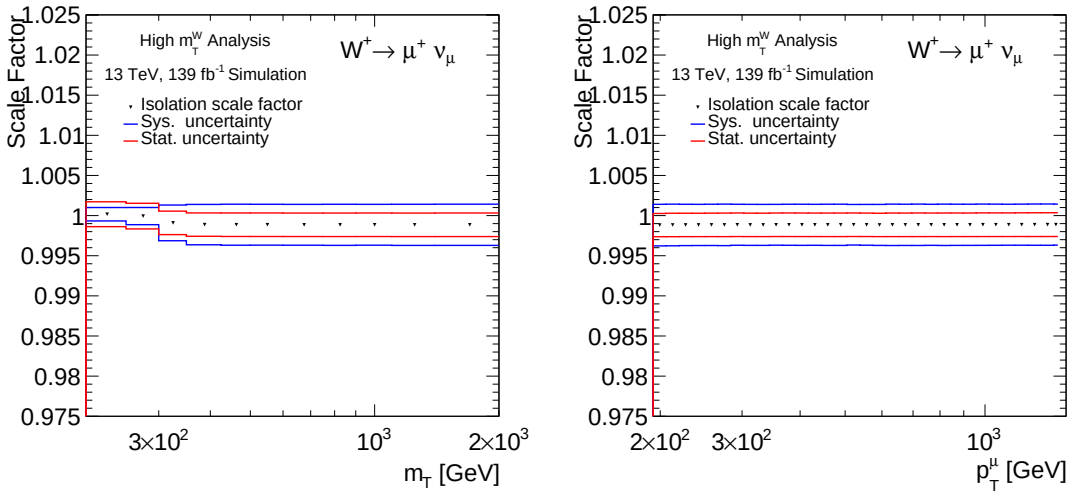

(a) (b)

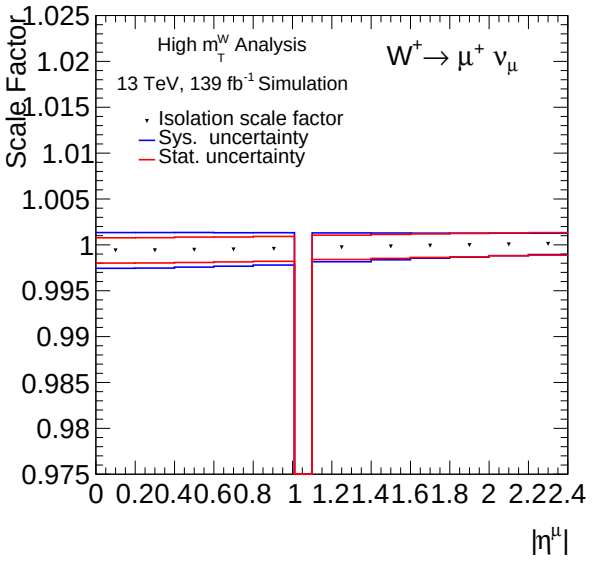

(c)

Figure 6.3.: Average isolation selection efficiency scale factors as a function of transverse mass m_T^W (a), p_T^μ (b) and $|\eta^\mu|$ (c). These plots are for $W^+ \rightarrow \mu\nu$ for the combined Monte Carlo campaigns MC16a, MC16d, MC16e. The individual systematics and statistical uncertainty for one standard deviation are shown in blue and red.

conserved. Thus, when all p_T is summed in an event, any missing energy is attributed to the neutrino p_T. A cut was taken on $E_T^{miss} > 85$ GeV in this analysis to reduce the background events.

6.1.10. Transverse Mass

The invariant mass cannot be fully reconstructed for $W \to \mu\nu$ processes due to the missing energy. However, the transverse mass is a quantity that can be reconstructed to discriminate W bosons from background events and perform a cross-section measurement. The transverse mass is defined in Equation 6.4 below:

$$m_T^W = \sqrt{2 p_T^\mu E_T^{miss} \left(1 - \cos\left(\phi^\mu - \phi^{E_T^{miss}}\right)\right)} \tag{6.4}$$

p_T^μ is the muon transverse momentum. E_T^{miss} is the magnitude of the missing energy vector. ϕ^μ is the muon azimuthal angle and $\phi^{E_T^{miss}}$ is the missing energy azimuthal angle. When the neutrino momentum has zero longitudinal component, the transverse mass is equivalent to the invariant mass. Therefore, for a given invariant mass, the transverse mass is bound between 0 and m. In this analysis, a $m_T^W > 200$ GeV cut is used. This reduces events coming from backgrounds and the W mass peak.

6.1.11. Truth Level

It is helpful to define a fiducial truth level selection for the unfolding. The following selections are required, which have been chosen to resemble the reconstruction level cuts:

Fiducial Truth Level Cuts

- 200 GeV $< m_T^W <$ 2000 GeV
- $p_{\mathrm{T}}\left(\nu_{\mathrm{born}}\right) > 85$ GeV
- $p_{\mathrm{T}}\left(\ell_{\mathrm{born}}\right) > 65$ GeV
- $\left|\eta\left(\ell_{\mathrm{born}}\right)\right| < 2.4$

An underflow bin called the "shadow" bin was used during the unfolding procedure. For the truth and reconstructed level, the m_T^W cut is lowered. Therefore, the m_T^W bin for 150-200 GeV used to stabilise the unfolding is included. The shadow bin is not to be included in the final or published results. Therefore the final fiducial level starts at $m_T^W = 200$ GeV.

7. Multijet Background Estimate

This section details the process for estimating the QCD multijet background, this is also sometimes referred as fake lepton backgroundd. The multijet background is not well described in Monte Carlo. Therefore, a "data-driven" method is performed to determine the multijet background accurately. A "data-driven" method is one where reconstructed data is used directly to derive a multijet estimate. The following sections introduce the multijet, detail the inputs of the matrix method, the real/fake lepton efficiency and the final results in data are then shown. This chapter also explains the systematic uncertainties for this estimation.

7.1. Introduction

Event signatures with several jets are considered multijet events. These events arise because of QCD interactions, and at the LHC multijet events have a large cross-section. Multijet events have falsely identified leptons or have non-prompt leptons (fake leptons) which pass as part of an interesting physics signal, making them a background in most LHC analyses. The final state for this measurement is $W^{\pm} \rightarrow \mu\nu$. When a multijet process also has a muon and neutrino in its final state, this will contaminate the signal.

The multijet background or fake muon background for this analysis arises from semi-leptonic decays of bottom and charm quarks, when a hadron (pion or kaon) is formed when a jet decays into a lepton and when there are fake muons from jets. The b and c quarks can undergo semi-leptonic decays where, a quark transforms into a different quark (e.g. $c \rightarrow s$ or $b \rightarrow c$), emitting a lepton (electron or muon) and a neutrino. While the neutrino goes undetected, the accompanying muon is detected. These muons are considered fake because they are not directly produced at the primary vertex. The pions and kaons can undergo decay in flight within the tracking regions. Specifically, these particles can decay into muons and neutrinos. When these decays occur within the detector's tracking regions, the resulting muons from pion and kaon decays can mistakenly be identified as primary vertex muons. This misidentification contributes to the multijet background. When jets are detected in ATLAS, their signature is a collection of particle tracks in the MS and ID subdetectors. The energy deposited in the calorimeters is also used to identify the jets. The particles will have a cone shape and, using specialised algorithms, can identify jets. However, the reconstruction of jets is not perfect, and some particles can be misidentified and contribute to the fake muon back-

ground. Punch-through hadrons also contribute to the multijet background. These are hadrons that have a large enough energy to pass through the calorimeter and deposit energy in the muon spectrometer. These hadrons can be misidentified as muons.

For multijet events with fake electrons, there are also various sources. These include fake electrons from b and c quark decays, electrons from photon conversions and electrons from misidentified jets. Fake elections from b and c quark decays are similar to the fake muon b and c quark decays, but the final signature involves an electron and a neutrino instead. Electrons from photon conversions occur when a photon transforms into an electron-positron pair. The electron generated in this conversion process can contribute to the fake electron signals. Electrons from misidentified jets can occur in various ways, such as when there are few charged tracks in the jet or little energy in the hadronic compartments. Electrons tend to deposit most of their energy in the electromagnetic calorimeter, while hadronic jets distribute energy more widely. When there is insufficient energy in hadronic compartments this might lead to misidentification.

Missing energy in multijet events could contaminate the signal because it can mimic the final state for this measurement which involves a neutrino, also resulting in missing energy. One source of $E_{\mathrm{T}}^{\mathrm{miss}}$ is in multijet events involving neutrinos, such as in the decay of W bosons or heavy-flavour hadrons. Another source of $E_{\mathrm{T}}^{\mathrm{miss}}$ is the mismeasurement of jets. Inaccuracies in measuring the energy of jets can lead to mismeasurement of the total transverse energy in the event, resulting in $E_{\mathrm{T}}^{\mathrm{miss}}$. Other undetected particles, such as any particles that escape the detector without leaving a detectable signature, also contribute to $E_{\mathrm{T}}^{\mathrm{miss}}$.

The multijet has a larger cross-section than the other background processes in this analysis. The selection in Chapter 6 reduces the multijet background events in a few ways. The leptons resulting from a hard collision will be isolated, whereas jets are seen as a cluster of energy. Therefore, selecting isolated events reduces multijet contamination. The muon d_0 significance follows a Gaussian shape centred at zero. Muons from the signal have a small impact parameter, whereas jets have a large impact parameter. The large cuts on transverse momentum, missing energy and transverse mass will reduce the multijet background as the multijet dominates in lower regions. However, it is not possible to altogether remove the multijet background. The multijet processes are not well described in Monte Carlo. Therefore, a data-driven technique has been adopted for estimation, where the number of events is derived from measured data.

7.2. Matrix Method

"Real" leptons are prompt and isolated leptons from the primary interaction vertex from the $W^{\pm}$ boson. "Fake" leptons are any non-prompt lepton produced in heavy flavour meson decays or from an object misreconstructed as a lepton coming from converted photons from various origins, from decays of pions or kaons to muons. Real

Criteria	Requirement
Loose level	`HighPt` quality
	No isolation
Tight level	`HighPt` quality
	`FCTightTrackOnly_FixedRad` isolation

Table 7.1.: Loose and tight selections for the multijet estimation.

events in the following are any event where the lepton is real and fake events are those with one fake lepton.

Overlap Removal

It should be noted that the overlap removal between a muon and a jet has been omitted. The standard overlap has been discussed in Section 6.1. When dealing with the fake muon estimation, it is crucial to compare a muon and a jet. The standard overlap removal procedure is such that if the number of tracks is less than 3 and the muon is ghost-associated or $\Delta R(\text{jet}, \mu) < 0.2$, the jet is rejected.

Ghost-association is a method used in dense hadronic environments to match jets with calorimeter objects. This involves introducing infinitesimally small "ghosts" representing jets. These "ghosts" are the track jet 4-vectors in the event, with the track jet p_T set to an infinitesimal amount. This effectively retains only the direction of the track jets, ensuring that the reconstruction is not altered by the ghosts when the calorimeter clusters, along with ghosts, are reclustered. Following this, reclustering with the anti-k_t algorithm [75] with $R = 1.0$ is performed. This technique ensures robust matching with irregular jet boundaries and facilitates precise measurements in the analysis [108].

Alternatively, the muon is rejected against the jet if the surviving object is within $\Delta R(\text{jet}, \mu) < 0.4$. These selections do not affect the signal selection because an isolated muon is required in the signal region. However, as fake muons mostly have jet origins, they will likely be close to the jet and would eliminate many fake muons via overlap removal. It is vital in the matrix method to define a QCD-enriched region with a large number of fake muons. Therefore, standard overlap removal is not used in this analysis.

7.2.1. Matrix Method Strategy

The matrix method requires a tight and a loose level, defined in Table 7.1. The isolation has been used as a discriminant for tight and loose selections due to its ability to strongly separate between real and fake muons.

The matrix method is given by lowering the isolation and/or identification requirements. A matrix, shown in Equation 7.1, can then be used to relate the number of real and fake muons (N_R/N_F) and the number of loose and tight muons (N_L/N_T).

$$\begin{pmatrix} N_T \\ N_L \end{pmatrix} = \begin{pmatrix} \epsilon_R & \epsilon_F \\ 1-\epsilon_R & 1-\epsilon_F \end{pmatrix} \begin{pmatrix} N_R \\ N_F \end{pmatrix} \tag{7.1}$$

N_R and N_F are mutually exclusive, therefore the N_T and N_L must be too. Therefore, N_L is the number of events that pass the loose selection but fail the tight selection. N_T is defined as the number of events that pass the tight selection. ϵ_R is the real efficiency calculated by taking the ratio of the number of real events which pass the tight selection to those which pass the loose selection. The fake efficiency ϵ_F is calculated similarly but takes the number of fake events, shown in Equation 7.2.

$$\epsilon_{R/F} = \frac{N^T_{R/F}}{N^L_{R/F}} \tag{7.2}$$

Here $N^L_{R/F}$ are those events that solely pass the loose level selection. Events for $N^T_{R/F}$ must pass the tight selection and, by definition, are a subset of the $N^L_{R/F}$. This includes all events that pass or fail the tight selection, thereby correctly defining efficiency. Therefore, the number of tight events will be given by the number of real events multiplied by the real efficiency summed with the number of fake events multiplied by the fake efficiency. The efficiencies allow the ability to take the number of real or fake events and calculate how many pass the tight selection. The matrix also gives this in Equation 7.2, which defines Equation 7.3.

$$N_T = \epsilon_R N_R + \epsilon_F N_F \tag{7.3}$$

The number of real or fake leptons is not available in the data. However, the number of tight and loose leptons is available. By inverting the matrix, Equation 7.4 gives the number of fake leptons.

$$\begin{pmatrix} N_R \\ N_F \end{pmatrix} = \frac{1}{\epsilon_R(1-\epsilon_F) - \epsilon_F(1-\epsilon_R)} \begin{pmatrix} 1-\epsilon_F & -\epsilon_F \\ \epsilon_R - 1 & \epsilon_R \end{pmatrix} \begin{pmatrix} N_T \\ N_L \end{pmatrix} \tag{7.4}$$

To estimate the final number of multijet events, the number of fake leptons passing the tight level (the event selection of this analysis) must be calculated. This is given by Equation 7.5.

$$\epsilon_F N_F = \frac{\epsilon_F}{\epsilon_R - \epsilon_F} \left[\epsilon_R (N_L + N_T) - N_T\right] \tag{7.5}$$

For the matrix method to successfully estimate the multijet background, it is crucial to have a good estimate of the real and fake efficiencies from the number of loose and tight events. The efficiencies are calculated from the data and MC and are usually estimated in each variable in a special region, enriching the real or fake lepton. The efficiencies are assumed to be transferred to the signal region by calculating an event weight per bin. This is based on whether the tight selection is passed, shown in Equa-

tion 7.6 or if it fails the tight selection shown in Equation 7.7.

$$w_{MM}^{T} = \frac{\epsilon_F\,(\epsilon_R - 1)}{\epsilon_R - \epsilon_F} \tag{7.6}$$

$$w_{MM}^{L} = \frac{\epsilon_F \epsilon_R}{\epsilon_R - \epsilon_F} \tag{7.7}$$

The weight w_{MM}^{T} is for events that pass the tight selection ($N_T = 1, N_L = 0$) and w_{MM}^{L} is applied to events that pass the loose selection but fail the tight selection ($N_T = 0, N_L = 1$). These weights are applied to W^+ and W^- data (for tight and tight not loose events) to get charge-separated multijet distributions and will account for any differences between charges.

7.3. Multijet Estimate

The multijet estimate was carried out separately for each Monte Carlo campaign and finally summed for the estimation in Run-2. Plots for MC16e only have been included in this section. Plots for MC16a and MC16d can be found in Appendix C.

7.3.1. Real Efficiency

The real muon efficiency, ϵ_R, is the efficiency for a real, loose muon to make the tight selection. It is measured using only simulation, by combining both charges $W^{\pm}$ in the signal Monte Carlo. Real muons should dominate these samples; summing the charges gives better statistics.
The following selections have been applied to the MC samples for the real efficiency calculation:

- $m_W^{Inv} > 120$ GeV
- $p_T > 65$ GeV
- $\Delta R_{\mu_{truth}\mu_{reco}} < 0.1$
- No $E_{\mathrm{T}}^{\mathrm{miss}}$ & m_T^W selection

Only the high-mass slices have been used; therefore, the truth invariant mass is greater than 120 GeV. The cut on $p_T > 65$ GeV is kept the same as the selection in Chapter 6. The $E_{\mathrm{T}}^{\mathrm{miss}}$ and m_T^W are not used for the calculation of the real efficiency. Also a truth matching with $\Delta R\left(\mu_{\mathrm{truth}}, \mu_{\mathrm{reco}}\right) < 0.1$ was applied.

The method used is the following:

- run over each sample with the tight/loose criteria

- ⋆ calculate the real efficiency by dividing the tight and loose

The real muon efficiency for MC16e is shown in Figure 7.1. To cover all dependencies in the fake efficiency, detailed in Section 7.3.2, the efficiency is binned three-dimensionally in $p_{\mathrm{T}}, |\eta|$ and $\Delta\Phi\left(\mu, E_{\mathrm{T}}^{\mathrm{miss}}\right)$. Each line represents a different $|\eta|$ region and each plot show a different $\Delta\Phi\left(\mu, E_{\mathrm{T}}^{\mathrm{miss}}\right)$ region. For all regions, the efficiency is close to unity, $\epsilon_R > 0.99$ and as p_{T} increases, the efficiency also increases. For higher $|\eta|$ values, the efficiency tends to be smaller. In the higher $\Delta\Phi\left(\mu, E_{\mathrm{T}}^{\mathrm{miss}}\right)$ regions, the efficiency also tends to be larger. High efficiency is expected as most real muons should be isolated therefore passing the tight criterion.

7.3.2. Fake Efficiency

The ϵ_F, fake muon efficiency is for a fake, loose muon to make the tight selection. A good estimate of the fake muon efficiency is important. Therefore, a sample with a large number of fake muons is necessary. The fake muon contribution to the data is small, so if the real muon contribution to the data is subtracted, a sample of fake muons will be obtained. The Monte Carlo well models real muons in the signal and backgrounds. Therefore, the estimate of fake muons comes from the data, while the simulation (Monte Carlo) is used to model and subtract the contributions of real muons from both signal and background events. The calculation method is as follows:

- ⋆ Run over data and all MC
- ⋆ Calculate loose and tight histograms
- ⋆ Get the difference between MC and Data to be identfied as fakes
- ⋆ Calculate the fake efficiency by dividing the number of tight and loose fakes

To further increase the fake muon contribution, a fake enriched region is defined as follows:

- ⋆ $E_T^{miss} < 65$GeV
- ⋆ $p_T > 65$GeV
- ⋆ $d_0^{\mathrm{sig}} > 1.5$
- ⋆ at least one jet with $p_T > 40$GeV and $\Delta R($ Jet,$\mu) > 0.2$
- ⋆ No m_T cut

Here the fake muon contribution is expected to be substantially more than in the signal region. The $E_{\mathrm{T}}^{\mathrm{miss}}$ cut selects a region orthogonal to the signal region. The cut on $p_T > 65$ GeV is the same as the selection in Chapter 6. The cut on d_0^{sig} chooses events

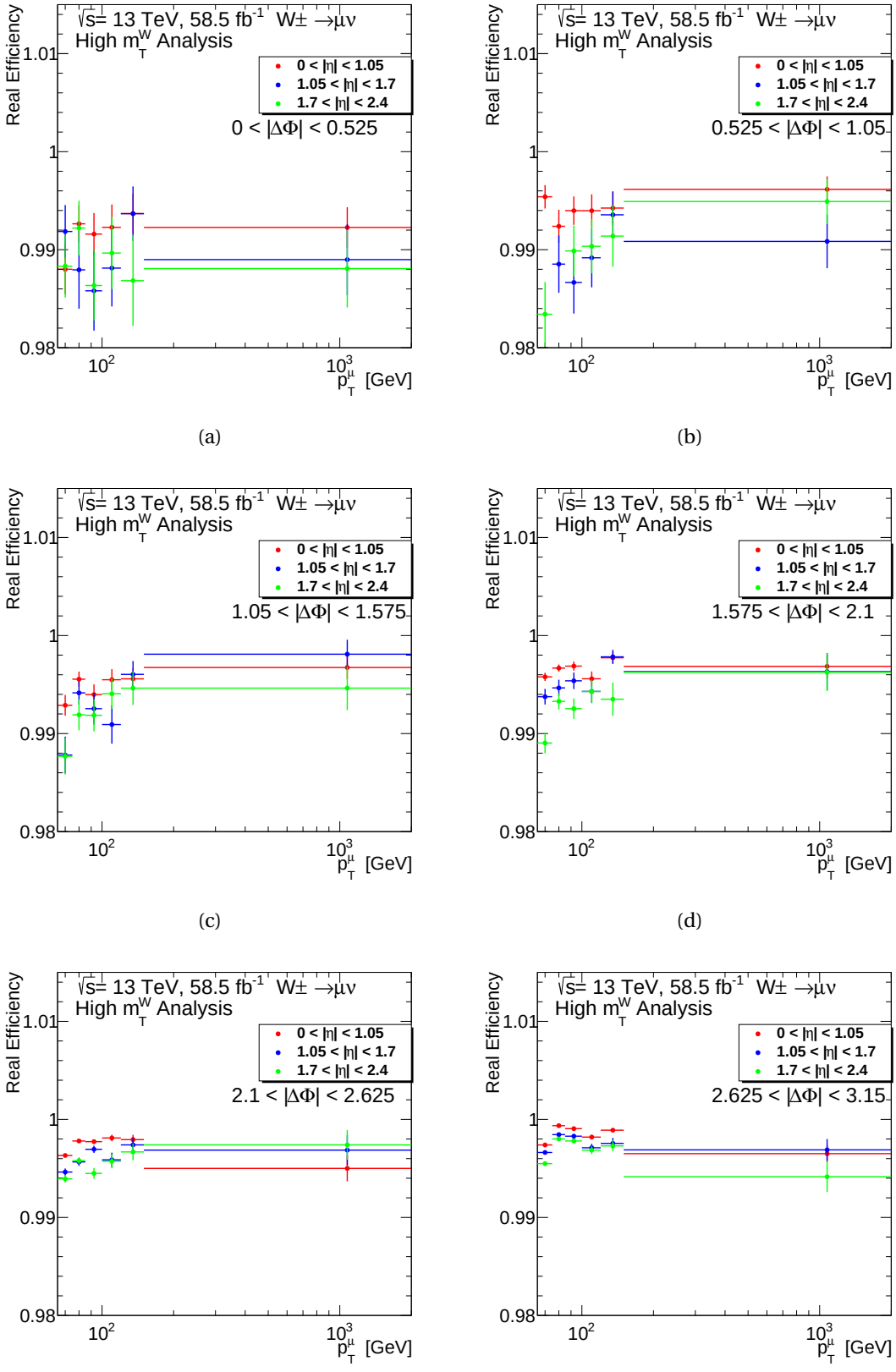

Figure 7.1.: Real muon efficiency for calculating the matrix method for MC16e. The real efficiency has been binned three dimensionally in $p_{\mathrm{T}}, |\eta|$ and $\Delta\Phi\left(\mu, E_{\mathrm{T}}^{\mathrm{miss}}\right)$. Each figure shows a different $\Delta\Phi\left(\mu, E_{\mathrm{T}}^{\mathrm{miss}}\right)$ region. The red line shows the $0 < |\eta| < 1.05$, the blue line shows the $1.05 < |\eta| < 1.7$ and the green line the $1.7 < |\eta| < 2.4$.

with non-prompt muons. Heavy flavour jets are a dominant source of fake muons; therefore, an additional jet is selected to enrich a dijet topology. The jet is also required to have no overlap with the fake muon such that $\Delta R(\text{ jet},\mu) > 0.2$. This ensures there are two jets, one jet where the fake muon originates, plus an additional one. Standard overlap removal is removed from this analysis so that this selection could be taken for a fake muon-enriched region. This definition of a QCD enriched region is arbitrary, so systematic variations are defined in Section 7.5.

The fake muon efficiency for MC16e is shown in Figure 7.2. The fake efficiency has been binned as a function of p_{T} and is shown for different $\Delta\Phi\left(\mu, E_{\mathrm{T}}^{\mathrm{miss}}\right)$ regions. The fake efficiency has a strong dependence on p_{T}, at lower p_{T} the efficiency is lowest $\epsilon_F < 0.1$ and at higher p_{T} the efficiency is largest. Dependence on $|\eta|$ and $\Delta\Phi\left(\mu, E_{\mathrm{T}}^{\mathrm{miss}}\right)$ is also seen, but not as strongly as p_{T}. For the dependence in $|\eta|$, represented by the coloured lines, the central $0 < |\eta| < 1.05$ region has the lowest values in efficiency, whilst the $1.7 < |\eta| < 2.4$ has the higher values in efficiency. For the dependence in $\Delta\Phi\left(\mu, E_{\mathrm{T}}^{\mathrm{miss}}\right)$, shown in each figure, the smallest $\Delta\Phi\left(\mu, E_{\mathrm{T}}^{\mathrm{miss}}\right)$ region shows the lowest fake efficiency. Conversely, the largest $\Delta\Phi\left(\mu, E_{\mathrm{T}}^{\mathrm{miss}}\right)$ region has the largest fake efficiency. The binning for these plots have been chosen in compromise with describing all the dependencies but still maintaining sufficient statistics in each bin for the calculation. In the lowest p_{T} region, the binning is finest, and there is only one bin for high p_{T} starting at 200 GeV. This ensures that in the highest p_{T} region, the efficiency does not approach too close to unity. If the fake efficiency approaches unity, it would also approach the value of the real efficiency, which would result in an unstable multijet calculation, as described in Equation 7.5.

7.4. Multijet Results

The multijet estimate has been computed as described in the previous sections and presented in the following Figure 7.3, Figure 7.4 for W^+ and Figure 7.5, Figure 7.6 for W^-. Chapter 9 presents the control distributions, including this multijet background estimate, showing good agreement between the data and prediction. Comparing the distributions for W^+ and W^-, there are no significant shape differences, with each distribution peaking around the same value. One important difference between the charges is that there are overall more events in W^+ than in W^-. Taking the transverse mass distribution, shown in Figure 7.3d and Figure 7.5d, there is an approximately 2.5% difference in the number of events in the 200 GeV bin. Thus, the multijet estimation has a charge asymmetry in the regions with a high number of predicted events (low m_T), which is in line with the findings of this thesis. In the larger m_T bins, the difference between charges becomes close to 0%. Due to the expected low number of multijet events in this region, there is inadequate statistical data to observe any asymmetry.

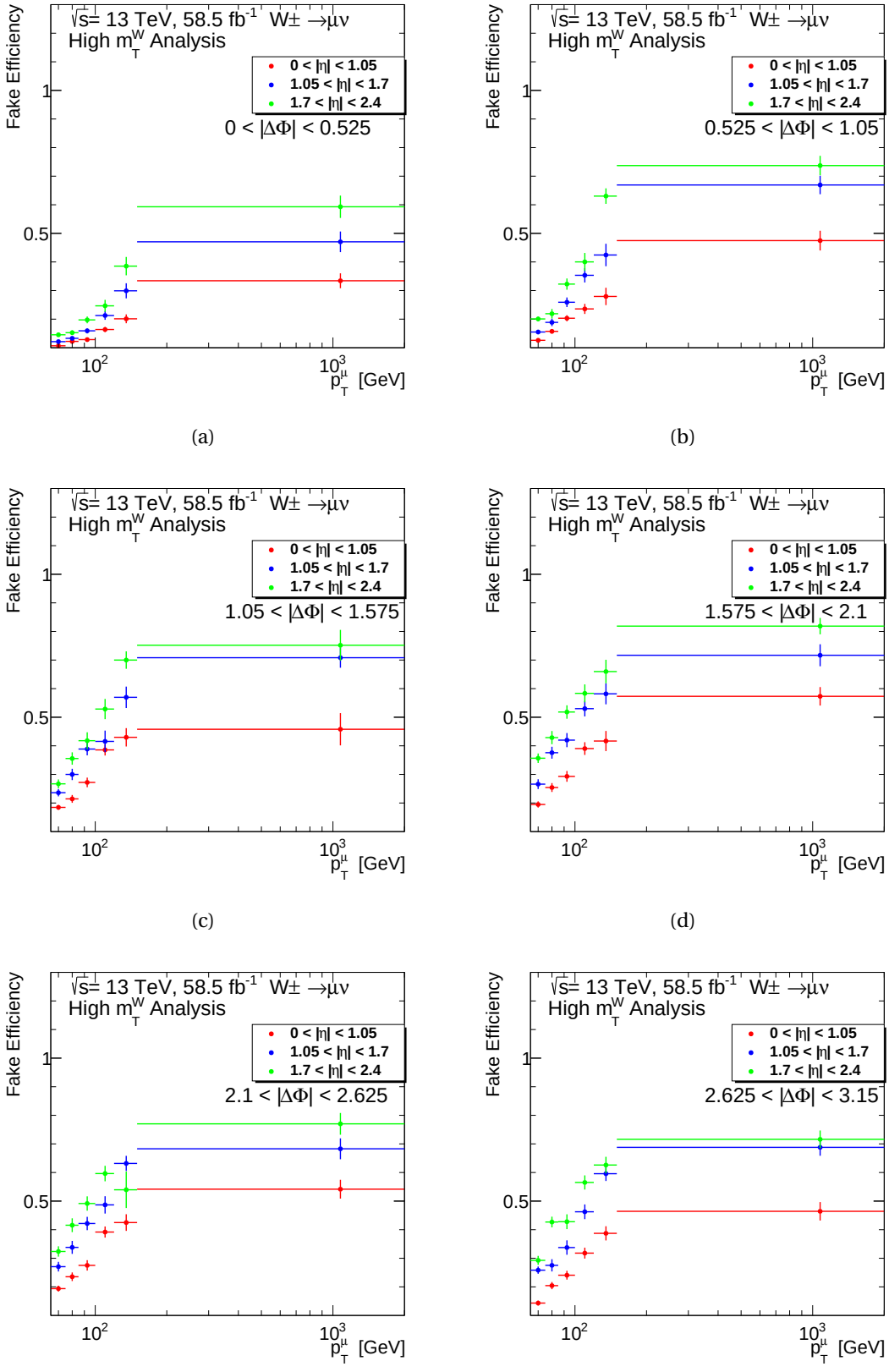

Figure 7.2.: Fake muon efficiency for calculating the matrix method for MC16e. The fake efficiency has been binned three dimensionally in $p_{\mathrm{T}}, |\eta|$ and $\Delta\Phi\left(\mu, E_{\mathrm{T}}^{\mathrm{miss}}\right)$. Each figure shows a different $\Delta\Phi\left(\mu, E_{\mathrm{T}}^{\mathrm{miss}}\right)$ region. The red line shows the $0 < |\eta| < 1.05$, the blue line shows the $1.05 < |\eta| < 1.7$ and the green line the $1.7 < |\eta| < 2.4$.

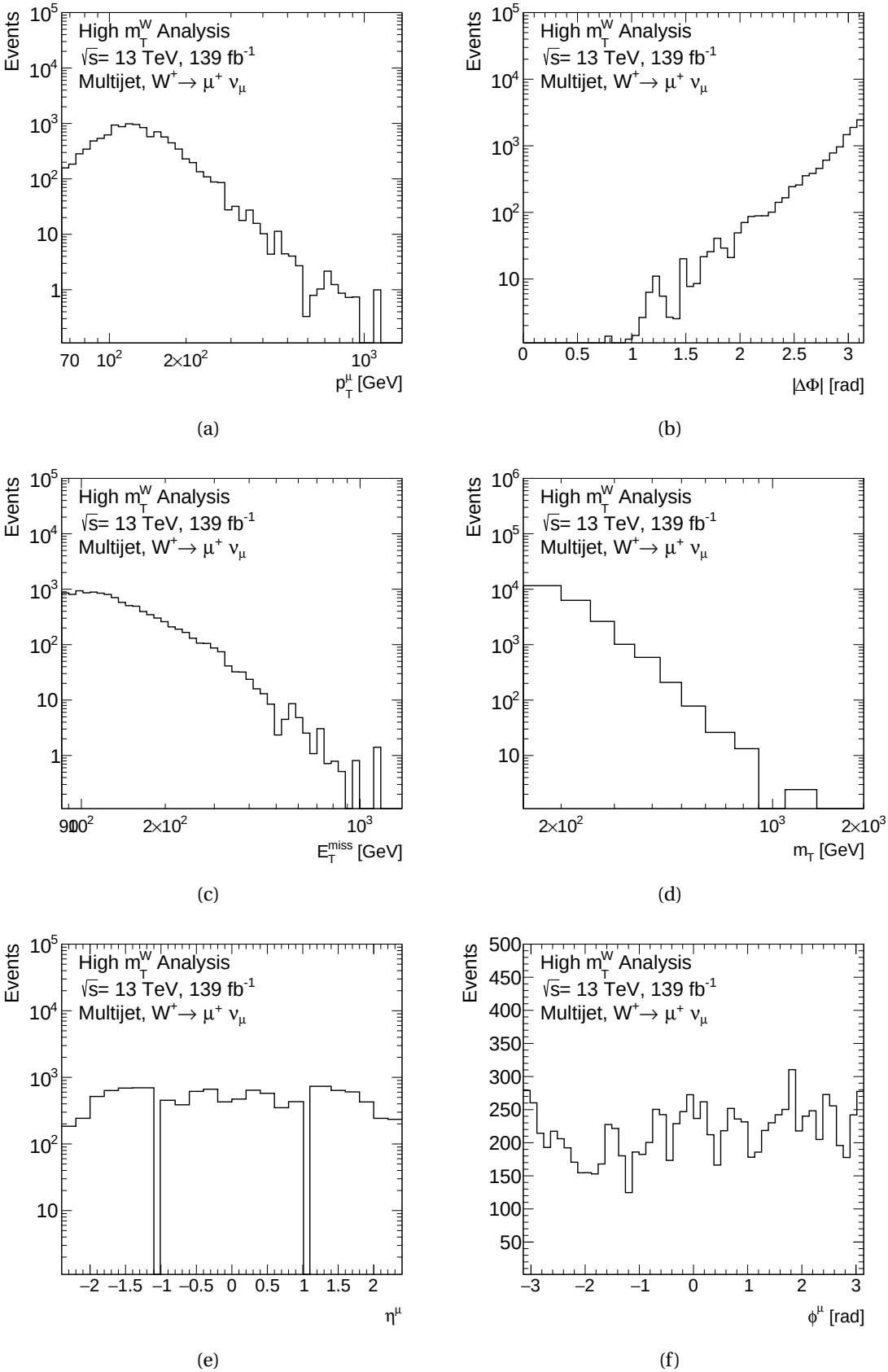

Figure 7.3.: Multijet background estimation for $W^+ \rightarrow \mu^+ \nu$ in p_T^μ, $|\Delta\phi|$, E_T^{miss}, m_T, η^μ and ϕ^μ. These distributions were calculated by summing the final multijet estimates for MC16a, MC16d, and MC16e.

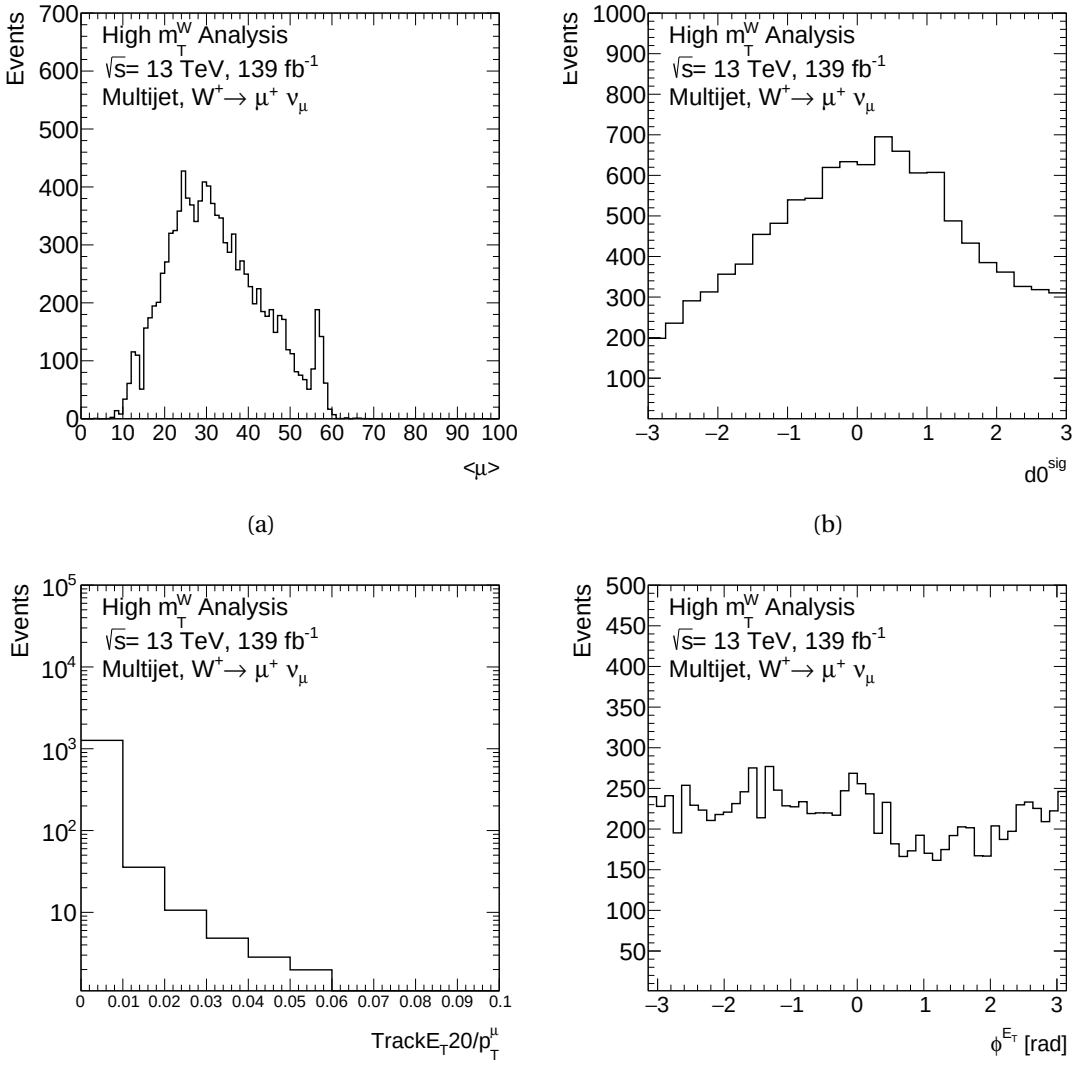

(a) (b)

(c) (d)

Figure 7.4.: Multijet background estimation for $W^+ \rightarrow \mu^+\nu$ in $<\mu>$, $d0^{sig}$, $TrackE_T20/p_T^\mu$ and $\phi^{E_T^{miss}}$. These distributions were calculated by summing the final multijet estimates for MC16a, MC16d, and MC16e.

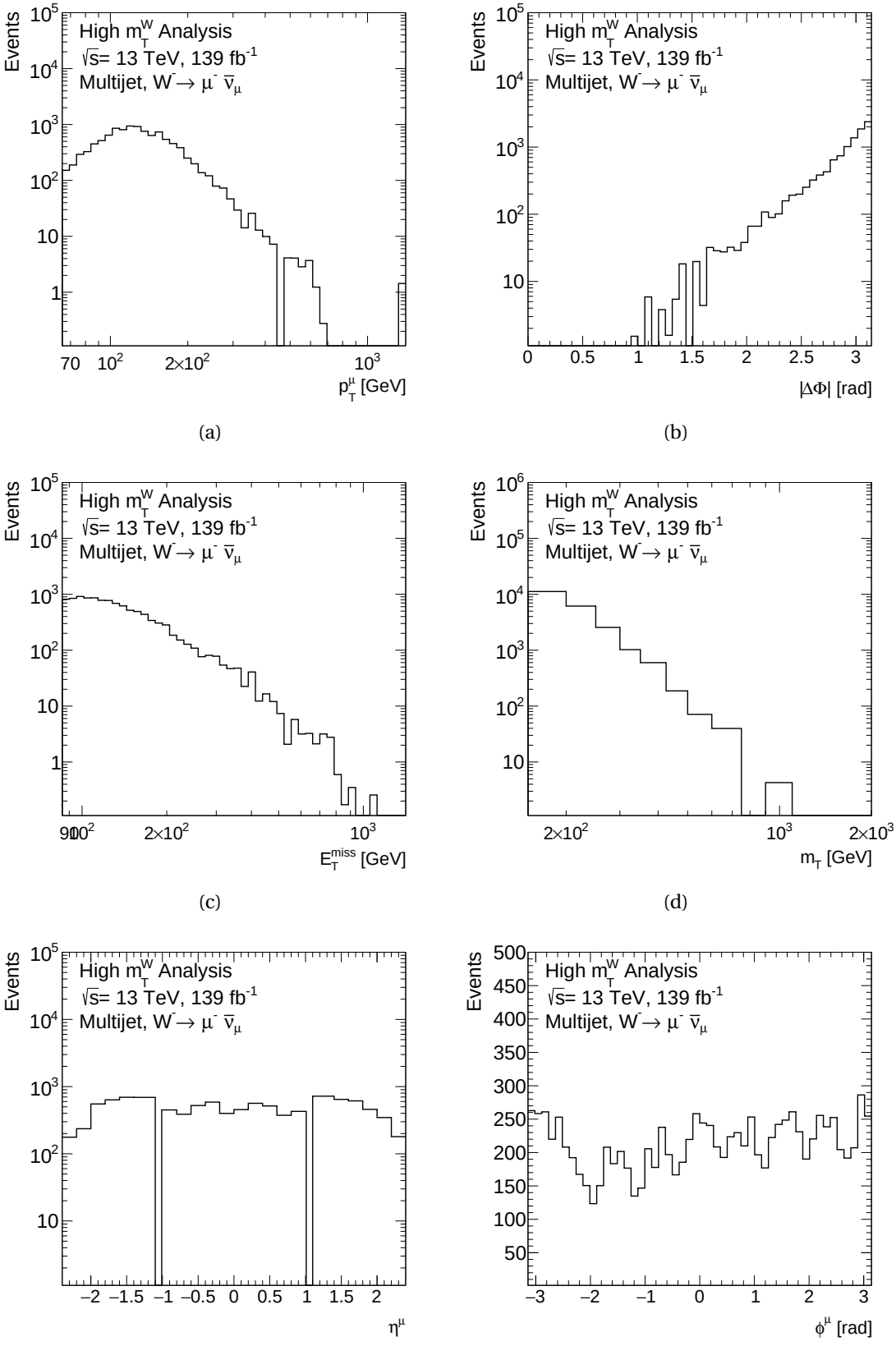

Figure 7.5.: Multijet background estimation for $W^- \to \mu^- \bar{\nu}$ in p_T^μ, $|\Delta\phi|$, E_T^{miss}, m_T, η^μ and ϕ^μ. These distributions were calculated by summing the final multijet estimates for MC16a, MC16d, and MC16e.

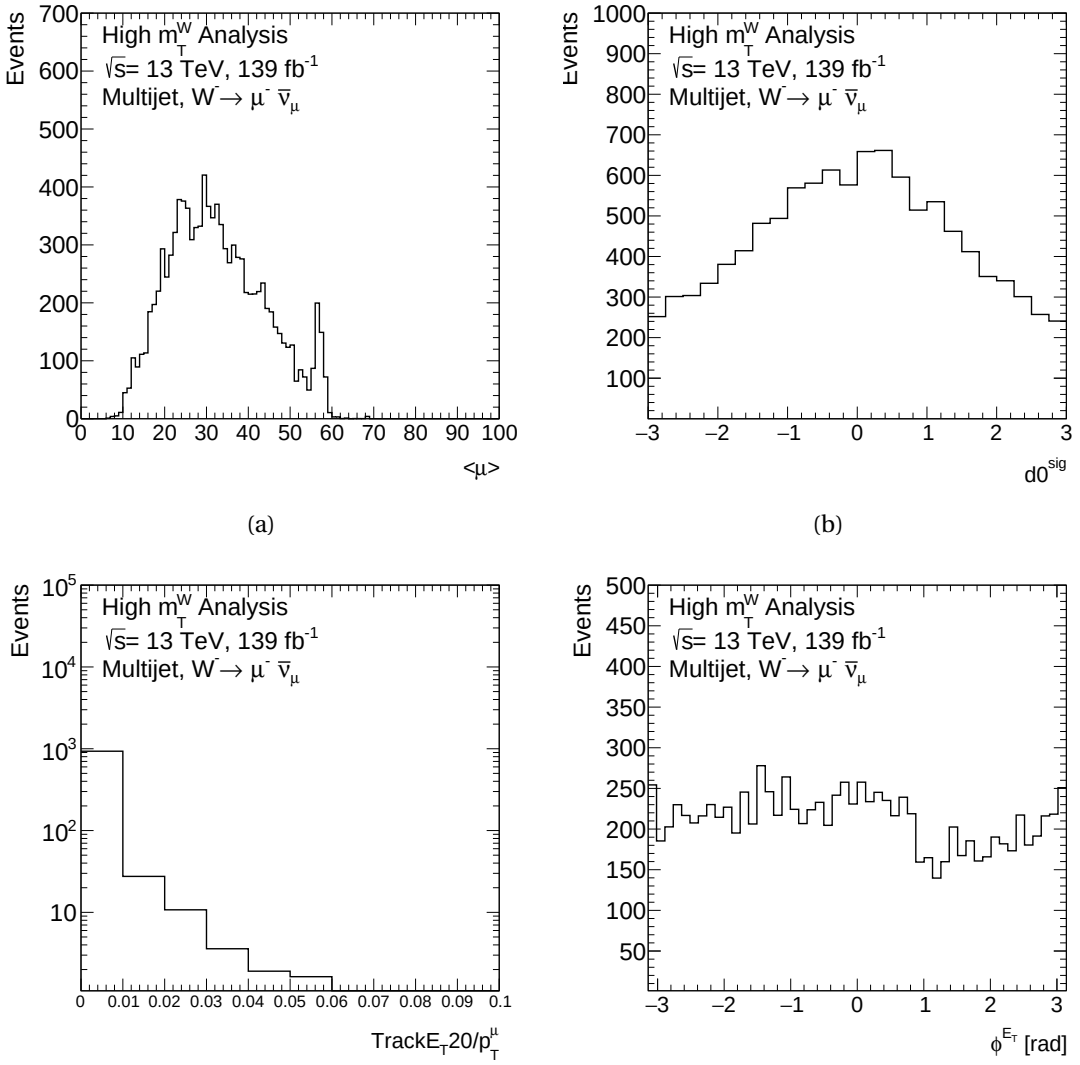

(a) (b)

(c) (d)

Figure 7.6.: Multijet background estimation for $W^- \to \mu^- \bar{\nu}$ in $<\mu>$, $d0^{sig}$, $TrackE_T20/p_T^{\mu}$ and $\phi^{E_T^{miss}}$. These distributions were calculated by summing the final multijet estimates for MC16a, MC16d, and MC16e.

7.5. Multijet Systematic Uncertainties

A QCD-enriched region was defined in estimating the fake efficiency; see Section 7.3.2. The definition of the enriched region is, to a degree, arbitrary. The calculation of the fake efficiency is dependent on the choice of the region selected. The region is modified by changing each selection individually to account for this dependence. These changes are systematic variations. The following variations have been applied, one by one, to calculate the multijet systematics:

- $E_T^{miss} < 55$ GeV
- $E_T^{miss} < 75$ GeV
- $p_T > 75$ GeV
- $|d_0^{sig}| > 1.4$
- $|d_0^{sig}| > 1.6$
- ΔR(Jet,μ) > 0.2 and at least one jet with $p_T > 30$ GeV
- ΔR(Jet,μ) > 0.2 and at least one jet with $p_T > 50$ GeV

After the variation, the difference is taken with respect to the nominal multijet background. The results of this are shown in Figure 7.7. The largest systematic variation comes from the changes in jet p_T and is around 10% in m_T around 200 GeV. The total contribution of the multijet, as shown in Figure 9.1, is around 5% to the total data. Therefore, the relative systematic uncertainty is expected to be around 0.5-1%.

The systematic variations for the final cross-section and asymmetry measurement are also shown in Figure 7.8 and Figure 7.9. These variations have been calculated by taking the multijet input for each calculation of the cross-section or asymmetry and varying it individually. The difference again is taken with respect to the nominal. The largest variation comes from the changes jet p_T, around 0.5-1% in m_T around 200 GeV. The multijet is one of the dominant uncertainties in the lower and intermediate-mass range around $200 - 500$ GeV.

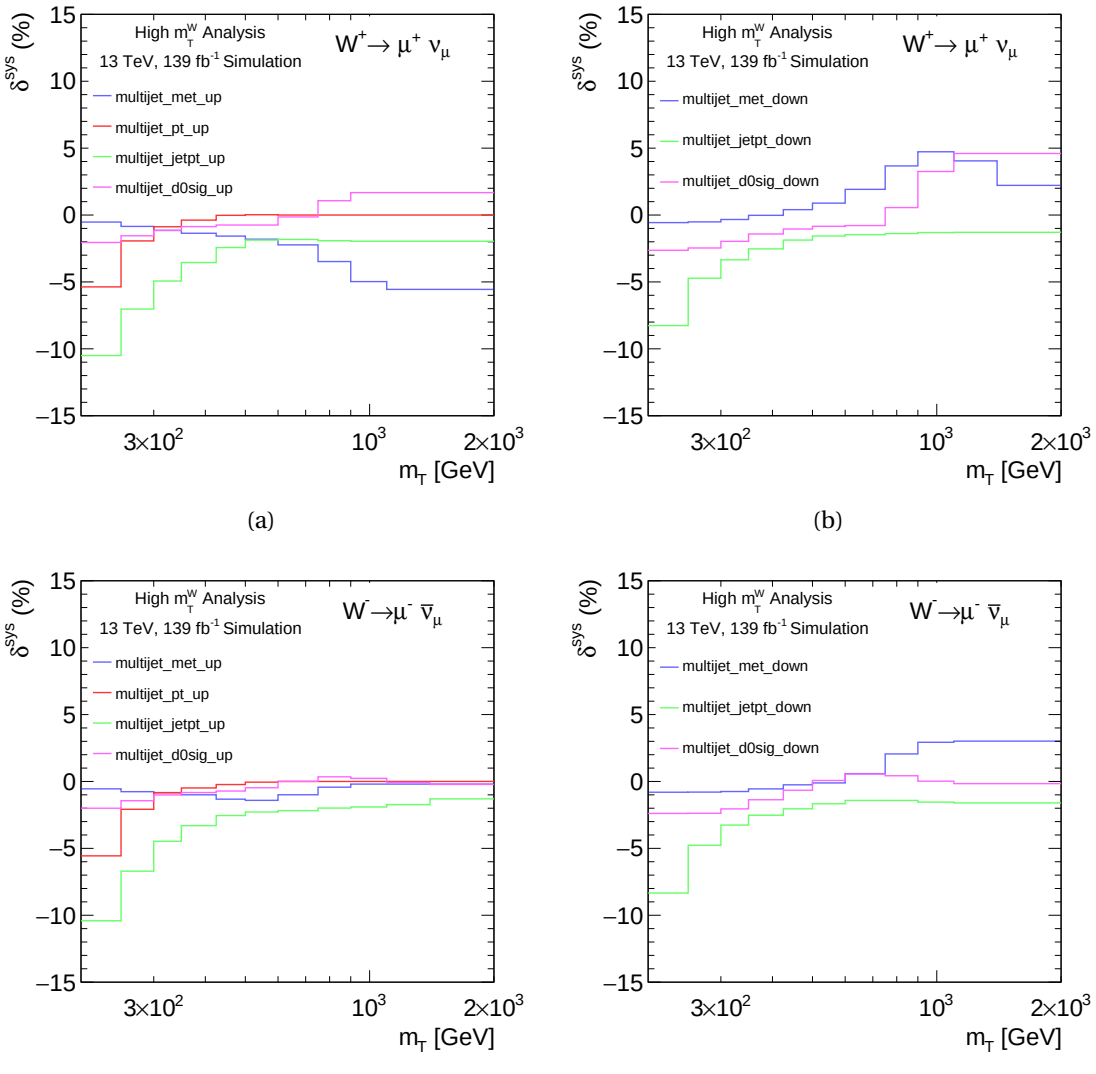

Figure 7.7.: Systematic uncertainties for the multijet background. These uncertainties are for Run-2 data for W^+ (top row) and W^- (bottom row). The plots on the left are for the "up" variation and the right-hand side shows the "down" variation." These uncertainties have been calculated for the control distributions in Chapter 9.

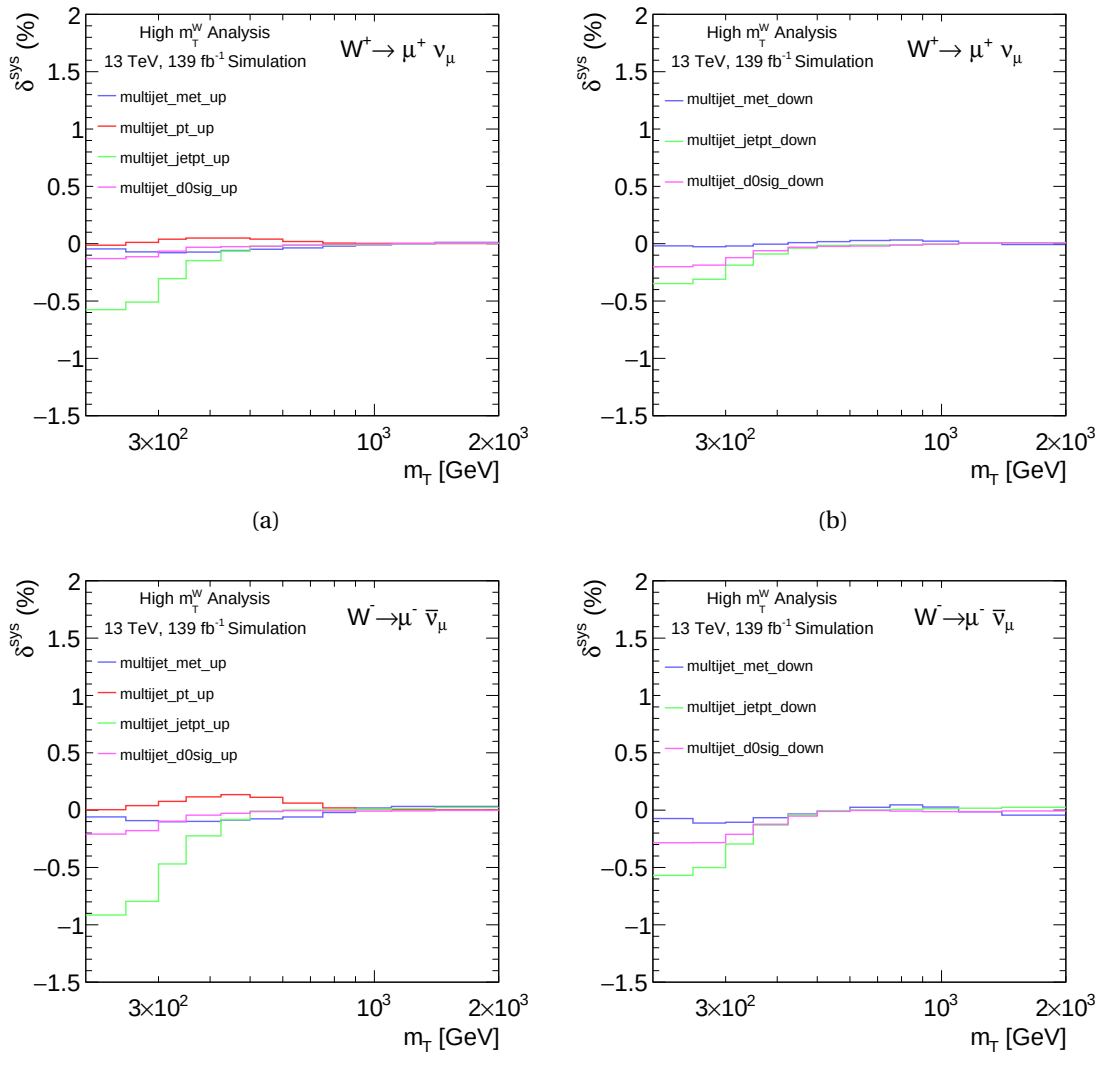

Figure 7.8.: Systematic uncertainties for the multijet background. These uncertainties are for Run-2 data for W^+ (top row) and W^- (bottom row). The plots on the left are for the "up" variation and the right-hand side shows the "down" variation." These uncertainties have been calculated for the cross-sections in Chapter 10.

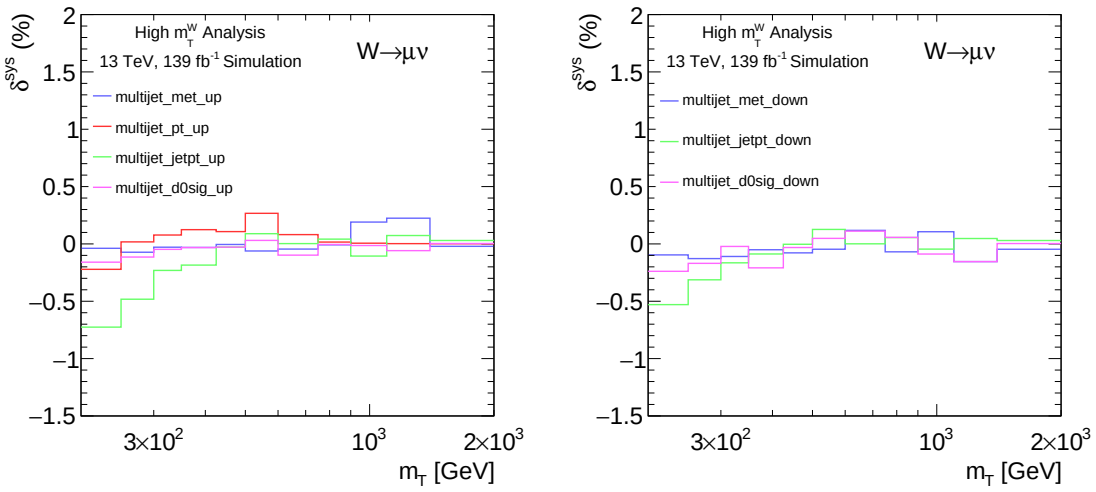

(a) (b)

Figure 7.9.: Systematic uncertainties for the multijet background. These uncertainties are for Run-2 data for W^+ (top row) and W^- (bottom row). The plots on the left are for the "up" variation and the right-hand side shows the "down" variation." These uncertainties have been calculated for the asymmetry in Chapter 10.

8. Systematic Uncertainties

The final result of a precision measurement relies on how the uncertainties affect the final result. This chapter details all of the systematic uncertainties considered in this analysis. The origin and their impact on the analysis have also been discussed.

8.1. Systematic Uncertainty Definition

The systematic uncertainties affect the cross section and asymmetry results through the shape of the distributions and the normalisation. The experimental systematic uncertainties have been applied to the Monte Carlo signal. The uncertainties considered for this analysis vary for nominal yields by one standard deviation "up" and "down" for each given uncertainty. Both charges are shown though there is no substantial difference in most of the uncertainties; any differences have been stated. Smoothed and symmetrised uncertainties have also been explicitly stated, except for one-sided systematics and asymmetry uncertainties.

The standard `ROOT` smoothing algorithm `353QH, twice` is used for smoothing [109]. The `353QH` smoothing algorithm uses a multi-step process to reduce variance in probability density estimation. It involves three components; running medians, running means and quadratic interpolation. The "353" in the algorithm refers to running medians of three, then medians of five, followed by three again. The "Q" refers to the quadratic interpolation, which addresses the shortcomings of the running medians. The "H" refers to Hanning or running means, which handles the problem of monotonic sequences. The "twicing" technique is used to reduce the problem of over-smoothing the real peaks and valleys or regions with large second derivatives. This process involves smoothing the residuals (the difference between the original data sequence and the initial `353QH` smoothed sequence) and adding the result to the previous smooth. [110].

To calculate the uncertainty of a single bin, the following Equation 8.1 is used:

$$\delta^i = \frac{N^i_{sys} - N^i_{nom}}{N^i_{\text{nom}}} \tag{8.1}$$

δ^i is the uncertainty in a bin "i" and helps to study individual systematics effects on the cross-section and asymmetry bin by bin. N^i_{nom} and N^i_{sys} are the number of entries for the nominal where no systematic variation is applied and "sys" where the systematic variation is applied.

In the following Equation 8.2, the up and down systematic uncertainty is averaged bin by bin to get a symmetric systematic uncertainty:

$$\delta^i_{sym} = \frac{\left|\delta^i_{up}\right| + \left|\delta^i_{down}\right|}{2} \tag{8.2}$$

Symmtrising is used to express the systematic variations so that the values are symmetric for the up and down variations. Therefore, for the symmetrised systematics, positive and negative signs are assigned to the symmetrised down and up variations. Symmetrised and smoothed uncertainties are calculated for the control distributions and cross-sections.

To combine the individual systematics and get the total systematic uncertainty for each bin, each systematic is added in quadrature, shown in Equation 8.3:

$$\delta^i_{total} = \sqrt{\sum_{x=1}^{n} \left(\delta^i\right)^2} \tag{8.3}$$

Where δ^i_{total} is the total uncertainty for each bin, the sum runs over all the systematics considered, and δ^i is the systematic uncertainty for an individual systematic in each bin. δ^i_{total} is used for the final cross-section and charge asymmetry systematic uncertainties.

The up or down shift in the systematic parameter can result in different signs of the cross-section shifts for W^+ and W^- which could underestimate/overestimate the systematic uncertainty in the charge asymmetry. Therefore, the up or down shift sign needs to be considered for the charge asymmetry. When summing over all systematics shown in Equation 8.3, for each bin, the positive terms and negative terms for each up and down systematic are instead added in quadrature, except when up and down has the same sign where the largest difference is used. Finally, a conservative approach is taken and the maximum positive or negative total sum is taken.

The number of signal events passing the selection criteria depends on the kinematic cuts, e.g. $p^\mu_T, \eta^\mu, E^{\text{miss}}_T$. This represents a source of uncertainty in the number of events because some systematic uncertainties affect the experimental determination of the value. This arises because when considering fixed cuts, the final number of events after applying a specific selection criterion can change due to the fluctuation of the kinematic variable. Counting the number of events is a linear function and it can be assumed that the uncertainties of each kinematic variable are uncorrelated and independent of each other. Taking this approximation yields vanishingly small covariances between the variables; therefore, the correlation between the different errors is also small. This approximation is reasonable as the determination of different kinematic variables and muon identification is independent, e.g. the p^μ_T and E^{miss}_T calculation should be independent. The transverse mass calculation depends on the missing energy and the muon kinematics calculations, so correlations between these must be considered. The

Category	Systematic
Muons	MUON_ID
	MUON_MS
	MUON_SAGITTA_RESBIAS
	MUON_SAGITTA_DATASTAT
	MUON_SCALE
	leptonSF_MU_SF_ID_STAT
	leptonSF_MU_SF_ID_SYST
	leptonSF_MU_SF_Isol_STAT
	leptonSF_MU_SF_Isol_SYST
	leptonSF_MU_SF_Trigger_STAT
	leptonSF_MU_SF_Trigger_SYST
	leptonSF_MU_SF_TTVA_STAT
	leptonSF_MU_SF_TTVA_SYST

Table 8.1.: List of the experimental systematic uncertainties on the muons.

correlations between the charges would also need to be considered for the asymmetry. However, the approach used in this thesis, where these are treated as uncorrelated, yields a conservative value because taking into account correlations would reduce the total errors.

8.2. Experimental Systematic Uncertainties

In the ATLAS detector, it is impossible to achieve perfect modelling, giving rise to experimental uncertainties. Corrections (like the scale factors) to mitigate these uncertainties implicate systematic and statistical uncertainties. This section briefly describes all of the relevant experimental systematic uncertainties for the measurement in this thesis.

8.2.1. Muon Uncertainties

In Table 8.1 muon systematic uncertainties have been listed. For the scale factors, the discrimination between statistical and systematic contributions is made.

Muon Momentum and Scale Resolution

The calibration for muon momentum is calculated using data and MC samples for $Z \to \mu\mu$ and $J/\Psi \to \mu\mu$ decays. The statistical error has also been added to the systematic uncertainty. Statistical errors arise from the alignment of the MS chambers where there is a resolution correction uncertainty, the arbitrary invariant mass window choice from which a systematic uncertainty is calculated by taking ± 5 GeV of this quantity and scale uncertainties from non-linear effects when fitting the ID correction separately in

$Z \to \mu\mu$ and $J/\Psi \to \mu\mu$ samples. The following figures show the relative systematic variations for the muon calibration for the up and down variations for both positive and negative charges, Figure 8.1a, Figure 8.1b and Figure 8.4a, Figure 8.4b. The MUON_MS variation contributes around 1% for the high m_T region. The MUON_SCALE variation has a negligible contribution [71].

Muon Scale Factors

Four muon efficiency scale factor variations are considered, the muon identification and three selection efficiencies variations from the isolation, trigger and track-to-track vertex association. The MCP group provided the uncertainties and the systematic variations extracted for the given Drell-Yan selection criteria. Figure 8.1a, Figure 8.1b and Figure 8.4a, Figure 8.4b show the identification, isolation and trigger systematic uncertainties. In Figure 8.2a, Figure 8.2b and Figure 8.5a, Figure 8.5b the statistical component of the uncertainties are shown for the identification, isolation, trigger and TTVA along with the systematic component for TTVA uncertainty. The muon identification systematic uncertainty has the larger contribution, with a contribution of up to $\approx 4\%$ in the high m_T region.

There are various sources of systematic and statistical uncertainties for the muon identification scale factor uncertainties. Statistical uncertainty is associated with calculating the identification $Z \to \mu\mu$ and $J/\Psi \to \mu\mu$ data and MC samples. There is also uncertainty in the background subtraction. A definite cone size is used for the tag and probe method (detailed in Section 3.11.7), and a variation of $\pm 50\%$ is used to calculate the systematic uncertainty. For muons of $p_T > 200$ GeV, a 2-3% uncertainty is used to account for the upper limit on the identification efficiency scale factor variation for high muon momenta extracted from the MC.

In the muon isolation scale factor uncertainties, the backgrounds are varied within their uncertainties. The tag and probe method selection criteria are also varied to calculate a systematic uncertainty. The statistical contribution of the systematic uncertainty is also included.

For the muon trigger scale factor uncertainties, variations on the tag and probe selections are used for systematics from the background. The systematic uncertainties from the event topology and the p_T dependence are also considered. The statistical contribution of the systematic uncertainty is also included.

In the muon TTVA scale factor uncertainties, the backgrounds vary within the uncertainties and by shifting the tag and probe method selections. The statistical contribution to the systematics is also considered.

Muon Sagitta

For the sagitta bias, a correction is applied as recommended by the MCP [69] group, which is applied to the data. The source of the uncertainties comes from the resolution of the muon momentum and the calculation of the correction itself. These are calculated by comparing the magnitude of the corrections for the positive and negative channels at the detector level. These corrections result in two uncertainties in the signal MC, MUON_SAGITTA_RESBIAS and MUON_SAGITTA_DATASTAT. The sagitta resbias is, by far, the largest systematic uncertainty in the high m_T region as shown in Figure 8.1c, Figure 8.1d and Figure 8.4c, Figure 8.4d. The sagitta has a different impact depending on the charge. This leads to opposite behaviour in the up and down variation observed for the W^+ and W^- selections. The value of these uncertainties in W^+ reaches $\approx 10\%$ in the down variation and for W^-, reaches $\approx 15\%$ for the up variation in the high m_T region. For the sagitta data statistical uncertainties, seen in Figure 8.1g, Figure 8.1h and Figure 8.4g, Figure 8.4h, the value is largest in W^-, reaching about 1% for the high m_T region.

8.2.2. Muon Charge Misidentification

Charge misidentification is the incorrect assignment of the electric charge. In data, charge misidentification occurs when the charge of a muon before entering the detector is different from the charge measured in the detector. Similarly, in Monte Carlo simulations, charge misidentification happens when the charge of a generated muon differs from the charge assigned after reconstruction. For the muon charge asymmetry, where two muons of opposite charge are considered, the charge misidentification is relevant. The charge of the muon is reconstructed from the curvature of the associated track. A misidentification can occur from matching an incorrect track to the muon candidate, from a mismeasurement of the curvature of the muon candidate track or misalignments in the detector systems. This leads to a charge-dependent bias and a correction can be calculated.

One approach for estimating muons with misidentified charge involves ensuring a consistent measurement between the MS and ID, allowing for an independent cross-check. In a prior study of W charge asymmetry at $\sqrt{s} = 7$ TeV, the researchers utilised redundant ID and MS momentum measurements, resulting in a charge misidentification rate below 10^{-4} within the p_T range of $20-90$ GeV. This had a negligible impact on the asymmetry measurement [111].

In this analysis, high p_T muons pose a challenge due to their reduced curvature in the magnetic field. As the momentum of a particle increases, its track becomes less curved, making it more difficult to accurately measure the charge and momentum. Consequently, it is expected that the muon charge misidentification rate would be larger for high p_T muons. Despite the important role muons play in many ATLAS analyses, there

is currently no solid estimation available for muon charge misidentification.

However, there are studies which have been carried out to estimate the charge misidentification for electrons. The charge of an electron is reconstructed from the curvature of the associated track in the ID. A misidentification can occur from matching an incorrect track to the electron candidate or from a mismeasurement of the curvature of the electron candidate track. In pair production resulting from bremsstrahlung, three tracks in close proximity can occur, which leads to ambiguity in charge assignment. To estimate the probability of charge misidentification, a sample of $Z \rightarrow ee$ events is used. The number of events where both electrons have the same electric charge is compared to the number of events where they have opposite charges. The charge misidentification for electrons is estimated to be in the range of 10^{-3} to 10^{-2} as measured by the EGamma group [112].

If a calculation of the muon charge misidentification were to be performed, an alternative method could be used. This would involve using the $Z \rightarrow \mu^+\mu^-$ sample where the Z boson decays to two muons of opposite charge. The charge misidentification rate can be calculated by comparing the number of events with same-charge muons to opposite-charge muons, providing a measure of muon misidentification.

Based on the study of W charge asymmetry at $\sqrt{s} = 7$ TeV and the lower estimate of charge misidentification in muon compared to electrons, it is expected that the correction for charge misidentification would have a minimal impact on the final results of this asymmetry measurement. Therefore, the charge misidentification systematic uncertainty has not been considered in this thesis. This decision is also justified by the dominant contributions of the statistical uncertainties (up to 40%) and the systematic uncertainties related to the sagitta bias correction (up to 33%) in the asymmetry measurement.

8.2.3. Missing Energy Uncertainties

The E_T^{miss} is calculated using leptons, photons and jets from which arise uncertainties which are propagated to the E_T^{miss} uncertainties. More uncertainties arise from the reconstruction of the soft term, calculated by comparing the Monte Carlo and data simulation using the balance of the soft term and the hard objects. The $E_{\text{T}}^{\text{miss}}$ soft term systematic uncertainties are listed in Table 8.2. The relative impact of the E_T^{miss} systematic uncertainties are shown in Figure 8.1e, Figure 8.1f and Figure 8.4e, Figure 8.4f. The value of these uncertainties is largest in W^-, reaching about 1.5% for the low m_T region. Similar behaviour is observed for the W^+ and W^- selections.

8.2.4. Jet Uncertainties

The 36 systematic uncertainties for the jet energy scale (JES) and jet energy resolution (JER) have been listed in Table 8.3. This thesis uses the Category Reduction scheme

Category	Systematic
$E_{\mathrm{T}}^{\mathrm{miss}}$	SoftTrk_Scale
	SoftTrk_ResoPara
	SoftTrk_ResoPerp

Table 8.2.: List of experimental systematic uncertainties on the $E_{\mathrm{T}}^{\mathrm{miss}}$ soft term.

based on 28 nuisance parameters for the JES. The SimpleJER scheme is used based on eight nuisance parameters for the JER. The jet systematic uncertainty are shown in Figure 8.2, Figure 8.3 and Figure 8.5, Figure 8.6. For both the JES and JER systematics, the uncertainty is largest at low m_T^W and approaches zero at high m_T^W. The JER EffectiveNP_1 is one of the largest uncertainties, reaching $\approx 2\%$ in the low m_T^W region.

The number of jet uncertainties is very large. Therefore, their processing is computationally intensive. The ATLAS Jet and Etmiss Combined Performance [77] group have a recommended set of systematics which merge individual systematics to reduce the computational resources required. This analysis utilises these systematics and the official naming conventions provided by the group.

Jet uncertainties can account for assumptions made in the event topology, MC simulations and reconstruction algorithms. The uncertainties from pileup are also considered for the mismodelling of the number of primary vertices, the number of interactions and residual p_T dependences. Another source of systematics affecting the jets arises from the objects' scale and resolution (muons, electrons and photons). There are also uncertainties regarding the efficiency of the JVT cut applied to select jets. Uncertainties from the statistical limitations of the data and MC samples, which are limited and used to perform the calibrations, have also been included.

Variations taken for the jet systematics include the JET_JER_EffectiveNP_1,2,3,4,5,6,7. These uncertainties arise from pileup, $Z/\gamma+$ jet and multijet in situ calibrations, accounting for assumptions made in the MC simulation, event topology and sample statistics. These uncertainties account for electron, muon, and photon energy scale uncertainties. The nuisance parameters associated with these systematics are combined and a reduction is performed, taking the largest components and keeping these whilst averaging the rest of the components into a single nuisance parameter (np) [113].

For the JET_EtaIntercalibration_NonClosure a jet correction is used to account for biases in the jet η reconstruction which arise from the transition between different calorimeter environments and sudden changes in calorimeter granularity, the non-closure of the corrections is accounted for by this jet uncertainty.

In the JET_JER_DataVsMC, uncertainties arise from using different MC generators to study the agreement with data for the several kinematic jet variables.

Category	Systematic
Jet Energy Scale	BJES_Response
	EffectiveNP_Detector1
	EffectiveNP_Detector2
	EffectiveNP_Mixed1
	EffectiveNP_Mixed2
	EffectiveNP_Mixed3
	EffectiveNP_Modelling1
	EffectiveNP_Modelling2
	EffectiveNP_Modelling3
	EffectiveNP_Modelling4
	EffectiveNP_Statistical1
	EffectiveNP_Statistical2
	EffectiveNP_Statistical3
	EffectiveNP_Statistical4
	EffectiveNP_Statistical5
	EffectiveNP_Statistical6
	EtaIntercalibration_Modelling
	EtaIntercalibration_NonClosure_highE
	EtaIntercalibration_NonClosure_negEta
	EtaIntercalibration_NonClosure_posEta
	EtaIntercalibration_TotalStat
	Flavor_Composition
	Flavor_Response
	Pileup_OffsetMu
	Pileup_OffsetNPV
	Pileup_PtTerm
	Pileup_RhoTopology
Jet Energy Resolution	DataVsMC
	Detector 1
	EffectiveNP_1
	EffectiveNP_2
	EffectiveNP_3
	EffectiveNP_4
	EffectiveNP_5
	EffectiveNP_6
	EffectiveNP_7restTerm

Table 8.3.: List of experimental systematic uncertainties for the jet energy scale and jet energy resolution.

8.2.5. Pileup Reweighting

The pileup reweighting is an additional data scale factor which improves the agreement between data and simulation of the pileup distributions shown in Section 9. This correction aims to match the number of primary vertices as a function of pileup interactions and to include mismodelling by inelastic interactions. The systematic variations of the pileup weight are taken from the pileup reweighting tool [114]. The relative systematic uncertainty coming from the pileup can be seen in Figure 8.2a, Figure 8.2b and Figure 8.5a, Figure 8.5b. The maximum variation seen in these figures in the up and down is of the order of 1%.

8.2.6. Luminosity

The total integrated luminosity used is 139.0 fb^{-1}. The primary luminosity measurement is completed using the LUCID-2 detector [115]. When comparing the different subdetectors and algorithms, an uncertainty is obtained. The uncertainty for the combined 2015-2018 dataset is 1.7% [45].

8.3. Fake Muon Background Systematic Uncertainties

In Chapter 7, the calculation of the multijet using the matrix method is described. This method requires a calculation of real and fake efficiencies. In particular, the fake efficiencies are defined using a QCD-enriched region from which systematic variations are calculated. The resulting systematic uncertainties are detailed in Section 7.5. The uncertainties for the fake muon background are estimated using a data-driven method as described in Section 7.5.

8.4. Theoretical Systematic Uncertainties

For this analysis, no theory uncertainties are included. In the Powheg+Pythia8 signal Monte Carlo samples used, no theory uncertainties were included in the form of generator weights. However, alternative Monte Carlo is available, SHERPA 2.2.11 and Powheg+Herwig7, which can account for generator and shower uncertainties. The SHERPA 2.2.11 uses internal showering provided by SHERPA and the PDF set NNPDF3.0. The Powheg+Herwig7 is generated using Powheg-Box v2 at NLO QCD and showered with Herwig 7 using the PDF set CT18NNLO. The alternative Monte Carlo also stores generator weights which can estimate theory uncertainties for the μ_R and μ_F scales, the strong coupling constant α_s, EW corrections and the used PDFs. The alternative MC has not yet been evaluated for the full Run-2 dataset and there are still some open issues. In this thesis, theory uncertainties have not been included in the measurements

presented but are expected to not alter the results presented. This estimation is based on the results presented by the $\sqrt{s} = 8$ TeV measurement of the cross-section and charge asymmetry of W bosons where the total theoretical uncertainties shown is up to 7% [5]. This is small compared to the uncertainties presented in this chapter. A similar study for the theoretical uncertainties in the $\sqrt{s} = 13$ TeV measurement is expected to be performed in the future.

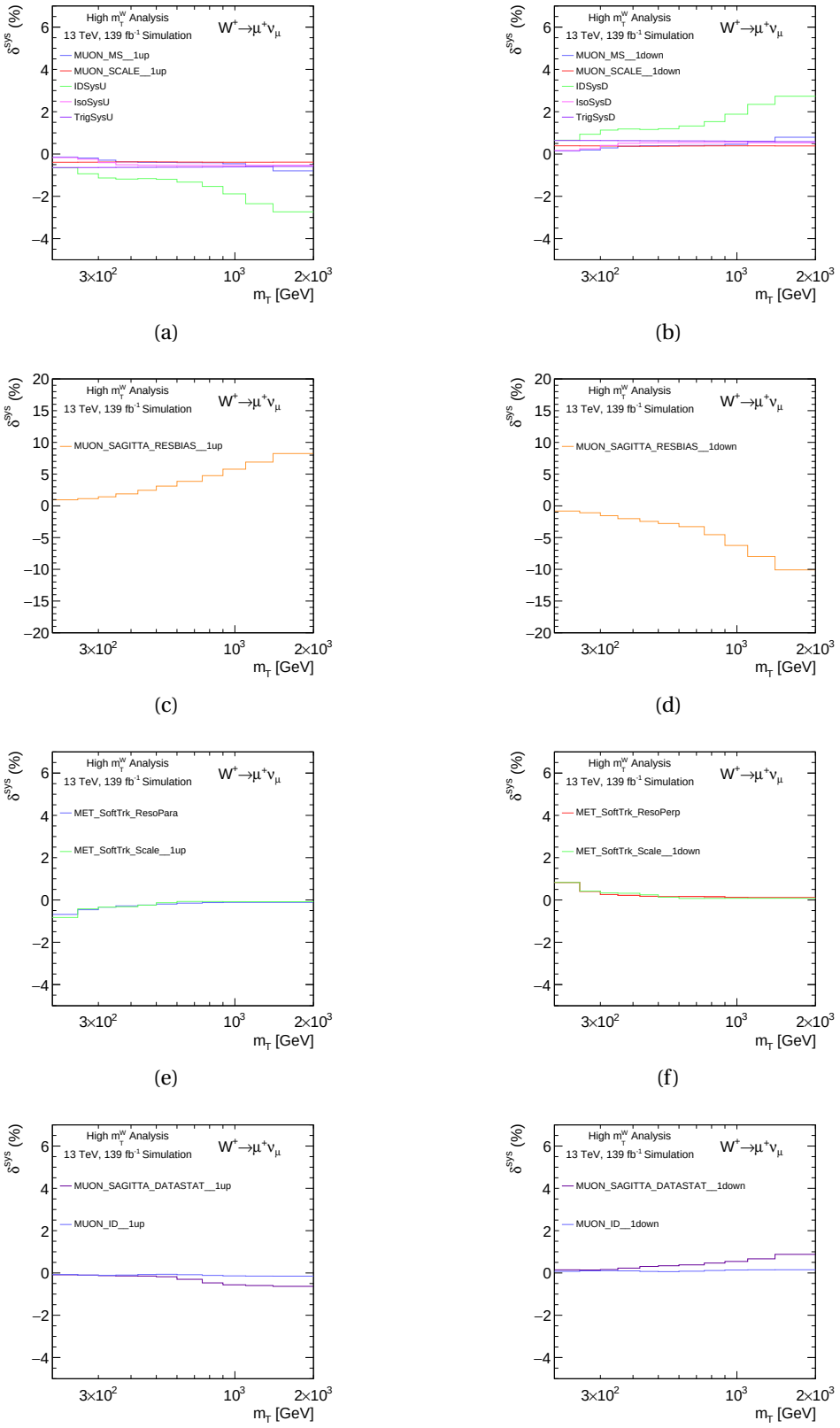

Figure 8.1.: Individual contributions to the systematic variations in Run-2 for $W^+ \to \mu^+ \nu$ in the measurement binning for m_T. The plots on the left show the up variations and those on the right show the down variations. All values are presented in percentages. Plots (a) and (b) show the muon scale and resolution uncertainties along with the muon scale identification, isolation and trigger scale factor uncertainties. Plots (c) and (d) display the muon sagitta resolution bias uncertainty. Plots (e) and (f) show the missing energy soft track uncertainties. The labels in the legend of both plots are the conventional names given by the JetEtMiss group. "MET" stands for missing energy, "SofTrk" refers to soft track E_T^{miss} and "ResoPara" and "ResoPerp" refers to the resolution uncertainty on the parallel and perpendicular component. Plots (g) and (h) display the muon sagitta data statistical and muon identification uncertainty.

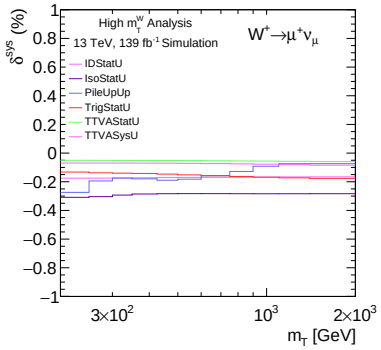

(a)

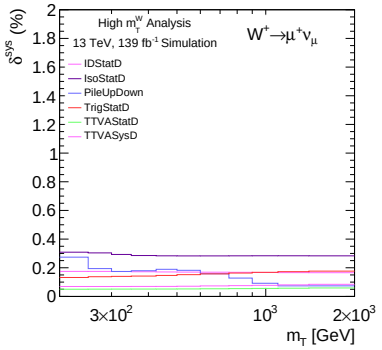

(b)

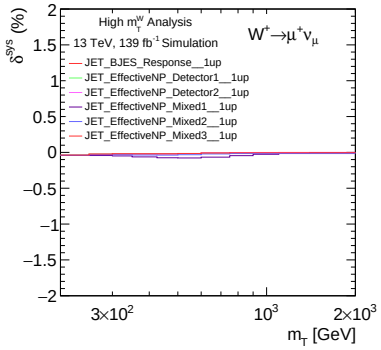

(c)

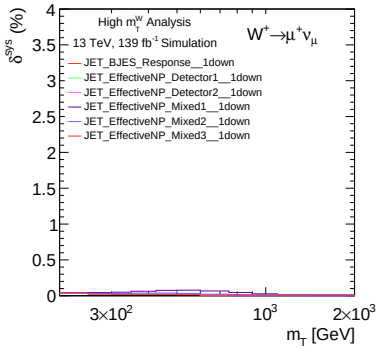

(d)

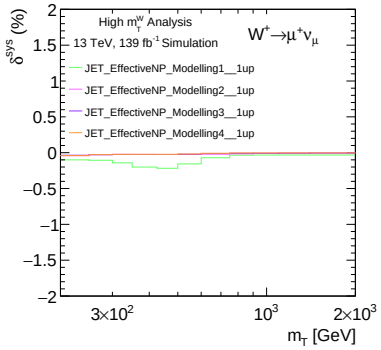

(e)

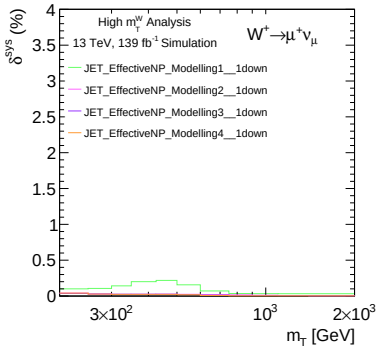

(f)

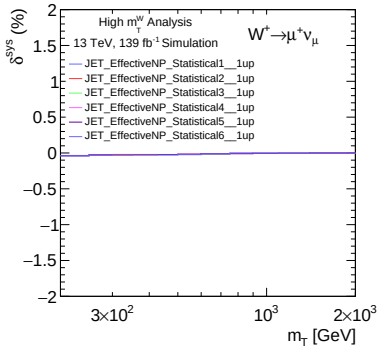

(g)

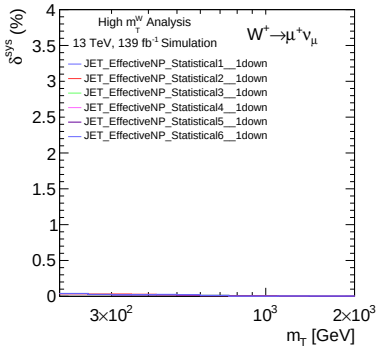

(h)

Figure 8.2.: Individual contributions to the systematic variations in Run-2 for $W^+ \to \mu^+ \nu$ in the measurement binning for m_T. The plots on the left show the up variations and those on the right show the down variations. All values are presented in percentages. Plots (a) and (b) show the scale factor uncertainties for the muon identification, isolation, trigger and TTVA statistical uncertainties. It also shows the TTVA systematic uncertainty and the pileup uncertainty. Plots (c) to (h) display the effect of the jet's systematic uncertainties.

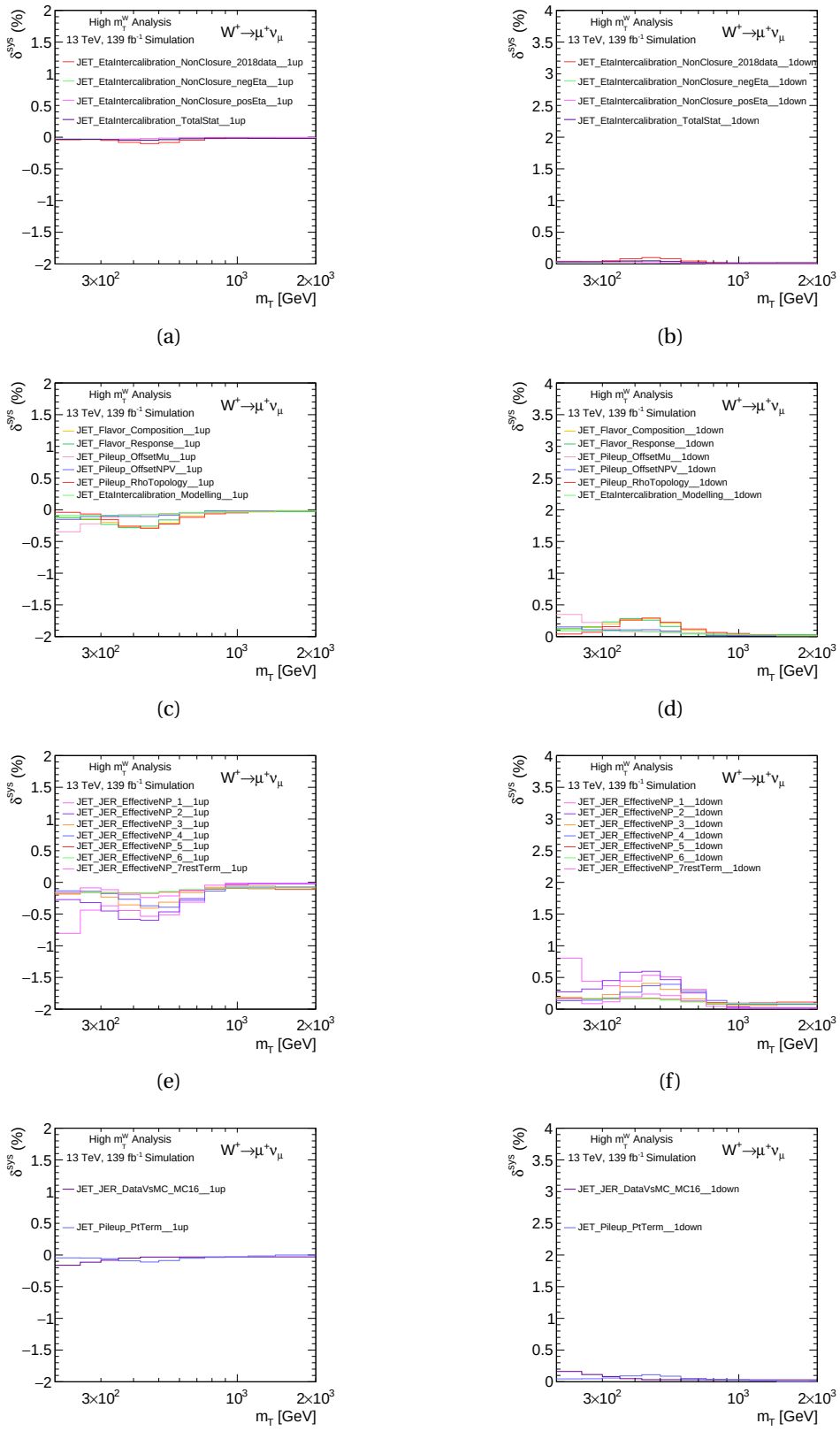

Figure 8.3.: Individual contributions to the systematic variations in Run-2 for $W^+ \to \mu^+\nu$ in the measurement binning for m_T. The plots on the left show the up variations and those on the right show the down variations. All values are presented in percentages. Plots (a) to (h) display the effect of the jet's systematic uncertainties.

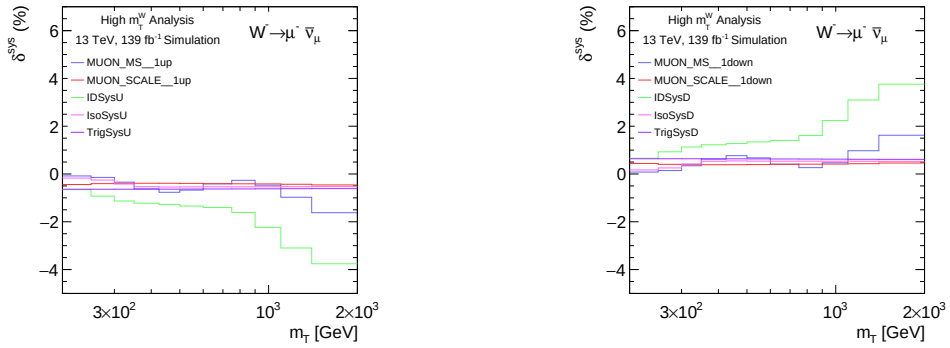

(a)

(b)

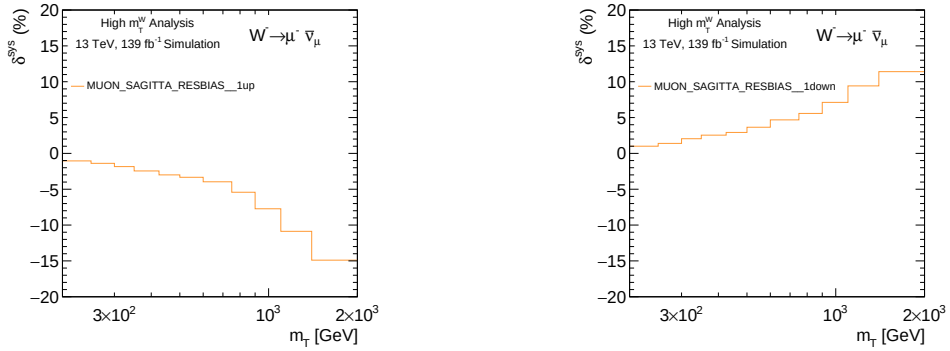

(c)

(d)

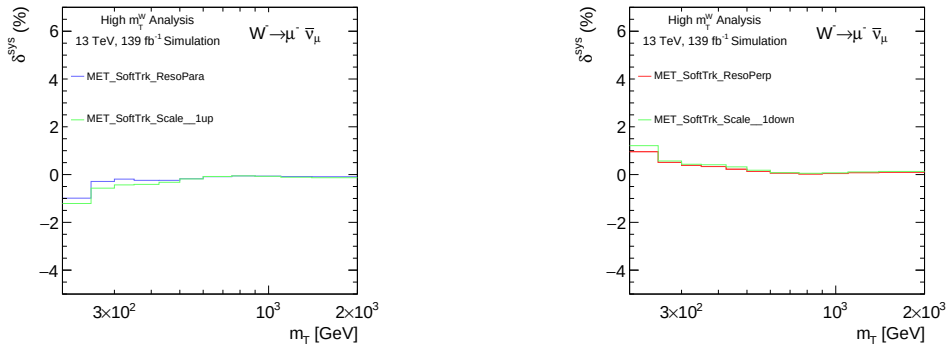

(e)

(f)

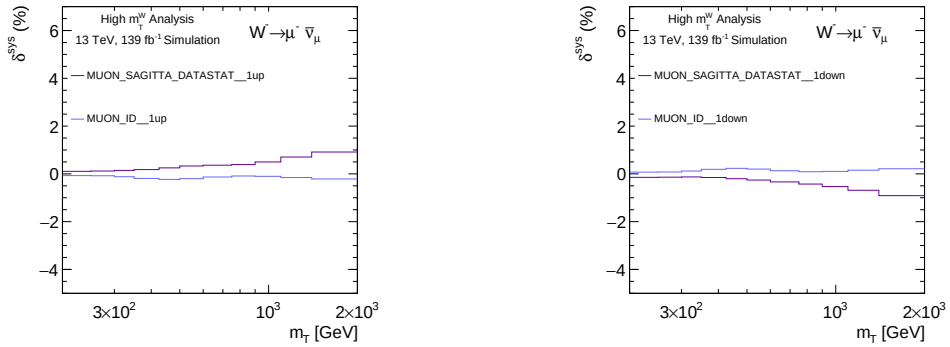

(g)

(h)

Figure 8.4.: Individual contributions to the systematic variations in Run-2 for $W^- \to \mu^- \bar{\nu}$ in the measurement binning for m_T. The plots on the left show the up variations and those on the right show the down variations. All values are presented in percentages. Plots (a) and (b) show the muon scale and resolution uncertainties along with the muon scale identification, isolation and trigger scale factor uncertainties. Plots (c) and (d) display the muon sagitta resolution bias uncertainty. Plots (e) and (f) show the missing energy soft track uncertainties. The labels in the legend of both plots are the conventional names given by the JetEtMiss group. "MET" stands for missing energy, "SofTrk" refers to soft track E_T^{miss} and "ResoPara" and "ResoPerp" refers to the resolution uncertainty on the parallel and perpendicular component. Plots (g) and (h) display the muon sagitta data statistical and muon identification uncertainty.

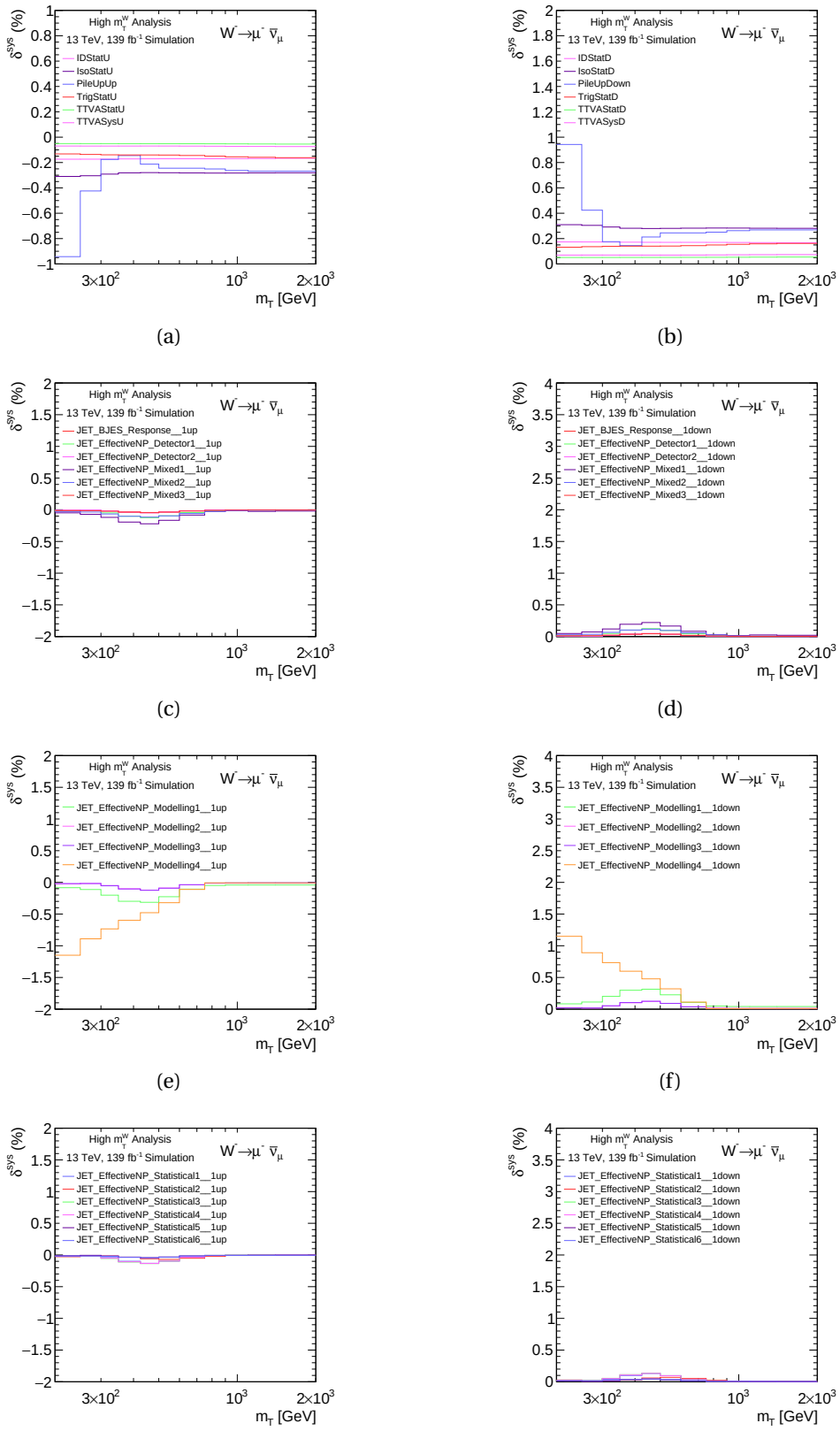

Figure 8.5.: Individual contributions to the systematic variations in Run-2 for $W^- \to \mu^- \bar{\nu}$ in the measurement binning for m_T. The plots on the left show the up variations and those on the right show the down variations. All values are presented in percentages. Plots (a) and (b) show the scale factor uncertainties for the muon identification, isolation, trigger and TTVA statistical uncertainties. Also shown are the TTVA systematic uncertainty and the pileup uncertainty. Plots (c) to (h) display the effect of the jet's systematic uncertainties.

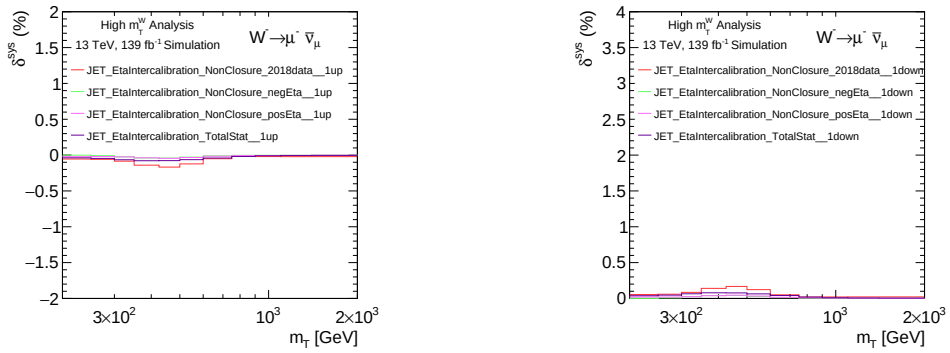

(a)

(b)

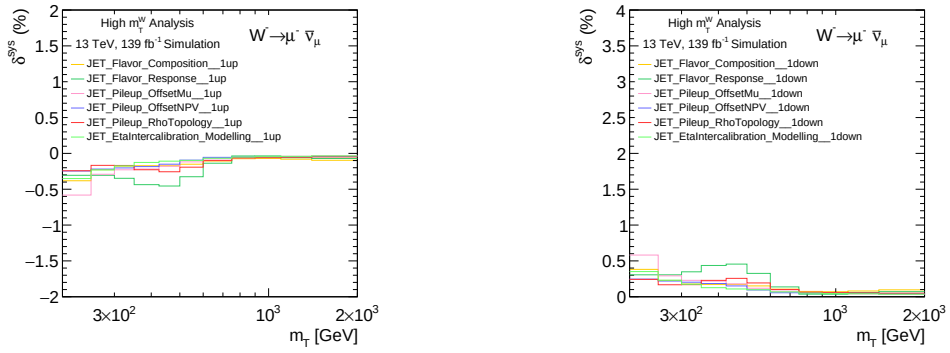

(c)

(d)

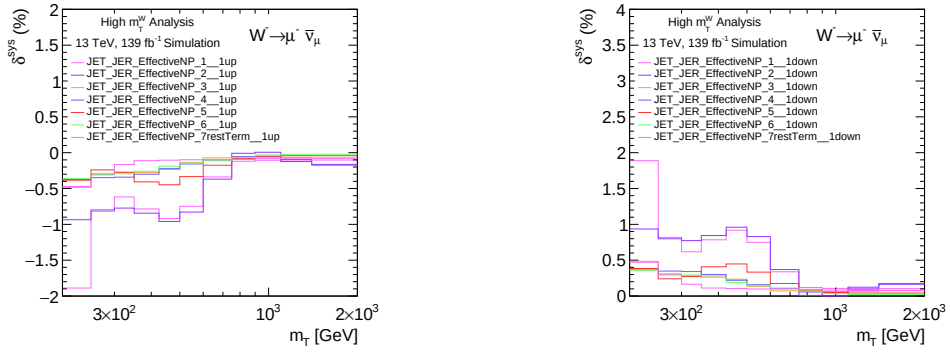

(e)

(f)

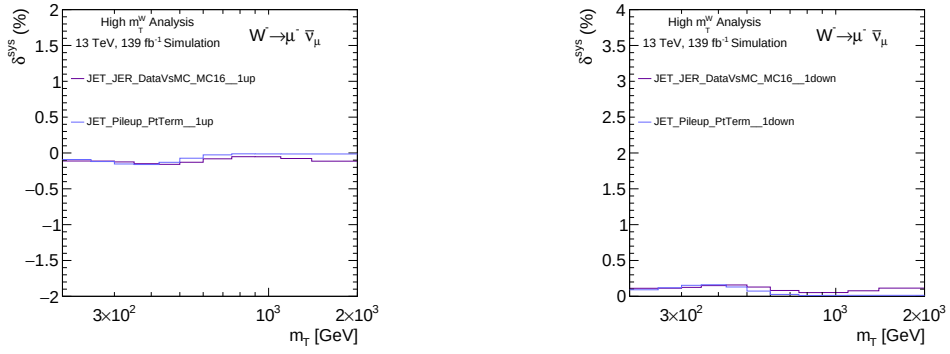

(g)

(h)

Figure 8.6.: Individual contributions to the systematic variations in Run-2 for $W^- \to \mu^- \bar{\nu}$ in the measurement binning for m_T. The plots on the left show the up variations and those on the right show the down variations. All values are presented in percentages. Plots (a) to (h) display the effect of the jet's systematic uncertainties.

9. Control Distributions

The following chapter presents key kinematic distributions with cutflows for this analysis. The kinematic distributions show the agreement between data collected by the ATLAS detector and cross-section predictions convoluted with the detector's response by comparing the number of events in each distribution. This is vital for checking the validity of the W boson selection criteria, cross-section measurements and charge asymmetry measurement. The cutflows summarise each selection criterion's effect on the total number of events selected. These are shown for the data and all Monte-Carlo samples used.

9.1. Monte Carlo to Data Comparison

The selections presented in Chapter 6 define a signal region with sufficient statistics in the signal process ($W^+ \to \mu^+\nu$ and $W^- \to \mu^-\bar{\nu}$) where the cross-section will be measured. The control distributions all use a 200 GeV m_T^W cut. The shadow bin, used for stabilising the unfolding, is not considered here. The MC-data comparison distributions in this chapter are shown, charge-separated, for the full Run-2 period. Appendix E shows the individual Monte-Carlo campaign distributions.

The following control distributions are shown for W^+ in Figures 9.2 and 9.3 and W^- in Figures 9.4 and 9.5. The Monte Carlo predictions are scaled to the pp cross-section, the data luminosity and weighted as presented in Section 5 using Equation 5.3. It is important to note that the data has a sagitta bias correction applied, which ensures a good MC-Data comparison, particularly in W^-. The uncertainty bands shown for each distribution include the statistical uncertainty, the systematic uncertainty and the uncertainty from the multijet calculation. Experimental systematic uncertainties are considered for measuring the muon, E_T^{miss} and jets in the signal MC discussed in Chapter 8. Additional data-driven systematic uncertainties for the multijet background are also considered, as discussed in Chapter 7. No theoretical or unfolding uncertainties are currently included; however, these are expected to have a minimal impact on the distributions (around a few percent).

The fraction of predicted MC event yields to the data are shown for each charge in Figure 9.1a and Figure 9.1b. As expected, the signal process has the largest contribution of approximately 60% in the signal region. The most dominant background process for both charges is $t\bar{t}$ with a contribution of approximately 20%. An 8% contribution

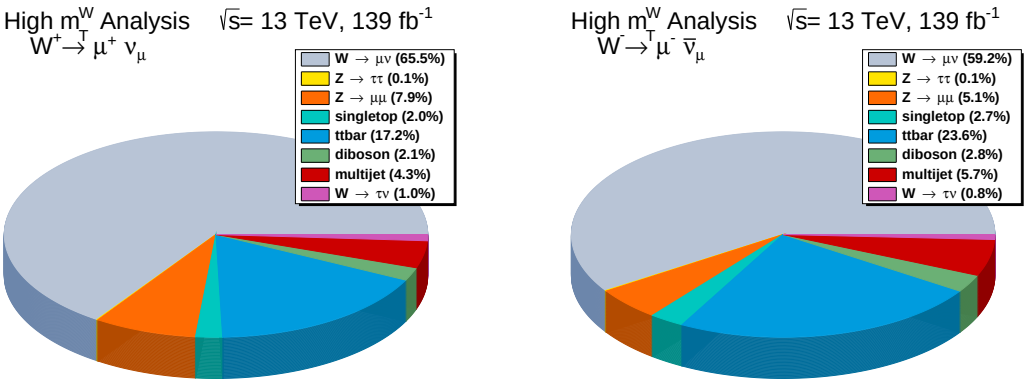

(a) (b)

Figure 9.1.: Chart showing relative contributions of all Monte Carlo in the signal region for Run-2 (139 fb^{-1}), for muon charge (a) W^+ and (b) W^-.

follows this in the $Z \to \mu\mu$ background in W^+ and a 5.7% contribution in the multijet background in W^-.

The kinematic variables considered are:

Muon transverse momentum, p_T^μ

The p_T^μ selection is one of the most significant cuts taken in this analysis. The control distribution for p_T^μ is shown in Figure 9.2a and Figure 9.4a for W^+ and W^- respectively. At lower transverse momentum values ($\approx$ 100 GeV), there is a peak and the contribution to the background here is also the largest. The distribution peaks at approximately half of the 200 GeV m_T^W selection taken. The agreement between the data and the prediction is shown in the lower panel. There is good agreement in the regions with most statistics. At lower and higher p_T^μ the difference between the values becomes more substantial. However, this is expected and is within the range of statistical and systematic uncertainties.

Difference of azimuthal angle between the muon and event missing energy, $|\Delta\phi|$

This distribution, shown in Figure 9.2b and Figure 9.4b for W^+ and W^- respectively, is peaked around π. When muons and neutrinos are produced in the $W \to \mu\nu$ process, they are mostly expected to be back to back. Therefore, the azimuthal separation angle between them will be close to π, reflected by the peak in events in the distribution. This peak is shown for the signal process and all the electroweak backgrounds. The data and prediction agreement is shown in the lower panel for both W^+ and W^-. The agreement is at the per cent level in the highest statistic region, $|\Delta\phi| \approx \pi$. At smaller $|\Delta\phi|$, there is a larger difference between data and prediction ($\approx$ 20%).

Event missing transverse energy, E_T^{miss}

The missing energy of an event is described in Section 6.1.9 and acts as an approxi-

mation to the transverse neutrino momentum. The E_T^{miss} selects $W \rightarrow \mu\nu$ events. The muon and neutrino kinematics are similar for this process; therefore, the distributions shown in Figure 9.2c and Figure 9.4c are likewise peaked at $\approx$ 100 GeV. The data and prediction agreement in the lower panel show agreement at the per cent level in the highest statistic region. The difference between the values becomes more substantial at lower and higher E_T^{miss}. However, this is expected and is within the range of statistical and systematic uncertainties.

Event transverse mass, m_T

The event transverse mass is an important distribution used in the final cross-section and charge asymmetry measurements. The m_T is defined in Equation 6.4 and is dependent on $p_T^{\mu}, E_T^{\text{miss}}$ and $\Delta\phi$. All three of these distributions must first be consistent before m_T is considered. The m_T is also used to select $W \rightarrow \mu\nu$ events. The distributions in in Figure 9.2d and Figure 9.4d for W^+ and W^- respectively show the m_T distribution. The binning for this m_T distribution is the same as the binning for the final cross-section and charge asymmetry measurements. An explanation on how the binning was chosen is given in Section 10.4.

The distribution peaks around the lower m_T cut at $\approx$ 200 GeV. Following the p_T^{μ} and E_T^{miss} distributions, most background events are also in the lower m_T region. The data and prediction in the lower panel of the distributions agree within a per cent level in the region with the most statistics. At higher m_T, the difference becomes larger ($\approx$ 10%) and is within the range of the statistical and systematic uncertainties.

Muon pseudorapidity, η^{μ}

The muon pseudorapidity has been defined in Equation 3.4. The distributions shown in Figure 9.2e and Figure 9.4e are for W^+ and W^- respectively. These are used to check the geometrical distribution of the final state muons. The distributions are flat as expected because η^{μ} is an angular variable. The build of the ATLAS detector is such that muons are detected equally well in the region $|\eta^{\mu}| < 2.4$. The MS does not allow an optimal reconstruction in the region between $1.01 < |\eta^{\mu}| < 1.1$; therefore, muons in this region are vetoed. In the lower panel of these figures, the agreement between the data and prediction is at a per cent level for all bins.

Muon azimuthal angle, ϕ^{μ}

The ϕ^{μ} distributions are shown in Figure 9.2f and Figure 9.4f are for W^+ and W^- respectively. The flat distributions for the muon azimuthal angle arise as there is no preference on a ϕ^{μ} value for $W\pm \rightarrow \mu\nu$ events in the signal or background. The ATLAS detector's construction also allows it to reconstruct objects equally well for the full azimuthal angle leading to a flat distribution. The data and prediction ratios, as shown in the lower panel of the distributions, agree within a few per cent.

Pileup, $< \mu >$

The pileup, as described in Section 3.3 and Equation 5.1, is shown in distributions Figure 9.3a and Figure 9.5a for W^+ and W^- respectively. The pileup is used to match the

pileup conditions in each data-taking year shown in Figure 5.1. The distributions peak around $<\mu>=20$. In the lower panel of these figures, the agreement between the data and prediction in the most statistically significant region is within a few per cent. In the lower statistics region, the difference becomes larger but is mostly within the range of the statistical and systematic uncertainties.

d0 significance, $d0^{sig}$

The $d0^{sig}$ as defined in Equation 6.1 discriminates between the multijet background and signal events. The $d0^{sig}$ distributions are shown in Figure 9.3b and Figure 9.5b for W^+ and W^- respectively. The distribution is Gaussian, with the highest statistics being in the region where $d0^{sig}=0$ for both the signal and background events. The data and prediction in the lower panel of the distributions agree within a per cent level in the region with the most statistics. As the distribution approaches the tails at $d0^{sig}=\pm 3$ the difference becomes larger ($\approx 15\%$).

Muon isolation per transverse momentum, $TrackE_T20/p_T^{\mu}$

The muon isolation is described in Section 6.1.7. The distributions for $TrackE_T20/p_T^{\mu}$ are shown in Figure 9.3c and Figure 9.5c for W^+ and W^- respectively. As expected, the event's peak was below 0.01 due to most of the energy from muons being isolated. In the lower panel, where the data and prediction theory is shown, the agreement in the most statistically significant region below 0.01 is within a few per cent. In the regions with fewer statistics, the difference between data and prediction becomes larger ($\approx 15\%$)

Missing energy azimuthal angle, $\phi^{E_T^{miss}}$

The $\phi^{E_T^{miss}}$ distributions are shown in Figure 9.3d and Figure 9.5d for W^+ and W^- respectively. The flat distributions for the missing azimuthal angle, approximating the neutrinos missing azimuthal angle, are expected due to no preference for the value in this process and the ATLAS detectors construction, allowing it to reconstruct objects equally well. The data and prediction ratios, as shown in the lower panel of the distributions, agree within a few per cent for all $\phi^{E_T^{miss}}$ bins.

9.2. Cutflows

The following two tables are cutflows for W^+ in Table 9.1 and W^- in Table 9.2. These tables show each selection's effect on the data, signal MC and backgrounds. The efficiencies of each cut have also been included in brackets. In the final rows, the total efficiency has been calculated by taking the initial number of events and dividing it by the final number of events left after all selections.

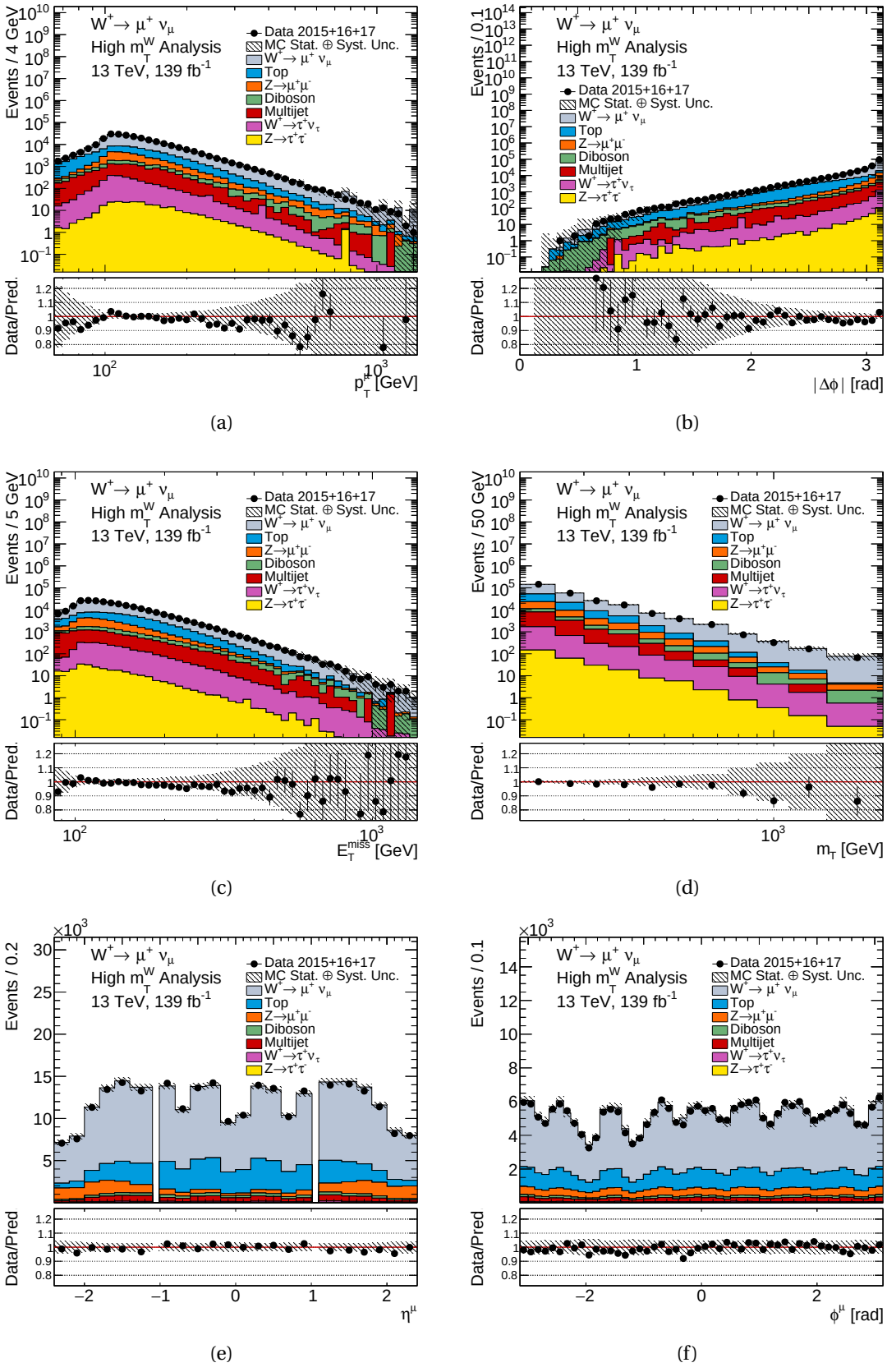

Figure 9.2.: $W^+ \to \mu^+\nu$ control distributions for p_T^μ, $|\Delta\phi|$, E_T^{miss}, m_T, η^μ and ϕ^μ. The data contribution is shown with black points, the signal and the background contributions with solid lines. In the shaded band, systematic experimental uncertainties have been combined with the MC statistical uncertainties. The statistical data uncertainties are shown on the data points. Luminosity uncertainties have not been included.

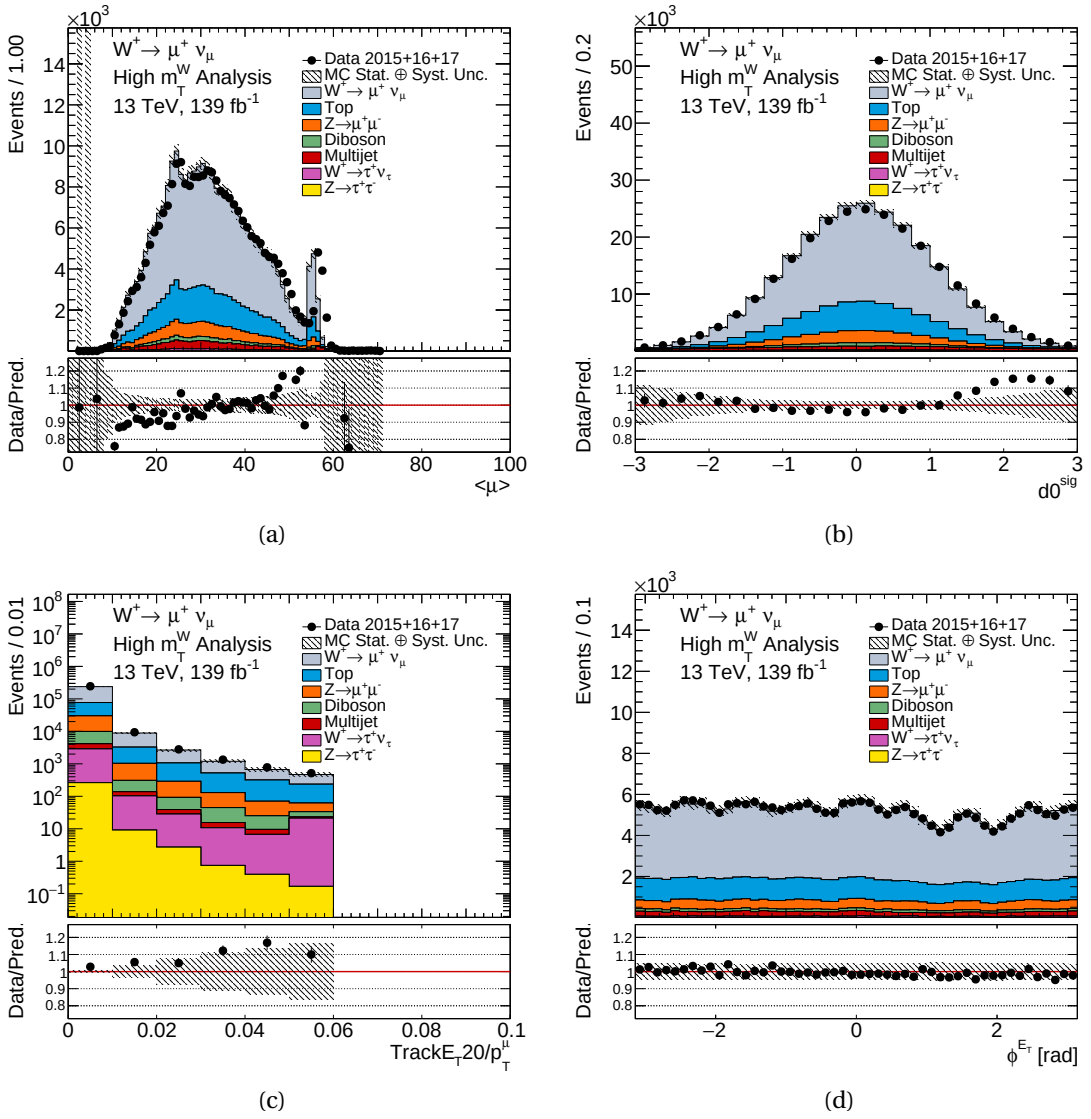

Figure 9.3.: $W^+ \to \mu^+\nu$ control distributions for $<\mu>$, $d0^{sig}$, $TrackE_T20/p_T^{\mu}$ and $\phi^{E_T^{miss}}$. The data contribution is shown with black points, the signal and the background contributions with solid lines. In the shaded band, systematic experimental uncertainties have been combined with the MC statistical uncertainties. The statistical data uncertainties are shown on the data points. Luminosity uncertainties have not been included.

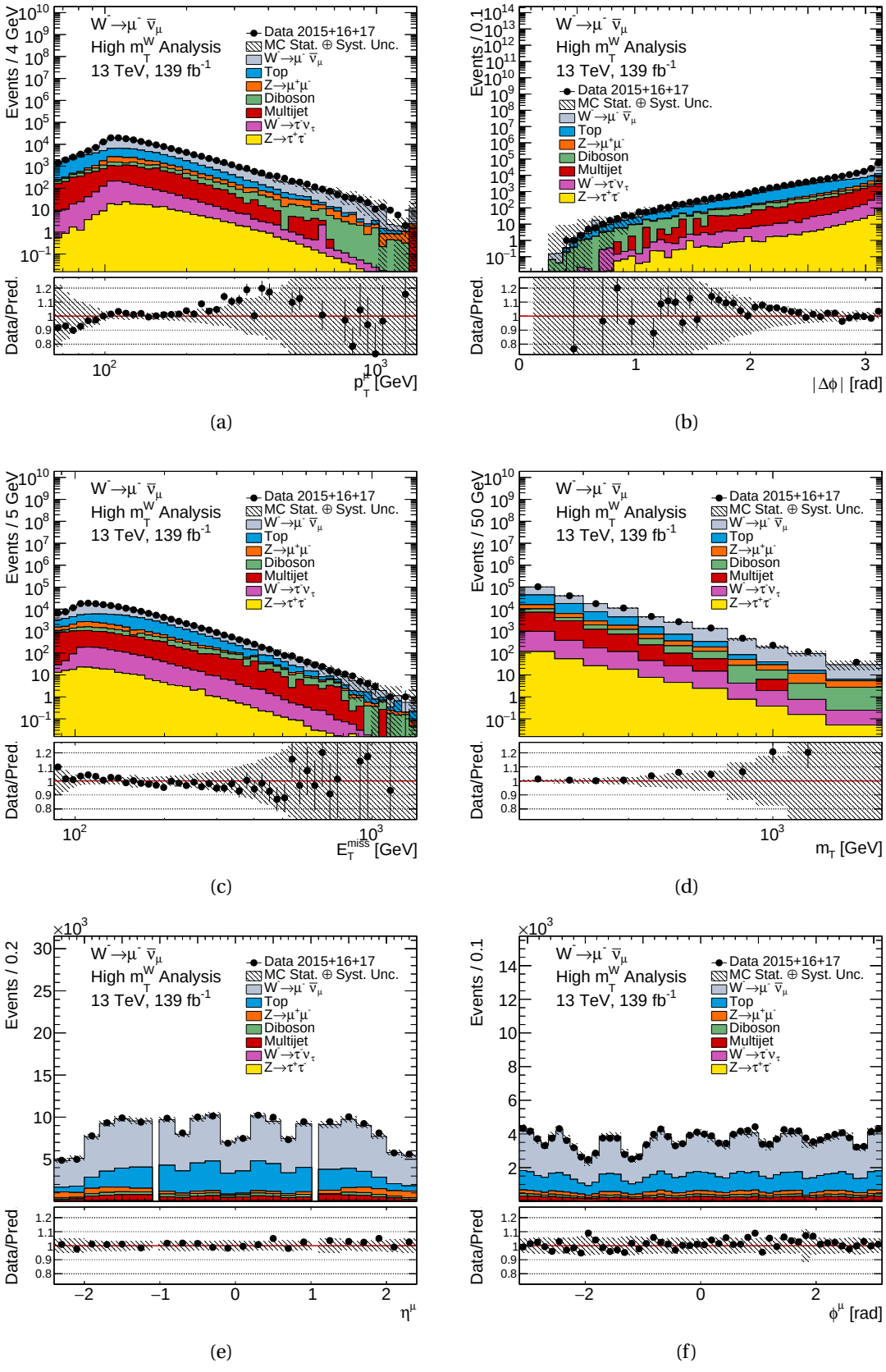

Figure 9.4.: $W^- \to \mu^- \bar{\nu}$ control distributions for p_T^μ, $|\Delta\phi|$, E_T^{miss}, m_T, η^μ and ϕ^μ. The data contribution is shown with black points, the signal and the background contributions with solid lines. In the shaded band, systematic experimental uncertainties have been combined with the MC statistical uncertainties. The statistical data uncertainties are shown on the data points. Luminosity uncertainties have not been included.

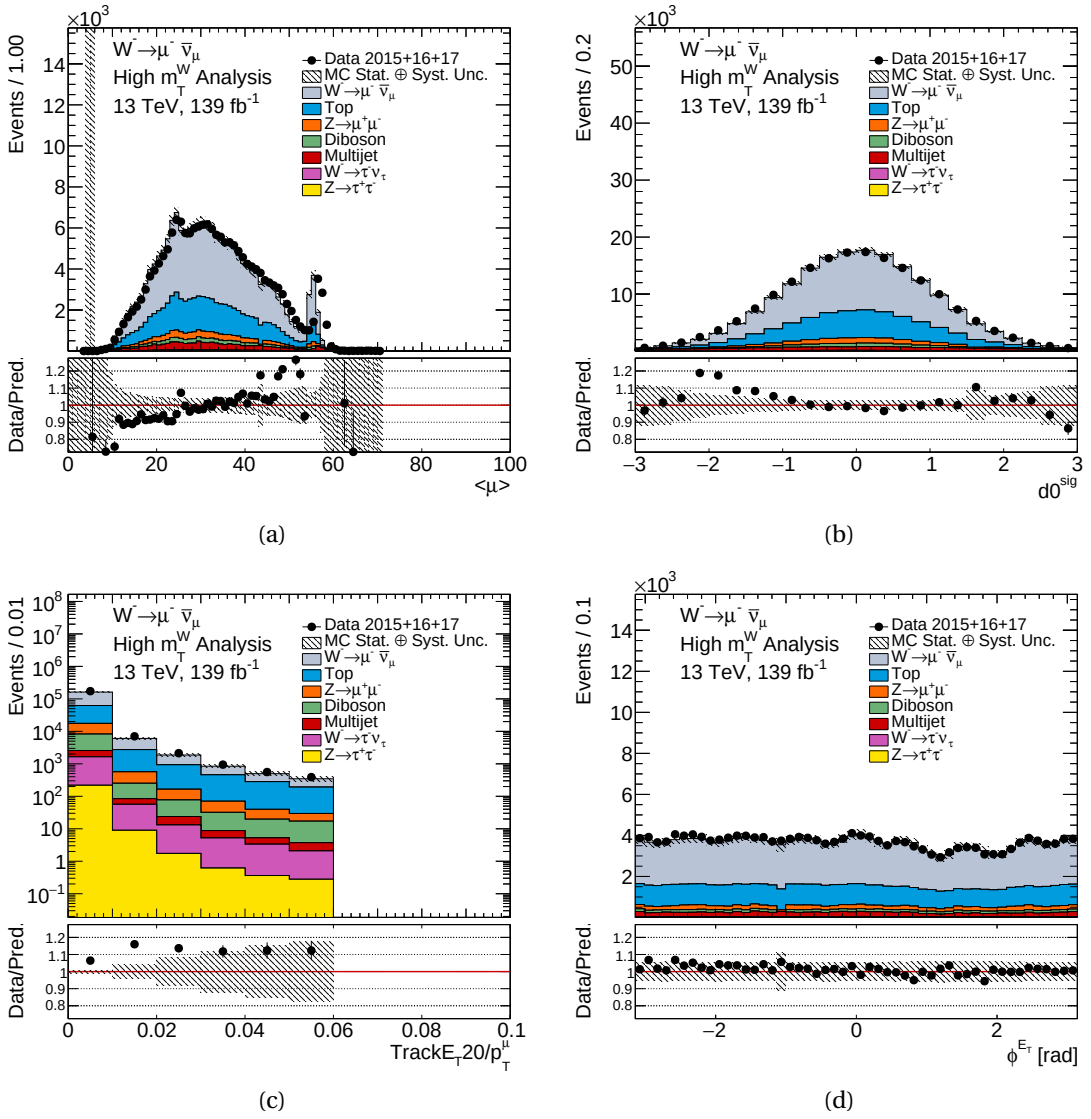

Figure 9.5.: $W^- \to \mu^- \bar{\nu}$ control distributions for $< \mu >$, $d0^{sig}$, $TrackE_T20/p_T^{\mu}$ and $\phi^{E_T^{miss}}$. The data contribution is shown with black points, the signal and the background contributions with solid lines. In the shaded band, systematic experimental uncertainties have been combined with the MC statistical uncertainties. The statistical data uncertainties are shown on the data points. Luminosity uncertainties have not been included.

	Data	$W^+ \to \mu\nu$	$W^+ \to \tau\nu$	$Z \to \mu\mu$	$Z \to \tau\tau$	Top	Diboson
Initial	$5.56 \cdot 10^9$ (NA)	$1.87 \cdot 10^8$ (NA)	$3.93 \cdot 10^7$ (NA)	$1.22 \cdot 10^9$ (NA)	$3.96 \cdot 10^7$ (NA)	$4.59 \cdot 10^8$ (NA)	$2.77 \cdot 10^8$ (NA)
GRL	$5.44 \cdot 10^9$ (97.96%)	$1.87 \cdot 10^8$ (100%)	$3.93 \cdot 10^7$ (100%)	$1.22 \cdot 10^9$ (100%)	$3.96 \cdot 10^7$ (100%)	$4.59 \cdot 10^8$ (100%)	$2.77 \cdot 10^8$ (100%)
Good Calo	$5.44 \cdot 10^9$ (99.93%)	$1.87 \cdot 10^8$ (100%)	$3.93 \cdot 10^7$ (100%)	$1.22 \cdot 10^9$ (100%)	$3.96 \cdot 10^7$ (100%)	$4.59 \cdot 10^8$ (100%)	$2.77 \cdot 10^8$ (100%)
PriVtx	$5.44 \cdot 10^9$ (100%)	$1.87 \cdot 10^8$ (100%)	$3.93 \cdot 10^7$ (100%)	$1.22 \cdot 10^9$ (100%)	$3.96 \cdot 10^7$ (100%)	$4.59 \cdot 10^8$ (100%)	$2.77 \cdot 10^8$ (100%)
Reco Level	$5.44 \cdot 10^9$ (100%)	$1.87 \cdot 10^8$ (100%)	$3.93 \cdot 10^7$ (100%)	$1.22 \cdot 10^9$ (100%)	$3.96 \cdot 10^7$ (100%)	$4.59 \cdot 10^8$ (100%)	$2.77 \cdot 10^8$ (100%)
Trigger	$1.83 \cdot 10^9$ (33.59%)	$7.42 \cdot 10^7$ (39.7%)	$1.80 \cdot 10^6$ (4.568%)	$7.28 \cdot 10^8$ (59.68%)	$9.19 \cdot 10^6$ (23.21%)	$1.53 \cdot 10^8$ (33.39%)	$1.06 \cdot 10^8$ (38.11%)
MU_N 20 == 1	$1.29 \cdot 10^9$ (70.73%)	$6.97 \cdot 10^7$ (93.99%)	$1.28 \cdot 10^6$ (71.29%)	$2.68 \cdot 10^8$ (36.83%)	$5.73 \cdot 10^6$ (62.36%)	$1.37 \cdot 10^8$ (89.27%)	$7.02 \cdot 10^7$ (66.55%)
EL_N 20 == 0	$1.29 \cdot 10^9$ (99.88%)	$6.97 \cdot 10^7$ (99.99%)	$1.28 \cdot 10^6$ (99.97%)	$2.68 \cdot 10^8$ (99.92%)	$5.30 \cdot 10^6$ (92.49%)	$1.28 \cdot 10^8$ (93.36%)	$6.08 \cdot 10^7$ (86.62%)
MU_N 30 == 1	$9.88 \cdot 10^8$ (76.57%)	$5.88 \cdot 10^7$ (84.34%)	$8.27 \cdot 10^5$ (64.66%)	$2.14 \cdot 10^8$ (79.76%)	$4.17 \cdot 10^6$ (78.6%)	$1.15 \cdot 10^8$ (89.63%)	$5.30 \cdot 10^7$ (87.2%)
MU_N 65 == 1	$6.74 \cdot 10^7$ (6.815%)	$1.11 \cdot 10^7$ (18.82%)	$2.36 \cdot 10^5$ (28.52%)	$2.13 \cdot 10^7$ (9.955%)	$2.25 \cdot 10^6$ (53.87%)	$4 \cdot 10^7$ (34.93%)	$1.66 \cdot 10^7$ (31.23%)
MU_N Tight 65 == 1	$6.74 \cdot 10^7$ (100%)	$1.11 \cdot 10^7$ (100%)	$2.36 \cdot 10^5$ (100%)	$2.13 \cdot 10^7$ (100%)	$2.25 \cdot 10^6$ (100%)	$4 \cdot 10^7$ (100%)	$1.66 \cdot 10^7$ (100%)
Trigger match	$6.73 \cdot 10^7$ (99.89%)	$1.11 \cdot 10^7$ (100%)	$2.36 \cdot 10^5$ (99.99%)	$2.11 \cdot 10^7$ (99.1%)	$2.21 \cdot 10^6$ (98.25%)	$3.99 \cdot 10^7$ (99.78%)	$1.65 \cdot 10^7$ (99.72%)
JetCleaning: Loose Bad	$6.65 \cdot 10^7$ (98.8%)	$1.10 \cdot 10^7$ (99.65%)	$2.35 \cdot 10^5$ (99.65%)	$2.09 \cdot 10^7$ (99.38%)	$2.19 \cdot 10^6$ (99.46%)	$3.97 \cdot 10^7$ (99.54%)	$1.64 \cdot 10^7$ (99.47%)
NOBADMUON	$6.65 \cdot 10^7$ (99.99%)	$1.10 \cdot 10^7$ (99.79%)	$2.35 \cdot 10^5$ (99.78%)	$2.09 \cdot 10^7$ (99.96%)	$2.19 \cdot 10^6$ (99.65%)	$3.97 \cdot 10^7$ (100%)	$1.64 \cdot 10^7$ (99.99%)
Save	$6.65 \cdot 10^7$ (100%)	$1.10 \cdot 10^7$ (100%)	$2.35 \cdot 10^5$ (100%)	$2.09 \cdot 10^7$ (100%)	$2.19 \cdot 10^6$ (100%)	$3.97 \cdot 10^7$ (100%)	$1.64 \cdot 10^7$ (100%)
Lepton Veto	$4.06 \cdot 10^7$ (61.03%)	$9.09 \cdot 10^6$ (82.63%)	$1.95 \cdot 10^5$ (83.12%)	$1.66 \cdot 10^7$ (79.32%)	$1.79 \cdot 10^6$ (81.92%)	$3.27 \cdot 10^7$ (82.25%)	$1.36 \cdot 10^7$ (82.81%)
Charge Selection	$2.08 \cdot 10^7$ (51.29%)	$9.09 \cdot 10^6$ (100%)	$1.95 \cdot 10^5$ (99.98%)	$8.96 \cdot 10^6$ (53.96%)	$9.23 \cdot 10^5$ (51.55%)	$1.64 \cdot 10^7$ (50.03%)	$6.56 \cdot 10^6$ (48.2%)
$\lvert\eta\rvert^\mu < 2.4$	$2.08 \cdot 10^7$ (100%)	$9.09 \cdot 10^6$ (100%)	$1.95 \cdot 10^5$ (100%)	$8.96 \cdot 10^6$ (100%)	$9.23 \cdot 10^5$ (100%)	$1.64 \cdot 10^7$ (100%)	$6.56 \cdot 10^6$ (100%)
$p_T^\mu > 65$ GeV	$2.08 \cdot 10^7$ (100%)	$9.09 \cdot 10^6$ (100%)	$1.95 \cdot 10^5$ (100%)	$8.96 \cdot 10^6$ (100%)	$9.23 \cdot 10^5$ (100%)	$1.64 \cdot 10^7$ (100%)	$6.56 \cdot 10^6$ (100%)
$E_T^{miss} > 85$ GeV	$1.81 \cdot 10^6$ (8.708%)	$4.48 \cdot 10^6$ (49.3%)	$1.60 \cdot 10^5$ (82.23%)	$1.74 \cdot 10^6$ (19.38%)	$6.68 \cdot 10^5$ (72.33%)	$3.85 \cdot 10^6$ (23.57%)	$1.63 \cdot 10^6$ (24.86%)
$m_T > 200$ GeV	$2.60 \cdot 10^5$ (14.35%)	$3.18 \cdot 10^6$ (71.05%)	$1.44 \cdot 10^5$ (89.67%)	$1.35 \cdot 10^6$ (77.71%)	$2.79 \cdot 10^5$ (41.71%)	$4.50 \cdot 10^5$ (11.66%)	$4.73 \cdot 10^5$ (29.04%)
Total Efficiency	0.0047%	1.7%	0.37%	0.11%	0.7%	0.098%	0.17%
ProcessMC/TotalMC	NA	54.16%	2.446%	22.95%	4.74%	7.651%	8.055%
Data/TotalMC	4.425%						

Table 9.1.: Cutflow table for Run-2 data for the W^+ selection showing the effect each selection has on the number of events. The first column lists the name of the selection. The rest of the columns show the number of events for each sample and for each selection. The relative efficiency is shown as a percentage next to each number of events. The relative efficiency is calculated as the number of events after the current cut divided by the number of events in the previous cuts. The three rows at the bottom of the table show the total efficiency, ProcessMC/TotalMC and Data/TotalMC. The total efficiency is calculated by taking the number of events after all cuts have been applied divided by the number of events before any cut. The ProcessMC/TotalMC row shows the number of events in each Monte Carlo sample divided by the total sum of events of the Monte Carlo samples after all the selection cuts. The Data/TotalMC row is the total number of data events divided by the sum of the total number of Monte Carlo events after all the selection cuts. All Monte Carlo samples are normalised to the luminosity of the data and include the pileup and generator weights.

	Data	$W^- \to \mu\nu$	$W^- \to \tau\nu$	$Z \to \mu\mu$	$Z \to \tau\tau$	Top	Diboson
Initial	$5.56 \cdot 10^9$ (NA)	$1.56 \cdot 10^8$ (NA)	$2.75 \cdot 10^7$ (NA)	$1.22 \cdot 10^9$ (NA)	$3.96 \cdot 10^7$ (NA)	$4.59 \cdot 10^8$ (NA)	$2.77 \cdot 10^8$ (NA)
GRL	$5.44 \cdot 10^9$ (97.96%)	$1.56 \cdot 10^8$ (100%)	$2.75 \cdot 10^7$ (100%)	$1.22 \cdot 10^9$ (100%)	$3.96 \cdot 10^7$ (100%)	$4.59 \cdot 10^8$ (100%)	$2.77 \cdot 10^8$ (100%)
Good Calo	$5.44 \cdot 10^9$ (99.93%)	$1.56 \cdot 10^8$ (100%)	$2.75 \cdot 10^7$ (100%)	$1.22 \cdot 10^9$ (100%)	$3.96 \cdot 10^7$ (100%)	$4.59 \cdot 10^8$ (100%)	$2.77 \cdot 10^8$ (100%)
PriVtx	$5.44 \cdot 10^9$ (100%)	$1.56 \cdot 10^8$ (100%)	$2.75 \cdot 10^7$ (100%)	$1.22 \cdot 10^9$ (100%)	$3.96 \cdot 10^7$ (100%)	$4.59 \cdot 10^8$ (100%)	$2.77 \cdot 10^8$ (100%)
Reco Level	$5.44 \cdot 10^9$ (100%)	$1.56 \cdot 10^8$ (100%)	$2.75 \cdot 10^7$ (100%)	$1.22 \cdot 10^9$ (100%)	$3.96 \cdot 10^7$ (100%)	$4.59 \cdot 10^8$ (100%)	$2.77 \cdot 10^8$ (100%)
Trigger	$1.83 \cdot 10^9$ (33.59%)	$6.20 \cdot 10^7$ (39.89%)	$1.44 \cdot 10^6$ (5.259%)	$7.28 \cdot 10^8$ (59.68%)	$9.19 \cdot 10^6$ (23.21%)	$1.53 \cdot 10^8$ (33.39%)	$1.06 \cdot 10^8$ (38.11%)
MU_N 20 == 1	$1.29 \cdot 10^9$ (70.73%)	$5.85 \cdot 10^7$ (94.25%)	$1.01 \cdot 10^6$ (69.83%)	$2.68 \cdot 10^8$ (36.83%)	$5.73 \cdot 10^6$ (62.36%)	$1.37 \cdot 10^8$ (89.27%)	$7.02 \cdot 10^7$ (66.55%)
EL_N 20 == 0	$1.29 \cdot 10^9$ (99.88%)	$5.85 \cdot 10^7$ (99.98%)	$1.01 \cdot 10^6$ (99.96%)	$2.68 \cdot 10^8$ (99.92%)	$5.30 \cdot 10^6$ (92.49%)	$1.28 \cdot 10^8$ (93.36%)	$6.08 \cdot 10^7$ (86.62%)
MU_N 30 == 1	$9.88 \cdot 10^8$ (76.57%)	$5.09 \cdot 10^7$ (86.99%)	$6.87 \cdot 10^5$ (68.13%)	$2.14 \cdot 10^8$ (79.76%)	$4.17 \cdot 10^6$ (78.6%)	$1.15 \cdot 10^8$ (89.63%)	$5.30 \cdot 10^7$ (87.2%)
MU_N 65 == 1	$6.74 \cdot 10^7$ (6.815%)	$1.08 \cdot 10^7$ (21.2%)	$2.28 \cdot 10^5$ (33.23%)	$2.13 \cdot 10^7$ (9.955%)	$2.25 \cdot 10^6$ (53.87%)	$4 \cdot 10^7$ (34.93%)	$1.66 \cdot 10^7$ (31.23%)
MU_N Tight 65 == 1	$6.74 \cdot 10^7$ (100%)	$1.08 \cdot 10^7$ (100%)	$2.28 \cdot 10^5$ (100%)	$2.13 \cdot 10^7$ (100%)	$2.25 \cdot 10^6$ (100%)	$4 \cdot 10^7$ (100%)	$1.66 \cdot 10^7$ (100%)
Trigger match	$6.73 \cdot 10^7$ (99.89%)	$1.08 \cdot 10^7$ (100%)	$2.28 \cdot 10^5$ (99.99%)	$2.11 \cdot 10^7$ (99.1%)	$2.21 \cdot 10^6$ (98.25%)	$3.99 \cdot 10^7$ (99.78%)	$1.65 \cdot 10^7$ (99.72%)
JetCleaning: Loose Bad	$6.65 \cdot 10^7$ (98.8%)	$1.07 \cdot 10^7$ (99.64%)	$2.27 \cdot 10^5$ (99.64%)	$2.09 \cdot 10^7$ (99.38%)	$2.19 \cdot 10^6$ (99.46%)	$3.97 \cdot 10^7$ (99.54%)	$1.64 \cdot 10^7$ (99.47%)
NOBADMUON	$6.65 \cdot 10^7$ (99.99%)	$1.07 \cdot 10^7$ (99.71%)	$2.27 \cdot 10^5$ (99.63%)	$2.09 \cdot 10^7$ (99.96%)	$2.19 \cdot 10^6$ (99.65%)	$3.97 \cdot 10^7$ (100%)	$1.64 \cdot 10^7$ (99.99%)
Save	$6.65 \cdot 10^7$ (100%)	$1.07 \cdot 10^7$ (100%)	$2.27 \cdot 10^5$ (100%)	$2.09 \cdot 10^7$ (100%)	$2.19 \cdot 10^6$ (100%)	$3.97 \cdot 10^7$ (100%)	$1.64 \cdot 10^7$ (100%)
Lepton Veto	$4.06 \cdot 10^7$ (61.03%)	$8.83 \cdot 10^6$ (82.41%)	$1.84 \cdot 10^5$ (81.37%)	$1.66 \cdot 10^7$ (79.32%)	$1.79 \cdot 10^6$ (81.92%)	$3.27 \cdot 10^7$ (82.25%)	$1.36 \cdot 10^7$ (82.81%)
Charge Selection	$1.98 \cdot 10^7$ (48.71%)	$8.83 \cdot 10^6$ (100%)	$1.84 \cdot 10^5$ (99.97%)	$7.64 \cdot 10^6$ (46.04%)	$8.68 \cdot 10^5$ (48.45%)	$1.63 \cdot 10^7$ (49.97%)	$7.05 \cdot 10^6$ (51.8%)
$\lvert\eta\rvert^\mu < 2.4$	$1.98 \cdot 10^7$ (100%)	$8.83 \cdot 10^6$ (100%)	$1.84 \cdot 10^5$ (100%)	$7.64 \cdot 10^6$ (100%)	$8.68 \cdot 10^5$ (100%)	$1.63 \cdot 10^7$ (100%)	$7.05 \cdot 10^6$ (100%)
$p_T^\mu > 65$ GeV	$1.98 \cdot 10^7$ (100%)	$8.83 \cdot 10^6$ (100%)	$1.84 \cdot 10^5$ (100%)	$7.64 \cdot 10^6$ (100%)	$8.68 \cdot 10^5$ (100%)	$1.63 \cdot 10^7$ (100%)	$7.05 \cdot 10^6$ (100%)
$E_T^{miss} > 85$ GeV	$1.37 \cdot 10^6$ (6.922%)	$4.20 \cdot 10^6$ (47.56%)	$1.52 \cdot 10^5$ (82.55%)	$7.89 \cdot 10^5$ (10.33%)	$6.39 \cdot 10^5$ (73.58%)	$3.79 \cdot 10^6$ (23.21%)	$1.66 \cdot 10^6$ (23.51%)
$m_T > 200$ GeV	$1.84 \cdot 10^5$ (13.45%)	$3.01 \cdot 10^6$ (71.66%)	$1.38 \cdot 10^5$ (90.38%)	$6.04 \cdot 10^5$ (76.48%)	$2.65 \cdot 10^5$ (41.56%)	$4.47 \cdot 10^5$ (11.78%)	$5.05 \cdot 10^5$ (30.46%)
Total Efficiency	0.0033%	1.9%	0.5%	0.05%	0.67%	0.097%	0.18%
ProcessMC/TotalMC	NA	60.58%	2.769%	12.16%	5.343%	8.991%	10.16%
Data/TotalMC	3.705%						

Table 9.2.: Cutflow table for Run-2 data for the W^- selection showing the effect each selection has on the number of events. The first column lists the name of the selection. The rest of the columns show the number of events for each sample and for each selection. The relative efficiency is shown as a percentage next to each number of events. The relative efficiency is calculated as the number of events after the current cut divided by the number of events in the previous cuts. The three rows at the bottom of the table show the total efficiency, ProcessMC/TotalMC and Data/TotalMC. The total efficiency is calculated by taking the number of events after all cuts have been applied divided by the number of events before any cut. The ProcessMC/TotalMC row shows the number of events in each Monte Carlo sample divided by the total sum of events of the Monte Carlo samples after all the selection cuts. The Data/TotalMC row is the total number of data events divided by the sum of the total number of Monte Carlo events after all the selection cuts. All Monte Carlo samples are normalised to the luminosity of the data and include the pileup and generator weights.

9.2.1. Event Selection Efficiency and Pileup

In this section, the event selection efficiency as a function of the pileup is considered. Figure 9.6 illustrates the event selection efficiency as a function of the average pileup for the $W \to \mu\nu$ processes, in the full Run-2 period. The efficiency ($\varepsilon_{\text{Selection}}$) is defined as the ratio of simulated events meeting all selection criteria to the total simulated $W \to \mu\nu$ events. This is expressed in Equation 9.1.

$$\varepsilon_{\text{Selection}} = \frac{N_{\text{Selected}}}{N_{\text{Total}}} \tag{9.1}$$

Here, N_{Selected} represents the number of events passing all selection criteria, and N_{Total} is the total number of simulated events. This efficiency is calculated independently for both positive and negative charges, using the event selections as defined in Chapter 6.1.

The efficiency remains relatively consistent across the 20-50 $< \mu >$ range for both positive and negative charges. This is expected as the event selection criteria is independent of pileup and this is where the statistics dominate. The average efficiency within this range is approximately 0.017 (1.7%) for W^+ and 0.019 (1.9%) for W^-, matching the values presented in the total efficiency row of Table 9.1 for the positive charge and Table 9.2 for negative charge.

Examining the region $< \mu >$ less than 10 there is a higher efficiency, but with larger uncertainty due to limited statistics. In contrast, the efficiency experiences a dip followed by an increase in the $< \mu >$ higher than 50 region. This region also has larger uncertainties due to fewer statistics. A comparison with Figure 5.2 indicates that around $< \mu >$ greater than 53, the 2017 statistics begin to dominate over 2018. The lower efficiency in this region is attributed to the 2017 period being less efficient at data recording, a result of several improvements made to data-taking during that time. In the average $< \mu >$ greater than 80 range the statistics in 2018 dominate once again and the efficiency increases. To see this in more detail, efficiencies of the individual Monte Carlo campaigns (MC16a, MC16d, and MC16e), which contribute to the full Run-2 period, are shown in Appendix E.5 and show the same trend.

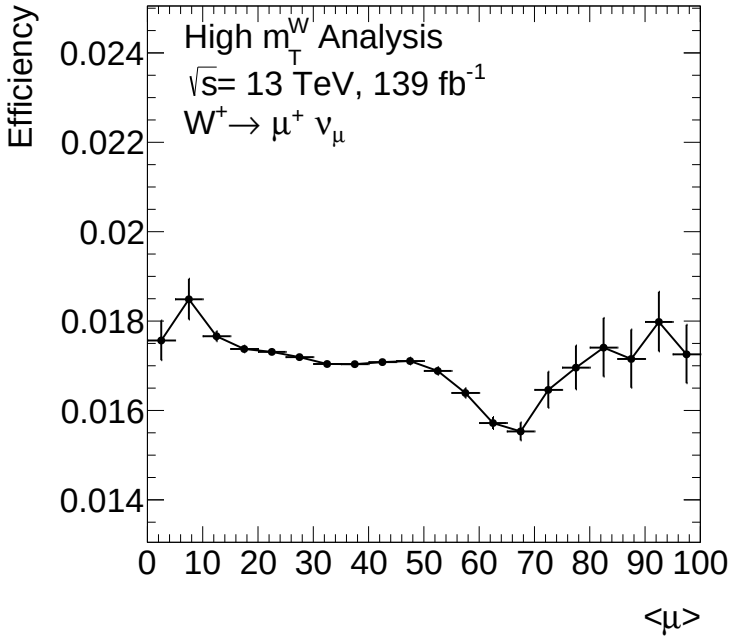

(a) $W^+ \rightarrow \mu^+ \nu$

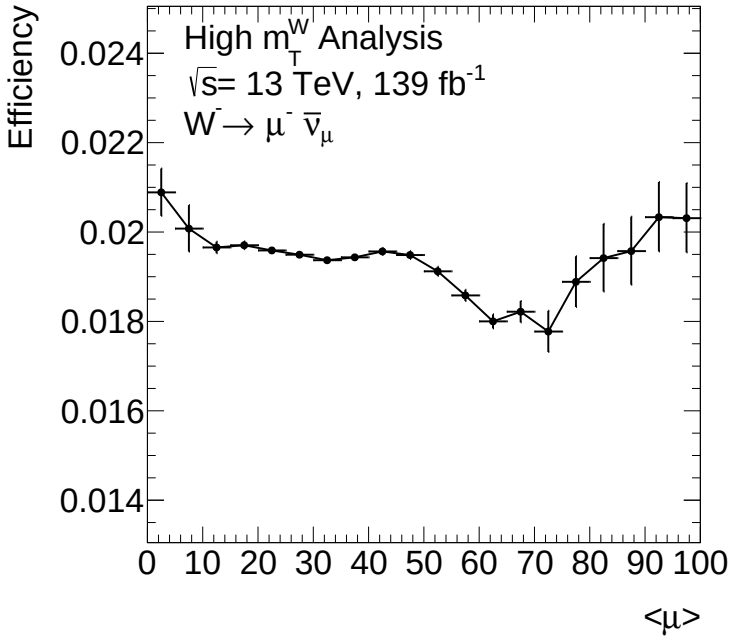

(b) $W^- \rightarrow \mu^- \bar{\nu}$

Figure 9.6.: Event selection efficiency as a function of the average $< \mu >$ for Run-2 (139^{-1}). The efficiency is defined as the number of events passing all event selections divided by the total number of simulated $W^+ \rightarrow \mu^+ \nu_\mu$ (top) and $W^- \rightarrow \mu^- \bar{\nu}_\mu$ (bottom) events. Errors have been calculated using the Bayesian Error approach implemented in TGraphAsymmErrors [84].

10. Cross-Section and Charge Asymmetry

This chapter presents the high-mass Drell-Yan charged current cross-sections and muon charge asymmetry measurements. Firstly, the procedure for extracting the cross-sections is explained. This involves corrections, the truth level, an explanation of the binning used, details about the iterative Bayesian unfolding procedure and a closure test. Next, the calculation of the systematic uncertainties is also included. Finally, the unfolded cross-section and muon charge asymmetry is shown and the conclusions of the measurement are explained.

10.1. Extraction of Cross-Section and Asymmetry

10.1.1. Cross-Section Calculation

For the estimation of the Drell-Yan cross-sections, the following Equation 10.1 is used:

$$\frac{d\sigma}{dx_j} = \frac{1}{\Delta x_j \cdot \mathscr{L}_{int} \cdot \mathscr{BR} \cdot S_j} \sum_i R_{ij}^{-1} \cdot P_{in}^i \cdot \left(N_{data}^i - N_{bkg}^i\right) \tag{10.1}$$

where Δx_j is the bin width, $\mathscr{L}_{int}$ the integrated luminosity and $\mathscr{BR}$ is the branching ratio. The sum uses the bin indexes i for the measured reconstruction level and j for the generated truth level. $N_{data}^i - N_{bkg}^i$ is the difference between the measurement data and all background events, which gives the number of reconstructed signal events per bin. The response matrix is R_{ij} and represents the probability that an event is generated and reconstructed in different bins. The inverse of this matrix applied to the measured data per bin is used to correct for migrations in the data through the IBU method [116]. The response matrix follows the same range and binning as the reconstruction and truth level, $m_T^W = 150 - 2000$ GeV. The correction factors are purity, P_{in}^i, and stability, S_j, discussed in Section 10.2.

10.1.2. Asymmetry Calculation

For the calculation of the muon charge asymmetry, As_μ, the following Equation 10.2 is used:

$$As_\mu = \frac{\sigma_{W^+} - \sigma_{W^-}}{\sigma_{W^+} + \sigma_{W^-}} \tag{10.2}$$

Here σ_{W^+} is the cross-section for the $W^+ \rightarrow \mu^+\nu$ production, and σ_{W^-} is the cross-section for the $W^- \rightarrow \mu^-\bar{\nu}$ production which are calculated using Equation 10.1.

10.2. Stability, Purity and Acceptance

In determining the cross-section within the fiducial volume defined in Section 6.1.11, a correction is needed to account for the differences between the reconstruction and fiducial level selections. Some events will migrate from the bin they were generated to other bins and need to be corrected for. The levels of migration can be gauged by measuring the number of events that are reconstructed and generated in the same bin. Migrations are discussed in further detail in Section 10.4.1. A correction for the generated events, which will not be reconstructed at all due to the detector's imperfect detector efficiency, is also necessary.

The factor S_j is the stability. The stability accounts for the number of generated events at the truth level which are not reconstructed, e.g. due to the measurement reconstruction or efficiency. The following Equation 10.3 defines the stability:

$$S_j = \frac{N^j_{reco \wedge truth[150,2000]}}{N^j_{\text{truth }[150,2000]}} \tag{10.3}$$

The fiducial truth level selection defined in Section 6.1.11 and the reconstruction selection defined in Section 6.1 are used in the definition. The bin-wise efficiency is found by taking the quotient of the events that pass both the reconstruction and fiducial truth level, with all events passing the fiducial truth level.

The factor P^i_{in} is the purity. The purity is accounts for the number of reconstructed events not reconstructed in the same bin on the truth level. The purity can correct for the events smearing into the measurement range on the reconstruction level but are generated around the mass peak in m_T^W below 150 GeV. The following Equation 10.4 defines the purity:

$$P^i_{in} = \frac{N^i_{reco \wedge truth[150,2000]}}{N^i_{\text{reco }[150,2000]}} \tag{10.4}$$

Again the same truth level selections (Section 6.1.11) and reconstruction selections (Section 6.1) are used. The purity is calculated by taking the quotient of the events that pass both the reconstruction and fiducial truth level with all reconstructed events per bin.

The acceptance, also known as the correction factor, is the fraction of generated events to reconstructed events in a bin. It is used for correcting events selected at the reconstruction level but not at the truth level. It is also used to make a bin-by-bin correction of the detector-level events to bring them to the truth level. The bin-by-bin unfolding

was used in this analysis to cross-check to ensure `RooUnfold` had been implemented correctly. The results between the bin-by-bin unfolding the author implemented and `RooUnfold` were identical, validating the `RooUnfold` implementation. The bin-by-bin unfolding is unsuitable for the final measurement because it cannot account for potential bin migrations, which are present in the high m_T region (see Section 10.4.1). The acceptance can be defined as the quotient between the stability and purity or Equation 10.3 divided by Equation 10.4, which becomes Equation 10.5.

$$A^i = \frac{N^i_{\text{truth [150,2000]}}}{N^i_{\text{reco [150,2000]}}} \tag{10.5}$$

The correction factors have been obtained using the signal MC. The stability, purity and acceptance were all calculated as a function of the truth m_T^W in the bin range 60 – 2000 GeV. Including the bin from 60 – 150 GeV allows for the peak and its migrations to be seen. The positive muon charge has been shown here as no substantial difference is observed between the lepton charges (see Appendix F.1 for the negative charge).

In Figure 10.1, the stability S_j, shown in the lower pad, can be observed with an efficiency of around 40% throughout the measurement range. The smallest stability value is observed in the shadow bin at 33% indicating a large fraction of events that are generated but not considered in the reconstruction. Small efficiency at low m_T^W is expected due to the acceptance cuts on reconstruction level, e.g. $p_{\mathrm{T}}^{\mu}, E_{\mathrm{T}}^{\mathrm{miss}}$ and m_T^W. The upper pad shows the events in the truth m_T^W against the reconstruction m_T^W where yellow indicates many events while blue indicates fewer events. The numbers in each bin show the events in the same reconstruction and truth bin divided by all truth events in the m_T^W bin. Therefore, the numbers in the diagonal of this 2D plot give stability in the lower pad.

The purity P^i_{in} is shown in Figure 10.2 in the lower pad, where the purity is largest ($\approx$ 96%) at low m_T^W and decreases to around 60%. This is expected from the migration, discussed in Section 10.4.1, as there are many migrating events from bin to bin on the reconstruction level. The effect of smearing from the mass peak decreases for the higher m_T^W bins. The upper pad shows the events in the truth m_T^W against the reconstruction m_T^W where yellow indicates many events while blue indicates fewer events. The numbers in each bin represent the calculation of events in the same reconstruction and truth bin divided by the total number of reconstructed events in that m_T^W bin. Therefore, the diagonal of this 2D plot gives the purity in the lower pad. This matrix calculates the iterative Bayesian unfolding discussed in Section 10.6.

The acceptance, A^i, is shown in the lower pad of Figure 10.3. The acceptance is smallest in the shadow bin at 41% and is around 55% for the following bins. This is expected and follows from the purity and stability in the previous Figure 10.2 and Figure 10.1.

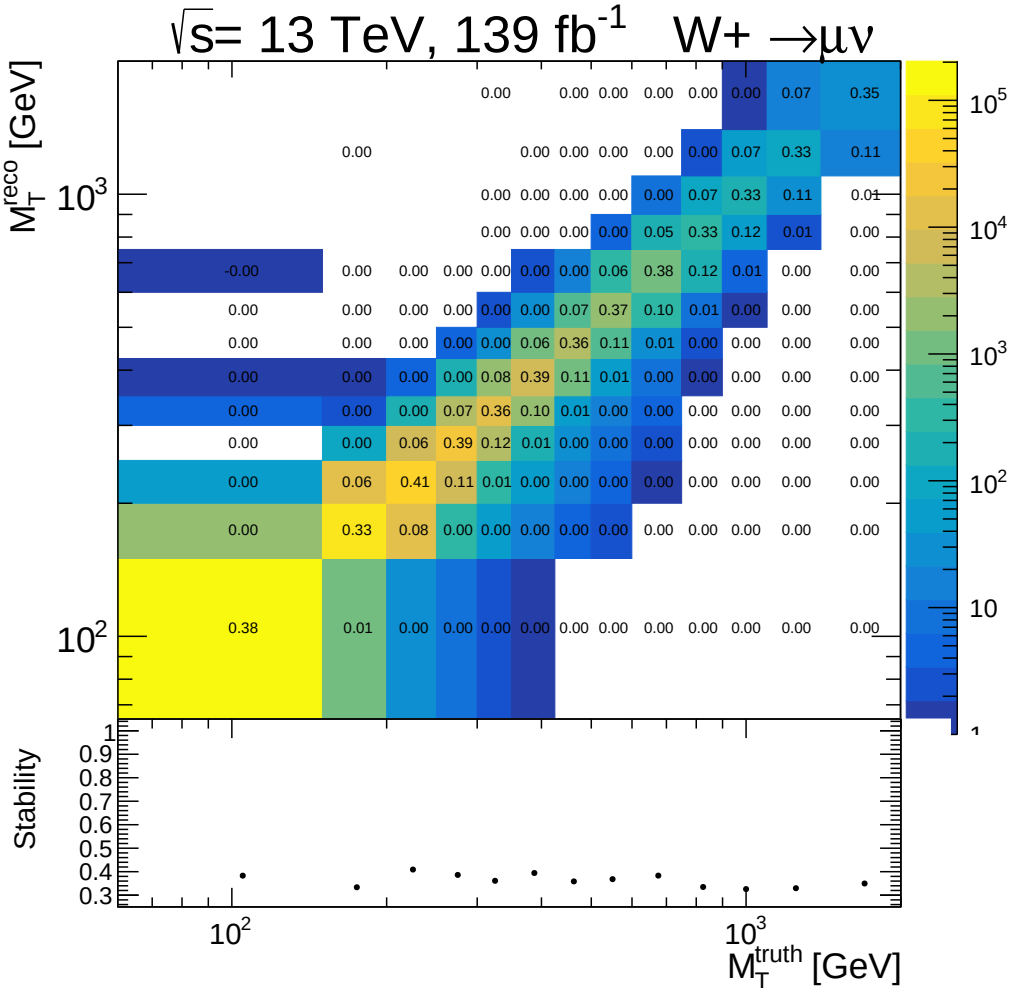

Figure 10.1.: Stability for the $W^+ \to \mu^+ \nu$ signal process. The upper panel shows the m_T^W truth level vs the m_T^W reconstruction level events. The given numbers show the ratio of the number of events in each bin to the total number of truth events in the given mass bin. The diagonal of the upper panel gives the stability in the lower panel.

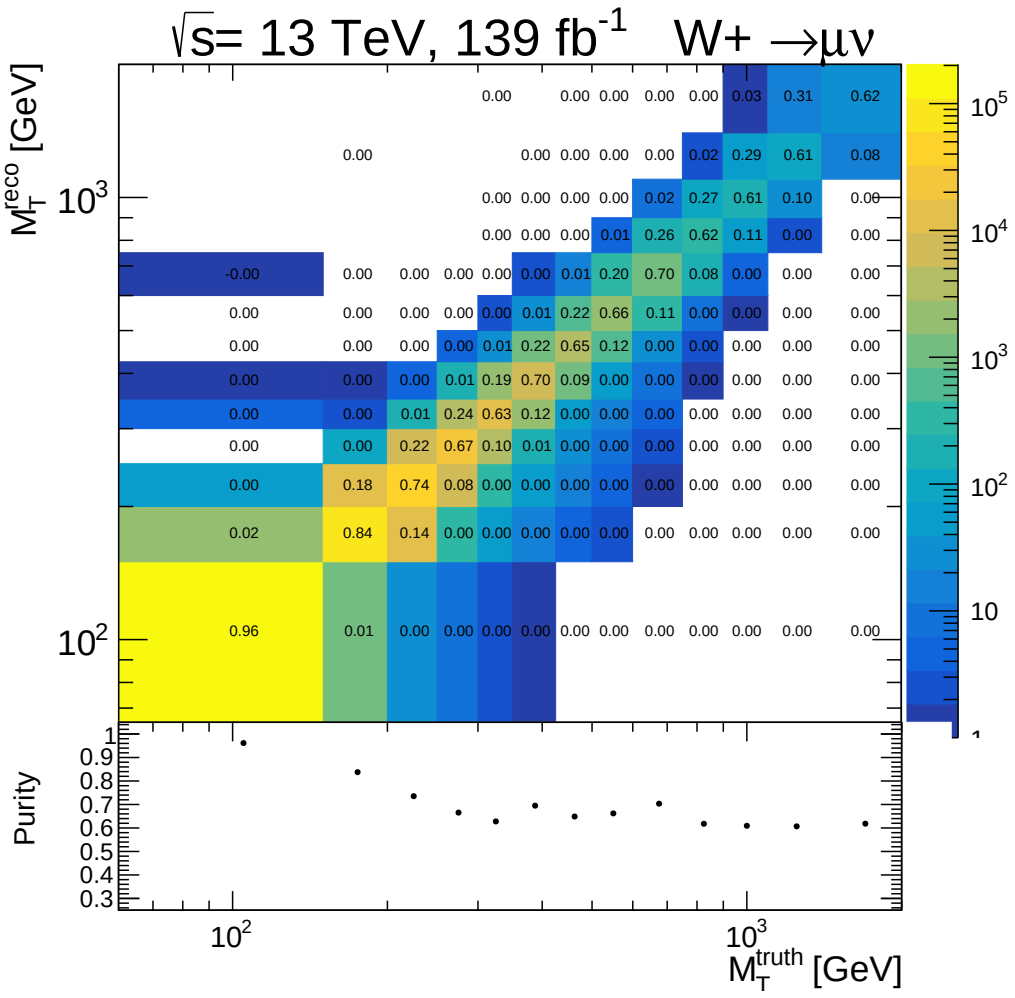

Figure 10.2.: Purity for the $W^+ \to \mu^+ \nu$ signal process. The upper panel shows the m_T^W truth level vs the m_T^W reconstruction level events. The given numbers show the ratio of the number of events in each bin to the total number of reconstructed events in the given mass bin. The diagonal of the upper panel gives the purity in the lower panel.

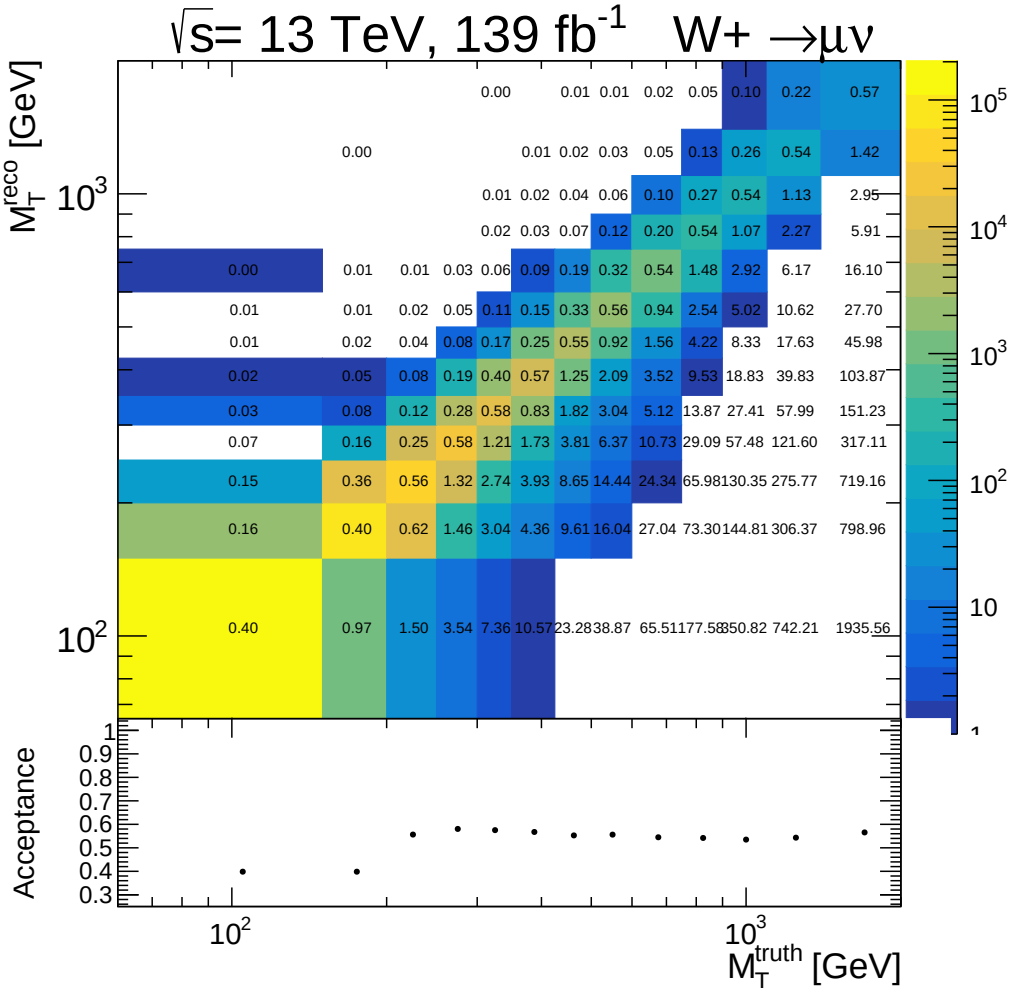

Figure 10.3.: Acceptance for the $W^+ \to \mu^+\nu$ signal process. The upper panel shows the m_T^W truth level vs the m_T^W reconstruction level events. The lower panel shows the ratio of the total number of truth events in each bin to the total number of reconstructed events in each bin.

10.3. Truth Level Definition

The boundaries of the fiducial volume are performed on the truth level Monte Carlo. The truth level refers to a simulation where the events are simulated without any detector constraints. There are several possible truth-level definitions which differ depending on the way the photons radiated by the final state leptons are handled. These are the following:

- Born level: before final state radiation (FSR)
- Bare level: after final state radiation
- Dressed level: bare lepton with all photons originating from the same decay vertex in a cone of $\Delta R < 0.1$ also added to the reconstruction

Figure 10.4 shows the distributions for the truth invariant mass of the W boson for the positive and negative charge channels. Each line is used to represent a different definition of the truth level. No cuts have been applied to these distributions, which leave a visible maximum at the mass of the W boson at 80 GeV. The lower panel shows the bare and dressed level ratio to the born level. The bare level invariant mass distribution is higher than the born level for events below the mass peak of 80 GeV. The shift in the whole distribution at lower masses corresponds to the bare level's final state radiation. The lepton could carry less energy than the born level corresponding to a lower calculated invariant mass. As the mass increases above 80 GeV, the differences between the bare and born levels decrease.

Additional radiated photons are added again to the bare level lepton in the dressed level. Therefore, the energy will increase compared to the bare level mass, shifting the dressed level mass distribution to higher masses. If all radiated photons are included in the dressed level, it would become identical to the born level. However, this is impossible, so the dressed distribution is between bare and born level, as demonstrated by the ratio panel in Figure 10.4.

For this analysis, the truth level refers to the born level, and all unfolded cross-sections and asymmetry measurements have been measured using this born level only.

10.4. Optimisation of Binning

The cross-section is measured differentially in the transverse mass of the W boson, so a binning suitable for this variable is used. The binning chosen, shown below in Equation 10.6 for this analysis, matches the high m_T^W analysis group to make all the results comparable [117].

$$m_T^W = [(150,)200, 250, 300, 350, 425, 500, 600, 750, 900, 1100, 1400, 2000] \text{ GeV} \tag{10.6}$$

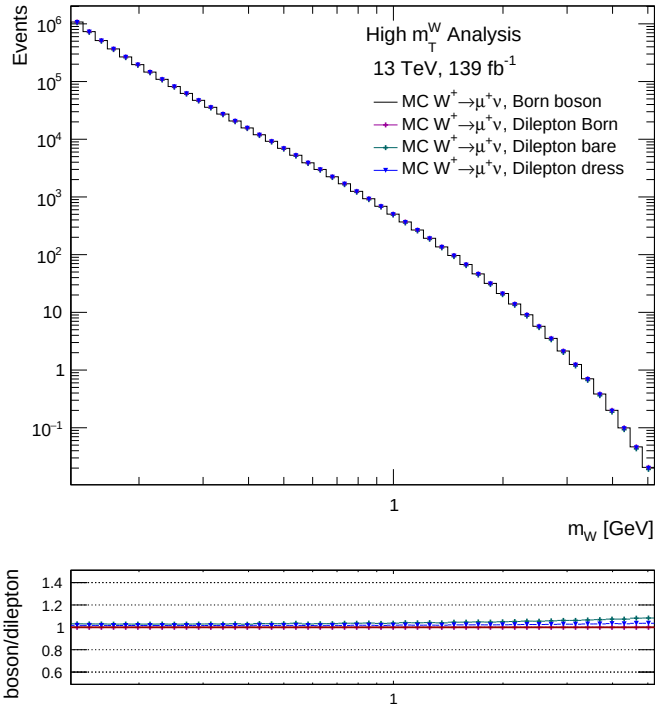

(a)

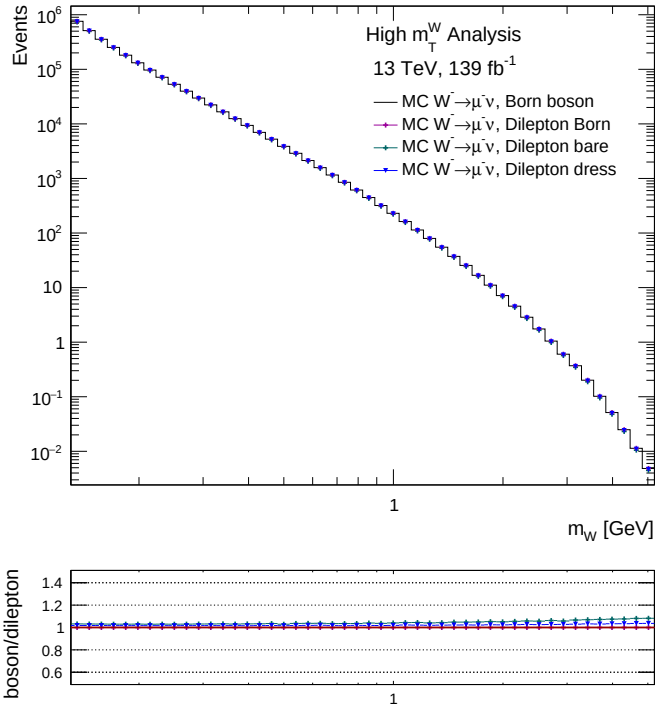

(b)

Figure 10.4.: Truth invariant mass distributions for the W boson for both charges using the bare, born or dressed level truth level definitions.

The following criteria were considered in choosing the binning:

- Experimental resolution of reconstructed events
- Bin-wise migration caused by reconstruction
- Statistical uncertainty in the data

A bin width was chosen to be larger than the resolution in each level bin. The bin-wise migrations and statistical uncertainties were also required to be reasonably small. The final binning is decided after checks on these criteria, with data and prediction also being compared in this particular binning which can be found in the Internal Note of the high m_T^W analysis [117].

10.4.1. Migration

An important feature to consider in this analysis is the so-called "bin migration", which is characterised by the fraction of events reconstructed and generated in different bins. The value of a variable is often different on reconstruction and truth levels. For a binned measurement, this results in a probability that an event gets generated in a bin but reconstructed in a different bin. The migration is important to understand so that the detector response can be corrected. The bin migration should be kept reasonably low for the unfolding to be accurate. To monitor the bin migration, a migration matrix M_{ij}, can be established, giving a mathematical connection between the variable's value on the truth level and after accounting for detector effects, i.e. reconstruction level. The entries in this matrix give the probability of an truth event in bin j having a corresponding reconstructed event located in bin i.

This migration matrix is created using the Monte Carlo signal. The reconstructed event is plotted against the corresponding truth event for the kinematic variable to create a 2D histogram where the binning is identical in both axes to get a $N \times N$ matrix. The ratio of events in the bin to the total number of reconstructed events is calculated and can be found in each bin. Therefore, every bin in each truth event row is normalised to unity. This normalisation is used to see directly where events originate. It should be noted this is not the response matrix used for unfolding which is later explained in Section 10.6.

The migration matrix, calculated in Figure 10.5, uses the transverse mass for W^+ bosons and is denoted as $M_{\text{reco, truth}}$. The measurement binning has been used with the addition of two low m_T^W bins. The migrations shown in this matrix are a restricting factor when choosing the binning. This matrix is constructed using the usual signal region selection (Section 6.1) but with the m_T^W cut lowered to 60 GeV. There have been no fiducial truth level selections (Section 6.1.11) applied to this matrix. This enables the migration effect from the peak of the W boson to be explicitly seen. The migrations

from the peak are largest at lower m_T^W. However, it is worth noting that migrations from the peak sample are still visible at very high m_T^W seen by the presence of non-zero values of the first column of the matrix. Taking only the diagonal elements of the matrix gives the purity. Purity is lowest in the shadow bin and the highest m_T^W bin. This is where the effects of migration are most greatly seen. The binning chosen needed to keep the purity at sufficiently large values to yield reasonable purities. This can be seen in the matrix as the purities, in general, have been kept above 50%.

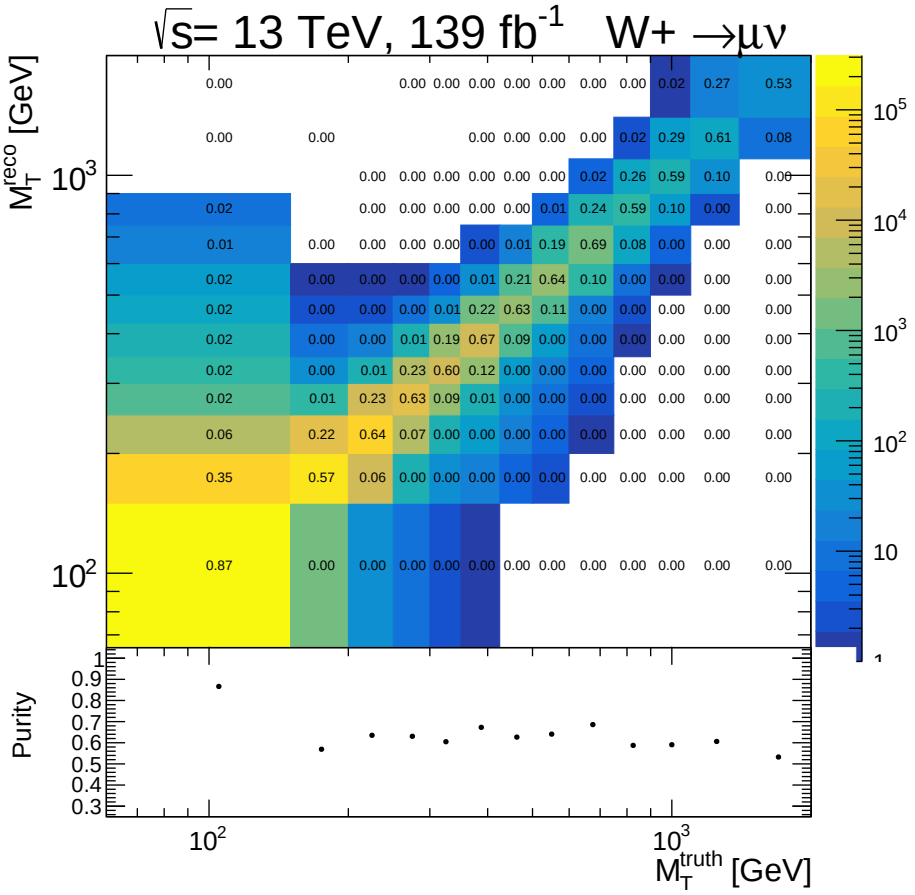

Figure 10.5.: Migration matrix $M_{\text{reco,truth}}$ for the $W^+ \to \mu^+\nu$ signal process. The upper panel shows the m_T^W truth level vs the m_T^W reconstruction level events. The given numbers show the ratio of the number of events in each bin to the total number of reconstructed events in the given mass bin. The diagonal of the upper panel gives the purity in the lower panel.

The purity is generally a few per cent lower for the negative charge in Figure 10.6 compared to the positive charge in Figure 10.5. The distribution of the truth level m_T^W is strictly falling in the region above the mass peak of the W boson. The charge difference arises from the slight differences in the steepness of the mass distributions of the two charges. This originates from the production mechanism of the W boson. More W^+ boson events are produced because the proton consists of two up valence quarks but

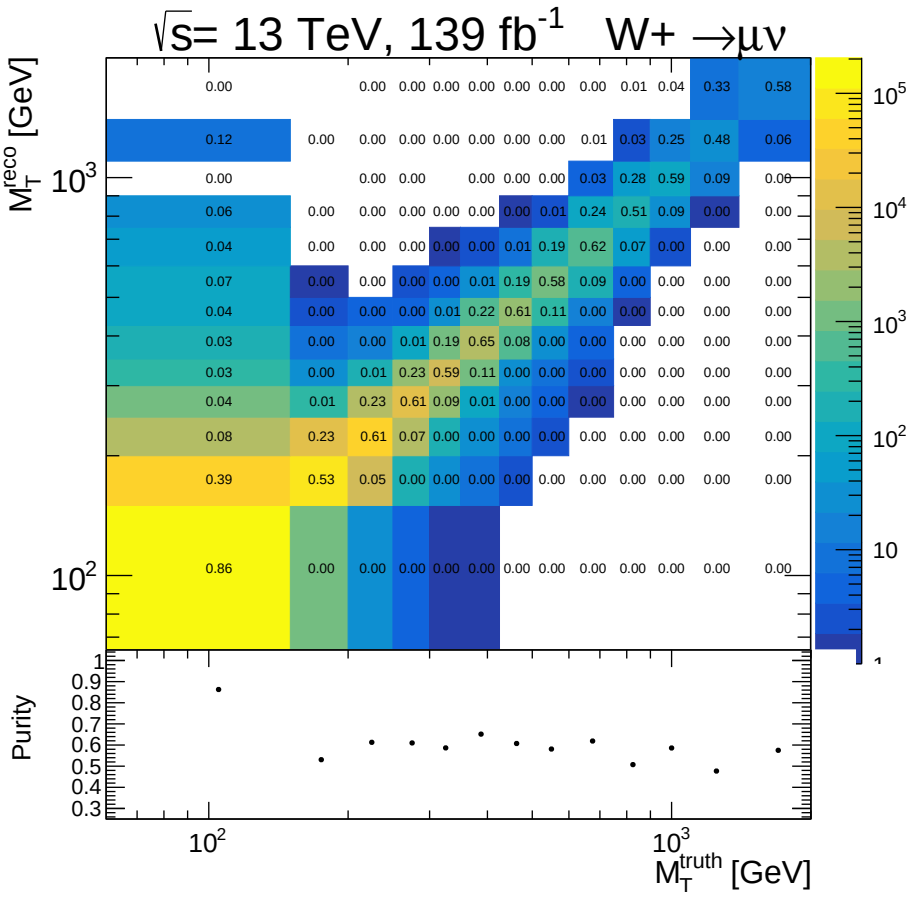

Figure 10.6.: Migration matrix $M_{\text{reco,truth}}$ for the $W^- \to \mu^- \bar{\nu}$ signal process. The upper panel shows the m_T^W truth level vs the m_T^W reconstruction level events. The given numbers show the ratio of the number of events in each bin to the total number of reconstructed events in the given mass bin. The diagonal of the upper panel gives the purity in the lower panel.

only one down valence quark. A large Bjorken-x (see Section 2.2) is needed to produce the W boson for very high masses. When looking at the PDFs, shown in Figure 2.2, the valence quarks dominate in the region of high Bjorken-x. At low Bjorken-x, the sea quarks become more dominant and are symmetric in the charges, so at lower mass, the difference in the production rates of the W^+ and W^- bosons are expected to be less pronounced. Therefore, the distribution of the W^- mass needs to be steeper, which results in higher migration effects and lower purities. The migration matrices for the individual Monte Carlo campaigns can be found in Appendix F.2.

10.5. Iterative Bayesian Unfolding

The ATLAS detector does not provide a perfect reconstruction of events, so a correction, called unfolding, for the detector efficiency and acceptance effects which transforms the measured reconstruction level to the truth level, is necessary. As seen in Equation 10.1, inverting the response matrix R_{ij} is an essential step for calculating the truth level cross-section. For this analysis, the method used is the iterative Bayesian unfolding (IBU) [116], which is implemented through `RooUnfold` [118]. This method can adequately unfold if non-negligible migrations between bins are present, see Section 10.4.1 for more detail on migrations.

The mathematical framework for IBU is based on Bayes' theorem and is expressed by effects E and causes C. The effects can be linked to the reconstruction-level events and the causes to the truth-level events. The number of reconstructed events N_i corresponds to the effects E_i and n_E is the number of bins on the reconstruction level. The number of predicted events in bin j of the truth distribution is C_j and the number of causes or truth bins is n_C. The number of truth-level bins and reconstruction-level bins is identical. The effects E_i can be measured, but the causes C_j cannot be measured directly in data. In Equation 10.7, Bayes' theorem defines the probability for a cause C_j to produce an effect E_i where $P_0(C_j)$ is, in general, an arbitrary initial distribution for the truth level.

$$P(C_j \mid E_i) = \frac{P(E_i \mid C_j) \cdot P_0(C_j)}{\sum_{k=0}^{n_C} P(E_i \mid C_k) \cdot P_0(C_k)} \tag{10.7}$$

$P(E_i \mid C_j)$ is the probability for a cause to result in a certain effect which can be obtained as a migration matrix built from the Monte Carlo signal, see Section 10.6. In the denominator of this equation, a summation over all truth level bins is made to get a normalised probability.

To estimate the number of truth level events in a bin $j, \hat{N}(C_j)$ the following Equation 10.8 is used.

$$\hat{N}(C_j) = \frac{1}{\epsilon_j} \sum_{i=0}^{n_E} P(C_j \mid E_i) N(E_i) \tag{10.8}$$

Here $N(E_i)$ is the corrected for fraction of unmatched events per bin of the reconstructed data and is equivalent to $P_{in}^{i}(N_{data,i} - N_{bkg,i})$ seen in Equation 10.1. $N(E_i)$ is taken and multiplied with the probability $P(C_j \mid E_i)$ which corresponds to an element of the inverted matrix R_{ij}^{-1}. Therefore, this multiplication expresses the number of events that migrate from a specific bin i on the reconstruction level to a specific bin j on the truth level. A summation of all effects (reconstruction level bins) is made per truth bin to cover all migrations in the distribution. For this procedure, the only events considered are those selected on the truth level and, in particular, the reconstruction level is

considered. Finally, the estimated number of causes or the unfolded number of events is corrected for the events that are not reconstructed by multiplying with the inverse of the efficiency defined as the ratio of reconstructed to truth events.

The estimated number of truth-level events can be optimised by using an iterative procedure. The probability for an event to be generated in bin i is given by taking the quotient of the estimated number of events per bin and the total number of estimated events shown in Equation 10.9.

$$\hat{P}(C_j) = \frac{\hat{N}(C_j)}{\sum_{j=1}^{n_C} \hat{N}(C_j)} \tag{10.9}$$

From Equation 10.7, it is known that an adequate initial probability distribution, $P_0(C_j)$, is essential. The truth distribution of the signal MC sample is used as the initial guess $P_0(C_j)$ in the first iteration in `RooUnfold`. In the second iteration $P_0(C_j)$ is set to the newly calculated $\hat{P}(C_j)$. This step is repeated until a certain termination criterion is fulfilled e.g. the total uncertainty or a χ^2 distribution reaches a minimum.

10.6. Response Matrix for the Iterative Bayesian Unfolding

For the IBU, it is important to define a matrix used to give the probability of an event migrating from one bin to another. However, the response matrix is defined differently from the migration matrix $M_{\text{reco,truth}}$ previously shown in Section 10.4.1. The migration matrix is used to understand the migration effects per bin, particularly for the W boson mass peak. The response matrix considers events generated and reconstructed in the measurement range of $m_T^W = 150 - 2000$ GeV and must pass all cuts on reconstruction and truth level selections. The response matrix is the inverse of the matrix shown in Figure 10.2 and is calculated using the signal MC. Note that the first bin from $m_T^W = 60 - 150$ GeV is shown for display purposes but is not used in the IBU. The response matrix for the negative charge and each Monte Carlo campaign can be found in Appendix F.1. Due to the truth level selections being applied to the response matrix, the migrations from the mass peak, i.e. truth $m_T^W < 150$ GeV, are not included leading to purities that are considerably larger in the response matrix compared to the migration matrix $M_{\text{reco,truth}}$ in Figure 10.5.

10.7. Shadow Bin

A "shadow" bin is a bin outside of the measurement range and has the purpose of stabilising the unfolding procedure. This additional bin allows more sophisticated handling of the migrations from outside the fiducial volume. A shadow bin in the transverse mass of 150 – 200 GeV, just below the measurement range, is used for this measurement.

In this measurement, there are considerable bin migrations as discussed in Section 10.4.1, especially in the low m_T^W region. Events originating from outside the fiducial volume into the measurement range, which is not accounted for in the unfolding procedure, will lead to mismeasurements. From the response matrix shown in Figure 10.2, the events migrating into the 200 GeV bin from the lower bin are of order 20%. The correction factor P_{in}^i is applied once and not iteratively in the IBU. This should be kept as high as possible to handle the migration in the iterative procedure. If the shadow bin were not included, many events would not be accounted for in P_{in}^i, which would lower the value of the correction factor P_{in}^i. Therefore, it was decided to use the shadow bin in this analysis because it yields a more sophisticated handling of migrations across bins in the low m_T^W region.

The selections taken in this analysis and the range of the shadow bin were carefully considered. It was important to populate the shadow bin with enough events, so the fiducial cuts on p_{T} of the muon and neutrino were kept reasonably low. Naively, having fiducial $p_{\mathrm{T}}^{\mu/\nu}$ cuts to match the m_T^W e.g. $p_{\mathrm{T}}^{\mu} + p_{\mathrm{T}}^{\nu} \approx m_T^W = 200$ GeV would be reasonable. However, this would leave a shadow bin with few events from 150-200 GeV. Therefore, it was important to lower not just the m_T^W cut but also the $p_{\mathrm{T}}^{\mu/\nu}$ cuts. There is also the possibility to include the full mass peak by adding an additional shadow bin in m_T^W from $60-200$ GeV. By including this additional shadow bin the migrations from the full mass peak could be handled iteratively in the IBU. However, this is ill-advised for two reasons. Firstly, the $p_{\mathrm{T}}^{\mu/\nu}$ cuts would have to be lowered considerably for there to be no in-smearing. However, this measurement focuses on the high m_T^W region, so very low fiducial cuts on $p_{\mathrm{T}}^{\mu/\nu}$ are not wanted. The reconstruction level also provides restrictions for $p_{\mathrm{T}}^{\mu/\nu}$ because the lepton triggers used are only for events with transverse momentum greater than 65 GeV. Also, there are known issues in the region of low $E_{\mathrm{T}}^{\mathrm{miss}}$ where the $E_{\mathrm{T}}^{\mathrm{miss}}$ is not modelled very well. Secondly, the matrix method utilised in this measurement described in Section 7 cannot provide a reasonable multijet estimate in the W boson mass peak.

10.8. Technical Closure Test

A technical closure test is presented to ensure that the unfolding implemented via `RooUnfold` behaves as expected with no issues introduced by the unfolding procedure. The test uses the Monte Carlo signal, where the reconstructed distribution in place of the real measured data is used. The IBU unfolding process is carried out on the reconstruction distribution and the unfolded results are compared to the initial truth distribution. Perfect closure is expected where the unfolded and truth distributions should be in perfect agreement. This can be seen in Figure 10.7. The unfolded results using the transverse mass of the W boson for the reconstruction distribution and the truth level are shown for each charge. In the lower panel of the plots, a ratio is calculated be-

tween the unfolded output and initial truth level distribution. This ratio is as expected at unity for the whole m_T^W spectrum. Therefore, closure has been observed and the IBU in `RooUnfold` has been implemented correctly. The full systematic and statistical uncertainties are not included in the closure test.

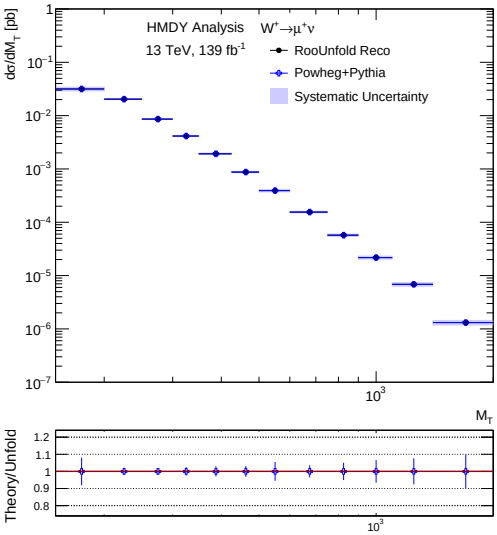

(a)

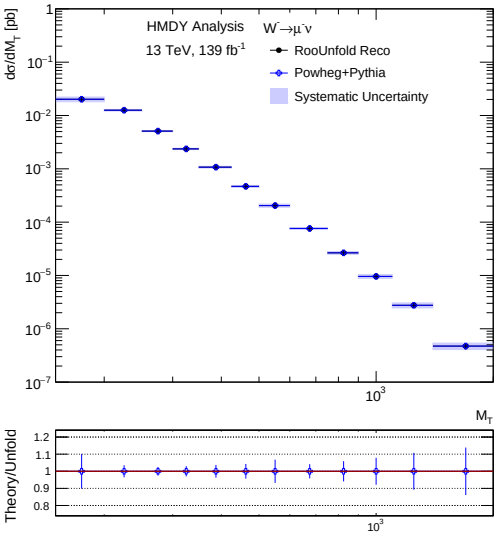

(b)

Figure 10.7.: Closure test for unfolding using `RooUnfold`. Here the reconstruction Monte Carlo has been used in place of real measured data. The unfolding matrix is constructed using truth (`POWHEG+PYTHIA`) and reconstruction-level information. Therefore, by definition, the reconstruction events must identically unfold to the truth level, as shown in the ratio panel. The full systematic and statistical uncertainties are not included.

10.9. Results

10.9.1. Unfolded Differential Cross-Section

This section presents the results of the cross-section measurements in m_T^W bins for the charged-current Drell-Yan process. The number of iterations could not be optimised in the course of this thesis; however, using two iterations was decided based on a similar study undertaken by the high m_T^W analysis group [117].

The final cross-sections are shown in Figure 10.8 for the m_T^W range of 200 GeV to 2000 GeV. The cross-sections for both charges fall by four orders of magnitude. It can be observed, as expected, that in the positively charged W boson in Figure 10.8a, the production cross-section is larger than the negatively charged W boson in Figure 10.8b.

The statistical and systematic uncertainties, as described in Chapter 8, have also been shown in the measurement results. The cross-section uncertainties are calculated with Equation 10.1. The black uncertainty bars represent the statistical uncertainty and the light blue band represents the systematic uncertainty. The total uncertainty combines these uncertainties using a sum in quadrature of all the error sources and is represented by the dark blue band. The numerical values for the measurement cross-sections, the relative systematic and statistical uncertainty per bin, the number of measured data events, Monte Carlo simulation for reconstructed and truth events and the background number of events are given in Table 10.1 and Table 10.2 for the positive and negative charges respectively. The various contributions of the systematic uncertainties have been grouped based on their origin and summed in quadrature for ease of being displayed in Table 10.3 for the positive charge and in Table 10.4 for the negative charge. The full tables showing each individual experimental systematic uncertainty contribution can be found in Appendix F.3.1. The most dominant source of systematic uncertainty is the muon sagitta bias correction which is the second largest uncertainty in the first bin (behind the multijet)and extends up to around 7% to 8% in W^+ and around 14% to 15% in W^-. The statistical uncertainty increases above the systematic uncertainty in the final measurement bin to around 13% and 19% for W^+ and W^-, respectively. When comparing the total uncertainty bands between the two charges, it is clear that the uncertainties are larger in W^-.

The lower panel of the plots show the ratio comparing the unfolded measured data to the truth level of the signal Monte Carlo which was simulated using `POWHEG-BOX` and `PYTHIA8`. This thesis has not included systematic theoretical uncertainties available, but they are expected to be small (a few per cent). The deviations between Monte Carlo and unfolded data are covered by the systematic and statistical uncertainties reasonably well in most of the bins. Slight deviations in the higher m_T^W bins were already seen in the comparison plots in Section 9. Overall the results in the positive channel have less substantial deviations between the truth and unfolded data, particularly in the highest m_T^W bin. The positive channel also has, in general, too large cross-sections in the truth

Monte Carlo. The opposite can be observed in the negative channel, where there are generally too small cross-sections seen from the ratio in many bins being substantially below unity. It is not clear why there are such noticeable differences between the results of the two muons charges.

10.9.2. Muon Charge Asymmetry

For this section, the muon charge asymmetry measurement results are presented using m_T^W bins for the charged-current Drell-Yan process. The muon charge asymmetry is shown in Figure 10.9 for the m_T^W range of 200 GeV to 2000 GeV. The statistical and systematic uncertainties, as described in Chapter 8, have also been shown in the measurement results. The muon charge asymmetry uncertainties derive from the uncertainties of the cross sections and are calculated with Equation 10.2. The black uncertainty bars represent the statistical uncertainty and the light blue band represents the systematic uncertainty. The total uncertainty combines these uncertainties using a sum in quadrature of all the error sources and is represented by the dark blue band. The numerical values for the asymmetry measurement and the relative systematic and statistical uncertainty per bin are given in Table 10.5. The various contributions of the systematic uncertainties have been grouped based on their origin and summed in quadrature for ease of being displayed in Table 10.6. The full tables showing each individual experimental systematic uncertainty contribution can be found in Appendix F.3.1. The most dominant source of systematic uncertainty is the muon sagitta bias correction, which reaches around 33%. The statistical uncertainty increases above the systematic uncertainty in the final measurement bin to around 40%. The theoretical value of the asymmetry shows an upward trend which is not reflected in the central value of the measured data; however, the total uncertainties cover this difference.

The lower panel of the plots show the ratio comparing the unfolded measured data to the truth level of the signal Monte Carlo which was simulated using POWHEG-BOX and PYTHIA8. Theoretical systematic uncertainties available have not been included but are expected to be small. The deviations between Monte Carlo and unfolded data are covered by the systematic and statistical uncertainties reasonably well in most of the bins. There is a difference in the 1 TeV bin which follows from the cross-section measurements presented but is not presently understood. The charge asymmetry measured follows the results already shown in the measurement cross-sections.

10.9.3. Summary

In this section, the results shown above are condensed into Table 10.7. This table presents the cross-sections for W^+ and W^- and the charge asymmetry measurements for each measurement bin in the m_T^W range of 200 GeV to 2000 GeV. Each value is also presented

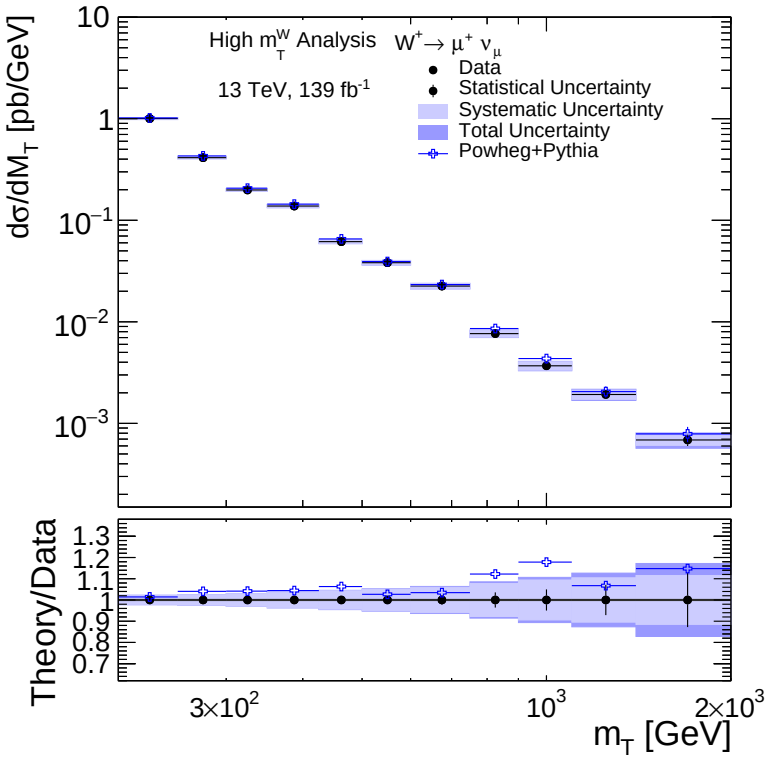

(a) W^+

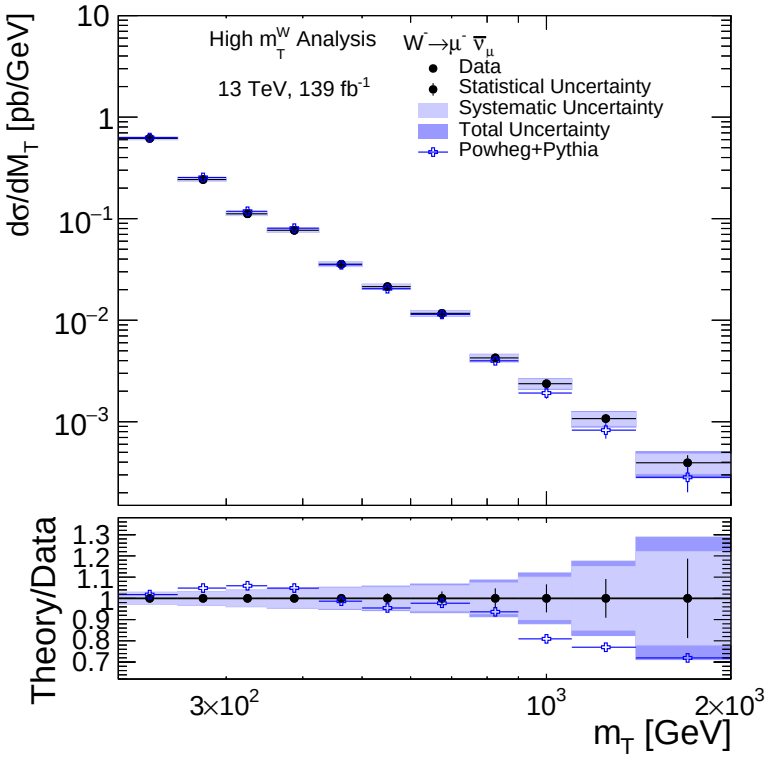

(b) W^-

Figure 10.8.: Unfolded 1D cross sections binned in m_T^W calculated using Equation 10.1. Statistical and systematic uncertainties are included in the uncertainty band. The dark blue band shows the total uncertainty. The ratio is taken between the measured data and the truth (prediction) distributions.

alongside the corresponding contribution of the statistical uncertainty first, followed by the systematic up and down uncertainties.

10.9.4. Measurement Conclusions

The measurements presented here for the charged-current cross-sections and muon charge asymmetry provide a good agreement between data and prediction. The largest systematic uncertainty arises from the muon sagitta bias correction and is dominant in the highest m_T^W regions. The statistical uncertainty is particularly dominant for the asymmetry in the highest m_T^W regions. These measurements, carried out differentially in the transverse mass of the W boson, are related to the momentum fraction that a particle carries inside the proton. These results provide the capability to constrain further the parton distribution functions relating to the up and down quarks and antiquarks, which are responsible for producing positive and negative muons through the charged Drell-Yan process. The results for the muon charge asymmetry in m_T^W have not been presented before in the literature and are being presented here for the first time. The cross-section measurements have never been reported in literature using the full 13 TeV dataset and are presented here first.

	σ_{Data} [pb]	σ_{MC} [pb]	δ_{sys}^{up} [%]	δ_{sys}^{down} [%]	δ_{stat} [%]	N^{Data}	N^{reco}	N^{truth}	N^{BG}
$200 \leq M_T < 250$	1.0041	1.0185	2.20	1.57	0.38	145577	92583	141531	53744
$250 \leq M_T < 300$	0.4137	0.4305	2.41	1.95	0.58	57698	36720	59828	22112
$300 \leq M_T < 350$	0.1989	0.2072	2.48	2.45	0.79	25815	17200	28788	9218
$350 \leq M_T < 425$	0.1381	0.1442	2.81	2.83	0.98	16711	11752	20044	5394
$425 \leq M_T < 500$	0.0616	0.0655	3.29	3.17	1.38	6824	5212	9107	1928
$500 \leq M_T < 600$	0.0382	0.0392	3.70	3.44	1.72	3945	3134	5453	890
$600 \leq M_T < 750$	0.0225	0.0233	4.39	4.04	2.26	2138	1808	3235	387
$750 \leq M_T < 900$	0.0077	0.0086	5.64	5.35	3.57	731	680	1194	117
$900 \leq M_T < 1100$	0.0037	0.0043	6.71	6.60	4.98	322	333	604	40
$1100 \leq M_T < 1400$	0.0019	0.0021	7.28	7.49	7.14	167	155	286	18
$1400 \leq M_T < 2000$	0.0007	0.0008	7.82	8.46	12.77	66	72	110	5

Table 10.1.: This table contains the cross-section values for $W^+ \to \mu^+ \nu$. The first column displays the muon mass bins; the second and third columns are the data measured and predicted cross-sections computed with Equation 10.1; the fourth, fifth and sixth columns show the up, down and statistical uncertainties in percentage, respectively; last right four columns contain the data, reconstructed, truth and background number of events in that order.

	σ_{Data} [pb]	σ_{MC} [pb]	δ_{sys}^{up} [%]	δ_{sys}^{down} [%]	δ_{stat} [%]	N^{Data}	N^{reco}	N^{truth}	N^{BG}
$200 \leq M_T < 250$	0.6177	0.6285	3.13	2.20	0.51	104811	59236	87346	46049
$250 \leq M_T < 300$	0.2430	0.2548	3.59	2.88	0.81	40626	22432	35402	18936
$300 \leq M_T < 350$	0.1116	0.1183	3.84	3.61	1.14	17762	10150	16434	8081
$350 \leq M_T < 425$	0.0769	0.0806	3.87	3.90	1.41	11234	6773	11199	4734
$425 \leq M_T < 500$	0.0356	0.0351	3.77	4.01	1.92	4639	2934	4883	1658
$500 \leq M_T < 600$	0.0214	0.0204	3.57	4.19	2.36	2664	1800	2841	775
$600 \leq M_T < 750$	0.0117	0.0114	3.81	4.62	3.24	1377	985	1586	367
$750 \leq M_T < 900$	0.0043	0.0040	4.96	5.30	4.71	470	358	554	93
$900 \leq M_T < 1100$	0.0024	0.0019	6.99	7.10	6.60	226	148	266	44
$1100 \leq M_T < 1400$	0.0011	0.0008	10.40	10.71	9.13	114	79	115	17
$1400 \leq M_T < 2000$	0.0004	0.0003	15.11	15.91	18.71	38	23	39	7

Table 10.2.: This table contains the cross-section values for $W^- \to \mu^- \nu$. The first column displays the muon mass bins; the second and third columns are the data measured and predicted cross-sections computed with Equation 10.1; the fourth, fifth and sixth columns show the up, down and statistical uncertainties in percentage, respectively; last right four columns contain the data, reconstructed, truth and background number of events in that order.

Systematic Group	$200 \leq M_T < 250$	$250 \leq M_T < 300$	$300 \leq M_T < 350$	$350 \leq M_T < 425$	$425 \leq M_T < 500$	$500 \leq M_T < 600$	$600 \leq M_T < 750$	$750 \leq M_T < 900$	$900 \leq M_T < 1100$	$1100 \leq M_T < 1400$	$1400 \leq M_T < 2000$
Muon	−0.80 0.80	−0.99 0.99	−1.11 1.11	−1.16 1.16	−1.16 1.16	−1.16 1.16	−1.20 1.20	−1.32 1.32	−1.56 1.56	−1.92 1.92	−2.28 2.28
Sagitta Bias	−0.95 0.83	−1.17 1.12	−1.49 1.67	−2.09 2.20	−2.77 2.65	−3.36 3.09	−4.17 3.82	−5.47 5.16	−6.52 6.41	−7.02 7.23	−7.48 8.14
Missing Energy	−0.82 0.67	−0.52 0.45	−0.31 0.52	−0.27 0.21	−0.10 0.10	−0.08 0.07	−0.05 0.06	−0.16 0.19	−0.11 0.09	−0.17 0.19	−0.16 0.16
Pileup	−0.12 0.12	−0.12 0.12	−0.12 0.12	−0.14 0.14	−0.16 0.16	−0.17 0.17	−0.17 0.17	−0.14 0.14	−0.09 0.09	−0.06 0.06	−0.06 0.06
Jet	−0.45 0.45	−0.53 0.53	−0.61 0.61	−0.73 0.73	−0.77 0.77	−0.66 0.66	−0.47 0.47	−0.27 0.27	−0.13 0.13	−0.08 0.08	−0.08 0.08
Multijet	−1.56 0.70	−1.70 1.05	−1.49 1.16	−1.26 1.11	−1.08 1.01	−0.77 0.72	−0.40 0.34	−0.22 0.21	−0.13 0.10	−0.05 0.11	−0.13 0.13

Table 10.3.: This table contains the contribution of grouped experimental systematic uncertainties in each bin for $W^+ \to \mu^+ \nu$. The systematics were computed with Equation 10.1 and then summed in quadrature for each group. The first column is the name of the systematic. All values are presented in percentages.

Systematic Group	$200 \leq M_T < 250$	$250 \leq M_T < 300$	$300 \leq M_T < 350$	$350 \leq M_T < 425$	$425 \leq M_T < 500$	$500 \leq M_T < 600$	$600 \leq M_T < 750$	$750 \leq M_T < 900$	$900 \leq M_T < 1100$	$1100 \leq M_T < 1400$	$1400 \leq M_T < 2000$
Muon	−0.80 0.80	−0.97 0.97	−1.12 1.12	−1.27 1.27	−1.36 1.36	−1.35 1.35	−1.28 1.28	−1.36 1.36	−1.81 1.81	−2.53 2.53	−3.11 3.11
Sagitta Bias	−1.11 1.16	−1.54 1.57	−2.05 2.29	−2.50 2.78	−2.82 3.11	−2.98 3.69	−3.49 4.34	−4.74 5.10	−6.75 6.86	−10.08 10.40	−14.78 15.59
Missing Energy	−0.80 0.85	−0.37 0.44	−0.42 0.30	−0.28 0.37	−0.33 0.67	−0.29 0.24	−0.14 0.11	−0.02 0.07	−0.03 0.05	−0.22 0.15	−0.11 0.10
Pileup	−0.32 0.32	−0.27 0.27	−0.18 0.18	−0.17 0.17	−0.19 0.19	−0.19 0.19	−0.19 0.19	−0.19 0.19	−0.20 0.20	−0.23 0.23	−0.24 0.24
Jet	−0.81 0.81	−0.85 0.85	−0.86 0.86	−0.89 0.89	−0.90 0.90	−0.75 0.75	−0.43 0.43	−0.18 0.18	−0.11 0.11	−0.13 0.13	−0.23 0.23
Multijet	−2.56 1.17	−2.94 1.97	−2.88 2.39	−2.49 2.22	−1.85 1.81	−1.14 1.21	−0.70 0.80	−0.43 0.43	−0.11 0.31	−0.19 0.18	−0.45 0.45

Table 10.4.: This table contains the contribution of grouped experimental systematic uncertainties in each bin for $W^- \to \mu^- \nu$. Systematics were computed with Equation 10.1 and then summed in quadrature for each group. The first column is the name of the systematic. All values are presented in percentage.

	$As_{\mu,Data}$	$As_{\mu,MC}$	δ_{sys}^{up} [%]	δ_{sys}^{down} [%]	δ_{stat} [%]
$200 \leq M_T < 250$	0.24	0.24	4.60	4.67	1.31
$250 \leq M_T < 300$	0.26	0.26	5.63	4.78	1.88
$300 \leq M_T < 350$	0.28	0.27	5.71	7.02	2.41
$350 \leq M_T < 425$	0.28	0.28	8.77	9.00	2.94
$425 \leq M_T < 500$	0.27	0.30	9.15	7.70	4.34
$500 \leq M_T < 600$	0.28	0.31	10.92	18.39	5.13
$600 \leq M_T < 750$	0.32	0.34	11.43	12.03	6.15
$750 \leq M_T < 900$	0.29	0.37	20.56	20.45	10.36
$900 \leq M_T < 1100$	0.22	0.39	28.55	29.76	18.70
$1100 \leq M_T < 1400$	0.28	0.43	35.27	35.72	20.62
$1400 \leq M_T < 2000$	0.27	0.47	31.68	33.53	40.66

Table 10.5.: This table contains the muon charge asymmetry values. The first column displays the muon mass bins; the second and third columns are the data measured and predicted cross-sections computed with Equation 10.2; the fourth, fifth and sixth columns show the up, down and statistical uncertainties in percentage, respectively.

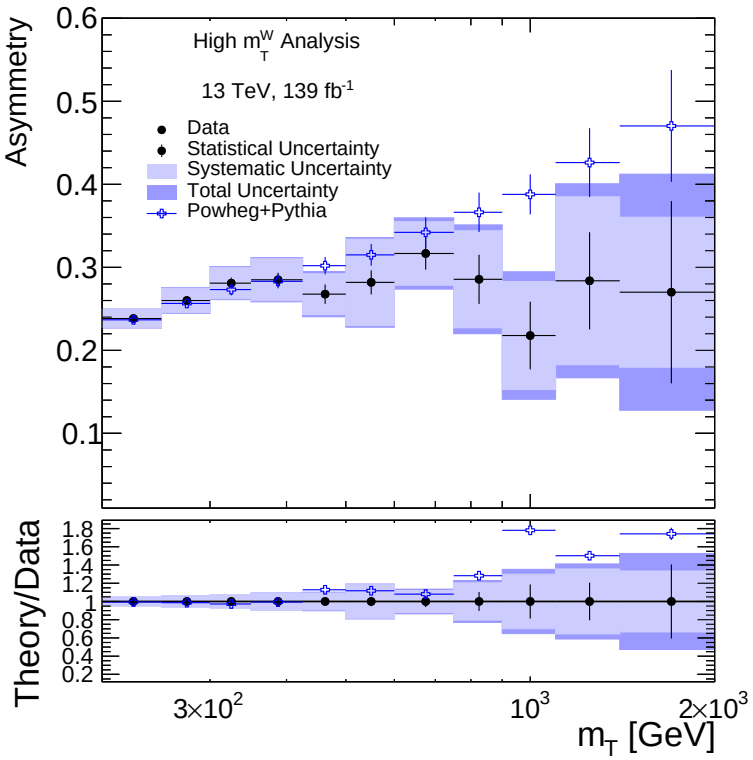

Figure 10.9.: Muon charge aymmetry binned in m_T^W calculated using Equation 10.2. Statistical and systematic uncertainties are included in the uncertainty band. Statistical and systematic uncertainties are included in the uncertainty band. The dark blue band shows the total uncertainty. The ratio is between the measured data and the truth (prediction) distributions.

Systematic Group	$200 \leq M_T < 250$	$250 \leq M_T < 300$	$300 \leq M_T < 350$	$350 \leq M_T < 425$	$425 \leq M_T < 500$	$500 \leq M_T < 600$	$600 \leq M_T < 750$	$750 \leq M_T < 900$	$900 \leq M_T < 1100$	$1100 \leq M_T < 1400$	$1400 \leq M_T < 2000$
Muon	−0.18	−0.24	−1.11	−0.31	−0.83	−2.62	−0.25	−0.37	−0.86	−2.33	−1.68
	0.22	0.38	0.35	0.40	1.15	1.83	0.42	0.42	1.16	2.13	1.48
Sagitta Bias	−3.93	−3.98	−6.17	−8.73	−6.75	−17.90	−11.96	−20.42	−29.67	−35.62	−33.52
	3.66	5.07	5.64	8.64	8.61	10.54	11.38	20.54	28.56	35.19	31.61
Missing Energy	−0.77	−0.91	−0.86	−0.47	−1.30	−0.45	−0.30	−0.38	−0.18	−0.18	−0.13
	0.91	0.86	0.96	0.44	1.31	0.53	0.22	0.39	0.14	0.17	0.11
Pileup	−0.91	−1.30	−0.26	−0.21	−1.72	−0.26	−0.38	−0.17	−0.33	−0.21	−0.11
	0.33	0.79	0.48	0.53	0.75	0.76	0.64	0.10	0.56	1.18	0.25
Jet	−2.84	−1.84	−1.42	−1.13	−3.16	−3.62	−0.63	−1.17	−0.95	−0.46	−0.31
	2.73	1.72	1.56	1.36	3.05	3.23	0.72	1.14	0.63	0.39	0.28
Multijet	−0.81	−1.62	−2.19	−1.70	−1.36	−0.65	−1.26	−0.42	−1.08	−0.95	−0.43
	1.78	2.26	2.46	1.94	1.40	0.47	1.18	0.45	1.06	0.95	0.43

Table 10.6.: This table contains the contribution of grouped uncertainties in each bin for the asymmetry. Systematics were computed with Equation 10.2 and then summed in quadrature for each group. The first column is the name of the systematic. All the values are presented in percentages.

	σ_{W^-} [pb]	σ_{W^+} [pb]	As_μ
$200 \leq M_T < 250$	$0.6177 \pm 0.0031^{+0.0193}_{-0.0136}$	$1.0041 \pm 0.0038^{+0.0221}_{-0.0158}$	$0.2383 \pm 0.0007^{+0.0110}_{-0.0111}$
$250 \leq M_T < 300$	$0.2430 \pm 0.0020^{+0.0087}_{-0.0070}$	$0.4137 \pm 0.0024^{+0.0100}_{-0.0081}$	$0.2600 \pm 0.0013^{+0.0146}_{-0.0124}$
$300 \leq M_T < 350$	$0.1116 \pm 0.0013^{+0.0043}_{-0.0040}$	$0.1989 \pm 0.0016^{+0.0049}_{-0.0049}$	$0.2809 \pm 0.0019^{+0.0160}_{-0.0197}$
$350 \leq M_T < 425$	$0.0769 \pm 0.0011^{+0.0030}_{-0.0030}$	$0.1381 \pm 0.0014^{+0.0039}_{-0.0039}$	$0.2850 \pm 0.0024^{+0.0250}_{-0.0256}$
$425 \leq M_T < 500$	$0.0356 \pm 0.0007^{+0.0013}_{-0.0014}$	$0.0616 \pm 0.0009^{+0.0020}_{-0.0020}$	$0.2677 \pm 0.0031^{+0.0245}_{-0.0206}$
$500 \leq M_T < 600$	$0.0214 \pm 0.0005^{+0.0008}_{-0.0009}$	$0.0382 \pm 0.0007^{+0.0014}_{-0.0013}$	$0.2819 \pm 0.0041^{+0.0308}_{-0.0518}$
$600 \leq M_T < 750$	$0.0117 \pm 0.0004^{+0.0004}_{-0.0005}$	$0.0225 \pm 0.0005^{+0.0010}_{-0.0009}$	$0.3167 \pm 0.0062^{+0.0362}_{-0.0381}$
$750 \leq M_T < 900$	$0.0043 \pm 0.0002^{+0.0002}_{-0.0002}$	$0.0077 \pm 0.0003^{+0.0004}_{-0.0004}$	$0.2855 \pm 0.0084^{+0.0587}_{-0.0584}$
$900 \leq M_T < 1100$	$0.0024 \pm 0.0002^{+0.0002}_{-0.0002}$	$0.0037 \pm 0.0002^{+0.0002}_{-0.0002}$	$0.2178 \pm 0.0089^{+0.0622}_{-0.0648}$
$1100 \leq M_T < 1400$	$0.0011 \pm 9.8074 \cdot 10^{-5}{}^{+0.0001}_{-0.0001}$	$0.0019 \pm 0.0001^{+0.0001}_{-0.0001}$	$0.2838 \pm 0.0166^{+0.1001}_{-0.1014}$
$1400 \leq M_T < 2000$	$0.0004 \pm 7.3825 \cdot 10^{-5}{}^{+5.9631 \cdot 10^{-5}}_{-6.2790 \cdot 10^{-5}}$	$0.0007 \pm 8.7647 \cdot 10^{-5}{}^{+5.3707 \cdot 10^{-5}}_{-5.8049 \cdot 10^{-5}}$	$0.2700 \pm 0.0296^{+0.0855}_{-0.0905}$

Table 10.7.: This table displays a summary of the charged current Drell-Yan cross-sections and the muon charge asymmetry measurements. The first column is the muon mass binning; the second and the third columns are the $W^- \to \mu^- \nu$ and $W^+ \to \mu^+ \nu$ cross-sections, respectively, calculated utilising Equation 10.1; the fourth column is the muon charge asymmetry computed with Equation 10.2. The numbers are presented in the following order: the value of the process, the data statistical uncertainty and the systematic uncertainties up and down.

11. Conclusion

Modern accelerators and detectors have reached levels of development and sophistication such that physicists can prove robust quantum field theories and provide guidance on constructing new ones. The Large Hadron Collider and the ATLAS detector's successful operation have been paramount for obtaining the results in this thesis. The calibration of physics objects calculated by the ATLAS performance groups, particularly the muons seen in the detector, has unprecedented precision for the Run-2 analyses.

A one-dimensional differential cross-section and muon charge asymmetry measurement for charged-current Drell-Yan processes in the muonic decay channel at high transverse masses $m_{\mathrm{T}}^{\mathrm{W}}$ in the range from 200 GeV to 2000 GeV has been successfully obtained and presented in this thesis. The analysis used 139 fb^{-1} of data from pp collisions recorded by the ATLAS detector, which constitutes the full Run-2 dataset which was collected between 2015-2018 with centre-of-mass energy $\sqrt{s} = 13$ TeV.

The precise measurement of the cross-section and asymmetry allows insight into the proton's structure, which is essential for future measurements and searches at hadron colliders. These results also will help provide direct constraints on the parton distribution functions of the proton. They will also be able to provide sensitivity to electroweak and effective field theory parameters. The measurements presented here aim to include the high-mass region, unlike the previous results by ATLAS and CMS mentioned in Section 2.5. The results in this thesis have never been presented before using centre-of-mass energy $\sqrt{s} = 13$ TeV for the full Run-2 data and the charge asymmetry has never been reported for the transverse mass of the W boson in the high-mass tail.

The number of events predicted by Standard Model processes is estimated using Monte Carlo simulations and a data-driven method. The background modelling for the multijet background uses a data-driven method estimated via the Matrix Method. The multijet background is composed of fake muons originating from jet activities, as opposed to real muons from the decay of W or Z bosons. Overall a reasonable agreement between the data and prediction can be observed in the control distributions.

The Iterative Bayesian Unfolding is used on the born lepton level for the unfolding. The unfolding corrects for measurement efficiency, detector smearing and acceptance caused by the analysis-specific selection criteria. This method for unfolding is adequate if non-negligible migration effects between bins are present. Migrations were investigated and shown to be present in this thesis. The unfolded cross-sections and asymmetry were calculated in an optimised $m_{\mathrm{T}}^{\mathrm{W}}$ binning. The results in this thesis are

preliminary until the number of unfolding iterations is properly optimised.

The statistical and systematic uncertainties have been included. Experimental systematic uncertainties from the measurements of muons, muon sagitta bias, missing transverse energy, pileup, and jets are included. Systematic uncertainties for the multijet estimation were also included. Theoretical systematic uncertainties were not included but are expected to have little impact, especially compared to the large uncertainties arising from other sources. The largest systematic uncertainties arise from the muon sagitta bias correction, which particularly dominates in the highest $m_{\mathrm{T}}^{\mathrm{W}}$ bin ranging from 1400 – 2000 GeV. The muon sagitta bias correction for W^+ bosons reaches up to around 7% to 8% in W^+ and around 14% to 15% in W^-, reaching up to around 33% for the muon charge asymmetry. For the muon charge asymmetry, in the highest $m_{\mathrm{T}}^{\mathrm{W}}$ bin, the statistical uncertainty increases above the systematic uncertainty in the final measurement bin to around 40%.

The unfolded cross-sections and charge asymmetry are finally compared to the born lepton level from the signal Monte Carlo which was simulated using POWHEG-BOX and PYTHIA8. The agreement between the measured and predicted cross-sections is reasonable within the considered uncertainties. An interesting difference between the positive and negative W bosons is visible where the positive charge shows a trend of overestimated predicted cross-sections and the negative charge a trend of an underestimated predicted cross-section. This trend is reflected explicitly in the muon charge asymmetry results. The agreement between the measured and predicted muon charge asymmetry is also reasonable within considered uncertainties.

The work contained in this thesis was conducted as part of a broader analysis group in ATLAS for Standard Model measurements in the W/Z physics group for high m_T^W. The author's contributions were to provide a muon asymmetry measurement, a cross-check for the cross-sections in the muon channel, provide an alternative multijet estimation and systematic uncertainties, to help with studies on the choice of optimal working points, provide distributions with cutflows which breakdown each MC campaign used for Run-2 estimation and help with the requesting/maintaining the derived samples for the charged-current Drell-Yan phase space. Contributions to these and other areas were obtained from other analysis team members, for which the author is grateful.

There are multiple areas where this analysis could be further improved. Firstly, an improvement in the calculation of the muon sagitta bias correction, which the Muon Combined Performance group provides, will reduce the systematic uncertainties in the highest $m_{\mathrm{T}}^{\mathrm{W}}$ region. Significant statistical uncertainties exist, particularly in the muon charge asymmetry results. Half the statistical uncertainty would require approximately four times an increase in statistics. Including the LHC Run-3 dataset would increase the statistics for this analysis. However, combining the Run-2 and Run-3 datasets leads to a factor 2 increase in statistics which would not be enough to lower the statistical uncertainty substantially. Furthermore, systematic theoretical uncertainties on the signal

process must be considered to classify and interpret the results entirely in the future. The systematic theoretical uncertainties must include variations of the initial and final state radiation, the factorisation and renormalisation scales, alternative PDF models and alternative Monte Carlo generators. The results in the charged-current Drell-Yan muonic channel analysis and a parallel electron channel analysis will also be combined. An extension of this analysis is also to perform this measurement as a double-differential measurement in the transverse mass of the W boson and the pseudorapidity of the muon. There is also currently an effort to measure the tau channel for the Drell-Yan process. Currently, a number of PhD students are working on these areas, including EFT interpretation. The combined electron and muon analysis results aim to be published in a peer-reviewed journal as a world-leading result.

A. Appendix: Samples

The following is a list of all data and Monte Carlo signal and background samples used for the measurement. The data samples are listed first with each year being specified. The Monte Carlo samples have been listed based on the process and then further sectioned based on the Monte Carlo campaign.

A.1. Data samples

A.1.1. 2015

- data15_13TeV.periodD.physics_Main.PhysCont.DAOD_STDM4.grp23_v01_p4238
- data15_13TeV.periodE.physics_Main.PhysCont.DAOD_STDM4.grp23_v01_p4238
- data15_13TeV.periodF.physics_Main.PhysCont.DAOD_STDM4.grp23_v01_p4238
- data15_13TeV.periodG.physics_Main.PhysCont.DAOD_STDM4.grp23_v01_p4238
- data15_13TeV.periodH.physics_Main.PhysCont.DAOD_STDM4.grp23_v01_p4238
- data15_13TeV.periodJ.physics_Main.PhysCont.DAOD_STDM4.grp23_v01_p4238

A.1.2. 2016

- data16_13TeV.periodA.physics_Main.PhysCont.DAOD_STDM4.grp23_v01_p4238
- data16_13TeV.periodB.physics_Main.PhysCont.DAOD_STDM4.grp23_v01_p4238
- data16_13TeV.periodC.physics_Main.PhysCont.DAOD_STDM4.grp23_v01_p4238
- data16_13TeV.periodD.physics_Main.PhysCont.DAOD_STDM4.grp23_v01_p4238
- data16_13TeV.periodE.physics_Main.PhysCont.DAOD_STDM4.grp23_v01_p4238
- data16_13TeV.periodF.physics_Main.PhysCont.DAOD_STDM4.grp23_v01_p4238
- data16_13TeV.periodG.physics_Main.PhysCont.DAOD_STDM4.grp23_v01_p4238
- data16_13TeV.periodI.physics_Main.PhysCont.DAOD_STDM4.grp23_v01_p4238
- data16_13TeV.periodK.physics_Main.PhysCont.DAOD_STDM4.grp23_v01_p4238
- data16_13TeV.periodL.physics_Main.PhysCont.DAOD_STDM4.grp23_v01_p4238

A.1.3. 2017

- data17_13TeV.periodB.physics_Main.PhysCont.DAOD_STDM4.grp23_v01_p4238
- data17_13TeV.periodC.physics_Main.PhysCont.DAOD_STDM4.grp23_v01_p4238
- data17_13TeV.periodD.physics_Main.PhysCont.DAOD_STDM4.grp23_v01_p4238
- data17_13TeV.periodE.physics_Main.PhysCont.DAOD_STDM4.grp23_v01_p4238
- data17_13TeV.periodF.physics_Main.PhysCont.DAOD_STDM4.grp23_v01_p4238

- data17_13TeV.periodH.physics_Main.PhysCont.DAOD_STDM4.grp23_v01_p4238
- data17_13TeV.periodI.physics_Main.PhysCont.DAOD_STDM4.grp23_v01_p4238
- data17_13TeV.periodK.physics_Main.PhysCont.DAOD_STDM4.grp23_v01_p4238

A.1.4. 2018

- data18_13TeV.periodB.physics_Main.PhysCont.DAOD_STDM4.grp23_v01_p4238
- data18_13TeV.periodC.physics_Main.PhysCont.DAOD_STDM4.grp23_v01_p4238
- data18_13TeV.periodD.physics_Main.PhysCont.DAOD_STDM4.grp23_v01_p4238
- data18_13TeV.periodF.physics_Main.PhysCont.DAOD_STDM4.grp23_v01_p4238
- data18_13TeV.periodI.physics_Main.PhysCont.DAOD_STDM4.grp23_v01_p4238
- data18_13TeV.periodK.physics_Main.PhysCont.DAOD_STDM4.grp23_v01_p4238
- data18_13TeV.periodL.physics_Main.PhysCont.DAOD_STDM4.grp23_v01_p4238
- data18_13TeV.periodM.physics_Main.PhysCont.DAOD_STDM4.grp23_v01_p4238
- data18_13TeV.periodO.physics_Main.PhysCont.DAOD_STDM4.grp23_v01_p4238
- data18_13TeV.periodQ.physics_Main.PhysCont.DAOD_STDM4.grp23_v01_p4238

A.2. Signal samples

A.2.1. $W \to \mu\nu$

MC16a:

W^+

- mc16_13TeV.361101.PowhegPythia8EvtGen_AZNLOCTEQ6L1_Wplusmunu.deriv.DAOD_STDM4.e3601_s3126_r9364_r9315_p4239
- mc16_13TeV.301100.PowhegPythia8EvtGen_AZNLOCTEQ6L1_Wplusmunu_120M180.deriv.DAOD_STDM4.e3663_s3126_r9364_r9315_p4239
- mc16_13TeV.301101.PowhegPythia8EvtGen_AZNLOCTEQ6L1_Wplusmunu_180M250.deriv.DAOD_STDM4.e3663_s3126_r9364_r9315_p4239
- mc16_13TeV.301102.PowhegPythia8EvtGen_AZNLOCTEQ6L1_Wplusmunu_250M400.deriv.DAOD_STDM4.e3663_s3126_r9364_r9315_p4239
- mc16_13TeV.301103.PowhegPythia8EvtGen_AZNLOCTEQ6L1_Wplusmunu_400M600.deriv.DAOD_STDM4.e3663_s3126_r9364_r9315_p4239
- mc16_13TeV.301104.PowhegPythia8EvtGen_AZNLOCTEQ6L1_Wplusmunu_600M800.deriv.DAOD_STDM4.e3663_s3126_r9364_r9315_p4239
- mc16_13TeV.301105.PowhegPythia8EvtGen_AZNLOCTEQ6L1_Wplusmunu_800M1000.deriv.DAOD_STDM4.e3663_s3126_r9364_r9315_p4239
- mc16_13TeV.301106.PowhegPythia8EvtGen_AZNLOCTEQ6L1_Wplusmunu_1000M1250.deriv.DAOD_STDM4.e3663_s3126_r9364_r9315_p4239
- mc16_13TeV.301107.PowhegPythia8EvtGen_AZNLOCTEQ6L1_Wplusmunu_1250M1500.deriv.DAOD_STDM4.e3663_s3126_r9364_r9315_p4239
- mc16_13TeV.301108.PowhegPythia8EvtGen_AZNLOCTEQ6L1_Wplusmunu_1500M1750.deriv.DAOD_STDM4.e3663_s3126_r9364_r9315_p4239
- mc16_13TeV.301109.PowhegPythia8EvtGen_AZNLOCTEQ6L1_Wplusmunu_1750M2000.deriv.DAOD_STDM4.e3663_s3126_r9364_r9315_p4239
- mc16_13TeV.301110.PowhegPythia8EvtGen_AZNLOCTEQ6L1_Wplusmunu_2000M2250.deriv.DAOD_STDM4.e3663_s3126_r9364_r9315_p4239
- mc16_13TeV.301111.PowhegPythia8EvtGen_AZNLOCTEQ6L1_Wplusmunu_2250M2500.deriv.DAOD_STDM4.e3663_s3126_r9364_r9315_p4239
- mc16_13TeV.301112.PowhegPythia8EvtGen_AZNLOCTEQ6L1_Wplusmunu_2500M2750.deriv.DAOD_STDM4.e3663_s3126_r9364_r9315_p4239
- mc16_13TeV.301113.PowhegPythia8EvtGen_AZNLOCTEQ6L1_Wplusmunu_2750M3000.deriv.DAOD_STDM4.e3663_s3126_r9364_r9315_p4239
- mc16_13TeV.301114.PowhegPythia8EvtGen_AZNLOCTEQ6L1_Wplusmunu_3000M3500.deriv.DAOD_STDM4.e3663_s3126_r9364_r9315_p4239
- mc16_13TeV.301116.PowhegPythia8EvtGen_AZNLOCTEQ6L1_Wplusmunu_4000M4500.deriv.DAOD_STDM4.e3663_s3126_r9364_r9315_p4239

- mc16_13TeV.301115.PowhegPythia8EvtGen_AZNLOCTEQ6L1_Wplusmunu_3500M4000.deriv.DAOD_STDM4.e3663_s3126_r9364_r9315_p4239
- mc16_13TeV.301117.PowhegPythia8EvtGen_AZNLOCTEQ6L1_Wplusmunu_4500M5000.deriv.DAOD_STDM4.e3663_s3126_r9364_r9315_p4239
- mc16_13TeV.301118.PowhegPythia8EvtGen_AZNLOCTEQ6L1_Wplusmunu_5000M.deriv.DAOD_STDM4.e3663_s3126_r9364_r9315_p4239

W^-

- mc16_13TeV.361104.PowhegPythia8EvtGen_AZNLOCTEQ6L1_Wminusmunu.deriv.DAOD_STDM4.e3601_s3126_r9364_r9315_p4239
- mc16_13TeV.301120.PowhegPythia8EvtGen_AZNLOCTEQ6L1_Wminmunu_120M180.deriv.DAOD_STDM4.e3663_s3126_r9364_r9315_p4239
- mc16_13TeV.301121.PowhegPythia8EvtGen_AZNLOCTEQ6L1_Wminmunu_180M250.deriv.DAOD_STDM4.e3663_s3126_r9364_r9315_p4239
- mc16_13TeV.301122.PowhegPythia8EvtGen_AZNLOCTEQ6L1_Wminmunu_250M400.deriv.DAOD_STDM4.e3663_s3126_r9364_r9315_p4239
- mc16_13TeV.301123.PowhegPythia8EvtGen_AZNLOCTEQ6L1_Wminmunu_400M600.deriv.DAOD_STDM4.e3663_s3126_r9364_r9315_p4239
- mc16_13TeV.301124.PowhegPythia8EvtGen_AZNLOCTEQ6L1_Wminmunu_600M800.deriv.DAOD_STDM4.e3663_s3126_r9364_r9315_p4239
- mc16_13TeV.301125.PowhegPythia8EvtGen_AZNLOCTEQ6L1_Wminmunu_800M1000.deriv.DAOD_STDM4.e3663_s3126_r9364_r9315_p4239
- mc16_13TeV.301126.PowhegPythia8EvtGen_AZNLOCTEQ6L1_Wminmunu_1000M1250.deriv.DAOD_STDM4.e3663_s3126_r9364_r9315_p4239
- mc16_13TeV.301127.PowhegPythia8EvtGen_AZNLOCTEQ6L1_Wminmunu_1250M1500.deriv.DAOD_STDM4.e3663_s3126_r9364_r9315_p4239
- mc16_13TeV.301128.PowhegPythia8EvtGen_AZNLOCTEQ6L1_Wminmunu_1500M1750.deriv.DAOD_STDM4.e3663_s3126_r9364_r9315_p4239
- mc16_13TeV.301129.PowhegPythia8EvtGen_AZNLOCTEQ6L1_Wminmunu_1750M2000.deriv.DAOD_STDM4.e3663_s3126_r9364_r9315_p4239
- mc16_13TeV.301134.PowhegPythia8EvtGen_AZNLOCTEQ6L1_Wminmunu_3000M3500.deriv.DAOD_STDM4.e3663_s3126_r9364_r9315_p4239
- mc16_13TeV.301132.PowhegPythia8EvtGen_AZNLOCTEQ6L1_Wminmunu_2500M2750.deriv.DAOD_STDM4.e3663_s3126_r9364_r9315_p4239
- mc16_13TeV.301133.PowhegPythia8EvtGen_AZNLOCTEQ6L1_Wminmunu_2750M3000.deriv.DAOD_STDM4.e3663_s3126_r9364_r9315_p4239
- mc16_13TeV.301135.PowhegPythia8EvtGen_AZNLOCTEQ6L1_Wminmunu_3500M4000.deriv.DAOD_STDM4.e3663_s3126_r9364_r9315_p4239
- mc16_13TeV.301131.PowhegPythia8EvtGen_AZNLOCTEQ6L1_Wminmunu_2250M2500.deriv.DAOD_STDM4.e3663_s3126_r9364_r9315_p4239
- mc16_13TeV.301136.PowhegPythia8EvtGen_AZNLOCTEQ6L1_Wminmunu_4000M4500.deriv.DAOD_STDM4.e3663_s3126_r9364_r9315_p4239
- mc16_13TeV.301137.PowhegPythia8EvtGen_AZNLOCTEQ6L1_Wminmunu_4500M5000.deriv.DAOD_STDM4.e3663_s3126_r9364_r9315_p4239
- mc16_13TeV.301138.PowhegPythia8EvtGen_AZNLOCTEQ6L1_Wminmunu_5000M.deriv.DAOD_STDM4.e3663_s3126_r9364_r9315_p4239

MC16d:

W^+

- mc16_13TeV.361101.PowhegPythia8EvtGen_AZNLOCTEQ6L1_Wplusmunu.deriv.DAOD_STDM4.e3601_s3126_r10201_r10210_p4239
- mc16_13TeV.301100.PowhegPythia8EvtGen_AZNLOCTEQ6L1_Wplusmunu_120M180.deriv.DAOD_STDM4.e3663_e5984_s3126_r10201_r10210_p4239
- mc16_13TeV.301101.PowhegPythia8EvtGen_AZNLOCTEQ6L1_Wplusmunu_180M250.deriv.DAOD_STDM4.e3663_e5984_s3126_r10201_r10210_p4239
- mc16_13TeV.301102.PowhegPythia8EvtGen_AZNLOCTEQ6L1_Wplusmunu_250M400.deriv.DAOD_STDM4.e3663_e5984_s3126_r10201_r10210_p4239
- mc16_13TeV.301103.PowhegPythia8EvtGen_AZNLOCTEQ6L1_Wplusmunu_400M600.deriv.DAOD_STDM4.e3663_e5984_s3126_r10201_r10210_p4239
- mc16_13TeV.301104.PowhegPythia8EvtGen_AZNLOCTEQ6L1_Wplusmunu_600M800.deriv.DAOD_STDM4.e3663_e5984_s3126_r10201_r10210_p4239
- mc16_13TeV.301105.PowhegPythia8EvtGen_AZNLOCTEQ6L1_Wplusmunu_800M1000.deriv.DAOD_STDM4.e3663_e5984_s3126_r10201_r10210_p4239
- mc16_13TeV.301106.PowhegPythia8EvtGen_AZNLOCTEQ6L1_Wplusmunu_1000M1250.deriv.DAOD_STDM4.e3663_e5984_s3126_r10201_r10210_p4239
- mc16_13TeV.301107.PowhegPythia8EvtGen_AZNLOCTEQ6L1_Wplusmunu_1250M1500.deriv.DAOD_STDM4.e3663_e5984_s3126_r10201_r10210_p4239
- mc16_13TeV.301108.PowhegPythia8EvtGen_AZNLOCTEQ6L1_Wplusmunu_1500M1750.deriv.DAOD_STDM4.e3663_e5984_s3126_r10201_r10210_p4239
- mc16_13TeV.301109.PowhegPythia8EvtGen_AZNLOCTEQ6L1_Wplusmunu_1750M2000.deriv.DAOD_STDM4.e3663_e5984_s3126_r10201_r10210_p4239
- mc16_13TeV.301110.PowhegPythia8EvtGen_AZNLOCTEQ6L1_Wplusmunu_2000M2250.deriv.DAOD_STDM4.e3663_e5984_s3126_r10201_r10210_p4239
- mc16_13TeV.301111.PowhegPythia8EvtGen_AZNLOCTEQ6L1_Wplusmunu_2250M2500.deriv.DAOD_STDM4.e3663_e5984_s3126_r10201_r10210_p4239

- mc16_13TeV.301112.PowhegPythia8EvtGen_AZNLOCTEQ6L1_Wplusmunu_2500M2750.deriv.DAOD_STDM4.e3663_e5984_s3126_r10201_r10210_p4239
- mc16_13TeV.301113.PowhegPythia8EvtGen_AZNLOCTEQ6L1_Wplusmunu_2750M3000.deriv.DAOD_STDM4.e3663_e5984_s3126_r10201_r10210_p4239
- mc16_13TeV.301114.PowhegPythia8EvtGen_AZNLOCTEQ6L1_Wplusmunu_3000M3500.deriv.DAOD_STDM4.e3663_e5984_s3126_r10201_r10210_p4239
- mc16_13TeV.301115.PowhegPythia8EvtGen_AZNLOCTEQ6L1_Wplusmunu_3500M4000.deriv.DAOD_STDM4.e3663_e5984_s3126_r10201_r10210_p4239
- mc16_13TeV.301116.PowhegPythia8EvtGen_AZNLOCTEQ6L1_Wplusmunu_4000M4500.deriv.DAOD_STDM4.e3663_e5984_s3126_r10201_r10210_p4239
- mc16_13TeV.301117.PowhegPythia8EvtGen_AZNLOCTEQ6L1_Wplusmunu_4500M5000.deriv.DAOD_STDM4.e3663_e5984_s3126_r10201_r10210_p4239
- mc16_13TeV.301118.PowhegPythia8EvtGen_AZNLOCTEQ6L1_Wplusmunu_5000M.deriv.DAOD_STDM4.e3663_e5984_s3126_r10201_r10210_p4239

W^-

- mc16_13TeV.361104.PowhegPythia8EvtGen_AZNLOCTEQ6L1_Wminusmunu.deriv.DAOD_STDM4.e3601_s3126_r10201_r10210_p4239
- mc16_13TeV.301120.PowhegPythia8EvtGen_AZNLOCTEQ6L1_Wminmunu_120M180.deriv.DAOD_STDM4.e3663_e5984_s3126_r10201_r10210_p4239
- mc16_13TeV.301121.PowhegPythia8EvtGen_AZNLOCTEQ6L1_Wminmunu_180M250.deriv.DAOD_STDM4.e3663_e5984_s3126_r10201_r10210_p4239
- mc16_13TeV.301122.PowhegPythia8EvtGen_AZNLOCTEQ6L1_Wminmunu_250M400.deriv.DAOD_STDM4.e3663_e5984_s3126_r10201_r10210_p4239
- mc16_13TeV.301123.PowhegPythia8EvtGen_AZNLOCTEQ6L1_Wminmunu_400M600.deriv.DAOD_STDM4.e3663_e5984_s3126_r10201_r10210_p4239
- mc16_13TeV.301124.PowhegPythia8EvtGen_AZNLOCTEQ6L1_Wminmunu_600M800.deriv.DAOD_STDM4.e3663_e5984_s3126_r10201_r10210_p4239
- mc16_13TeV.301125.PowhegPythia8EvtGen_AZNLOCTEQ6L1_Wminmunu_800M1000.deriv.DAOD_STDM4.e3663_e5984_s3126_r10201_r10210_p4239
- mc16_13TeV.301126.PowhegPythia8EvtGen_AZNLOCTEQ6L1_Wminmunu_1000M1250.deriv.DAOD_STDM4.e3663_e5984_s3126_r10201_r10210_p4239
- mc16_13TeV.301127.PowhegPythia8EvtGen_AZNLOCTEQ6L1_Wminmunu_1250M1500.deriv.DAOD_STDM4.e3663_e5984_s3126_r10201_r10210_p4239
- mc16_13TeV.301128.PowhegPythia8EvtGen_AZNLOCTEQ6L1_Wminmunu_1500M1750.deriv.DAOD_STDM4.e3663_e5984_s3126_r10201_r10210_p4239
- mc16_13TeV.301129.PowhegPythia8EvtGen_AZNLOCTEQ6L1_Wminmunu_1750M2000.deriv.DAOD_STDM4.e3663_e5984_s3126_r10201_r10210_p4239
- mc16_13TeV.301130.PowhegPythia8EvtGen_AZNLOCTEQ6L1_Wminmunu_2000M2250.deriv.DAOD_STDM4.e3663_e5984_s3126_r10201_r10210_p4239
- mc16_13TeV.301131.PowhegPythia8EvtGen_AZNLOCTEQ6L1_Wminmunu_2250M2500.deriv.DAOD_STDM4.e3663_e5984_s3126_r10201_r10210_p4239
- mc16_13TeV.301132.PowhegPythia8EvtGen_AZNLOCTEQ6L1_Wminmunu_2500M2750.deriv.DAOD_STDM4.e3663_e5984_s3126_r10201_r10210_p4239
- mc16_13TeV.301133.PowhegPythia8EvtGen_AZNLOCTEQ6L1_Wminmunu_2750M3000.deriv.DAOD_STDM4.e3663_e5984_s3126_r10201_r10210_p4239
- mc16_13TeV.301134.PowhegPythia8EvtGen_AZNLOCTEQ6L1_Wminmunu_3000M3500.deriv.DAOD_STDM4.e3663_e5984_s3126_r10201_r10210_p4239
- mc16_13TeV.301135.PowhegPythia8EvtGen_AZNLOCTEQ6L1_Wminmunu_3500M4000.deriv.DAOD_STDM4.e3663_e5984_s3126_r10201_r10210_p4239
- mc16_13TeV.301136.PowhegPythia8EvtGen_AZNLOCTEQ6L1_Wminmunu_4000M4500.deriv.DAOD_STDM4.e3663_e5984_s3126_r10201_r10210_p4239
- mc16_13TeV.301137.PowhegPythia8EvtGen_AZNLOCTEQ6L1_Wminmunu_4500M5000.deriv.DAOD_STDM4.e3663_e5984_s3126_r10201_r10210_p4239
- mc16_13TeV.301138.PowhegPythia8EvtGen_AZNLOCTEQ6L1_Wminmunu_5000M.deriv.DAOD_STDM4.e3663_e5984_s3126_r10201_r10210_p4239

MC16e:

W^+

- mc16_13TeV.361101.PowhegPythia8EvtGen_AZNLOCTEQ6L1_Wplusmunu.deriv.DAOD_STDM4.e3601_e5984_s3126_r10724_r10726_p4239
- mc16_13TeV.301100.PowhegPythia8EvtGen_AZNLOCTEQ6L1_Wplusmunu_120M180.deriv.DAOD_STDM4.e3663_e5984_s3126_r10724_r10726_p4239
- mc16_13TeV.301101.PowhegPythia8EvtGen_AZNLOCTEQ6L1_Wplusmunu_180M250.deriv.DAOD_STDM4.e3663_e5984_s3126_r10724_r10726_p4239
- mc16_13TeV.301102.PowhegPythia8EvtGen_AZNLOCTEQ6L1_Wplusmunu_250M400.deriv.DAOD_STDM4.e3663_e5984_s3126_r10724_r10726_p4239
- mc16_13TeV.301103.PowhegPythia8EvtGen_AZNLOCTEQ6L1_Wplusmunu_400M600.deriv.DAOD_STDM4.e3663_e5984_s3126_r10724_r10726_p4239
- mc16_13TeV.301104.PowhegPythia8EvtGen_AZNLOCTEQ6L1_Wplusmunu_600M800.deriv.DAOD_STDM4.e3663_e5984_s3126_r10724_r10726_p4239
- mc16_13TeV.301105.PowhegPythia8EvtGen_AZNLOCTEQ6L1_Wplusmunu_800M1000.deriv.DAOD_STDM4.e3663_e5984_s3126_r10724_r10726_p4239
- mc16_13TeV.301106.PowhegPythia8EvtGen_AZNLOCTEQ6L1_Wplusmunu_1000M1250.deriv.DAOD_STDM4.e3663_e5984_s3126_r10724_r10726_p4239

- mc16_13TeV.301107.PowhegPythia8EvtGen_AZNLOCTEQ6L1_Wplusmunu_1250M1500.deriv.DAOD_STDM4.e3663_e5984_s3126_r10724_r10726_p4239
- mc16_13TeV.301108.PowhegPythia8EvtGen_AZNLOCTEQ6L1_Wplusmunu_1500M1750.deriv.DAOD_STDM4.e3663_e5984_s3126_r10724_r10726_p4239
- mc16_13TeV.301109.PowhegPythia8EvtGen_AZNLOCTEQ6L1_Wplusmunu_1750M2000.deriv.DAOD_STDM4.e3663_e5984_s3126_r10724_r10726_p4239
- mc16_13TeV.301110.PowhegPythia8EvtGen_AZNLOCTEQ6L1_Wplusmunu_2000M2250.deriv.DAOD_STDM4.e3663_e5984_s3126_r10724_r10726_p4239
- mc16_13TeV.301111.PowhegPythia8EvtGen_AZNLOCTEQ6L1_Wplusmunu_2250M2500.deriv.DAOD_STDM4.e3663_e5984_s3126_r10724_r10726_p4239
- mc16_13TeV.301112.PowhegPythia8EvtGen_AZNLOCTEQ6L1_Wplusmunu_2500M2750.deriv.DAOD_STDM4.e3663_e5984_s3126_r10724_r10726_p4239
- mc16_13TeV.301113.PowhegPythia8EvtGen_AZNLOCTEQ6L1_Wplusmunu_2750M3000.deriv.DAOD_STDM4.e3663_e5984_s3126_r10724_r10726_p4239
- mc16_13TeV.301114.PowhegPythia8EvtGen_AZNLOCTEQ6L1_Wplusmunu_3000M3500.deriv.DAOD_STDM4.e3663_e5984_s3126_r10724_r10726_p4239
- mc16_13TeV.301115.PowhegPythia8EvtGen_AZNLOCTEQ6L1_Wplusmunu_3500M4000.deriv.DAOD_STDM4.e3663_e5984_s3126_r10724_r10726_p4239
- mc16_13TeV.301116.PowhegPythia8EvtGen_AZNLOCTEQ6L1_Wplusmunu_4000M4500.deriv.DAOD_STDM4.e3663_e5984_s3126_r10724_r10726_p4239
- mc16_13TeV.301117.PowhegPythia8EvtGen_AZNLOCTEQ6L1_Wplusmunu_4500M5000.deriv.DAOD_STDM4.e3663_e5984_s3126_r10724_r10726_p4239
- mc16_13TeV.301118.PowhegPythia8EvtGen_AZNLOCTEQ6L1_Wplusmunu_5000M.deriv.DAOD_STDM4.e3663_e5984_s3126_r10724_r10726_p4239

W^-

- mc16_13TeV.361104.PowhegPythia8EvtGen_AZNLOCTEQ6L1_Wminusmunu.deriv.DAOD_STDM4.e3601_e5984_s3126_r10724_r10726_p4239
- mc16_13TeV.301120.PowhegPythia8EvtGen_AZNLOCTEQ6L1_Wminmunu_120M180.deriv.DAOD_STDM4.e3663_e5984_s3126_r10724_r10726_p4239
- mc16_13TeV.301121.PowhegPythia8EvtGen_AZNLOCTEQ6L1_Wminmunu_180M250.deriv.DAOD_STDM4.e3663_e5984_s3126_r10724_r10726_p4239
- mc16_13TeV.301122.PowhegPythia8EvtGen_AZNLOCTEQ6L1_Wminmunu_250M400.deriv.DAOD_STDM4.e3663_e5984_s3126_r10724_r10726_p4239
- mc16_13TeV.301123.PowhegPythia8EvtGen_AZNLOCTEQ6L1_Wminmunu_400M600.deriv.DAOD_STDM4.e3663_e5984_s3126_r10724_r10726_p4239
- mc16_13TeV.301124.PowhegPythia8EvtGen_AZNLOCTEQ6L1_Wminmunu_600M800.deriv.DAOD_STDM4.e3663_e5984_s3126_r10724_r10726_p4239
- mc16_13TeV.301125.PowhegPythia8EvtGen_AZNLOCTEQ6L1_Wminmunu_800M1000.deriv.DAOD_STDM4.e3663_e5984_s3126_r10724_r10726_p4239
- mc16_13TeV.301126.PowhegPythia8EvtGen_AZNLOCTEQ6L1_Wminmunu_1000M1250.deriv.DAOD_STDM4.e3663_e5984_s3126_r10724_r10726_p4239
- mc16_13TeV.301127.PowhegPythia8EvtGen_AZNLOCTEQ6L1_Wminmunu_1250M1500.deriv.DAOD_STDM4.e3663_e5984_s3126_r10724_r10726_p4239
- mc16_13TeV.301128.PowhegPythia8EvtGen_AZNLOCTEQ6L1_Wminmunu_1500M1750.deriv.DAOD_STDM4.e3663_e5984_s3126_r10724_r10726_p4239
- mc16_13TeV.301129.PowhegPythia8EvtGen_AZNLOCTEQ6L1_Wminmunu_1750M2000.deriv.DAOD_STDM4.e3663_e5984_s3126_r10724_r10726_p4239
- mc16_13TeV.301130.PowhegPythia8EvtGen_AZNLOCTEQ6L1_Wminmunu_2000M2250.deriv.DAOD_STDM4.e3663_e5984_s3126_r10724_r10726_p4239
- mc16_13TeV.301131.PowhegPythia8EvtGen_AZNLOCTEQ6L1_Wminmunu_2250M2500.deriv.DAOD_STDM4.e3663_e5984_s3126_r10724_r10726_p4239
- mc16_13TeV.301132.PowhegPythia8EvtGen_AZNLOCTEQ6L1_Wminmunu_2500M2750.deriv.DAOD_STDM4.e3663_e5984_s3126_r10724_r10726_p4239
- mc16_13TeV.301133.PowhegPythia8EvtGen_AZNLOCTEQ6L1_Wminmunu_2750M3000.deriv.DAOD_STDM4.e3663_e5984_s3126_r10724_r10726_p4239
- mc16_13TeV.301134.PowhegPythia8EvtGen_AZNLOCTEQ6L1_Wminmunu_3000M3500.deriv.DAOD_STDM4.e3663_e5984_s3126_r10724_r10726_p4239
- mc16_13TeV.301135.PowhegPythia8EvtGen_AZNLOCTEQ6L1_Wminmunu_3500M4000.deriv.DAOD_STDM4.e3663_e5984_s3126_r10724_r10726_p4239
- mc16_13TeV.301136.PowhegPythia8EvtGen_AZNLOCTEQ6L1_Wminmunu_4000M4500.deriv.DAOD_STDM4.e3663_e5984_s3126_r10724_r10726_p4239
- mc16_13TeV.301137.PowhegPythia8EvtGen_AZNLOCTEQ6L1_Wminmunu_4500M5000.deriv.DAOD_STDM4.e3663_e5984_s3126_r10724_r10726_p4239
- mc16_13TeV.301138.PowhegPythia8EvtGen_AZNLOCTEQ6L1_Wminmunu_5000M.deriv.DAOD_STDM4.e3663_e5984_s3126_r10724_r10726_p4239

A.3. Background samples

A.3.1. $t\bar{t}$

MC16a:

- mc16_13TeV.410470.PhPy8EG_A14_ttbar_hdamp258p75_nonallhad.deriv.DAOD_STDM4.e6337_s3126_r9364_p4237

MC16d:

- mc16_13TeV.410470.PhPy8EG_A14_ttbar_hdamp258p75_nonallhad.deriv.DAOD_STDM4.e6337_e5984_s3126_r10201_r10210_p4237

MC16e:

- mc16_13TeV.410470.PhPy8EG_A14_ttbar_hdamp258p75_nonallhad.deriv.DAOD_STDM4.e6337_e5984_s3126_r10724_r10726_p4237

A.3.2. Single Top

MC16a:

- mc16_13TeV.410644.PowhegPythia8EvtGen_A14_singletop_schan_lept_top.deriv.DAOD_STDM4.e6527_s3126_r9364_p4237
- mc16_13TeV.410645.PowhegPythia8EvtGen_A14_singletop_schan_lept_antitop.deriv.DAOD_STDM4.e6527_s3126_r9364_p4237
- mc16_13TeV.410646.PowhegPythia8EvtGen_A14_Wt_DR_inclusive_top.deriv.DAOD_STDM4.e6552_s3126_r9364_p4237
- mc16_13TeV.410647.PowhegPythia8EvtGen_A14_Wt_DR_inclusive_antitop.deriv.DAOD_STDM4.e6552_s3126_r9364_p4237
- mc16_13TeV.410658.PhPy8EG_A14_tchan_BW50_lept_top.deriv.DAOD_STDM4.e6671_s3126_r9364_p4237
- mc16_13TeV.410659.PhPy8EG_A14_tchan_BW50_lept_antitop.deriv.DAOD_STDM4.e6671_s3126_r9364_p4237

MC16d:

- mc16_13TeV.410644.PowhegPythia8EvtGen_A14_singletop_schan_lept_top.deriv.DAOD_STDM4.e6527_e5984_s3126_r10201_r10210_p4237
- mc16_13TeV.410645.PowhegPythia8EvtGen_A14_singletop_schan_lept_antitop.deriv.DAOD_STDM4.e6527_s3126_r10201_r10210_p4237
- mc16_13TeV.410646.PowhegPythia8EvtGen_A14_Wt_DR_inclusive_top.deriv.DAOD_STDM4.e6552_e5984_s3126_r10201_r10210_p4237
- mc16_13TeV.410647.PowhegPythia8EvtGen_A14_Wt_DR_inclusive_antitop.deriv.DAOD_STDM4.e6552_e5984_s3126_r10201_r10210_p4237
- mc16_13TeV.410658.PhPy8EG_A14_tchan_BW50_lept_top.deriv.DAOD_STDM4.e6671_e5984_s3126_r10201_r10210_p4237
- mc16_13TeV.410659.PhPy8EG_A14_tchan_BW50_lept_antitop.deriv.DAOD_STDM4.e6671_e5984_s3126_r10201_r10210_p4237

MC16e:

- mc16_13TeV.410644.PowhegPythia8EvtGen_A14_singletop_schan_lept_top.deriv.DAOD_STDM4.e6527_e5984_s3126_r10724_r10726_p4237
- mc16_13TeV.410645.PowhegPythia8EvtGen_A14_singletop_schan_lept_antitop.deriv.DAOD_STDM4.e6527_e5984_s3126_r10724_r10726_p4237
- mc16_13TeV.410646.PowhegPythia8EvtGen_A14_Wt_DR_inclusive_top.deriv.DAOD_STDM4.e6552_e5984_s3126_r10724_r10726_p4237
- mc16_13TeV.410647.PowhegPythia8EvtGen_A14_Wt_DR_inclusive_antitop.deriv.DAOD_STDM4.e6552_e5984_s3126_r10724_r10726_p4237
- mc16_13TeV.410658.PhPy8EG_A14_tchan_BW50_lept_top.deriv.DAOD_STDM4.e6671_e5984_s3126_r10724_r10726_p4237
- mc16_13TeV.410659.PhPy8EG_A14_tchan_BW50_lept_antitop.deriv.DAOD_STDM4.e6671_e5984_s3126_r10724_r10726_p4237

A.3.3. Z+Jets

MC16a:

$Z \to \mu\mu$

- mc16_13TeV.361107.PowhegPythia8EvtGen_AZNLOCTEQ6L1_Zmumu.deriv.DAOD_STDM4.e3601_s3126_r9364_p4239
- mc16_13TeV.301020.PowhegPythia8EvtGen_AZNLOCTEQ6L1_DYmumu_120M180.deriv.DAOD_STDM4.e3649_s3126_r9364_p4239
- mc16_13TeV.301021.PowhegPythia8EvtGen_AZNLOCTEQ6L1_DYmumu_180M250.deriv.DAOD_STDM4.e3649_s3126_r9364_p4239
- mc16_13TeV.301022.PowhegPythia8EvtGen_AZNLOCTEQ6L1_DYmumu_250M400.deriv.DAOD_STDM4.e3649_s3126_r9364_p4239
- mc16_13TeV.301023.PowhegPythia8EvtGen_AZNLOCTEQ6L1_DYmumu_400M600.deriv.DAOD_STDM4.e3649_s3126_r9364_p4239
- mc16_13TeV.301024.PowhegPythia8EvtGen_AZNLOCTEQ6L1_DYmumu_600M800.deriv.DAOD_STDM4.e3649_s3126_r9364_p4239
- mc16_13TeV.301025.PowhegPythia8EvtGen_AZNLOCTEQ6L1_DYmumu_800M1000.deriv.DAOD_STDM4.e3649_s3126_r9364_p4239
- mc16_13TeV.301026.PowhegPythia8EvtGen_AZNLOCTEQ6L1_DYmumu_1000M1250.deriv.DAOD_STDM4.e3649_s3126_r9364_p4239
- mc16_13TeV.301027.PowhegPythia8EvtGen_AZNLOCTEQ6L1_DYmumu_1250M1500.deriv.DAOD_STDM4.e3649_s3126_r9364_p4239
- mc16_13TeV.301028.PowhegPythia8EvtGen_AZNLOCTEQ6L1_DYmumu_1500M1750.deriv.DAOD_STDM4.e3649_s3126_r9364_p4239
- mc16_13TeV.301029.PowhegPythia8EvtGen_AZNLOCTEQ6L1_DYmumu_1750M2000.deriv.DAOD_STDM4.e3649_s3126_r9364_p4239
- mc16_13TeV.301030.PowhegPythia8EvtGen_AZNLOCTEQ6L1_DYmumu_2000M2250.deriv.DAOD_STDM4.e3649_s3126_r9364_p4239
- mc16_13TeV.301031.PowhegPythia8EvtGen_AZNLOCTEQ6L1_DYmumu_2250M2500.deriv.DAOD_STDM4.e3649_s3126_r9364_p4239
- mc16_13TeV.301032.PowhegPythia8EvtGen_AZNLOCTEQ6L1_DYmumu_2500M2750.deriv.DAOD_STDM4.e3649_s3126_r9364_p4239
- mc16_13TeV.301033.PowhegPythia8EvtGen_AZNLOCTEQ6L1_DYmumu_2750M3000.deriv.DAOD_STDM4.e3649_s3126_r9364_p4239
- mc16_13TeV.301034.PowhegPythia8EvtGen_AZNLOCTEQ6L1_DYmumu_3000M3500.deriv.DAOD_STDM4.e3649_s3126_r9364_p4239
- mc16_13TeV.301035.PowhegPythia8EvtGen_AZNLOCTEQ6L1_DYmumu_3500M4000.deriv.DAOD_STDM4.e3649_s3126_r9364_p4239
- mc16_13TeV.301036.PowhegPythia8EvtGen_AZNLOCTEQ6L1_DYmumu_4000M4500.deriv.DAOD_STDM4.e3649_s3126_r9364_p4239
- mc16_13TeV.301037.PowhegPythia8EvtGen_AZNLOCTEQ6L1_DYmumu_4500M5000.deriv.DAOD_STDM4.e3649_s3126_r9364_p4239
- mc16_13TeV.301038.PowhegPythia8EvtGen_AZNLOCTEQ6L1_DYmumu_5000M.deriv.DAOD_STDM4.e3649_s3126_r9364_p4239

$Z \to \tau\tau$

- mc16_13TeV.361108.PowhegPythia8EvtGen_AZNLOCTEQ6L1_Ztautau.deriv.DAOD_STDM4.e3601_s3126_r9364_p4237
- mc16_13TeV.301040.PowhegPythia8EvtGen_AZNLOCTEQ6L1_DYtautau_120M180.deriv.DAOD_STDM4.e3649_s3126_r9364_p4237
- mc16_13TeV.301041.PowhegPythia8EvtGen_AZNLOCTEQ6L1_DYtautau_180M250.deriv.DAOD_STDM4.e3649_s3126_r9364_p4237
- mc16_13TeV.301042.PowhegPythia8EvtGen_AZNLOCTEQ6L1_DYtautau_250M400.deriv.DAOD_STDM4.e3649_s3126_r9364_p4237
- mc16_13TeV.301043.PowhegPythia8EvtGen_AZNLOCTEQ6L1_DYtautau_400M600.deriv.DAOD_STDM4.e3649_s3126_r9364_p4237
- mc16_13TeV.301044.PowhegPythia8EvtGen_AZNLOCTEQ6L1_DYtautau_600M800.deriv.DAOD_STDM4.e3649_s3126_r9364_p4237
- mc16_13TeV.301045.PowhegPythia8EvtGen_AZNLOCTEQ6L1_DYtautau_800M1000.deriv.DAOD_STDM4.e3649_s3126_r9364_p4237
- mc16_13TeV.301046.PowhegPythia8EvtGen_AZNLOCTEQ6L1_DYtautau_1000M1250.deriv.DAOD_STDM4.e3649_s3126_r9364_p4237
- mc16_13TeV.301047.PowhegPythia8EvtGen_AZNLOCTEQ6L1_DYtautau_1250M1500.deriv.DAOD_STDM4.e3649_s3126_r9364_p4237
- mc16_13TeV.301048.PowhegPythia8EvtGen_AZNLOCTEQ6L1_DYtautau_1500M1750.deriv.DAOD_STDM4.e3649_s3126_r9364_p4237
- mc16_13TeV.301049.PowhegPythia8EvtGen_AZNLOCTEQ6L1_DYtautau_1750M2000.deriv.DAOD_STDM4.e3649_s3126_r9364_p4237
- mc16_13TeV.301050.PowhegPythia8EvtGen_AZNLOCTEQ6L1_DYtautau_2000M2250.deriv.DAOD_STDM4.e3649_s3126_r9364_p4237
- mc16_13TeV.301051.PowhegPythia8EvtGen_AZNLOCTEQ6L1_DYtautau_2250M2500.deriv.DAOD_STDM4.e3649_s3126_r9364_p4237
- mc16_13TeV.301052.PowhegPythia8EvtGen_AZNLOCTEQ6L1_DYtautau_2500M2750.deriv.DAOD_STDM4.e3649_s3126_r9364_p4237

- mc16_13TeV.301053.PowhegPythia8EvtGen_AZNLOCTEQ6L1_DYtautau_2750M3000.deriv.DAOD_STDM4.e3649_s3126_r9364_p4237
- mc16_13TeV.301054.PowhegPythia8EvtGen_AZNLOCTEQ6L1_DYtautau_3000M3500.deriv.DAOD_STDM4.e3649_s3126_r9364_p4237
- mc16_13TeV.301055.PowhegPythia8EvtGen_AZNLOCTEQ6L1_DYtautau_3500M4000.deriv.DAOD_STDM4.e3649_s3126_r9364_p4237
- mc16_13TeV.301056.PowhegPythia8EvtGen_AZNLOCTEQ6L1_DYtautau_4000M4500.deriv.DAOD_STDM4.e3649_s3126_r9364_p4237
- mc16_13TeV.301057.PowhegPythia8EvtGen_AZNLOCTEQ6L1_DYtautau_4500M5000.deriv.DAOD_STDM4.e3649_s3126_r9364_p4237
- mc16_13TeV.301058.PowhegPythia8EvtGen_AZNLOCTEQ6L1_DYtautau_5000M.deriv.DAOD_STDM4.e3649_s3126_r9364_p4237

MC16d:

$Z \rightarrow \mu\mu$

- mc16_13TeV.361107.PowhegPythia8EvtGen_AZNLOCTEQ6L1_Zmumu.deriv.DAOD_STDM4.e3601_e5984_s3126_r10201_r10210_p4239
- mc16_13TeV.301020.PowhegPythia8EvtGen_AZNLOCTEQ6L1_DYmumu_120M180.deriv.DAOD_STDM4.e3649_e5984_s3126_r10201_r10210_p4239
- mc16_13TeV.301021.PowhegPythia8EvtGen_AZNLOCTEQ6L1_DYmumu_180M250.deriv.DAOD_STDM4.e3649_e5984_s3126_r10201_r10210_p4239
- mc16_13TeV.301022.PowhegPythia8EvtGen_AZNLOCTEQ6L1_DYmumu_250M400.deriv.DAOD_STDM4.e3649_e5984_s3126_r10201_r10210_p4239
- mc16_13TeV.301023.PowhegPythia8EvtGen_AZNLOCTEQ6L1_DYmumu_400M600.deriv.DAOD_STDM4.e3649_e5984_s3126_r10201_r10210_p4239
- mc16_13TeV.301024.PowhegPythia8EvtGen_AZNLOCTEQ6L1_DYmumu_600M800.deriv.DAOD_STDM4.e3649_e5984_s3126_r10201_r10210_p4239
- mc16_13TeV.301025.PowhegPythia8EvtGen_AZNLOCTEQ6L1_DYmumu_800M1000.deriv.DAOD_STDM4.e3649_e5984_s3126_r10201_r10210_p4239
- mc16_13TeV.301026.PowhegPythia8EvtGen_AZNLOCTEQ6L1_DYmumu_1000M1250.deriv.DAOD_STDM4.e3649_e5984_s3126_r10201_r10210_p4239
- mc16_13TeV.301027.PowhegPythia8EvtGen_AZNLOCTEQ6L1_DYmumu_1250M1500.deriv.DAOD_STDM4.e3649_e5984_s3126_r10201_r10210_p4239
- mc16_13TeV.301028.PowhegPythia8EvtGen_AZNLOCTEQ6L1_DYmumu_1500M1750.deriv.DAOD_STDM4.e3649_e5984_s3126_r10201_r10210_p4239
- mc16_13TeV.301029.PowhegPythia8EvtGen_AZNLOCTEQ6L1_DYmumu_1750M2000.deriv.DAOD_STDM4.e3649_e5984_s3126_r10201_r10210_p4239
- mc16_13TeV.301030.PowhegPythia8EvtGen_AZNLOCTEQ6L1_DYmumu_2000M2250.deriv.DAOD_STDM4.e3649_e5984_s3126_r10201_r10210_p4239
- mc16_13TeV.301031.PowhegPythia8EvtGen_AZNLOCTEQ6L1_DYmumu_2250M2500.deriv.DAOD_STDM4.e3649_e5984_s3126_r10201_r10210_p4239
- mc16_13TeV.301032.PowhegPythia8EvtGen_AZNLOCTEQ6L1_DYmumu_2500M2750.deriv.DAOD_STDM4.e3649_e5984_s3126_r10201_r10210_p4239
- mc16_13TeV.301034.PowhegPythia8EvtGen_AZNLOCTEQ6L1_DYmumu_3000M3500.deriv.DAOD_STDM4.e3649_e5984_s3126_r10201_r10210_p4239
- mc16_13TeV.301033.PowhegPythia8EvtGen_AZNLOCTEQ6L1_DYmumu_2750M3000.deriv.DAOD_STDM4.e3649_e5984_s3126_r10201_r10210_p4239
- mc16_13TeV.301035.PowhegPythia8EvtGen_AZNLOCTEQ6L1_DYmumu_3500M4000.deriv.DAOD_STDM4.e3649_e5984_s3126_r10201_r10210_p4239
- mc16_13TeV.301036.PowhegPythia8EvtGen_AZNLOCTEQ6L1_DYmumu_4000M4500.deriv.DAOD_STDM4.e3649_e5984_s3126_r10201_r10210_p4239
- mc16_13TeV.301037.PowhegPythia8EvtGen_AZNLOCTEQ6L1_DYmumu_4500M5000.deriv.DAOD_STDM4.e3649_e5984_s3126_r10201_r10210_p4239
- mc16_13TeV.301038.PowhegPythia8EvtGen_AZNLOCTEQ6L1_DYmumu_5000M.deriv.DAOD_STDM4.e3649_e5984_s3126_r10201_r10210_p4239

$Z \rightarrow \tau\tau$

- mc16_13TeV.361108.PowhegPythia8EvtGen_AZNLOCTEQ6L1_Ztautau.deriv.DAOD_STDM4.e3601_e5984_s3126_r10239_r10210_p4237
- mc16_13TeV.301040.PowhegPythia8EvtGen_AZNLOCTEQ6L1_DYtautau_120M180.deriv.DAOD_STDM4.e3649_s3126_r10239_r10210_p4237
- mc16_13TeV.301041.PowhegPythia8EvtGen_AZNLOCTEQ6L1_DYtautau_180M250.deriv.DAOD_STDM4.e3649_s3126_r10239_r10210_p4237
- mc16_13TeV.301042.PowhegPythia8EvtGen_AZNLOCTEQ6L1_DYtautau_250M400.deriv.DAOD_STDM4.e3649_s3126_r10239_r10210_p4237
- mc16_13TeV.301043.PowhegPythia8EvtGen_AZNLOCTEQ6L1_DYtautau_400M600.deriv.DAOD_STDM4.e3649_s3126_r10239_r10210_p4237
- mc16_13TeV.301044.PowhegPythia8EvtGen_AZNLOCTEQ6L1_DYtautau_600M800.deriv.DAOD_STDM4.e3649_s3126_r10239_r10210_p4237
- mc16_13TeV.301045.PowhegPythia8EvtGen_AZNLOCTEQ6L1_DYtautau_800M1000.deriv.DAOD_STDM4.e3649_s3126_r10239_r10210_p4237
- mc16_13TeV.301046.PowhegPythia8EvtGen_AZNLOCTEQ6L1_DYtautau_1000M1250.deriv.DAOD_STDM4.e3649_s3126_r10239_r10210_p4237

- mc16_13TeV.301047.PowhegPythia8EvtGen_AZNLOCTEQ6L1_DYtautau_1250M1500.deriv.DAOD_STDM4.e3649_s3126_r10239_r10210_p4237
- mc16_13TeV.301048.PowhegPythia8EvtGen_AZNLOCTEQ6L1_DYtautau_1500M1750.deriv.DAOD_STDM4.e3649_s3126_r10239_r10210_p4237
- mc16_13TeV.301049.PowhegPythia8EvtGen_AZNLOCTEQ6L1_DYtautau_1750M2000.deriv.DAOD_STDM4.e3649_s3126_r10239_r10210_p4237
- mc16_13TeV.301050.PowhegPythia8EvtGen_AZNLOCTEQ6L1_DYtautau_2000M2250.deriv.DAOD_STDM4.e3649_s3126_r10239_r10210_p4237
- mc16_13TeV.301051.PowhegPythia8EvtGen_AZNLOCTEQ6L1_DYtautau_2250M2500.deriv.DAOD_STDM4.e3649_s3126_r10239_r10210_p4237
- mc16_13TeV.301052.PowhegPythia8EvtGen_AZNLOCTEQ6L1_DYtautau_2500M2750.deriv.DAOD_STDM4.e3649_s3126_r10239_r10210_p4237
- mc16_13TeV.301053.PowhegPythia8EvtGen_AZNLOCTEQ6L1_DYtautau_2750M3000.deriv.DAOD_STDM4.e3649_s3126_r10239_r10210_p4237
- mc16_13TeV.301054.PowhegPythia8EvtGen_AZNLOCTEQ6L1_DYtautau_3000M3500.deriv.DAOD_STDM4.e3649_s3126_r10239_r10210_p4237
- mc16_13TeV.301055.PowhegPythia8EvtGen_AZNLOCTEQ6L1_DYtautau_3500M4000.deriv.DAOD_STDM4.e3649_s3126_r10239_r10210_p4237
- mc16_13TeV.301056.PowhegPythia8EvtGen_AZNLOCTEQ6L1_DYtautau_4000M4500.deriv.DAOD_STDM4.e3649_s3126_r10239_r10210_p4237
- mc16_13TeV.301057.PowhegPythia8EvtGen_AZNLOCTEQ6L1_DYtautau_4500M5000.deriv.DAOD_STDM4.e3649_s3126_r10239_r10210_p4237
- mc16_13TeV.301058.PowhegPythia8EvtGen_AZNLOCTEQ6L1_DYtautau_5000M.deriv.DAOD_STDM4.e3649_s3126_r10239_r10210_p4237

MC16e:

$Z \to \mu\mu$

- mc16_13TeV.361107.PowhegPythia8EvtGen_AZNLOCTEQ6L1_Zmumu.deriv.DAOD_STDM4.e3601_e5984_s3126_r10724_r10726_p4239
- mc16_13TeV.301020.PowhegPythia8EvtGen_AZNLOCTEQ6L1_DYmumu_120M180.deriv.DAOD_STDM4.e3649_e5984_s3126_r10724_r10726_p4239
- mc16_13TeV.301021.PowhegPythia8EvtGen_AZNLOCTEQ6L1_DYmumu_180M250.deriv.DAOD_STDM4.e3649_e5984_s3126_r10724_r10726_p4239
- mc16_13TeV.301022.PowhegPythia8EvtGen_AZNLOCTEQ6L1_DYmumu_250M400.deriv.DAOD_STDM4.e3649_e5984_s3126_r10724_r10726_p4239
- mc16_13TeV.301023.PowhegPythia8EvtGen_AZNLOCTEQ6L1_DYmumu_400M600.deriv.DAOD_STDM4.e3649_e5984_s3126_r10724_r10726_p4239
- mc16_13TeV.301024.PowhegPythia8EvtGen_AZNLOCTEQ6L1_DYmumu_600M800.deriv.DAOD_STDM4.e3649_e5984_s3126_r10724_r10726_p4239
- mc16_13TeV.301025.PowhegPythia8EvtGen_AZNLOCTEQ6L1_DYmumu_800M1000.deriv.DAOD_STDM4.e3649_e5984_s3126_r10724_r10726_p4239
- mc16_13TeV.301026.PowhegPythia8EvtGen_AZNLOCTEQ6L1_DYmumu_1000M1250.deriv.DAOD_STDM4.e3649_e5984_s3126_r10724_r10726_p4239
- mc16_13TeV.301027.PowhegPythia8EvtGen_AZNLOCTEQ6L1_DYmumu_1250M1500.deriv.DAOD_STDM4.e3649_e5984_s3126_r10724_r10726_p4239
- mc16_13TeV.301028.PowhegPythia8EvtGen_AZNLOCTEQ6L1_DYmumu_1500M1750.deriv.DAOD_STDM4.e3649_e5984_s3126_r10724_r10726_p4239
- mc16_13TeV.301029.PowhegPythia8EvtGen_AZNLOCTEQ6L1_DYmumu_1750M2000.deriv.DAOD_STDM4.e3649_e5984_s3126_r10724_r10726_p4239
- mc16_13TeV.301030.PowhegPythia8EvtGen_AZNLOCTEQ6L1_DYmumu_2000M2250.deriv.DAOD_STDM4.e3649_e5984_s3126_r10724_r10726_p4239
- mc16_13TeV.301031.PowhegPythia8EvtGen_AZNLOCTEQ6L1_DYmumu_2250M2500.deriv.DAOD_STDM4.e3649_e5984_s3126_r10724_r10726_p4239
- mc16_13TeV.301032.PowhegPythia8EvtGen_AZNLOCTEQ6L1_DYmumu_2500M2750.deriv.DAOD_STDM4.e3649_e5984_s3126_r10724_r10726_p4239
- mc16_13TeV.301033.PowhegPythia8EvtGen_AZNLOCTEQ6L1_DYmumu_2750M3000.deriv.DAOD_STDM4.e3649_e5984_s3126_r10724_r10726_p4239
- mc16_13TeV.301034.PowhegPythia8EvtGen_AZNLOCTEQ6L1_DYmumu_3000M3500.deriv.DAOD_STDM4.e3649_e5984_s3126_r10724_r10726_p4239
- mc16_13TeV.301035.PowhegPythia8EvtGen_AZNLOCTEQ6L1_DYmumu_3500M4000.deriv.DAOD_STDM4.e3649_e5984_s3126_r10724_r10726_p4239
- mc16_13TeV.301036.PowhegPythia8EvtGen_AZNLOCTEQ6L1_DYmumu_4000M45000.deriv.DAOD_STDM4.e3649_e5984_s3126_r10724_r10726_p4239
- mc16_13TeV.301037.PowhegPythia8EvtGen_AZNLOCTEQ6L1_DYmumu_4500M5000.deriv.DAOD_STDM4.e3649_e5984_s3126_r10724_r10726_p4239
- mc16_13TeV.301038.PowhegPythia8EvtGen_AZNLOCTEQ6L1_DYmumu_5000M.deriv.DAOD_STDM4.e3649_e5984_s3126_r10724_r10726_p4239

$Z \to \tau\tau$

- mc16_13TeV.361108.PowhegPythia8EvtGen_AZNLOCTEQ6L1_Ztautau.deriv.DAOD_STDM4.e3601_e5984_s3126_r10724_r10726_p4237
- mc16_13TeV.301040.PowhegPythia8EvtGen_AZNLOCTEQ6L1_DYtautau_120M180.deriv.DAOD_STDM4.e3649_e5984_s3126_r10724_r10726_p4237
- mc16_13TeV.301041.PowhegPythia8EvtGen_AZNLOCTEQ6L1_DYtautau_180M250.deriv.DAOD_STDM4.e3649_e5984_s3126_r10724_r10726_p4237

- mc16_13TeV.301042.PowhegPythia8EvtGen_AZNLOCTEQ6L1_DYtautau_250M400.deriv.DAOD_STDM4.e3649_e5984_s3126_r10724_r10726_p4237
- mc16_13TeV.301043.PowhegPythia8EvtGen_AZNLOCTEQ6L1_DYtautau_400M600.deriv.DAOD_STDM4.e3649_e5984_s3126_r10724_r10726_p4237
- mc16_13TeV.301044.PowhegPythia8EvtGen_AZNLOCTEQ6L1_DYtautau_600M800.deriv.DAOD_STDM4.e3649_e5984_s3126_r10724_r10726_p4237
- mc16_13TeV.301045.PowhegPythia8EvtGen_AZNLOCTEQ6L1_DYtautau_800M1000.deriv.DAOD_STDM4.e3649_e5984_s3126_r10724_r10726_p4237
- mc16_13TeV.301046.PowhegPythia8EvtGen_AZNLOCTEQ6L1_DYtautau_1000M1250.deriv.DAOD_STDM4.e3649_e5984_s3126_r10724_r10726_p4237
- mc16_13TeV.301047.PowhegPythia8EvtGen_AZNLOCTEQ6L1_DYtautau_1250M1500.deriv.DAOD_STDM4.e3649_e5984_s3126_r10724_r10726_p4237
- mc16_13TeV.301048.PowhegPythia8EvtGen_AZNLOCTEQ6L1_DYtautau_1500M1750.deriv.DAOD_STDM4.e3649_e5984_s3126_r10724_r10726_p4237
- mc16_13TeV.301049.PowhegPythia8EvtGen_AZNLOCTEQ6L1_DYtautau_1750M2000.deriv.DAOD_STDM4.e3649_e5984_s3126_r10724_r10726_p4237
- mc16_13TeV.301050.PowhegPythia8EvtGen_AZNLOCTEQ6L1_DYtautau_2000M2250.deriv.DAOD_STDM4.e3649_e5984_s3126_r10724_r10726_p4237
- mc16_13TeV.301051.PowhegPythia8EvtGen_AZNLOCTEQ6L1_DYtautau_2250M2500.deriv.DAOD_STDM4.e3649_e5984_s3126_r10724_r10726_p4237
- mc16_13TeV.301052.PowhegPythia8EvtGen_AZNLOCTEQ6L1_DYtautau_2500M2750.deriv.DAOD_STDM4.e3649_e5984_s3126_r10724_r10726_p4237
- mc16_13TeV.301053.PowhegPythia8EvtGen_AZNLOCTEQ6L1_DYtautau_2750M3000.deriv.DAOD_STDM4.e3649_e5984_s3126_r10724_r10726_p4237
- mc16_13TeV.301054.PowhegPythia8EvtGen_AZNLOCTEQ6L1_DYtautau_3000M3500.deriv.DAOD_STDM4.e3649_e5984_s3126_r10724_r10726_p4237
- mc16_13TeV.301055.PowhegPythia8EvtGen_AZNLOCTEQ6L1_DYtautau_3500M4000.deriv.DAOD_STDM4.e3649_e5984_s3126_r10724_r10726_p4237
- mc16_13TeV.301056.PowhegPythia8EvtGen_AZNLOCTEQ6L1_DYtautau_4000M4500.deriv.DAOD_STDM4.e3649_e5984_s3126_r10724_r10726_p4237
- mc16_13TeV.301057.PowhegPythia8EvtGen_AZNLOCTEQ6L1_DYtautau_4500M5000.deriv.DAOD_STDM4.e3649_e5984_s3126_r10724_r10726_p4237
- mc16_13TeV.301058.PowhegPythia8EvtGen_AZNLOCTEQ6L1_DYtautau_5000M.deriv.DAOD_STDM4.e3649_e5984_s3126_r10724_r10726_p4237

A.3.4. Diboson

MC16a:

- mc16_13TeV.364250.Sherpa_222_NNPDF30NNLO_llll.deriv.DAOD_STDM4.e5894_s3126_r9364_p4237
- mc16_13TeV.364253.Sherpa_222_NNPDF30NNLO_lllv.deriv.DAOD_STDM4.e5916_s3126_r9364_p4237
- mc16_13TeV.364254.Sherpa_222_NNPDF30NNLO_llvv.deriv.DAOD_STDM4.e5916_s3126_r9364_p4237
- mc16_13TeV.364255.Sherpa_222_NNPDF30NNLO_lvvv.deriv.DAOD_STDM4.e5916_s3126_r9364_p4237
- mc16_13TeV.363360.Sherpa_221_NNPDF30NNLO_WplvWmqq.deriv.DAOD_STDM4.e5983_s3126_r9364_p4237
- mc16_13TeV.363359.Sherpa_221_NNPDF30NNLO_WpqqWmlv.deriv.DAOD_STDM4.e5583_s3126_r9364_p4237
- mc16_13TeV.363356.Sherpa_221_NNPDF30NNLO_ZqqZll.deriv.DAOD_STDM4.e5525_s3126_r9364_r9315_p4237
- mc16_13TeV.363358.Sherpa_221_NNPDF30NNLO_WqqZll.deriv.DAOD_STDM4.e5525_s3126_r9364_r9315_p4237
- mc16_13TeV.363489.Sherpa_221_NNPDF30NNLO_WlvZqq.deriv.DAOD_STDM4.e5525_s3126_r9364_p4237

MC16d:

- mc16_13TeV.364250.Sherpa_222_NNPDF30NNLO_llll.deriv.DAOD_STDM4.e5894_e5984_s3126_r10201_r10210_p4237
- mc16_13TeV.364253.Sherpa_222_NNPDF30NNLO_lllv.deriv.DAOD_STDM4.e5916_e5984_s3126_r10201_r10210_p4237
- mc16_13TeV.364254.Sherpa_222_NNPDF30NNLO_llvv.deriv.DAOD_STDM4.e5916_e5984_s3126_r10201_r10210_p4237
- mc16_13TeV.364255.Sherpa_222_NNPDF30NNLO_lvvv.deriv.DAOD_STDM4.e5916_e5984_s3126_r10201_r10210_p4237
- mc16_13TeV.363360.Sherpa_221_NNPDF30NNLO_WplvWmqq.deriv.DAOD_STDM4.e5983_e5984_s3126_r10201_r10210_p4237
- mc16_13TeV.363359.Sherpa_221_NNPDF30NNLO_WpqqWmlv.deriv.DAOD_STDM4.e5583_e5984_s3126_r10201_r10210_p4237
- mc16_13TeV.363356.Sherpa_221_NNPDF30NNLO_ZqqZll.deriv.DAOD_STDM4.e5525_s3126_r10201_r10210_p4239
- mc16_13TeV.363358.Sherpa_221_NNPDF30NNLO_WqqZll.deriv.DAOD_STDM4.e5525_e5984_s3126_r10201_r10210_p4239

- mc16_13TeV.363489.Sherpa_221_NNPDF30NNLO_WlvZqq.deriv.DAOD_STDM4.e5525_e5984_s3126_r10201_r10210_p4237

MC16e:

- mc16_13TeV.364250.Sherpa_222_NNPDF30NNLO_llll.deriv.DAOD_STDM4.e5894_e5984_s3126_r10724_r10726_p4237
- mc16_13TeV.364253.Sherpa_222_NNPDF30NNLO_lllv.deriv.DAOD_STDM4.e5916_e5984_s3126_r10724_r10726_p4237
- mc16_13TeV.364254.Sherpa_222_NNPDF30NNLO_llvv.deriv.DAOD_STDM4.e5916_e5984_s3126_r10724_r10726_p4237
- mc16_13TeV.364255.Sherpa_222_NNPDF30NNLO_lvvv.deriv.DAOD_STDM4.e5916_e5984_s3126_r10724_r10726_p4237
- mc16_13TeV.363360.Sherpa_221_NNPDF30NNLO_WplvWmqq.deriv.DAOD_STDM4.e5983_e5984_s3126_r10724_r10726_p4237
- mc16_13TeV.363359.Sherpa_221_NNPDF30NNLO_WpqqWmlv.deriv.DAOD_STDM4.e5583_e5984_s3126_r10724_r10726_p4237
- mc16_13TeV.363356.Sherpa_221_NNPDF30NNLO_ZqqZll.deriv.DAOD_STDM4.e5525_e5984_s3126_r10724_r10726_p4237
- mc16_13TeV.363358.Sherpa_221_NNPDF30NNLO_WqqZll.deriv.DAOD_STDM4.e5525_e5984_s3126_r10724_r10726_p4237
- mc16_13TeV.363489.Sherpa_221_NNPDF30NNLO_WlvZqq.deriv.DAOD_STDM4.e5525_e5984_s3126_r10724_r10726_p4237

A.3.5. $W \to \tau\nu$

MC16a:

W^+

- mc16_13TeV.361102.PowhegPythia8EvtGen_AZNLOCTEQ6L1_Wplustaunu.deriv.DAOD_STDM4.e3601_s3126_r9364_p4239
- mc16_13TeV.301140.PowhegPythia8EvtGen_AZNLOCTEQ6L1_Wplustaunu_120M180.deriv.DAOD_STDM4.e3663_s3126_r9364_p4239
- mc16_13TeV.301141.PowhegPythia8EvtGen_AZNLOCTEQ6L1_Wplustaunu_180M250.deriv.DAOD_STDM4.e3663_s3126_r9364_p4239
- mc16_13TeV.301142.PowhegPythia8EvtGen_AZNLOCTEQ6L1_Wplustaunu_250M400.deriv.DAOD_STDM4.e3663_s3126_r9364_p4239
- mc16_13TeV.301143.PowhegPythia8EvtGen_AZNLOCTEQ6L1_Wplustaunu_400M600.deriv.DAOD_STDM4.e3663_s3126_r9364_p4239
- mc16_13TeV.301144.PowhegPythia8EvtGen_AZNLOCTEQ6L1_Wplustaunu_600M800.deriv.DAOD_STDM4.e3663_s3126_r9364_p4239
- mc16_13TeV.301145.PowhegPythia8EvtGen_AZNLOCTEQ6L1_Wplustaunu_800M1000.deriv.DAOD_STDM4.e3663_s3126_r9364_p4239
- mc16_13TeV.301146.PowhegPythia8EvtGen_AZNLOCTEQ6L1_Wplustaunu_1000M1250.deriv.DAOD_STDM4.e3663_s3126_r9364_p4239
- mc16_13TeV.301147.PowhegPythia8EvtGen_AZNLOCTEQ6L1_Wplustaunu_1250M1500.deriv.DAOD_STDM4.e3663_s3126_r9364_p4239
- mc16_13TeV.301148.PowhegPythia8EvtGen_AZNLOCTEQ6L1_Wplustaunu_1500M1750.deriv.DAOD_STDM4.e3663_s3126_r9364_p4239
- mc16_13TeV.301149.PowhegPythia8EvtGen_AZNLOCTEQ6L1_Wplustaunu_1750M2000.deriv.DAOD_STDM4.e3663_s3126_r9364_p4239
- mc16_13TeV.301150.PowhegPythia8EvtGen_AZNLOCTEQ6L1_Wplustaunu_2000M2250.deriv.DAOD_STDM4.e3663_s3126_r9364_p4239
- mc16_13TeV.301151.PowhegPythia8EvtGen_AZNLOCTEQ6L1_Wplustaunu_2250M2500.deriv.DAOD_STDM4.e3663_s3126_r9364_p4239
- mc16_13TeV.301152.PowhegPythia8EvtGen_AZNLOCTEQ6L1_Wplustaunu_2500M2750.deriv.DAOD_STDM4.e3663_s3126_r9364_p4239
- mc16_13TeV.301153.PowhegPythia8EvtGen_AZNLOCTEQ6L1_Wplustaunu_2750M3000.deriv.DAOD_STDM4.e3663_s3126_r9364_p4239
- mc16_13TeV.301154.PowhegPythia8EvtGen_AZNLOCTEQ6L1_Wplustaunu_3000M3500.deriv.DAOD_STDM4.e3663_s3126_r9364_p4239
- mc16_13TeV.301155.PowhegPythia8EvtGen_AZNLOCTEQ6L1_Wplustaunu_3500M4000.deriv.DAOD_STDM4.e3663_s3126_r9364_p4239
- mc16_13TeV.301156.PowhegPythia8EvtGen_AZNLOCTEQ6L1_Wplustaunu_4000M4500.deriv.DAOD_STDM4.e3663_s3126_r9364_p4239
- mc16_13TeV.301157.PowhegPythia8EvtGen_AZNLOCTEQ6L1_Wplustaunu_4500M5000.deriv.DAOD_STDM4.e3663_s3126_r9364_p4239
- mc16_13TeV.301158.PowhegPythia8EvtGen_AZNLOCTEQ6L1_Wplustaunu_5000M.deriv.DAOD_STDM4.e3663_s3126_r9364_p4239

W^-

- mc16_13TeV.361105.PowhegPythia8EvtGen_AZNLOCTEQ6L1_Wminustaunu.deriv.DAOD_STDM4.e3601_s3126_r9364_p4239

- mc16_13TeV.301160.PowhegPythia8EvtGen_AZNLOCTEQ6L1_Wmintaunu_120M180.deriv.DAOD_STDM4.e3663_s3126_r9364_p4239
- mc16_13TeV.301161.PowhegPythia8EvtGen_AZNLOCTEQ6L1_Wmintaunu_180M250.deriv.DAOD_STDM4.e3663_s3126_r9364_p4239
- mc16_13TeV.301162.PowhegPythia8EvtGen_AZNLOCTEQ6L1_Wmintaunu_250M400.deriv.DAOD_STDM4.e3663_s3126_r9364_p4239
- mc16_13TeV.301163.PowhegPythia8EvtGen_AZNLOCTEQ6L1_Wmintaunu_400M600.deriv.DAOD_STDM4.e3663_s3126_r9364_p4239
- mc16_13TeV.301164.PowhegPythia8EvtGen_AZNLOCTEQ6L1_Wmintaunu_600M800.deriv.DAOD_STDM4.e3663_s3126_r9364_p4239
- mc16_13TeV.301165.PowhegPythia8EvtGen_AZNLOCTEQ6L1_Wmintaunu_800M1000.deriv.DAOD_STDM4.e3663_s3126_r9364_p4239
- mc16_13TeV.301166.PowhegPythia8EvtGen_AZNLOCTEQ6L1_Wmintaunu_1000M1250.deriv.DAOD_STDM4.e3663_s3126_r9364_p4239
- mc16_13TeV.301167.PowhegPythia8EvtGen_AZNLOCTEQ6L1_Wmintaunu_1250M1500.deriv.DAOD_STDM4.e3663_s3126_r9364_p4239
- mc16_13TeV.301168.PowhegPythia8EvtGen_AZNLOCTEQ6L1_Wmintaunu_1500M1750.deriv.DAOD_STDM4.e3663_s3126_r9364_p4239
- mc16_13TeV.301169.PowhegPythia8EvtGen_AZNLOCTEQ6L1_Wmintaunu_1750M2000.deriv.DAOD_STDM4.e3663_s3126_r9364_p4239
- mc16_13TeV.301170.PowhegPythia8EvtGen_AZNLOCTEQ6L1_Wmintaunu_2000M2250.deriv.DAOD_STDM4.e3663_s3126_r9364_p4239
- mc16_13TeV.301171.PowhegPythia8EvtGen_AZNLOCTEQ6L1_Wmintaunu_2250M2500.deriv.DAOD_STDM4.e3663_s3126_r9364_p4239
- mc16_13TeV.301172.PowhegPythia8EvtGen_AZNLOCTEQ6L1_Wmintaunu_2500M2750.deriv.DAOD_STDM4.e3663_s3126_r9364_p4239
- mc16_13TeV.301173.PowhegPythia8EvtGen_AZNLOCTEQ6L1_Wmintaunu_2750M3000.deriv.DAOD_STDM4.e3663_s3126_r9364_p4239
- mc16_13TeV.301174.PowhegPythia8EvtGen_AZNLOCTEQ6L1_Wmintaunu_3000M3500.deriv.DAOD_STDM4.e3663_s3126_r9364_p4239
- mc16_13TeV.301175.PowhegPythia8EvtGen_AZNLOCTEQ6L1_Wmintaunu_3500M4000.deriv.DAOD_STDM4.e3663_s3126_r9364_p4239
- mc16_13TeV.301176.PowhegPythia8EvtGen_AZNLOCTEQ6L1_Wmintaunu_4000M4500.deriv.DAOD_STDM4.e3663_s3126_r9364_p4239
- mc16_13TeV.301177.PowhegPythia8EvtGen_AZNLOCTEQ6L1_Wmintaunu_4500M5000.deriv.DAOD_STDM4.e3663_s3126_r9364_p4239
- mc16_13TeV.301178.PowhegPythia8EvtGen_AZNLOCTEQ6L1_Wmintaunu_5000M.deriv.DAOD_STDM4.e3663_s3126_r9364_p4239

MC16d:

W^+

- mc16_13TeV.361102.PowhegPythia8EvtGen_AZNLOCTEQ6L1_Wplustaunu.deriv.DAOD_STDM4.e3601_e5984_s3126_r10201_r10210_p4239
- mc16_13TeV.301140.PowhegPythia8EvtGen_AZNLOCTEQ6L1_Wplustaunu_120M180.deriv.DAOD_STDM4.e3663_e5984_s3126_r10201_r10210_p4239
- mc16_13TeV.301141.PowhegPythia8EvtGen_AZNLOCTEQ6L1_Wplustaunu_180M250.deriv.DAOD_STDM4.e3663_e5984_s3126_r10201_r10210_p4239
- mc16_13TeV.301142.PowhegPythia8EvtGen_AZNLOCTEQ6L1_Wplustaunu_250M400.deriv.DAOD_STDM4.e3663_e5984_s3126_r10201_r10210_p4239
- mc16_13TeV.301143.PowhegPythia8EvtGen_AZNLOCTEQ6L1_Wplustaunu_400M600.deriv.DAOD_STDM4.e3663_e5984_s3126_r10201_r10210_p4239
- mc16_13TeV.301144.PowhegPythia8EvtGen_AZNLOCTEQ6L1_Wplustaunu_600M800.deriv.DAOD_STDM4.e3663_e5984_s3126_r10201_r10210_p4239
- mc16_13TeV.301145.PowhegPythia8EvtGen_AZNLOCTEQ6L1_Wplustaunu_800M1000.deriv.DAOD_STDM4.e3663_e5984_s3126_r10201_r10210_p4239
- mc16_13TeV.301146.PowhegPythia8EvtGen_AZNLOCTEQ6L1_Wplustaunu_1000M1250.deriv.DAOD_STDM4.e3663_e5984_s3126_r10201_r10210_p4239
- mc16_13TeV.301147.PowhegPythia8EvtGen_AZNLOCTEQ6L1_Wplustaunu_1250M1500.deriv.DAOD_STDM4.e3663_e5984_s3126_r10201_r10210_p4239
- mc16_13TeV.301148.PowhegPythia8EvtGen_AZNLOCTEQ6L1_Wplustaunu_1500M1750.deriv.DAOD_STDM4.e3663_e5984_s3126_r10201_r10210_p4239
- mc16_13TeV.301149.PowhegPythia8EvtGen_AZNLOCTEQ6L1_Wplustaunu_1750M2000.deriv.DAOD_STDM4.e3663_e5984_s3126_r10201_r10210_p4239
- mc16_13TeV.301150.PowhegPythia8EvtGen_AZNLOCTEQ6L1_Wplustaunu_2000M2250.deriv.DAOD_STDM4.e3663_e5984_s3126_r10201_r10210_p4239
- mc16_13TeV.301151.PowhegPythia8EvtGen_AZNLOCTEQ6L1_Wplustaunu_2250M2500.deriv.DAOD_STDM4.e3663_e5984_s3126_r10201_r10210_p4239
- mc16_13TeV.301152.PowhegPythia8EvtGen_AZNLOCTEQ6L1_Wplustaunu_2500M2750.deriv.DAOD_STDM4.e3663_e5984_s3126_r10201_r10210_p4239
- mc16_13TeV.301153.PowhegPythia8EvtGen_AZNLOCTEQ6L1_Wplustaunu_2750M3000.deriv.DAOD_STDM4.e3663_e5984_s3126_r10201_r10210_p4239
- mc16_13TeV.301154.PowhegPythia8EvtGen_AZNLOCTEQ6L1_Wplustaunu_3000M3500.deriv.DAOD_STDM4.e3663_e5984_s3126_r10201_r10210_p4239
- mc16_13TeV.301155.PowhegPythia8EvtGen_AZNLOCTEQ6L1_Wplustaunu_3500M4000.deriv.DAOD_STDM4.e3663_e5984_s3126_r10201_r10210_p4239

- mc16_13TeV.301156.PowhegPythia8EvtGen_AZNLOCTEQ6L1_Wplustaunu_4000M4500.deriv.DAOD_STDM4.e3663_e5984_s3126_r10201_r10210_p4239
- mc16_13TeV.301157.PowhegPythia8EvtGen_AZNLOCTEQ6L1_Wplustaunu_4500M5000.deriv.DAOD_STDM4.e3663_e5984_s3126_r10201_r10210_p4239
- mc16_13TeV.301158.PowhegPythia8EvtGen_AZNLOCTEQ6L1_Wplustaunu_5000M.deriv.DAOD_STDM4.e3663_e5984_s3126_r10201_r10210_p4239

W^-

- mc16_13TeV.361105.PowhegPythia8EvtGen_AZNLOCTEQ6L1_Wminustaunu.deriv.DAOD_STDM4.e3601_e5984_s3126_r10201_r10210_p4239
- mc16_13TeV.301160.PowhegPythia8EvtGen_AZNLOCTEQ6L1_Wmintaunu_120M180.deriv.DAOD_STDM4.e3663_e5984_s3126_r10201_r10210_p4239
- mc16_13TeV.301161.PowhegPythia8EvtGen_AZNLOCTEQ6L1_Wmintaunu_180M250.deriv.DAOD_STDM4.e3663_e5984_s3126_r10201_r10210_p4239
- mc16_13TeV.301162.PowhegPythia8EvtGen_AZNLOCTEQ6L1_Wmintaunu_250M400.deriv.DAOD_STDM4.e3663_e5984_s3126_r10201_r10210_p4239
- mc16_13TeV.301163.PowhegPythia8EvtGen_AZNLOCTEQ6L1_Wmintaunu_400M600.deriv.DAOD_STDM4.e3663_e5984_s3126_r10201_r10210_p4239
- mc16_13TeV.301164.PowhegPythia8EvtGen_AZNLOCTEQ6L1_Wmintaunu_600M800.deriv.DAOD_STDM4.e3663_e5984_s3126_r10201_r10210_p4239
- mc16_13TeV.301165.PowhegPythia8EvtGen_AZNLOCTEQ6L1_Wmintaunu_800M1000.deriv.DAOD_STDM4.e3663_e5984_s3126_r10201_r10210_p4239
- mc16_13TeV.301166.PowhegPythia8EvtGen_AZNLOCTEQ6L1_Wmintaunu_1000M1250.deriv.DAOD_STDM4.e3663_e5984_s3126_r10201_r10210_p4239
- mc16_13TeV.301167.PowhegPythia8EvtGen_AZNLOCTEQ6L1_Wmintaunu_1250M1500.deriv.DAOD_STDM4.e3663_e5984_s3126_r10201_r10210_p4239
- mc16_13TeV.301168.PowhegPythia8EvtGen_AZNLOCTEQ6L1_Wmintaunu_1500M1750.deriv.DAOD_STDM4.e3663_e5984_s3126_r10201_r10210_p4239
- mc16_13TeV.301169.PowhegPythia8EvtGen_AZNLOCTEQ6L1_Wmintaunu_1750M2000.deriv.DAOD_STDM4.e3663_e5984_s3126_r10201_r10210_p4239
- mc16_13TeV.301170.PowhegPythia8EvtGen_AZNLOCTEQ6L1_Wmintaunu_2000M2250.deriv.DAOD_STDM4.e3663_e5984_s3126_r10201_r10210_p4239
- mc16_13TeV.301171.PowhegPythia8EvtGen_AZNLOCTEQ6L1_Wmintaunu_2250M2500.deriv.DAOD_STDM4.e3663_e5984_s3126_r10201_r10210_p4239
- mc16_13TeV.301172.PowhegPythia8EvtGen_AZNLOCTEQ6L1_Wmintaunu_2500M2750.deriv.DAOD_STDM4.e3663_e5984_s3126_r10201_r10210_p4239
- mc16_13TeV.301173.PowhegPythia8EvtGen_AZNLOCTEQ6L1_Wmintaunu_2750M3000.deriv.DAOD_STDM4.e3663_e5984_s3126_r10201_r10210_p4239
- mc16_13TeV.301174.PowhegPythia8EvtGen_AZNLOCTEQ6L1_Wmintaunu_3000M3500.deriv.DAOD_STDM4.e3663_e5984_s3126_r10201_r10210_p4239
- mc16_13TeV.301175.PowhegPythia8EvtGen_AZNLOCTEQ6L1_Wmintaunu_3500M4000.deriv.DAOD_STDM4.e3663_e5984_s3126_r10201_r10210_p4239
- mc16_13TeV.301176.PowhegPythia8EvtGen_AZNLOCTEQ6L1_Wmintaunu_4000M4500.deriv.DAOD_STDM4.e3663_e5984_s3126_r10201_r10210_p4239
- mc16_13TeV.301177.PowhegPythia8EvtGen_AZNLOCTEQ6L1_Wmintaunu_4500M5000.deriv.DAOD_STDM4.e3663_e5984_s3126_r10201_r10210_p4239
- mc16_13TeV.301178.PowhegPythia8EvtGen_AZNLOCTEQ6L1_Wmintaunu_5000M.deriv.DAOD_STDM4.e3663_e5984_s3126_r10201_r10210_p4239

MC16e:

W^+

- mc16_13TeV.361102.PowhegPythia8EvtGen_AZNLOCTEQ6L1_Wplustaunu.deriv.DAOD_STDM4.e3601_e5984_s3126_r10724_r10726_p4239
- mc16_13TeV.301140.PowhegPythia8EvtGen_AZNLOCTEQ6L1_Wplustaunu_120M180.deriv.DAOD_STDM4.e3663_e5984_s3126_r10724_r10726_p4239
- mc16_13TeV.301141.PowhegPythia8EvtGen_AZNLOCTEQ6L1_Wplustaunu_180M250.deriv.DAOD_STDM4.e3663_e5984_s3126_r10724_r10726_p4239
- mc16_13TeV.301142.PowhegPythia8EvtGen_AZNLOCTEQ6L1_Wplustaunu_250M400.deriv.DAOD_STDM4.e3663_e5984_s3126_r10724_r10726_p4239
- mc16_13TeV.301143.PowhegPythia8EvtGen_AZNLOCTEQ6L1_Wplustaunu_400M600.deriv.DAOD_STDM4.e3663_e5984_s3126_r10724_r10726_p4239
- mc16_13TeV.301144.PowhegPythia8EvtGen_AZNLOCTEQ6L1_Wplustaunu_600M800.deriv.DAOD_STDM4.e3663_e5984_s3126_r10724_r10726_p4239
- mc16_13TeV.301145.PowhegPythia8EvtGen_AZNLOCTEQ6L1_Wplustaunu_800M1000.deriv.DAOD_STDM4.e3663_e5984_s3126_r10724_r10726_p4239
- mc16_13TeV.301146.PowhegPythia8EvtGen_AZNLOCTEQ6L1_Wplustaunu_1000M1250.deriv.DAOD_STDM4.e3663_e5984_s3126_r10724_r10726_p4239
- mc16_13TeV.301147.PowhegPythia8EvtGen_AZNLOCTEQ6L1_Wplustaunu_1250M1500.deriv.DAOD_STDM4.e3663_e5984_s3126_r10724_r10726_p4239
- mc16_13TeV.301148.PowhegPythia8EvtGen_AZNLOCTEQ6L1_Wplustaunu_1500M1750.deriv.DAOD_STDM4.e3663_e5984_s3126_r10724_r10726_p4239
- mc16_13TeV.301149.PowhegPythia8EvtGen_AZNLOCTEQ6L1_Wplustaunu_1750M2000.deriv.DAOD_STDM4.e3663_e5984_s3126_r10724_r10726_p4239
- mc16_13TeV.301150.PowhegPythia8EvtGen_AZNLOCTEQ6L1_Wplustaunu_2000M2250.deriv.DAOD_STDM4.e3663_e5984_s3126_r10724_r10726_p4239

- mc16_13TeV.301151.PowhegPythia8EvtGen_AZNLOCTEQ6L1_Wplustaunu_2250M2500.deriv.DAOD_STDM4.e3663_e5984_s3126_r10724_r10726_p4239
- mc16_13TeV.301152.PowhegPythia8EvtGen_AZNLOCTEQ6L1_Wplustaunu_2500M2750.deriv.DAOD_STDM4.e3663_e5984_s3126_r10724_r10726_p4239
- mc16_13TeV.301153.PowhegPythia8EvtGen_AZNLOCTEQ6L1_Wplustaunu_2750M3000.deriv.DAOD_STDM4.e3663_e5984_s3126_r10724_r10726_p4239
- mc16_13TeV.301154.PowhegPythia8EvtGen_AZNLOCTEQ6L1_Wplustaunu_3000M3500.deriv.DAOD_STDM4.e3663_e5984_s3126_r10724_r10726_p4239
- mc16_13TeV.301155.PowhegPythia8EvtGen_AZNLOCTEQ6L1_Wplustaunu_3500M4000.deriv.DAOD_STDM4.e3663_e5984_s3126_r10724_r10726_p4239
- mc16_13TeV.301156.PowhegPythia8EvtGen_AZNLOCTEQ6L1_Wplustaunu_4000M4500.deriv.DAOD_STDM4.e3663_e5984_s3126_r10724_r10726_p4239
- mc16_13TeV.301157.PowhegPythia8EvtGen_AZNLOCTEQ6L1_Wplustaunu_4500M5000.deriv.DAOD_STDM4.e3663_e5984_s3126_r10724_r10726_p4239
- mc16_13TeV.301158.PowhegPythia8EvtGen_AZNLOCTEQ6L1_Wplustaunu_5000M.deriv.DAOD_STDM4.e3663_e5984_s3126_r10724_r10726_p4239

W^-

- mc16_13TeV.361105.PowhegPythia8EvtGen_AZNLOCTEQ6L1_Wminustaunu.deriv.DAOD_STDM4.e3601_e5984_s3126_r10724_r10726_p4239
- mc16_13TeV.301160.PowhegPythia8EvtGen_AZNLOCTEQ6L1_Wmintaunu_120M180.deriv.DAOD_STDM4.e3663_e5984_s3126_r10724_r10726_p4239
- mc16_13TeV.301161.PowhegPythia8EvtGen_AZNLOCTEQ6L1_Wmintaunu_180M250.deriv.DAOD_STDM4.e3663_e5984_s3126_r10724_r10726_p4239
- mc16_13TeV.301162.PowhegPythia8EvtGen_AZNLOCTEQ6L1_Wmintaunu_250M400.deriv.DAOD_STDM4.e3663_e5984_s3126_r10724_r10726_p4239
- mc16_13TeV.301163.PowhegPythia8EvtGen_AZNLOCTEQ6L1_Wmintaunu_400M600.deriv.DAOD_STDM4.e3663_e5984_s3126_r10724_r10726_p4239
- mc16_13TeV.301164.PowhegPythia8EvtGen_AZNLOCTEQ6L1_Wmintaunu_600M800.deriv.DAOD_STDM4.e3663_e5984_s3126_r10724_r10726_p4239
- mc16_13TeV.301165.PowhegPythia8EvtGen_AZNLOCTEQ6L1_Wmintaunu_800M1000.deriv.DAOD_STDM4.e3663_e5984_s3126_r10724_r10726_p4239
- mc16_13TeV.301166.PowhegPythia8EvtGen_AZNLOCTEQ6L1_Wmintaunu_1000M1250.deriv.DAOD_STDM4.e3663_e5984_s3126_r10724_r10726_p4239
- mc16_13TeV.301167.PowhegPythia8EvtGen_AZNLOCTEQ6L1_Wmintaunu_1250M1500.deriv.DAOD_STDM4.e3663_e5984_s3126_r10724_r10726_p4239
- mc16_13TeV.301168.PowhegPythia8EvtGen_AZNLOCTEQ6L1_Wmintaunu_1500M1750.deriv.DAOD_STDM4.e3663_e5984_s3126_r10724_r10726_p4239
- mc16_13TeV.301169.PowhegPythia8EvtGen_AZNLOCTEQ6L1_Wmintaunu_1750M2000.deriv.DAOD_STDM4.e3663_e5984_s3126_r10724_r10726_p4239
- mc16_13TeV.301170.PowhegPythia8EvtGen_AZNLOCTEQ6L1_Wmintaunu_2000M2250.deriv.DAOD_STDM4.e3663_e5984_s3126_r10724_r10726_p4239
- mc16_13TeV.301171.PowhegPythia8EvtGen_AZNLOCTEQ6L1_Wmintaunu_2250M2500.deriv.DAOD_STDM4.e3663_e5984_s3126_r10724_r10726_p4239
- mc16_13TeV.301172.PowhegPythia8EvtGen_AZNLOCTEQ6L1_Wmintaunu_2500M2750.deriv.DAOD_STDM4.e3663_e5984_s3126_r10724_r10726_p4239
- mc16_13TeV.301173.PowhegPythia8EvtGen_AZNLOCTEQ6L1_Wmintaunu_2750M3000.deriv.DAOD_STDM4.e3663_e5984_s3126_r10724_r10726_p4239
- mc16_13TeV.301174.PowhegPythia8EvtGen_AZNLOCTEQ6L1_Wmintaunu_3000M3500.deriv.DAOD_STDM4.e3663_e5984_s3126_r10724_r10726_p4239
- mc16_13TeV.301175.PowhegPythia8EvtGen_AZNLOCTEQ6L1_Wmintaunu_3500M4000.deriv.DAOD_STDM4.e3663_e5984_s3126_r10724_r10726_p4239
- mc16_13TeV.301176.PowhegPythia8EvtGen_AZNLOCTEQ6L1_Wmintaunu_4000M4500.deriv.DAOD_STDM4.e3663_e5984_s3126_r10724_r10726_p4239
- mc16_13TeV.301177.PowhegPythia8EvtGen_AZNLOCTEQ6L1_Wmintaunu_4500M5000.deriv.DAOD_STDM4.e3663_e5984_s3126_r10724_r10726_p4239
- mc16_13TeV.301178.PowhegPythia8EvtGen_AZNLOCTEQ6L1_Wmintaunu_5000M.deriv.DAOD_STDM4.e3663_e5984_s3126_r10724_r10726_p4239

B. Appendix: Scale Factors

Scale factor plots for selection efficiencies for the trigger, isolation, identification, TTVA, k-Factor, pile-up weight. The plots shown here are for the W^- negative charge for the combination of Monte Carlo campaigns, MC16a, MC16d, MC16e. The W^+ positive charge scale factor plots are shown in Chapter 5 for the k-Factor and Chapter 6 for the trigger and isolation. Each plot is shown as a function of the m_T^W, p_T and η^μ. No large differences except for the k-Factor are observed as expected between the charges.

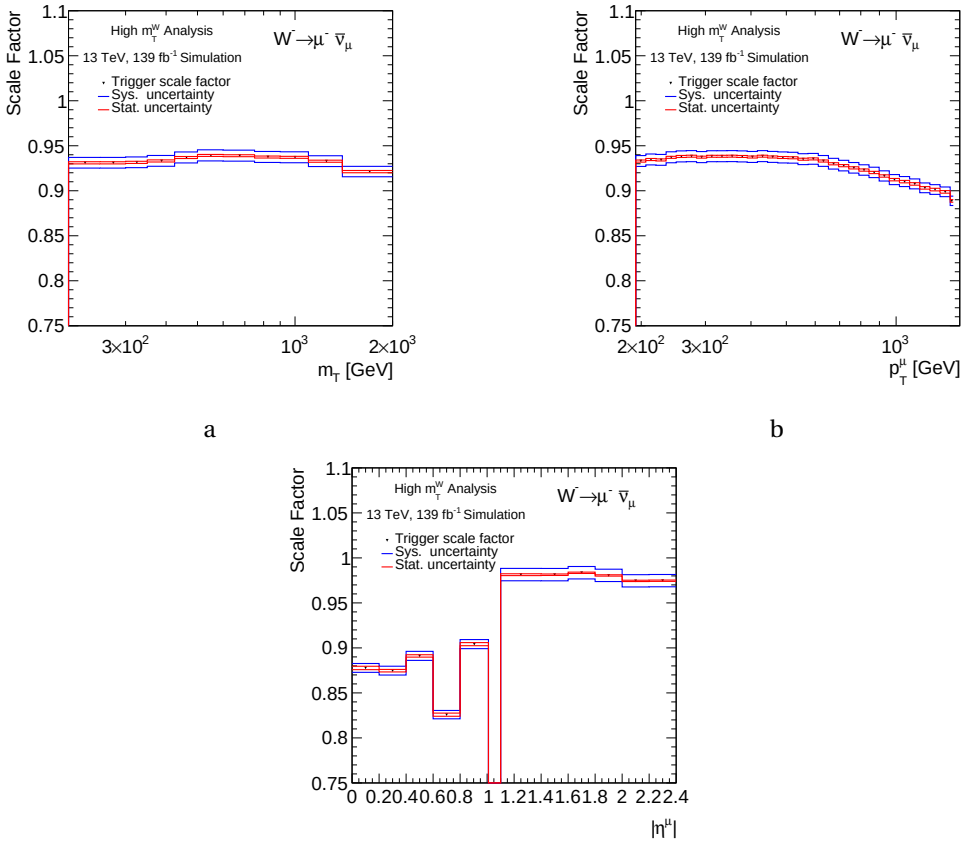

Figure B.1.: Scale Factor plots for average trigger cut efficiency. These plots are for $W^- \to \mu^- \bar{\nu}$ for the combination of Monte Carlo campaigns, MC16a, MC16d, MC16e. The plots show average trigger scale factors as a function of transverse mass m_T (a), p_T^μ (b) and $|\eta^\mu|$ (c). The individual systematics and statistical for one standard deviation are shown in blue and red.

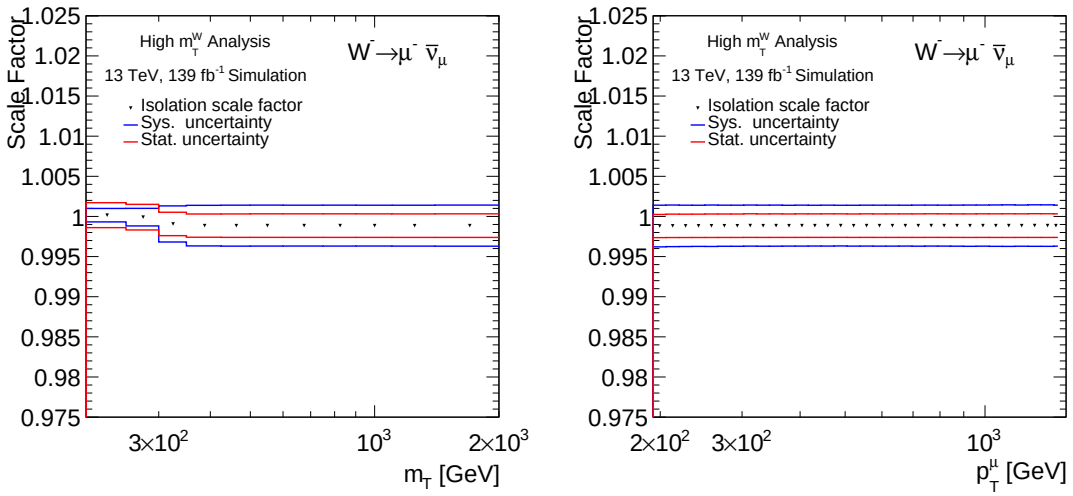

(a) (b)

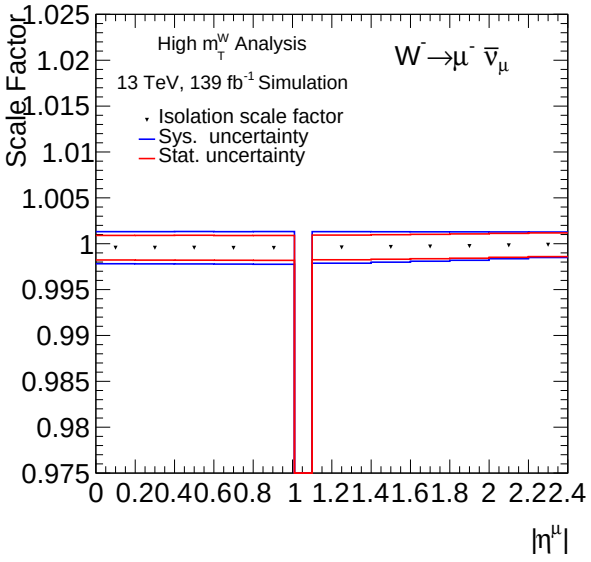

(c)

Figure B.2.: Scale Factor plots for average isolation selection efficiency. These plots are for $W^- \to \mu^- \bar{\nu}$ for the combination of Monte Carlo campaigns, MC16a, MC16d, MC16e. The plots show average isolation scale factors as a function of transverse mass m_T (a), p_T^μ (b) and $|\eta^\mu|$ (c). The individual systematics and statistical for one standard deviation are shown in blue and red.

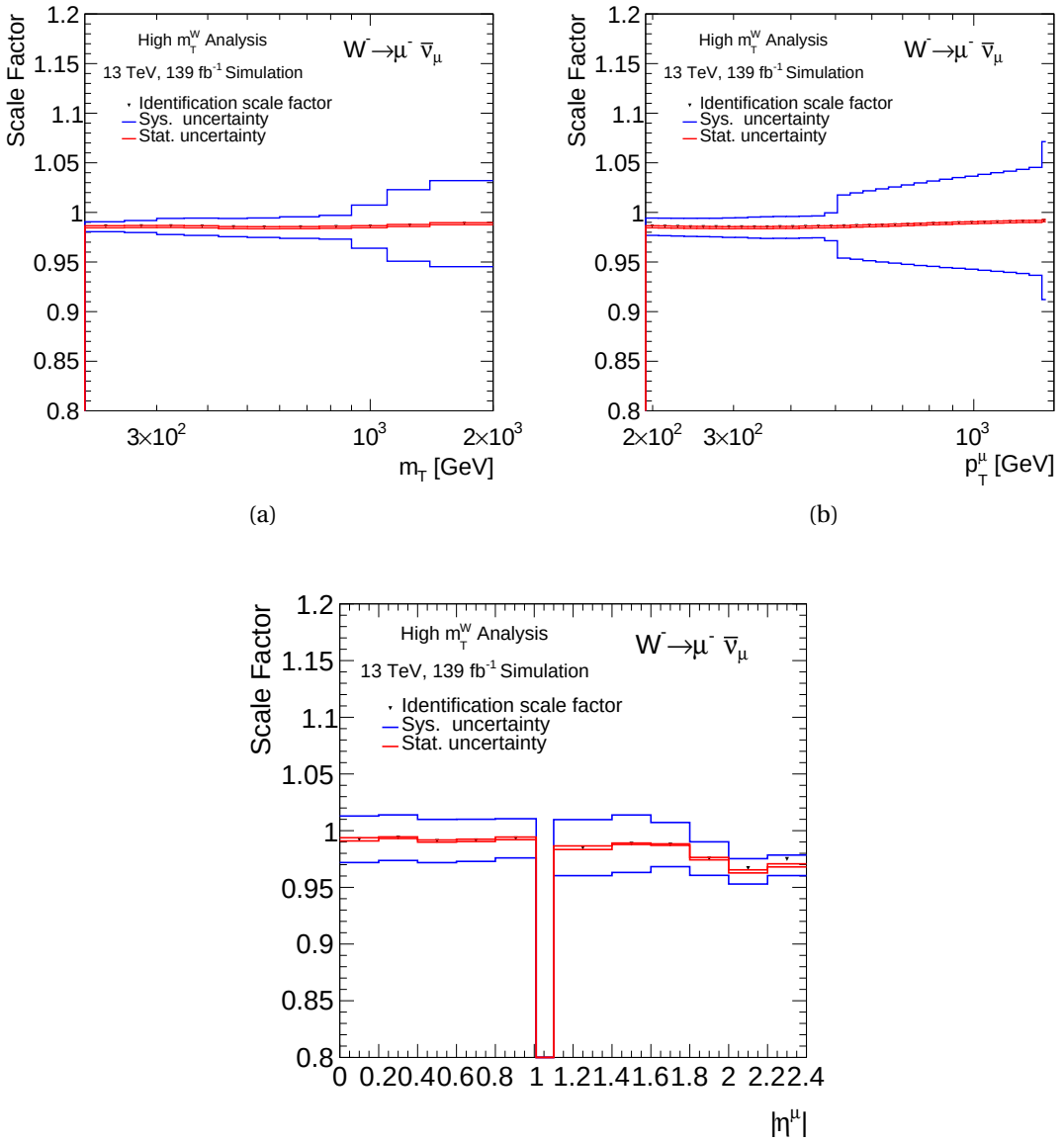

(a) (b)

(c)

Figure B.3.: Scale Factor plots for average muon identification selection efficiency. These plots are for $W^- \to \mu^- \bar{\nu}$ for the combination of Monte Carlo campaigns, MC16a, MC16d, MC16e. The plots show average isolation scale factors as a function of transverse mass m_T (a), p_T^μ (b) and $|\eta^\mu|$ (c). The individual systematics and statistical for one standard deviation are shown in blue and red.

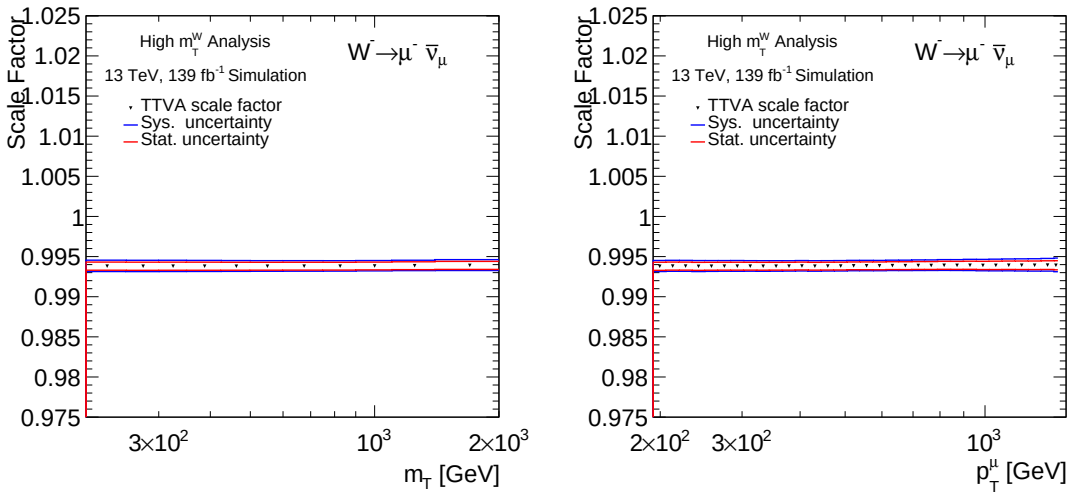

(a) (b)

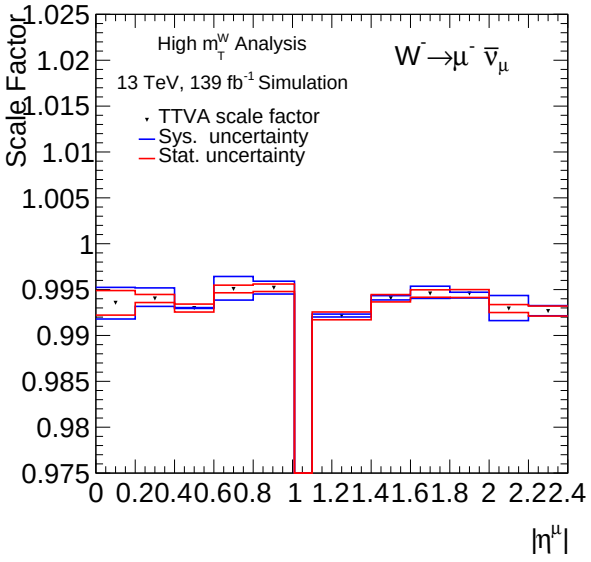

(c)

Figure B.4.: Scale Factor plots for average TTVA selection efficiency. These plots are for $W^- \to \mu^- \bar{\nu}$ for the combination of Monte Carlo campaigns, MC16a, MC16d, MC16e. The plots show average isolation scale factors as a function of transverse mass m_T (a), p_T^μ (b) and $|\eta^\mu|$ (c). The individual systematics and statistical for one standard deviation are shown in blue and red.

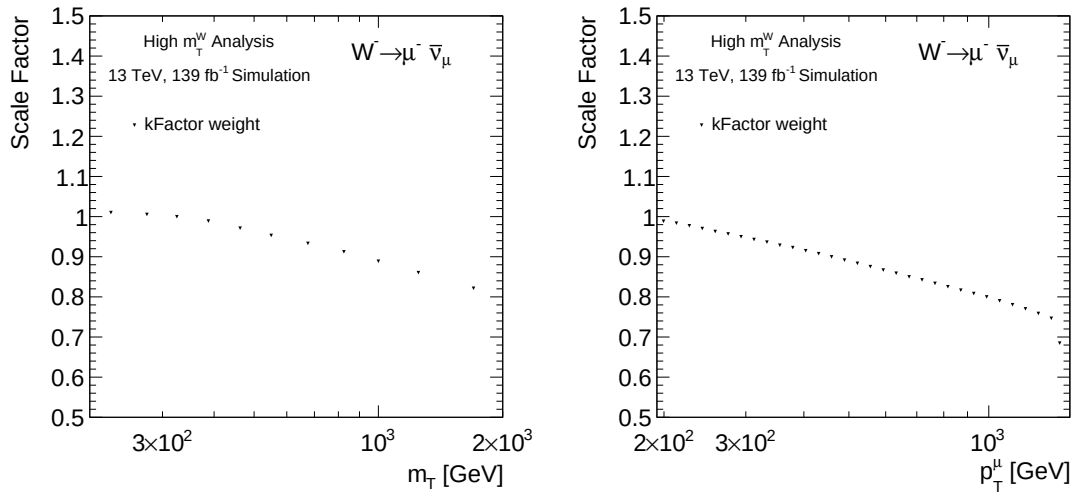

(a) (b)

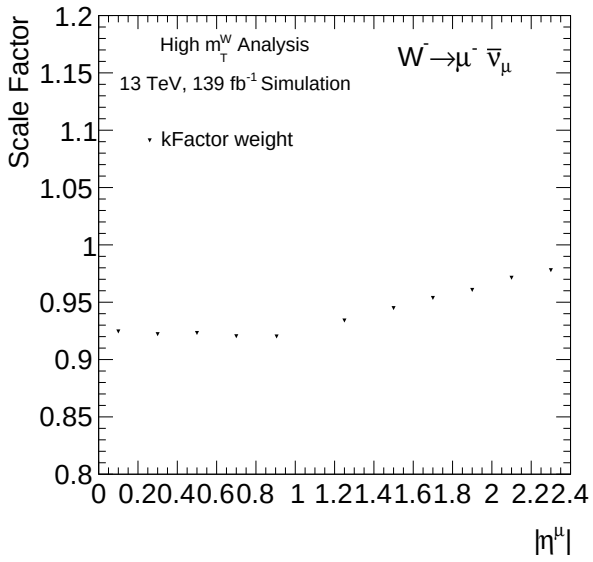

(c)

Figure B.5.: Scale Factor plots for average k-Factor efficiency. These plots are for $W^- \to \mu^- \bar{\nu}$ for the combination of Monte Carlo campaigns, MC16a, MC16d, MC16e. The plots show average k-Factor as a function of transverse mass m_T (a), p_T^μ (b) and $|\eta^\mu|$ (c).

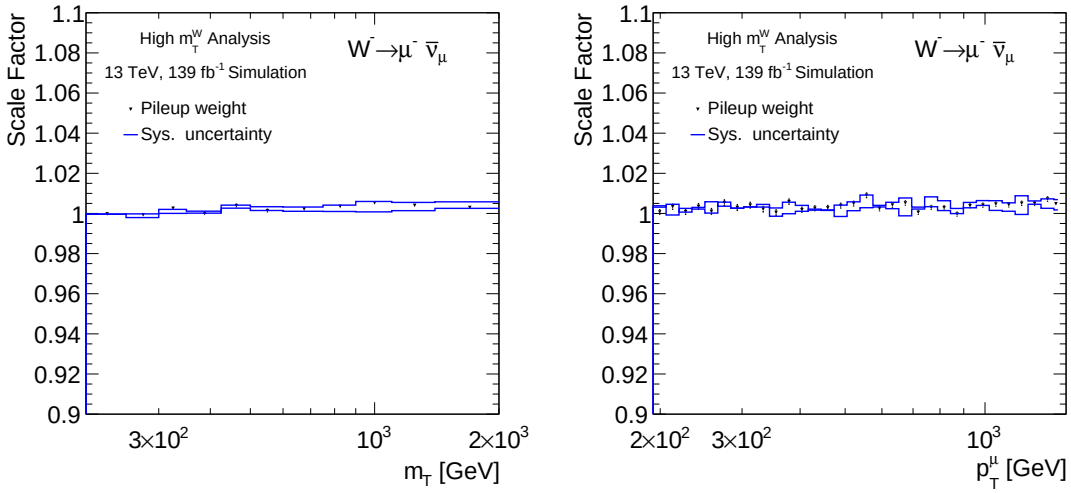

(a) (b)

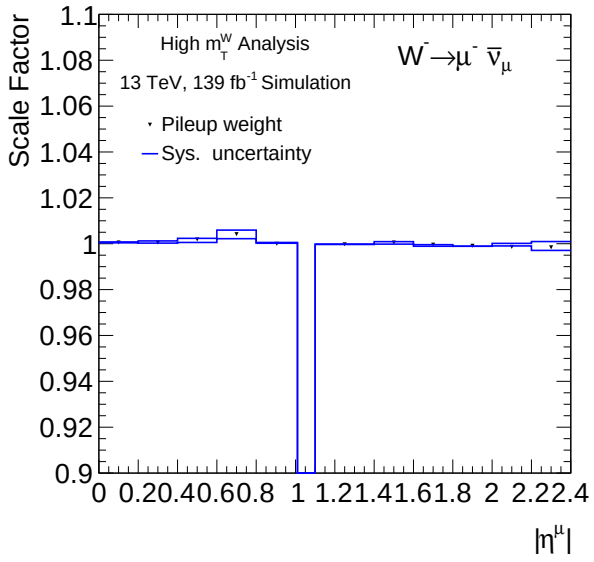

(c)

Figure B.6.: Plots for average pileup weight. These plots are for $W^- \to \mu^- \bar{\nu}$ for the combination of Monte Carlo campaigns, MC16a, MC16d, MC16e. The plots show average pileup weight as a function of transverse mass m_T (a), p_T^μ (b) and $|\eta^\mu|$ (c). The individual systematics and statistical for one standard deviation are shown in blue and red.

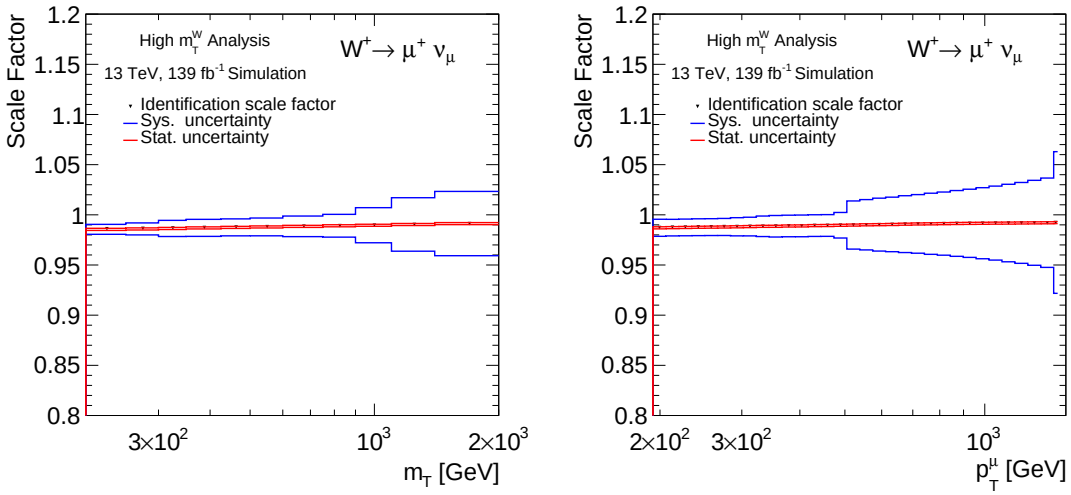

(a) (b)

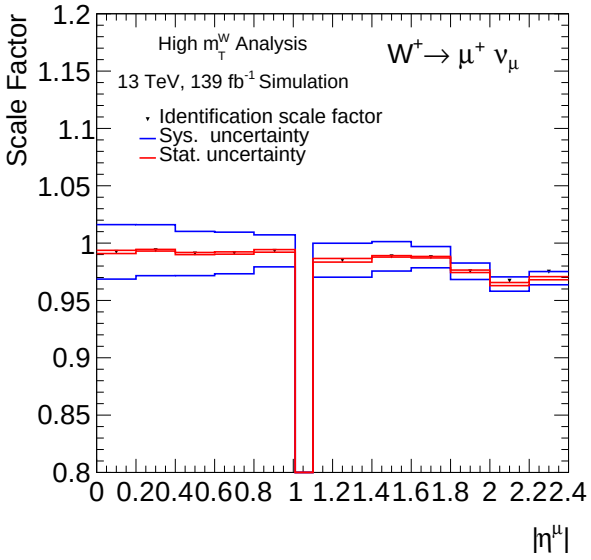

(c)

Figure B.7.: Scale Factor plots for average muon identification selection efficiency. These plots are for $W^+ \rightarrow \mu^+ \nu$ for the combination of Monte Carlo campaigns, MC16a, MC16d, MC16e. The plots show average isolation scale factors as a function of transverse mass m_T (a), p_T^μ (b) and $|\eta^\mu|$ (c). The individual systematics and statistical for one standard deviation are shown in blue and red.

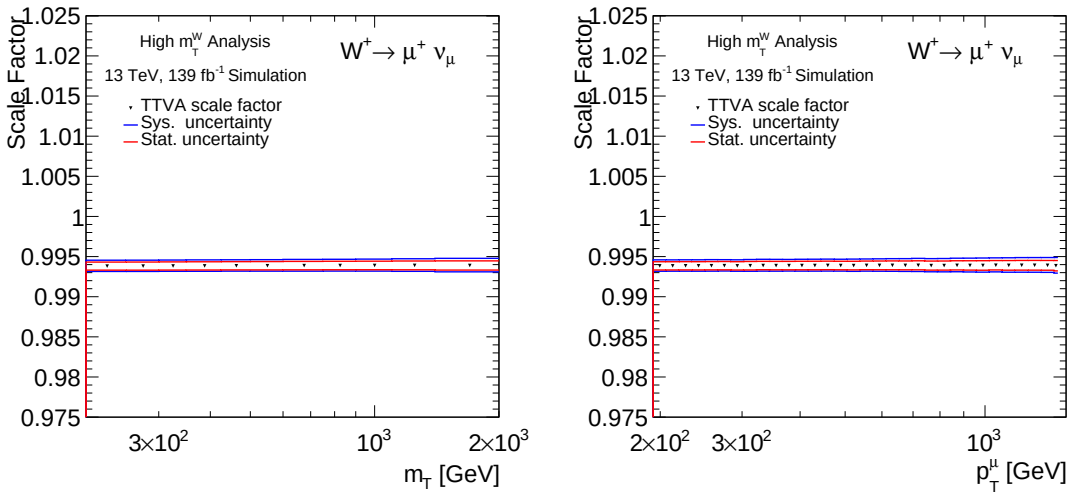

(a) (b)

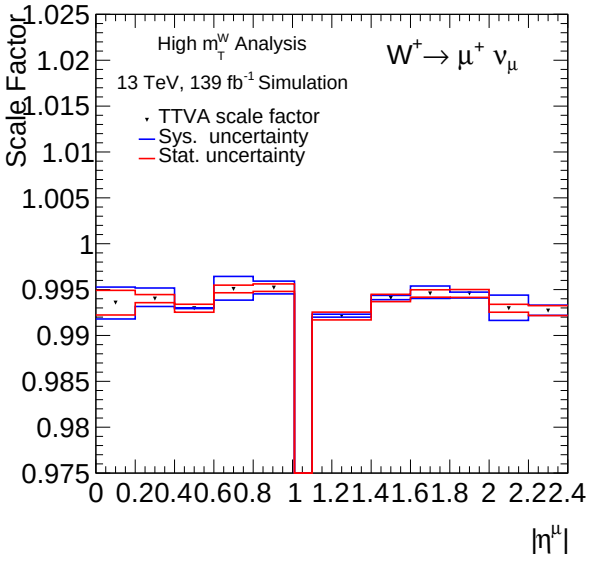

(c)

Figure B.8.: Scale Factor plots for average TTVA selection efficiency. These plots are for $W^+ \rightarrow \mu^+ \nu$ for the combination of Monte Carlo campaigns, MC16a, MC16d, MC16e. The plots show average isolation scale factors as a function of transverse mass m_T (a), p_T^μ (b) and $|\eta^\mu|$ (c). The individual systematics and statistical for one standard deviation are shown in blue and red.

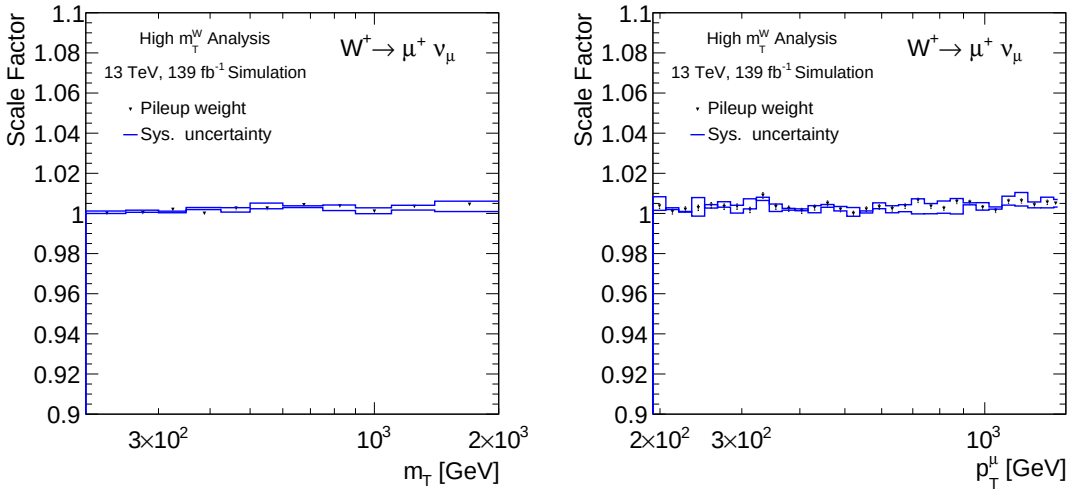

(a) (b)

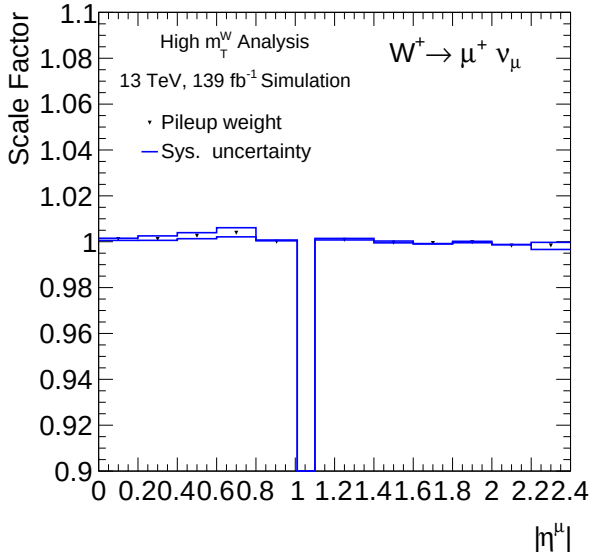

(c)

Figure B.9.: Plots for average pileup weight. These plots are for $W^+ \rightarrow \mu^+\nu$ for the combination of Monte Carlo campaigns, MC16a, MC16d, MC16e. The plots show average pileup weight as a function of transverse mass m_T (a), p_T^μ (b) and $|\eta^\mu|$ (c). The individual systematics and statistical for one standard deviation are shown in blue and red.

C. Appendix: Multijet Background Estimation

The multijet background estimation is detailed in Chapter 7. The matrix method is used in the calculation of this background, which involves determining the real and fake muon efficiencies. In this section, the real and fake efficiencies for the MC16a and MC16d Monte Carlo campaigns are shown. The MC16e campaign has been displayed in Section 7. The real efficiency was calculated using the selections detailed in Section 7.3.1, and the fake efficiency was calculated using the selections detailed in Section 7.3.2. The multijet background estimation was carried out individually for each Monte Carlo campaign and then combined to give the final estimation for the Run-2 (139 fb^{-1}). The final multijet background estimation is shown in Section 7.4. The real and fake efficiencies are binned three-dimensionally in $p_{\mathrm{T}}, |\eta|$ and $\Delta\Phi(\mu, E_{\mathrm{T}}^{\mathrm{miss}})$. Each figure shows a different $\Delta\Phi(\mu, E_{\mathrm{T}}^{\mathrm{miss}})$ region. The red line shows the $0 < |\eta| < 1.05$, the blue line shows the $1.05 < |\eta| < 1.7$, and the green line shows the $1.7 < |\eta| < 2.4$.

C.1. Real Efficiency

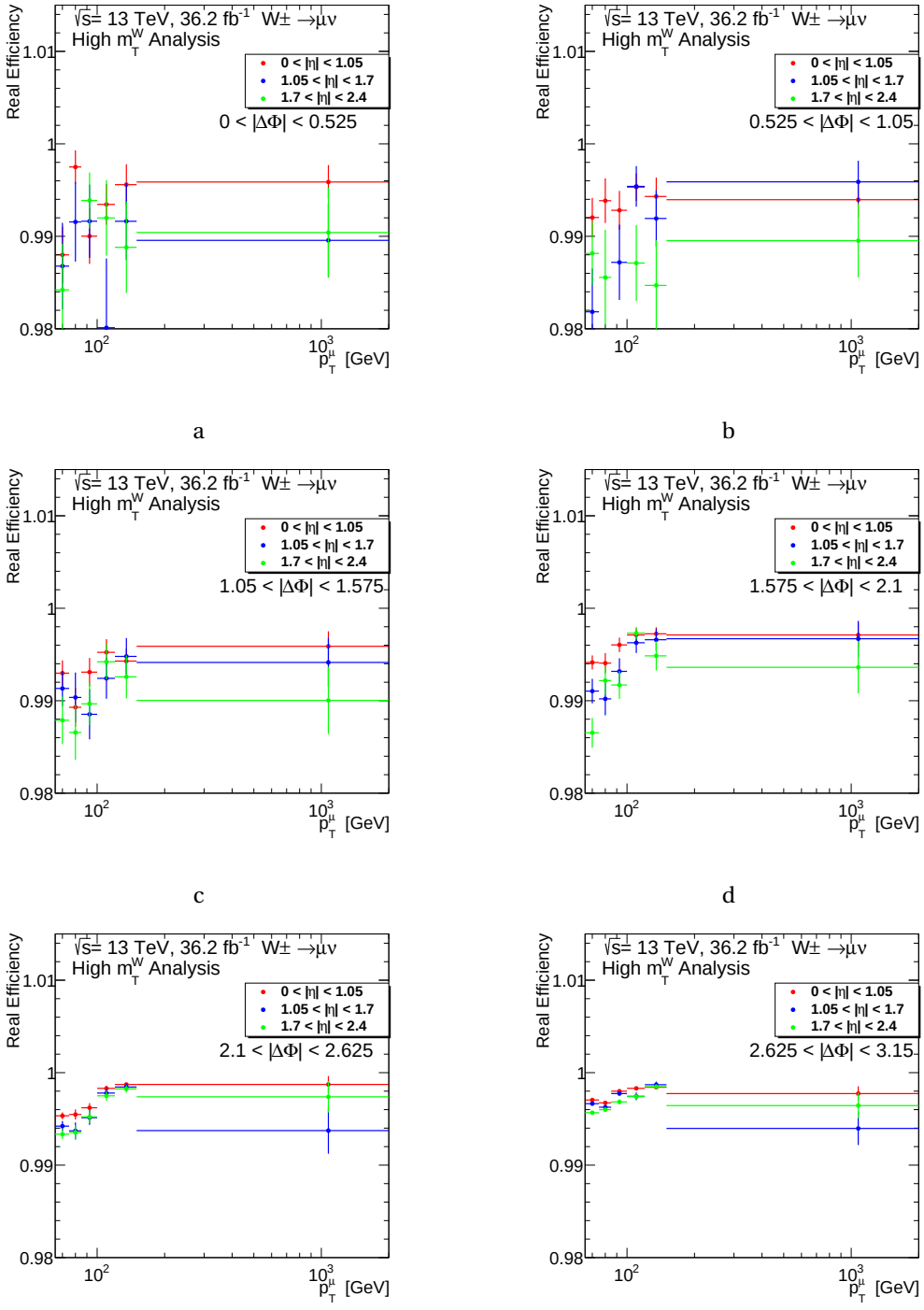

Figure C.1.: The real muon efficiency for the calculation of the matrix method for MC16a. The real efficiency has been binned three-dimensionally in $p_{\mathrm{T}}, |\eta|$ and $\Delta\Phi\left(\mu, E_{\mathrm{T}}^{\mathrm{miss}}\right)$. Each figure shows a different $\Delta\Phi\left(\mu, E_{\mathrm{T}}^{\mathrm{miss}}\right)$ region. The red line shows the $0 < |\eta| < 1.05$, the blue line shows the $1.05 < |\eta| < 1.7$ and the green line the $1.7 < |\eta| < 2.4$.

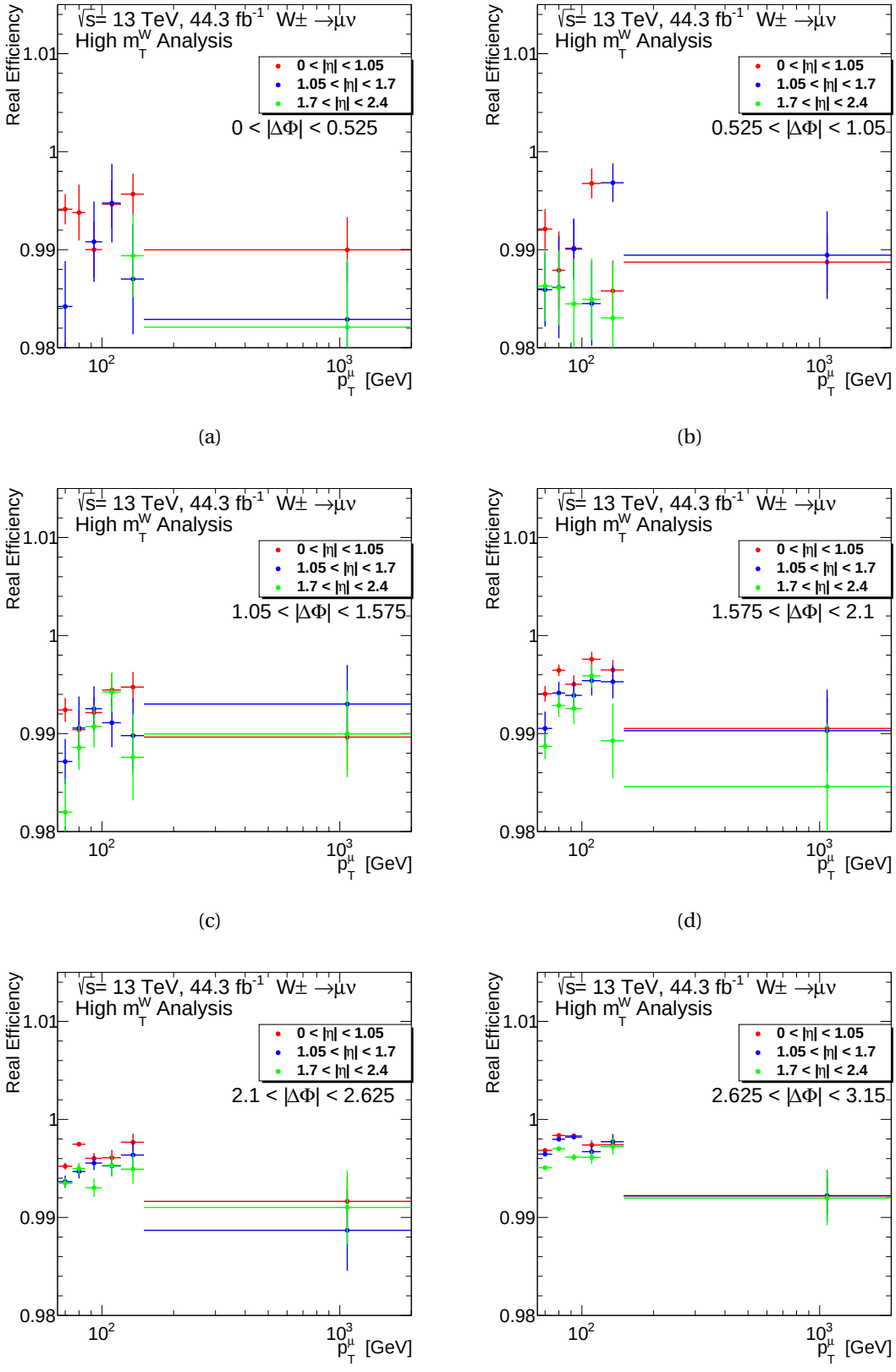

Figure C.2.: The real muon efficiency for the calculation of the matrix method for MC16d. The real efficiency has been binned three-dimensionally in $p_{\mathrm{T}}, |\eta|$ and $\Delta\Phi\left(\mu, E_{\mathrm{T}}^{\mathrm{miss}}\right)$. Each figure shows a different $\Delta\Phi\left(\mu, E_{\mathrm{T}}^{\mathrm{miss}}\right)$ region. The red line shows the $0 < |\eta| < 1.05$, the blue line shows the $1.05 < |\eta| < 1.7$ and the green line the $1.7 < |\eta| < 2.4$.

C.2. Fake Efficiency

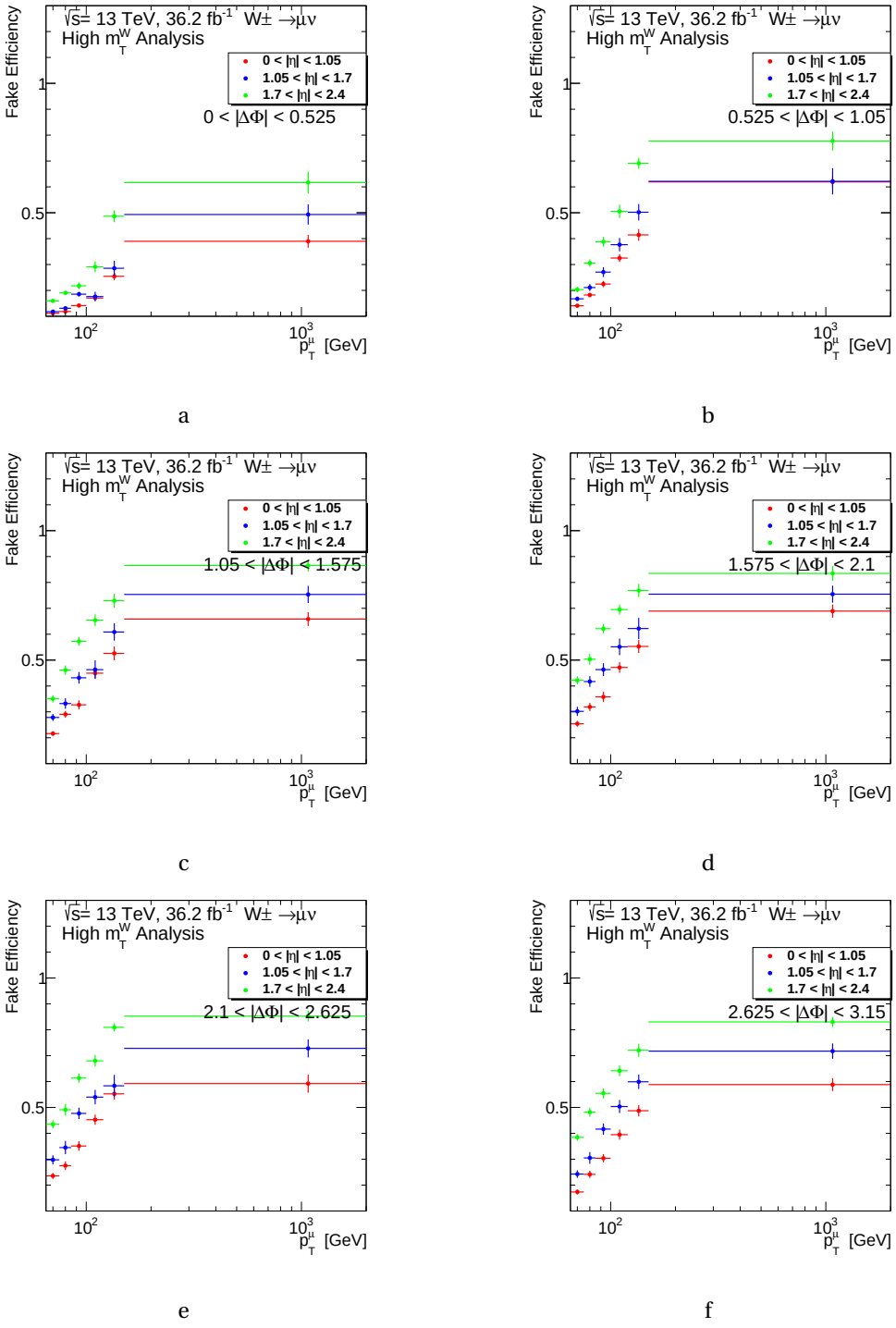

Figure C.3.: The fake muon efficiency for the calculation of the matrix method for MC16a. The fake efficiency has been binned three-dimensionally in $p_{\mathrm{T}}, |\eta|$ and $\Delta\Phi\left(\mu, E_{\mathrm{T}}^{\mathrm{miss}}\right)$. Each figure shows a different $\Delta\Phi\left(\mu, E_{\mathrm{T}}^{\mathrm{miss}}\right)$ region. The red line shows the $0 < |\eta| < 1.05$, the blue line shows the $1.05 < |\eta| < 1.7$ and the green line the $1.7 < |\eta| < 2.4$.

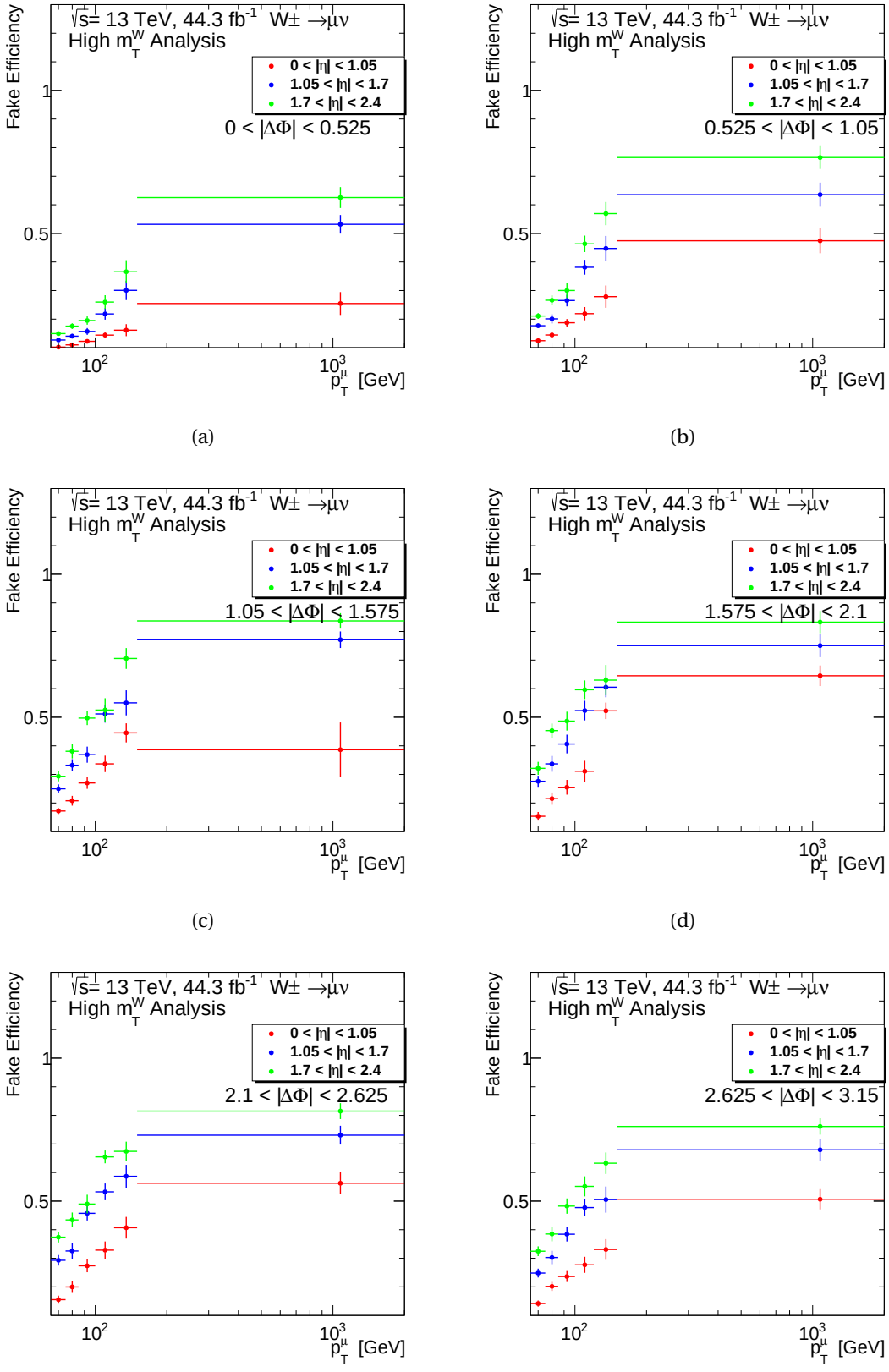

Figure C.4.: The fake muon efficiency for the calculation of the matrix method for MC16d. The fake efficiency has been binned three-dimensionally in $p_{\mathrm{T}}, |\eta|$ and $\Delta\Phi\left(\mu, E_{\mathrm{T}}^{\mathrm{miss}}\right)$. Each figure shows a different $\Delta\Phi\left(\mu, E_{\mathrm{T}}^{\mathrm{miss}}\right)$ region. The red line shows the $0 < |\eta| < 1.05$, the blue line shows the $1.05 < |\eta| < 1.7$ and the green line the $1.7 < |\eta| < 2.4$.

D. Appendix: Systematic Uncertainties

D.1. Individual Cross-Section Systematic Uncertainties

The systematic uncertainties have been discussed in Chapter 8. The following distributions are for the individual experimental systematic uncertainties for the cross-section measurement and are calculated using Equation 10.1. The uncertainties are shown for the W^+ and W^- bosons separately. The uncertainties are shown for the muon, sagitta and missing energy uncertainties in Figures D.1 for W^+ and D.4 for W^-. The uncertainties are shown for the scale factor identification, isolation, pile-up, trigger, TTVA and jet uncertainties in Figures D.2 for W^+ and D.5 for W^-. The uncertainties are shown for more jet uncertainties in Figures D.3 for W^+ and D.6 for W^-. The largest systematic is the muon resolution sagitta bias, up to 8% for W^+ and 16% for W^-.

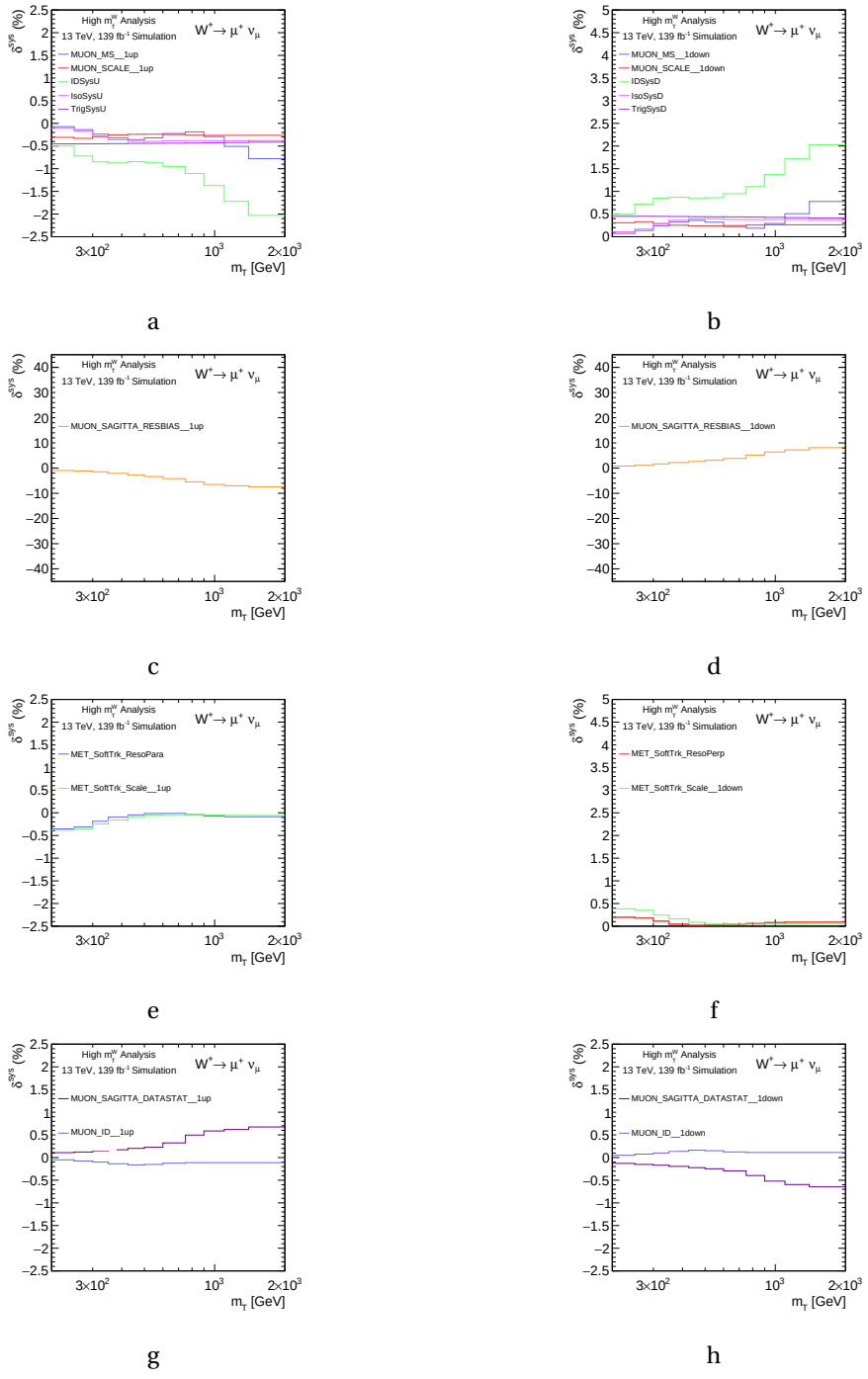

Figure D.1.: Individual contributions to the cross-section systematic variations in Run-2 for $W^+ \to \mu^+ \nu$ in the measurement binning for m_T. The plots on the left show the up variations and those on the right show the down variations. All values are presented in percentages. Plots (a) and (b) show the muon scale and resolution uncertainties along with the muon scale identification, isolation and trigger scale factor uncertainties. Plots (c) and (d) display the muon sagitta resolution bias uncertainty. Plots (e) and (f) show the missing energy soft track uncertainties. The labels in the legend of both plots are the conventional names given by the JetEtMiss group. "MET" stands for missing energy, "SofTrk" refers to soft track E_T^{miss} and “ResoPara” and “ResoPerp” refers to the resolution uncertainty on the parallel and perpendicular component. Plots (g) and (h) display the muon sagitta data statistical and muon identification uncertainty.

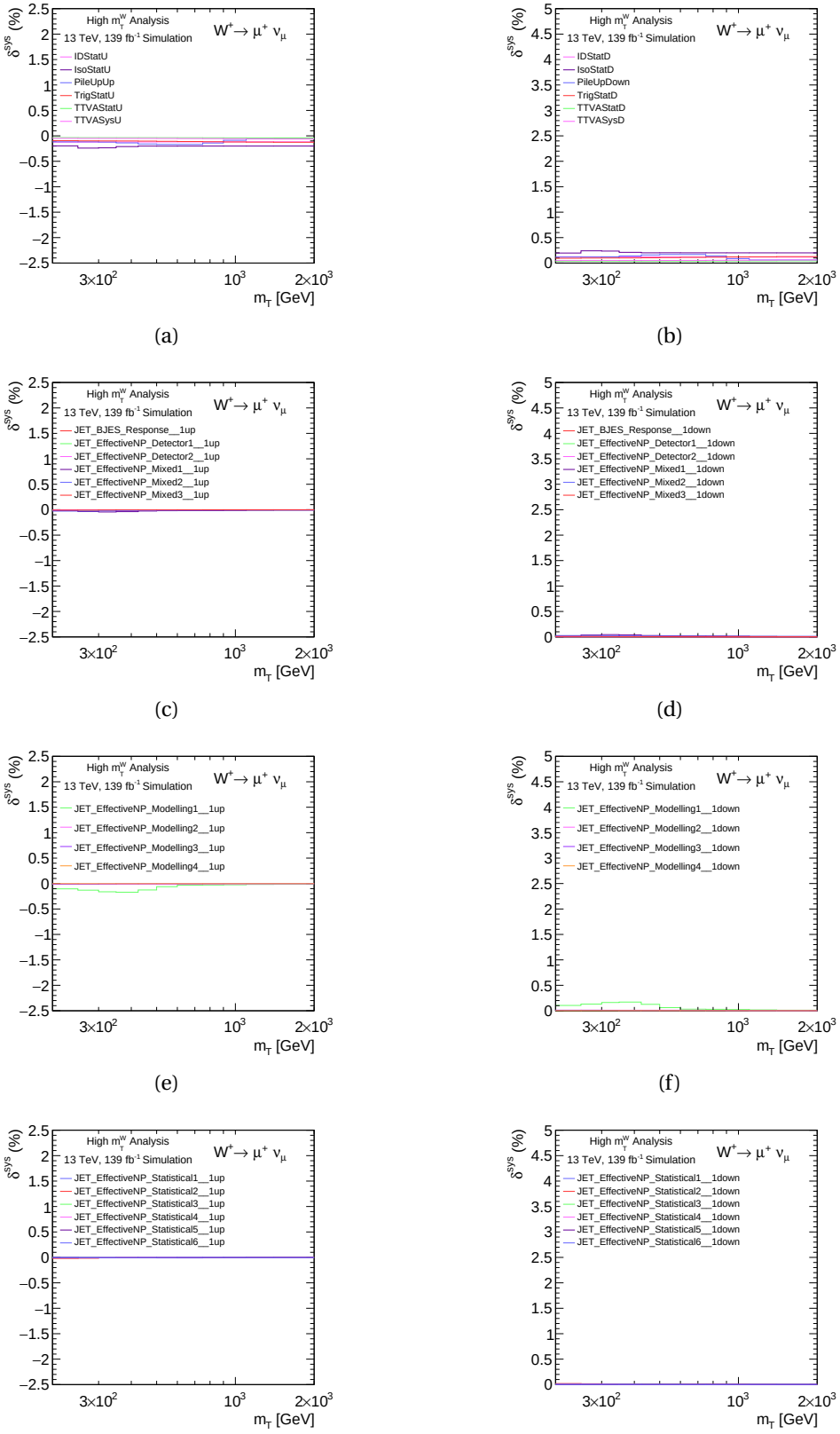

Figure D.2.: Individual contributions to the cross-section systematic variations in Run-2 for $W^+ \to \mu^+\nu$ in the measurement binning for m_T. The plots on the left show the up variations and those on the right show the down variations. All values are presented in percentages. Plots (a) and (b) show the scale factor uncertainties for the muon identification, isolation, trigger and TTVA statistical uncertainties. Also shows the TTVA systematic uncertainty and the pileup uncertainty. Plots (c) to (h) display the effect of the jet's systematic uncertainties.

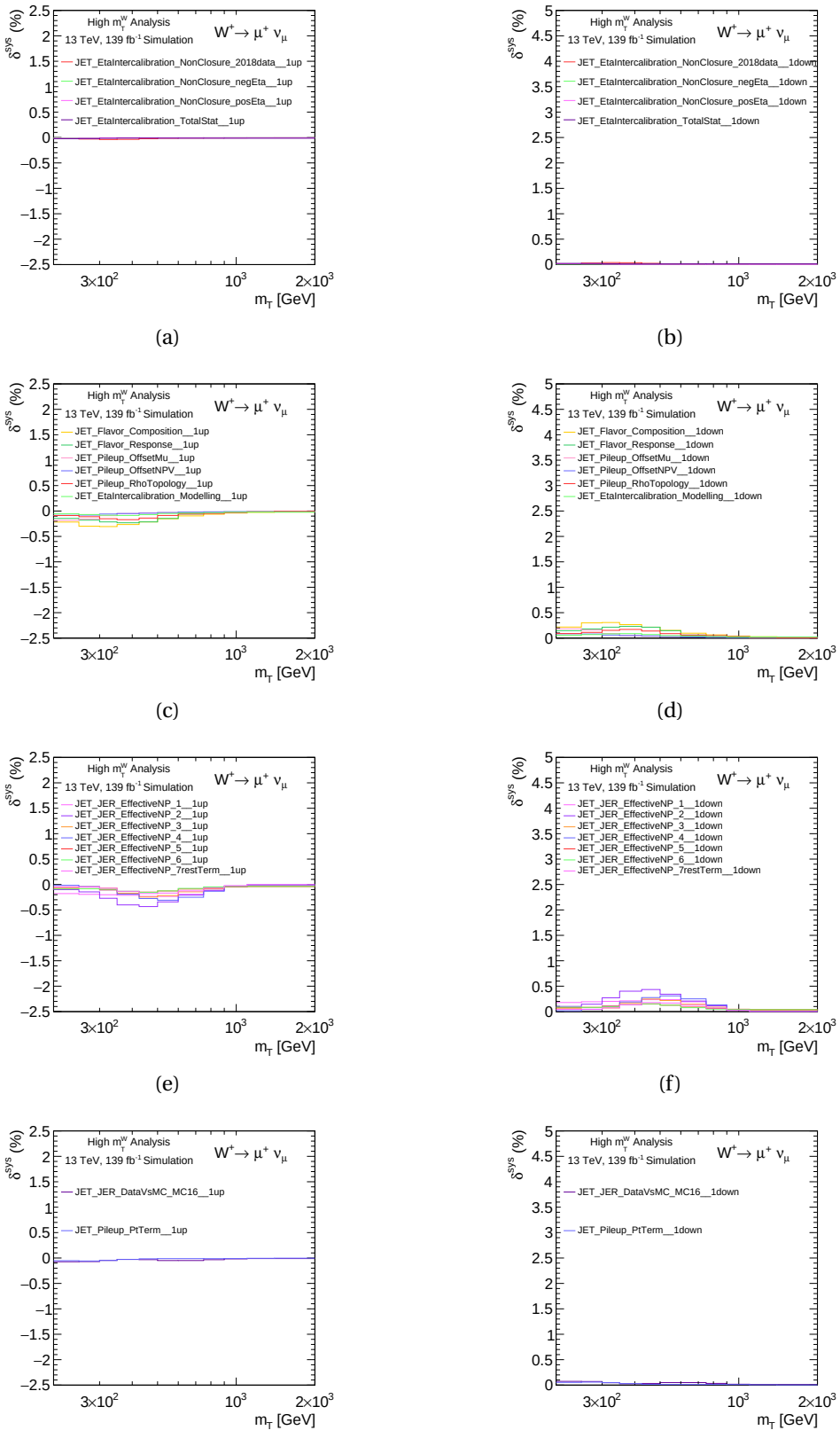

Figure D.3.: Individual contributions to the cross-section systematic variations in Run-2 for $W^+ \to \mu^+ \nu$ in the measurement binning for m_T. The plots on the left show the up variations and those on the right show the down variations. All values are presented in percentages. Plots (a) to (h) display the effect of the jet's systematic uncertainties.

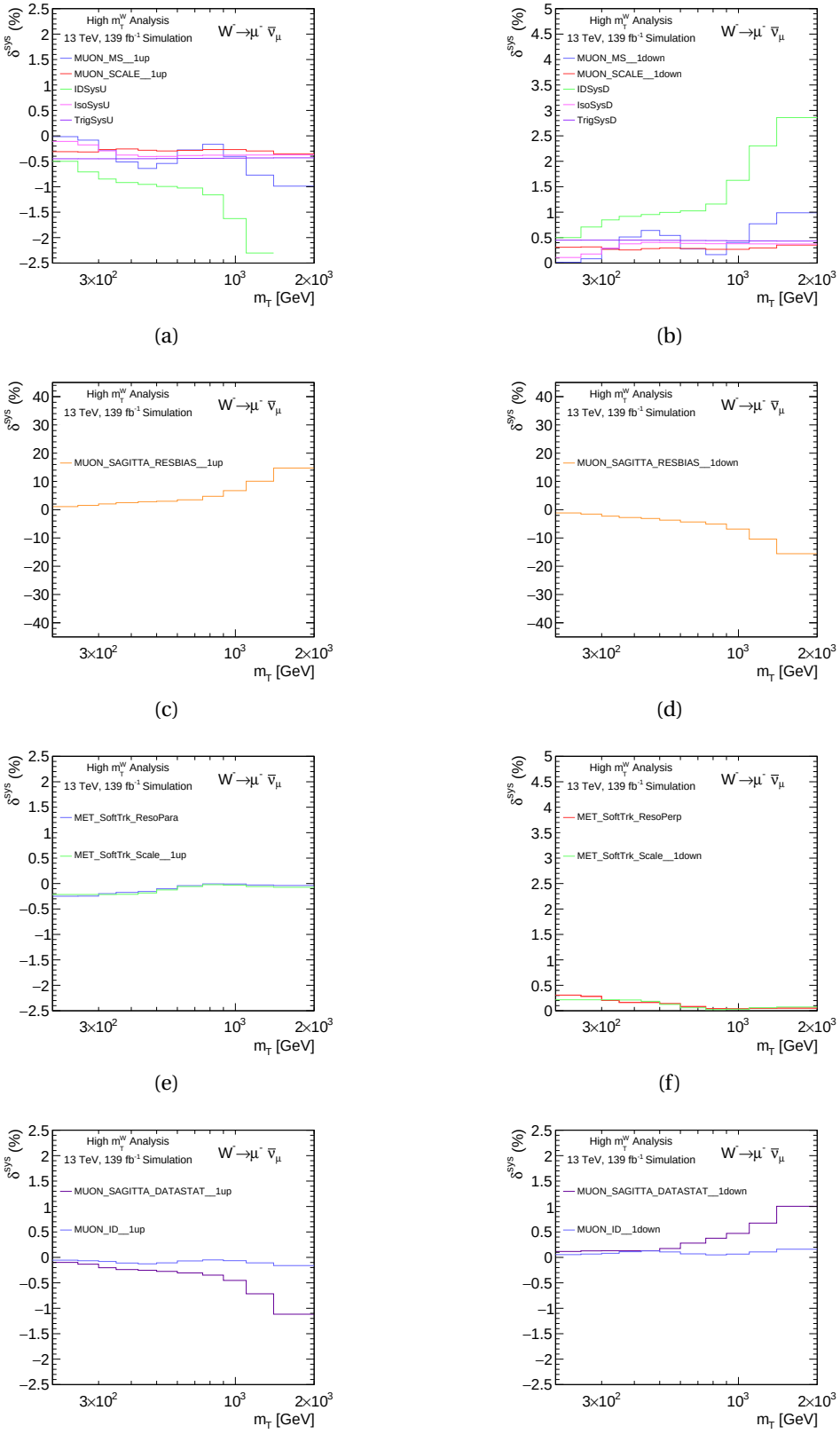

Figure D.4.: Individual contributions to the cross-section systematic variations in Run-2 for $W^- \to \mu^- \bar{\nu}$ in the measurement binning for m_T. The plots on the left show the up variations and those on the right show the down variations. All values are presented in percentages. Plots (a) and (b) show the muon scale and resolution uncertainties along with the muon scale identification, isolation and trigger scale factor uncertainties. Plots (c) and (d) display the muon sagitta resolution bias uncertainty. Plots (e) and (f) show the missing energy soft track uncertainties. The labels in the legend of both plots are the conventional names given by the JetEtMiss group. "MET" stands for missing energy, "SofTrk" refers to soft track E_T^{miss} and “ResoPara” and “ResoPerp” refers to the resolution uncertainty on the parallel and perpendicular component. Plots (g) and (h) display the muon sagitta data statistical and muon identification uncertainty.

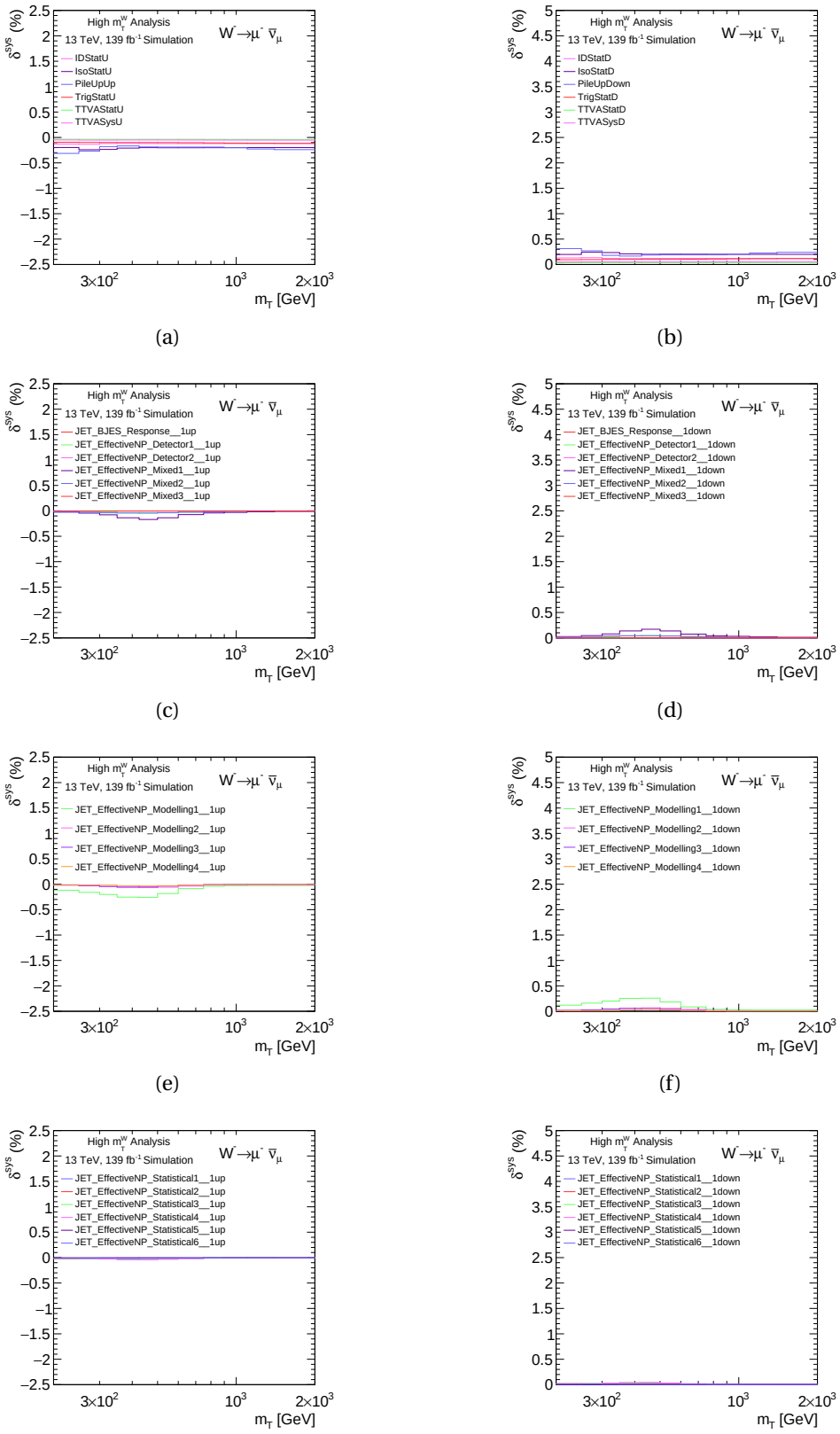

Figure D.5.: Individual contributions to the cross-section systematic variations in Run-2 for $W^- \to \mu^- \bar{\nu}$ in the measurement binning for m_T. The plots on the left show the up variations and those on the right show the down variations. All values are presented in percentages. Plots (a) and (b) show the scale factor uncertainties for the muon identification, isolation, trigger and TTVA statistical uncertainties. Also shown are the TTVA systematic uncertainty and the pileup uncertainty. Plots (c) to (h) display the effect of the jet's systematic uncertainties.

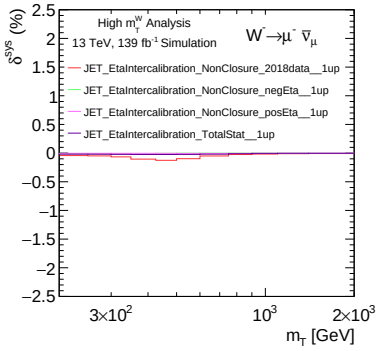

(a)

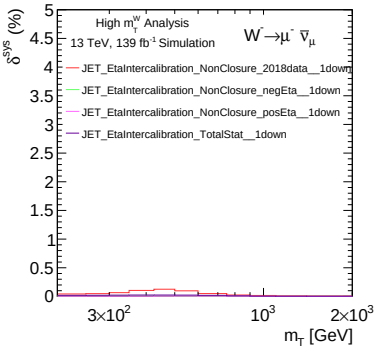

(b)

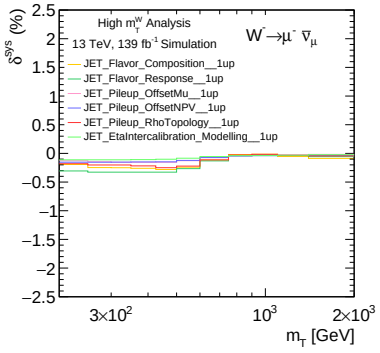

(c)

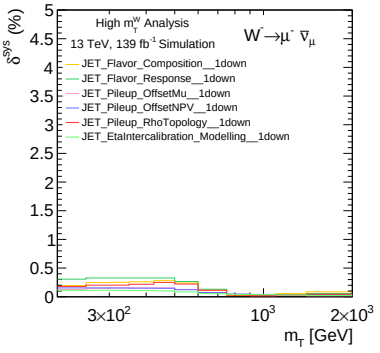

(d)

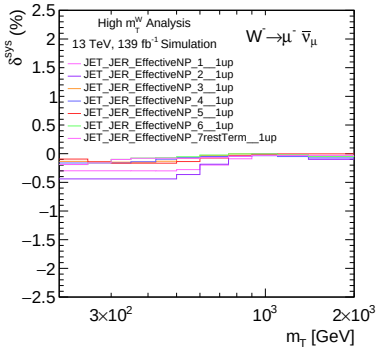

(e)

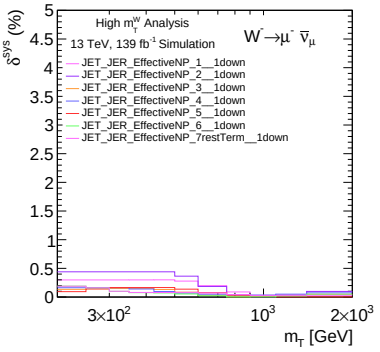

(f)

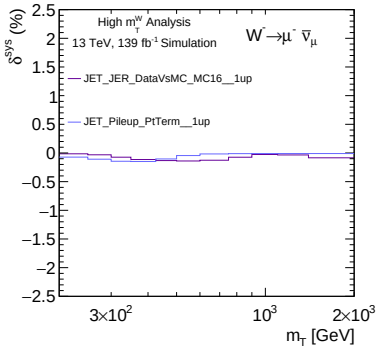

(g)

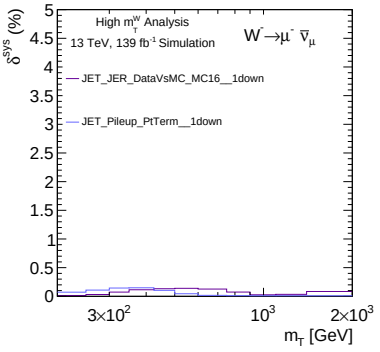

(h)

Figure D.6.: Individual contributions to the cross-section systematic variations in Run-2 for $W^- \to \mu^- \bar{\nu}$ in the measurement binning for m_T. The plots on the left show the up variations and those on the right show the down variations. All values are presented in percentages. Plots (a) to (h) display the effect of the jet's systematic uncertainties.

D.2. Individual Asymmetry Systematic Uncertainties

The systematic uncertainties have been discussed in Chapter 8. Distributions showing each individual experimental systematic uncertainty considered for this measurement are included in this section. The following distributions are for the experimental systematic uncertainties for the asymmertry measurement and are calculated using Equation 10.2. The uncertainties are shown for the W^+ and W^- bosons separately. The uncertainties are shown for the muon, sagitta and missing energy uncertainties in Figures D.7. The uncertainties are shown for the scale factor identification, isolation, pile-up, trigger, TTVA and jet uncertainties in Figures D.8. The uncertainties are shown for more jet uncertainties in Figures D.9. The largest systematic is the muon resolution sagitta bias, up to 35%.

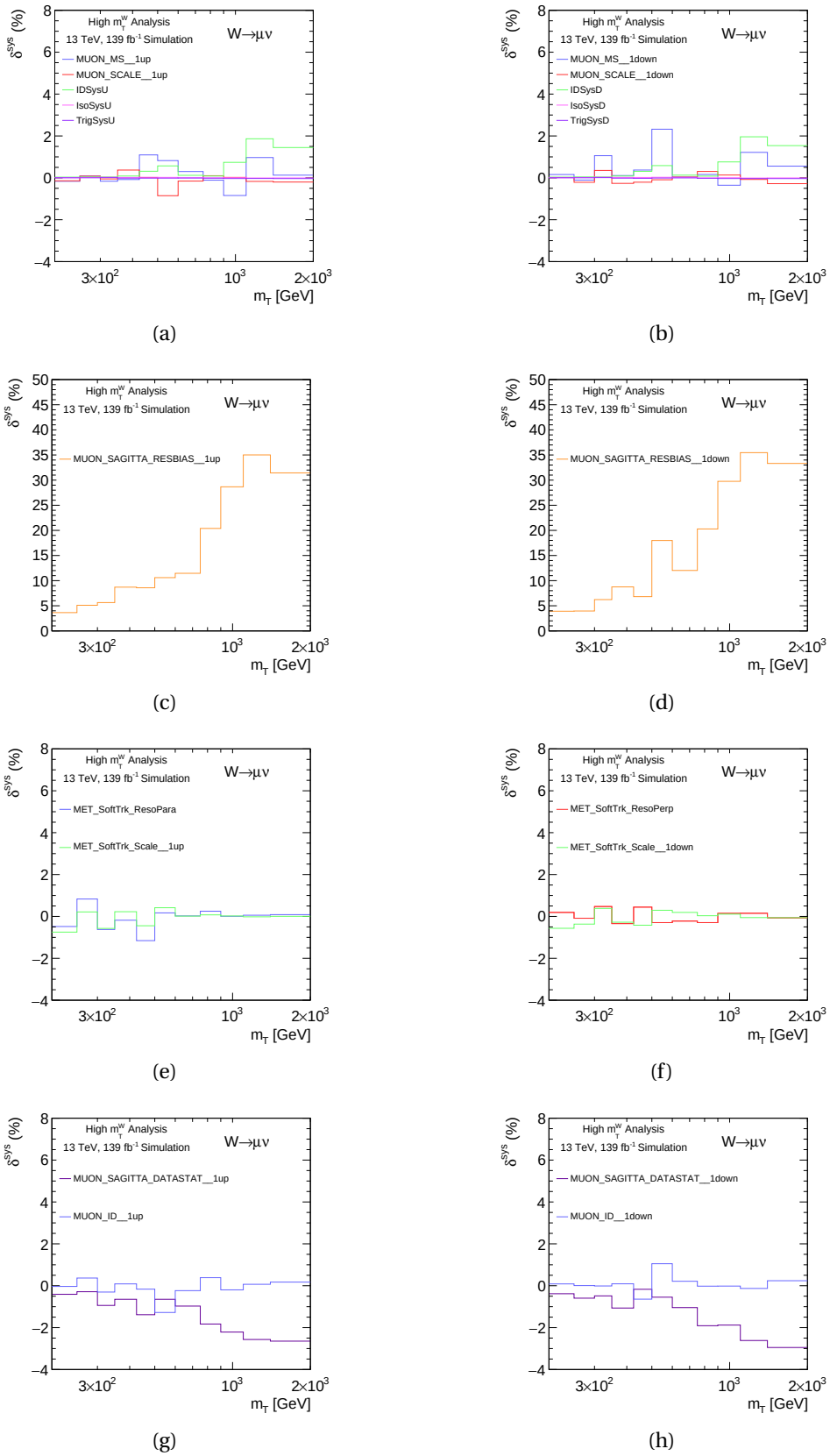

Figure D.7.: Individual contributions to the muon asymmetry systematic variations in Run-2 for $W \to \mu\nu$ in the measurement binning for m_T. The plots on the left show the up variations and those on the right show the down variations. All values are presented in percentages. Plots (a) and (b) show the muon scale and resolution uncertainties along with the muon scale identification, isolation and trigger scale factor uncertainties. Plots (c) and (d) display the muon sagitta resolution bias uncertainty. Plots (e) and (f) show the missing energy soft track uncertainties. The labels in the legend of both plots are the conventional names given by the JetEtMiss group. "MET" stands for missing energy, "SofTrk" refers to soft track E_T^{miss} and "ResoPara" and "ResoPerp" refers to the resolution uncertainty on the parallel and perpendicular component. Plots (g) and (h) display the muon sagitta data statistical and muon identification uncertainty.

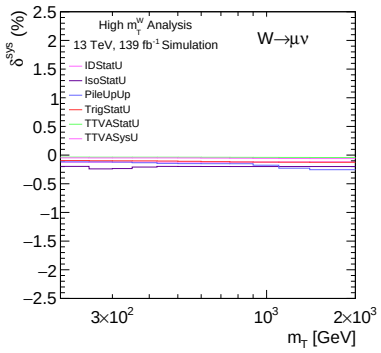

(a)

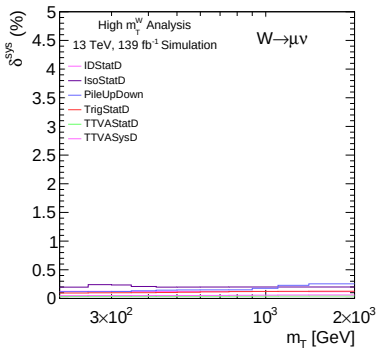

(b)

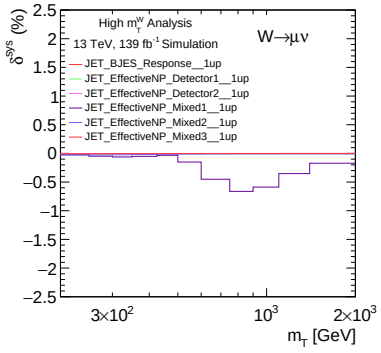

(c)

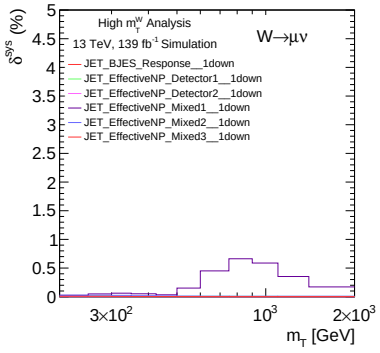

(d)

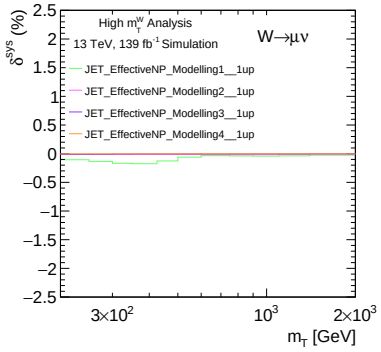

(e)

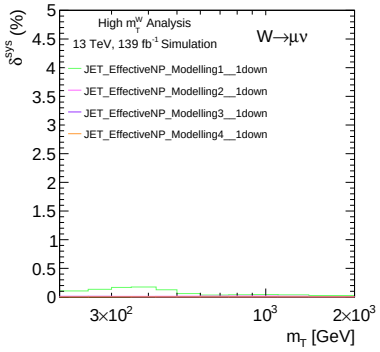

(f)

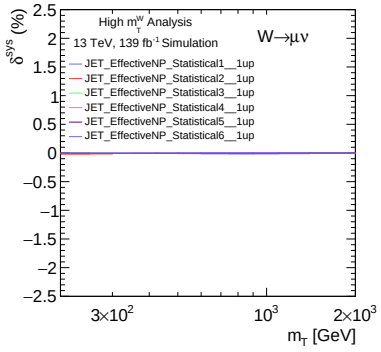

(g)

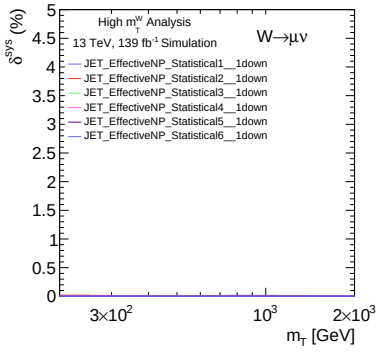

(h)

Figure D.8.: Individual contributions to the asymmetry systematic variations in Run-2 for $W \to \mu\nu$ in the measurement binning for m_T. The plots on the left show the up variations and those on the right show the down variations. All values are presented in percentages. Plots (a) and (b) show the scale factor uncertainties for the muon identification, isolation, trigger and TTVA statistical uncertainties. Also shown are the TTVA systematic uncertainty and the pileup uncertainty. Plots (c) to (h) display the effect of the jet's systematic uncertainties.

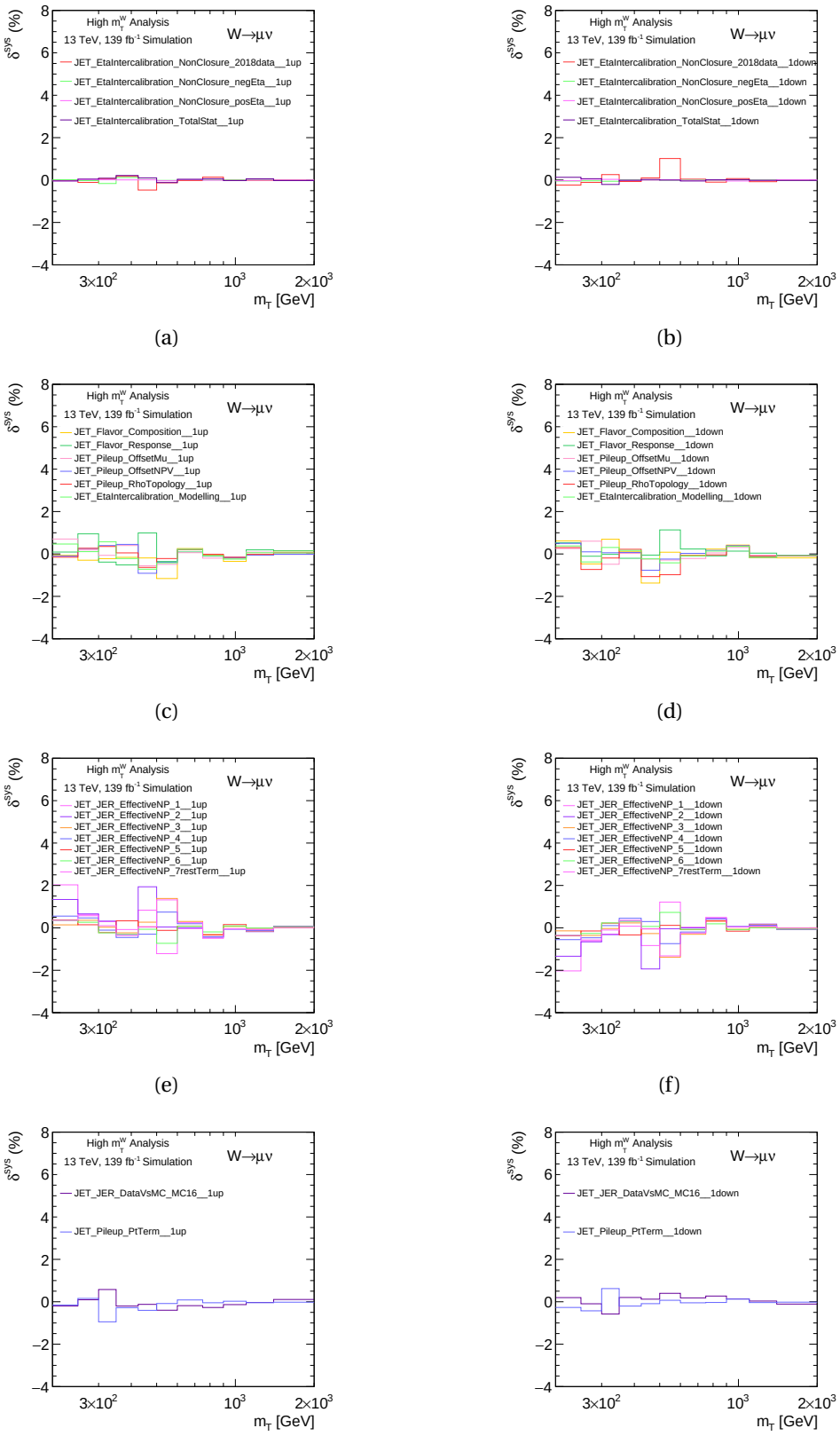

Figure D.9.: Individual contributions to the muon asymmetry systematic variations in Run-2 for $W \to \mu\nu$ in the measurement binning for m_T. The plots on the left show the up variations and those on the right show the down variations. All values are presented in percentages. Plots (a) to (h) display the effect of the jet's systematic uncertainties.

D.3. Systematic Uncertainties For Individual Monte Carlo Campaigns

The systematic uncertainties have been discussed in Chapter 8. The following distributions are of the systematic uncertainties for individual Monte Carlo campaigns MC16a, MC16d and MC16e. The uncertainties are shown for the W^+ and W^- bosons separately. The uncertainties are first shown for the muon, sagitta and missing energy uncertainties. Then uncertainties are shown for the scale factor identification, isolation, pile-up, trigger, TTVA and jet uncertainties. Finally, more jet systematic uncertainties are shown.

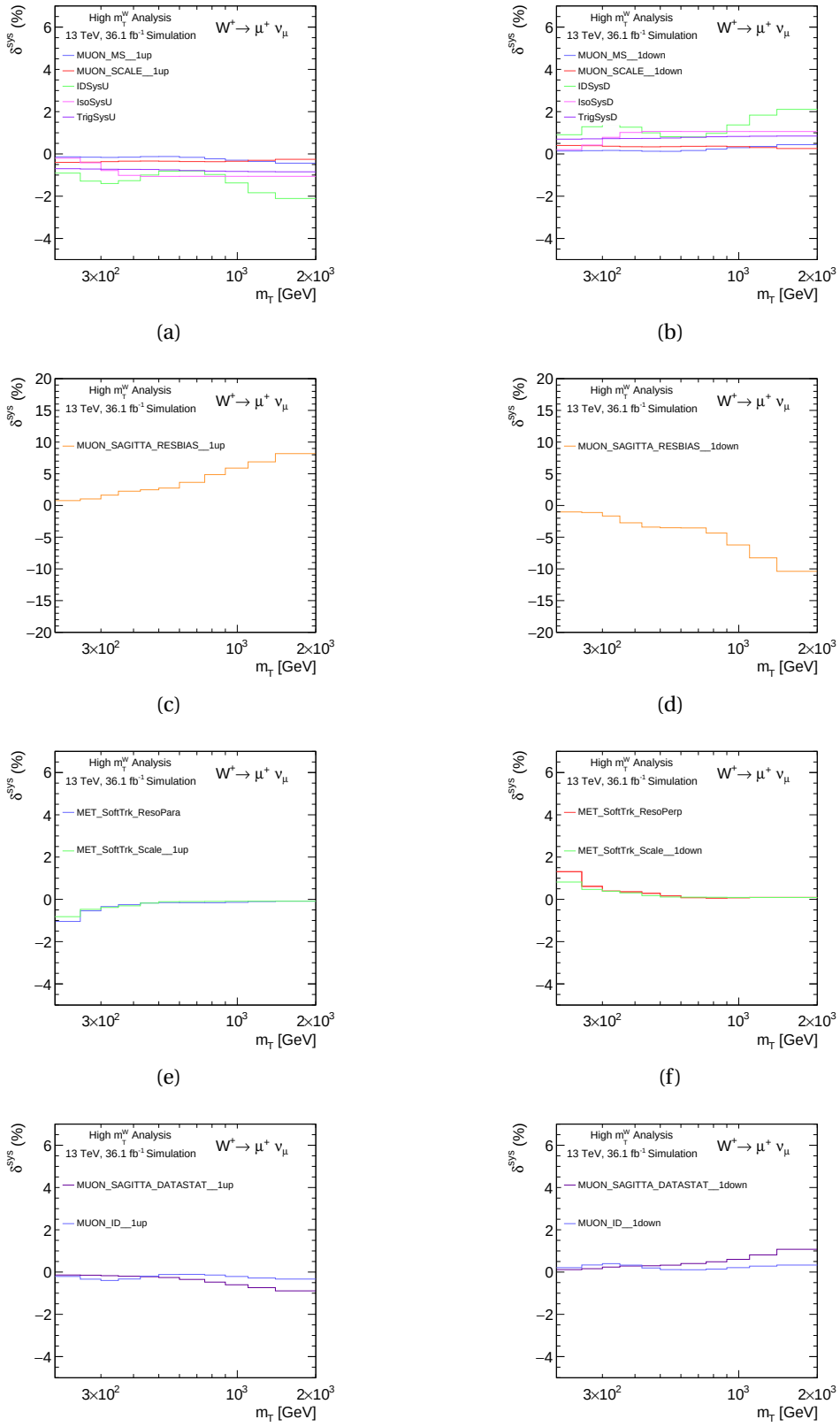

Figure D.10.: Individual contributions to the systematic variations in MC16a for $W^+ \to \mu^+\nu$ in the measurement binning for m_T. The plots on the left show the up variations and those on the right show the down variations. All values are presented in percentages. Plots (a) and (b) show the muon scale and resolution uncertainties along with the muon scale identification, isolation and trigger scale factor uncertainties. Plots (c) and (d) display the muon sagitta resolution bias uncertainty. Plots (e) and (f) show the missing energy soft track uncertainties. The labels in the legend of both plots are the conventional names given by the JetEtMiss group. "MET" stands for missing energy, "SofTrk" refers to soft track E_T^{miss} and "ResoPara" and "ResoPerp" refers to the resolution uncertainty on the parallel and perpendicular component. Plots (g) and (h) display the muon sagitta data statistical and muon identification uncertainty.

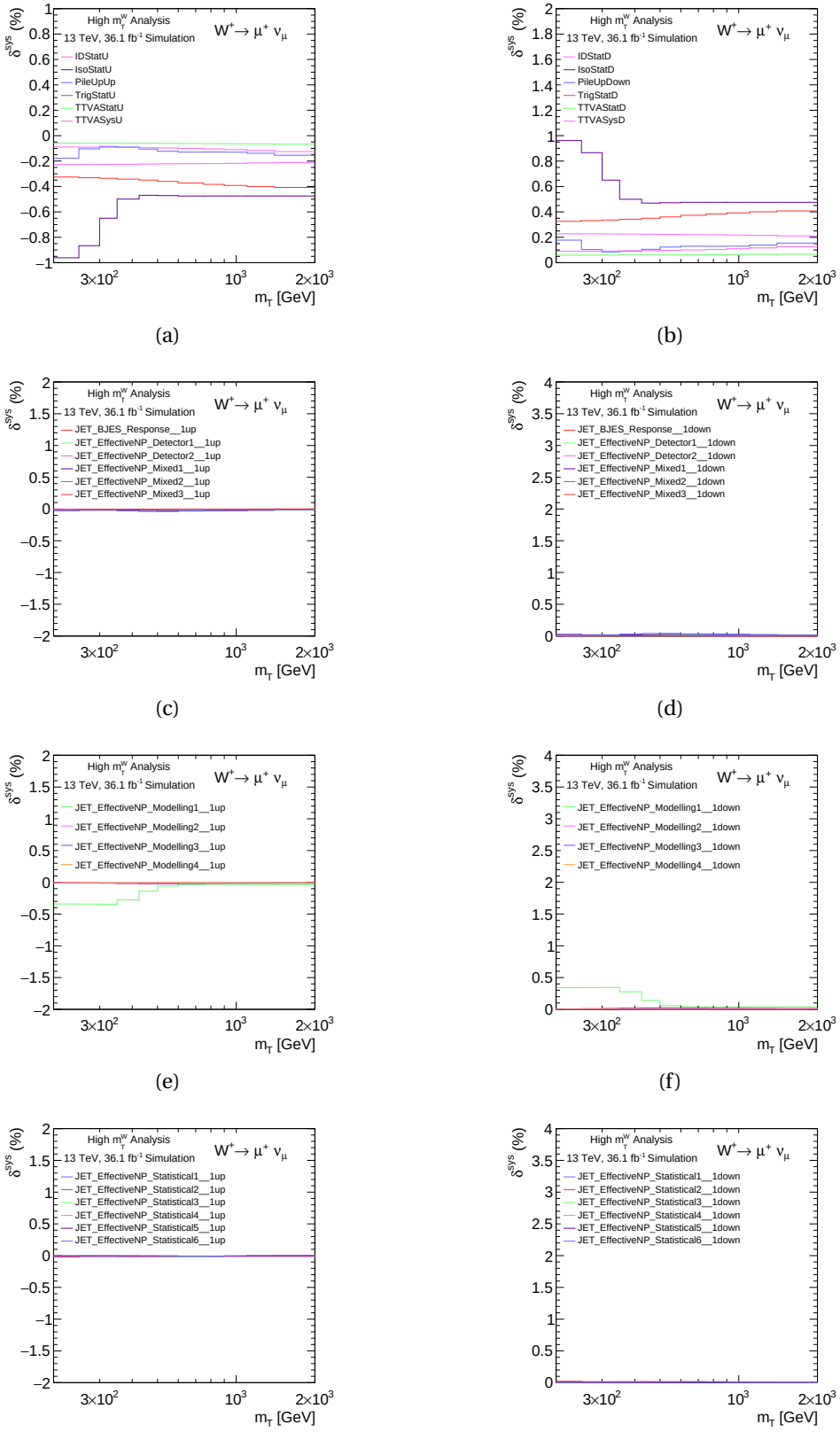

Figure D.11.: Individual contributions to the systematic variations in MC16a for $W^+ \to \mu^+ \nu$ in the measurement binning for m_T. The plots on the left show the up variations and those on the right show the down variations. All values are presented in percentages. Plots (a) and (b) show the scale factor uncertainties for the muon identification, isolation, trigger and TTVA statistical uncertainties. It also shows the TTVA systematic uncertainty and the pileup uncertainty. Plots (c) to (h) display the effect of the jet's systematic uncertainties.

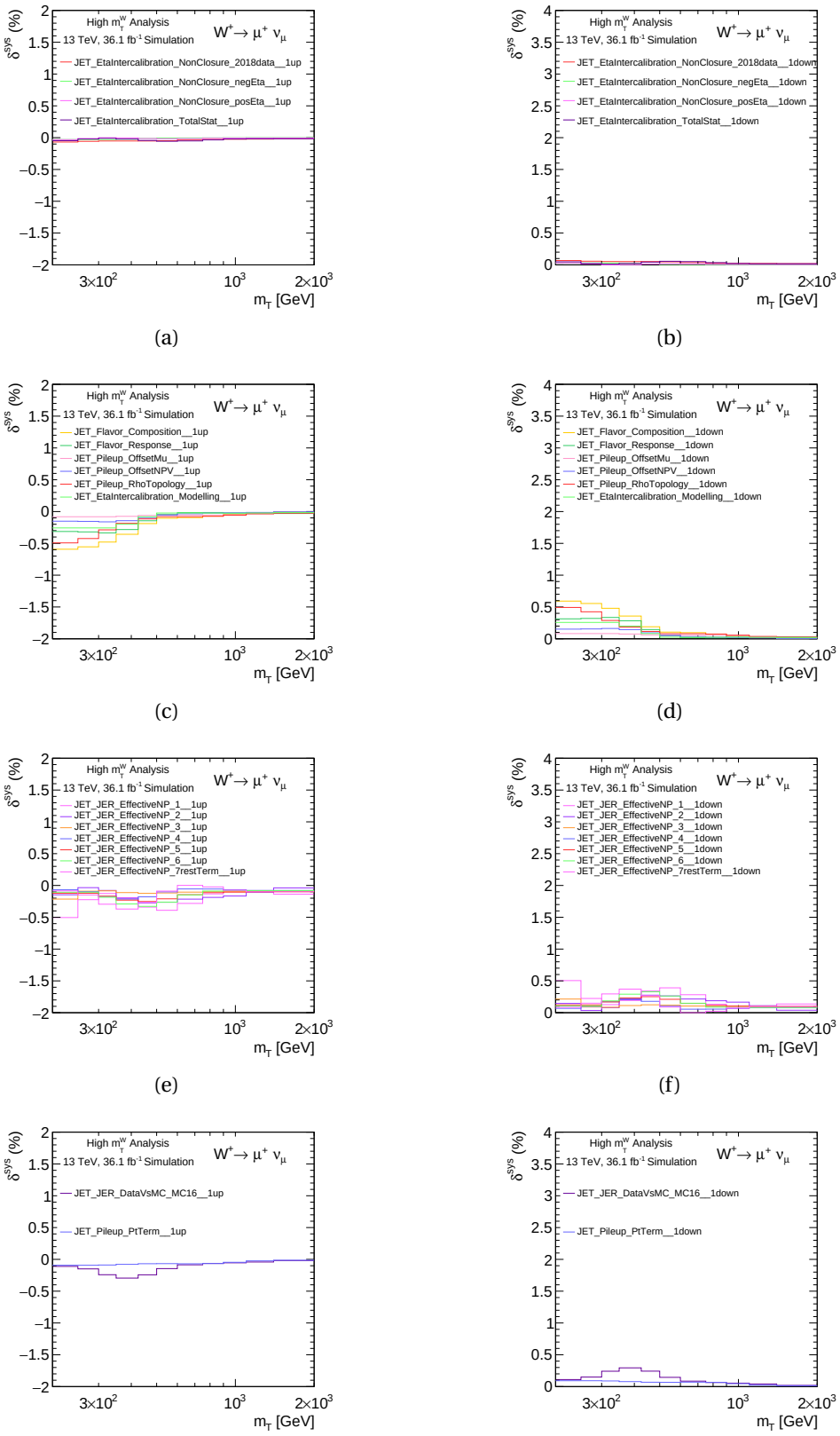

Figure D.12.: Individual contributions to the systematic variations in MC16a for $W^+ \to \mu^+\nu$ in the measurement binning for m_T. The plots on the left show the up variations and those on the right show the down variations. All values are presented in percentages. Plots (a) to (h) display the effect of the jet's systematic uncertainties.

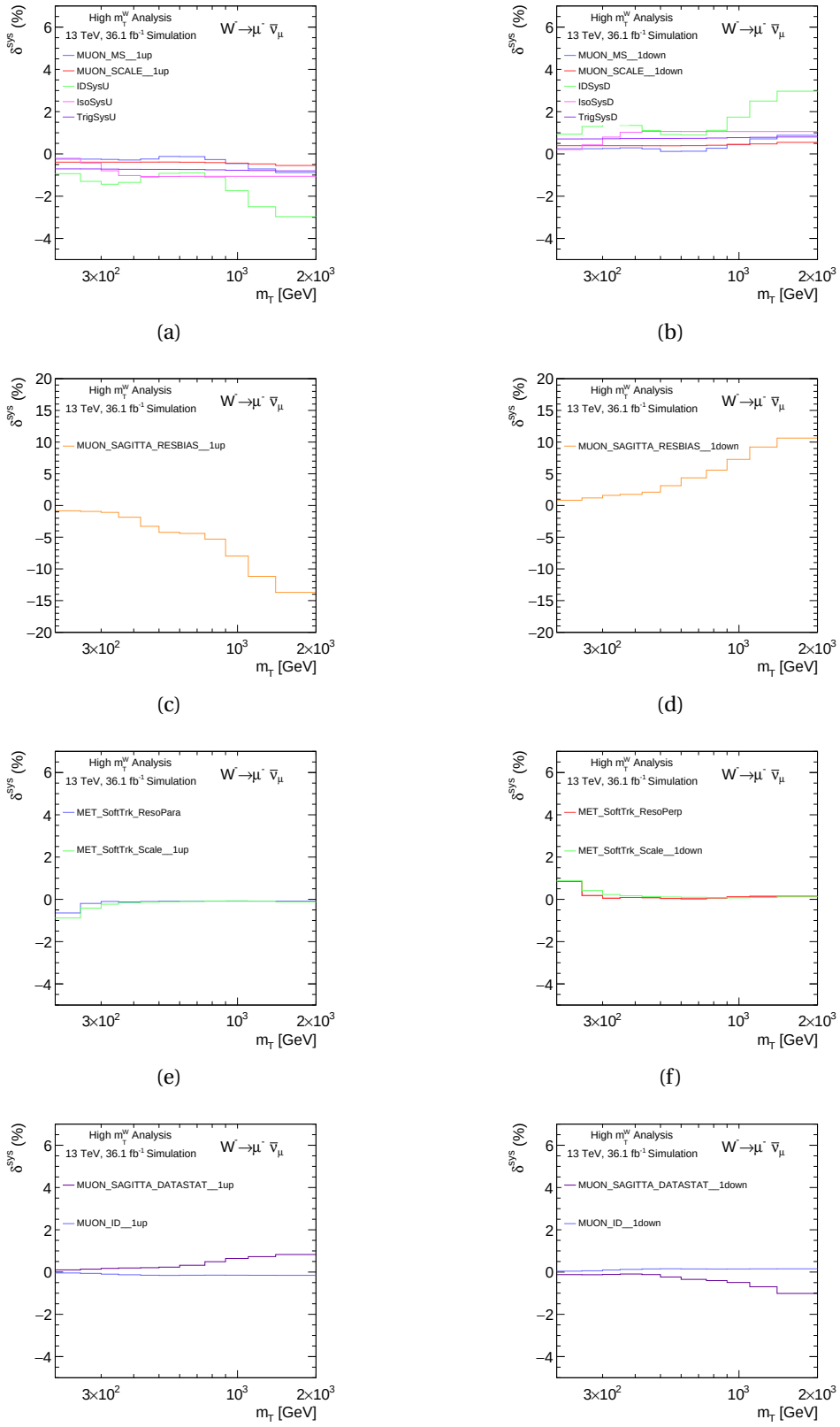

Figure D.13.: Individual contributions to the systematic variations in MC16a for $W^- \to \mu^- \bar{\nu}$ in the measurement binning for m_T. The plots on the left show the up variations and those on the right show the down variations. All values are presented in percentages. Plots (a) and (b) show the muon scale and resolution uncertainties along with the muon scale identification, isolation and trigger scale factor uncertainties. Plots (c) and (d) display the muon sagitta resolution bias uncertainty. Plots (e) and (f) show the missing energy soft track uncertainties. The labels in the legend of both plots are the conventional names given by the JetEtMiss group. "MET" stands for missing energy, "SofTrk" refers to soft track E_T^{miss} and "ResoPara" and "ResoPerp" refers to the resolution uncertainty on the parallel and perpendicular component. Plots (g) and (h) display the muon sagitta data statistical and muon identification uncertainty.

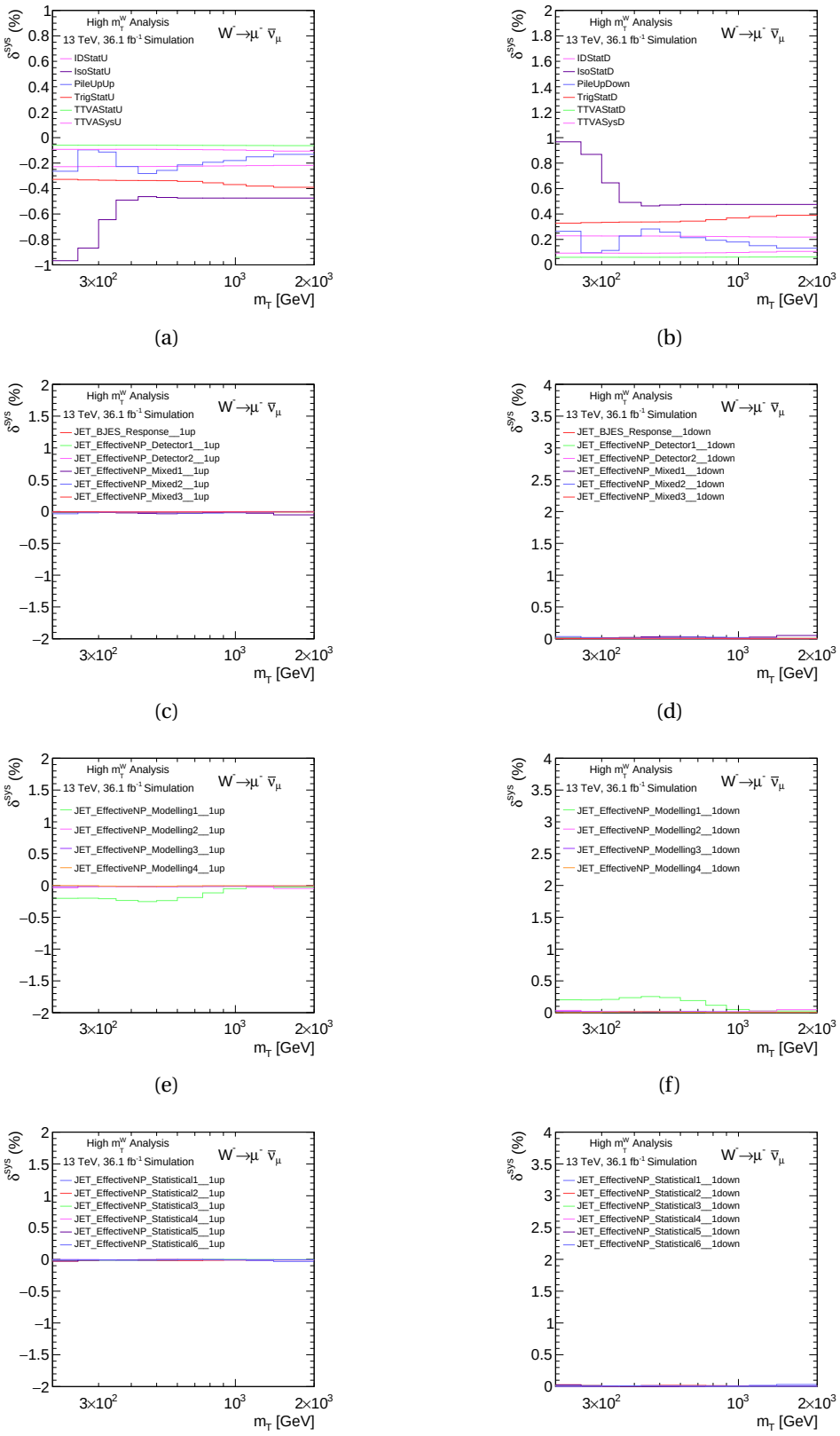

Figure D.14.: Individual contributions to the systematic variations in MC16a for $W^- \to \mu^- \bar{\nu}$ in the measurement binning for m_T. The plots on the left show the up variations and those on the right show the down variations. All values are presented in percentages. Plots (a) and (b) show the scale factor uncertainties for the muon identification, isolation, trigger and TTVA statistical uncertainties. Also shown are the TTVA systematic uncertainty and the pileup uncertainty. Plots (c) to (h) display the effect of the jet's systematic uncertainties.

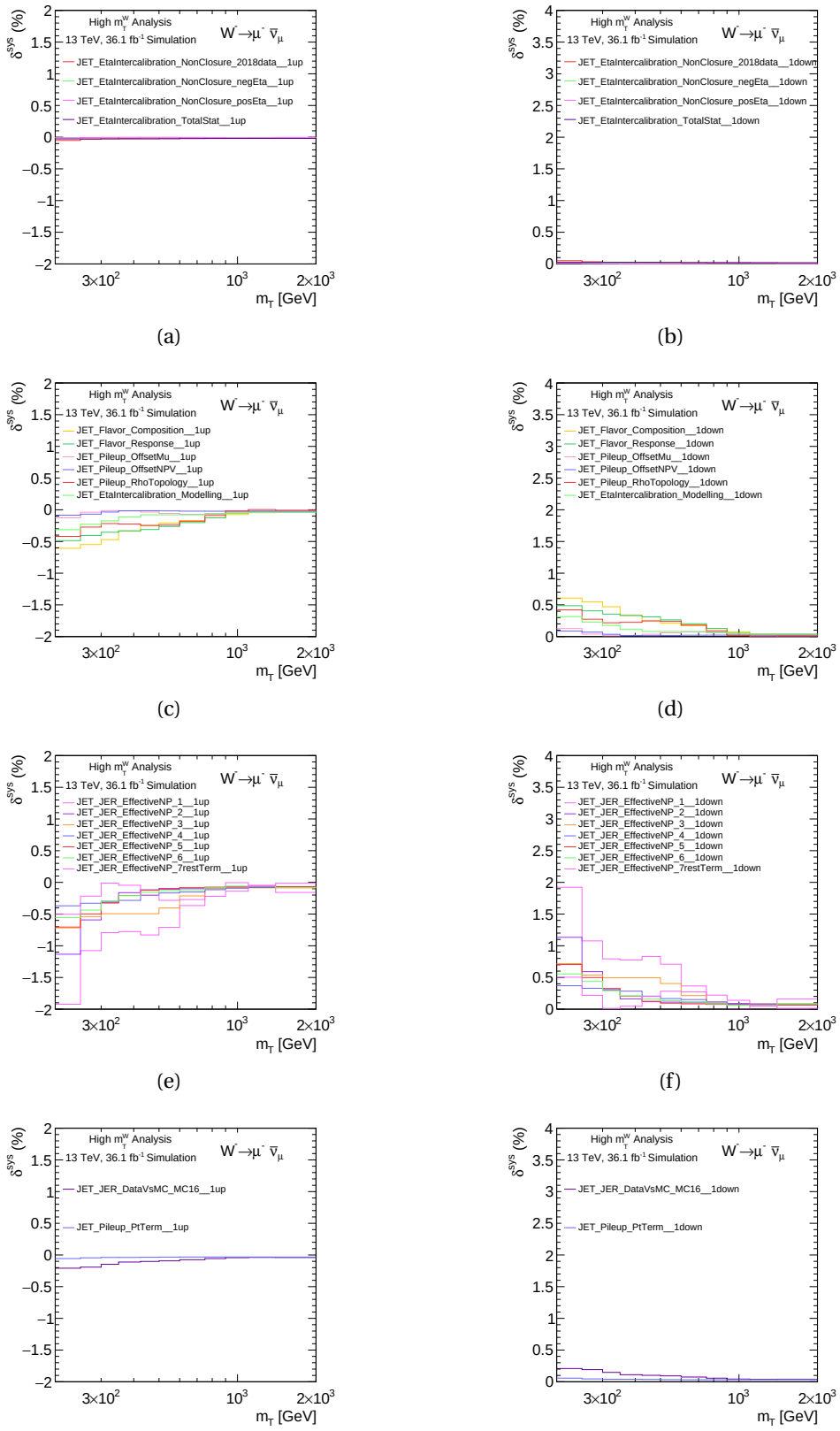

Figure D.15.: Individual contributions to the systematic variations in MC16a for $W^- \to \mu^- \bar{\nu}$ in the measurement binning for m_T. The plots on the left show the up variations and those on the right show the down variations. All values are presented in percentages. Plots (a) to (h) display the effect of the jet's systematic uncertainties.

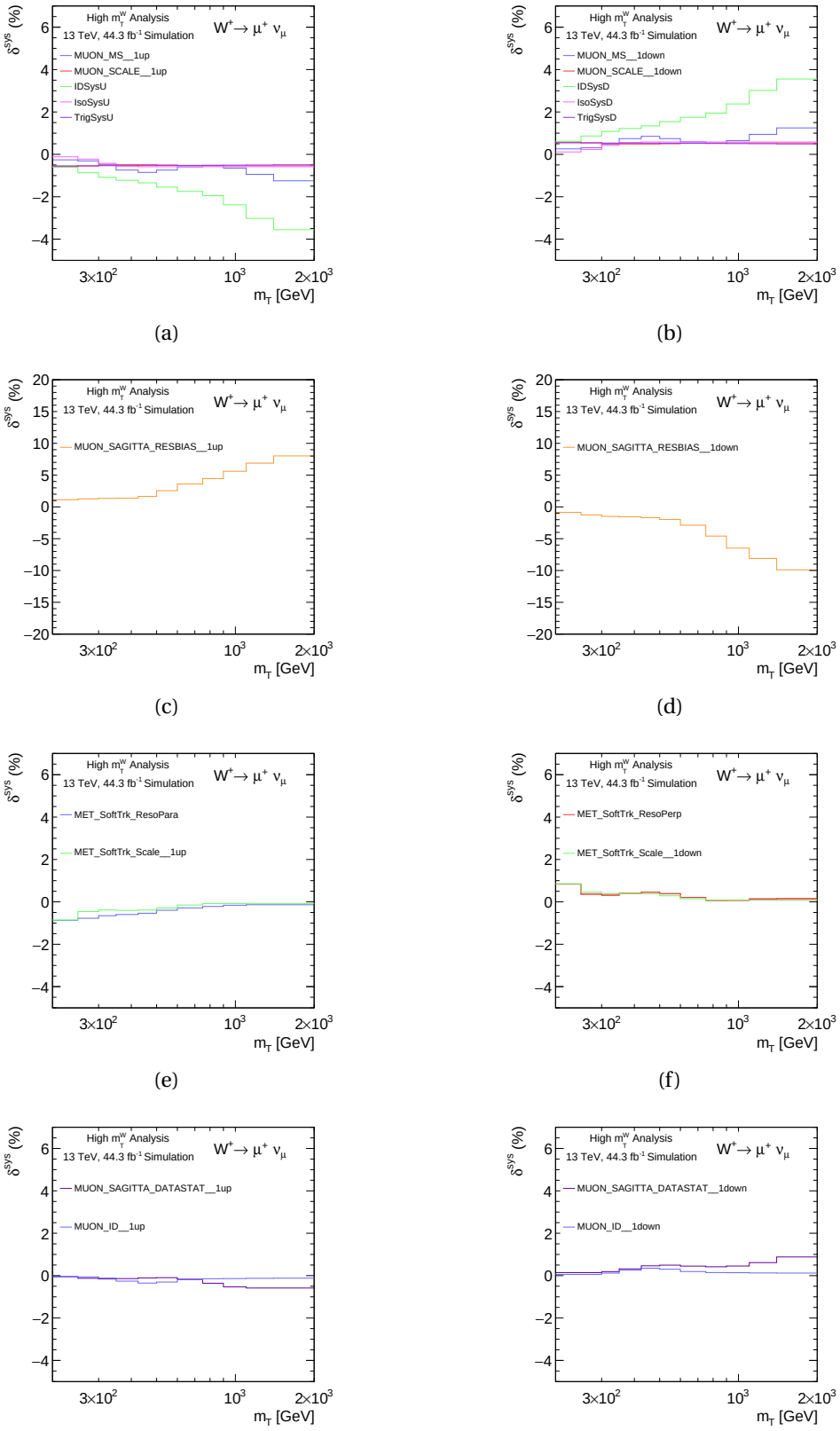

Figure D.16.: Individual contributions to the systematic variations in MC16d for $W^+ \to \mu^+\nu$ in the measurement binning for m_T. The plots on the left show the up variations and those on the right show the down variations. All values are presented in percentages. Plots (a) and (b) show the muon scale and resolution uncertainties along with the muon scale identification, isolation and trigger scale factor uncertainties. Plots (c) and (d) display the muon sagitta resolution bias uncertainty. Plots (e) and (f) show the missing energy soft track uncertainties. The labels in the legend of both plots are the conventional names given by the JetEtMiss group. "MET" stands for missing energy, "SofTrk" refers to soft track E_T^{miss} and "ResoPara" and "ResoPerp" refers to the resolution uncertainty on the parallel and perpendicular component.
Plots (g) and (h) display the muon sagitta data statistical and muon identification uncertainty.

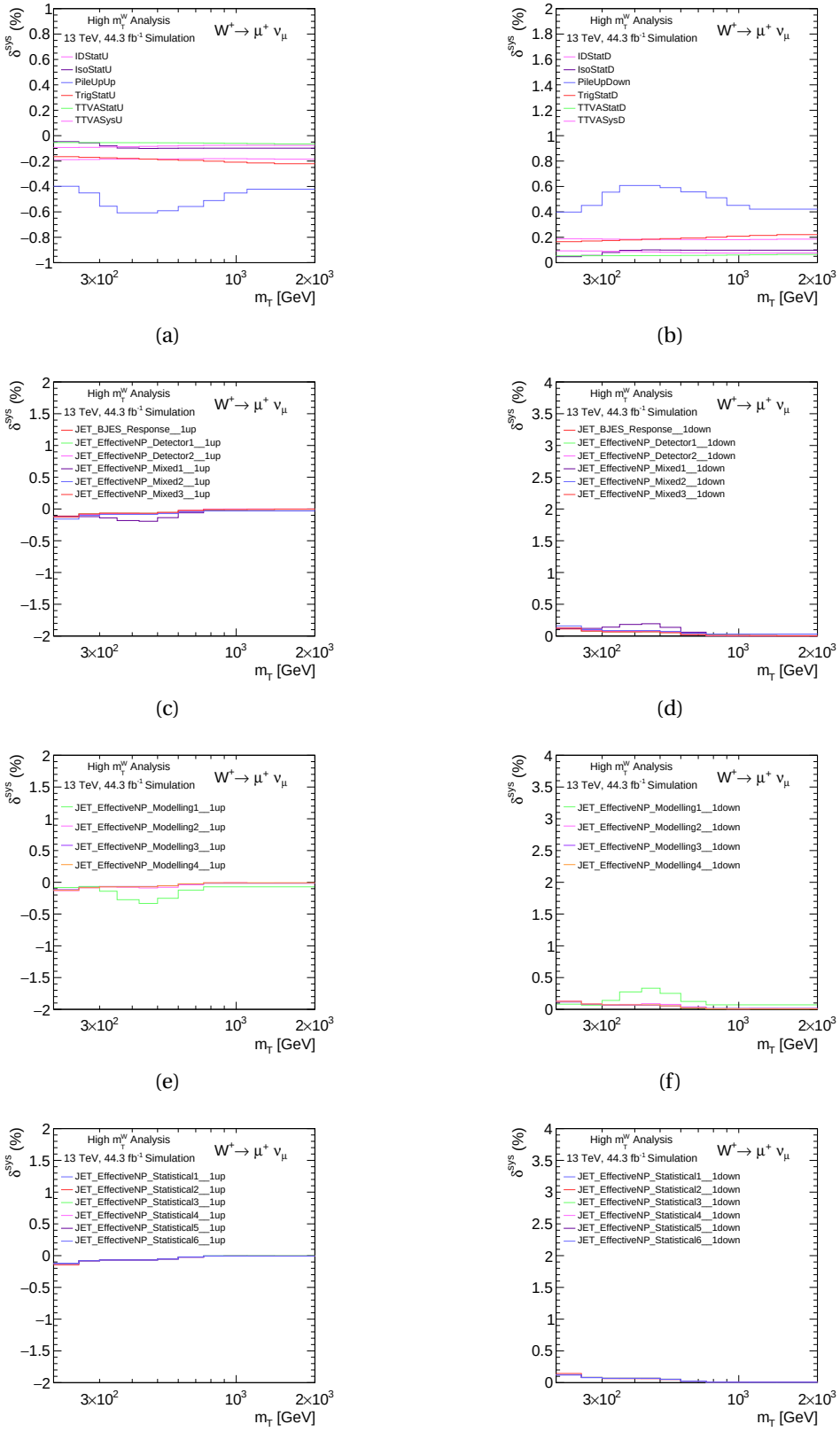

Figure D.17.: Individual contributions to the systematic variations in MC16d for $W^+ \to \mu^+ \nu$ in the measurement binning for m_T. The plots on the left show the up variations and those on the right show the down variations. All values are presented in percentages. Plots (a) and (b) show the scale factor uncertainties for the muon identification, isolation, trigger and TTVA statistical uncertainties. It also shows the TTVA systematic uncertainty and the pileup uncertainty. Plots (c) to (h) display the effect of the jet's systematic uncertainties.

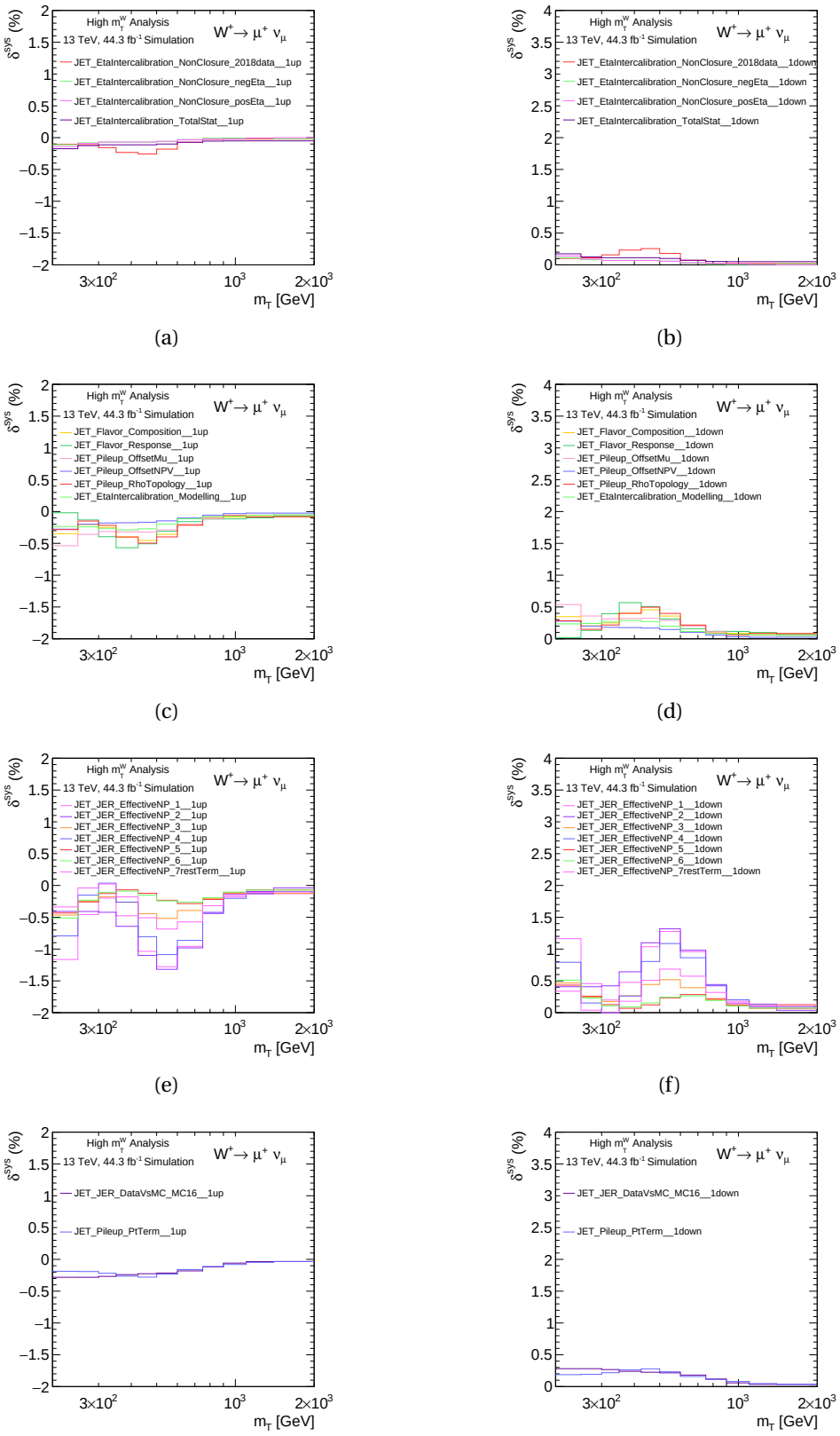

Figure D.18.: Individual contributions to the systematic variations in MC16d for $W^+ \to \mu^+\nu$ in the measurement binning for m_T. The plots on the left show the up variations and those on the right show the down variations. All values are presented in percentages. Plots (a) to (h) display the effect of the jet's systematic uncertainties.

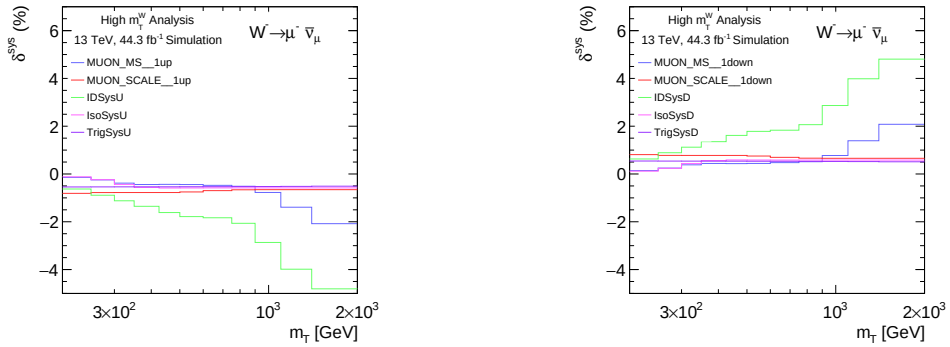

(a)

(b)

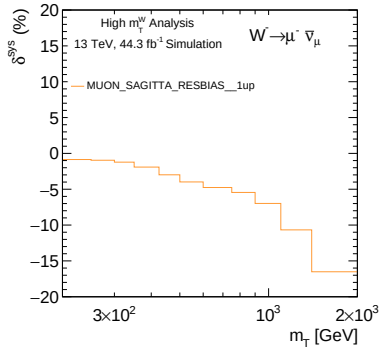

(c)

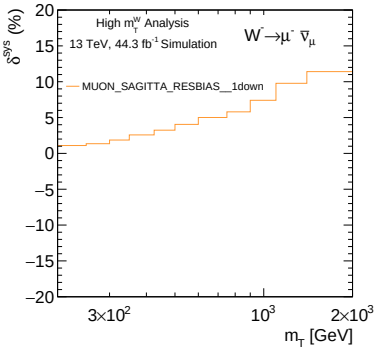

(d)

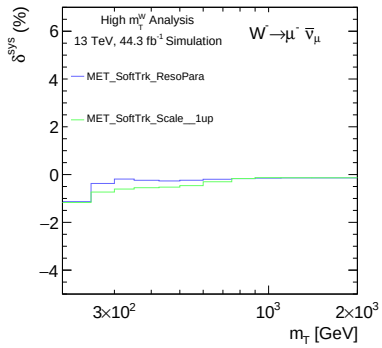

(e)

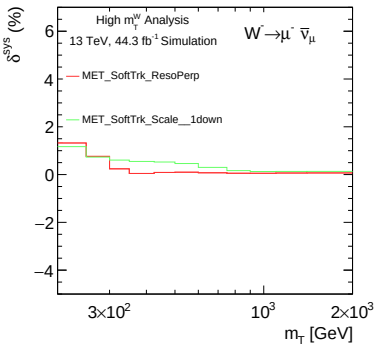

(f)

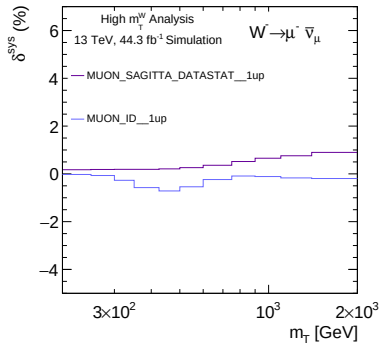

(g)

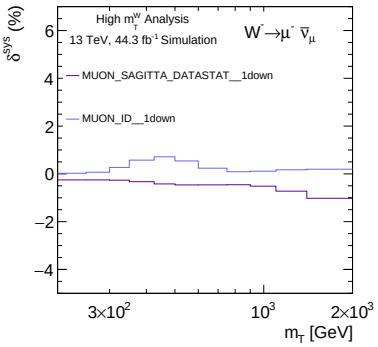

(h)

Figure D.19.: Individual contributions to the systematic variations in MC16d for $W^- \to \mu^- \bar{\nu}$ in the measurement binning for m_T. The plots on the left show the up variations and those on the right show the down variations. All values are presented in percentages. Plots (a) and (b) show the muon scale and resolution uncertainties along with the muon scale identification, isolation and trigger scale factor uncertainties. Plots (c) and (d) display the muon sagitta resolution bias uncertainty. Plots (e) and (f) show the missing energy soft track uncertainties. The labels in the legend of both plots are the conventional names given by the JetEtMiss group. "MET" stands for missing energy, "SofTrk" refers to soft track E_T^{miss} and "ResoPara" and "ResoPerp" refers to the resolution uncertainty on the parallel and perpendicular component. Plots (g) and (h) display the muon sagitta data statistical and muon identification uncertainty.

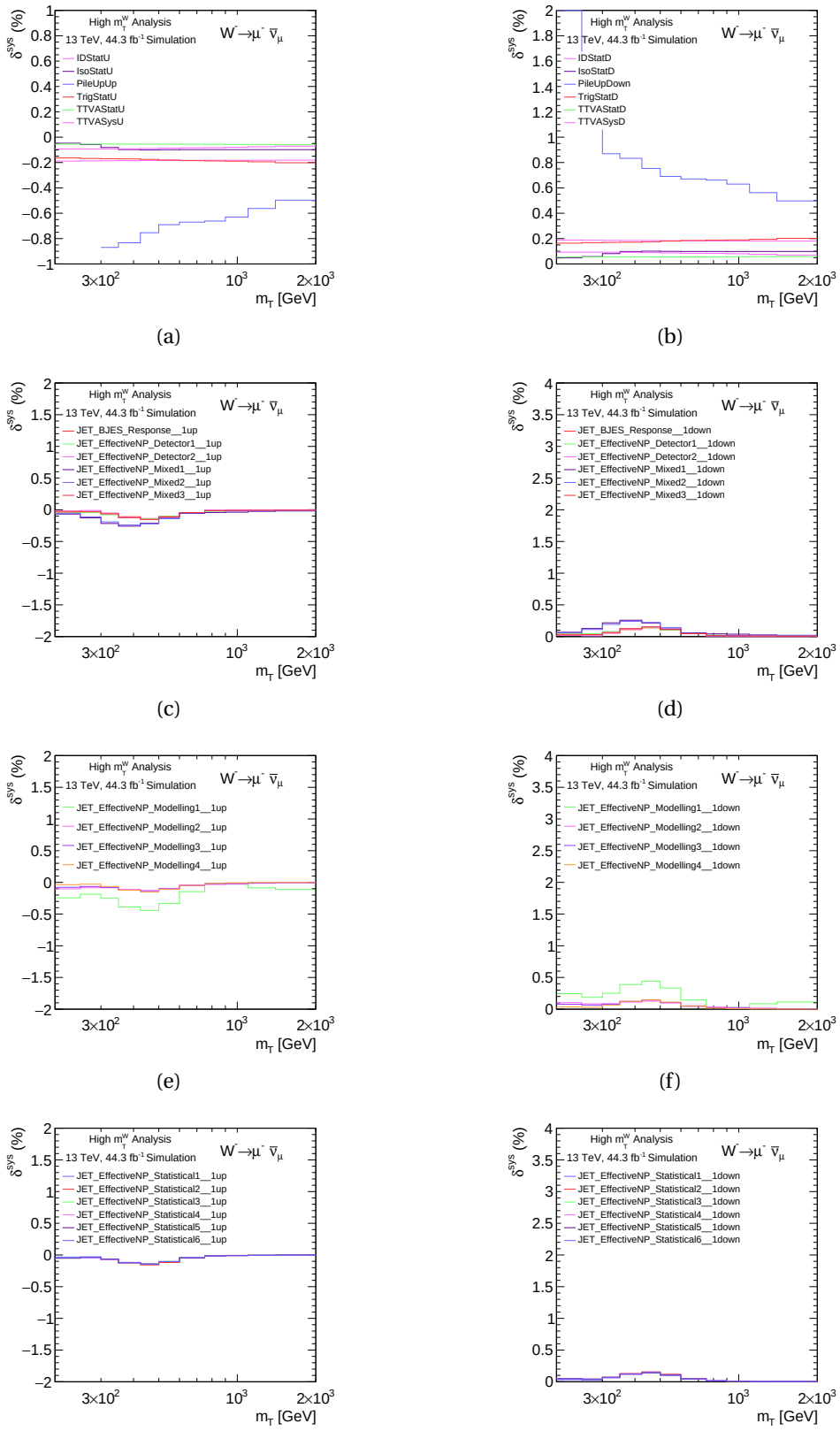

Figure D.20.: Individual contributions to the systematic variations in MC16d for $W^- \to \mu^- \bar{\nu}$ in the measurement binning for m_T. The plots on the left show the up variations and those on the right show the down variations. All values are presented in percentages. Plots (a) and (b) show the scale factor uncertainties for the muon identification, isolation, trigger and TTVA statistical uncertainties. Also shown are the TTVA systematic uncertainty and the pileup uncertainty. Plots (c) to (h) display the effect of the jet's systematic uncertainties.

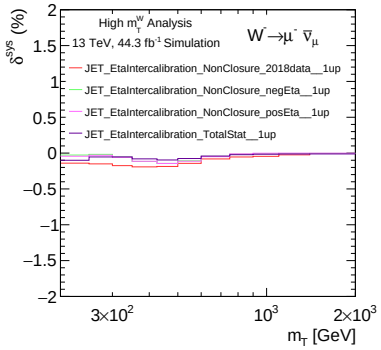

(a)

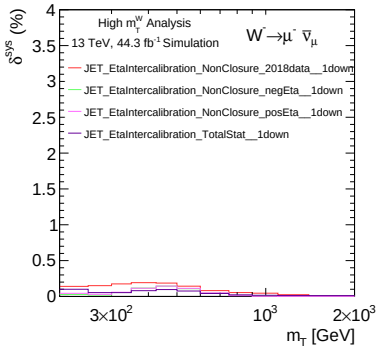

(b)

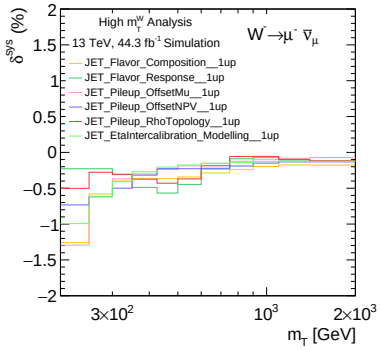

(c)

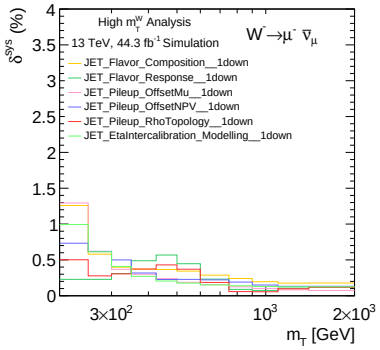

(d)

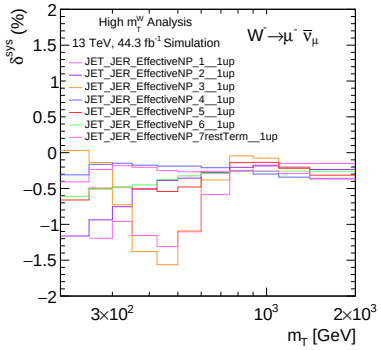

(e)

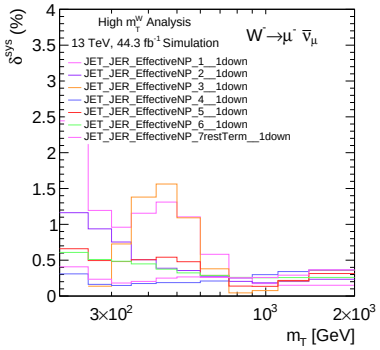

(f)

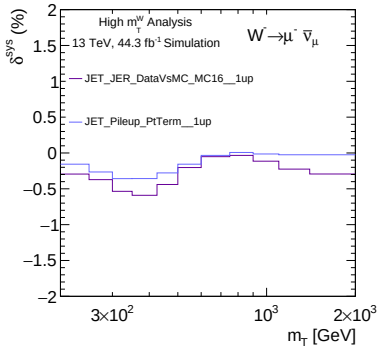

(g)

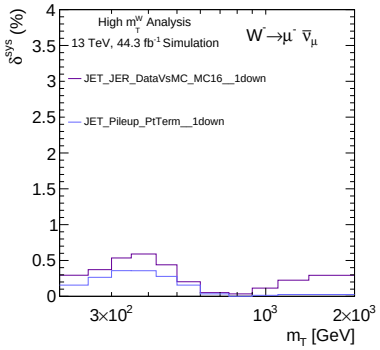

(h)

Figure D.21.: Individual contributions to the systematic variations in MC16d for $W^- \to \mu^- \bar{\nu}$ in the measurement binning for m_T. The plots on the left show the up variations and those on the right show the down variations. All values are presented in percentages. Plots (a) to (h) display the effect of the jet's systematic uncertainties.

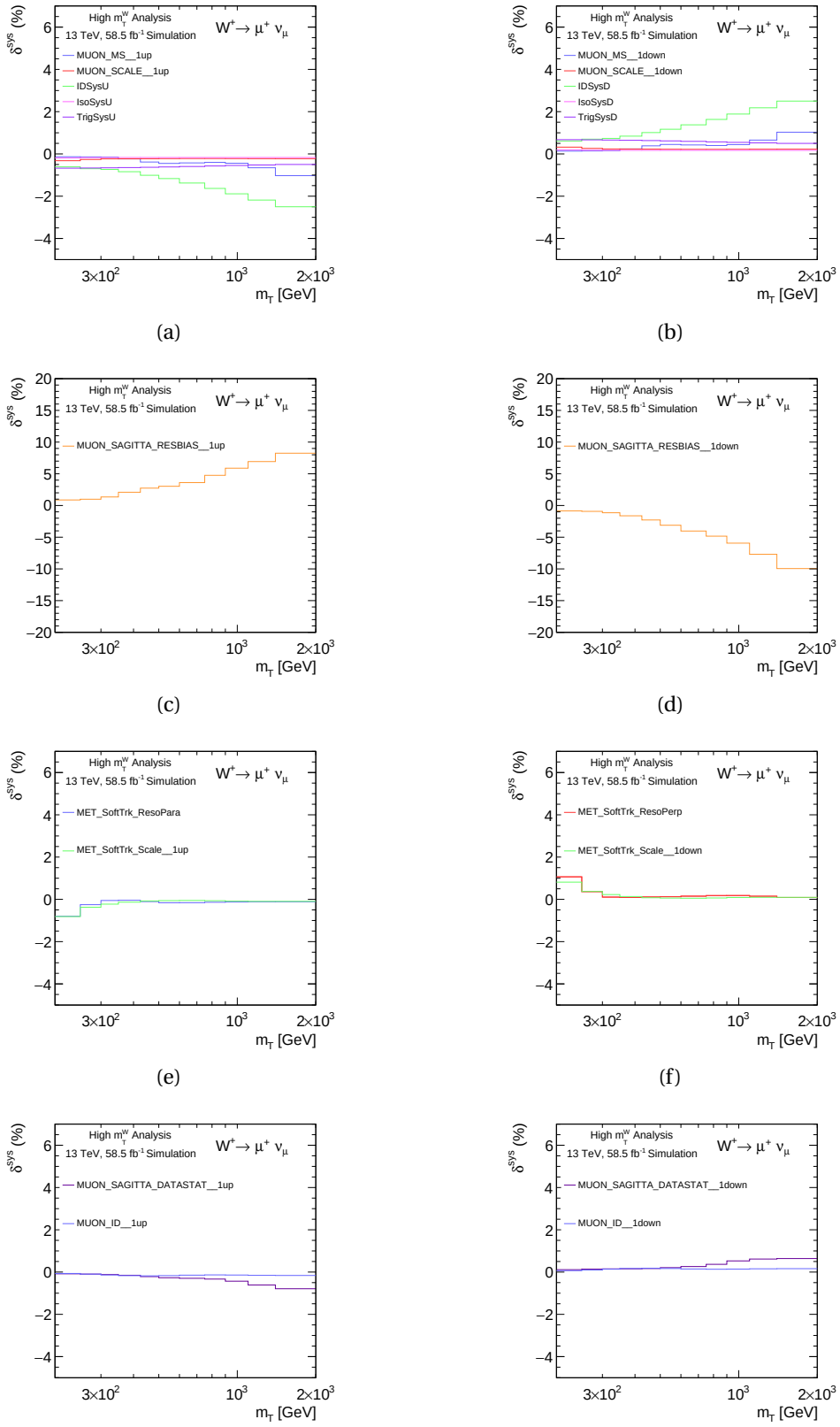

Figure D.22.: Individual contributions to the systematic variations in MC16e for $W^+ \to \mu^+\nu$ in the measurement binning for m_T. The plots on the left show the up variations and those on the right show the down variations. All values are presented in percentages. Plots (a) and (b) show the muon scale and resolution uncertainties along with the muon scale identification, isolation and trigger scale factor uncertainties. Plots (c) and (d) display the muon sagitta resolution bias uncertainty. Plots (e) and (f) show the missing energy soft track uncertainties. The labels in the legend of both plots are the conventional names given by the JetEtMiss group. "MET" stands for missing energy, "SofTrk" refers to soft track E_T^{miss} and "ResoPara" and "ResoPerp" refers to the resolution uncertainty on the parallel and perpendicular component. Plots (g) and (h) display the muon sagitta data statistical and muon identification uncertainty.

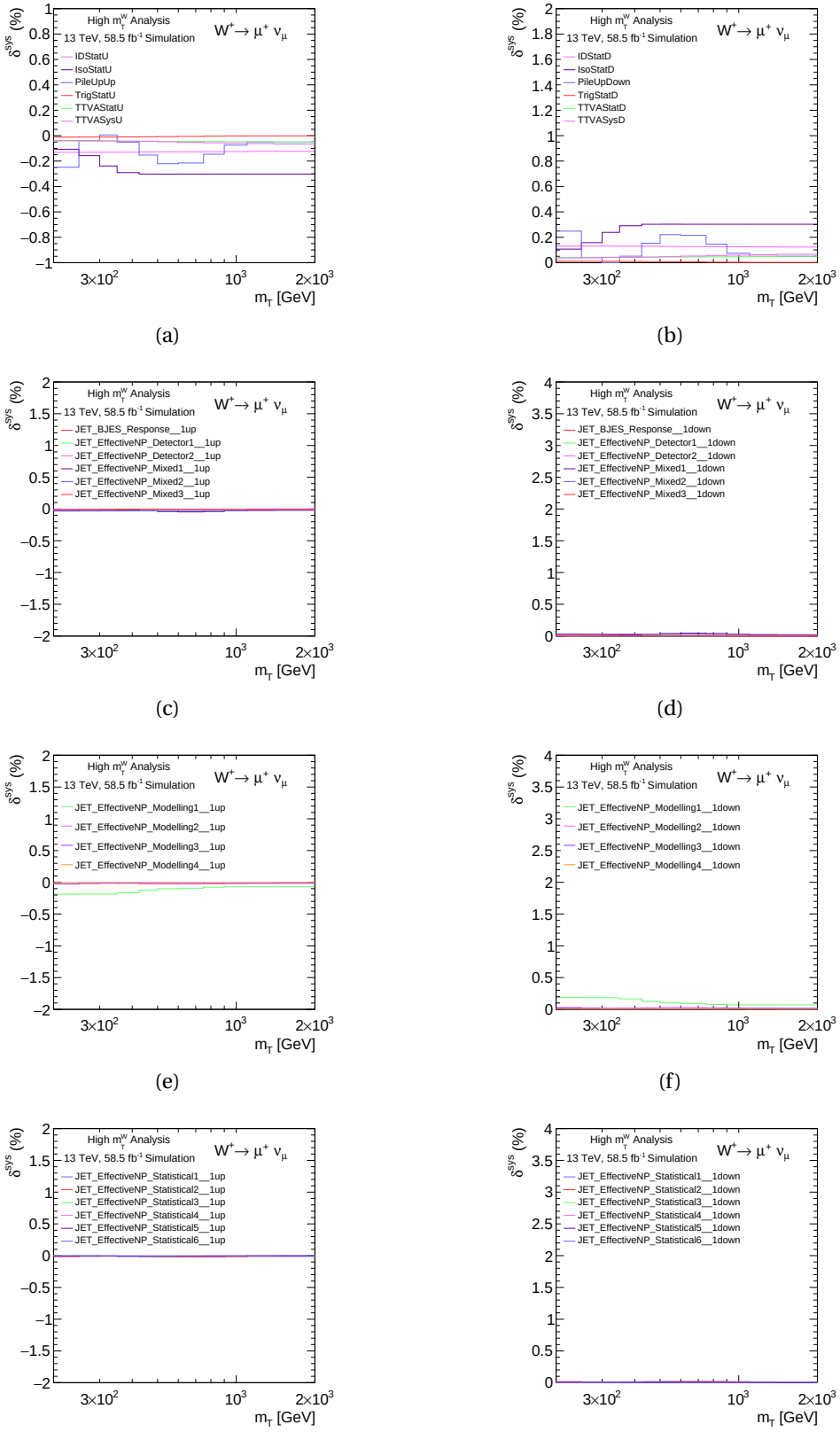

Figure D.23.: Individual contributions to the systematic variations in MC16e for $W^+ \to \mu^+ \nu$ in the measurement binning for m_T. The plots on the left show the up variations and those on the right show the down variations. All values are presented in percentages. Plots (a) and (b) show the scale factor uncertainties for the muon identification, isolation, trigger and TTVA statistical uncertainties. It also shows the TTVA systematic uncertainty and the pileup uncertainty. Plots (c) to (h) display the effect of the jet's systematic uncertainties.

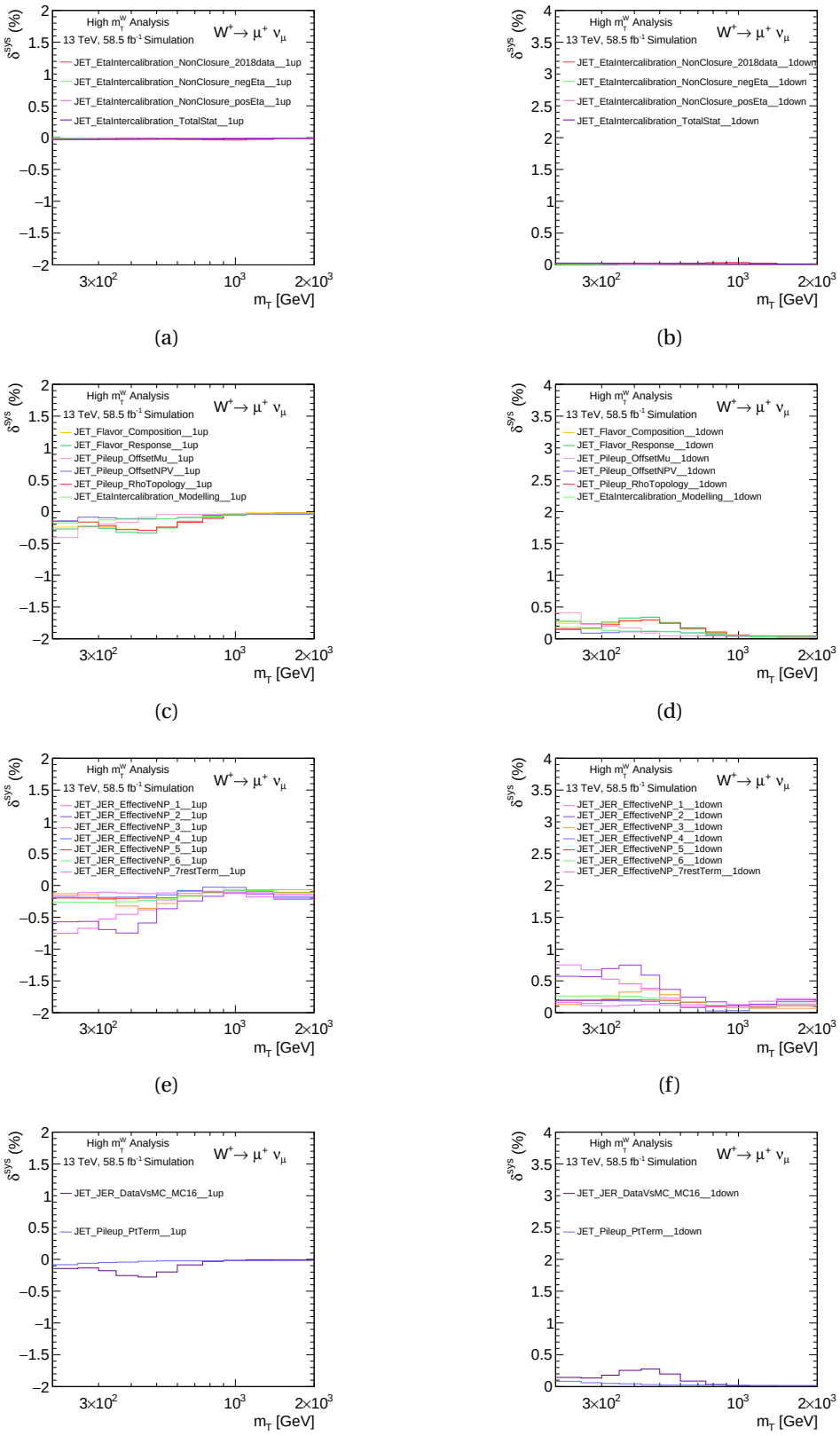

Figure D.24.: Individual contributions to the systematic variations in MC16e for $W^+ \to \mu^+\nu$ in the measurement binning for m_T. The plots on the left show the up variations and those on the right show the down variations. All values are presented in percentages. Plots (a) to (h) display the effect of the jet's systematic uncertainties.

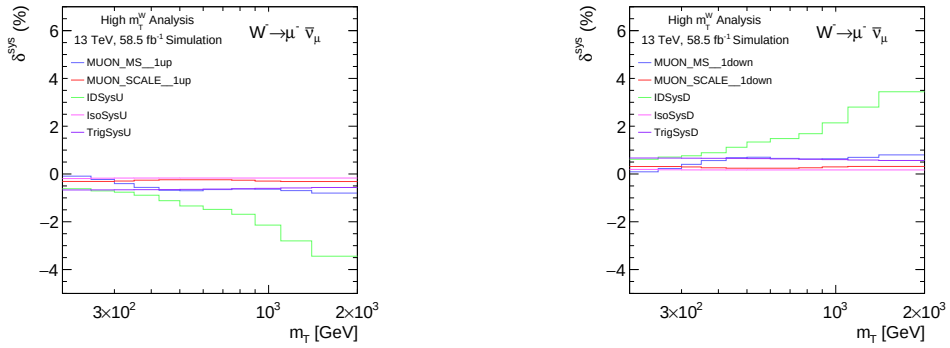

(a)

(b)

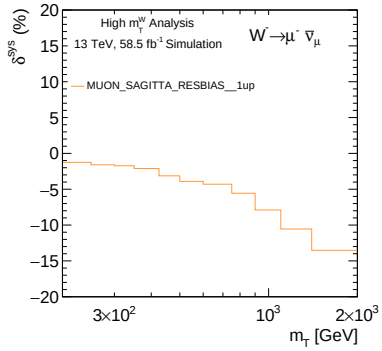

(c)

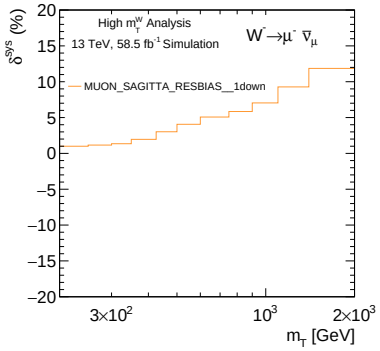

(d)

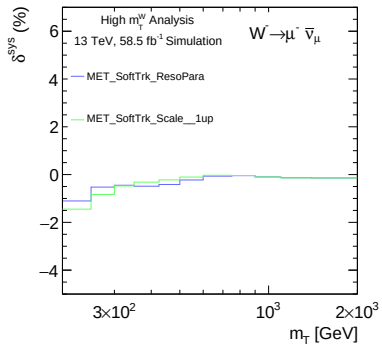

(e)

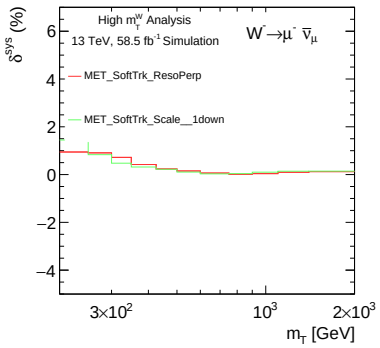

(f)

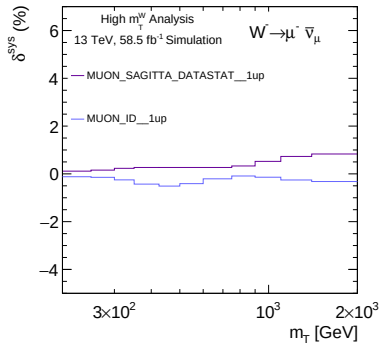

(g)

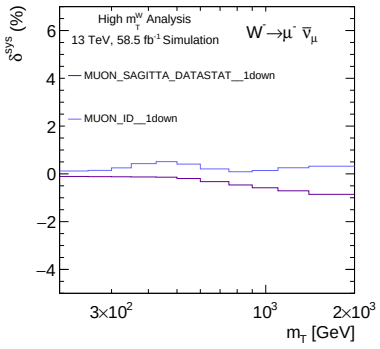

(h)

Figure D.25.: Individual contributions to the systematic variations in MC16e for $W^- \to \mu^- \bar{\nu}$ in the measurement binning for m_T. The plots on the left show the up variations and those on the right show the down variations. All values are presented in percentages. Plots (a) and (b) show the muon scale and resolution uncertainties along with the muon scale identification, isolation and trigger scale factor uncertainties. Plots (c) and (d) display the muon sagitta resolution bias uncertainty. Plots (e) and (f) show the missing energy soft track uncertainties. The labels in the legend of both plots are the conventional names given by the JetEtMiss group. "MET" stands for missing energy, "SofTrk" refers to soft track E_T^{miss} and "ResoPara" and "ResoPerp" refers to the resolution uncertainty on the parallel and perpendicular component. Plots (g) and (h) display the muon sagitta data statistical and muon identification uncertainty.

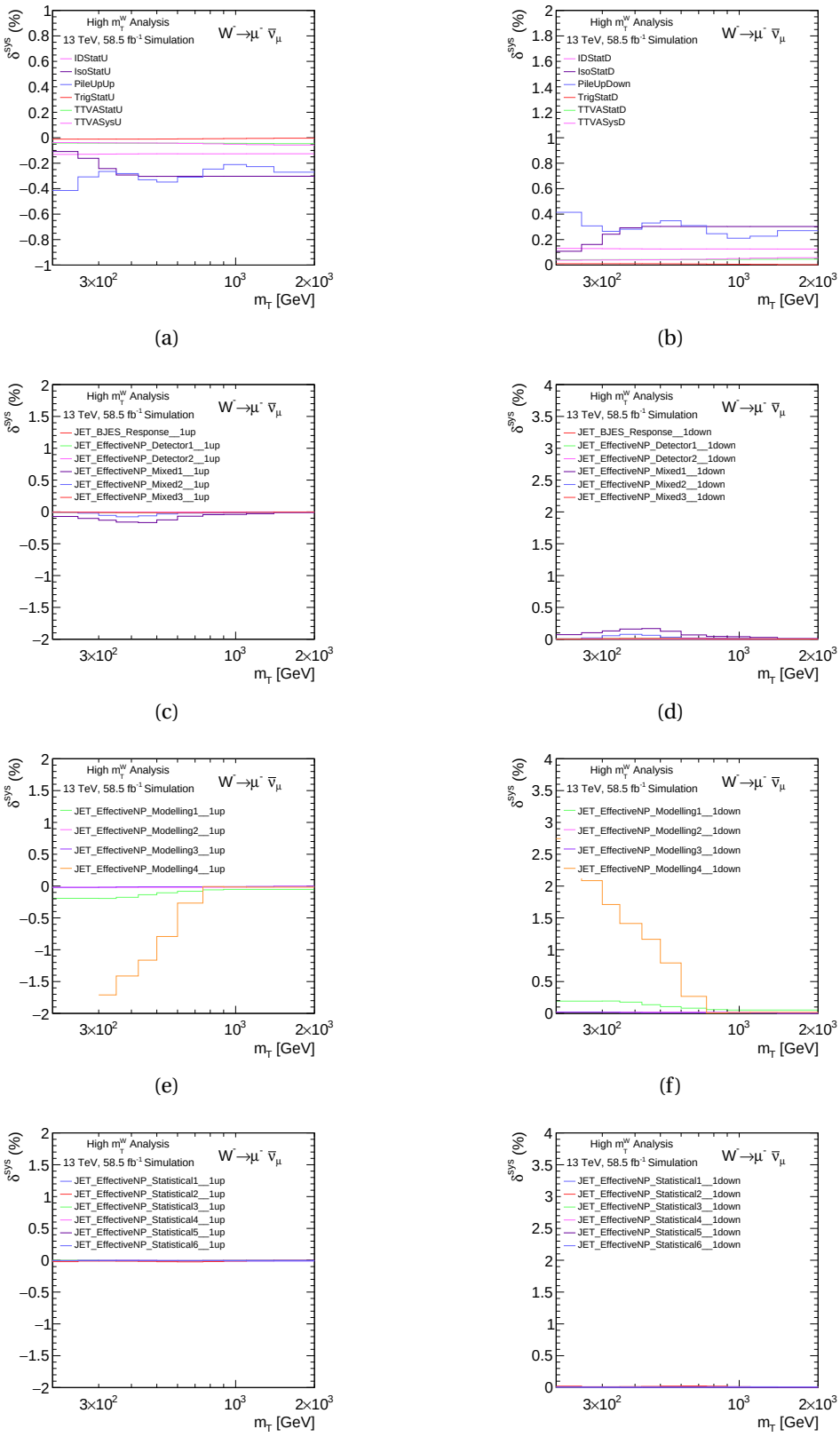

Figure D.26.: Individual contributions to the systematic variations in MC16e for $W^- \to \mu^- \bar{\nu}$ in the measurement binning for m_T. The plots on the left show the up variations and those on the right show the down variations. All values are presented in percentages. Plots (a) and (b) show the scale factor uncertainties for the muon identification, isolation, trigger and TTVA statistical uncertainties. Also shown are the TTVA systematic uncertainty and the pileup uncertainty. Plots (c) to (h) display the effect of the jet's systematic uncertainties.

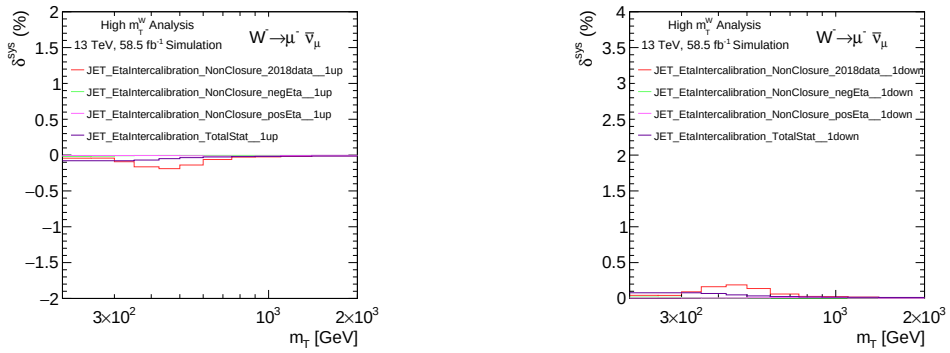

(a)

(b)

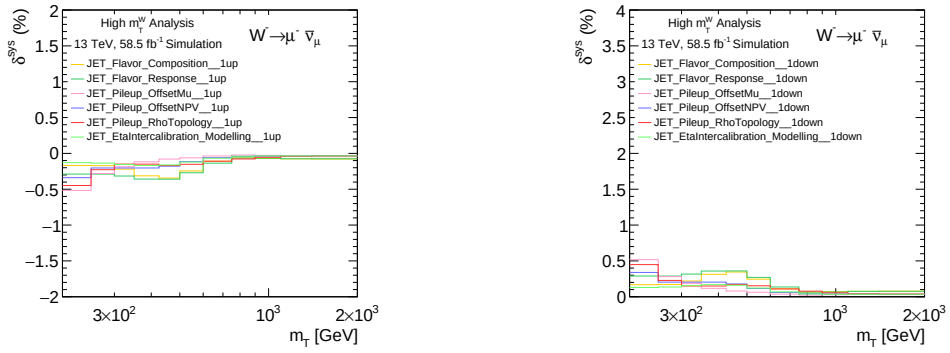

(c)

(d)

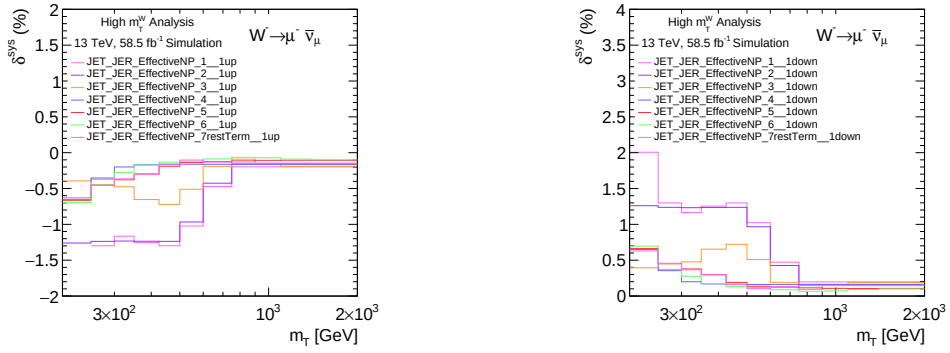

(e)

(f)

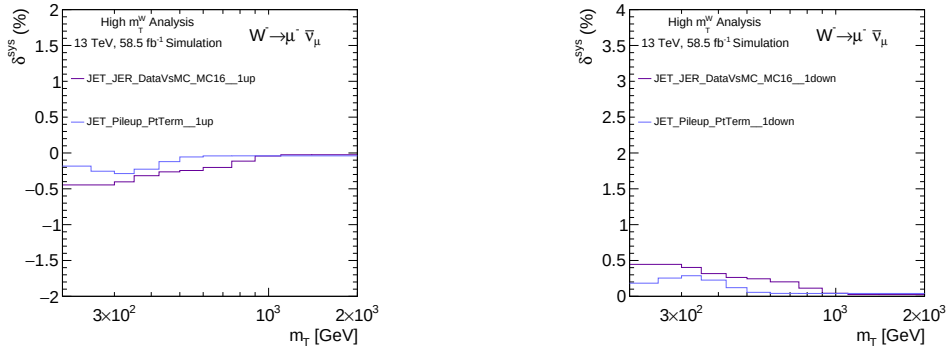

(g)

(h)

Figure D.27.: Individual contributions to the systematic variations in MC16e for $W^- \to \mu^- \bar{\nu}$ in the measurement binning for m_T. The plots on the left show the up variations and those on the right show the down variations. All values are presented in percentages. Plots (a) to (h) display the effect of the jet's systematic uncertainties.

D.4. Cross-Section Systematic Uncertainties For Individual Monte Carlo Campaigns

This section is for the distributions of the systematic uncertainties for individual Monte Carlo campaigns MC16a, MC16d and MC16e. The systematic uncertainties have been discussed in Chapter 8. The following distributions are for the experimental systematic uncertainties for the cross-section measurement and are calculated using Equation 10.1. The uncertainties are shown for the W^+ and W^- bosons separately. The uncertainties are first shown for the muon, sagitta and missing energy uncertainties. Then uncertainties are shown for the scale factor identification, isolation, pile-up, trigger, TTVA and jet uncertainties. Finally, more jet systematic uncertainties are shown.

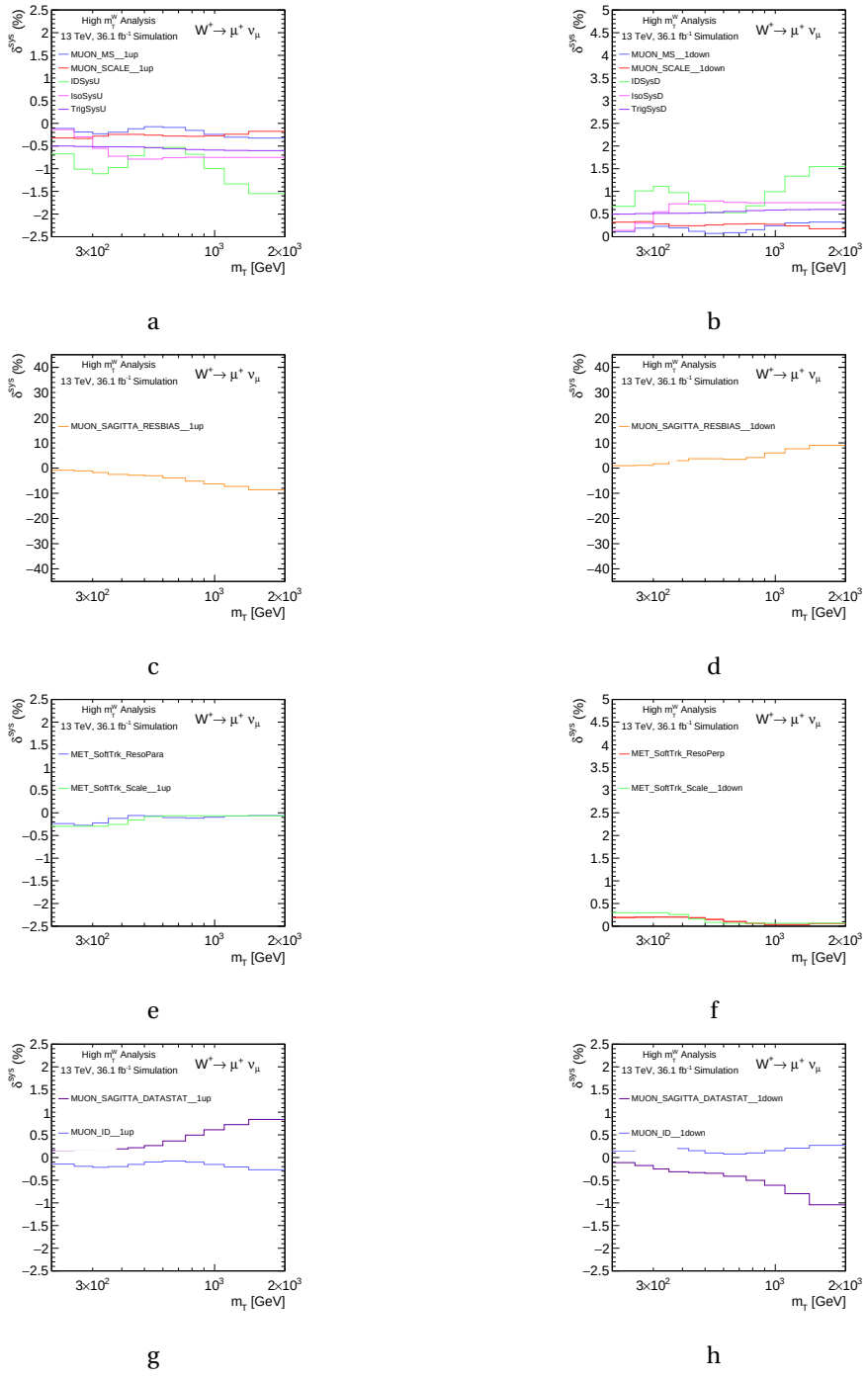

Figure D.28.: Individual contributions to the cross-section systematic variations in MC16a for $W^+ \to \mu^+ \nu$ in the measurement binning for m_T. The plots on the left show the up variations and those on the right show the down variations. All values are presented in percentages. Plots (a) and (b) show the muon scale and resolution uncertainties along with the muon scale identification, isolation and trigger scale factor uncertainties. Plots (c) and (d) display the muon sagitta resolution bias uncertainty. Plots (e) and (f) show the missing energy soft track uncertainties. The labels in the legend of both plots are the conventional names given by the JetEtMiss group. "MET" stands for missing energy, "SofTrk" refers to soft track E_T^{miss} and “ResoPara” and “ResoPerp” refers to the resolution uncertainty on the parallel and perpendicular component. Plots (g) and (h) display the muon sagitta data statistical and muon identification uncertainty.

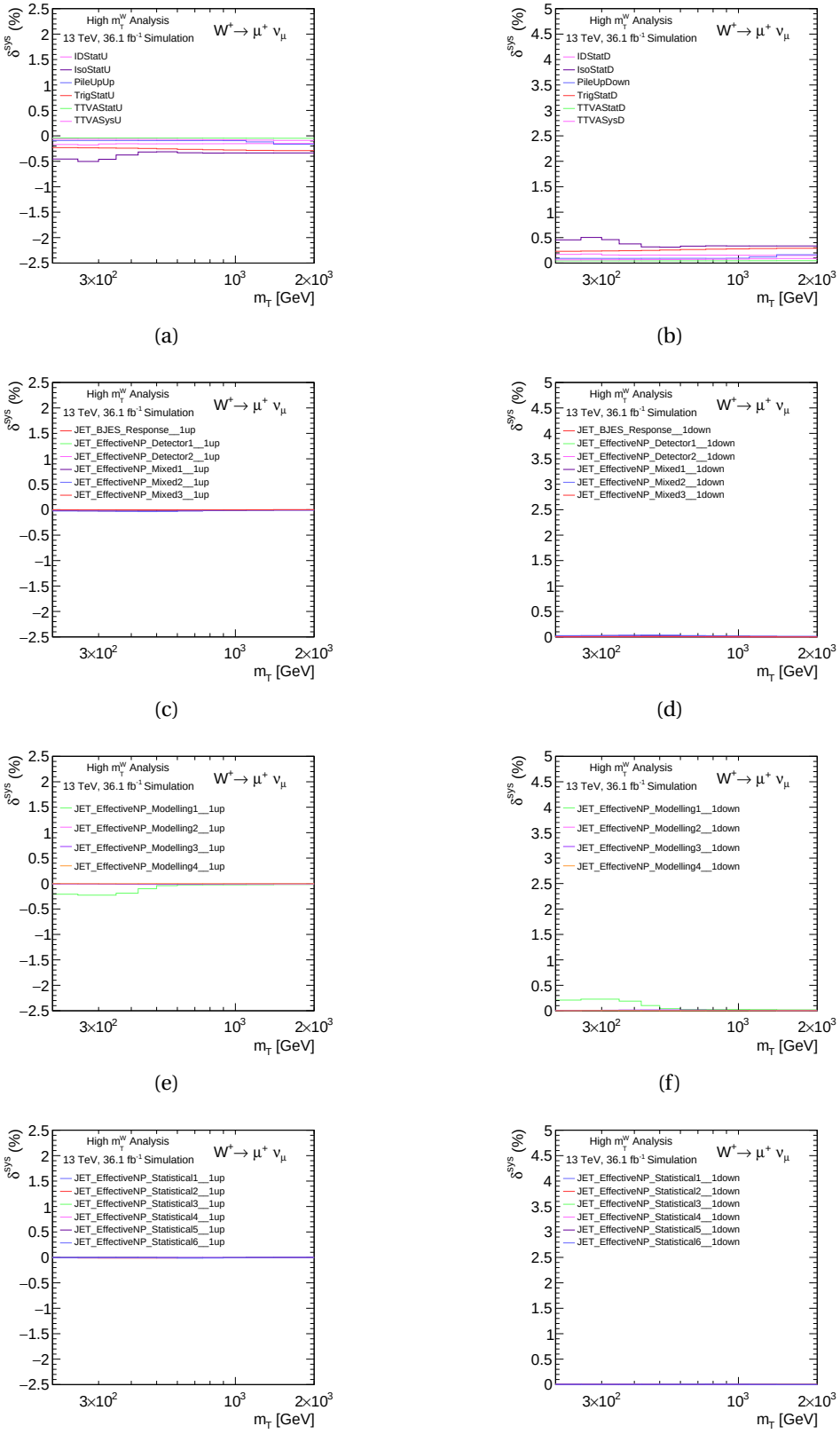

Figure D.29.: Individual contributions to the cross-section systematic variations in MC16a for $W^+ \to \mu^+ \nu$ in the measurement binning for m_T. The plots on the left show the up variations and those on the right show the down variations. All values are presented in percentages. Plots (a) and (b) show the scale factor uncertainties for the muon identification, isolation, trigger and TTVA statistical uncertainties. Also shows the TTVA systematic uncertainty and the pileup uncertainty. Plots (c) to (h) display the effect of the jet's systematic uncertainties.

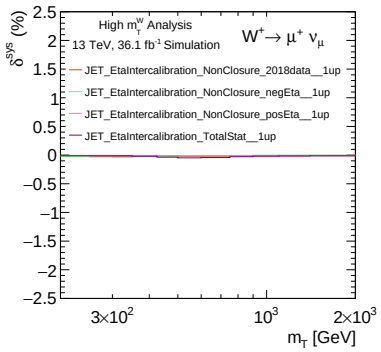

(a)

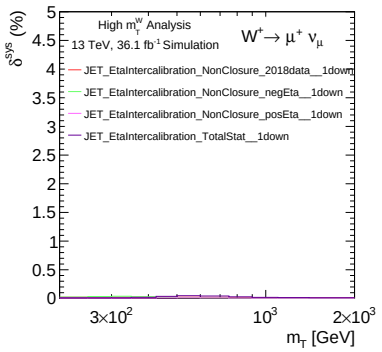

(b)

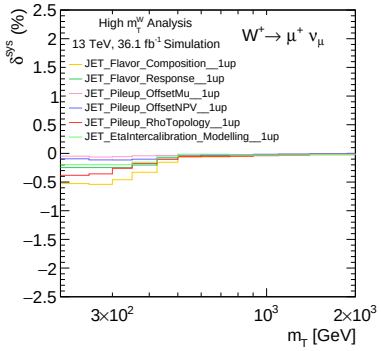

(c)

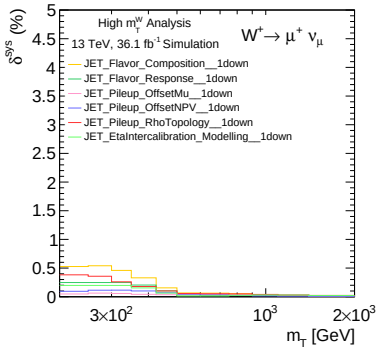

(d)

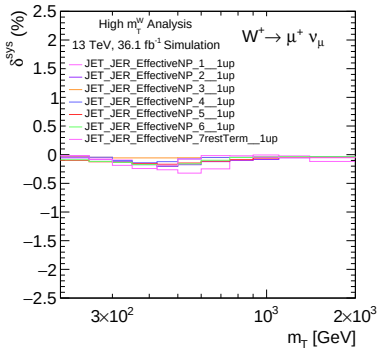

(e)

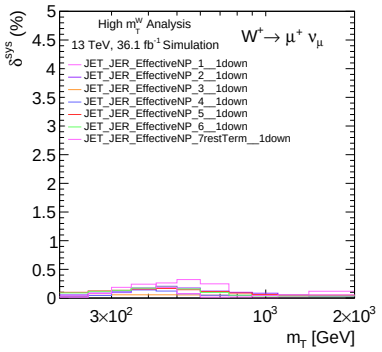

(f)

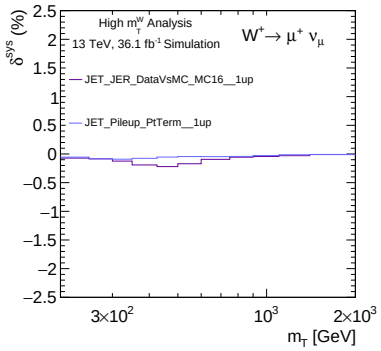

(g)

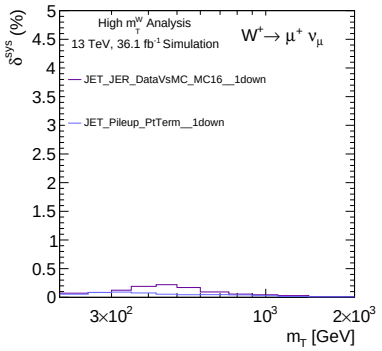

(h)

Figure D.30.: Individual contributions to the cross-section systematic variations in MC16a for $W^+ \to \mu^+\nu$ in the measurement binning for m_T. The plots on the left show the up variations and those on the right show the down variations. All values are presented in percentages. Plots (a) to (h) display the effect of the jet's systematic uncertainties.

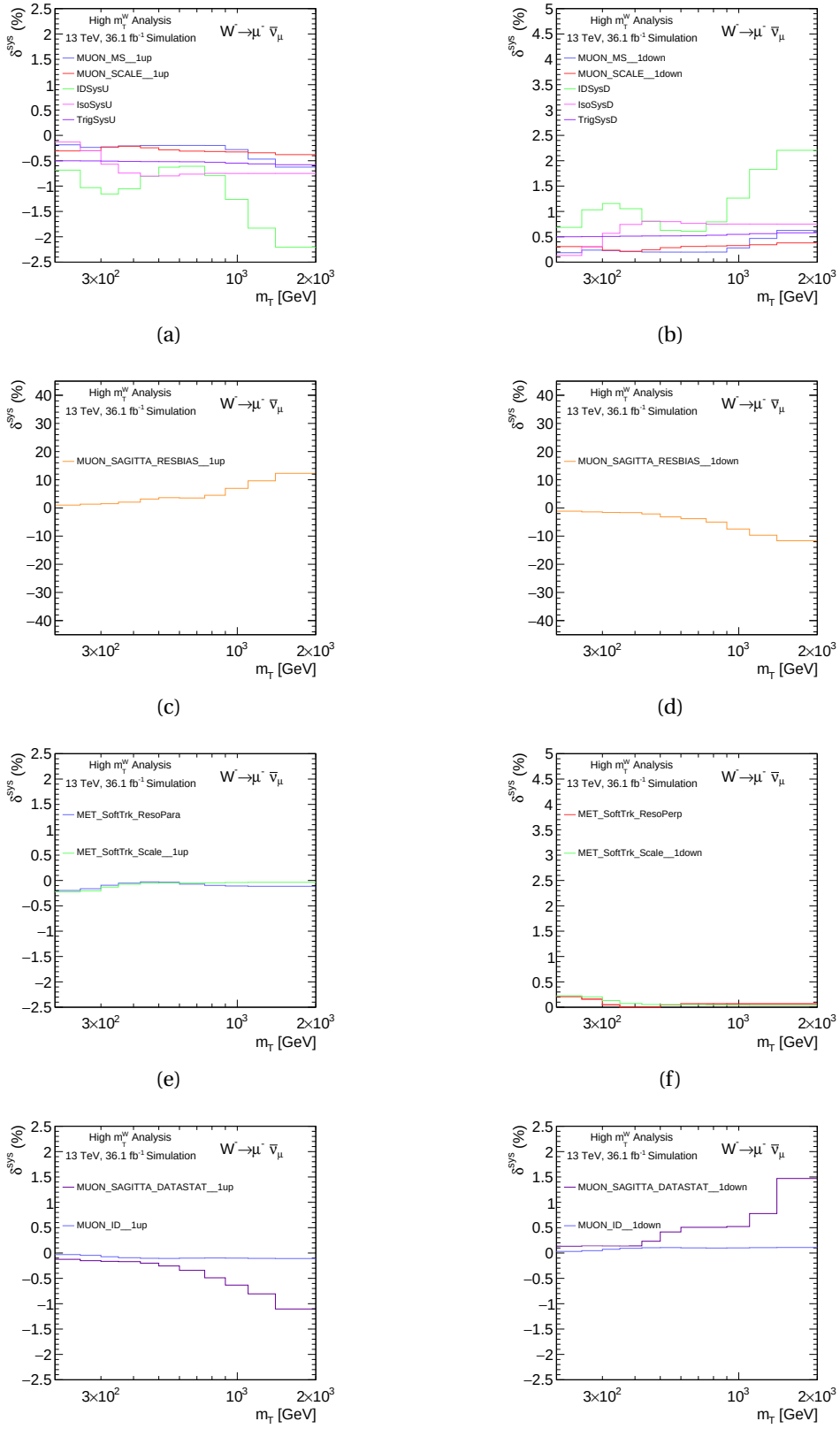

Figure D.31.: Individual contributions to the cross-section systematic variations in MC16a for $W^- \to \mu^- \bar{\nu}$ in the measurement binning for m_T. The plots on the left show the up variations and those on the right show the down variations. All values are presented in percentages. Plots (a) and (b) show the muon scale and resolution uncertainties along with the muon scale identification, isolation and trigger scale factor uncertainties. Plots (c) and (d) display the muon sagitta resolution bias uncertainty. Plots (e) and (f) show the missing energy soft track uncertainties. The labels in the legend of both plots are the conventional names given by the JetEtMiss group. "MET" stands for missing energy, "SofTrk" refers to soft track E_T^{miss} and “ResoPara” and “ResoPerp” refers to the resolution uncertainty on the parallel and perpendicular component. Plots (g) and (h) display the muon sagitta data statistical and muon identification uncertainty.

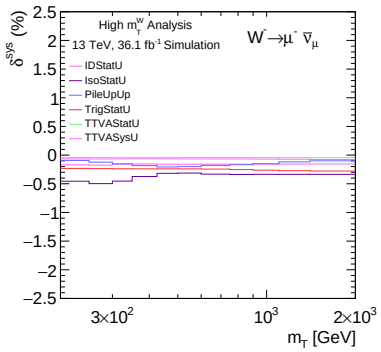

(a)

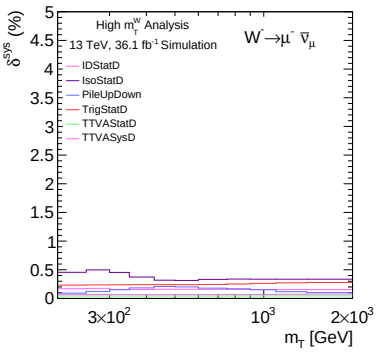

(b)

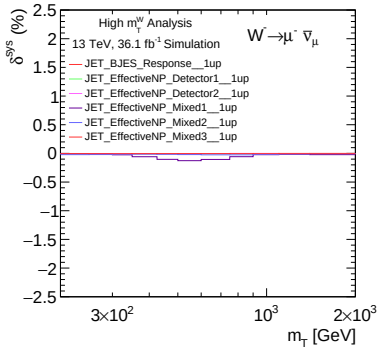

(c)

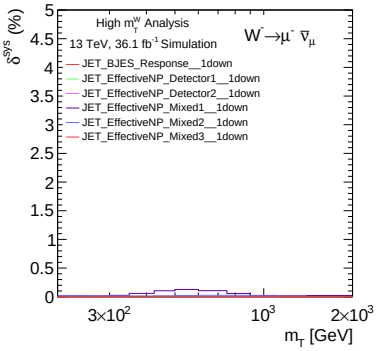

(d)

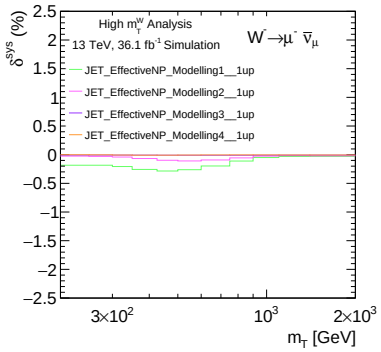

(e)

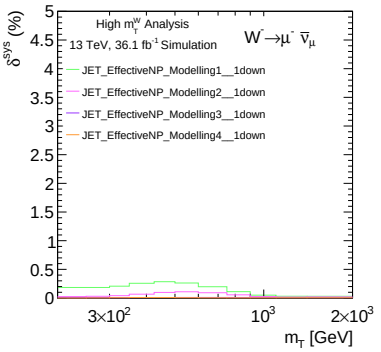

(f)

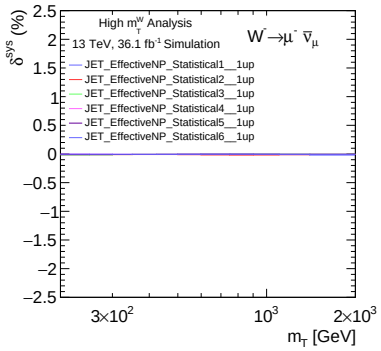

(g)

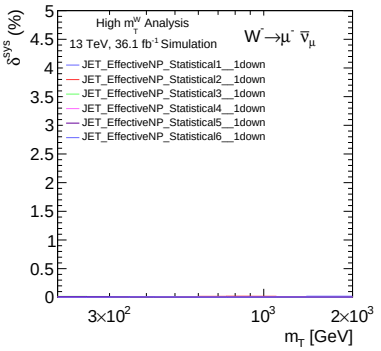

(h)

Figure D.32.: Individual contributions to the cross-section systematic variations in MC16a for $W^- \to \mu^- \bar{\nu}$ in the measurement binning for m_T. The plots on the left show the up variations and those on the right show the down variations. All values are presented in percentages. Plots (a) and (b) show the scale factor uncertainties for the muon identification, isolation, trigger and TTVA statistical uncertainties. Also shown are the TTVA systematic uncertainty and the pileup uncertainty. Plots (c) to (h) display the effect of the jet's systematic uncertainties.

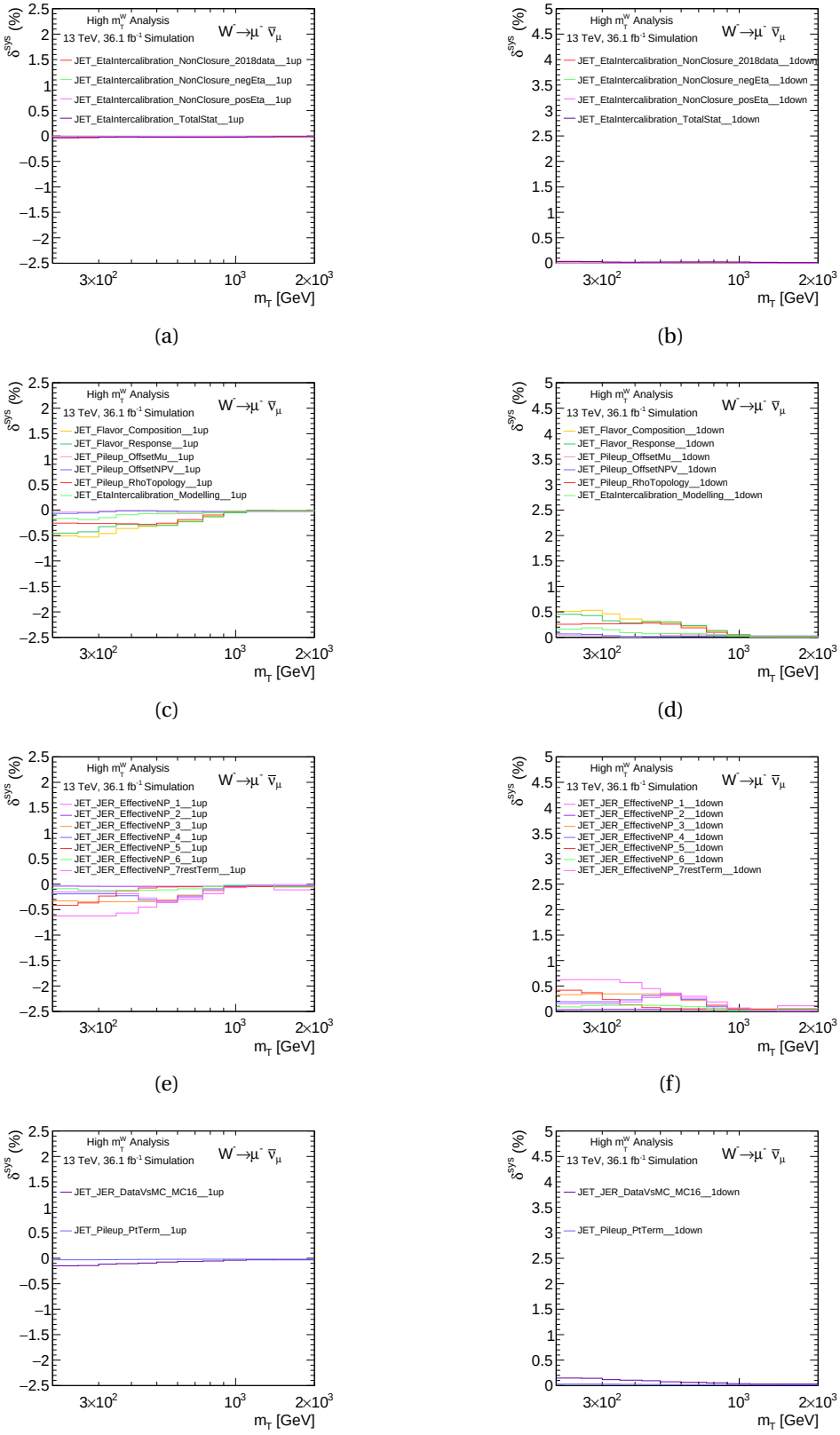

Figure D.33.: Individual contributions to the cross-section systematic variations in MC16a for $W^- \to \mu^- \bar{\nu}$ in the measurement binning for m_T. The plots on the left show the up variations and those on the right show the down variations. All values are presented in percentages. Plots (a) to (h) display the effect of the jet's systematic uncertainties.

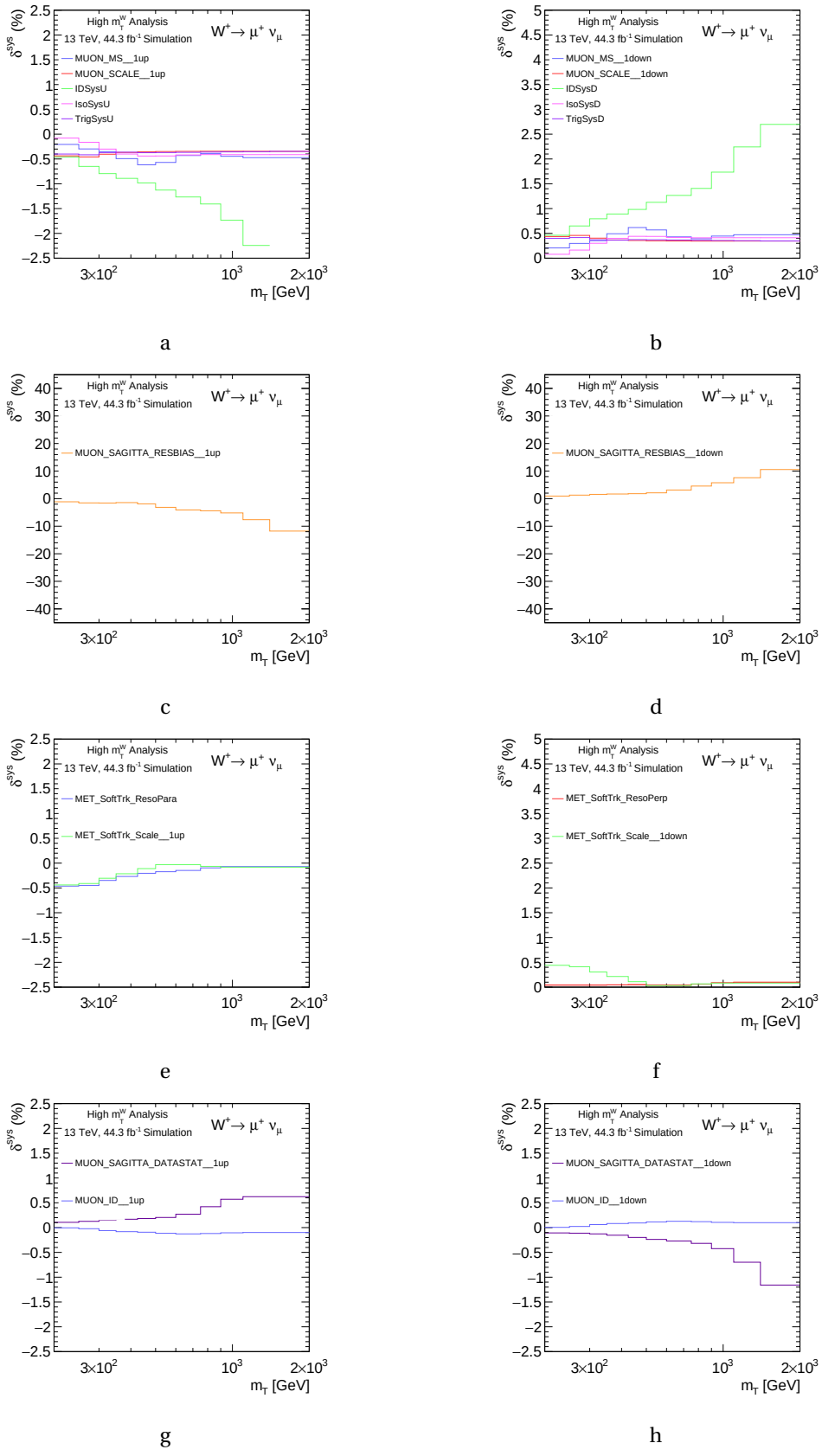

Figure D.34.: Individual contributions to the cross-section systematic variations in MC16d for $W^+ \to \mu^+\nu$ in the measurement binning for m_T. The plots on the left show the up variations and those on the right show the down variations. All values are presented in percentages. Plots (a) and (b) show the muon scale and resolution uncertainties along with the muon scale identification, isolation and trigger scale factor uncertainties. Plots (c) and (d) display the muon sagitta resolution bias uncertainty. Plots (e) and (f) show the missing energy soft track uncertainties. The labels in the legend of both plots are the conventional names given by the JetEtMiss group. "MET" stands for missing energy, "SofTrk" refers to soft track p_T and "ResoPara" and "ResoPerp" refers to the resolution uncertainty on the parallel and perpendicular component. Plots (g) and (h) display the muon sagitta data statistical and muon identification uncertainty.

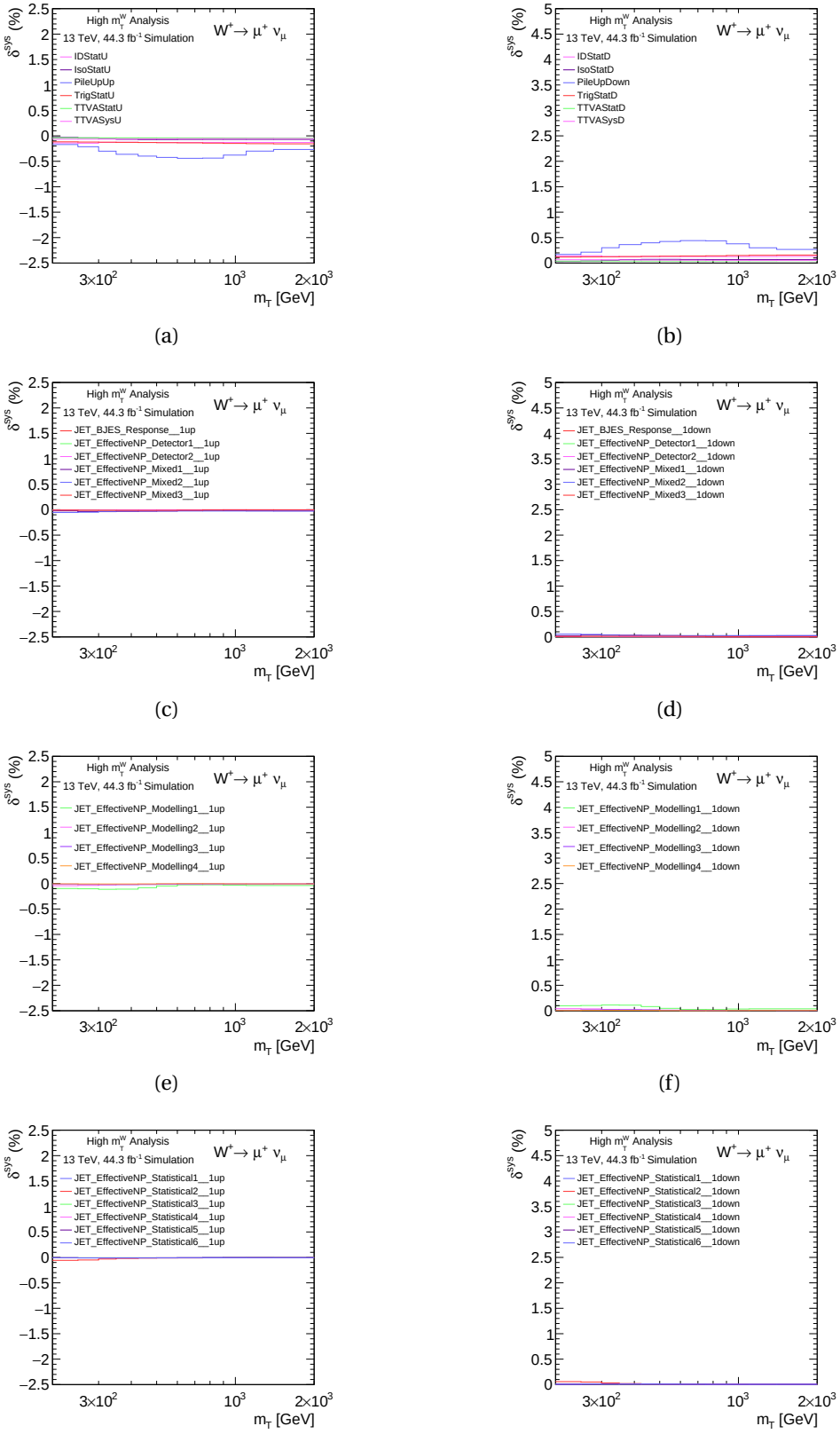

Figure D.35.: Individual contributions to the cross-section systematic variations in MC16d for $W^+ \to \mu^+\nu$ in the measurement binning for m_T. The plots on the left show the up variations and those on the right show the down variations. All values are presented in percentages. Plots (a) and (b) show the scale factor uncertainties for the muon identification, isolation, trigger and TTVA statistical uncertainties. Also shows the TTVA systematic uncertainty and the pileup uncertainty. Plots (c) to (h) display the effect of the jet's systematic uncertainties.

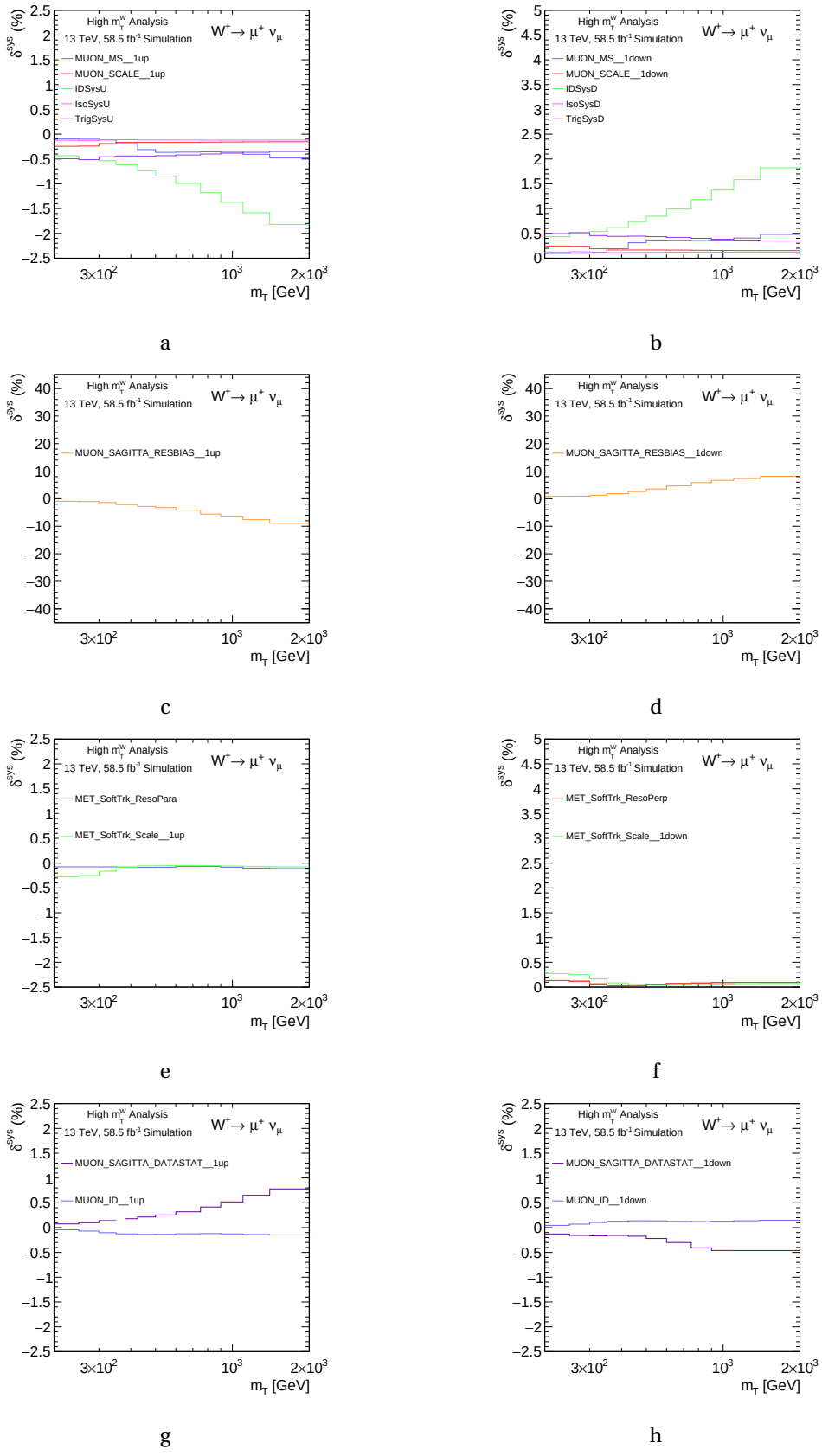

Figure D.40.: Individual contributions to the cross-section systematic variations in MC16e for $W^+ \to \mu^+\nu$ in the measurement binning for m_T. The plots on the left show the up variations and those on the right show the down variations. All values are presented in percentages. Plots (a) and (b) show the muon scale and resolution uncertainties along with the muon scale identification, isolation and trigger scale factor uncertainties. Plots (c) and (d) display the muon sagitta resolution bias uncertainty. Plots (e) and (f) show the missing energy soft track uncertainties. The labels in the legend of both plots are the conventional names given by the JetEtMiss group. "MET" stands for missing energy, "SofTrk" refers to soft track and "ResoPara" and "ResoPerp" refers to the resolution uncertainty on the parallel and perpendicular component. Plots (g) and (h) display the muon sagitta data statistical and muon identification uncertainty.

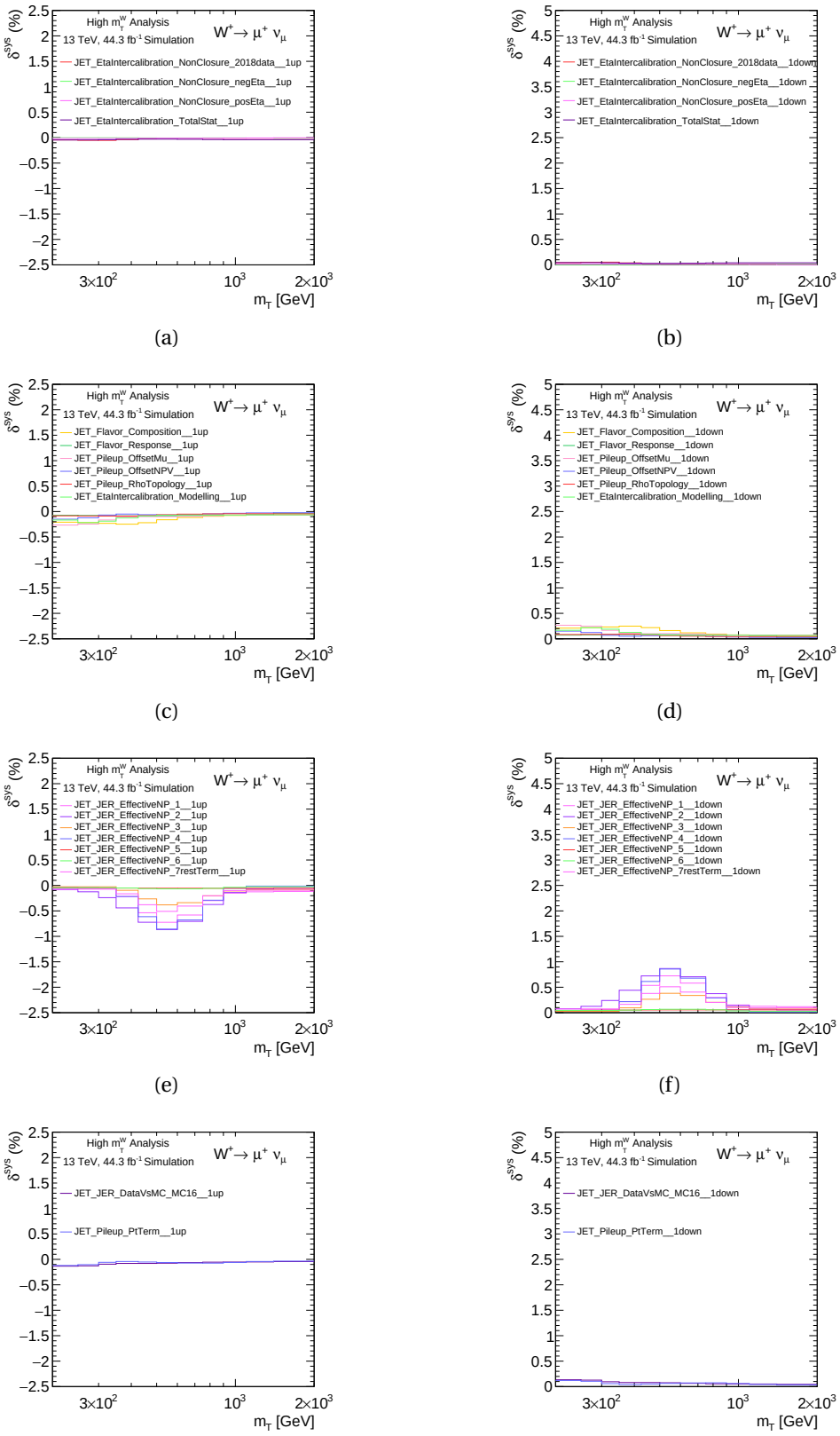

Figure D.36.: Individual contributions to the cross-section systematic variations in MC16d for $W^+ \to \mu^+\nu$ in the measurement binning for m_T. The plots on the left show the up variations and those on the right show the down variations. All values are presented in percentages. Plots (a) to (h) display the effect of the jet's systematic uncertainties.

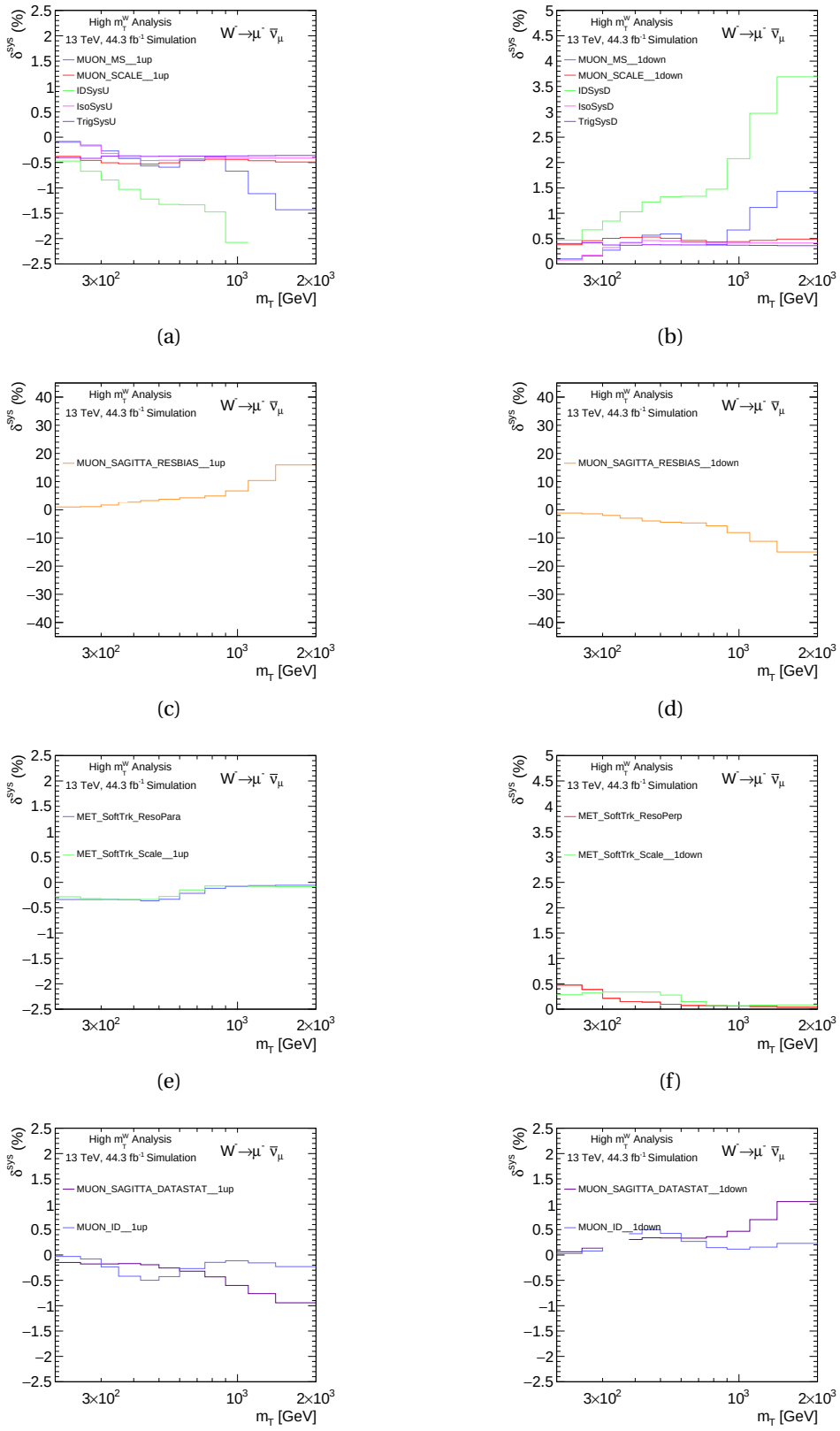

Figure D.37.: Individual contributions to the cross-section systematic variations in MC16d for $W^- \to \mu^- \bar{\nu}$ in the measurement binning for m_T. The plots on the left show the up variations and those on the right show the down variations. All values are presented in percentages. Plots (a) and (b) show the muon scale and resolution uncertainties along with the muon scale identification, isolation and trigger scale factor uncertainties. Plots (c) and (d) display the muon sagitta resolution bias uncertainty. Plots (e) and (f) show the missing energy soft track uncertainties. The labels in the legend of both plots are the conventional names given by the JetEtMiss group. "MET" stands for missing energy, "SofTrk" refers to soft track $\vec{p}_T^{223}$ and "ResoPara" and "ResoPerp" refers to the resolution uncertainty on the parallel and perpendicular component. Plots (g) and (h) display the muon sagitta data statistical and muon identification uncertainty.

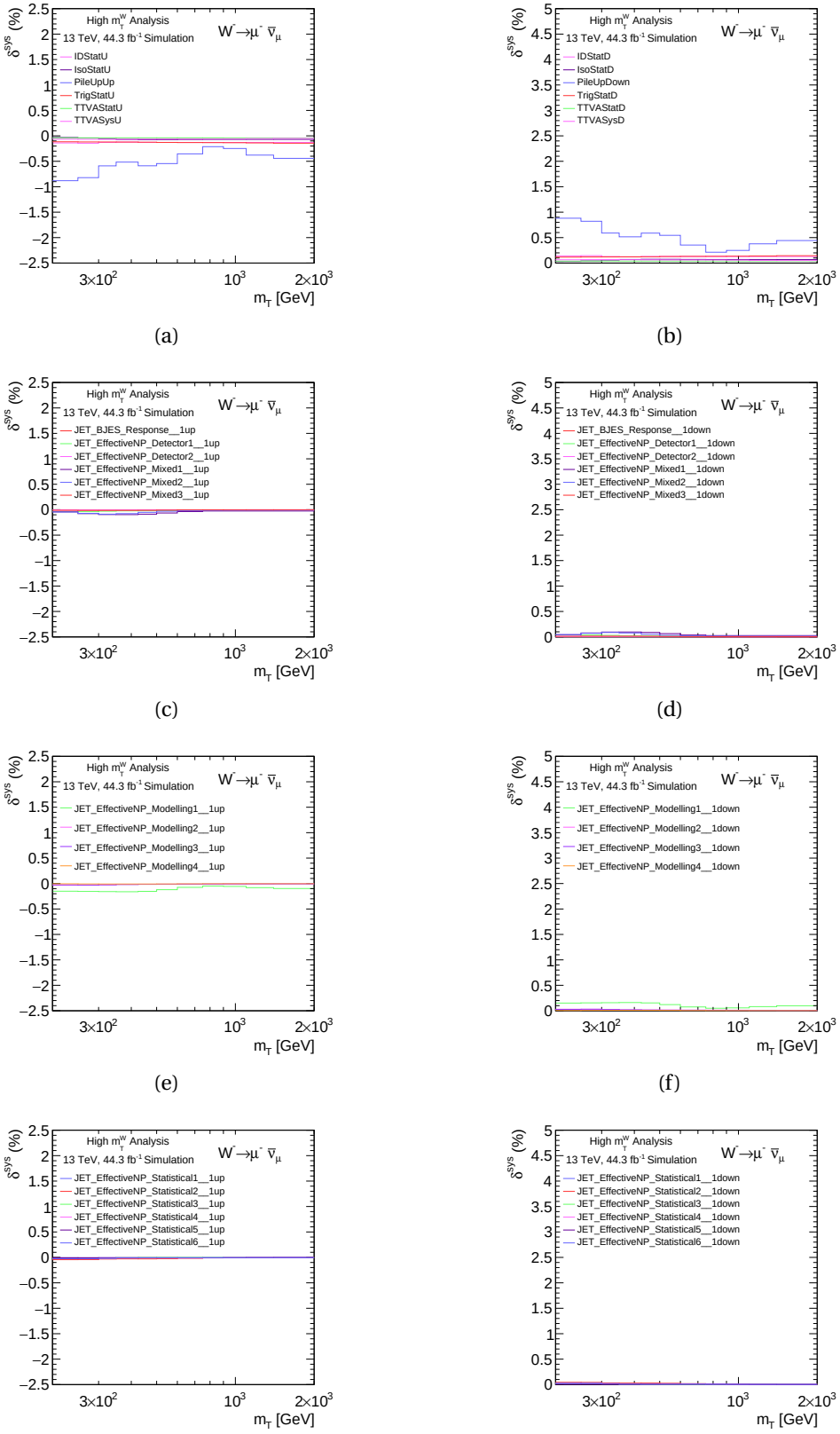

Figure D.38.: Individual contributions to the cross-section systematic variations in MC16d for $W^- \to \mu^- \bar{\nu}$ in the measurement binning for m_T. The plots on the left show the up variations and those on the right show the down variations. All values are presented in percentages. Plots (a) and (b) show the scale factor uncertainties for the muon identification, isolation, trigger and TTVA statistical uncertainties. Also shown are the TTVA systematic uncertainty and the pileup uncertainty. Plots (c) to (h) display the effect of the jet's systematic uncertainties.

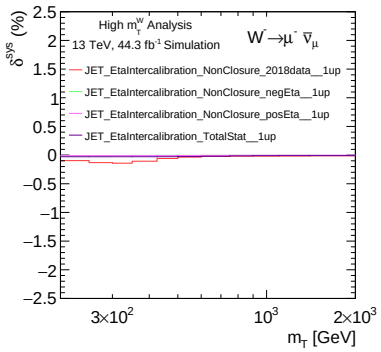

(a)

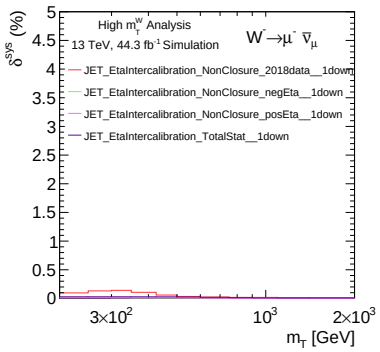

(b)

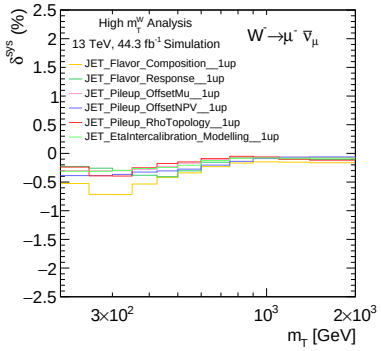

(c)

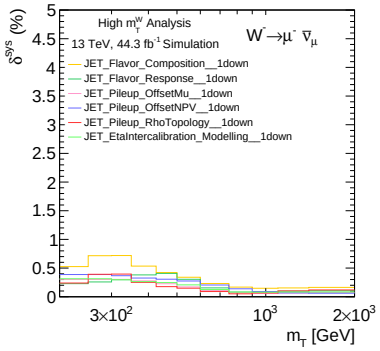

(d)

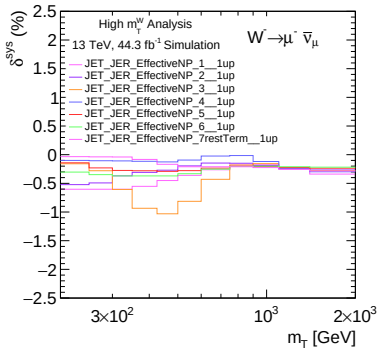

(e)

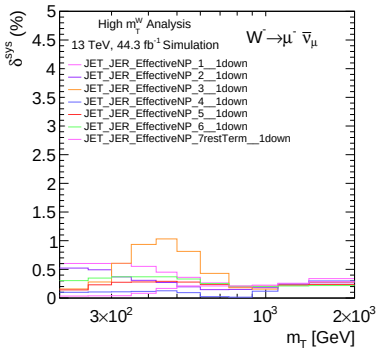

(f)

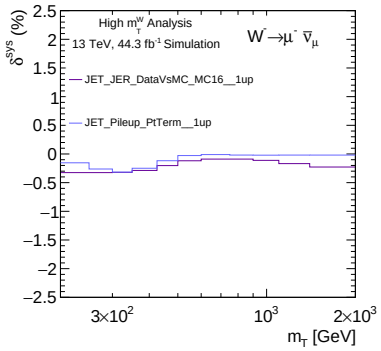

(g)

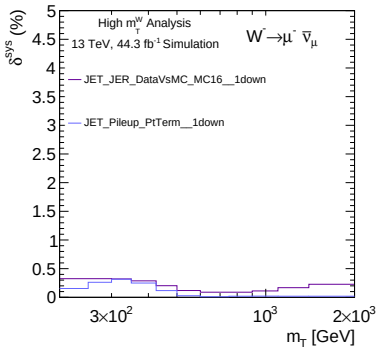

(h)

Figure D.39.: Individual contributions to the cross-section systematic variations in MC16d for $W^- \to \mu^- \bar{\nu}$ in the measurement binning for m_T. The plots on the left show the up variations and those on the right show the down variations. All values are presented in percentages. Plots (a) to (h) display the effect of the jet's systematic uncertainties.

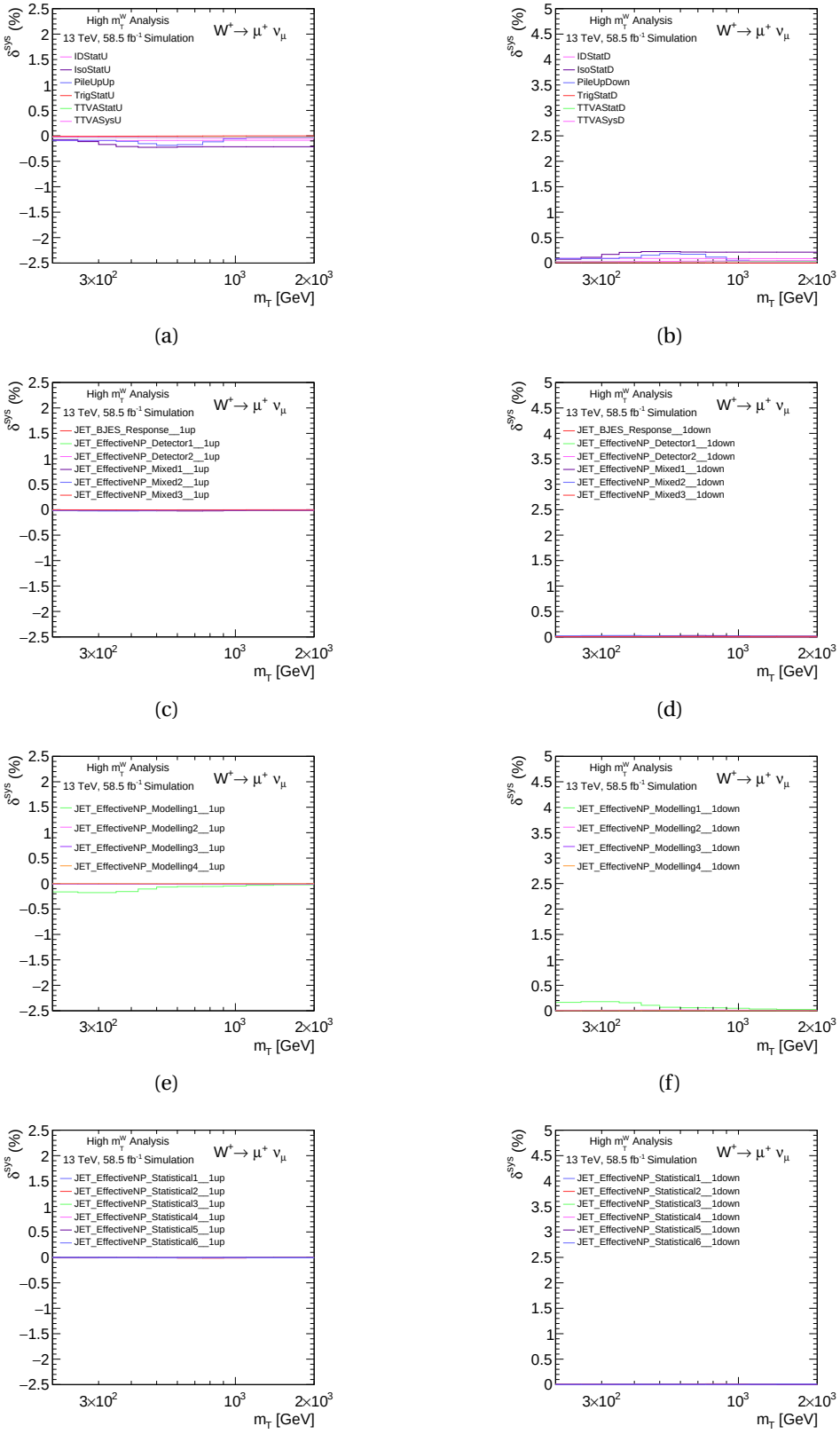

Figure D.41.: Individual contributions to the cross-section systematic variations in MC16e for $W^+ \to \mu^+ \nu$ in the measurement binning for m_T. The plots on the left show the up variations and those on the right show the down variations. All values are presented in percentages. Plots (a) and (b) show the scale factor uncertainties for the muon identification, isolation, trigger and TTVA statistical uncertainties. Also shows the TTVA systematic uncertainty and the pileup uncertainty. Plots (c) to (h) display the effect of the jet's systematic uncertainties.

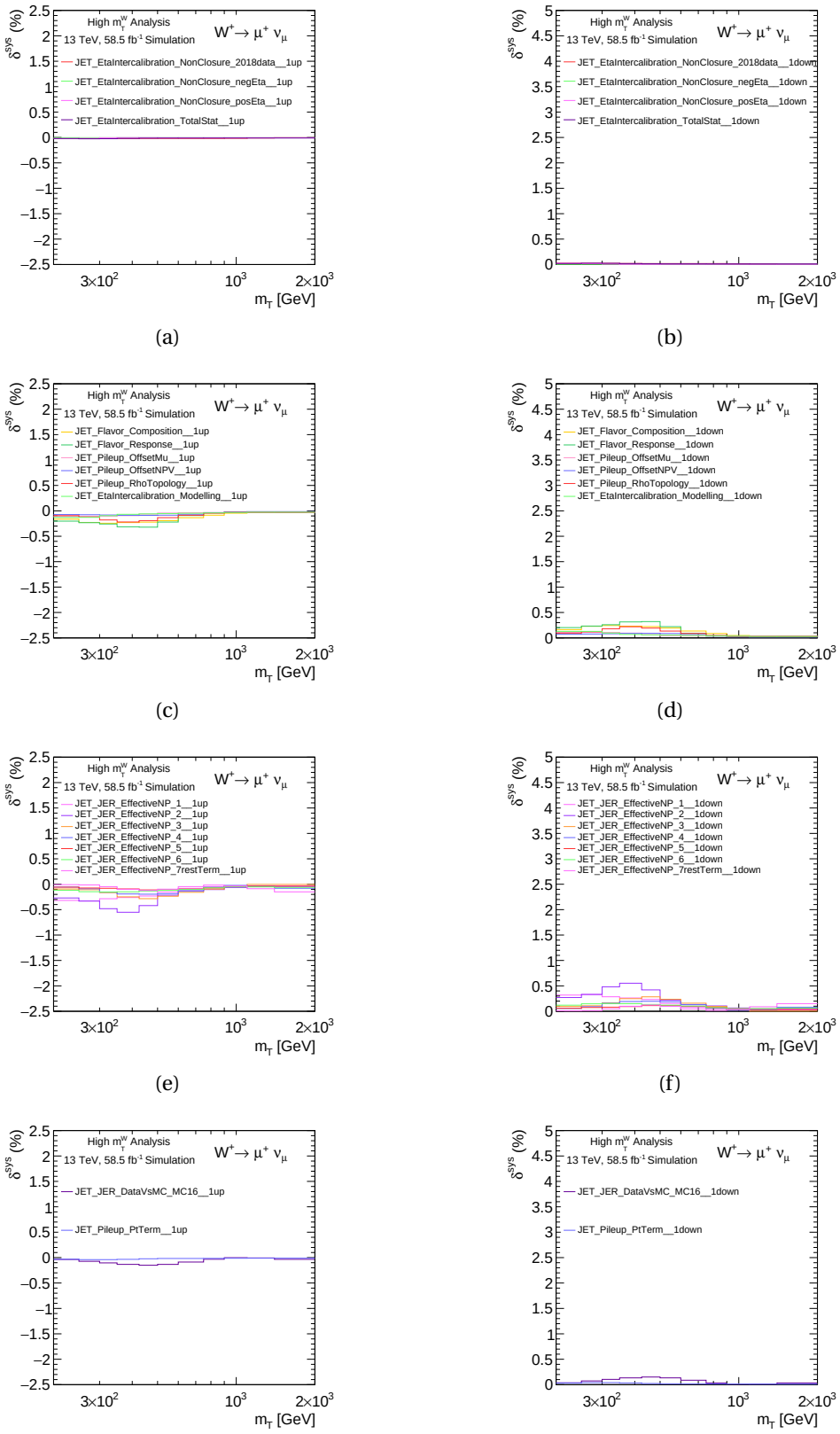

Figure D.42.: Individual contributions to the cross-section systematic variations in MC16e for $W^+ \to \mu^+\nu$ in the measurement binning for m_T. The plots on the left show the up variations and those on the right show the down variations. All values are presented in percentages. Plots (a) to (h) display the effect of the jet's systematic uncertainties.

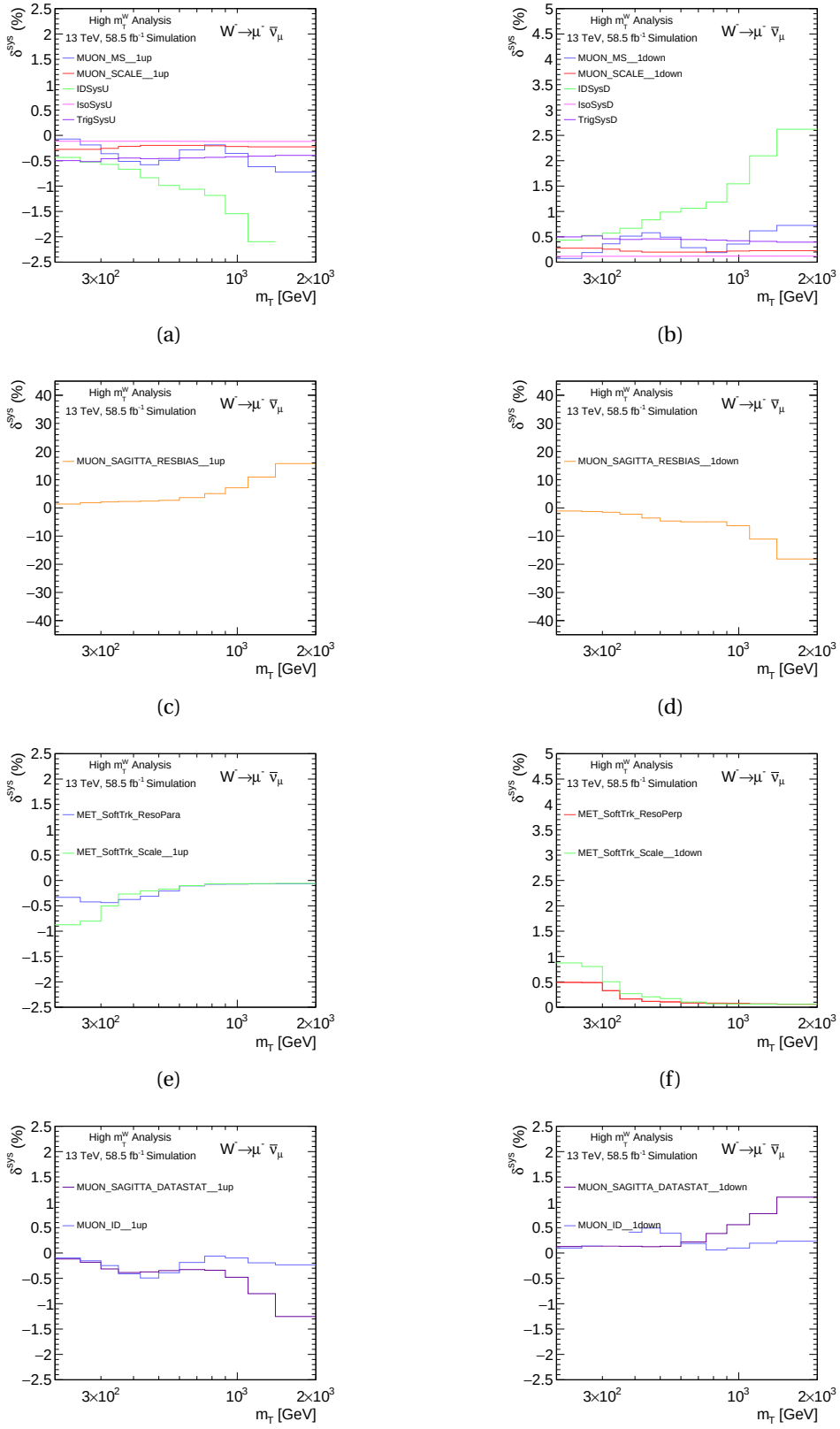

Figure D.43.: Individual contributions to the cross-section systematic variations in MC16e for $W^- \to \mu^- \bar{\nu}$ in the measurement binning for m_T. The plots on the left show the up variations and those on the right show the down variations. All values are presented in percentages. Plots (a) and (b) show the muon scale and resolution uncertainties along with the muon scale identification, isolation and trigger scale factor uncertainties. Plots (c) and (d) display the muon sagitta resolution bias uncertainty. Plots (e) and (f) show the missing energy soft track uncertainties. The labels in the legend of both plots are the conventional names given by the JetEtMiss group. "MET" stands for missing energy, "SofTrk" refers to soft track E_T^{miss} and “ResoPara” and “ResoPerp” refers to the resolution uncertainty on the parallel and perpendicular component. Plots (g) and (h) display the muon sagitta data statistical and muon identification uncertainty.

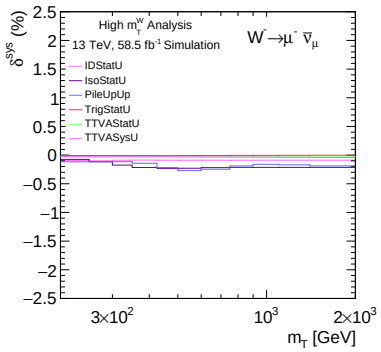

(a)

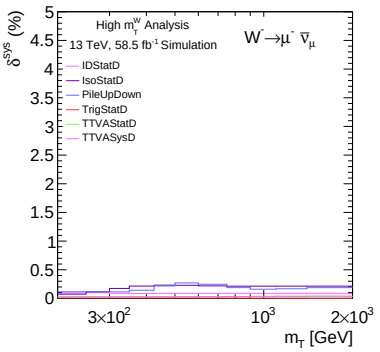

(b)

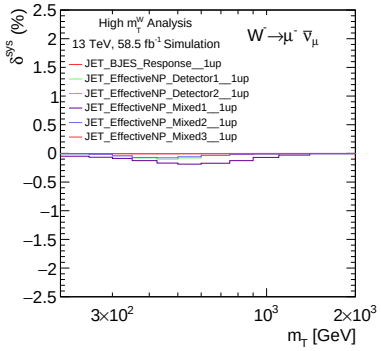

(c)

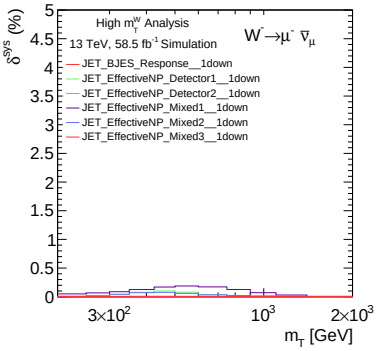

(d)

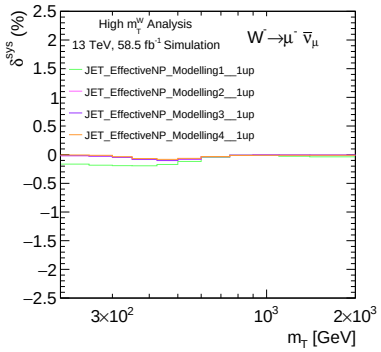

(e)

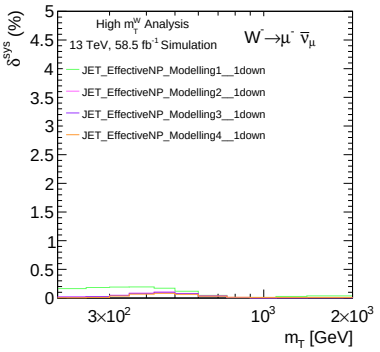

(f)

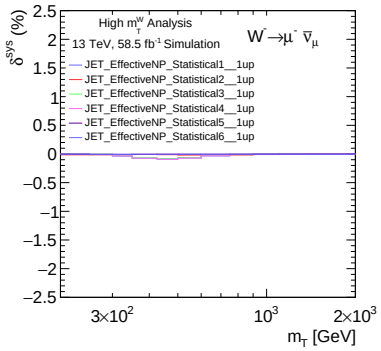

(g)

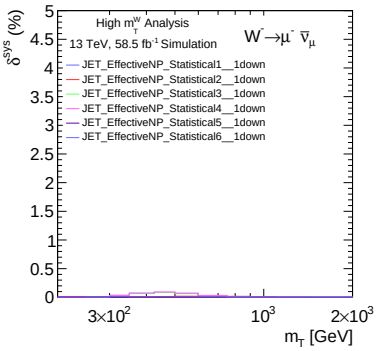

(h)

Figure D.44.: Individual contributions to the cross-section systematic variations in MC16e for $W^- \to \mu^- \bar{\nu}$ in the measurement binning for m_T. The plots on the left show the up variations and those on the right show the down variations. All values are presented in percentages. Plots (a) and (b) show the scale factor uncertainties for the muon identification, isolation, trigger and TTVA statistical uncertainties. Also shown are the TTVA systematic uncertainty and the pileup uncertainty. Plots (c) to (h) display the effect of the jet's systematic uncertainties.

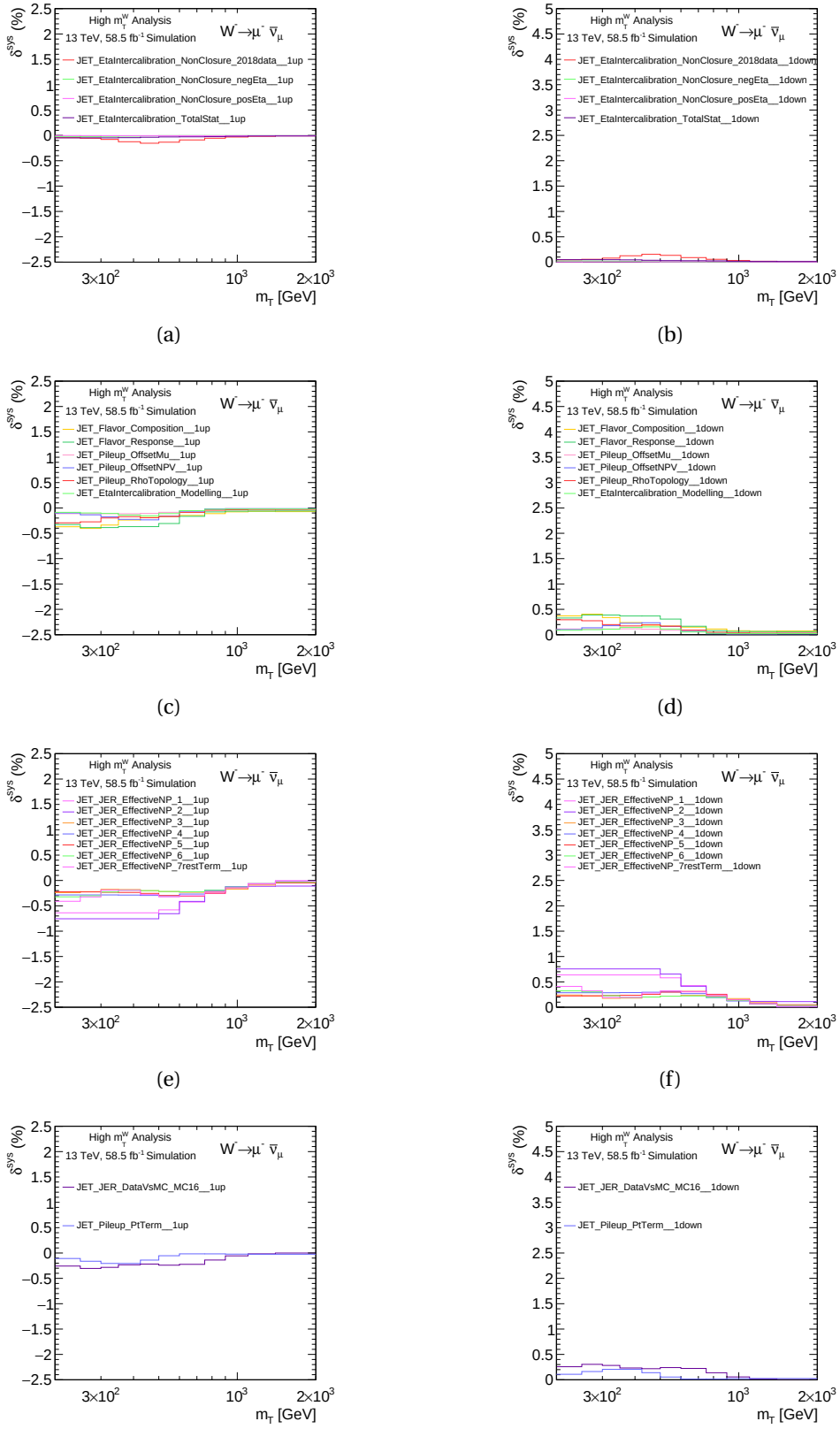

Figure D.45.: Individual contributions to the cross-section systematic variations in MC16e for $W^- \to \mu^- \bar{\nu}$ in the measurement binning for m_T. The plots on the left show the up variations and those on the right show the down variations. All values are presented in percentages. Plots (a) to (h) display the effect of the jet's systematic uncertainties.

D.5. Asymmetry Systematic Uncertainties For Individual Monte Carlo Campaigns

This section is for the distributions of the systematic uncertainties for individual Monte Carlo campaigns MC16a, MC16d and MC16e. The systematic uncertainties have been discussed in Chapter 8. The following distributions are for the experimental systematic uncertainties for the asymmetry measurement and are calculated using Equation 10.2. The uncertainties are first shown for the muon, sagitta and missing energy uncertainties. Then uncertainties are shown for the scale factor identification, isolation, pile-up, trigger, TTVA and jet uncertainties. Finally, more jet systematic uncertainties are shown.

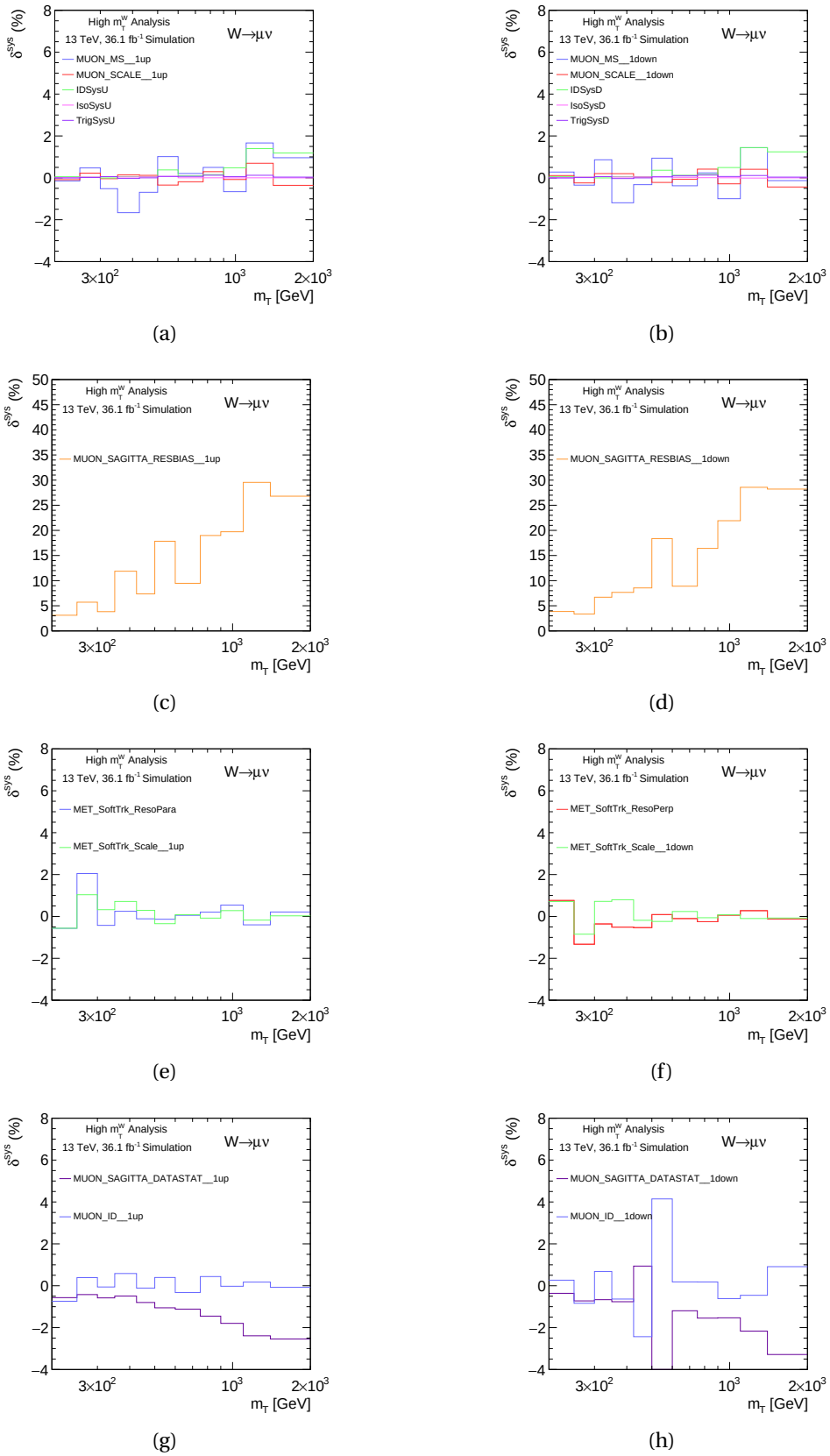

Figure D.46.: Individual contributions to the muon asymmetry systematic variations in MC16a for $W \to \mu\nu$ in the measurement binning for m_T. The plots on the left show the up variations and those on the right show the down variations. All values are presented in percentages. Plots (a) and (b) show the muon scale and resolution uncertainties along with the muon scale identification, isolation and trigger scale factor uncertainties. Plots (c) and (d) display the muon sagitta resolution bias uncertainty. Plots (e) and (f) show the missing energy soft track uncertainties. The labels in the legend of both plots are the conventional names given by the JetEtMiss group. "MET" stands for missing energy, "SofTrk" refers to soft track E_T^{miss} and “ResoPara” and “ResoPerp” refers to the resolution uncertainty on the parallel and perpendicular component. Plots (g) and (h) display the muon sagitta data statistical and muon identification uncertainty.

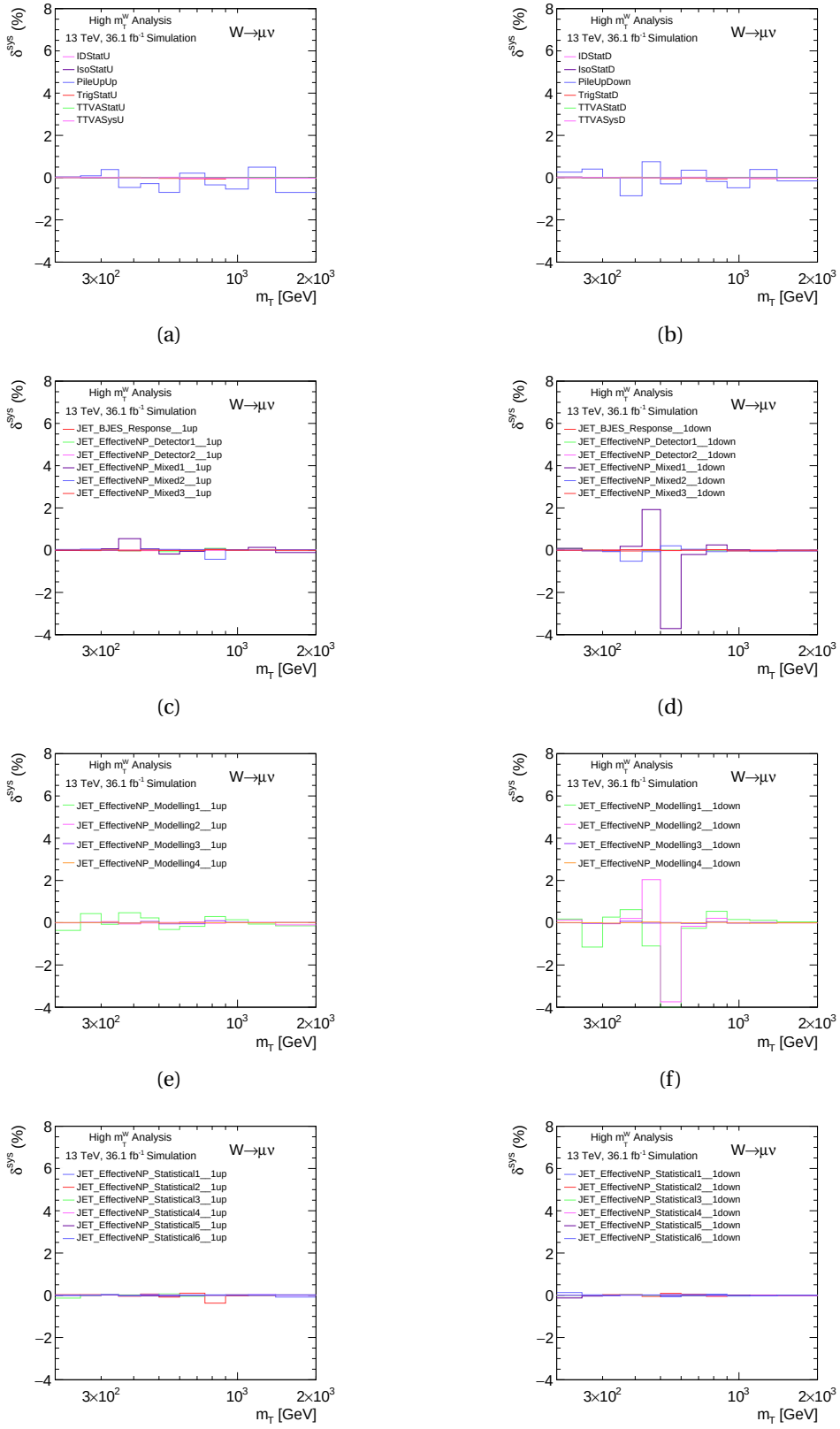

Figure D.47.: Individual contributions to the asymmetry systematic variations in MC16a for $W \to \mu\nu$ in the measurement binning for m_T. The plots on the left show the up variations and those on the right show the down variations. All values are presented in percentages. Plots (a) and (b) show the scale factor uncertainties for the muon identification, isolation, trigger and TTVA statistical uncertainties. Also shown are the TTVA systematic uncertainty and the pileup uncertainty. Plots (c) to (h) display the effect of the jet's systematic uncertainties.

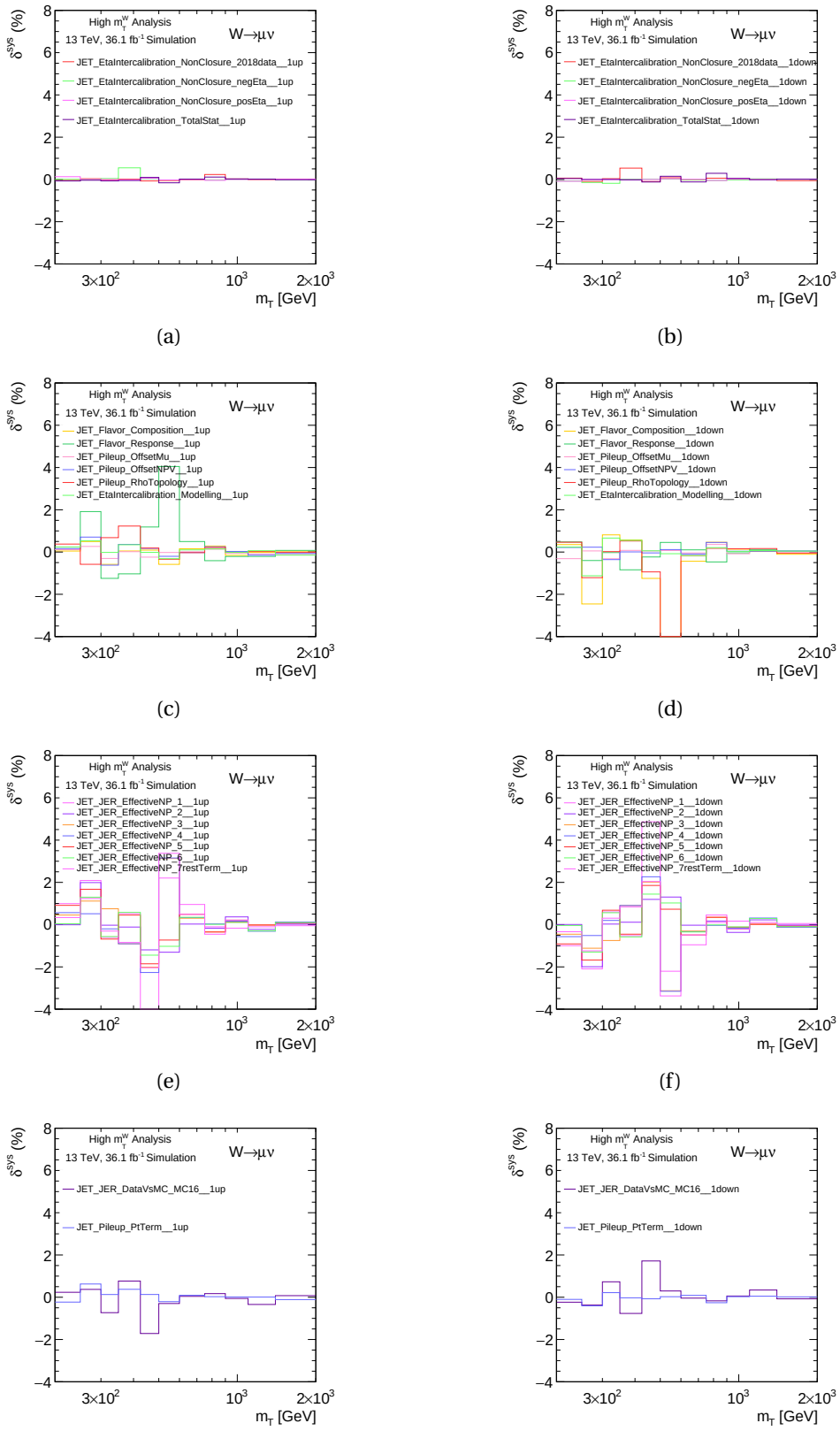

Figure D.48.: Individual contributions to the muon asymmetry systematic variations in MC16a for $W \to \mu\nu$ in the measurement binning for m_T. The plots on the left show the up variations and those on the right show the down variations. All values are presented in percentages. Plots (a) to (h) display the effect of the jet's systematic uncertainties.

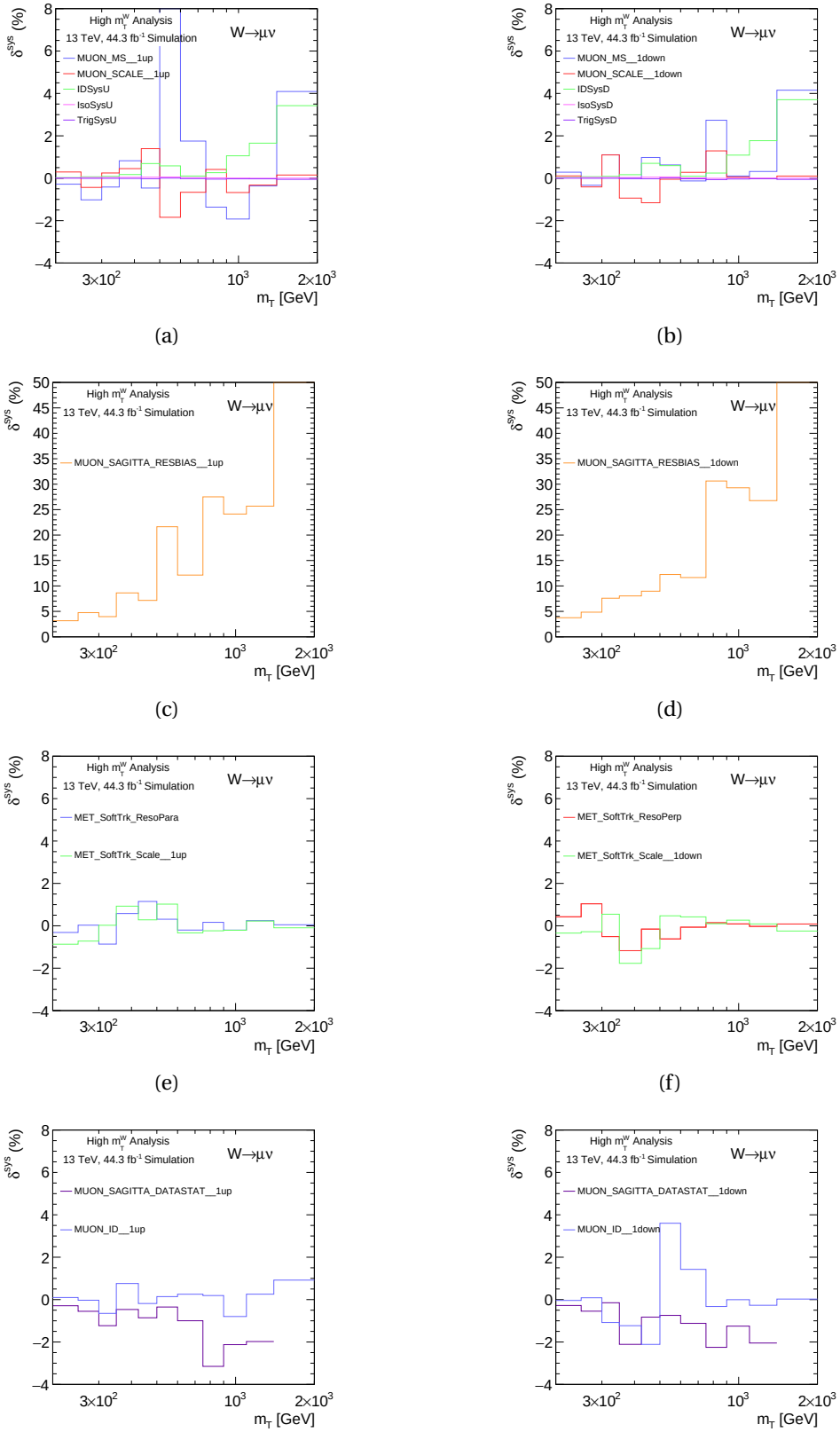

Figure D.49.: Individual contributions to the muon asymmetry systematic variations in MC16d for $W \to \mu\nu$ in the measurement binning for m_T. The plots on the left show the up variations and those on the right show the down variations. All values are presented in percentages. Plots (a) and (b) show the muon scale and resolution uncertainties along with the muon scale identification, isolation and trigger scale factor uncertainties. Plots (c) and (d) display the muon sagitta resolution bias uncertainty. Plots (e) and (f) show the missing energy soft track uncertainties. The labels in the legend of both plots are the conventional names given by the JetEtMiss group. "MET" stands for missing energy, "SofTrk" refers to soft track and "ResoPara" and "ResoPerp" refers to the resolution uncertainty on the parallel and perpendicular component. Plots (g) and (h) display the muon sagitta data statistical and muon identification uncertainty.

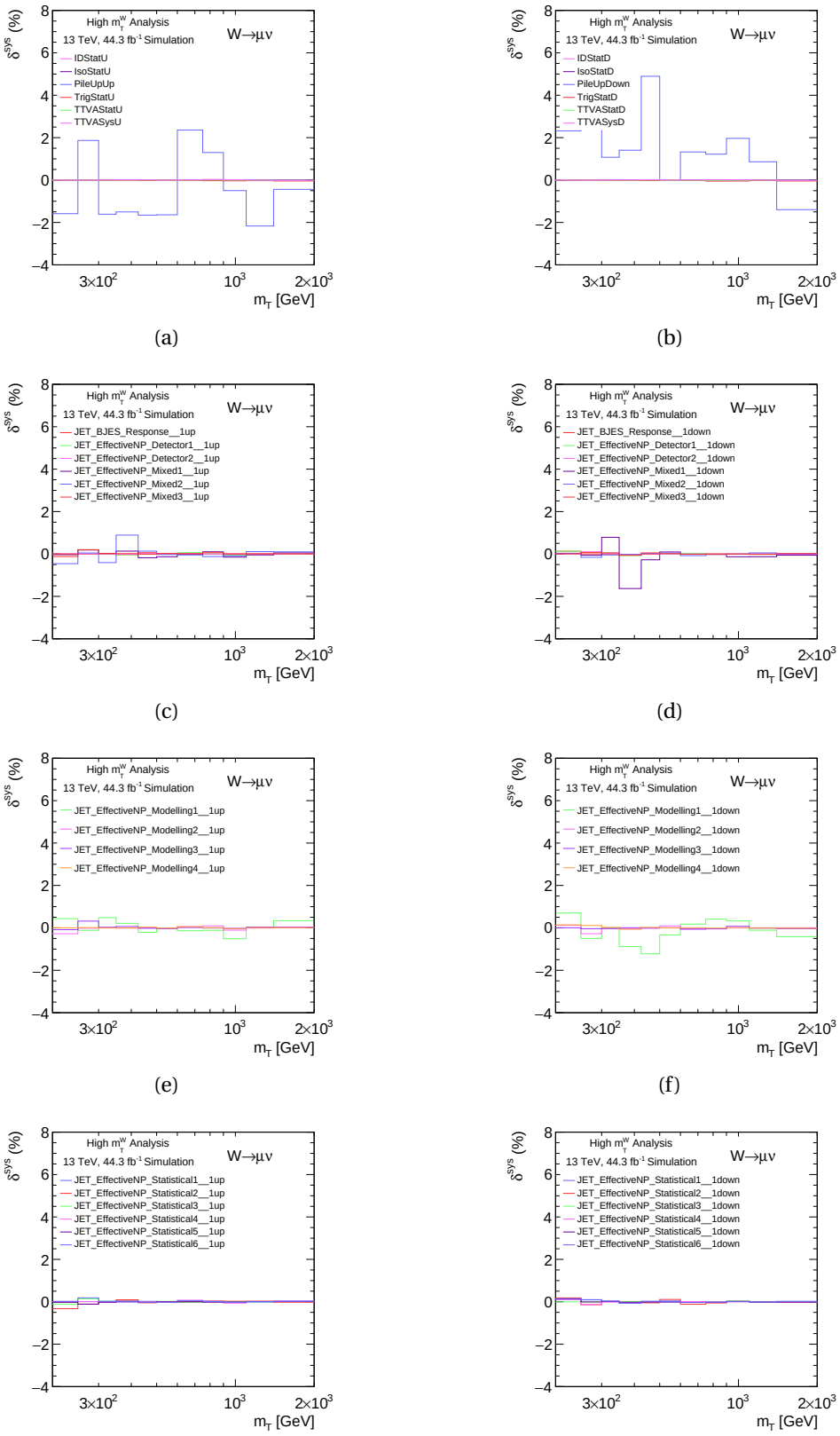

Figure D.50.: Individual contributions to the asymmetry systematic variations in MC16d for $W \to \mu\nu$ in the measurement binning for m_T. The plots on the left show the up variations and those on the right show the down variations. All values are presented in percentages. Plots (a) and (b) show the scale factor uncertainties for the muon identification, isolation, trigger and TTVA statistical uncertainties. Also shown are the TTVA systematic uncertainty and the pileup uncertainty. Plots (c) to (h) display the effect of the jet's systematic uncertainties.

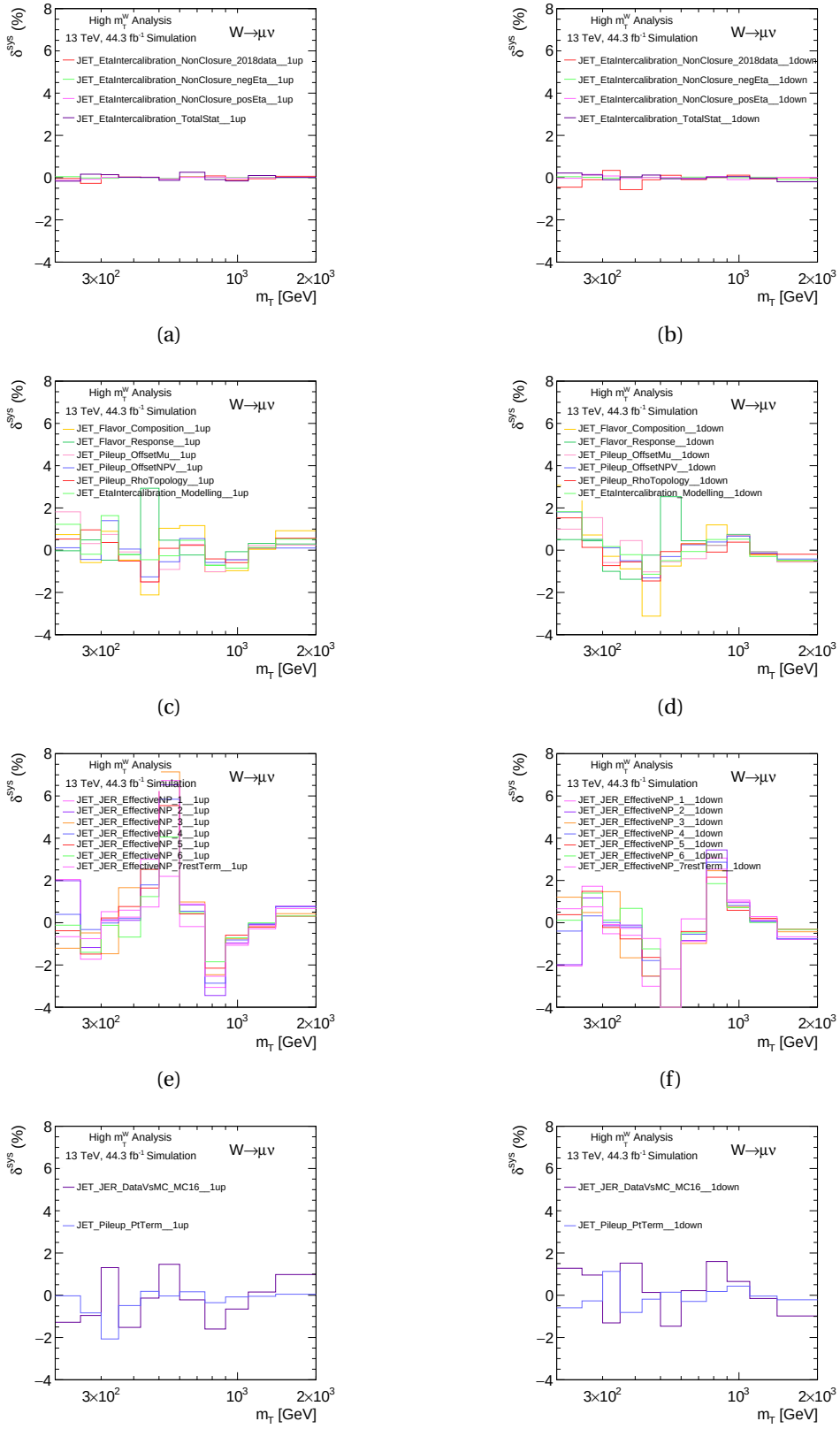

Figure D.51.: Individual contributions to the muon asymmetry systematic variations in MC16d for $W \to \mu\nu$ in the measurement binning for m_T. The plots on the left show the up variations and those on the right show the down variations. All values are presented in percentages. Plots (a) to (h) display the effect of the jet's systematic uncertainties.

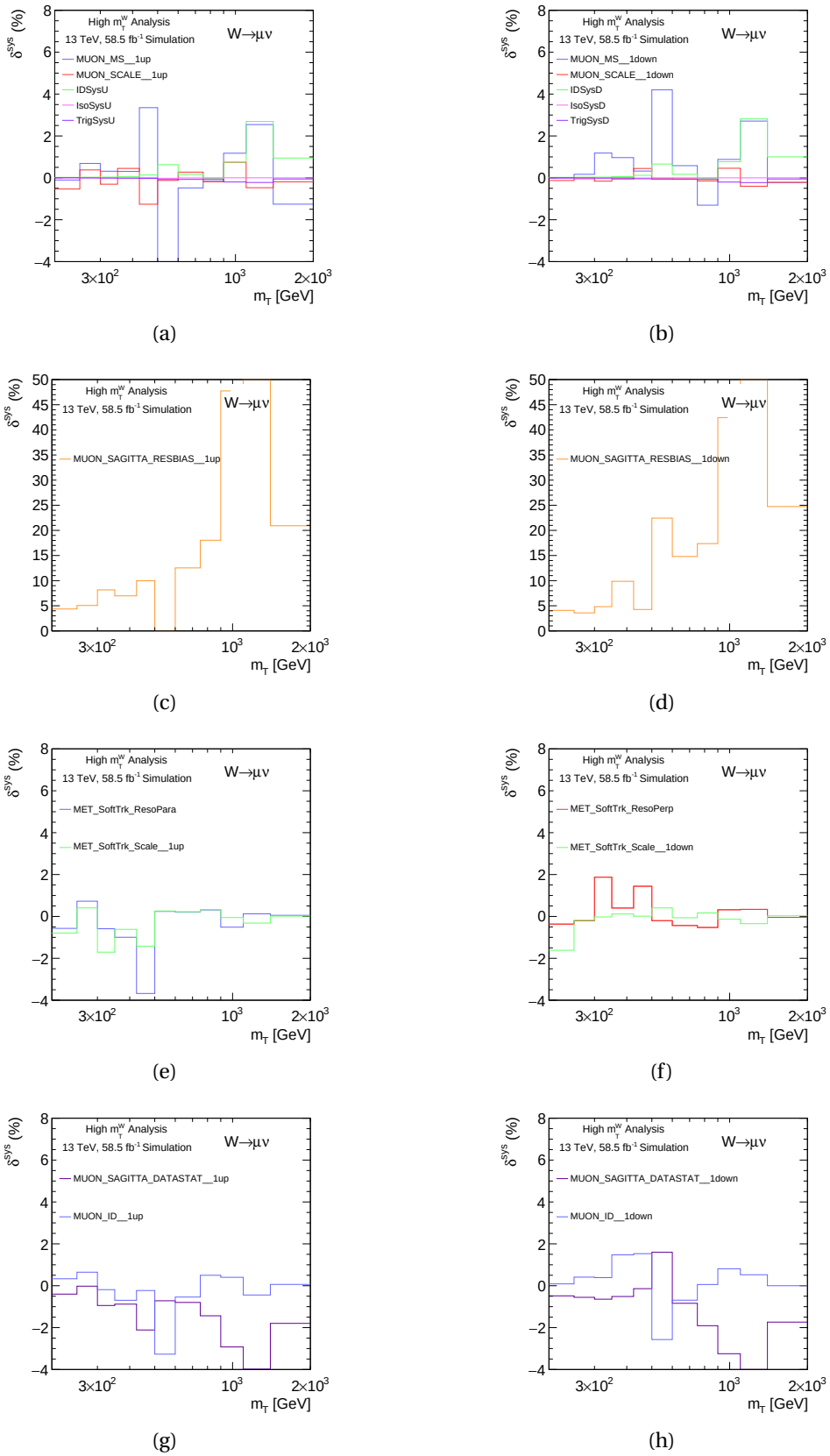

Figure D.52.: Individual contributions to the muon asymmetry systematic variations in MC16e for $W \to \mu\nu$ in the measurement binning for m_T. The plots on the left show the up variations and those on the right show the down variations. All values are presented in percentages. Plots (a) and (b) show the muon scale and resolution uncertainties along with the muon scale identification, isolation and trigger scale factor uncertainties. Plots (c) and (d) display the muon sagitta resolution bias uncertainty. Plots (e) and (f) show the missing energy soft track uncertainties. The labels in the legend of both plots are the conventional names given by the JetEtMiss group. "MET" stands for missing energy, "SofTrk" refers to soft track E_T^{miss} and “ResoPara” and “ResoPerp” refers to the resolution uncertainty on the parallel and perpendicular component. Plots (g) and (h) display the muon sagitta data statistical and muon identification uncertainty.

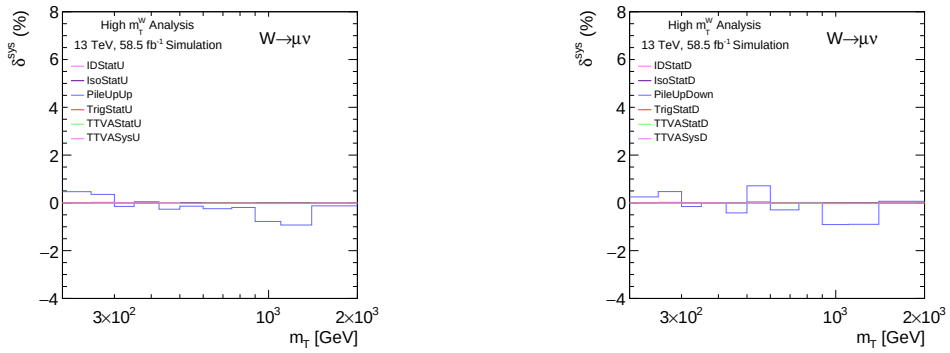

(a)

(b)

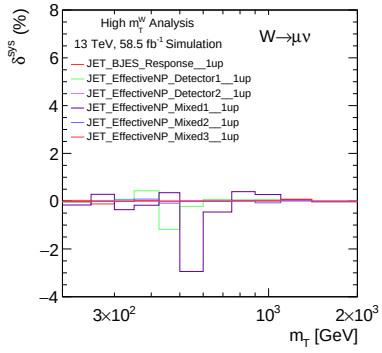

(c)

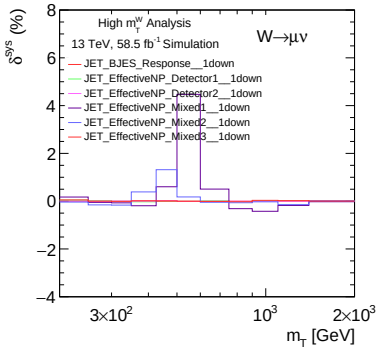

(d)

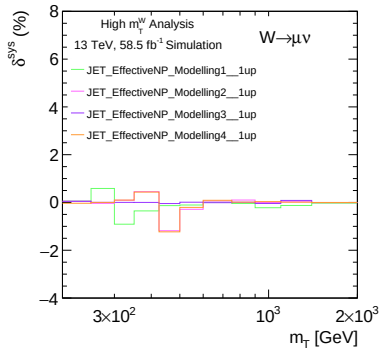

(e)

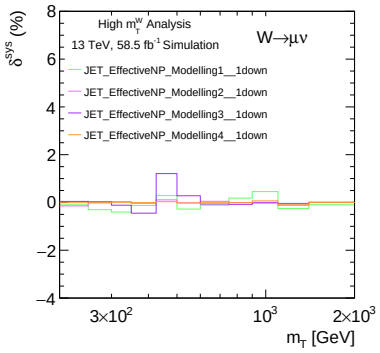

(f)

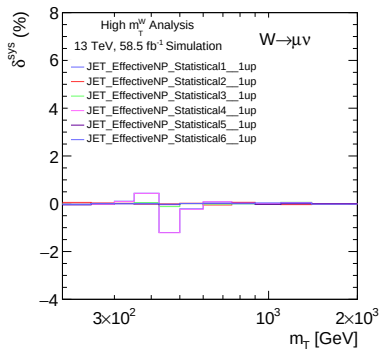

(g)

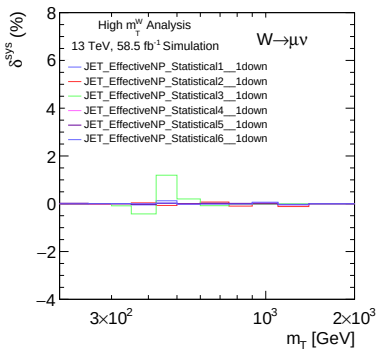

(h)

Figure D.53.: Individual contributions to the asymmetry systematic variations in MC16e for $W \to \mu\nu$ in the measurement binning for m_T. The plots on the left show the up variations and those on the right show the down variations. All values are presented in percentages. Plots (a) and (b) show the scale factor uncertainties for the muon identification, isolation, trigger and TTVA statistical uncertainties. Also shown are the TTVA systematic uncertainty and the pileup uncertainty. Plots (c) to (h) display the effect of the jet's systematic uncertainties.

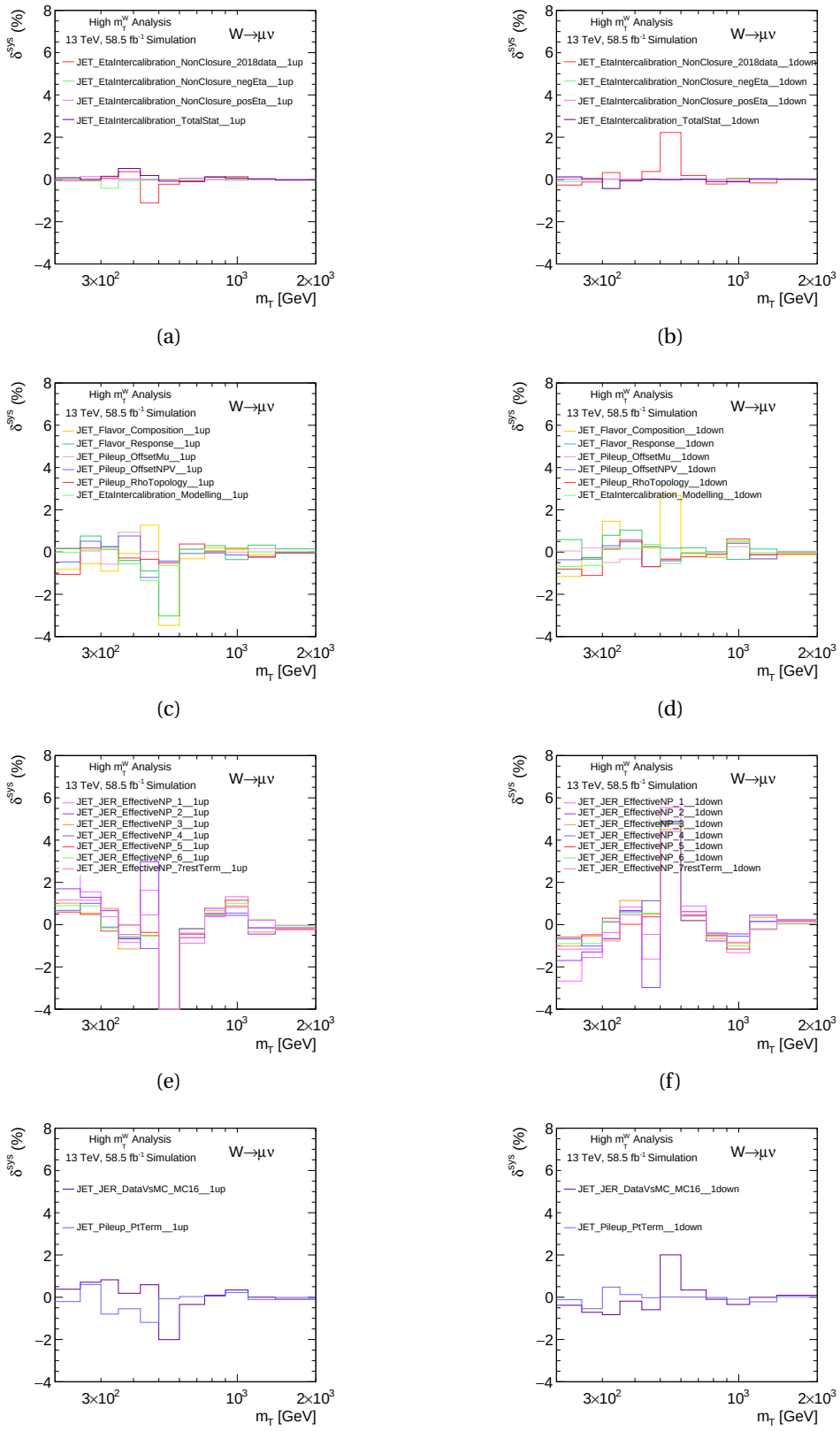

Figure D.54.: Individual contributions to the muon asymmetry systematic variations in MC16e for $W \to \mu\nu$ in the measurement binning for m_T. The plots on the left show the up variations and those on the right show the down variations. All values are presented in percentages. Plots (a) to (h) display the effect of the jet's systematic uncertainties.

E. Appendix: Control Distributions

The following section shows control distributions for each Monte Carlo campaign individually. The kinematic variables presented were discussed in Chapter 9. The plots for the positive charge process, negatively charged process and the combination of charges is displayed. Each Monte Carlo campaign shows reasonable agreement which is reflected by the control distributions presented in the main body of this work. The cutflows for each campaign and charge have also been included.

The relative contributions in the form of a pie chart has also been shown for each Monte Carlo campaign. Most samples' contribution is similar in each campaign except for the multijet which is considerably smaller in MC16a due to less statistics being available in this campaign.

E.1. MC16a

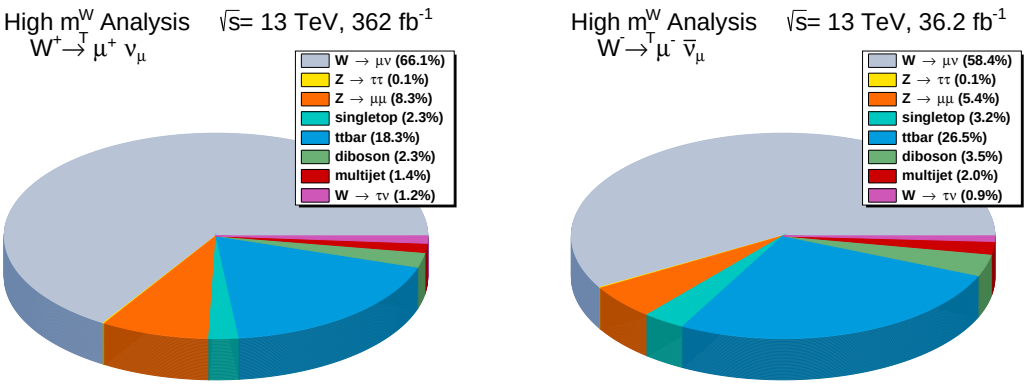

a b

Figure E.1.: Chart showing relative contributions of all Monte Carlo in the signal region for MC16a, for muon charge (a) W^+ and (b) W^-.

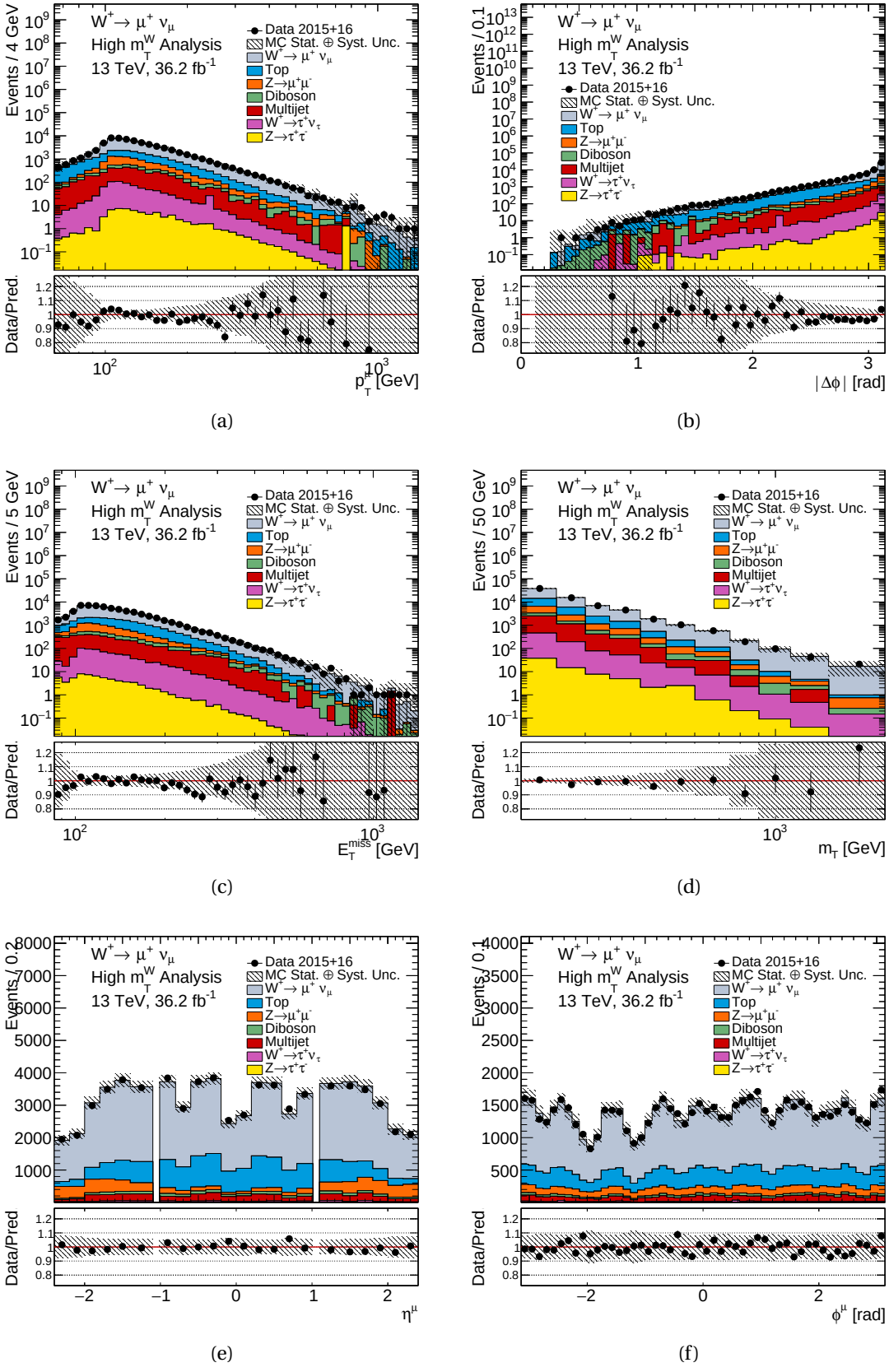

Figure E.2.: MC16a $W^+ \to \mu^+\nu$ control distributions for p_T^μ, $|\Delta\phi|$, E_T^{miss}, m_T, η^μ and ϕ^μ. The data contribution is shown with black points, the signal and the background contributions with solid lines. In the shaded band, systematic experimental uncertainties have been combined with the MC statistical uncertainties. The data statistical uncertainties are shown on the data points. Luminosity uncertainties have not been included.

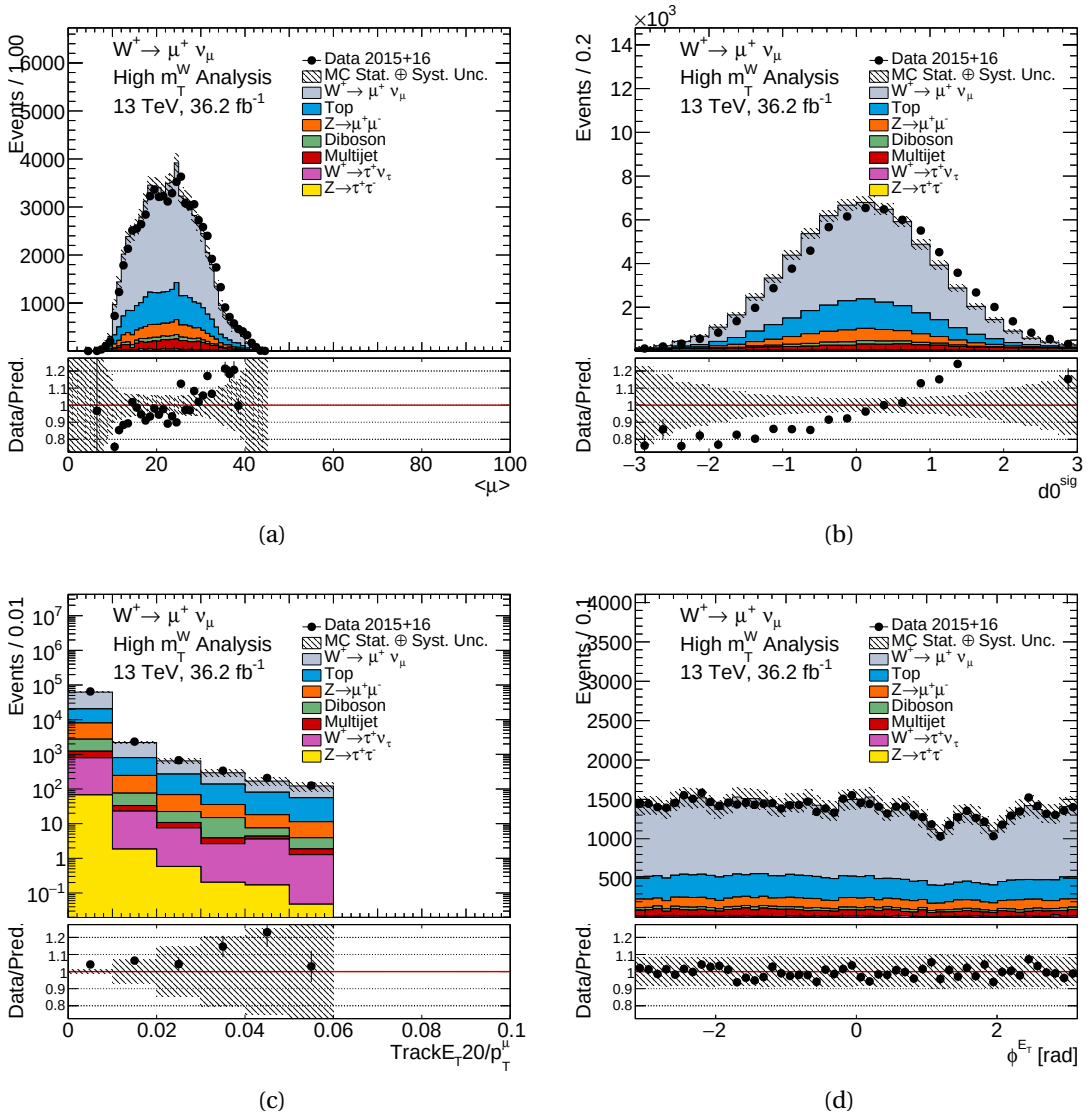

Figure E.3.: MC16a $W^+ \to \mu^+\nu$ control distributions for $<\mu>$, $d0^{sig}$, $TrackE_T20/p_T^{\mu}$ and $\phi^{E_T^{miss}}$. The data contribution is shown with black points, the signal and the background contributions with solid lines. In the shaded band, systematic experimental uncertainties have been combined with the MC statistical uncertainties. The data statistical uncertainties are shown on the data points. Luminosity uncertainties have not been included.

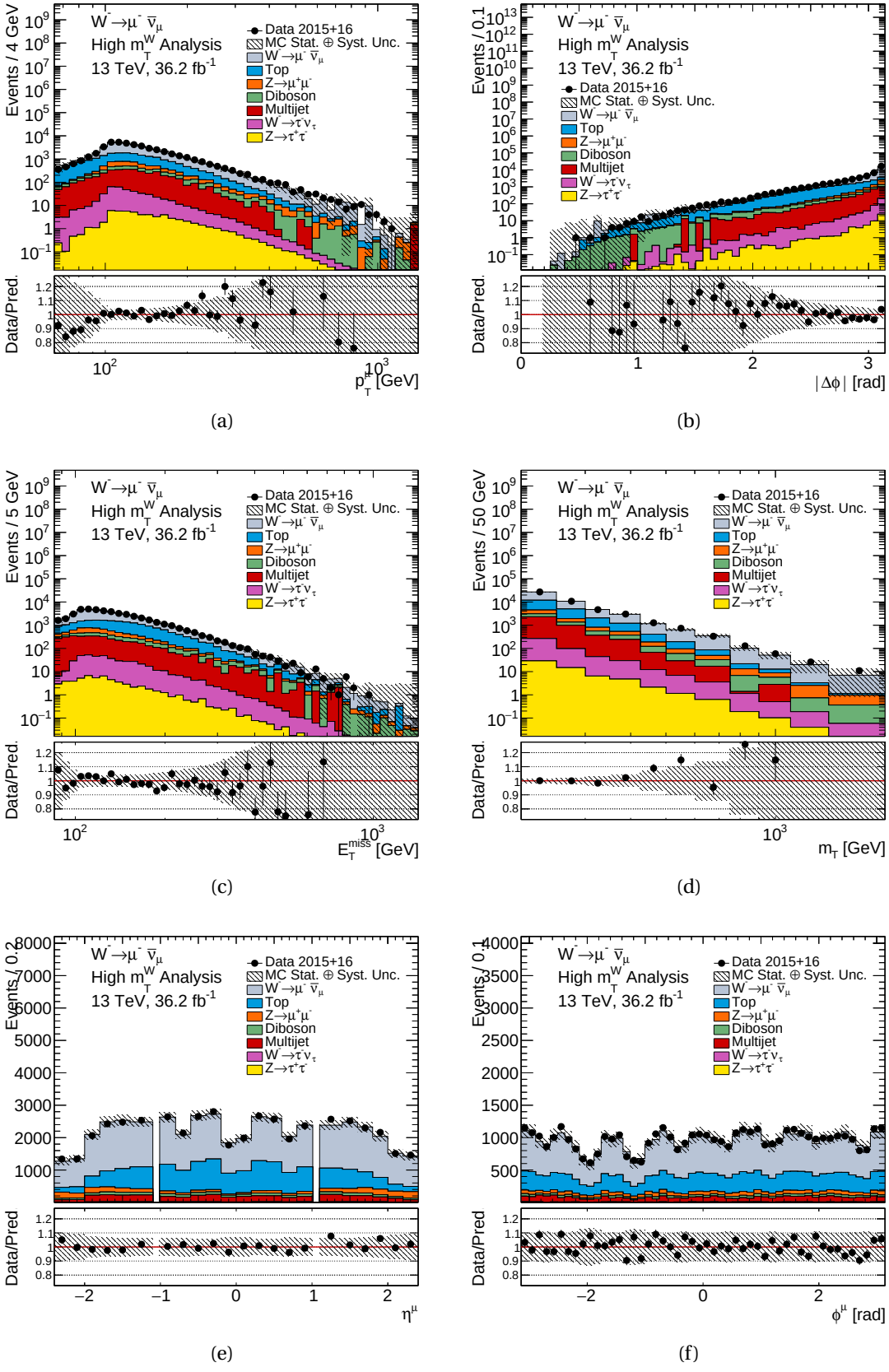

Figure E.4.: MC16a $W^- \to \mu^- \nu$ control distributions for p_T^μ, $|\Delta\phi|$, E_T^{miss}, m_T, η^μ and ϕ^μ. The data contribution is shown with black points, the signal and the background contributions with solid lines. In the shaded band, systematic experimental uncertainties have been combined with the MC statistical uncertainties. The data statistical uncertainties are shown on the data points. Luminosity uncertainties have not been included.

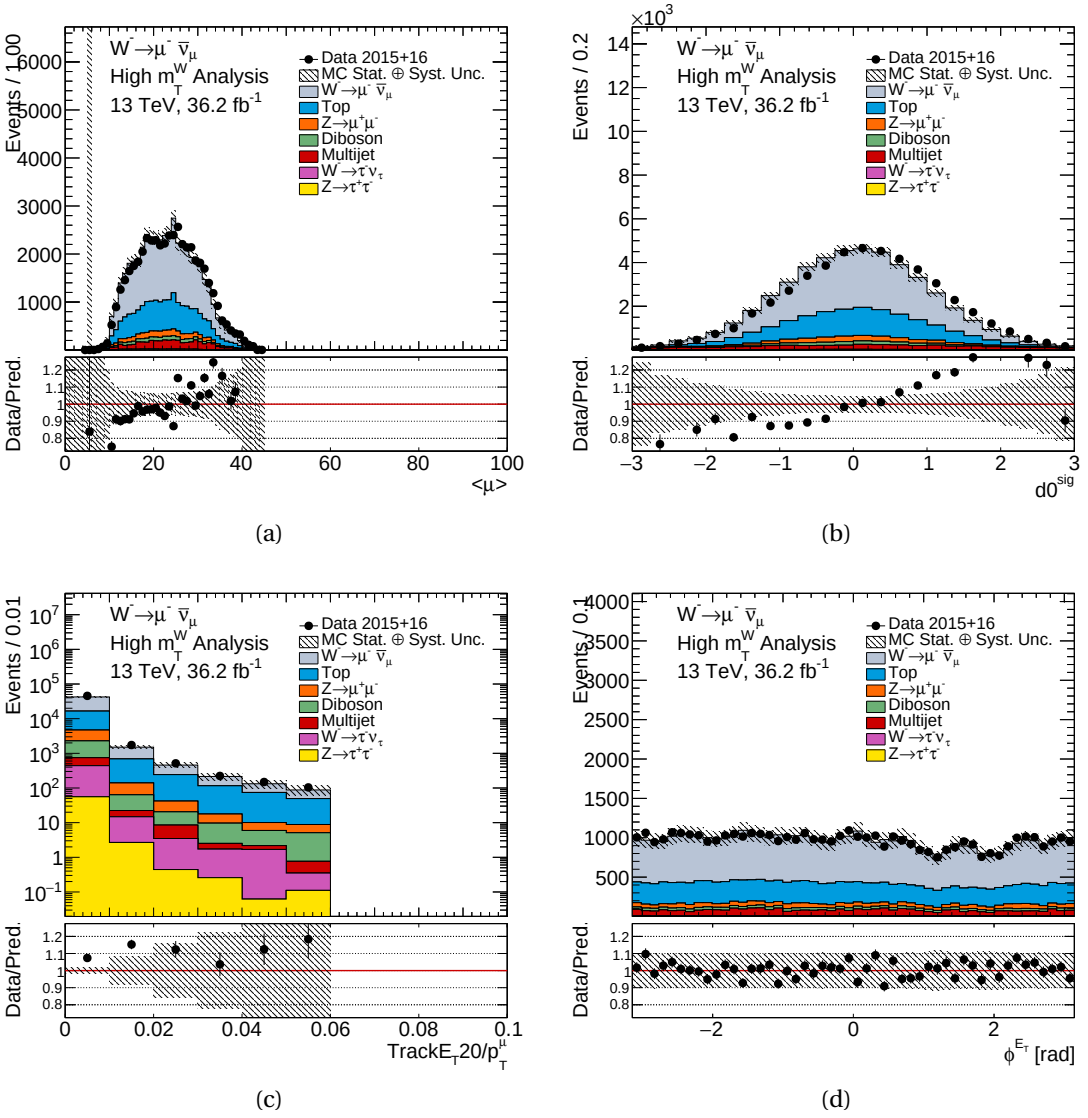

Figure E.5.: MC16a $W^- \to \mu^- \nu$ control distributions for $< \mu >$, $d0^{sig}$, $TrackE_T20/p_T^{\mu}$ and $\phi^{E_T^{miss}}$. The data contribution is shown with black points, the signal and the background contributions with solid lines. In the shaded band, systematic experimental uncertainties have been combined with the MC statistical uncertainties. The data statistical uncertainties are shown on the data points. Luminosity uncertainties have not been included.

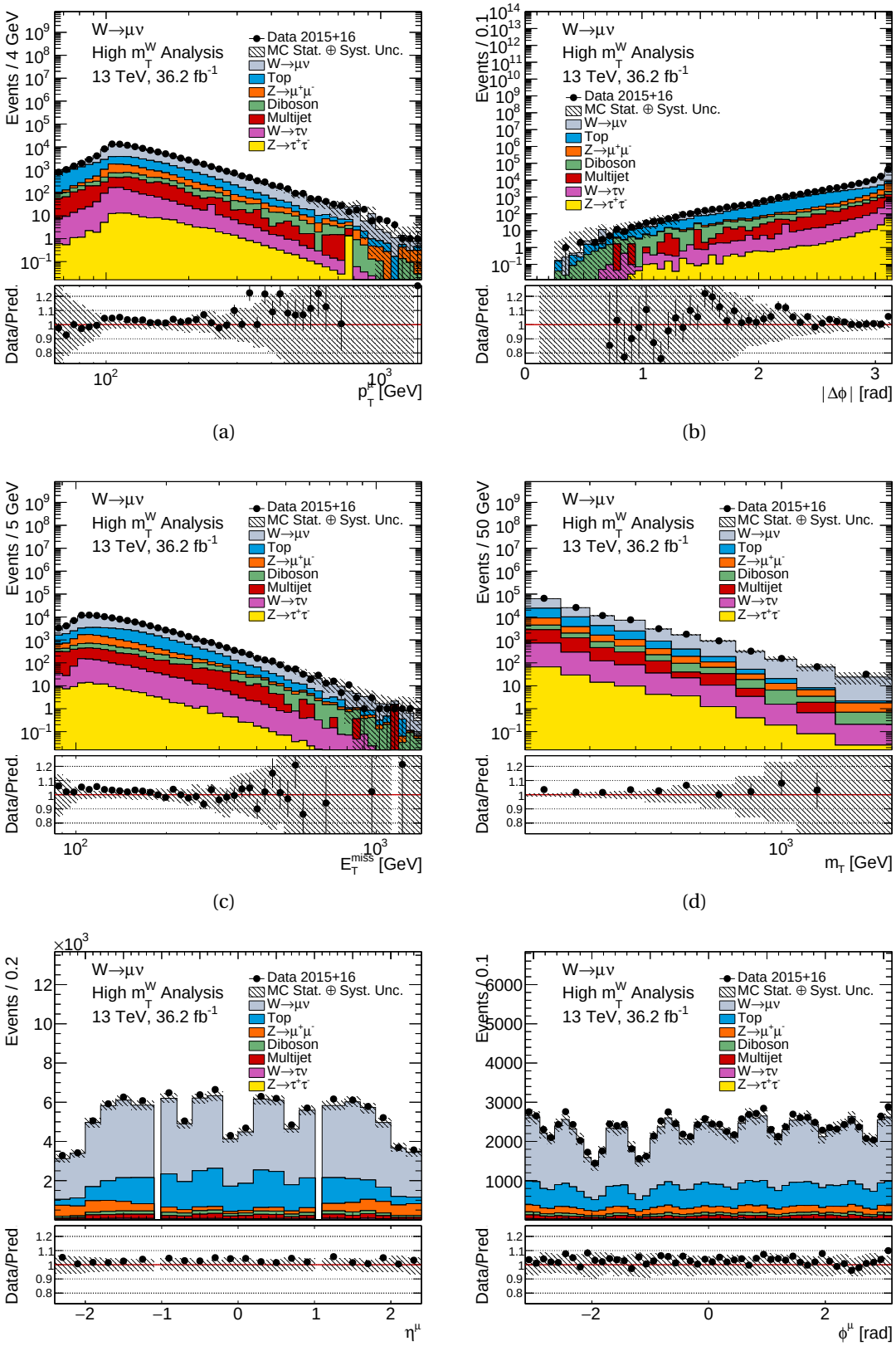

MC16a $W^{\pm} \to \mu\nu$ control distributions for p_T^{μ}, $|\Delta\phi|$, E_T^{miss}, m_T, η^{μ} and ϕ^{μ}.]MC16a combined charge $W^{\pm} \to \mu\nu$ control distributions for p_T^{μ}, $|\Delta\phi|$, E_T^{miss}, m_T, η^{μ} and ϕ^{μ}. The data contribution is shown with black points, the signal and the background contributions with solid lines. In the shaded band, systematic experimental uncertainties have been combined with the MC statistical uncertainties. The data statistical uncertainties are shown on the data points. Luminosity uncertainties have not been included.

Figure F.6 : [

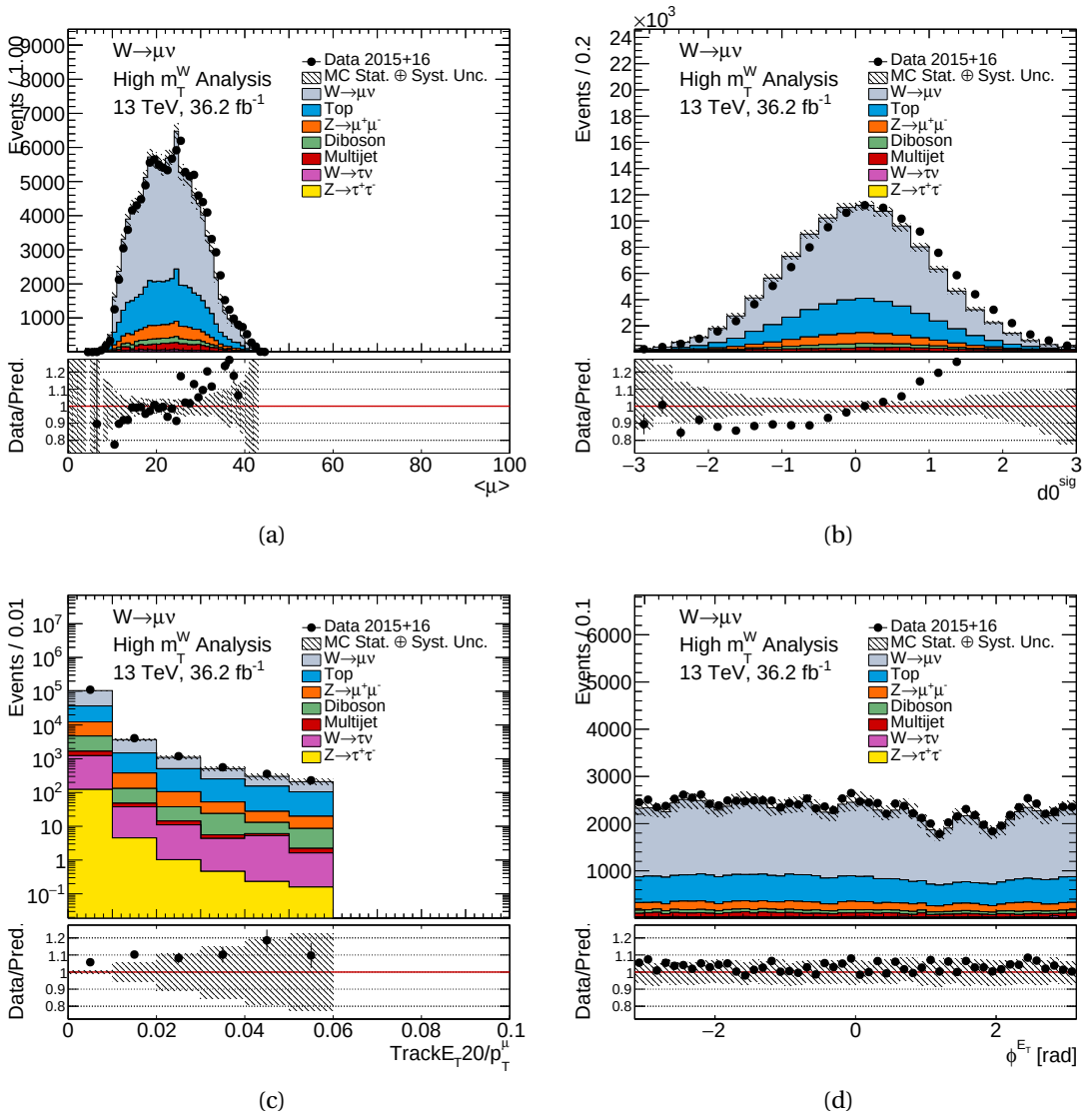

Figure E.7.: MC16a combined charge $W^{\pm} \to \mu\nu$ control distributions for $< \mu >$, $d0^{sig}$, $TrackE_T20/p_T^{\mu}$ and $\phi^{E_T^{miss}}$. The data contribution is shown with black points, the signal and the background contributions with solid lines. In the shaded band, systematic experimental uncertainties have been combined with the MC statistical uncertainties. The data statistical uncertainties are shown on the data points. Luminosity uncertainties have not been included.

	Data	$W^+ \to \mu\nu$	$W^+ \to \tau\nu$	$Z \to \mu\mu$	$Z \to \tau\tau$	Top	Diboson
Initial	$1.74 \cdot 10^9$ (NA)	$4.79 \cdot 10^7$ (NA)	$3.16 \cdot 10^7$ (NA)	$3.17 \cdot 10^8$ (NA)	$1.06 \cdot 10^7$ (NA)	$1.15 \cdot 10^8$ (NA)	$5.67 \cdot 10^7$ (NA)
GRL	$1.70 \cdot 10^9$ (97.81%)	$4.79 \cdot 10^7$ (100%)	$3.16 \cdot 10^7$ (100%)	$3.17 \cdot 10^8$ (100%)	$1.06 \cdot 10^7$ (100%)	$1.15 \cdot 10^8$ (100%)	$5.67 \cdot 10^7$ (100%)
Good Calo	$1.70 \cdot 10^9$ (99.89%)	$4.79 \cdot 10^7$ (100%)	$3.16 \cdot 10^7$ (100%)	$3.17 \cdot 10^8$ (100%)	$1.06 \cdot 10^7$ (100%)	$1.15 \cdot 10^8$ (100%)	$5.67 \cdot 10^7$ (100%)
PriVtx	$1.70 \cdot 10^9$ (100%)	$4.79 \cdot 10^7$ (100%)	$3.16 \cdot 10^7$ (100%)	$3.17 \cdot 10^8$ (100%)	$1.06 \cdot 10^7$ (100%)	$1.15 \cdot 10^8$ (100%)	$5.67 \cdot 10^7$ (100%)
Reco Level	$1.70 \cdot 10^9$ (100%)	$4.79 \cdot 10^7$ (100%)	$3.16 \cdot 10^7$ (100%)	$3.17 \cdot 10^8$ (100%)	$1.06 \cdot 10^7$ (100%)	$1.15 \cdot 10^8$ (100%)	$5.67 \cdot 10^7$ (100%)
Trigger	$5.18 \cdot 10^8$ (30.52%)	$1.92 \cdot 10^7$ (40%)	$4.82 \cdot 10^5$ (1.524%)	$1.91 \cdot 10^8$ (60.05%)	$2.51 \cdot 10^6$ (23.71%)	$3.84 \cdot 10^7$ (33.42%)	$2.20 \cdot 10^7$ (38.77%)
MU_N 20 == 1	$3.65 \cdot 10^8$ (70.55%)	$1.81 \cdot 10^7$ (94.42%)	$3.43 \cdot 10^5$ (71.21%)	$7.07 \cdot 10^7$ (37.1%)	$1.57 \cdot 10^6$ (62.34%)	$3.43 \cdot 10^7$ (89.35%)	$1.40 \cdot 10^7$ (63.9%)
EL_N 20 == 0	$3.65 \cdot 10^8$ (99.88%)	$1.81 \cdot 10^7$ (99.99%)	$3.43 \cdot 10^5$ (99.97%)	$7.07 \cdot 10^7$ (99.92%)	$1.45 \cdot 10^6$ (92.52%)	$3.20 \cdot 10^7$ (93.35%)	$1.20 \cdot 10^7$ (85.35%)
MU_N 30 == 1	$2.66 \cdot 10^8$ (72.88%)	$1.51 \cdot 10^7$ (83.57%)	$2.15 \cdot 10^5$ (62.55%)	$5.56 \cdot 10^7$ (78.72%)	$1.12 \cdot 10^6$ (77.51%)	$2.85 \cdot 10^7$ (88.88%)	$1.03 \cdot 10^7$ (86.12%)
MU_N 65 == 1	$1.80 \cdot 10^7$ (6.78%)	$2.86 \cdot 10^6$ (18.92%)	$6.21 \cdot 10^4$ (28.94%)	$5.62 \cdot 10^6$ (10.11%)	$6.12 \cdot 10^5$ (54.57%)	$9.89 \cdot 10^6$ (34.75%)	$3.25 \cdot 10^6$ (31.51%)
MU_N Tight 65 == 1	$1.80 \cdot 10^7$ (100%)	$2.86 \cdot 10^6$ (100%)	$6.21 \cdot 10^4$ (100%)	$5.62 \cdot 10^6$ (100%)	$6.12 \cdot 10^5$ (100%)	$9.89 \cdot 10^6$ (100%)	$3.25 \cdot 10^6$ (100%)
Trigger match	$1.80 \cdot 10^7$ (99.89%)	$2.86 \cdot 10^6$ (100%)	$6.21 \cdot 10^4$ (99.98%)	$5.56 \cdot 10^6$ (98.96%)	$6.01 \cdot 10^5$ (98.18%)	$9.87 \cdot 10^6$ (99.78%)	$3.24 \cdot 10^6$ (99.66%)
JetCleaning: Loose Bad	$1.79 \cdot 10^7$ (99.26%)	$2.85 \cdot 10^6$ (99.78%)	$6.20 \cdot 10^4$ (99.77%)	$5.54 \cdot 10^6$ (99.49%)	$5.99 \cdot 10^5$ (99.59%)	$9.84 \cdot 10^6$ (99.65%)	$3.23 \cdot 10^6$ (99.58%)
NOBADMUON	$1.79 \cdot 10^7$ (100%)	$2.85 \cdot 10^6$ (99.81%)	$6.19 \cdot 10^4$ (99.83%)	$5.53 \cdot 10^6$ (99.96%)	$5.97 \cdot 10^5$ (99.71%)	$9.84 \cdot 10^6$ (100%)	$3.23 \cdot 10^6$ (99.99%)
Save	$1.79 \cdot 10^7$ (100%)	$2.85 \cdot 10^6$ (100%)	$6.19 \cdot 10^4$ (100%)	$5.53 \cdot 10^6$ (100%)	$5.97 \cdot 10^5$ (100%)	$9.84 \cdot 10^6$ (100%)	$3.23 \cdot 10^6$ (100%)
Lepton Veto	$1.09 \cdot 10^7$ (61.09%)	$2.36 \cdot 10^6$ (82.79%)	$5.16 \cdot 10^4$ (83.36%)	$4.40 \cdot 10^6$ (79.53%)	$4.90 \cdot 10^5$ (82.09%)	$8.11 \cdot 10^6$ (82.4%)	$2.68 \cdot 10^6$ (82.92%)
Charge Selection	$5.60 \cdot 10^6$ (51.33%)	$2.36 \cdot 10^6$ (100%)	$5.16 \cdot 10^4$ (99.98%)	$2.39 \cdot 10^6$ (54.32%)	$2.53 \cdot 10^5$ (51.52%)	$4.09 \cdot 10^6$ (50.5%)	$1.35 \cdot 10^6$ (50.36%)
$\lvert\eta\rvert^\mu < 2.4$	$5.60 \cdot 10^6$ (100%)	$2.36 \cdot 10^6$ (100%)	$5.16 \cdot 10^4$ (100%)	$2.39 \cdot 10^6$ (100%)	$2.53 \cdot 10^5$ (100%)	$4.09 \cdot 10^6$ (100%)	$1.35 \cdot 10^6$ (100%)
$p_T^\mu > 65$ GeV	$5.60 \cdot 10^6$ (100%)	$2.36 \cdot 10^6$ (100%)	$5.16 \cdot 10^4$ (100%)	$2.39 \cdot 10^6$ (100%)	$2.53 \cdot 10^5$ (100%)	$4.09 \cdot 10^6$ (100%)	$1.35 \cdot 10^6$ (100%)
$E_T^{miss} > 85$ GeV	$4.68 \cdot 10^5$ (8.361%)	$1.16 \cdot 10^6$ (49.08%)	$4.24 \cdot 10^4$ (82.24%)	$4.92 \cdot 10^5$ (20.6%)	$1.81 \cdot 10^5$ (71.74%)	$9.26 \cdot 10^5$ (22.63%)	$3.29 \cdot 10^5$ (24.38%)
$m_T > 200$ GeV	$6.89 \cdot 10^4$ (14.7%)	$8.32 \cdot 10^5$ (71.86%)	$3.81 \cdot 10^4$ (89.83%)	$3.91 \cdot 10^5$ (79.31%)	$7.59 \cdot 10^4$ (41.9%)	$1.10 \cdot 10^5$ (11.87%)	$1.00 \cdot 10^5$ (30.55%)
Total Efficiency	0.004%	1.7%	0.12%	0.12%	0.72%	0.096%	0.18%
ProcessMC/TotalMC	NA	53.78%	2.463%	25.25%	4.906%	7.11%	6.487%
Data/TotalMC	4.453%						

Table E.1.: Cutflow table for 2015 and 2016 data for the W^+ selection showing the effect each selection has on the number of events. The first column lists the name of the selection. The rest of the columns show the number of events for each sample and for each selection. The relative efficiency is shown as a percentage next to each number of events. The relative efficiency is calculated as the number of events after the current cut divided by the number of events in the previous cuts. The three rows at the bottom of the table show the total efficiency, ProcessMC/TotalMC and Data/TotalMC. The total efficiency is calculated by taking the number of events after all cuts have been applied divided by the number of events before any cut. The ProcessMC/TotalMC row shows the number of events in each Monte Carlo sample divided by the total sum of events of the Monte Carlo samples after all the selection cuts. The Data/TotalMC row is the total number of data events divided by the sum of the total number of Monte Carlo events after all the selection cuts. All Monte Carlo samples are normalised to the luminosity of the data and include the pileup and generator weights.

	Data	$W^- \to \mu\nu$	$W^- \to \tau\nu$	$Z \to \mu\mu$	$Z \to \tau\tau$	Top	Diboson
Initial	$1.74 \cdot 10^9$ (NA)	$3.99 \cdot 10^7$ (NA)	$2.17 \cdot 10^7$ (NA)	$3.17 \cdot 10^8$ (NA)	$1.06 \cdot 10^7$ (NA)	$1.15 \cdot 10^8$ (NA)	$5.67 \cdot 10^7$ (NA)
GRL	$1.70 \cdot 10^9$ (97.81%)	$3.99 \cdot 10^7$ (100%)	$2.17 \cdot 10^7$ (100%)	$3.17 \cdot 10^8$ (100%)	$1.06 \cdot 10^7$ (100%)	$1.15 \cdot 10^8$ (100%)	$5.67 \cdot 10^7$ (100%)
Good Calo	$1.70 \cdot 10^9$ (99.89%)	$3.99 \cdot 10^7$ (100%)	$2.17 \cdot 10^7$ (100%)	$3.17 \cdot 10^8$ (100%)	$1.06 \cdot 10^7$ (100%)	$1.15 \cdot 10^8$ (100%)	$5.67 \cdot 10^7$ (100%)
PriVtx	$1.70 \cdot 10^9$ (100%)	$3.99 \cdot 10^7$ (100%)	$2.17 \cdot 10^7$ (100%)	$3.17 \cdot 10^8$ (100%)	$1.06 \cdot 10^7$ (100%)	$1.15 \cdot 10^8$ (100%)	$5.67 \cdot 10^7$ (100%)
Reco Level	$1.70 \cdot 10^9$ (100%)	$3.99 \cdot 10^7$ (100%)	$2.17 \cdot 10^7$ (100%)	$3.17 \cdot 10^8$ (100%)	$1.06 \cdot 10^7$ (100%)	$1.15 \cdot 10^8$ (100%)	$5.67 \cdot 10^7$ (100%)
Trigger	$5.18 \cdot 10^8$ (30.52%)	$1.60 \cdot 10^7$ (40.07%)	$3.85 \cdot 10^5$ (1.776%)	$1.91 \cdot 10^8$ (60.05%)	$2.51 \cdot 10^6$ (23.71%)	$3.84 \cdot 10^7$ (33.42%)	$2.20 \cdot 10^7$ (38.77%)
MU_N 20 == 1	$3.65 \cdot 10^8$ (70.55%)	$1.51 \cdot 10^7$ (94.68%)	$2.69 \cdot 10^5$ (69.91%)	$7.07 \cdot 10^7$ (37.1%)	$1.57 \cdot 10^6$ (62.34%)	$3.43 \cdot 10^7$ (89.35%)	$1.40 \cdot 10^7$ (63.9%)
EL_N 20 == 0	$3.65 \cdot 10^8$ (99.88%)	$1.51 \cdot 10^7$ (99.98%)	$2.69 \cdot 10^5$ (99.96%)	$7.07 \cdot 10^7$ (99.92%)	$1.45 \cdot 10^6$ (92.52%)	$3.20 \cdot 10^7$ (93.35%)	$1.20 \cdot 10^7$ (85.35%)
MU_N 30 == 1	$2.66 \cdot 10^8$ (72.88%)	$1.31 \cdot 10^7$ (86.38%)	$1.78 \cdot 10^5$ (66.3%)	$5.56 \cdot 10^7$ (78.72%)	$1.12 \cdot 10^6$ (77.51%)	$2.85 \cdot 10^7$ (88.88%)	$1.03 \cdot 10^7$ (86.12%)
MU_N 65 == 1	$1.80 \cdot 10^7$ (6.78%)	$2.78 \cdot 10^6$ (21.28%)	$6.01 \cdot 10^4$ (33.68%)	$5.62 \cdot 10^6$ (10.11%)	$6.12 \cdot 10^5$ (54.57%)	$9.89 \cdot 10^6$ (34.75%)	$3.25 \cdot 10^6$ (31.51%)
MU_N Tight 65 == 1	$1.80 \cdot 10^7$ (100%)	$2.78 \cdot 10^6$ (100%)	$6.01 \cdot 10^4$ (100%)	$5.62 \cdot 10^6$ (100%)	$6.12 \cdot 10^5$ (100%)	$9.89 \cdot 10^6$ (100%)	$3.25 \cdot 10^6$ (100%)
Trigger match	$1.80 \cdot 10^7$ (99.89%)	$2.78 \cdot 10^6$ (100%)	$6.01 \cdot 10^4$ (100%)	$5.56 \cdot 10^6$ (98.96%)	$6.01 \cdot 10^5$ (98.18%)	$9.87 \cdot 10^6$ (99.78%)	$3.24 \cdot 10^6$ (99.66%)
JetCleaning: Loose Bad	$1.79 \cdot 10^7$ (99.26%)	$2.78 \cdot 10^6$ (99.77%)	$5.99 \cdot 10^4$ (99.78%)	$5.54 \cdot 10^6$ (99.49%)	$5.99 \cdot 10^5$ (99.59%)	$9.84 \cdot 10^6$ (99.65%)	$3.23 \cdot 10^6$ (99.58%)
NOBADMUON	$1.79 \cdot 10^7$ (100%)	$2.77 \cdot 10^6$ (99.74%)	$5.97 \cdot 10^4$ (99.69%)	$5.53 \cdot 10^6$ (99.96%)	$5.97 \cdot 10^5$ (99.71%)	$9.84 \cdot 10^6$ (100%)	$3.23 \cdot 10^6$ (99.99%)
Save	$1.79 \cdot 10^7$ (100%)	$2.77 \cdot 10^6$ (100%)	$5.97 \cdot 10^4$ (100%)	$5.53 \cdot 10^6$ (100%)	$5.97 \cdot 10^5$ (100%)	$9.84 \cdot 10^6$ (100%)	$3.23 \cdot 10^6$ (100%)
Lepton Veto	$1.09 \cdot 10^7$ (61.09%)	$2.29 \cdot 10^6$ (82.51%)	$4.87 \cdot 10^4$ (81.48%)	$4.40 \cdot 10^6$ (79.53%)	$4.90 \cdot 10^5$ (82.09%)	$8.11 \cdot 10^6$ (82.4%)	$2.68 \cdot 10^6$ (82.92%)
Charge Selection	$5.31 \cdot 10^6$ (48.67%)	$2.29 \cdot 10^6$ (100%)	$4.87 \cdot 10^4$ (99.98%)	$2.01 \cdot 10^6$ (45.68%)	$2.38 \cdot 10^5$ (48.49%)	$4.01 \cdot 10^6$ (49.5%)	$1.33 \cdot 10^6$ (49.64%)
$\lvert\eta\rvert^\mu < 2.4$	$5.31 \cdot 10^6$ (100%)	$2.29 \cdot 10^6$ (100%)	$4.87 \cdot 10^4$ (100%)	$2.01 \cdot 10^6$ (100%)	$2.38 \cdot 10^5$ (100%)	$4.01 \cdot 10^6$ (100%)	$1.33 \cdot 10^6$ (100%)
$p_T^\mu > 65$ GeV	$5.31 \cdot 10^6$ (100%)	$2.29 \cdot 10^6$ (100%)	$4.87 \cdot 10^4$ (100%)	$2.01 \cdot 10^6$ (100%)	$2.38 \cdot 10^5$ (100%)	$4.01 \cdot 10^6$ (100%)	$1.33 \cdot 10^6$ (100%)
$E_T^{miss} > 85$ GeV	$3.50 \cdot 10^5$ (6.592%)	$1.08 \cdot 10^6$ (47.29%)	$4.02 \cdot 10^4$ (82.62%)	$2.24 \cdot 10^5$ (11.14%)	$1.74 \cdot 10^5$ (73.03%)	$8.94 \cdot 10^5$ (22.29%)	$3.24 \cdot 10^5$ (24.37%)
$m_T > 200$ GeV	$4.83 \cdot 10^4$ (13.79%)	$7.83 \cdot 10^5$ (72.43%)	$3.63 \cdot 10^4$ (90.37%)	$1.79 \cdot 10^5$ (79.89%)	$7.22 \cdot 10^4$ (41.61%)	$1.07 \cdot 10^5$ (11.93%)	$1.06 \cdot 10^5$ (32.87%)
Total Efficiency	0.0028%	2%	0.17%	0.056%	0.68%	0.093%	0.19%
ProcessMC/TotalMC	NA	60.99%	2.832%	13.94%	5.627%	8.318%	8.293%
Data/TotalMC	3.762%						

Table E.2.: Cutflow table for 2015 and 2016 data for the W^- selection showing the effect each selection has on the number of events. The first column lists the name of the selection. The rest of the columns show the number of events for each sample and for each selection. The relative efficiency is shown as a percentage next to each number of events. The relative efficiency is calculated as the number of events after the current cut divided by the number of events in the previous cuts. The three rows at the bottom of the table show the total efficiency, ProcessMC/TotalMC and Data/TotalMC. The total efficiency is calculated by taking the number of events after all cuts have been applied divided by the number of events before any cut. The ProcessMC/TotalMC row shows the number of events in each Monte Carlo sample divided by the total sum of events of the Monte Carlo samples after all the selection cuts. The Data/TotalMC row is the total number of data events divided by the sum of the total number of Monte Carlo events after all the selection cuts. All Monte Carlo samples are normalised to the luminosity of the data and include the pileup and generator weights.

	Data	$W^{\pm} \to \mu\nu$	$W^{\pm} \to \tau\nu$	$Z \to \mu\mu$	$Z \to \tau\tau$	Top	Diboson
Initial	$3.47 \cdot 10^9$ (NA)	$8.78 \cdot 10^7$ (NA)	$5.33 \cdot 10^7$ (NA)	$6.35 \cdot 10^8$ (NA)	$2.12 \cdot 10^7$ (NA)	$2.30 \cdot 10^8$ (NA)	$1.13 \cdot 10^8$ (NA)
GRL	$3.40 \cdot 10^9$ (97.81%)	$8.78 \cdot 10^7$ (100%)	$5.33 \cdot 10^7$ (100%)	$6.35 \cdot 10^8$ (100%)	$2.12 \cdot 10^7$ (100%)	$2.30 \cdot 10^8$ (100%)	$1.13 \cdot 10^8$ (100%)
Good Calo	$3.39 \cdot 10^9$ (99.89%)	$8.78 \cdot 10^7$ (100%)	$5.33 \cdot 10^7$ (100%)	$6.35 \cdot 10^8$ (100%)	$2.12 \cdot 10^7$ (100%)	$2.30 \cdot 10^8$ (100%)	$1.13 \cdot 10^8$ (100%)
PriVtx	$3.39 \cdot 10^9$ (100%)	$8.78 \cdot 10^7$ (100%)	$5.33 \cdot 10^7$ (100%)	$6.35 \cdot 10^8$ (100%)	$2.12 \cdot 10^7$ (100%)	$2.30 \cdot 10^8$ (100%)	$1.13 \cdot 10^8$ (100%)
Reco Level	$3.39 \cdot 10^9$ (100%)	$8.78 \cdot 10^7$ (100%)	$5.33 \cdot 10^7$ (100%)	$6.35 \cdot 10^8$ (100%)	$2.12 \cdot 10^7$ (100%)	$2.30 \cdot 10^8$ (100%)	$1.13 \cdot 10^8$ (100%)
Trigger	$1.04 \cdot 10^9$ (30.52%)	$3.52 \cdot 10^7$ (40.03%)	$8.67 \cdot 10^5$ (1.627%)	$3.81 \cdot 10^8$ (60.05%)	$5.02 \cdot 10^6$ (23.71%)	$7.68 \cdot 10^7$ (33.42%)	$4.40 \cdot 10^7$ (38.77%)
MU_N 20 == 1	$7.30 \cdot 10^8$ (70.55%)	$3.32 \cdot 10^7$ (94.54%)	$6.13 \cdot 10^5$ (70.63%)	$1.41 \cdot 10^8$ (37.1%)	$3.13 \cdot 10^6$ (62.34%)	$6.86 \cdot 10^7$ (89.35%)	$2.81 \cdot 10^7$ (63.9%)
EL_N 20 == 0	$7.29 \cdot 10^8$ (99.88%)	$3.32 \cdot 10^7$ (99.99%)	$6.12 \cdot 10^5$ (99.97%)	$1.41 \cdot 10^8$ (99.92%)	$2.90 \cdot 10^6$ (92.52%)	$6.41 \cdot 10^7$ (93.35%)	$2.40 \cdot 10^7$ (85.35%)
MU_N 30 == 1	$5.32 \cdot 10^8$ (72.88%)	$2.82 \cdot 10^7$ (84.85%)	$3.93 \cdot 10^5$ (64.19%)	$1.11 \cdot 10^8$ (78.72%)	$2.24 \cdot 10^6$ (77.51%)	$5.69 \cdot 10^7$ (88.88%)	$2.06 \cdot 10^7$ (86.12%)
MU_N 65 == 1	$3.60 \cdot 10^7$ (6.78%)	$5.64 \cdot 10^6$ (20.02%)	$1.22 \cdot 10^5$ (31.09%)	$1.12 \cdot 10^7$ (10.11%)	$1.23 \cdot 10^6$ (54.57%)	$1.98 \cdot 10^7$ (34.75%)	$6.50 \cdot 10^6$ (31.51%)
MU_N Tight 65 == 1	$3.60 \cdot 10^7$ (100%)	$5.64 \cdot 10^6$ (100%)	$1.22 \cdot 10^5$ (100%)	$1.12 \cdot 10^7$ (100%)	$1.23 \cdot 10^6$ (100%)	$1.98 \cdot 10^7$ (100%)	$6.50 \cdot 10^6$ (100%)
Trigger match	$3.60 \cdot 10^7$ (99.89%)	$5.64 \cdot 10^6$ (100%)	$1.22 \cdot 10^5$ (99.99%)	$1.11 \cdot 10^7$ (98.96%)	$1.20 \cdot 10^6$ (98.18%)	$1.97 \cdot 10^7$ (99.78%)	$6.48 \cdot 10^6$ (99.66%)
JetCleaning: Loose Bad	$3.57 \cdot 10^7$ (99.26%)	$5.63 \cdot 10^6$ (99.77%)	$1.22 \cdot 10^5$ (99.77%)	$1.11 \cdot 10^7$ (99.49%)	$1.20 \cdot 10^6$ (99.59%)	$1.97 \cdot 10^7$ (99.65%)	$6.45 \cdot 10^6$ (99.58%)
NOBADMUON	$3.57 \cdot 10^7$ (100%)	$5.62 \cdot 10^6$ (99.78%)	$1.22 \cdot 10^5$ (99.76%)	$1.11 \cdot 10^7$ (99.96%)	$1.19 \cdot 10^6$ (99.71%)	$1.97 \cdot 10^7$ (100%)	$6.45 \cdot 10^6$ (99.99%)
Save	$3.57 \cdot 10^7$ (100%)	$5.62 \cdot 10^6$ (100%)	$1.22 \cdot 10^5$ (100%)	$1.11 \cdot 10^7$ (100%)	$1.19 \cdot 10^6$ (100%)	$1.97 \cdot 10^7$ (100%)	$6.45 \cdot 10^6$ (100%)
Lepton Veto	$2.18 \cdot 10^7$ (61.09%)	$4.64 \cdot 10^6$ (82.65%)	$1.00 \cdot 10^5$ (82.43%)	$8.80 \cdot 10^6$ (79.53%)	$9.80 \cdot 10^5$ (82.09%)	$1.62 \cdot 10^7$ (82.4%)	$5.35 \cdot 10^6$ (82.92%)
Charge Selection	$1.09 \cdot 10^7$ (50%)	$4.64 \cdot 10^6$ (100%)	$1.00 \cdot 10^5$ (99.98%)	$4.40 \cdot 10^6$ (50%)	$4.90 \cdot 10^5$ (50%)	$8.11 \cdot 10^6$ (50%)	$2.68 \cdot 10^6$ (50%)
$\lvert\eta\rvert^{\mu} < 2.4$	$1.09 \cdot 10^7$ (100%)	$4.64 \cdot 10^6$ (100%)	$1.00 \cdot 10^5$ (100%)	$4.40 \cdot 10^6$ (100%)	$4.90 \cdot 10^5$ (100%)	$8.11 \cdot 10^6$ (100%)	$2.68 \cdot 10^6$ (100%)
$p_T^{\mu} > 65$ GeV	$1.09 \cdot 10^7$ (100%)	$4.64 \cdot 10^6$ (100%)	$1.00 \cdot 10^5$ (100%)	$4.40 \cdot 10^6$ (100%)	$4.90 \cdot 10^5$ (100%)	$8.11 \cdot 10^6$ (100%)	$2.68 \cdot 10^6$ (100%)
$E_T^{miss} > 85$ GeV	$8.19 \cdot 10^5$ (7.5%)	$2.24 \cdot 10^6$ (48.2%)	$8.26 \cdot 10^4$ (82.42%)	$7.16 \cdot 10^5$ (16.28%)	$3.55 \cdot 10^5$ (72.36%)	$1.82 \cdot 10^6$ (22.46%)	$6.52 \cdot 10^5$ (24.38%)
$m_T > 200$ GeV	$1.17 \cdot 10^5$ (14.31%)	$1.61 \cdot 10^6$ (72.14%)	$7.44 \cdot 10^4$ (90.09%)	$5.69 \cdot 10^5$ (79.49%)	$1.48 \cdot 10^5$ (41.76%)	$2.17 \cdot 10^5$ (11.9%)	$2.07 \cdot 10^5$ (31.7%)
Total Efficiency	0.0034%	1.8%	0.14%	0.09%	0.7%	0.094%	0.18%
ProcessMC/TotalMC	NA	57.05%	2.63%	20.12%	5.233%	7.658%	7.306%
Data/TotalMC	4.139%						

Table E.3.: Cutflow table for 2015 and 2016 data for the $W^{\pm}$ selection showing the effect each selection has on the number of events. The first column lists the name of the selection. The rest of the columns show the number of events for each sample and for each selection. The relative efficiency is shown as a percentage next to each number of events. The relative efficiency is calculated as the number of events after the current cut divided by the number of events in the previous cuts. The three rows at the bottom of the table show the total efficiency, ProcessMC/TotalMC and Data/TotalMC. The total efficiency is calculated by taking the number of events after all cuts have been applied divided by the number of events before any cut. The ProcessMC/TotalMC row shows the number of events in each Monte Carlo sample divided by the total sum of events of the Monte Carlo samples after all the selection cuts. The Data/TotalMC row is the total number of data events divided by the sum of the total number of Monte Carlo events after all the selection cuts. All Monte Carlo samples are normalised to the luminosity of the data and include the pileup and generator weights.

E.2. MC16d

This section shows the relative contribution of all samples, the control distributions and the cutflows for the MC16d campaign. The positive charge is presented first, followed by the negative charge and finally the combination of these two charges is shown. The kinematic variables presented were discussed in Chapter 9. The control distributions show reasonable agreement between data and prediction.

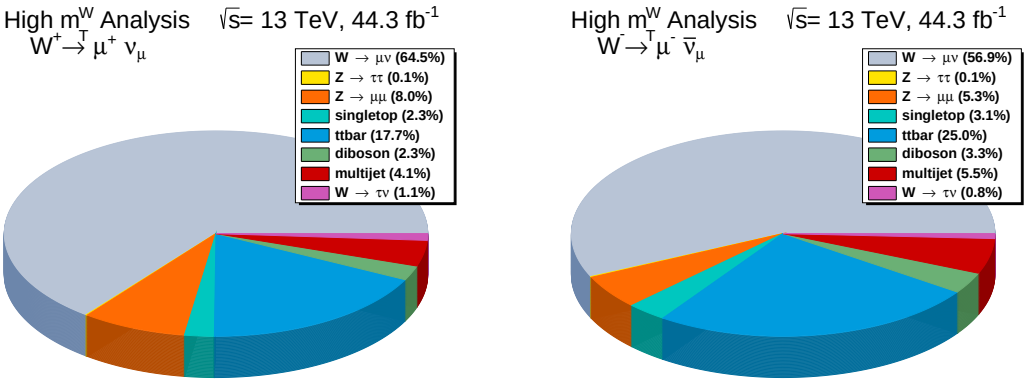

a b

Figure E.8.: Chart showing relative contributions of all Monte Carlo in the signal region for MC16d, for muon charge (a) W^+ and (b) W^-.

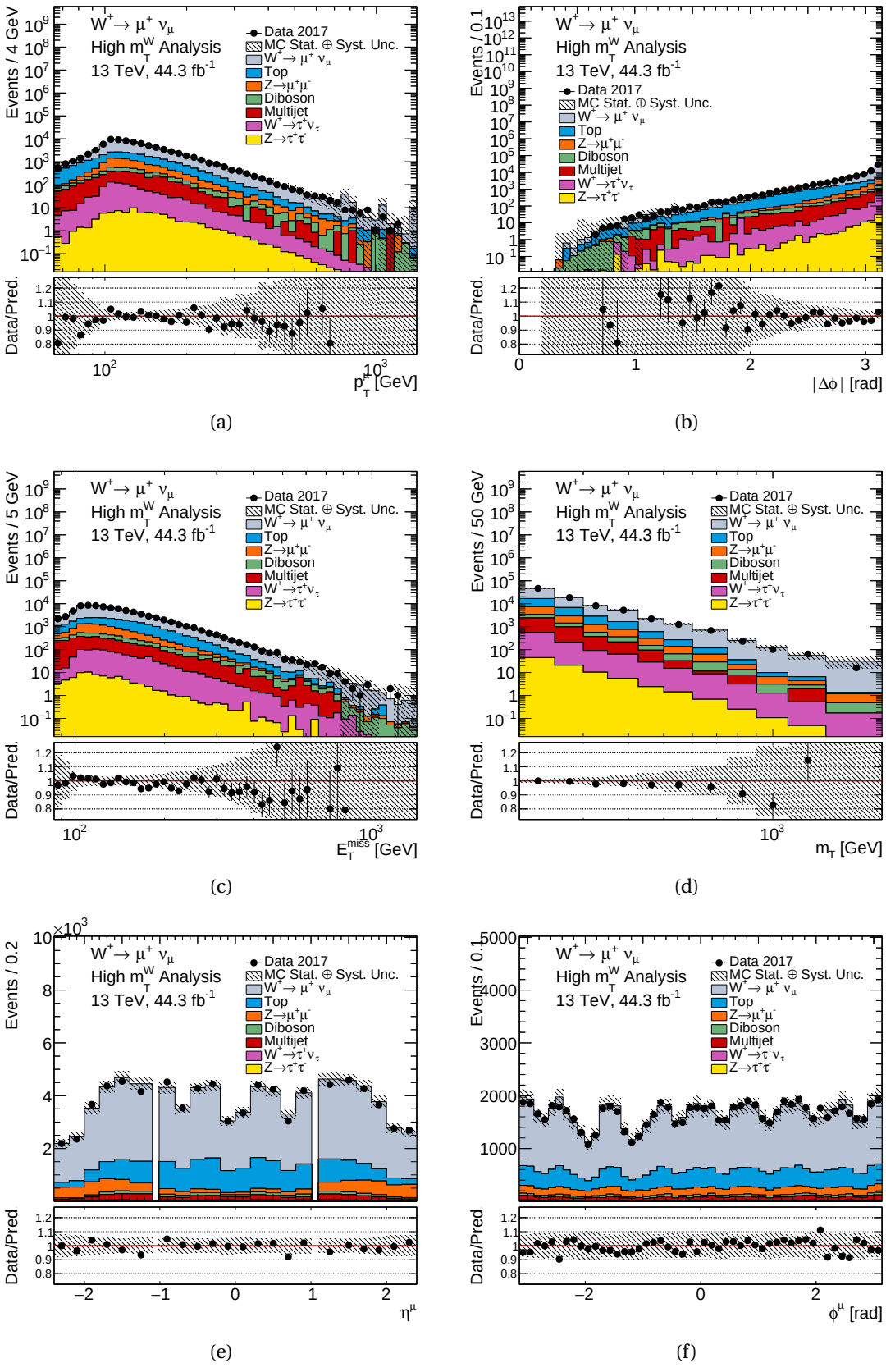

Figure E.9.: MC16d $W^+ \to \mu^+\nu$ control distributions for p_T^μ, $|\Delta\phi|$, E_T^{miss}, m_T, η^μ and ϕ^μ. The data contribution is shown with black points, the signal and the background contributions with solid lines. In the shaded band, systematic experimental uncertainties have been combined with the MC statistical uncertainties. The data statistical uncertainties are shown on the data points. Luminosity uncertainties have not been included.

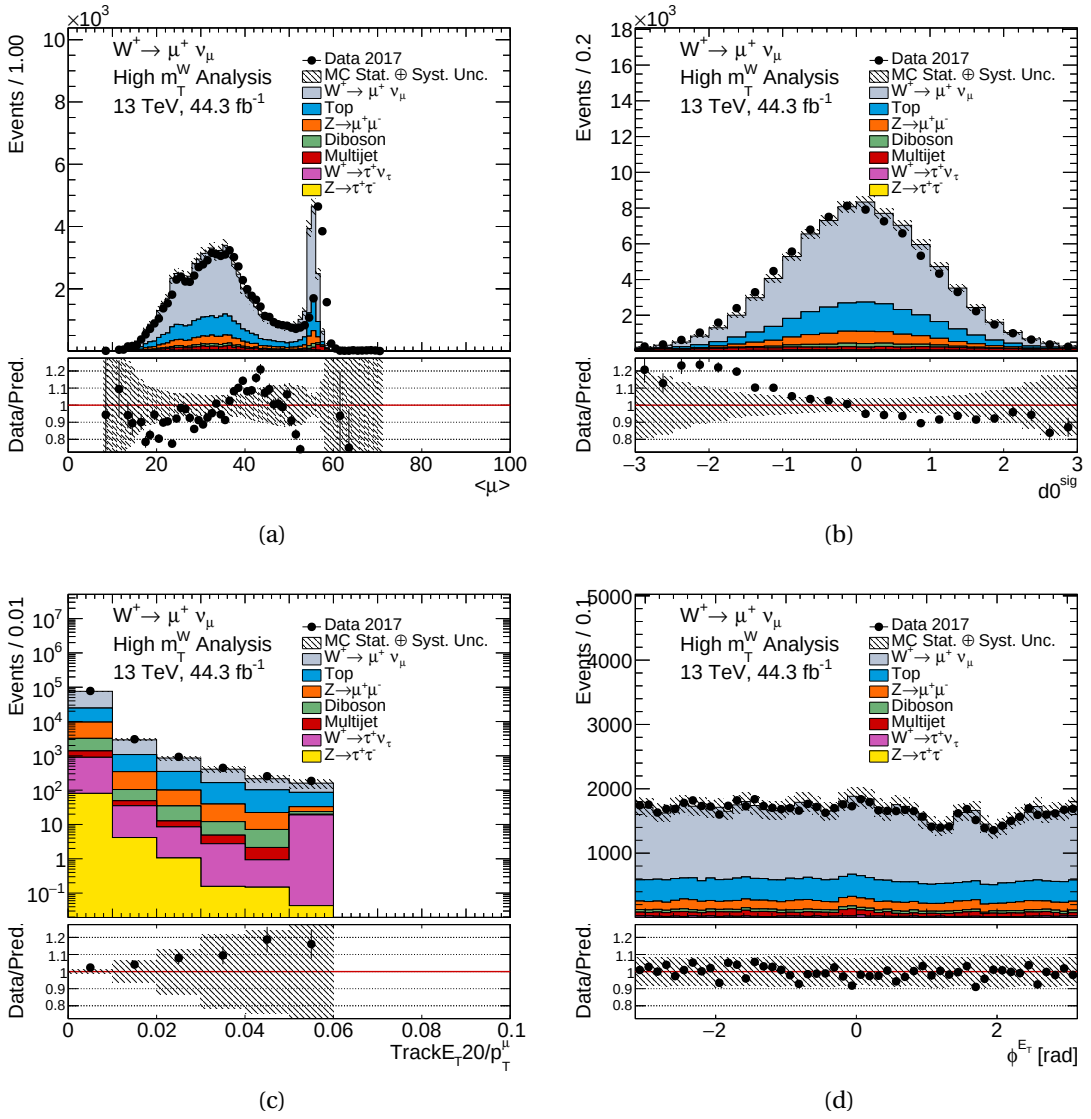

Figure E.10.: MC16d $W^+ \to \mu^+\nu$ control distributions for $<\mu>$, $d0^{sig}$, $TrackE_T20/p_T^{\mu}$ and $\phi^{E_T^{miss}}$. The data contribution is shown with black points, the signal and the background contributions with solid lines. In the shaded band, systematic experimental uncertainties have been combined with the MC statistical uncertainties. The data statistical uncertainties are shown on the data points. Luminosity uncertainties have not been included.

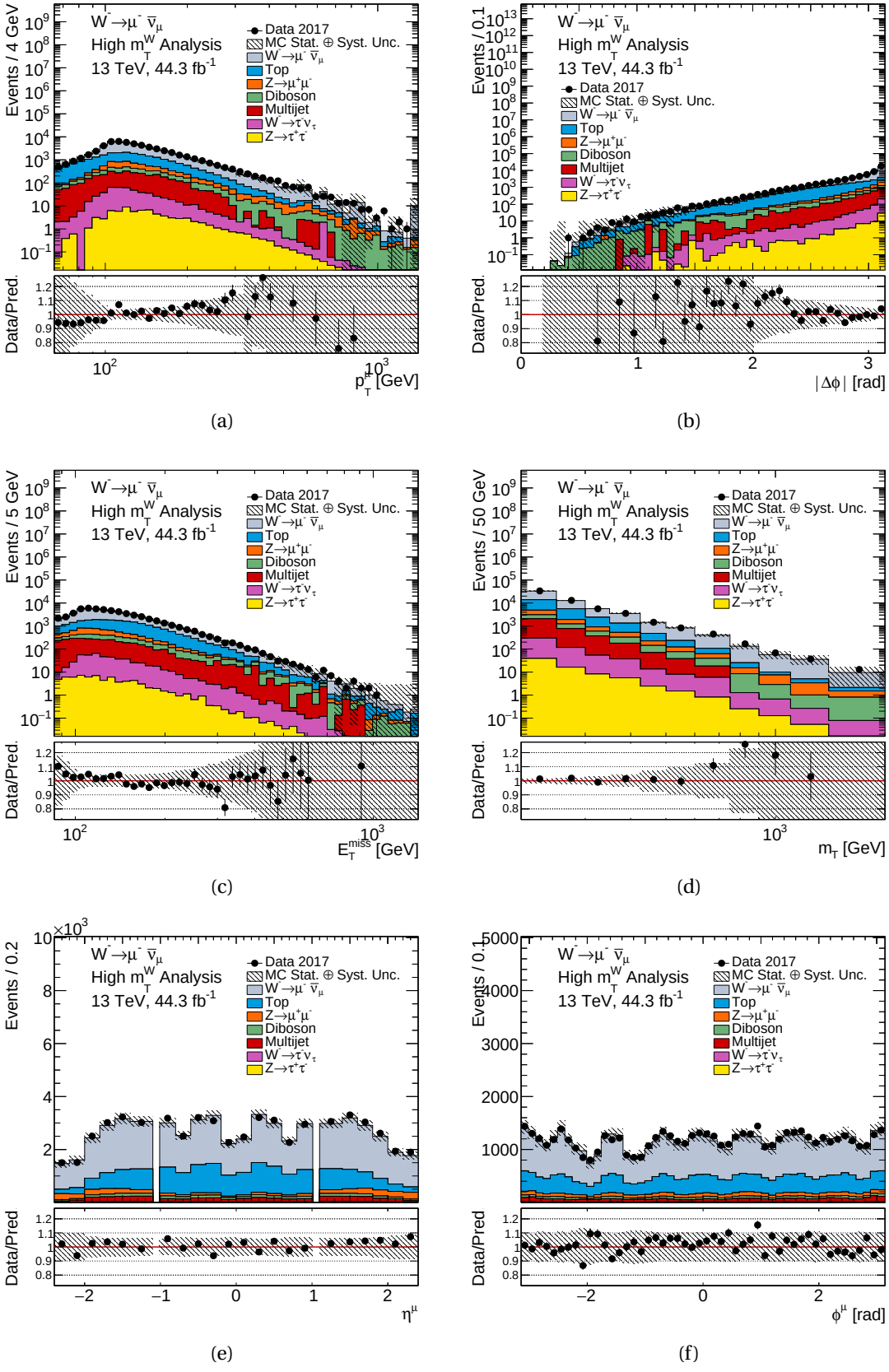

Figure E.11.: MC16d $W^- \to \mu^- \nu$ control distributions for p_T^μ, $|\Delta\phi|$, E_T^{miss}, m_T, η^μ and ϕ^μ. The data contribution is shown with black points, the signal and the background contributions with solid lines. In the shaded band, systematic experimental uncertainties have been combined with the MC statistical uncertainties. The data statistical uncertainties are shown on the data points. Luminosity uncertainties have not been included.

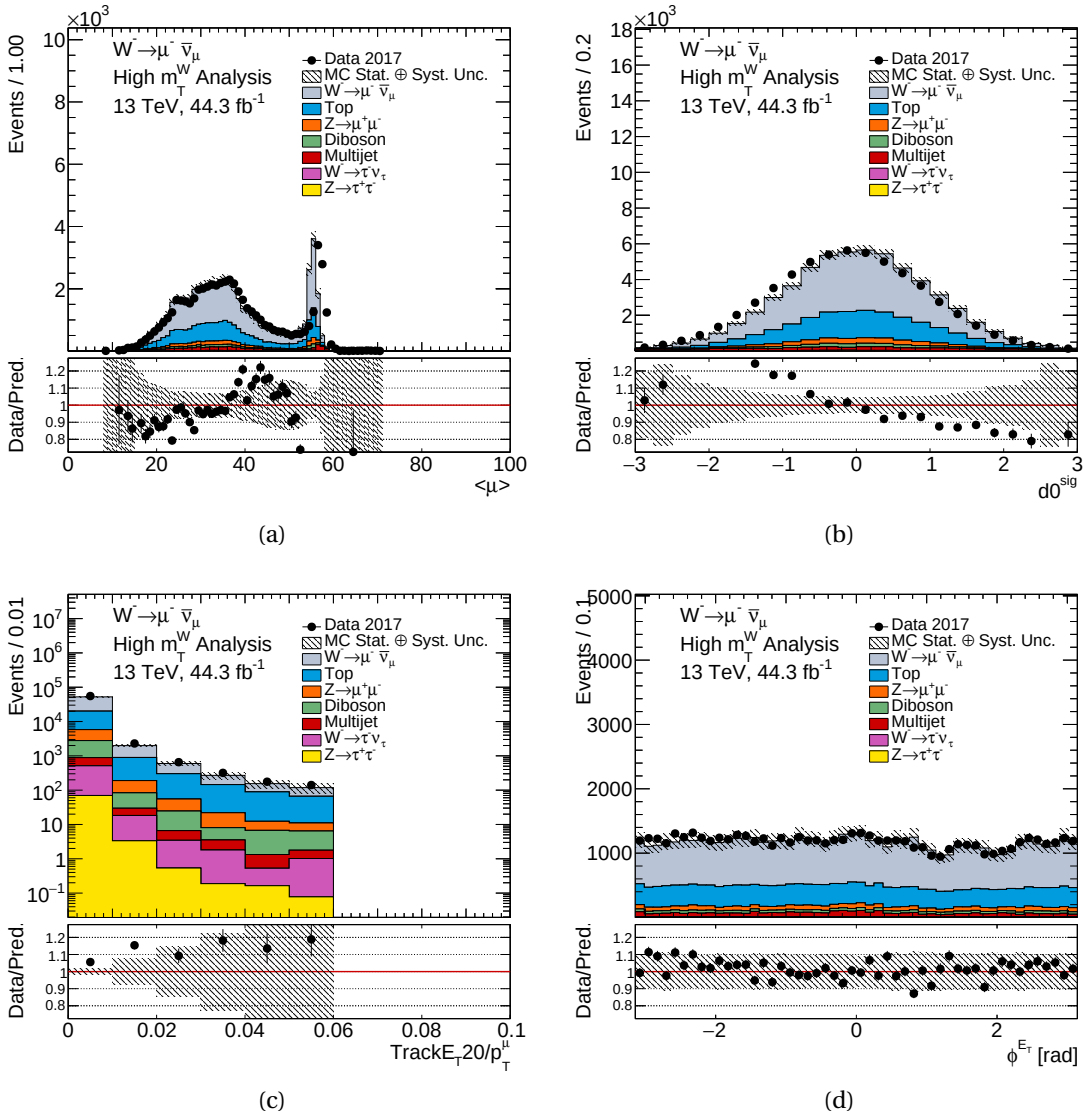

Figure E.12.: MC16d $W^- \to \mu^- \nu$ control distributions for $< \mu >$, $d0^{sig}$, $TrackE_T20/p_T^{\mu}$ and $\phi^{E_T^{miss}}$. The data contribution is shown with black points, the signal and the background contributions with solid lines. In the shaded band, systematic experimental uncertainties have been combined with the MC statistical uncertainties. The data statistical uncertainties are shown on the data points. Luminosity uncertainties have not been included.

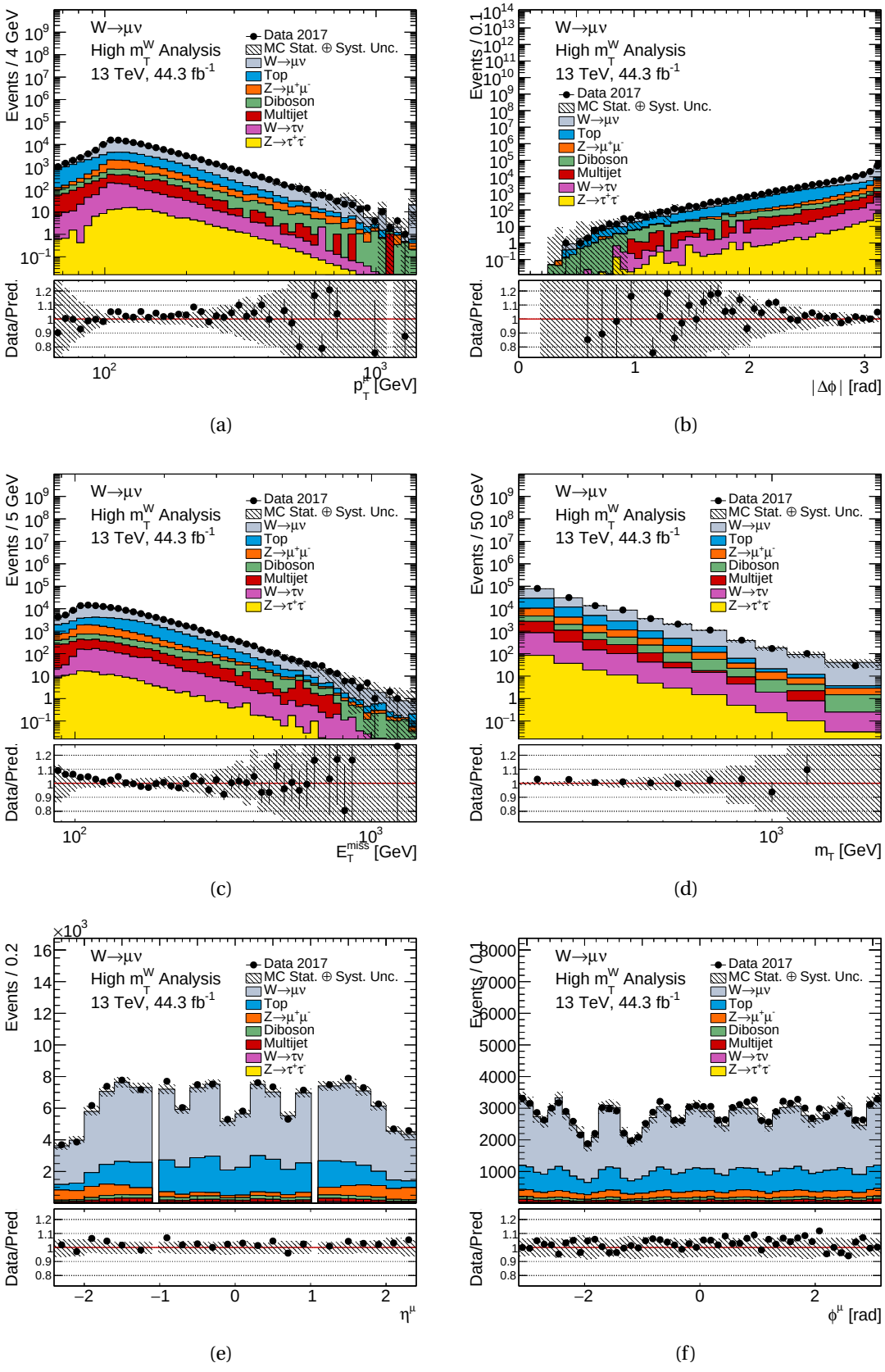

Figure E.13.: MC16d combined charge $W^{\pm} \to \mu\nu$ control distributions for p_T^{μ}, $|\Delta\phi|$, E_T^{miss}, m_T, η^{μ} and ϕ^{μ}. The data contribution is shown with black points, the signal and the background contributions with solid lines. In the shaded band, systematic experimental uncertainties have been combined with the MC statistical uncertainties. The data statistical uncertainties are shown on the data points. Luminosity uncertainties have not been included.

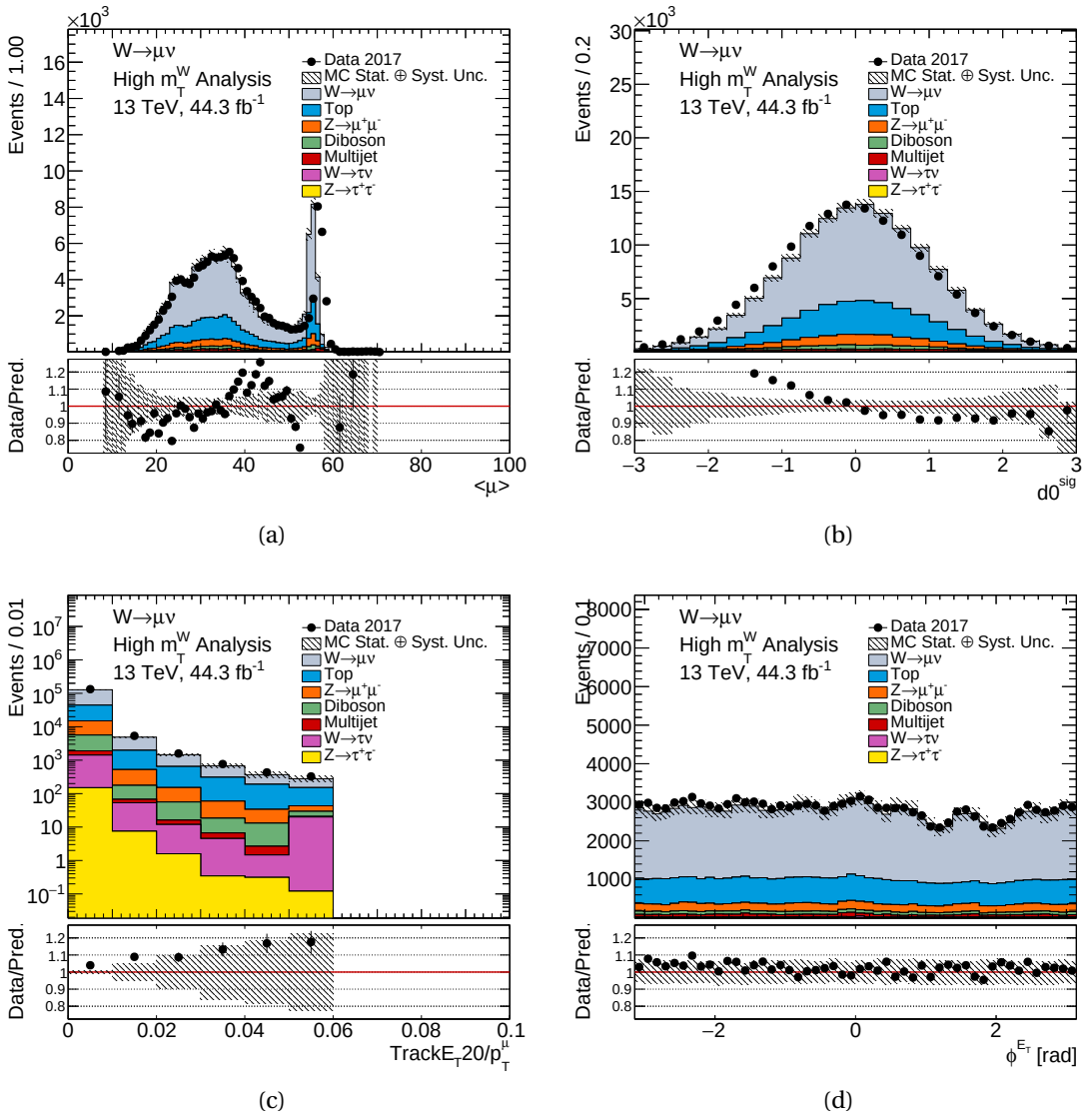

Figure E.14.: MC16d combined charge $W^{\pm} \to \mu\nu$ control distributions for $< \mu >$, $d0^{sig}$, $TrackE_T20/p_T^{\mu}$ and $\phi^{E_T^{miss}}$. The data contribution is shown with black points, the signal and the background contributions with solid lines. In the shaded band, systematic experimental uncertainties have been combined with the MC statistical uncertainties. The data statistical uncertainties are shown on the data points. Luminosity uncertainties have not been included.

	Data	$W^+ \to \mu\nu$	$W^+ \to \tau\nu$	$Z \to \mu\mu$	$Z \to \tau\tau$	Top	Diboson
Initial	$1.69 \cdot 10^9$ (NA)	$5.93 \cdot 10^7$ (NA)	$3.17 \cdot 10^6$ (NA)	$3.94 \cdot 10^8$ (NA)	$1.15 \cdot 10^7$ (NA)	$1.47 \cdot 10^8$ (NA)	$1.34 \cdot 10^8$ (NA)
GRL	$1.64 \cdot 10^9$ (96.86%)	$5.93 \cdot 10^7$ (100%)	$3.17 \cdot 10^6$ (100%)	$3.94 \cdot 10^8$ (100%)	$1.16 \cdot 10^7$ (100%)	$1.47 \cdot 10^8$ (100%)	$1.34 \cdot 10^8$ (100%)
Good Calo	$1.64 \cdot 10^9$ (99.94%)	$5.93 \cdot 10^7$ (100%)	$3.17 \cdot 10^6$ (100%)	$3.94 \cdot 10^8$ (100%)	$1.16 \cdot 10^7$ (100%)	$1.47 \cdot 10^8$ (100%)	$1.34 \cdot 10^8$ (100%)
PriVtx	$1.64 \cdot 10^9$ (100%)	$5.93 \cdot 10^7$ (100%)	$3.17 \cdot 10^6$ (100%)	$3.94 \cdot 10^8$ (100%)	$1.16 \cdot 10^7$ (100%)	$1.47 \cdot 10^8$ (100%)	$1.34 \cdot 10^8$ (100%)
Reco Level	$1.64 \cdot 10^9$ (100%)	$5.93 \cdot 10^7$ (100%)	$3.17 \cdot 10^6$ (100%)	$3.94 \cdot 10^8$ (100%)	$1.16 \cdot 10^7$ (100%)	$1.47 \cdot 10^8$ (100%)	$1.34 \cdot 10^8$ (100%)
Trigger	$5.50 \cdot 10^8$ (33.59%)	$2.31 \cdot 10^7$ (38.98%)	$5.29 \cdot 10^5$ (16.68%)	$2.33 \cdot 10^8$ (58.99%)	$2.60 \cdot 10^6$ (22.55%)	$4.88 \cdot 10^7$ (33.13%)	$5.03 \cdot 10^7$ (37.48%)
MU_N 20 == 1	$3.97 \cdot 10^8$ (72.07%)	$2.17 \cdot 10^7$ (93.82%)	$3.81 \cdot 10^5$ (71.96%)	$8.52 \cdot 10^7$ (36.63%)	$1.64 \cdot 10^6$ (62.91%)	$4.36 \cdot 10^7$ (89.33%)	$3.42 \cdot 10^7$ (68.02%)
EL_N 20 == 0	$3.96 \cdot 10^8$ (99.87%)	$2.17 \cdot 10^7$ (99.99%)	$3.81 \cdot 10^5$ (99.97%)	$8.51 \cdot 10^7$ (99.92%)	$1.52 \cdot 10^6$ (92.69%)	$4.07 \cdot 10^7$ (93.37%)	$3.02 \cdot 10^7$ (88.29%)
MU_N 30 == 1	$3.11 \cdot 10^8$ (78.45%)	$1.83 \cdot 10^7$ (84.65%)	$2.46 \cdot 10^5$ (64.59%)	$6.83 \cdot 10^7$ (80.25%)	$1.19 \cdot 10^6$ (78.24%)	$3.67 \cdot 10^7$ (90.08%)	$2.65 \cdot 10^7$ (87.69%)
MU_N 65 == 1	$2.15 \cdot 10^7$ (6.912%)	$3.34 \cdot 10^6$ (18.19%)	$6.36 \cdot 10^4$ (25.87%)	$6.52 \cdot 10^6$ (9.548%)	$6.14 \cdot 10^5$ (51.7%)	$1.29 \cdot 10^7$ (35.17%)	$8.22 \cdot 10^6$ (31.04%)
MU_N Tight 65 == 1	$2.15 \cdot 10^7$ (100%)	$3.34 \cdot 10^6$ (100%)	$6.36 \cdot 10^4$ (100%)	$6.52 \cdot 10^6$ (100%)	$6.14 \cdot 10^5$ (100%)	$1.29 \cdot 10^7$ (100%)	$8.22 \cdot 10^6$ (100%)
Trigger match	$2.15 \cdot 10^7$ (99.89%)	$3.34 \cdot 10^6$ (100%)	$6.36 \cdot 10^4$ (99.99%)	$6.47 \cdot 10^6$ (99.23%)	$6.04 \cdot 10^5$ (98.28%)	$1.29 \cdot 10^7$ (99.79%)	$8.20 \cdot 10^6$ (99.75%)
JetCleaning: Loose Bad	$2.12 \cdot 10^7$ (98.67%)	$3.32 \cdot 10^6$ (99.59%)	$6.34 \cdot 10^4$ (99.63%)	$6.43 \cdot 10^6$ (99.36%)	$6 \cdot 10^5$ (99.41%)	$1.28 \cdot 10^7$ (99.5%)	$8.15 \cdot 10^6$ (99.44%)
NOBADMUON	$2.12 \cdot 10^7$ (99.99%)	$3.32 \cdot 10^6$ (99.81%)	$6.32 \cdot 10^4$ (99.75%)	$6.43 \cdot 10^6$ (99.98%)	$5.98 \cdot 10^5$ (99.63%)	$1.28 \cdot 10^7$ (100%)	$8.15 \cdot 10^6$ (99.99%)
Save	$2.12 \cdot 10^7$ (100%)	$3.32 \cdot 10^6$ (100%)	$6.32 \cdot 10^4$ (100%)	$6.43 \cdot 10^6$ (100%)	$5.98 \cdot 10^5$ (100%)	$1.28 \cdot 10^7$ (100%)	$8.15 \cdot 10^6$ (100%)
Lepton Veto	$1.29 \cdot 10^7$ (60.71%)	$2.74 \cdot 10^6$ (82.52%)	$5.25 \cdot 10^4$ (83%)	$5.08 \cdot 10^6$ (79.05%)	$4.89 \cdot 10^5$ (81.81%)	$1.05 \cdot 10^7$ (82.2%)	$6.75 \cdot 10^6$ (82.83%)
Charge Selection	$6.59 \cdot 10^6$ (51.27%)	$2.74 \cdot 10^6$ (100%)	$5.25 \cdot 10^4$ (99.98%)	$2.69 \cdot 10^6$ (53%)	$2.52 \cdot 10^5$ (51.55%)	$5.25 \cdot 10^6$ (49.89%)	$3.10 \cdot 10^6$ (45.95%)
$\lvert\eta\rvert^\mu < 2.4$	$6.59 \cdot 10^6$ (100%)	$2.74 \cdot 10^6$ (100%)	$5.25 \cdot 10^4$ (100%)	$2.69 \cdot 10^6$ (100%)	$2.52 \cdot 10^5$ (100%)	$5.25 \cdot 10^6$ (100%)	$3.10 \cdot 10^6$ (100%)
$p_T^\mu > 65$ GeV	$6.59 \cdot 10^6$ (100%)	$2.74 \cdot 10^6$ (100%)	$5.25 \cdot 10^4$ (100%)	$2.69 \cdot 10^6$ (100%)	$2.52 \cdot 10^5$ (100%)	$5.25 \cdot 10^6$ (100%)	$3.10 \cdot 10^6$ (100%)
$E_T^{miss} > 85$ GeV	$5.88 \cdot 10^5$ (8.924%)	$1.30 \cdot 10^6$ (47.62%)	$4.23 \cdot 10^4$ (80.72%)	$4.13 \cdot 10^5$ (15.34%)	$1.82 \cdot 10^5$ (72.24%)	$1.26 \cdot 10^6$ (23.92%)	$7.39 \cdot 10^5$ (23.83%)
$m_T > 200$ GeV	$8.27 \cdot 10^4$ (14.07%)	$8.98 \cdot 10^5$ (68.87%)	$3.76 \cdot 10^4$ (88.85%)	$3.10 \cdot 10^5$ (75.01%)	$7.59 \cdot 10^4$ (41.65%)	$1.46 \cdot 10^5$ (11.58%)	$2.04 \cdot 10^5$ (27.66%)
Total Efficiency	0.0049%	1.5%	1.2%	0.079%	0.66%	0.099%	0.15%
ProcessMC/TotalMC	NA	53.72%	2.251%	18.55%	4.54%	8.711%	12.23%
Data/TotalMC	4.951%						

Table E.4.: Cutflow table for 2017 data for the W^+ selection showing the effect each selection has on the number of events. The first column lists the name of the selection. The rest of the columns show the number of events for each sample and for each selection. The relative efficiency is shown as a percentage next to each number of events. The relative efficiency is calculated as the number of events after the current cut divided by the number of events in the previous cuts. The three rows at the bottom of the table show the total efficiency, ProcessMC/TotalMC and Data/TotalMC. The total efficiency is calculated by taking the number of events after all cuts have been applied divided by the number of events before any cut. The ProcessMC/TotalMC row shows the number of events in each Monte Carlo sample divided by the total sum of events of the Monte Carlo samples after all the selection cuts. The Data/TotalMC row is the total number of data events divided by the sum of the total number of Monte Carlo events after all the selection cuts. All Monte Carlo samples are normalised to the luminosity of the data and include the pileup and generator weights.

	Data	$W^- \to \mu\nu$	$W^- \to \tau\nu$	$Z \to \mu\mu$	$Z \to \tau\tau$	Top	Diboson
Initial	$1.69 \cdot 10^9$ (NA)	$4.92 \cdot 10^7$ (NA)	$2.37 \cdot 10^6$ (NA)	$3.94 \cdot 10^8$ (NA)	$1.15 \cdot 10^7$ (NA)	$1.47 \cdot 10^8$ (NA)	$1.34 \cdot 10^8$ (NA)
GRL	$1.64 \cdot 10^9$ (96.86%)	$4.92 \cdot 10^7$ (100%)	$2.37 \cdot 10^6$ (100%)	$3.94 \cdot 10^8$ (100%)	$1.16 \cdot 10^7$ (100%)	$1.47 \cdot 10^8$ (100%)	$1.34 \cdot 10^8$ (100%)
Good Calo	$1.64 \cdot 10^9$ (99.94%)	$4.92 \cdot 10^7$ (100%)	$2.37 \cdot 10^6$ (100%)	$3.94 \cdot 10^8$ (100%)	$1.16 \cdot 10^7$ (100%)	$1.47 \cdot 10^8$ (100%)	$1.34 \cdot 10^8$ (100%)
PriVtx	$1.64 \cdot 10^9$ (100%)	$4.92 \cdot 10^7$ (100%)	$2.37 \cdot 10^6$ (100%)	$3.94 \cdot 10^8$ (100%)	$1.16 \cdot 10^7$ (100%)	$1.47 \cdot 10^8$ (100%)	$1.34 \cdot 10^8$ (100%)
Reco Level	$1.64 \cdot 10^9$ (100%)	$4.92 \cdot 10^7$ (100%)	$2.37 \cdot 10^6$ (100%)	$3.94 \cdot 10^8$ (100%)	$1.16 \cdot 10^7$ (100%)	$1.47 \cdot 10^8$ (100%)	$1.34 \cdot 10^8$ (100%)
Trigger	$5.50 \cdot 10^8$ (33.59%)	$1.93 \cdot 10^7$ (39.24%)	$4.24 \cdot 10^5$ (17.85%)	$2.33 \cdot 10^8$ (58.99%)	$2.60 \cdot 10^6$ (22.55%)	$4.88 \cdot 10^7$ (33.13%)	$5.03 \cdot 10^7$ (37.48%)
MU_N 20 == 1	$3.97 \cdot 10^8$ (72.07%)	$1.82 \cdot 10^7$ (94.09%)	$2.99 \cdot 10^5$ (70.49%)	$8.52 \cdot 10^7$ (36.63%)	$1.64 \cdot 10^6$ (62.91%)	$4.36 \cdot 10^7$ (89.33%)	$3.42 \cdot 10^7$ (68.02%)
EL_N 20 == 0	$3.96 \cdot 10^8$ (99.87%)	$1.82 \cdot 10^7$ (99.98%)	$2.99 \cdot 10^5$ (99.96%)	$8.51 \cdot 10^7$ (99.92%)	$1.52 \cdot 10^6$ (92.69%)	$4.07 \cdot 10^7$ (93.37%)	$3.02 \cdot 10^7$ (88.29%)
MU_N 30 == 1	$3.11 \cdot 10^8$ (78.45%)	$1.59 \cdot 10^7$ (87.23%)	$2.02 \cdot 10^5$ (67.82%)	$6.83 \cdot 10^7$ (80.25%)	$1.19 \cdot 10^6$ (78.24%)	$3.67 \cdot 10^7$ (90.08%)	$2.65 \cdot 10^7$ (87.69%)
MU_N 65 == 1	$2.15 \cdot 10^7$ (6.912%)	$3.25 \cdot 10^6$ (20.53%)	$6.17 \cdot 10^4$ (30.47%)	$6.52 \cdot 10^6$ (9.548%)	$6.14 \cdot 10^5$ (51.7%)	$1.29 \cdot 10^7$ (35.17%)	$8.22 \cdot 10^6$ (31.04%)
MU_N Tight 65 == 1	$2.15 \cdot 10^7$ (100%)	$3.25 \cdot 10^6$ (100%)	$6.17 \cdot 10^4$ (100%)	$6.52 \cdot 10^6$ (100%)	$6.14 \cdot 10^5$ (100%)	$1.29 \cdot 10^7$ (100%)	$8.22 \cdot 10^6$ (100%)
Trigger match	$2.15 \cdot 10^7$ (99.89%)	$3.25 \cdot 10^6$ (99.99%)	$6.17 \cdot 10^4$ (99.99%)	$6.47 \cdot 10^6$ (99.23%)	$6.04 \cdot 10^5$ (98.28%)	$1.29 \cdot 10^7$ (99.79%)	$8.20 \cdot 10^6$ (99.75%)
JetCleaning: Loose Bad	$2.12 \cdot 10^7$ (98.67%)	$3.24 \cdot 10^6$ (99.59%)	$6.14 \cdot 10^4$ (99.55%)	$6.43 \cdot 10^6$ (99.36%)	$6 \cdot 10^5$ (99.41%)	$1.28 \cdot 10^7$ (99.5%)	$8.15 \cdot 10^6$ (99.44%)
NOBADMUON	$2.12 \cdot 10^7$ (99.99%)	$3.23 \cdot 10^6$ (99.73%)	$6.12 \cdot 10^4$ (99.66%)	$6.43 \cdot 10^6$ (99.98%)	$5.98 \cdot 10^5$ (99.63%)	$1.28 \cdot 10^7$ (100%)	$8.15 \cdot 10^6$ (99.99%)
Save	$2.12 \cdot 10^7$ (100%)	$3.23 \cdot 10^6$ (100%)	$6.12 \cdot 10^4$ (100%)	$6.43 \cdot 10^6$ (100%)	$5.98 \cdot 10^5$ (100%)	$1.28 \cdot 10^7$ (100%)	$8.15 \cdot 10^6$ (100%)
Lepton Veto	$1.29 \cdot 10^7$ (60.71%)	$2.66 \cdot 10^6$ (82.43%)	$4.97 \cdot 10^4$ (81.26%)	$5.08 \cdot 10^6$ (79.05%)	$4.89 \cdot 10^5$ (81.81%)	$1.05 \cdot 10^7$ (82.2%)	$6.75 \cdot 10^6$ (82.83%)
Charge Selection	$6.26 \cdot 10^6$ (48.73%)	$2.66 \cdot 10^6$ (100%)	$4.97 \cdot 10^4$ (99.97%)	$2.39 \cdot 10^6$ (47%)	$2.37 \cdot 10^5$ (48.45%)	$5.28 \cdot 10^6$ (50.11%)	$3.65 \cdot 10^6$ (54.05%)
$\lvert\eta\rvert^\mu < 2.4$	$6.26 \cdot 10^6$ (100%)	$2.66 \cdot 10^6$ (100%)	$4.97 \cdot 10^4$ (100%)	$2.39 \cdot 10^6$ (100%)	$2.37 \cdot 10^5$ (100%)	$5.28 \cdot 10^6$ (100%)	$3.65 \cdot 10^6$ (100%)
$p_T^\mu > 65$ GeV	$6.26 \cdot 10^6$ (100%)	$2.66 \cdot 10^6$ (100%)	$4.97 \cdot 10^4$ (100%)	$2.39 \cdot 10^6$ (100%)	$2.37 \cdot 10^5$ (100%)	$5.28 \cdot 10^6$ (100%)	$3.65 \cdot 10^6$ (100%)
$E_T^{miss} > 85$ GeV	$4.46 \cdot 10^5$ (7.125%)	$1.23 \cdot 10^6$ (46.01%)	$4.04 \cdot 10^4$ (81.2%)	$1.88 \cdot 10^5$ (7.874%)	$1.74 \cdot 10^5$ (73.51%)	$1.24 \cdot 10^6$ (23.51%)	$7.79 \cdot 10^5$ (21.35%)
$m_T > 200$ GeV	$5.89 \cdot 10^4$ (13.19%)	$8.54 \cdot 10^5$ (69.66%)	$3.62 \cdot 10^4$ (89.7%)	$1.34 \cdot 10^5$ (71.02%)	$7.23 \cdot 10^4$ (41.51%)	$1.45 \cdot 10^5$ (11.71%)	$2.19 \cdot 10^5$ (28.06%)
Total Efficiency	0.0035%	1.7%	1.5%	0.034%	0.63%	0.099%	0.16%
ProcessMC/TotalMC	NA	58.49%	2.481%	9.149%	4.953%	9.954%	14.97%
Data/TotalMC	4.033%						

Table E.5.: Cutflow table for 2017 data for the W^- selection showing the effect each selection has on the number of events. The first column lists the name of the selection. The rest of the columns show the number of events for each sample and for each selection. The relative efficiency is shown as a percentage next to each number of events. The relative efficiency is calculated as the number of events after the current cut divided by the number of events in the previous cuts. The three rows at the bottom of the table show the total efficiency, ProcessMC/TotalMC and Data/TotalMC. The total efficiency is calculated by taking the number of events after all cuts have been applied divided by the number of events before any cut. The ProcessMC/TotalMC row shows the number of events in each Monte Carlo sample divided by the total sum of events of the Monte Carlo samples after all the selection cuts. The Data/TotalMC row is the total number of data events divided by the sum of the total number of Monte Carlo events after all the selection cuts. All Monte Carlo samples are normalised to the luminosity of the data and include the pileup and generator weights.

	Data	$W^{\pm} \to \mu\nu$	$W^{\pm} \to \tau\nu$	$Z \to \mu\mu$	$Z \to \tau\tau$	Top	Diboson
Initial	$3.38 \cdot 10^9$ (NA)	$1.08 \cdot 10^8$ (NA)	$5.54 \cdot 10^6$ (NA)	$7.88 \cdot 10^8$ (NA)	$2.31 \cdot 10^7$ (NA)	$2.95 \cdot 10^8$ (NA)	$2.68 \cdot 10^8$ (NA)
GRL	$3.28 \cdot 10^9$ (96.86%)	$1.09 \cdot 10^8$ (100%)	$5.55 \cdot 10^6$ (100%)	$7.88 \cdot 10^8$ (100%)	$2.31 \cdot 10^7$ (100%)	$2.95 \cdot 10^8$ (100%)	$2.68 \cdot 10^8$ (100%)
Good Calo	$3.28 \cdot 10^9$ (99.94%)	$1.09 \cdot 10^8$ (100%)	$5.55 \cdot 10^6$ (100%)	$7.88 \cdot 10^8$ (100%)	$2.31 \cdot 10^7$ (100%)	$2.95 \cdot 10^8$ (100%)	$2.68 \cdot 10^8$ (100%)
PriVtx	$3.28 \cdot 10^9$ (100%)	$1.09 \cdot 10^8$ (100%)	$5.55 \cdot 10^6$ (100%)	$7.88 \cdot 10^8$ (100%)	$2.31 \cdot 10^7$ (100%)	$2.95 \cdot 10^8$ (100%)	$2.68 \cdot 10^8$ (100%)
Reco Level	$3.28 \cdot 10^9$ (100%)	$1.09 \cdot 10^8$ (100%)	$5.55 \cdot 10^6$ (100%)	$7.88 \cdot 10^8$ (100%)	$2.31 \cdot 10^7$ (100%)	$2.95 \cdot 10^8$ (100%)	$2.68 \cdot 10^8$ (100%)
Trigger	$1.10 \cdot 10^9$ (33.59%)	$4.24 \cdot 10^7$ (39.1%)	$9.53 \cdot 10^5$ (17.19%)	$4.65 \cdot 10^8$ (58.99%)	$5.21 \cdot 10^6$ (22.55%)	$9.76 \cdot 10^7$ (33.13%)	$1.01 \cdot 10^8$ (37.48%)
MU_N 20 == 1	$7.93 \cdot 10^8$ (72.07%)	$3.99 \cdot 10^7$ (93.94%)	$6.79 \cdot 10^5$ (71.3%)	$1.70 \cdot 10^8$ (36.63%)	$3.28 \cdot 10^6$ (62.91%)	$8.72 \cdot 10^7$ (89.33%)	$6.84 \cdot 10^7$ (68.02%)
EL_N 20 == 0	$7.92 \cdot 10^8$ (99.87%)	$3.98 \cdot 10^7$ (99.99%)	$6.79 \cdot 10^5$ (99.96%)	$1.70 \cdot 10^8$ (99.92%)	$3.04 \cdot 10^6$ (92.69%)	$8.14 \cdot 10^7$ (93.37%)	$6.04 \cdot 10^7$ (88.29%)
MU_N 30 == 1	$6.21 \cdot 10^8$ (78.45%)	$3.42 \cdot 10^7$ (85.83%)	$4.48 \cdot 10^5$ (66.01%)	$1.37 \cdot 10^8$ (80.25%)	$2.38 \cdot 10^6$ (78.24%)	$7.34 \cdot 10^7$ (90.08%)	$5.30 \cdot 10^7$ (87.69%)
MU_N 65 == 1	$4.30 \cdot 10^7$ (6.912%)	$6.59 \cdot 10^6$ (19.28%)	$1.25 \cdot 10^5$ (27.95%)	$1.30 \cdot 10^7$ (9.548%)	$1.23 \cdot 10^6$ (51.7%)	$2.58 \cdot 10^7$ (35.17%)	$1.64 \cdot 10^7$ (31.04%)
MU_N Tight 65 == 1	$4.30 \cdot 10^7$ (100%)	$6.59 \cdot 10^6$ (100%)	$1.25 \cdot 10^5$ (100%)	$1.30 \cdot 10^7$ (100%)	$1.23 \cdot 10^6$ (100%)	$2.58 \cdot 10^7$ (100%)	$1.64 \cdot 10^7$ (100%)
Trigger match	$4.29 \cdot 10^7$ (99.89%)	$6.59 \cdot 10^6$ (100%)	$1.25 \cdot 10^5$ (99.99%)	$1.29 \cdot 10^7$ (99.23%)	$1.21 \cdot 10^6$ (98.28%)	$2.58 \cdot 10^7$ (99.79%)	$1.64 \cdot 10^7$ (99.75%)
JetCleaning: Loose Bad	$4.23 \cdot 10^7$ (98.67%)	$6.56 \cdot 10^6$ (99.59%)	$1.25 \cdot 10^5$ (99.59%)	$1.29 \cdot 10^7$ (99.36%)	$1.20 \cdot 10^6$ (99.41%)	$2.56 \cdot 10^7$ (99.5%)	$1.63 \cdot 10^7$ (99.44%)
NOBADMUON	$4.23 \cdot 10^7$ (99.99%)	$6.55 \cdot 10^6$ (99.77%)	$1.24 \cdot 10^5$ (99.71%)	$1.29 \cdot 10^7$ (99.98%)	$1.20 \cdot 10^6$ (99.63%)	$2.56 \cdot 10^7$ (100%)	$1.63 \cdot 10^7$ (99.99%)
Save	$4.23 \cdot 10^7$ (100%)	$6.55 \cdot 10^6$ (100%)	$1.24 \cdot 10^5$ (100%)	$1.29 \cdot 10^7$ (100%)	$1.20 \cdot 10^6$ (100%)	$2.56 \cdot 10^7$ (100%)	$1.63 \cdot 10^7$ (100%)
Lepton Veto	$2.57 \cdot 10^7$ (60.71%)	$5.40 \cdot 10^6$ (82.47%)	$1.02 \cdot 10^5$ (82.14%)	$1.02 \cdot 10^7$ (79.05%)	$9.78 \cdot 10^5$ (81.81%)	$2.11 \cdot 10^7$ (82.2%)	$1.35 \cdot 10^7$ (82.83%)
Charge Selection	$1.29 \cdot 10^7$ (50%)	$5.40 \cdot 10^6$ (100%)	$1.02 \cdot 10^5$ (99.97%)	$5.08 \cdot 10^6$ (50%)	$4.89 \cdot 10^5$ (50%)	$1.05 \cdot 10^7$ (50%)	$6.75 \cdot 10^6$ (50%)
$\lvert\eta\rvert^{\mu} < 2.4$	$1.29 \cdot 10^7$ (100%)	$5.40 \cdot 10^6$ (100%)	$1.02 \cdot 10^5$ (100%)	$5.08 \cdot 10^6$ (100%)	$4.89 \cdot 10^5$ (100%)	$1.05 \cdot 10^7$ (100%)	$6.75 \cdot 10^6$ (100%)
$p_T^{\mu} > 65$ GeV	$1.29 \cdot 10^7$ (100%)	$5.40 \cdot 10^6$ (100%)	$1.02 \cdot 10^5$ (100%)	$5.08 \cdot 10^6$ (100%)	$4.89 \cdot 10^5$ (100%)	$1.05 \cdot 10^7$ (100%)	$6.75 \cdot 10^6$ (100%)
$E_T^{miss} > 85$ GeV	$1.03 \cdot 10^6$ (8.048%)	$2.53 \cdot 10^6$ (46.83%)	$8.27 \cdot 10^4$ (80.96%)	$6.01 \cdot 10^5$ (11.83%)	$3.56 \cdot 10^5$ (72.86%)	$2.50 \cdot 10^6$ (23.71%)	$1.52 \cdot 10^6$ (22.49%)
$m_T > 200$ GeV	$1.42 \cdot 10^5$ (13.69%)	$1.75 \cdot 10^6$ (69.25%)	$7.38 \cdot 10^4$ (89.27%)	$4.44 \cdot 10^5$ (73.76%)	$1.48 \cdot 10^5$ (41.58%)	$2.91 \cdot 10^5$ (11.65%)	$4.23 \cdot 10^5$ (27.86%)
Total Efficiency	0.0042%	1.6%	1.3%	0.056%	0.64%	0.099%	0.16%
ProcessMC/TotalMC	NA	55.94%	2.358%	14.16%	4.733%	9.291%	13.51%
Data/TotalMC	4.523%						

Table E.6.: Cutflow table for 2017 data for the $W^{\pm}$ selection showing the effect each selection has on the number of events. The first column lists the name of the selection. The rest of the columns show the number of events for each sample and for each selection. The relative efficiency is shown as a percentage next to each number of events. The relative efficiency is calculated as the number of events after the current cut divided by the number of events in the previous cuts. The three rows at the bottom of the table show the total efficiency, ProcessMC/TotalMC and Data/TotalMC. The total efficiency is calculated by taking the number of events after all cuts have been applied divided by the number of events before any cut. The ProcessMC/TotalMC row shows the number of events in each Monte Carlo sample divided by the total sum of events of the Monte Carlo samples after all the selection cuts. The Data/TotalMC row is the total number of data events divided by the sum of the total number of Monte Carlo events after all the selection cuts. All Monte Carlo samples are normalised to the luminosity of the data and include the pileup and generator weights.

E.3. MC16e

This section shows the relative contribution of all samples, the control distributions and the cutflows for the MC16e campaign. The positive charge is presented first, followed by the negative charge and finally the combination of these two charges is shown. The kinematic variables presented were discussed in Chapter 9. The control distributions show reasonable agreement between data and prediction.

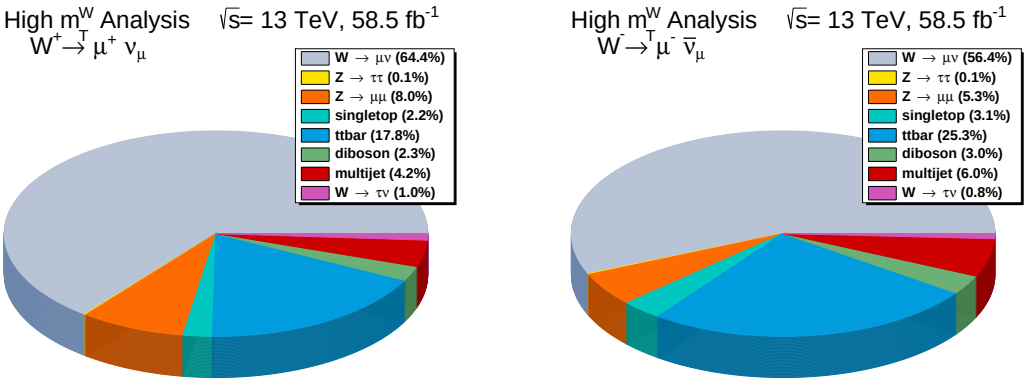

a b

Figure E.15.: Chart showing relative contributions of all Monte Carlo in the signal region for MC16e, for muon charge (a) W^+ and (b) W^-.

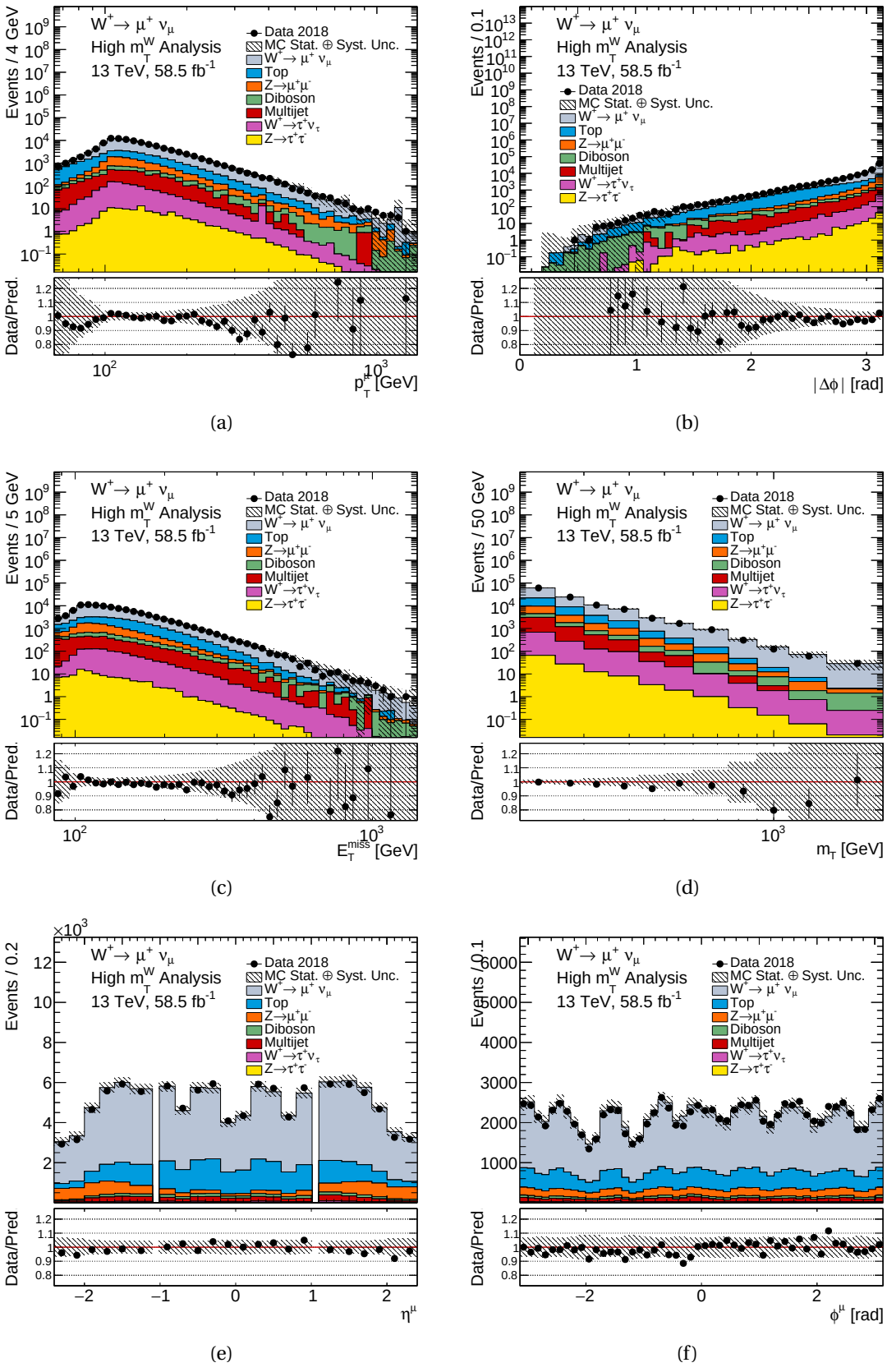

Figure E.16.: MC16e $W^+ \to \mu^+\nu$ control distributions for p_T^μ, $|\Delta\phi|$, E_T^{miss}, m_T, η^μ and ϕ^μ. The data contribution is shown with black points, the signal and the background contributions with solid lines. In the shaded band, systematic experimental uncertainties have been combined with the MC statistical uncertainties. The data statistical uncertainties are shown on the data points. Luminosity uncertainties have not been included.

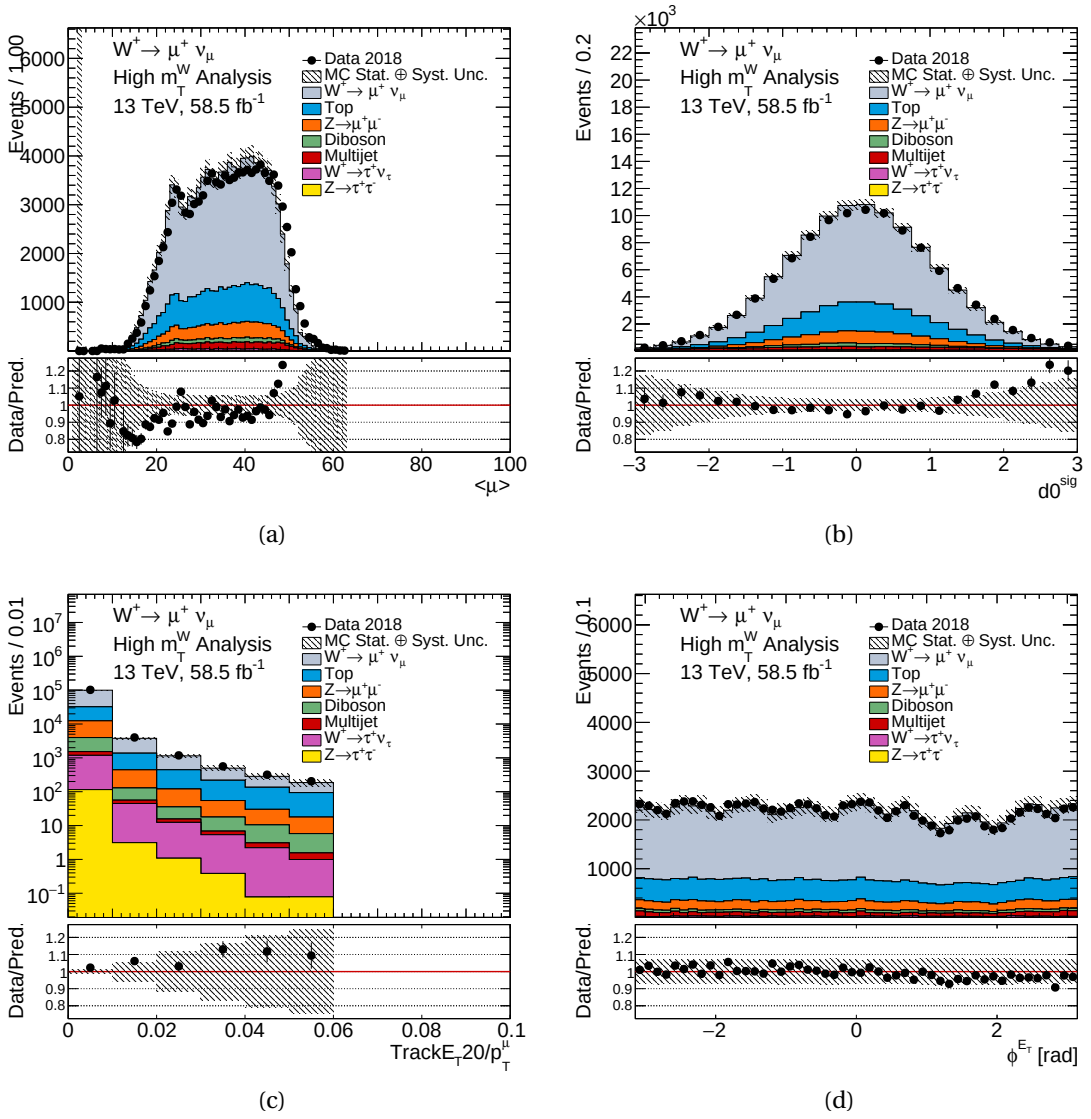

Figure E.17.: MC16e $W^+ \to \mu^+\nu$ control distributions for $<\mu>$, $d0^{sig}$, $TrackE_T20/p_T^{\mu}$ and $\phi^{E_T^{miss}}$. The data contribution is shown with black points, the signal and the background contributions with solid lines. In the shaded band, systematic experimental uncertainties have been combined with the MC statistical uncertainties. The data statistical uncertainties are shown on the data points. Luminosity uncertainties have not been included.

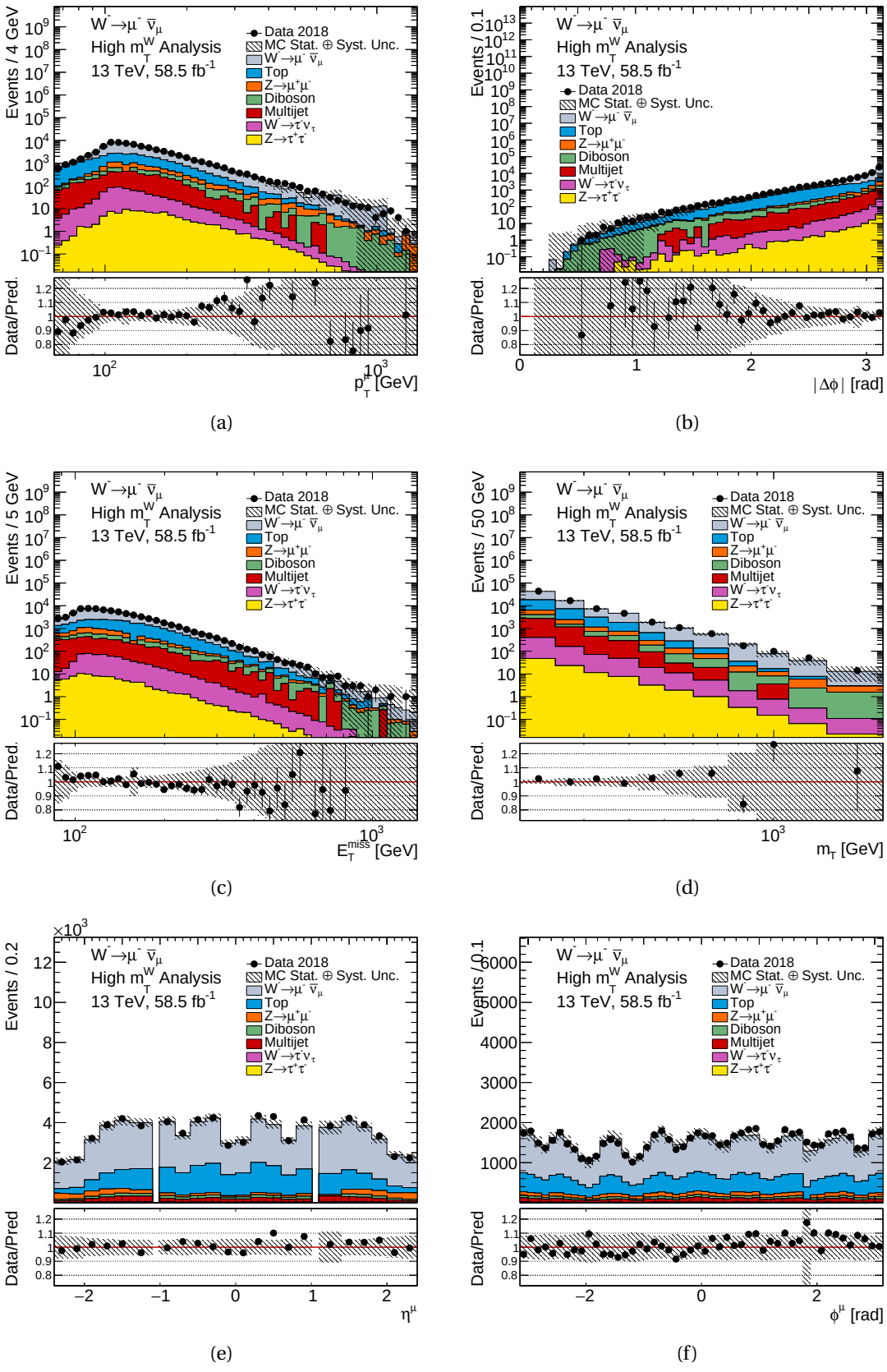

Figure E.18.: MC16e $W^- \to \mu^- \nu$ control distributions for p_T^μ, $|\Delta\phi|$, E_T^{miss}, m_T, η^μ and ϕ^μ. The data contribution is shown with black points, the signal and the background contributions with solid lines. In the shaded band, systematic experimental uncertainties have been combined with the MC statistical uncertainties. The data statistical uncertainties are shown on the data points. Luminosity uncertainties have not been included.

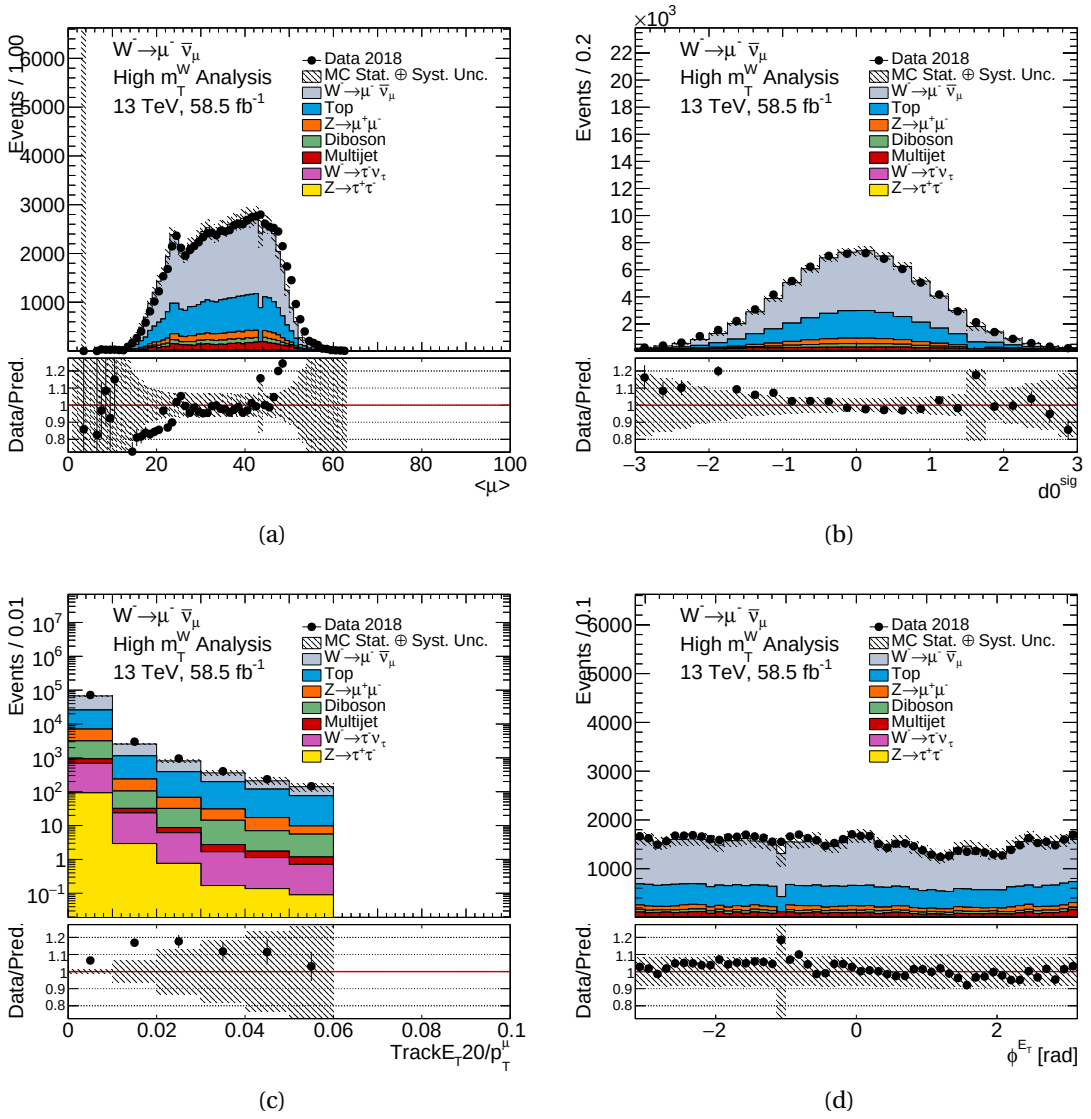

Figure E.19.: MC16e $W^- \to \mu^- \nu$ control distributions for $< \mu >$, $d0^{sig}$, $TrackE_T20/p_T^{\mu}$ and $\phi^{E_T^{miss}}$. The data contribution is shown with black points, the signal and the background contributions with solid lines. In the shaded band, systematic experimental uncertainties have been combined with the MC statistical uncertainties. The data statistical uncertainties are shown on the data points. Luminosity uncertainties have not been included.

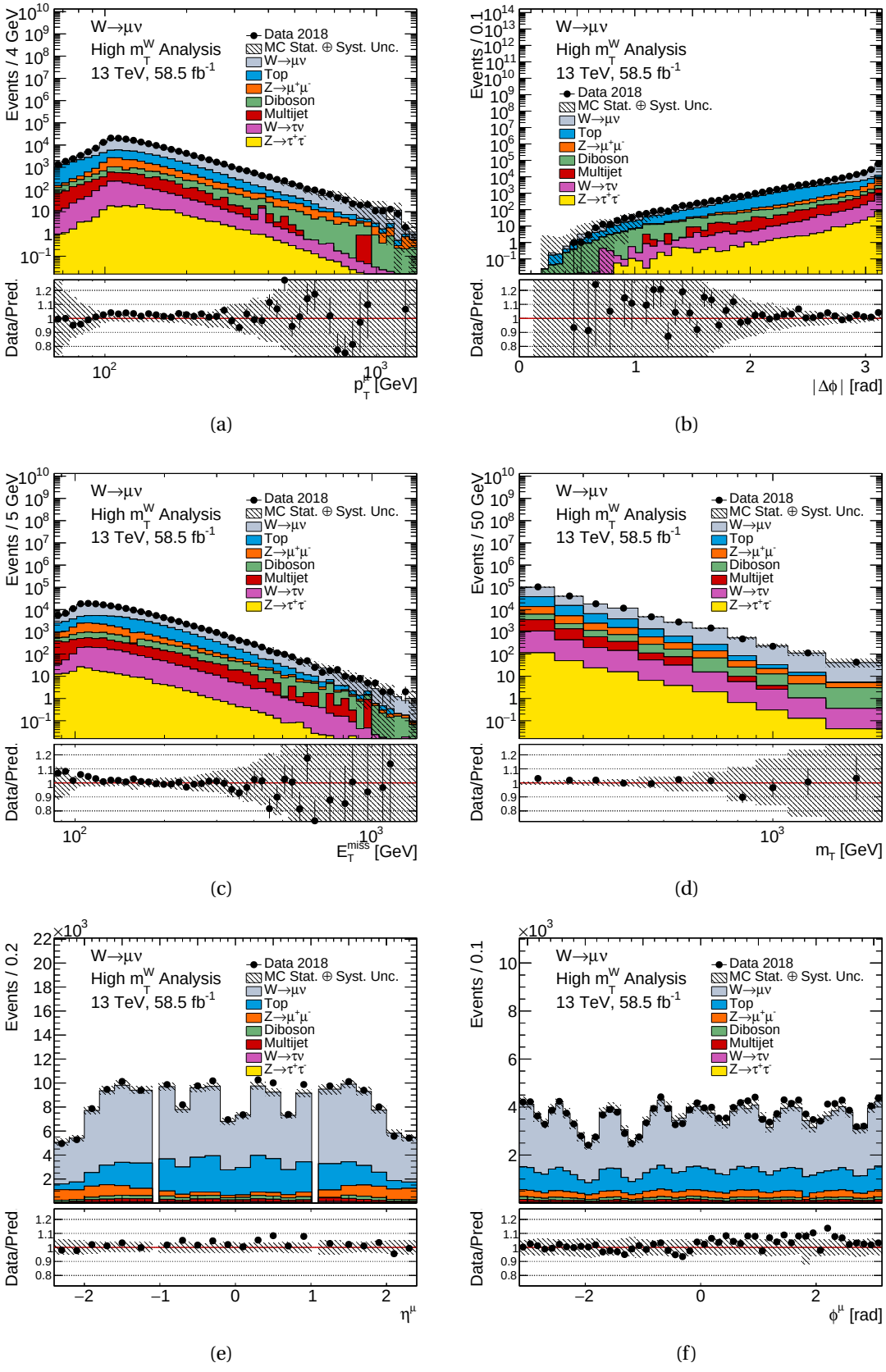

Figure E.20.: MC16e combined charge $W^{\pm} \to \mu\nu$ control distributions for p_T^{μ}, $|\Delta\phi|$, E_T^{miss}, m_T, η^{μ} and ϕ^{μ}. The data contribution is shown with black points, the signal and the background contributions with solid lines. In the shaded band, systematic experimental uncertainties have been combined with the MC statistical uncertainties. The data statistical uncertainties are shown on the data points. Luminosity uncertainties have not been included.

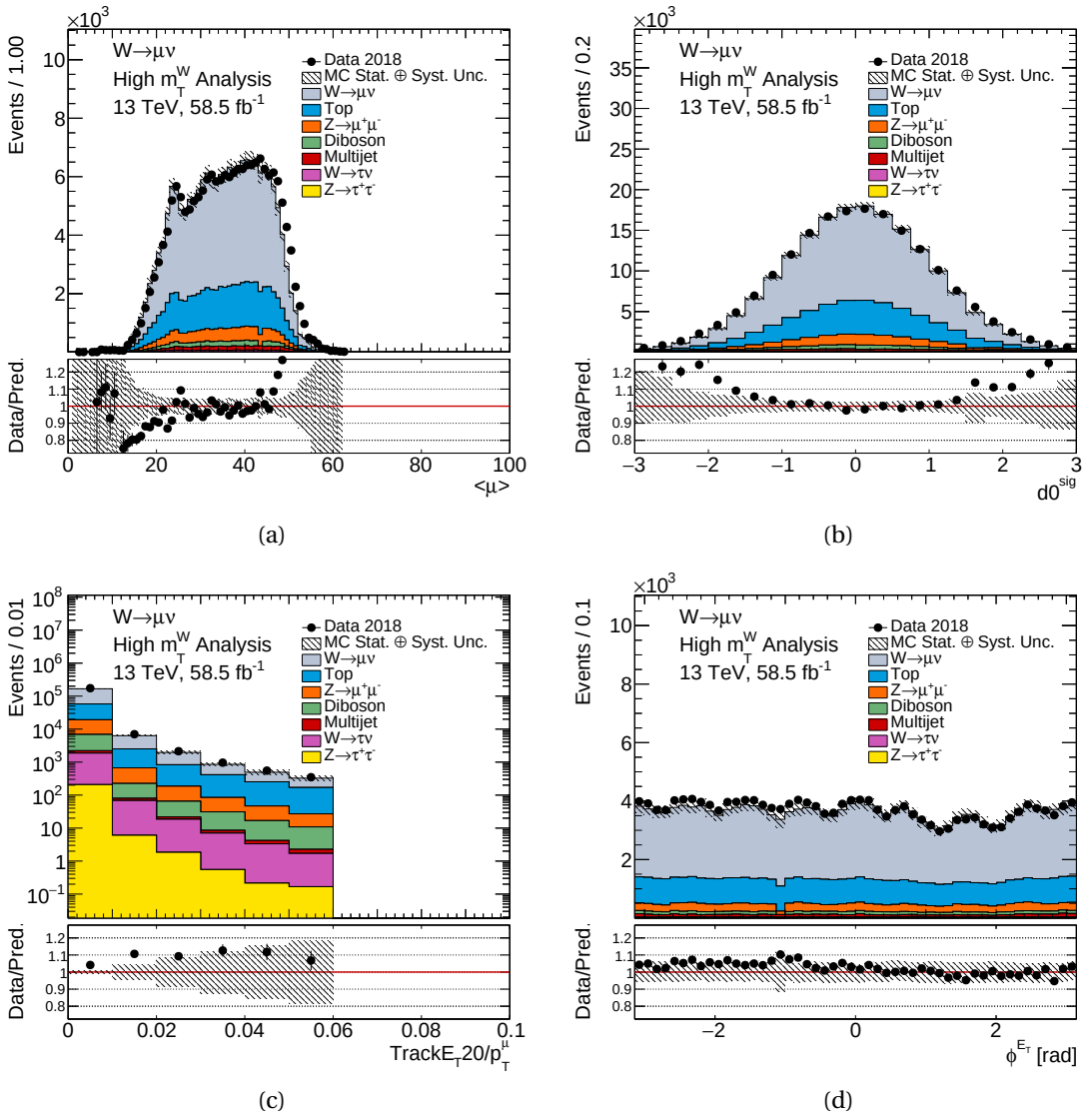

Figure E.21.: MC16e combined charge $W^{\pm} \to \mu\nu$ control distributions for $< \mu >$, $d0^{sig}$, $TrackE_T20/p_T^{\mu}$ and $\phi^{E_T^{miss}}$. The data contribution is shown with black points, the signal and the background contributions with solid lines. In the shaded band, systematic experimental uncertainties have been combined with the MC statistical uncertainties. The data statistical uncertainties are shown on the data points. Luminosity uncertainties have not been included.

	Data	$W^+ \to \mu\nu$	$W^+ \to \tau\nu$	$Z \to \mu\mu$	$Z \to \tau\tau$	Top	Diboson
Initial	$2.13 \cdot 10^9$ (NA)	$7.96 \cdot 10^7$ (NA)	$4.49 \cdot 10^6$ (NA)	$5.07 \cdot 10^8$ (NA)	$1.75 \cdot 10^7$ (NA)	$1.97 \cdot 10^8$ (NA)	$8.60 \cdot 10^7$ (NA)
GRL	$2.11 \cdot 10^9$ (98.95%)	$7.96 \cdot 10^7$ (100%)	$4.49 \cdot 10^6$ (100%)	$5.07 \cdot 10^8$ (100%)	$1.75 \cdot 10^7$ (100%)	$1.97 \cdot 10^8$ (100%)	$8.60 \cdot 10^7$ (100%)
Good Calo	$2.11 \cdot 10^9$ (99.96%)	$7.96 \cdot 10^7$ (100%)	$4.49 \cdot 10^6$ (100%)	$5.07 \cdot 10^8$ (100%)	$1.75 \cdot 10^7$ (100%)	$1.97 \cdot 10^8$ (100%)	$8.60 \cdot 10^7$ (100%)
PriVtx	$2.11 \cdot 10^9$ (100%)	$7.96 \cdot 10^7$ (100%)	$4.49 \cdot 10^6$ (100%)	$5.07 \cdot 10^8$ (100%)	$1.75 \cdot 10^7$ (100%)	$1.97 \cdot 10^8$ (100%)	$8.60 \cdot 10^7$ (100%)
Reco Level	$2.11 \cdot 10^9$ (100%)	$7.96 \cdot 10^7$ (100%)	$4.49 \cdot 10^6$ (100%)	$5.07 \cdot 10^8$ (100%)	$1.75 \cdot 10^7$ (100%)	$1.97 \cdot 10^8$ (100%)	$8.60 \cdot 10^7$ (100%)
Trigger	$7.60 \cdot 10^8$ (36.06%)	$3.19 \cdot 10^7$ (40.06%)	$7.84 \cdot 10^5$ (17.46%)	$3.04 \cdot 10^8$ (59.99%)	$4.08 \cdot 10^6$ (23.35%)	$6.61 \cdot 10^7$ (33.57%)	$3.33 \cdot 10^7$ (38.67%)
MU_N 20 == 1	$5.31 \cdot 10^8$ (69.88%)	$2.99 \cdot 10^7$ (93.85%)	$5.55 \cdot 10^5$ (70.89%)	$1.12 \cdot 10^8$ (36.8%)	$2.53 \cdot 10^6$ (62.03%)	$5.89 \cdot 10^7$ (89.18%)	$2.20 \cdot 10^7$ (66.08%)
EL_N 20 == 0	$5.30 \cdot 10^8$ (99.88%)	$2.99 \cdot 10^7$ (99.99%)	$5.55 \cdot 10^5$ (99.96%)	$1.12 \cdot 10^8$ (99.92%)	$2.34 \cdot 10^6$ (92.34%)	$5.50 \cdot 10^7$ (93.37%)	$1.86 \cdot 10^7$ (84.84%)
MU_N 30 == 1	$4.12 \cdot 10^8$ (77.7%)	$2.53 \cdot 10^7$ (84.57%)	$3.67 \cdot 10^5$ (66.01%)	$8.96 \cdot 10^7$ (80.04%)	$1.86 \cdot 10^6$ (79.51%)	$4.94 \cdot 10^7$ (89.73%)	$1.62 \cdot 10^7$ (87.11%)
MU_N 65 == 1	$2.79 \cdot 10^7$ (6.764%)	$4.86 \cdot 10^6$ (19.21%)	$1.10 \cdot 10^5$ (30.06%)	$9.11 \cdot 10^6$ (10.17%)	$1.02 \cdot 10^6$ (54.84%)	$1.72 \cdot 10^7$ (34.86%)	$5.09 \cdot 10^6$ (31.37%)
MU_N Tight 65 == 1	$2.79 \cdot 10^7$ (100%)	$4.86 \cdot 10^6$ (100%)	$1.10 \cdot 10^5$ (100%)	$9.11 \cdot 10^6$ (100%)	$1.02 \cdot 10^6$ (100%)	$1.72 \cdot 10^7$ (100%)	$5.09 \cdot 10^6$ (100%)
Trigger match	$2.78 \cdot 10^7$ (99.88%)	$4.86 \cdot 10^6$ (100%)	$1.10 \cdot 10^5$ (99.99%)	$9.03 \cdot 10^6$ (99.09%)	$1.00 \cdot 10^6$ (98.28%)	$1.72 \cdot 10^7$ (99.78%)	$5.08 \cdot 10^6$ (99.7%)
JetCleaning: Loose Bad	$2.75 \cdot 10^7$ (98.61%)	$4.84 \cdot 10^6$ (99.61%)	$1.10 \cdot 10^5$ (99.6%)	$8.97 \cdot 10^6$ (99.33%)	$9.95 \cdot 10^5$ (99.41%)	$1.71 \cdot 10^7$ (99.51%)	$5.05 \cdot 10^6$ (99.45%)
NOBADMUON	$2.74 \cdot 10^7$ (99.99%)	$4.83 \cdot 10^6$ (99.75%)	$1.09 \cdot 10^5$ (99.77%)	$8.96 \cdot 10^6$ (99.95%)	$9.91 \cdot 10^5$ (99.63%)	$1.71 \cdot 10^7$ (100%)	$5.05 \cdot 10^6$ (99.99%)
Save	$2.74 \cdot 10^7$ (100%)	$4.83 \cdot 10^6$ (100%)	$1.09 \cdot 10^5$ (100%)	$8.96 \cdot 10^6$ (100%)	$9.91 \cdot 10^5$ (100%)	$1.71 \cdot 10^7$ (100%)	$5.05 \cdot 10^6$ (100%)
Lepton Veto	$1.68 \cdot 10^7$ (61.23%)	$3.99 \cdot 10^6$ (82.6%)	$9.09 \cdot 10^4$ (83.07%)	$7.12 \cdot 10^6$ (79.39%)	$8.12 \cdot 10^5$ (81.89%)	$1.40 \cdot 10^7$ (82.2%)	$4.18 \cdot 10^6$ (82.71%)
Charge Selection	$8.62 \cdot 10^6$ (51.27%)	$3.99 \cdot 10^6$ (100%)	$9.09 \cdot 10^4$ (99.98%)	$3.87 \cdot 10^6$ (54.42%)	$4.19 \cdot 10^5$ (51.57%)	$7.00 \cdot 10^6$ (49.87%)	$2.11 \cdot 10^6$ (50.47%)
$\lvert\eta\rvert^\mu < 2.4$	$8.62 \cdot 10^6$ (100%)	$3.99 \cdot 10^6$ (100%)	$9.09 \cdot 10^4$ (100%)	$3.87 \cdot 10^6$ (100%)	$4.19 \cdot 10^5$ (100%)	$7.00 \cdot 10^6$ (100%)	$2.11 \cdot 10^6$ (100%)
$p_T^\mu > 65$ GeV	$8.62 \cdot 10^6$ (100%)	$3.99 \cdot 10^6$ (100%)	$9.09 \cdot 10^4$ (100%)	$3.87 \cdot 10^6$ (100%)	$4.19 \cdot 10^5$ (100%)	$7.00 \cdot 10^6$ (100%)	$2.11 \cdot 10^6$ (100%)
$E_T^{miss} > 85$ GeV	$7.56 \cdot 10^5$ (8.769%)	$2.02 \cdot 10^6$ (50.58%)	$7.55 \cdot 10^4$ (83.08%)	$8.30 \cdot 10^5$ (21.44%)	$3.05 \cdot 10^5$ (72.73%)	$1.67 \cdot 10^6$ (23.87%)	$5.63 \cdot 10^5$ (26.68%)
$m_T > 200$ GeV	$1.08 \cdot 10^5$ (14.35%)	$1.45 \cdot 10^6$ (71.98%)	$6.80 \cdot 10^4$ (90.03%)	$6.48 \cdot 10^5$ (78.1%)	$1.27 \cdot 10^5$ (41.63%)	$1.94 \cdot 10^5$ (11.61%)	$1.69 \cdot 10^5$ (29.97%)
Total Efficiency	0.0051%	1.8%	1.5%	0.13%	0.73%	0.099%	0.2%
ProcessMC/TotalMC	NA	54.65%	2.557%	24.38%	4.768%	7.301%	6.341%
Data/TotalMC	4.078%						

Table E.7.: Cutflow table for 2018 data for the W^+ selection showing the effect each selection has on the number of events. The first column lists the name of the selection. The rest of the columns show the number of events for each sample and for each selection. The relative efficiency is shown as a percentage next to each number of events. The relative efficiency is calculated as the number of events after the current cut divided by the number of events in the previous cuts. The three rows at the bottom of the table show the total efficiency, ProcessMC/TotalMC and Data/TotalMC. The total efficiency is calculated by taking the number of events after all cuts have been applied divided by the number of events before any cut. The ProcessMC/TotalMC row shows the number of events in each Monte Carlo sample divided by the total sum of events of the Monte Carlo samples after all the selection cuts. The Data/TotalMC row is the total number of data events divided by the sum of the total number of Monte Carlo events after all the selection cuts. All Monte Carlo samples are normalised to the luminosity of the data and include the pileup and generator weights.

	Data	$W^- \to \mu\nu$	$W^- \to \tau\nu$	$Z \to \mu\mu$	$Z \to \tau\tau$	Top	Diboson
Initial	$2.13 \cdot 10^9$ (NA)	$6.64 \cdot 10^7$ (NA)	$3.42 \cdot 10^6$ (NA)	$5.07 \cdot 10^8$ (NA)	$1.75 \cdot 10^7$ (NA)	$1.97 \cdot 10^8$ (NA)	$8.60 \cdot 10^7$ (NA)
GRL	$2.11 \cdot 10^9$ (98.95%)	$6.64 \cdot 10^7$ (100%)	$3.42 \cdot 10^6$ (100%)	$5.07 \cdot 10^8$ (100%)	$1.75 \cdot 10^7$ (100%)	$1.97 \cdot 10^8$ (100%)	$8.60 \cdot 10^7$ (100%)
Good Calo	$2.11 \cdot 10^9$ (99.96%)	$6.64 \cdot 10^7$ (100%)	$3.42 \cdot 10^6$ (100%)	$5.07 \cdot 10^8$ (100%)	$1.75 \cdot 10^7$ (100%)	$1.97 \cdot 10^8$ (100%)	$8.60 \cdot 10^7$ (100%)
PriVtx	$2.11 \cdot 10^9$ (100%)	$6.64 \cdot 10^7$ (100%)	$3.42 \cdot 10^6$ (100%)	$5.07 \cdot 10^8$ (100%)	$1.75 \cdot 10^7$ (100%)	$1.97 \cdot 10^8$ (100%)	$8.60 \cdot 10^7$ (100%)
Reco Level	$2.11 \cdot 10^9$ (100%)	$6.64 \cdot 10^7$ (100%)	$3.42 \cdot 10^6$ (100%)	$5.07 \cdot 10^8$ (100%)	$1.75 \cdot 10^7$ (100%)	$1.97 \cdot 10^8$ (100%)	$8.60 \cdot 10^7$ (100%)
Trigger	$7.60 \cdot 10^8$ (36.06%)	$2.67 \cdot 10^7$ (40.27%)	$6.36 \cdot 10^5$ (18.59%)	$3.04 \cdot 10^8$ (59.99%)	$4.08 \cdot 10^6$ (23.35%)	$6.61 \cdot 10^7$ (33.57%)	$3.33 \cdot 10^7$ (38.67%)
MU_N 20 == 1	$5.31 \cdot 10^8$ (69.88%)	$2.52 \cdot 10^7$ (94.1%)	$4.41 \cdot 10^5$ (69.35%)	$1.12 \cdot 10^8$ (36.8%)	$2.53 \cdot 10^6$ (62.03%)	$5.89 \cdot 10^7$ (89.18%)	$2.20 \cdot 10^7$ (66.08%)
EL_N 20 == 0	$5.30 \cdot 10^8$ (99.88%)	$2.52 \cdot 10^7$ (99.98%)	$4.41 \cdot 10^5$ (99.95%)	$1.12 \cdot 10^8$ (99.92%)	$2.34 \cdot 10^6$ (92.34%)	$5.50 \cdot 10^7$ (93.37%)	$1.86 \cdot 10^7$ (84.84%)
MU_N 30 == 1	$4.12 \cdot 10^8$ (77.7%)	$2.19 \cdot 10^7$ (87.18%)	$3.06 \cdot 10^5$ (69.46%)	$8.96 \cdot 10^7$ (80.04%)	$1.86 \cdot 10^6$ (79.51%)	$4.94 \cdot 10^7$ (89.73%)	$1.62 \cdot 10^7$ (87.11%)
MU_N 65 == 1	$2.79 \cdot 10^7$ (6.764%)	$4.74 \cdot 10^6$ (21.63%)	$1.06 \cdot 10^5$ (34.78%)	$9.11 \cdot 10^6$ (10.17%)	$1.02 \cdot 10^6$ (54.84%)	$1.72 \cdot 10^7$ (34.86%)	$5.09 \cdot 10^6$ (31.37%)
MU_N Tight 65 == 1	$2.79 \cdot 10^7$ (100%)	$4.74 \cdot 10^6$ (100%)	$1.06 \cdot 10^5$ (100%)	$9.11 \cdot 10^6$ (100%)	$1.02 \cdot 10^6$ (100%)	$1.72 \cdot 10^7$ (100%)	$5.09 \cdot 10^6$ (100%)
Trigger match	$2.78 \cdot 10^7$ (99.88%)	$4.74 \cdot 10^6$ (99.99%)	$1.06 \cdot 10^5$ (99.99%)	$9.03 \cdot 10^6$ (99.09%)	$1.00 \cdot 10^6$ (98.28%)	$1.72 \cdot 10^7$ (99.78%)	$5.08 \cdot 10^6$ (99.7%)
JetCleaning: Loose Bad	$2.75 \cdot 10^7$ (98.61%)	$4.72 \cdot 10^6$ (99.6%)	$1.06 \cdot 10^5$ (99.62%)	$8.97 \cdot 10^6$ (99.33%)	$9.95 \cdot 10^5$ (99.41%)	$1.71 \cdot 10^7$ (99.51%)	$5.05 \cdot 10^6$ (99.45%)
NOBADMUON	$2.74 \cdot 10^7$ (99.99%)	$4.71 \cdot 10^6$ (99.68%)	$1.06 \cdot 10^5$ (99.58%)	$8.96 \cdot 10^6$ (99.95%)	$9.91 \cdot 10^5$ (99.63%)	$1.71 \cdot 10^7$ (100%)	$5.05 \cdot 10^6$ (99.99%)
Save	$2.74 \cdot 10^7$ (100%)	$4.71 \cdot 10^6$ (100%)	$1.06 \cdot 10^5$ (100%)	$8.96 \cdot 10^6$ (100%)	$9.91 \cdot 10^5$ (100%)	$1.71 \cdot 10^7$ (100%)	$5.05 \cdot 10^6$ (100%)
Lepton Veto	$1.68 \cdot 10^7$ (61.23%)	$3.88 \cdot 10^6$ (82.34%)	$8.59 \cdot 10^4$ (81.38%)	$7.12 \cdot 10^6$ (79.39%)	$8.12 \cdot 10^5$ (81.89%)	$1.40 \cdot 10^7$ (82.2%)	$4.18 \cdot 10^6$ (82.71%)
Charge Selection	$8.19 \cdot 10^6$ (48.73%)	$3.88 \cdot 10^6$ (100%)	$8.59 \cdot 10^4$ (99.97%)	$3.24 \cdot 10^6$ (45.58%)	$3.93 \cdot 10^5$ (48.43%)	$7.04 \cdot 10^6$ (50.13%)	$2.07 \cdot 10^6$ (49.54%)
$\lvert\eta\rvert^\mu < 2.4$	$8.19 \cdot 10^6$ (100%)	$3.88 \cdot 10^6$ (100%)	$8.59 \cdot 10^4$ (100%)	$3.24 \cdot 10^6$ (100%)	$3.93 \cdot 10^5$ (100%)	$7.04 \cdot 10^6$ (100%)	$2.07 \cdot 10^6$ (100%)
$p_T^\mu > 65$ GeV	$8.19 \cdot 10^6$ (100%)	$3.88 \cdot 10^6$ (100%)	$8.59 \cdot 10^4$ (100%)	$3.24 \cdot 10^6$ (100%)	$3.93 \cdot 10^5$ (100%)	$7.04 \cdot 10^6$ (100%)	$2.07 \cdot 10^6$ (100%)
$E_T^{miss} > 85$ GeV	$5.72 \cdot 10^5$ (6.979%)	$1.89 \cdot 10^6$ (48.79%)	$7.16 \cdot 10^4$ (83.3%)	$3.77 \cdot 10^5$ (11.63%)	$2.91 \cdot 10^5$ (73.96%)	$1.66 \cdot 10^6$ (23.51%)	$5.54 \cdot 10^5$ (26.78%)
$m_T > 200$ GeV	$7.68 \cdot 10^4$ (13.44%)	$1.37 \cdot 10^6$ (72.52%)	$6.50 \cdot 10^4$ (90.78%)	$2.91 \cdot 10^5$ (77.17%)	$1.21 \cdot 10^5$ (41.55%)	$1.94 \cdot 10^5$ (11.75%)	$1.80 \cdot 10^5$ (32.43%)
Total Efficiency	0.0036%	2.1%	1.9%	0.057%	0.69%	0.099%	0.21%
ProcessMC/TotalMC	NA	61.71%	2.922%	13.1%	5.436%	8.747%	8.084%
Data/TotalMC	3.456%						

Table E.8.: Cutflow table for 2018 data for the W^- selection showing the effect each selection has on the number of events. The first column lists the name of the selection. The rest of the columns show the number of events for each sample and for each selection. The relative efficiency is shown as a percentage next to each number of events. The relative efficiency is calculated as the number of events after the current cut divided by the number of events in the previous cuts. The three rows at the bottom of the table show the total efficiency, ProcessMC/TotalMC and Data/TotalMC. The total efficiency is calculated by taking the number of events after all cuts have been applied divided by the number of events before any cut. The ProcessMC/TotalMC row shows the number of events in each Monte Carlo sample divided by the total sum of events of the Monte Carlo samples after all the selection cuts. The Data/TotalMC row is the total number of data events divided by the sum of the total number of Monte Carlo events after all the selection cuts. All Monte Carlo samples are normalised to the luminosity of the data and include the pileup and generator weights.

	Data	$W^{\pm} \to \mu\nu$	$W^{\pm} \to \tau\nu$	$Z \to \mu\mu$	$Z \to \tau\tau$	Top	Diboson
Initial	$4.26 \cdot 10^9$ (NA)	$1.46 \cdot 10^8$ (NA)	$7.91 \cdot 10^6$ (NA)	$1.01 \cdot 10^9$ (NA)	$3.49 \cdot 10^7$ (NA)	$3.94 \cdot 10^8$ (NA)	$1.72 \cdot 10^8$ (NA)
GRL	$4.21 \cdot 10^9$ (98.95%)	$1.46 \cdot 10^8$ (100%)	$7.91 \cdot 10^6$ (100%)	$1.02 \cdot 10^9$ (100%)	$3.49 \cdot 10^7$ (100%)	$3.94 \cdot 10^8$ (100%)	$1.72 \cdot 10^8$ (100%)
Good Calo	$4.21 \cdot 10^9$ (99.96%)	$1.46 \cdot 10^8$ (100%)	$7.91 \cdot 10^6$ (100%)	$1.02 \cdot 10^9$ (100%)	$3.49 \cdot 10^7$ (100%)	$3.94 \cdot 10^8$ (100%)	$1.72 \cdot 10^8$ (100%)
PriVtx	$4.21 \cdot 10^9$ (100%)	$1.46 \cdot 10^8$ (100%)	$7.91 \cdot 10^6$ (100%)	$1.02 \cdot 10^9$ (100%)	$3.49 \cdot 10^7$ (100%)	$3.94 \cdot 10^8$ (100%)	$1.72 \cdot 10^8$ (100%)
Reco Level	$4.21 \cdot 10^9$ (100%)	$1.46 \cdot 10^8$ (100%)	$7.91 \cdot 10^6$ (100%)	$1.02 \cdot 10^9$ (100%)	$3.49 \cdot 10^7$ (100%)	$3.94 \cdot 10^8$ (100%)	$1.72 \cdot 10^8$ (100%)
Trigger	$1.52 \cdot 10^9$ (36.06%)	$5.86 \cdot 10^7$ (40.15%)	$1.42 \cdot 10^6$ (17.95%)	$6.09 \cdot 10^8$ (59.99%)	$8.16 \cdot 10^6$ (23.35%)	$1.32 \cdot 10^8$ (33.57%)	$6.65 \cdot 10^7$ (38.67%)
MU_N 20 == 1	$1.06 \cdot 10^9$ (69.88%)	$5.51 \cdot 10^7$ (93.97%)	$9.96 \cdot 10^5$ (70.2%)	$2.24 \cdot 10^8$ (36.8%)	$5.06 \cdot 10^6$ (62.03%)	$1.18 \cdot 10^8$ (89.18%)	$4.39 \cdot 10^7$ (66.08%)
EL_N 20 == 0	$1.06 \cdot 10^9$ (99.88%)	$5.51 \cdot 10^7$ (99.99%)	$9.96 \cdot 10^5$ (99.96%)	$2.24 \cdot 10^8$ (99.92%)	$4.67 \cdot 10^6$ (92.34%)	$1.10 \cdot 10^8$ (93.37%)	$3.73 \cdot 10^7$ (84.84%)
MU_N 30 == 1	$8.24 \cdot 10^8$ (77.7%)	$4.72 \cdot 10^7$ (85.77%)	$6.73 \cdot 10^5$ (67.54%)	$1.79 \cdot 10^8$ (80.04%)	$3.71 \cdot 10^6$ (79.51%)	$9.87 \cdot 10^7$ (89.73%)	$3.25 \cdot 10^7$ (87.11%)
MU_N 65 == 1	$5.57 \cdot 10^7$ (6.764%)	$9.61 \cdot 10^6$ (20.33%)	$2.17 \cdot 10^5$ (32.21%)	$1.82 \cdot 10^7$ (10.17%)	$2.04 \cdot 10^6$ (54.84%)	$3.44 \cdot 10^7$ (34.86%)	$1.02 \cdot 10^7$ (31.37%)
MU_N Tight 65 == 1	$5.57 \cdot 10^7$ (100%)	$9.61 \cdot 10^6$ (100%)	$2.17 \cdot 10^5$ (100%)	$1.82 \cdot 10^7$ (100%)	$2.04 \cdot 10^6$ (100%)	$3.44 \cdot 10^7$ (100%)	$1.02 \cdot 10^7$ (100%)
Trigger match	$5.57 \cdot 10^7$ (99.88%)	$9.61 \cdot 10^6$ (100%)	$2.17 \cdot 10^5$ (99.99%)	$1.81 \cdot 10^7$ (99.09%)	$2.00 \cdot 10^6$ (98.28%)	$3.43 \cdot 10^7$ (99.78%)	$1.02 \cdot 10^7$ (99.7%)
JetCleaning: Loose Bad	$5.49 \cdot 10^7$ (98.61%)	$9.57 \cdot 10^6$ (99.61%)	$2.16 \cdot 10^5$ (99.61%)	$1.79 \cdot 10^7$ (99.33%)	$1.99 \cdot 10^6$ (99.41%)	$3.42 \cdot 10^7$ (99.51%)	$1.01 \cdot 10^7$ (99.45%)
NOBADMUON	$5.49 \cdot 10^7$ (99.99%)	$9.54 \cdot 10^6$ (99.72%)	$2.15 \cdot 10^5$ (99.68%)	$1.79 \cdot 10^7$ (99.95%)	$1.98 \cdot 10^6$ (99.63%)	$3.42 \cdot 10^7$ (100%)	$1.01 \cdot 10^7$ (99.99%)
Save	$5.49 \cdot 10^7$ (100%)	$9.54 \cdot 10^6$ (100%)	$2.15 \cdot 10^5$ (100%)	$1.79 \cdot 10^7$ (100%)	$1.98 \cdot 10^6$ (100%)	$3.42 \cdot 10^7$ (100%)	$1.01 \cdot 10^7$ (100%)
Lepton Veto	$3.36 \cdot 10^7$ (61.23%)	$7.87 \cdot 10^6$ (82.47%)	$1.77 \cdot 10^5$ (82.24%)	$1.42 \cdot 10^7$ (79.39%)	$1.62 \cdot 10^6$ (81.89%)	$2.81 \cdot 10^7$ (82.2%)	$8.36 \cdot 10^6$ (82.71%)
Charge Selection	$1.68 \cdot 10^7$ (50%)	$7.87 \cdot 10^6$ (100%)	$1.77 \cdot 10^5$ (99.97%)	$7.12 \cdot 10^6$ (50%)	$8.12 \cdot 10^5$ (50%)	$1.40 \cdot 10^7$ (50%)	$4.18 \cdot 10^6$ (50%)
$\lvert\eta\rvert^{\mu} < 2.4$	$1.68 \cdot 10^7$ (100%)	$7.87 \cdot 10^6$ (100%)	$1.77 \cdot 10^5$ (100%)	$7.12 \cdot 10^6$ (100%)	$8.12 \cdot 10^5$ (100%)	$1.40 \cdot 10^7$ (100%)	$4.18 \cdot 10^6$ (100%)
$p_T^{\mu} > 65$ GeV	$1.68 \cdot 10^7$ (100%)	$7.87 \cdot 10^6$ (100%)	$1.77 \cdot 10^5$ (100%)	$7.12 \cdot 10^6$ (100%)	$8.12 \cdot 10^5$ (100%)	$1.40 \cdot 10^7$ (100%)	$4.18 \cdot 10^6$ (100%)
$E_T^{miss} > 85$ GeV	$1.33 \cdot 10^6$ (7.897%)	$3.91 \cdot 10^6$ (49.7%)	$1.47 \cdot 10^5$ (83.19%)	$1.21 \cdot 10^6$ (16.97%)	$5.95 \cdot 10^5$ (73.33%)	$3.33 \cdot 10^6$ (23.69%)	$1.12 \cdot 10^6$ (26.73%)
$m_T > 200$ GeV	$1.85 \cdot 10^5$ (13.96%)	$2.83 \cdot 10^6$ (72.24%)	$1.33 \cdot 10^5$ (90.39%)	$9.40 \cdot 10^5$ (77.81%)	$2.48 \cdot 10^5$ (41.59%)	$3.89 \cdot 10^5$ (11.68%)	$3.48 \cdot 10^5$ (31.19%)
Total Efficiency	0.0043%	1.9%	1.7%	0.093%	0.71%	0.099%	0.2%
ProcessMC/TotalMC	NA	57.86%	2.723%	19.25%	5.072%	7.959%	7.135%
Data/TotalMC	3.795%						

Table E.9.: Cutflow table for 2018 data for the $W^{\pm}$ selection showing the effect each selection has on the number of events. The first column lists the name of the selection. The rest of the columns show the number of events for each sample and for each selection. The relative efficiency is shown as a percentage next to each number of events. The relative efficiency is calculated as the number of events after the current cut divided by the number of events in the previous cuts. The three rows at the bottom of the table show the total efficiency, ProcessMC/TotalMC and Data/TotalMC. The total efficiency is calculated by taking the number of events after all cuts have been applied divided by the number of events before any cut. The ProcessMC/TotalMC row shows the number of events in each Monte Carlo sample divided by the total sum of events of the Monte Carlo samples after all the selection cuts. The Data/TotalMC row is the total number of data events divided by the sum of the total number of Monte Carlo events after all the selection cuts. All Monte Carlo samples are normalised to the luminosity of the data and include the pileup and generator weights.

E.4. Run-2 Combined Charge Plots

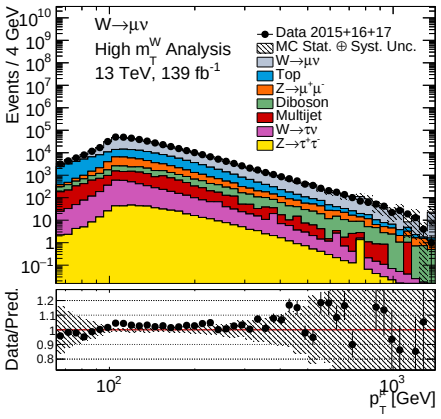

a

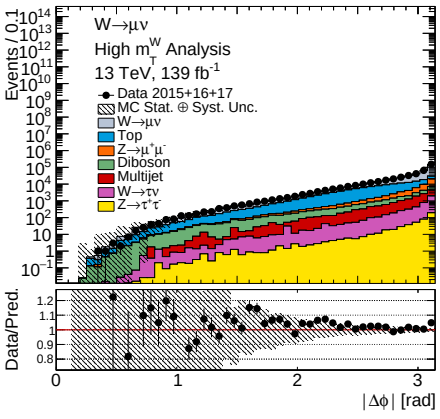

b

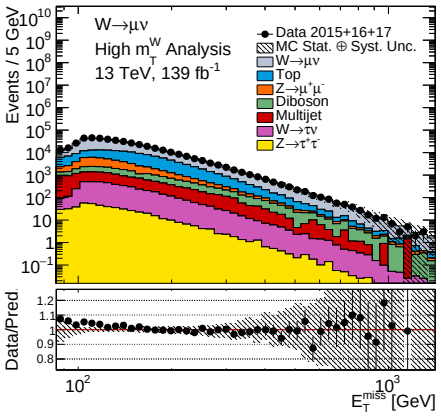

c

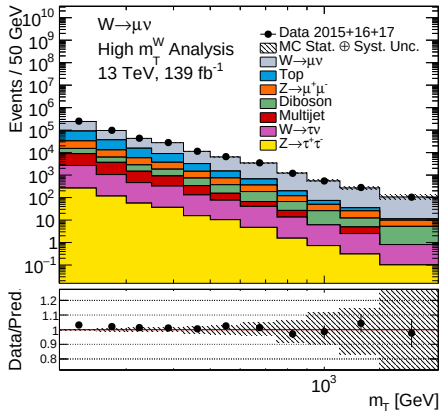

d

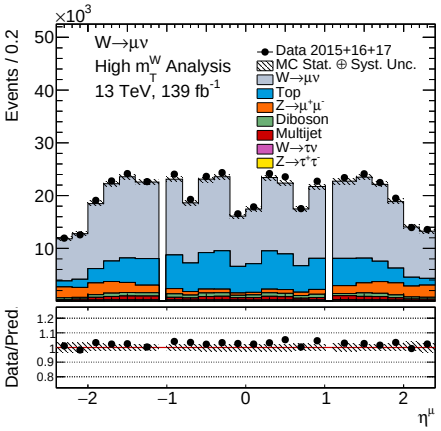

e

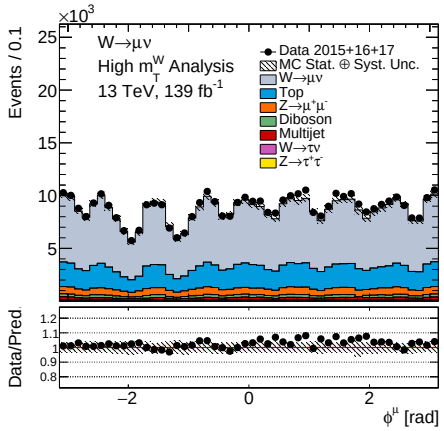

f

Figure E.22.: Control distributions for Run-2 for $W^{\pm} \to \mu\nu$ for p_T^{μ}, $|\Delta\phi|$, E_T^{miss}, m_T, η^{μ} and ϕ^{μ}. The data contribution is shown with black points, the signal and the background contributions with solid lines. In the shaded band, systematic experimental uncertainties have been combined with the MC statistical uncertainties. The data statistical uncertainties are shown on the data points. Luminosity uncertainties have not been included.

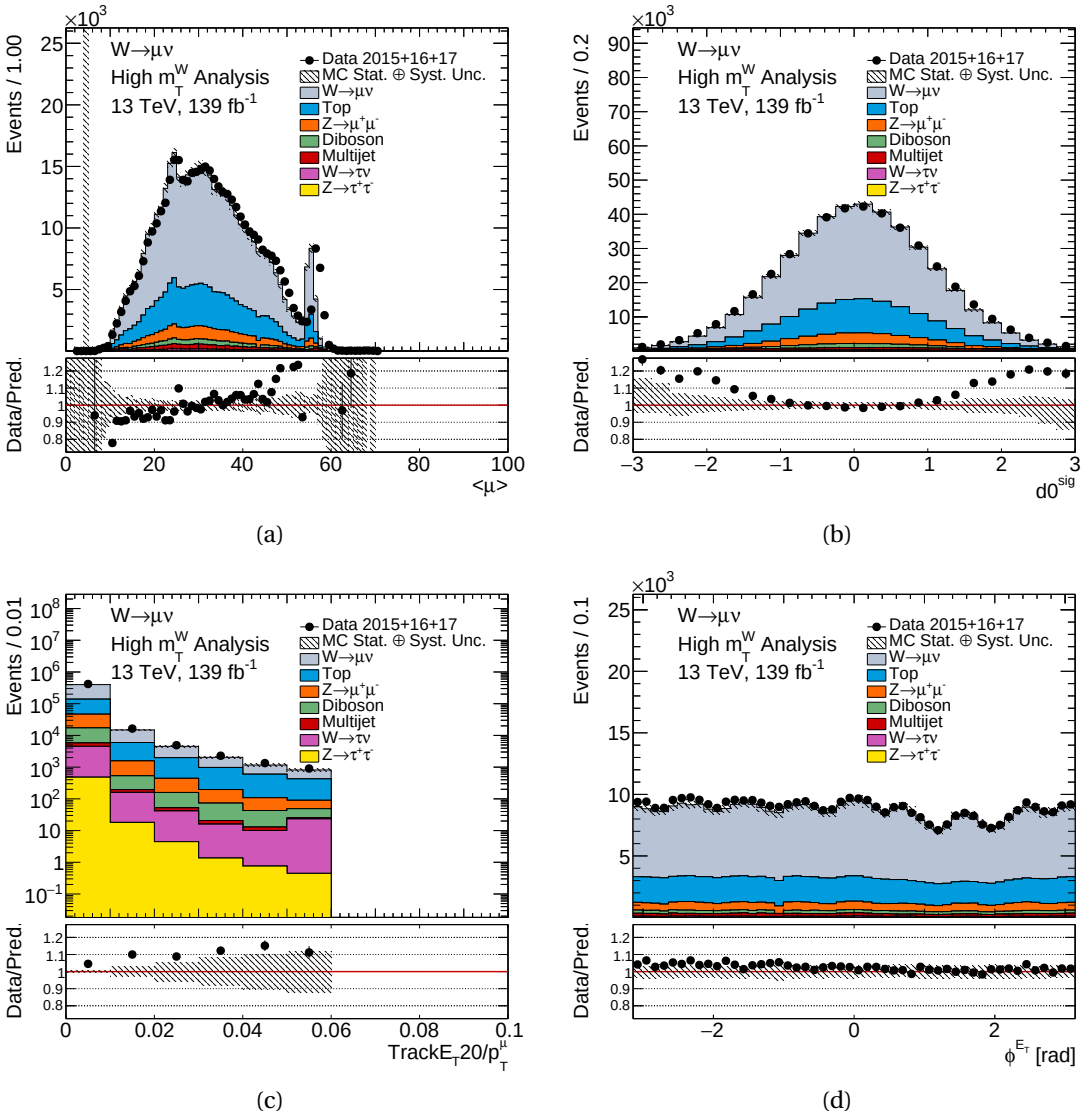

Figure E.23.: Control distributions for $W^{\pm} \to \mu\nu$ for $< \mu >$, $d0^{sig}$, $TrackE_T20/p_T^{\mu}$ and $\phi^{E_T^{miss}}$. The data contribution is shown with black points, the signal and the background contributions with solid lines. In the shaded band, systematic experimental uncertainties have been combined with the MC statistical uncertainties. The data statistical uncertainties are shown on the data points. Luminosity uncertainties have not been included.

	Data	$W^{\pm} \to \mu\nu$	$W^{\pm} \to \tau\nu$	$Z \to \mu\mu$	$Z \to \tau\tau$	Top	Diboson
Initial	$1.11 \cdot 10^{10}$ (NA)	$3.42 \cdot 10^{8}$ (NA)	$6.68 \cdot 10^{7}$ (NA)	$2.44 \cdot 10^{9}$ (NA)	$7.92 \cdot 10^{7}$ (NA)	$9.18 \cdot 10^{8}$ (NA)	$5.54 \cdot 10^{8}$ (NA)
GRL	$1.09 \cdot 10^{10}$ (97.96%)	$3.42 \cdot 10^{8}$ (100%)	$6.68 \cdot 10^{7}$ (100%)	$2.44 \cdot 10^{9}$ (100%)	$7.92 \cdot 10^{7}$ (100%)	$9.18 \cdot 10^{8}$ (100%)	$5.54 \cdot 10^{8}$ (100%)
Good Calo	$1.09 \cdot 10^{10}$ (99.93%)	$3.42 \cdot 10^{8}$ (100%)	$6.68 \cdot 10^{7}$ (100%)	$2.44 \cdot 10^{9}$ (100%)	$7.92 \cdot 10^{7}$ (100%)	$9.18 \cdot 10^{8}$ (100%)	$5.54 \cdot 10^{8}$ (100%)
PriVtx	$1.09 \cdot 10^{10}$ (100%)	$3.42 \cdot 10^{8}$ (100%)	$6.68 \cdot 10^{7}$ (100%)	$2.44 \cdot 10^{9}$ (100%)	$7.92 \cdot 10^{7}$ (100%)	$9.18 \cdot 10^{8}$ (100%)	$5.54 \cdot 10^{8}$ (100%)
Reco Level	$1.09 \cdot 10^{10}$ (100%)	$3.42 \cdot 10^{8}$ (100%)	$6.68 \cdot 10^{7}$ (100%)	$2.44 \cdot 10^{9}$ (100%)	$7.92 \cdot 10^{7}$ (100%)	$9.18 \cdot 10^{8}$ (100%)	$5.54 \cdot 10^{8}$ (100%)
Trigger	$3.66 \cdot 10^{9}$ (33.59%)	$1.36 \cdot 10^{8}$ (39.79%)	$3.24 \cdot 10^{6}$ (4.852%)	$1.46 \cdot 10^{9}$ (59.68%)	$1.84 \cdot 10^{7}$ (23.21%)	$3.07 \cdot 10^{8}$ (33.39%)	$2.11 \cdot 10^{8}$ (38.11%)
MU_N 20 == 1	$2.59 \cdot 10^{9}$ (70.73%)	$1.28 \cdot 10^{8}$ (94.1%)	$2.29 \cdot 10^{6}$ (70.64%)	$5.36 \cdot 10^{8}$ (36.83%)	$1.15 \cdot 10^{7}$ (62.36%)	$2.74 \cdot 10^{8}$ (89.27%)	$1.40 \cdot 10^{8}$ (66.55%)
EL_N 20 == 0	$2.58 \cdot 10^{9}$ (99.88%)	$1.28 \cdot 10^{8}$ (99.99%)	$2.29 \cdot 10^{6}$ (99.96%)	$5.35 \cdot 10^{8}$ (99.92%)	$1.06 \cdot 10^{7}$ (92.49%)	$2.56 \cdot 10^{8}$ (93.36%)	$1.22 \cdot 10^{8}$ (86.62%)
MU_N 30 == 1	$1.98 \cdot 10^{9}$ (76.57%)	$1.10 \cdot 10^{8}$ (85.55%)	$1.51 \cdot 10^{6}$ (66.19%)	$4.27 \cdot 10^{8}$ (79.76%)	$8.33 \cdot 10^{6}$ (78.6%)	$2.29 \cdot 10^{8}$ (89.63%)	$1.06 \cdot 10^{8}$ (87.2%)
MU_N 65 == 1	$1.35 \cdot 10^{8}$ (6.815%)	$2.18 \cdot 10^{7}$ (19.92%)	$4.64 \cdot 10^{5}$ (30.66%)	$4.25 \cdot 10^{7}$ (9.955%)	$4.49 \cdot 10^{6}$ (53.87%)	$8 \cdot 10^{7}$ (34.93%)	$3.31 \cdot 10^{7}$ (31.23%)
MU_N Tight 65 == 1	$1.35 \cdot 10^{8}$ (100%)	$2.18 \cdot 10^{7}$ (100%)	$4.64 \cdot 10^{5}$ (100%)	$4.25 \cdot 10^{7}$ (100%)	$4.49 \cdot 10^{6}$ (100%)	$8 \cdot 10^{7}$ (100%)	$3.31 \cdot 10^{7}$ (100%)
Trigger match	$1.35 \cdot 10^{8}$ (99.89%)	$2.18 \cdot 10^{7}$ (100%)	$4.64 \cdot 10^{5}$ (99.99%)	$4.21 \cdot 10^{7}$ (99.1%)	$4.41 \cdot 10^{6}$ (98.25%)	$7.98 \cdot 10^{7}$ (99.78%)	$3.30 \cdot 10^{7}$ (99.72%)
JetCleaning: Loose Bad	$1.33 \cdot 10^{8}$ (98.8%)	$2.18 \cdot 10^{7}$ (99.64%)	$4.62 \cdot 10^{5}$ (99.65%)	$4.19 \cdot 10^{7}$ (99.38%)	$4.39 \cdot 10^{6}$ (99.46%)	$7.95 \cdot 10^{7}$ (99.54%)	$3.29 \cdot 10^{7}$ (99.47%)
NOBADMUON	$1.33 \cdot 10^{8}$ (99.99%)	$2.17 \cdot 10^{7}$ (99.75%)	$4.61 \cdot 10^{5}$ (99.71%)	$4.19 \cdot 10^{7}$ (99.96%)	$4.37 \cdot 10^{6}$ (99.65%)	$7.95 \cdot 10^{7}$ (100%)	$3.29 \cdot 10^{7}$ (99.99%)
Save	$1.33 \cdot 10^{8}$ (100%)	$2.17 \cdot 10^{7}$ (100%)	$4.61 \cdot 10^{5}$ (100%)	$4.19 \cdot 10^{7}$ (100%)	$4.37 \cdot 10^{6}$ (100%)	$7.95 \cdot 10^{7}$ (100%)	$3.29 \cdot 10^{7}$ (100%)
Lepton Veto	$8.11 \cdot 10^{7}$ (61.03%)	$1.79 \cdot 10^{7}$ (82.52%)	$3.79 \cdot 10^{5}$ (82.26%)	$3.32 \cdot 10^{7}$ (79.32%)	$3.58 \cdot 10^{6}$ (81.92%)	$6.54 \cdot 10^{7}$ (82.25%)	$2.72 \cdot 10^{7}$ (82.81%)
Charge Selection	$4.06 \cdot 10^{7}$ (50%)	$1.79 \cdot 10^{7}$ (100%)	$3.79 \cdot 10^{5}$ (99.98%)	$1.66 \cdot 10^{7}$ (50%)	$1.79 \cdot 10^{6}$ (50%)	$3.27 \cdot 10^{7}$ (50%)	$1.36 \cdot 10^{7}$ (50%)
$\lvert\eta\rvert^{\mu} < 2.4$	$4.06 \cdot 10^{7}$ (100%)	$1.79 \cdot 10^{7}$ (100%)	$3.79 \cdot 10^{5}$ (100%)	$1.66 \cdot 10^{7}$ (100%)	$1.79 \cdot 10^{6}$ (100%)	$3.27 \cdot 10^{7}$ (100%)	$1.36 \cdot 10^{7}$ (100%)
$p_T^{\mu} > 65$ GeV	$4.06 \cdot 10^{7}$ (100%)	$1.79 \cdot 10^{7}$ (100%)	$3.79 \cdot 10^{5}$ (100%)	$1.66 \cdot 10^{7}$ (100%)	$1.79 \cdot 10^{6}$ (100%)	$3.27 \cdot 10^{7}$ (100%)	$1.36 \cdot 10^{7}$ (100%)
$E_T^{miss} > 85$ GeV	$3.18 \cdot 10^{6}$ (7.838%)	$8.68 \cdot 10^{6}$ (48.44%)	$3.12 \cdot 10^{5}$ (82.38%)	$2.53 \cdot 10^{6}$ (15.21%)	$1.31 \cdot 10^{6}$ (72.94%)	$7.65 \cdot 10^{6}$ (23.39%)	$3.29 \cdot 10^{6}$ (24.16%)
$m_T > 200$ GeV	$4.44 \cdot 10^{5}$ (13.96%)	$6.19 \cdot 10^{6}$ (71.34%)	$2.81 \cdot 10^{5}$ (90.02%)	$1.95 \cdot 10^{6}$ (77.32%)	$5.44 \cdot 10^{5}$ (41.64%)	$8.96 \cdot 10^{5}$ (11.72%)	$9.78 \cdot 10^{5}$ (29.76%)
Total Efficiency	0.004%	1.8%	0.42%	0.08%	0.69%	0.098%	0.18%
ProcessMC/TotalMC	NA	57.1%	2.594%	18.01%	5.016%	8.265%	9.021%
Data/TotalMC	4.095%						

Table E.10.: Cutflow table for Run-2 data for the $W^{\pm}$ selection showing the effect each selection has on the number of events. The first column lists the name of the selection. The rest of the columns show the number of events for each sample and for each selection. The relative efficiency is shown as a percentage next to each number of events. The relative efficiency is calculated as the number of events after the current cut divided by the number of events in the previous cuts. The three rows at the bottom of the table show the total efficiency, ProcessMC/TotalMC and Data/TotalMC. The total efficiency is calculated by taking the number of events after all cuts have been applied divided by the number of events before any cut. The ProcessMC/TotalMC row shows the number of events in each Monte Carlo sample divided by the total sum of events of the Monte Carlo samples after all the selection cuts. The Data/TotalMC row is the total number of data events divided by the sum of the total number of Monte Carlo events after all the selection cuts. All Monte Carlo samples are normalised to the luminosity of the data and include the pileup and generator weights.

E.5. Event Selection Efficiency for Individual MC Campaigns

Figure E.24 illustrates the event selection efficiency as a function of the average μ for the $W \to \mu\nu$ processes for the individual Monte Carlo campaigns (MC16a, MC16d, and MC16e), which contribute to the full Run-2 period. The efficiency is defined as the ratio of simulated events meeting all selection criteria, as detailed in Chapter 6.1, to the total simulated $W \to \mu\nu$ events. This efficiency is calculated charge independently.

The efficiency remains relatively consistent across the statistically significant average μ range for both positive and negative charges. For the negative charge the efficiency is slightly higher than the positive charge. The efficiency is also higher for the MC16e campaign, which is due to the fact that the MC16e campaign had improvements in data-taking and a larger cross-section than the MC16a and MC16d campaigns leading to more statistics especially in the highest average μ region. The lowest efficiency is observed for the MC16d campaign, particularly for the positive charge. The highest efficiency is observed for the MC16e campaign, in the negative charge.

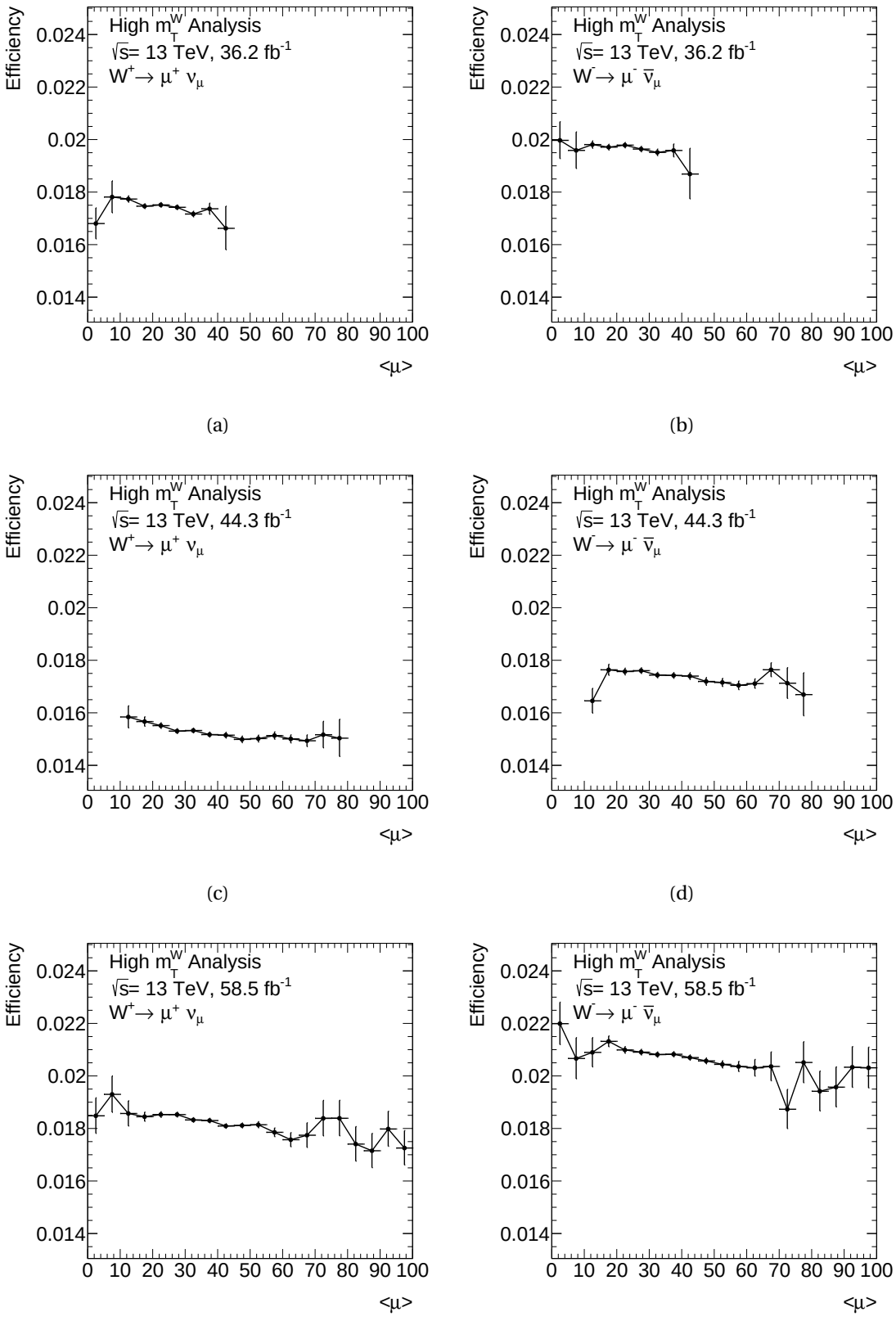

Figure E.24.: Event selection efficiency as a function of the pileup $< \mu >$ for MC16a (36.2^{-1}), MC16d (44.3^{-1}) and MC16e (58.5^{-1}). The efficiency is defined as the number of events passing all event selections divided by the total number of simulated $W^+ \rightarrow \mu^+ \nu_\mu$ (left) and $W^- \rightarrow \mu^- \bar{\nu}_\mu$ (right) events. Errors have been calculated using the Bayesian Error approach implemented in TGraphAsymmErrors [84].

F. Appendix: Results

F.1. Stability, Purity and Acceptance Correction Factors

Following the definitions in Chapter 10 corrections needed to account for differences between the reconstruction and fiducial level selections called the stability, purity and acceptance are calculated. In this section the results from each Monte Carlo campaign have been presented separately for both the positive and negative W boson Drell-Yan processes.

Results for the combination of all Monte Carlo campaigns for the negatively charge W boson have also been included for the stability in Figure F.19, the purity in Figure F.20 and the acceptance in Figure F.21.

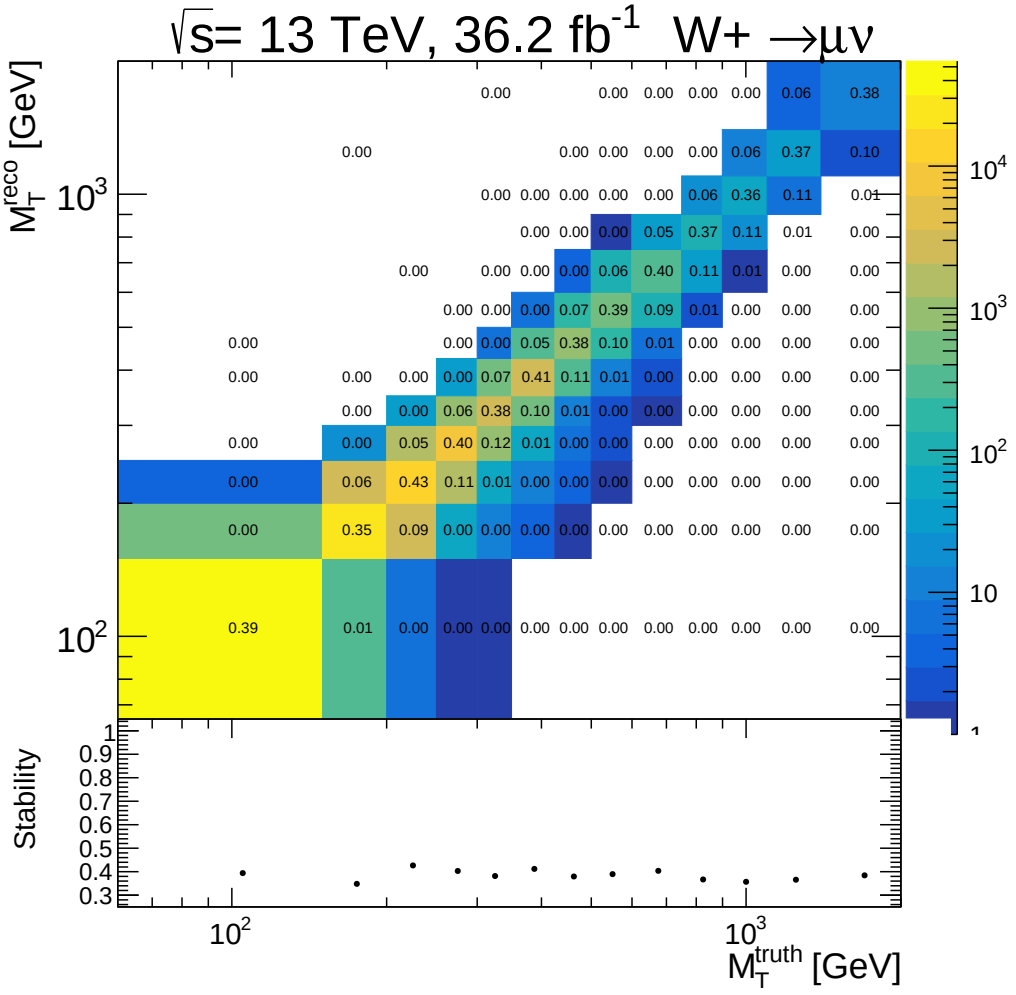

Figure F.1.: Stability for the $W^+ \to \mu^+ \nu$ MC16a signal process. The upper panel shows the m_T^W truth level vs the m_T^W reconstruction level events. The given numbers show the ratio of the number of events in each bin to the total number of truth events in the given mass bin. The diagonal of the upper panel gives the stability in the lower panel.

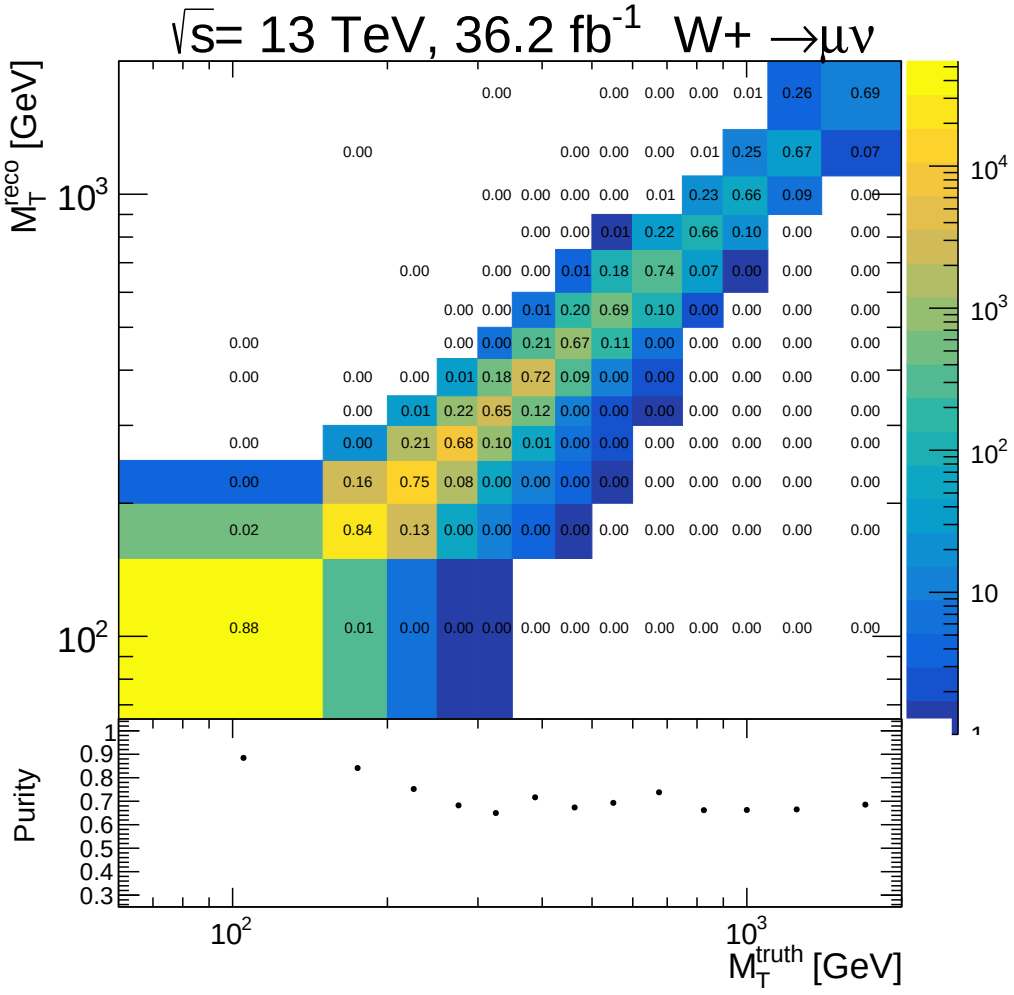

Figure F.2.: Purity for the $W^+ \to \mu^+\nu$ MC16a signal process. The upper panel shows the m_T^W truth level vs the m_T^W reconstruction level events. The given numbers show the ratio of the number of events in each bin to the total number of reconstructed event in the given mass bin. The diagonal of the upper panel gives the purity in the lower panel.

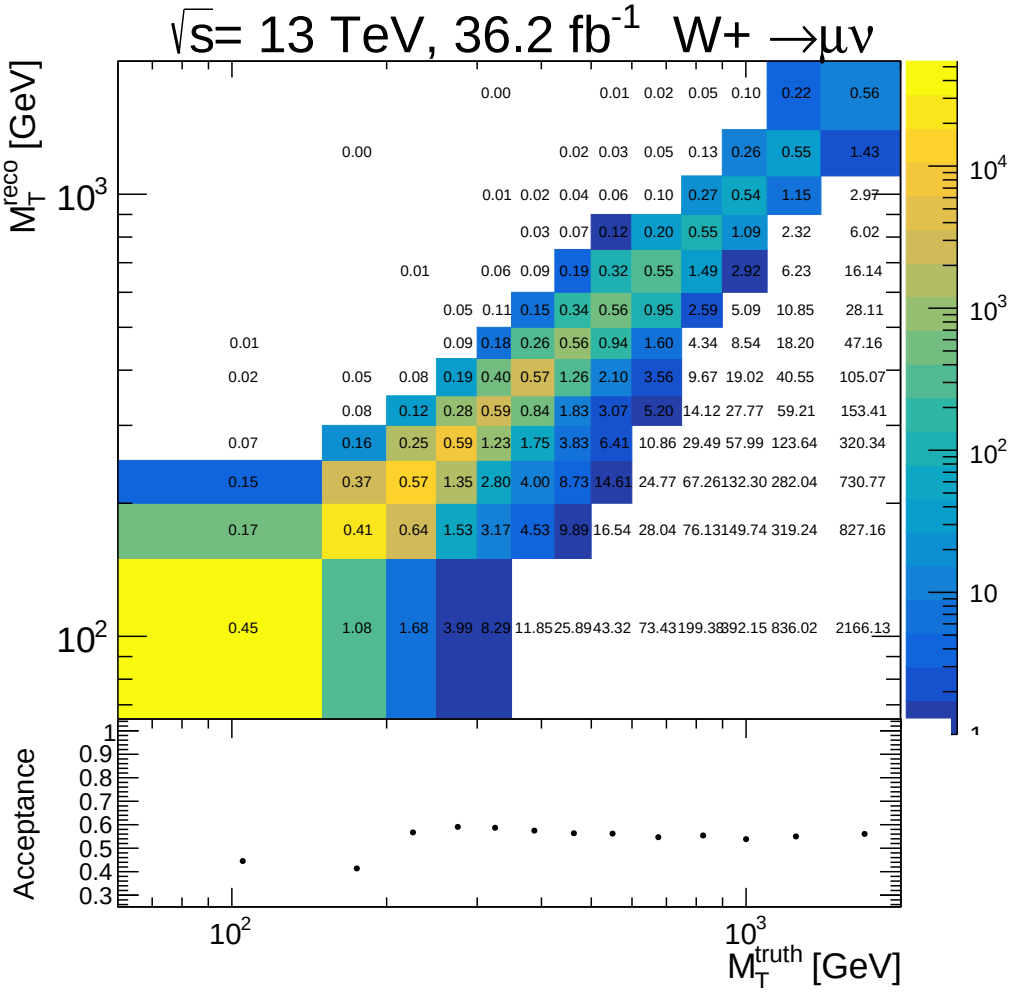

Figure F.3.: Acceptance for the $W^+ \to \mu^+ \nu$ MC16a signal process. The upper panel shows the m_T^W truth level vs the m_T^W reconstruction level events. The given numbers show the ratio of the total number of truth events in each bin to the total number of reconstructed events in each bin. The diagonal of the upper panel gives the acceptance in the lower panel.

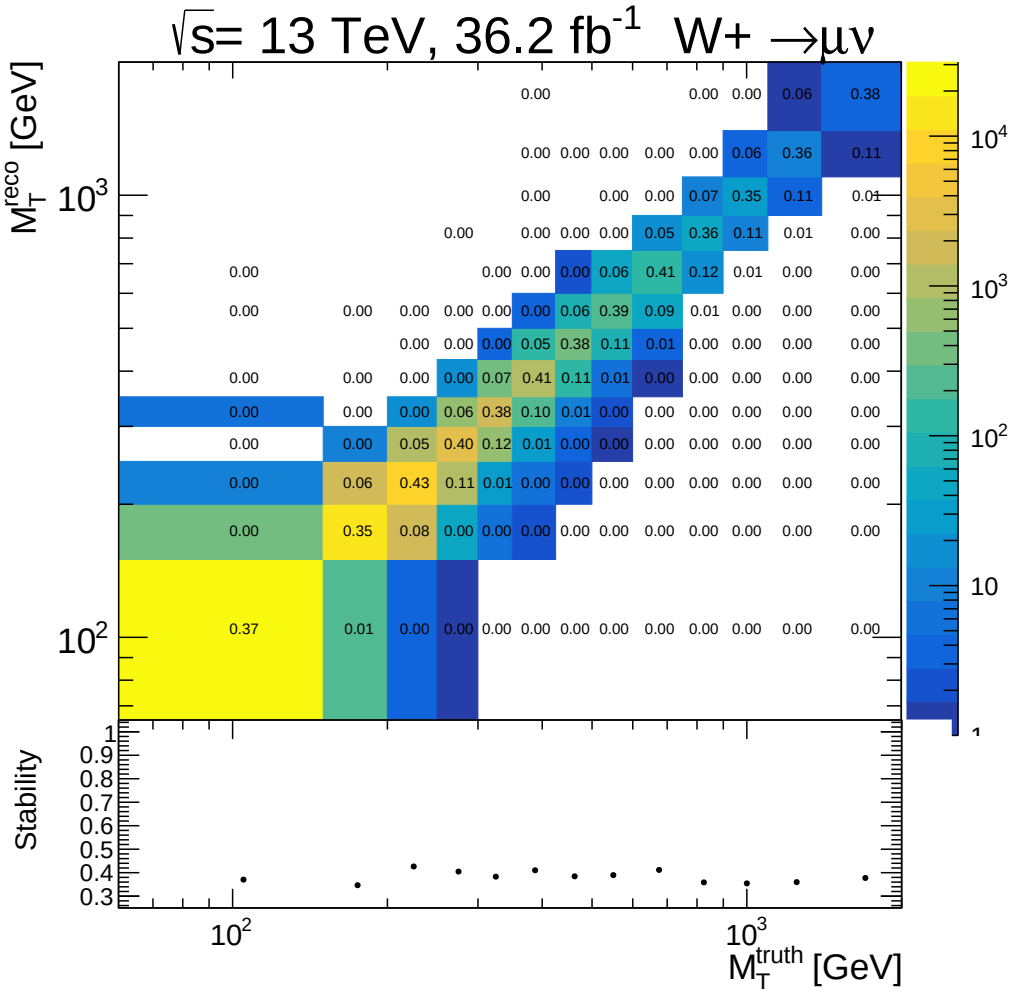

Figure F.4.: Stability for the $W^- \to \mu^- \bar{\nu}$ MC16a signal process. The upper panel shows the m_T^W truth level vs the m_T^W reconstruction level events. The given numbers show the ratio of the number of events in each bin to the total number of truth events in the given mass bin. The diagonal of the upper panel gives the stability in the lower panel.

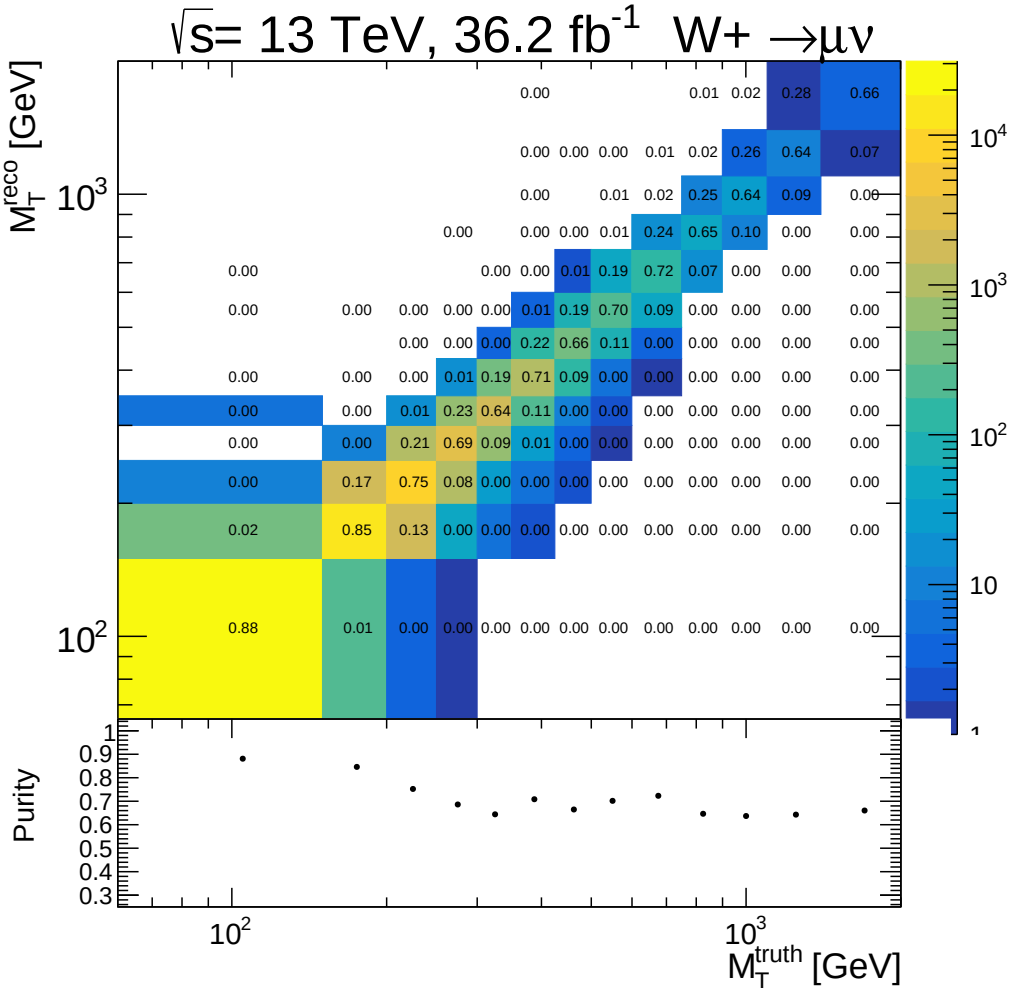

Figure F.5.: Purity for the $W^- \to \mu^- \bar{\nu}$ MC16a signal process. The upper panel shows the m_T^W truth level vs the m_T^W reconstruction level events. The given numbers show the ratio of the number of events in each bin to the total number of reconstructed event in the given mass bin. The diagonal of the upper panel gives the purity in the lower panel.

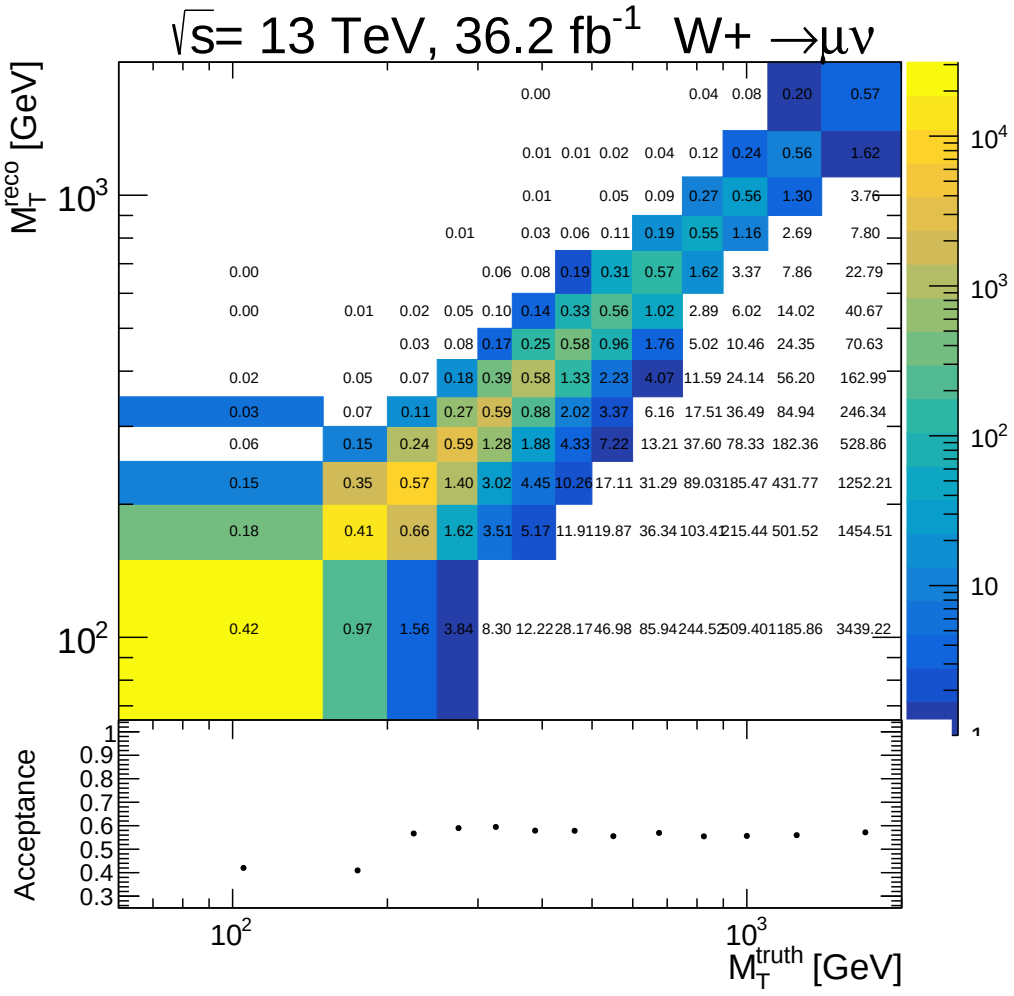

Figure F.6.: Acceptance for the $W^- \to \mu^- \bar{\nu}$ MC16a signal process. The upper panel shows the m_T^W truth level vs the m_T^W reconstruction level events. The given numbers show the ratio of the total number of truth events in each bin to the total number of reconstructed events in each bin. The diagonal of the upper panel gives the acceptance in the lower panel.

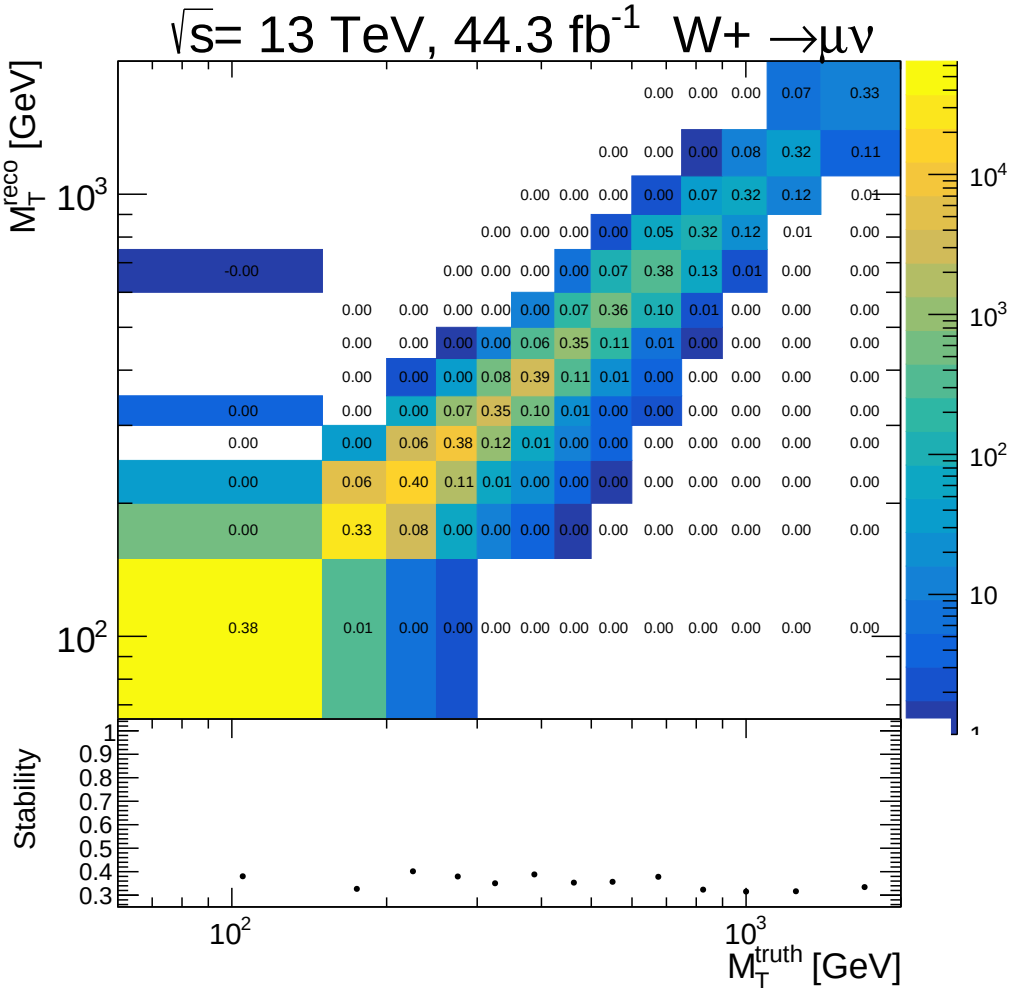

Figure F.7.: Stability for the $W^+ \to \mu^+ \nu$ MC16d signal process. The upper panel shows the m_T^W truth level vs the m_T^W reconstruction level events. The given numbers show the ratio of the number of events in each bin to the total number of truth events in the given mass bin. The diagonal of the upper panel gives the stability in the lower panel.

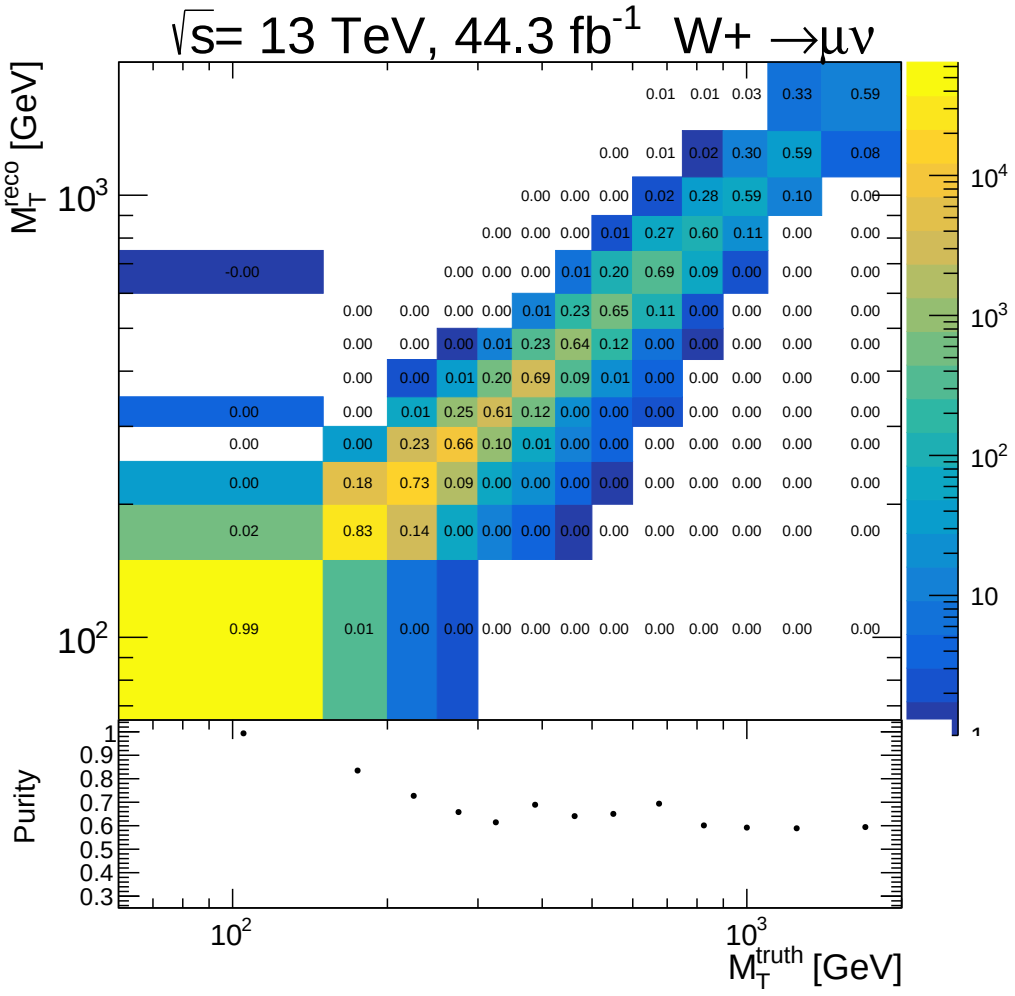

Figure F.8.: Purity for the $W^+ \to \mu^+ \nu$ MC16d signal process. The upper panel shows the m_T^W truth level vs the m_T^W reconstruction level events. The given numbers show the ratio of the number of events in each bin to the total number of reconstructed event in the given mass bin. The diagonal of the upper panel gives the purity in the lower panel.

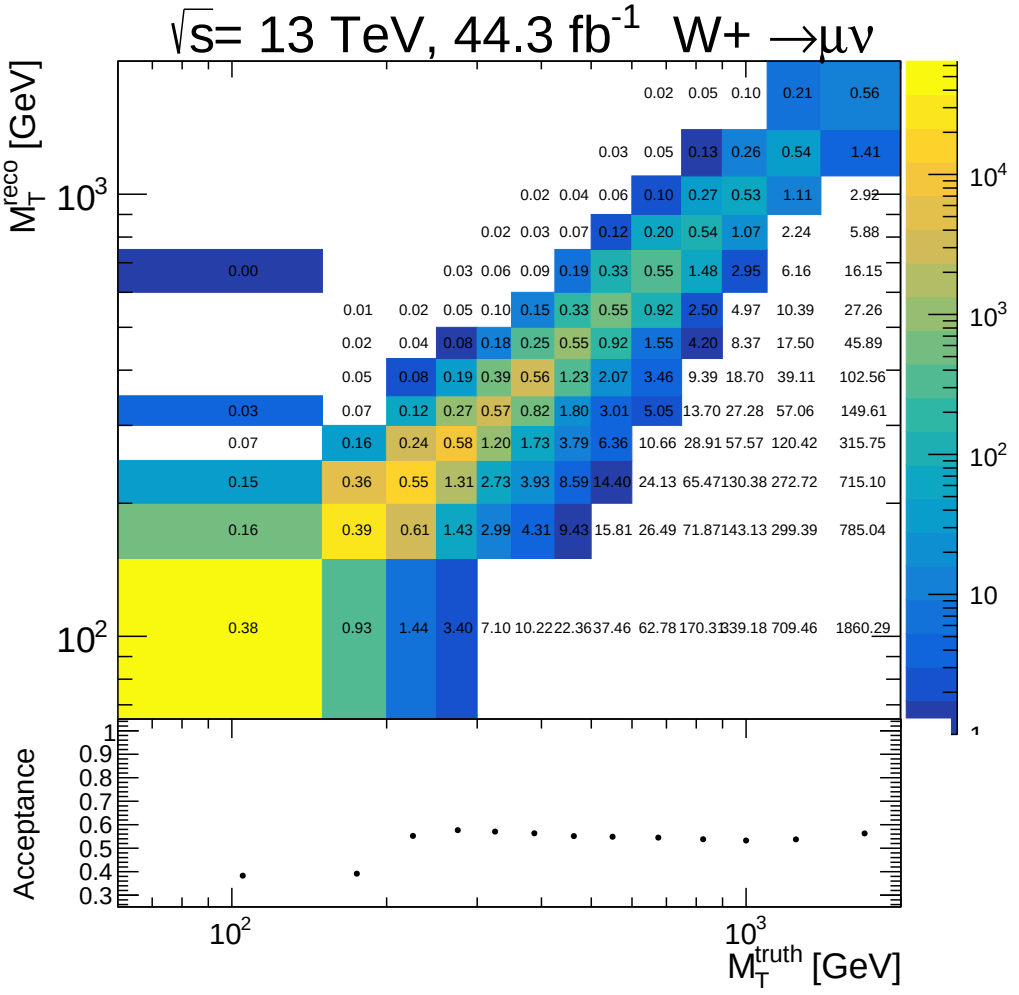

Figure F.9.: Acceptance for the $W^+ \to \mu^+ \nu$ MC16d signal process. The upper panel shows the m_T^W truth level vs the m_T^W reconstruction level events. The given numbers show the ratio of the total number of truth events in each bin to the total number of reconstructed events in each bin. The diagonal of the upper panel gives the acceptance in the lower panel.

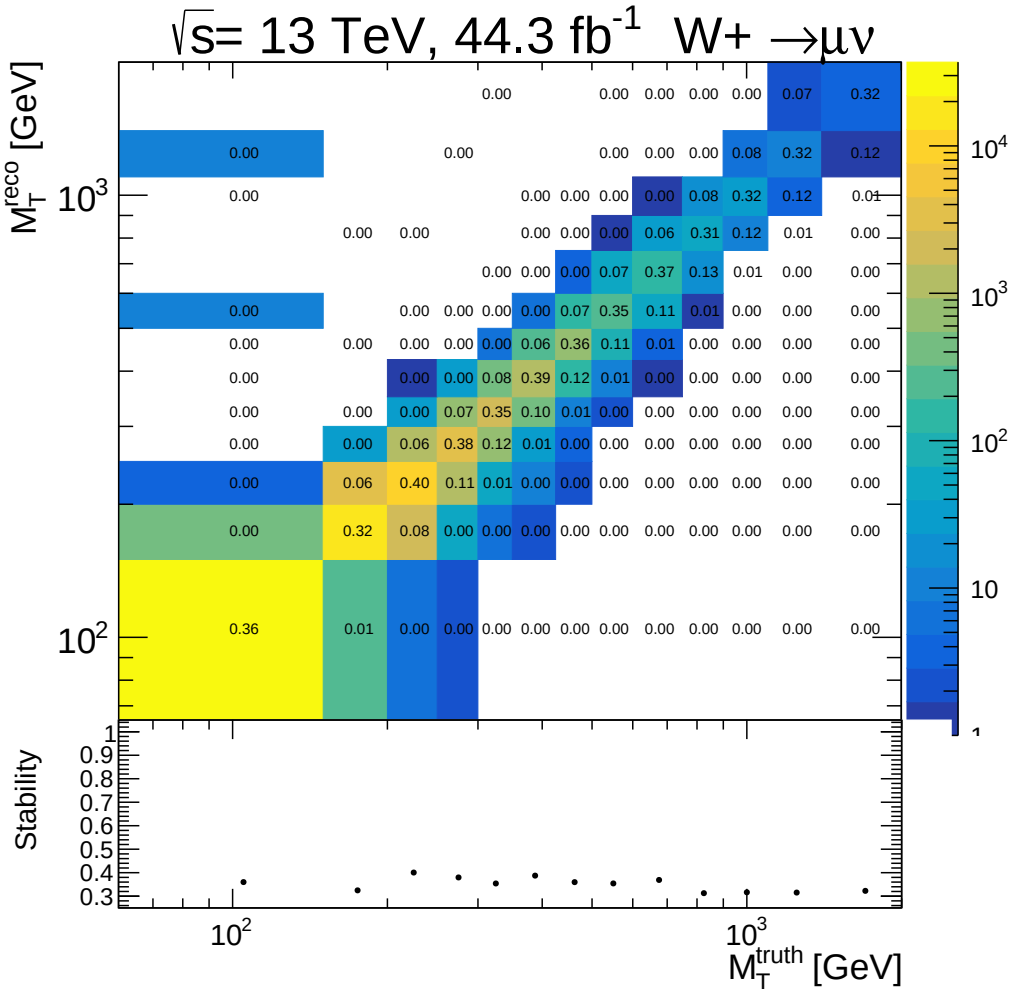

Figure F.10.: Stability for the $W^- \to \mu^- \bar{\nu}$ MC16d signal process. The upper panel shows the m_T^W truth level vs the m_T^W reconstruction level events. The given numbers show the ratio of the number of events in each bin to the total number of truth events in the given mass bin. The diagonal of the upper panel gives the stability in the lower panel.

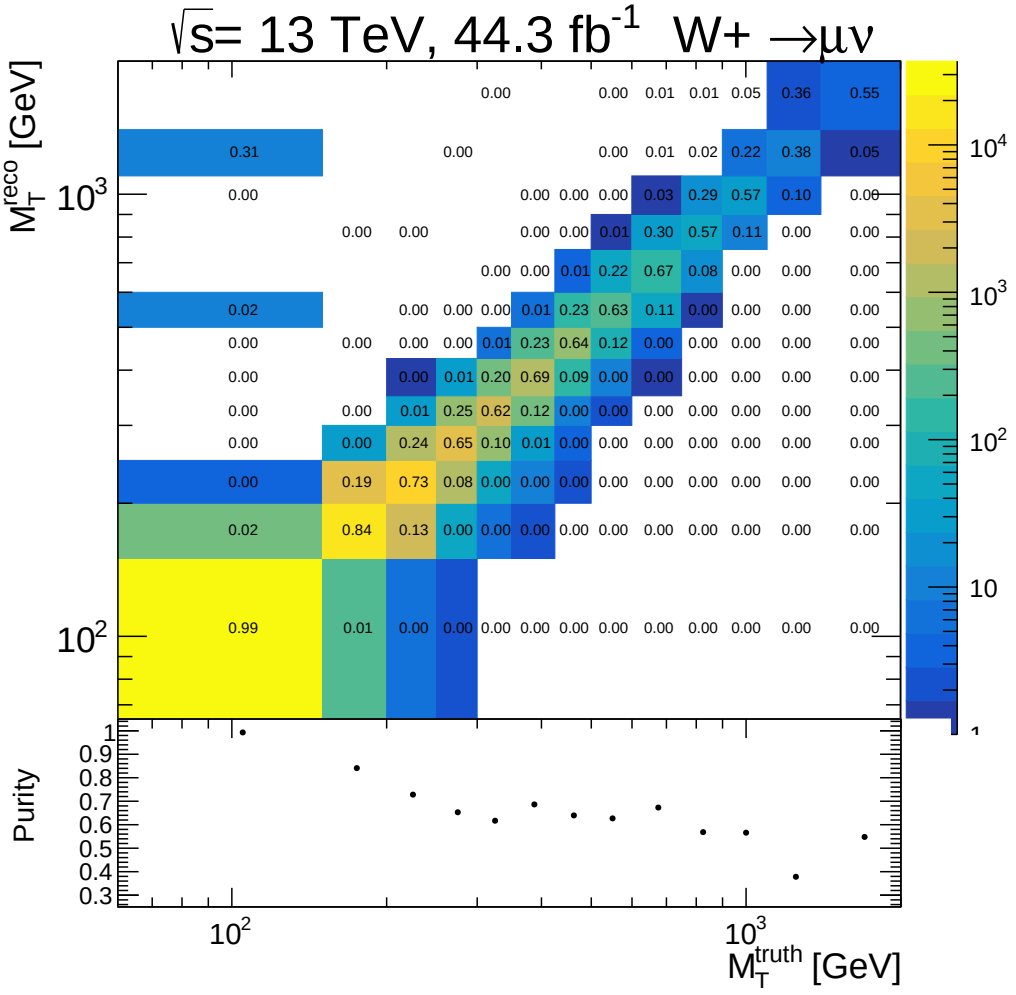

Figure F.11.: Purity for the $W^- \to \mu^- \bar{\nu}$ MC16d signal process. The upper panel shows the m_T^W truth level vs the m_T^W reconstruction level events. The given numbers show the ratio of the number of events in each bin to the total number of reconstructed event in the given mass bin. The diagonal of the upper panel gives the purity in the lower panel.

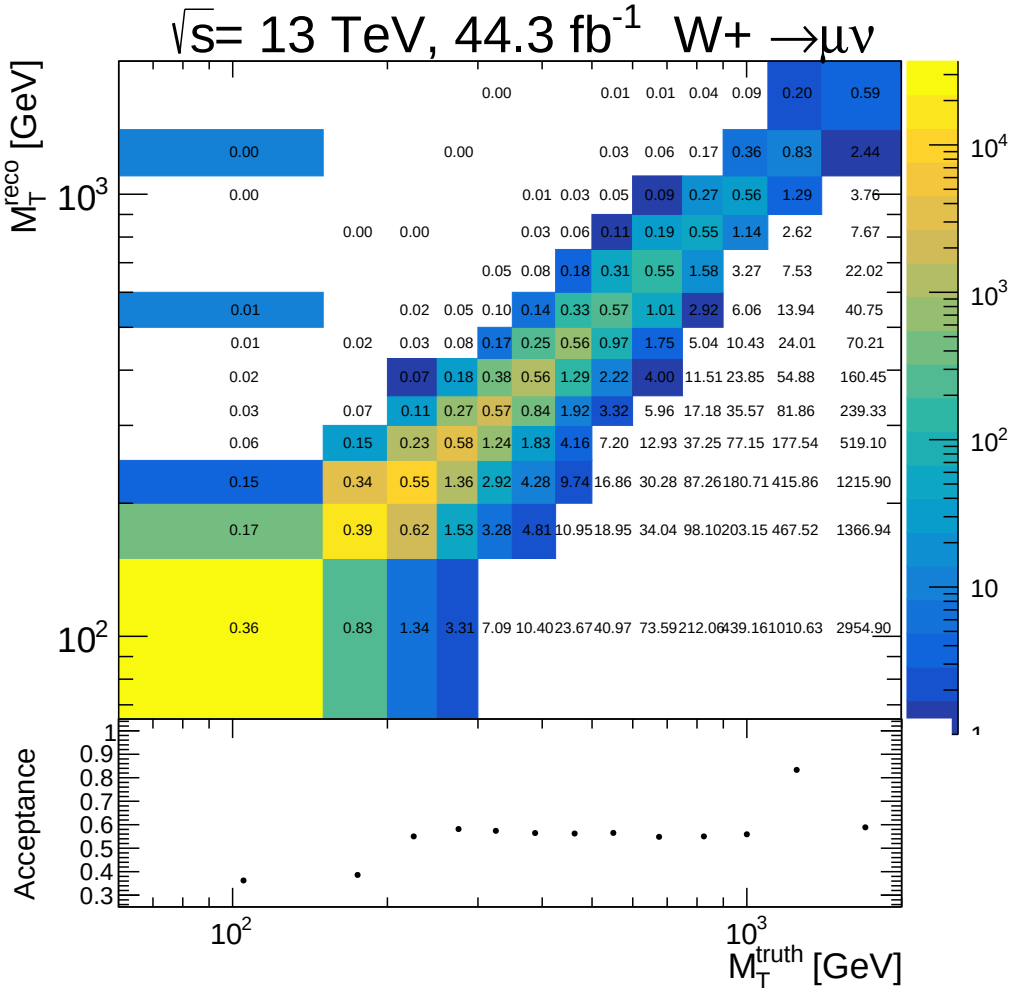

Figure F.12.: Acceptance for the $W^- \to \mu^- \bar{\nu}$ MC16d signal process. The upper panel shows the m_T^W truth level vs the m_T^W reconstruction level events. The given numbers show the ratio of the total number of truth events in each bin to the total number of reconstructed events in each bin. The diagonal of the upper panel gives the acceptance in the lower panel.

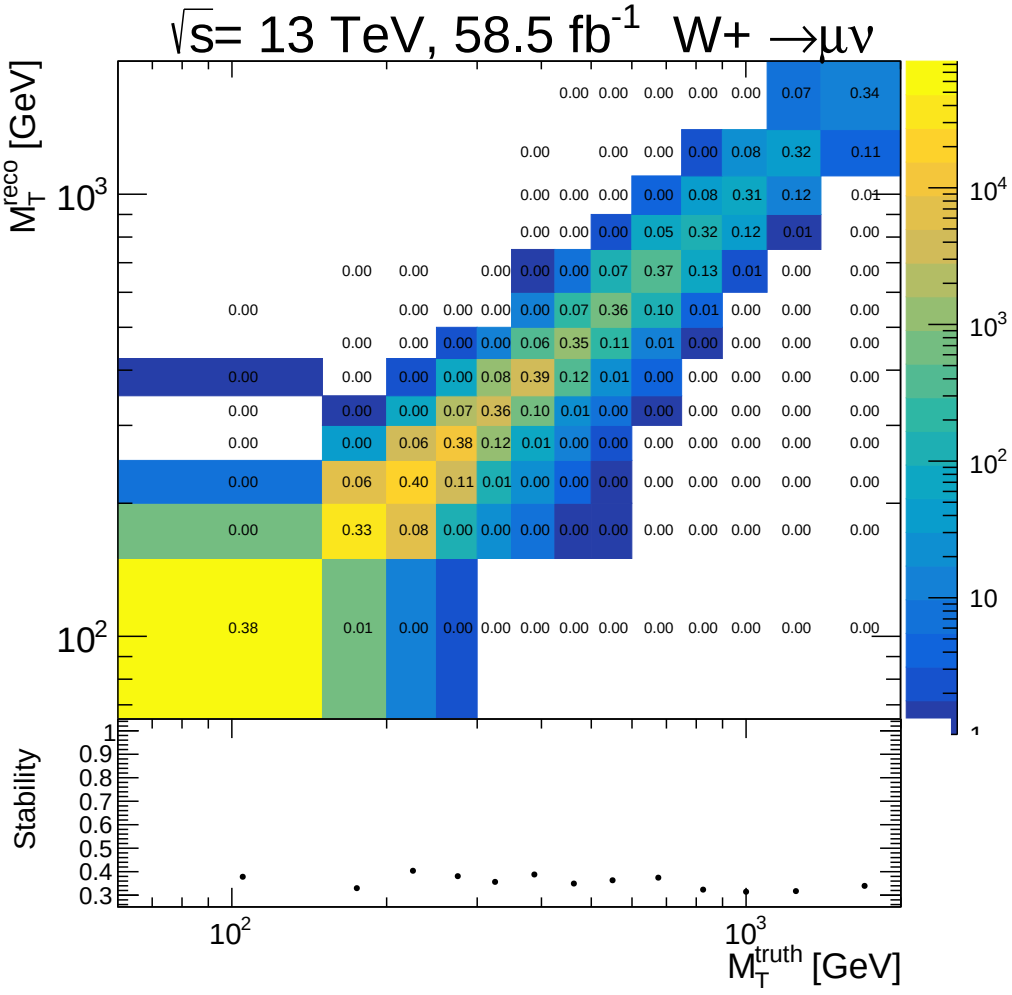

Figure F.13.: Stability for the $W^+ \to \mu^+\nu$ MC16e signal process. The upper panel shows the m_T^W truth level vs the m_T^W reconstruction level events. The given numbers show the ratio of the number of events in each bin to the total number of truth events in the given mass bin. The diagonal of the upper panel gives the stability in the lower panel.

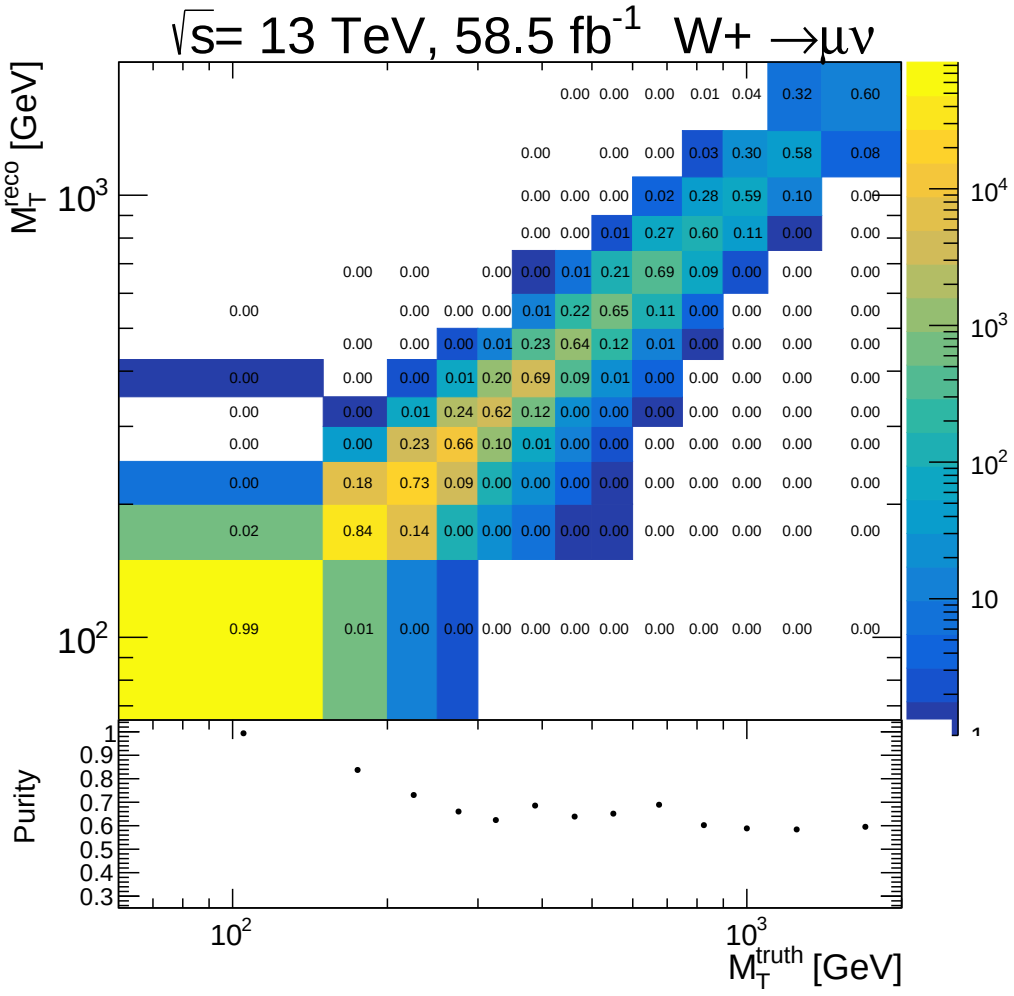

Figure F.14.: Purity for the $W^+ \to \mu^+\nu$ MC16e signal process. The upper panel shows the m_T^W truth level vs the m_T^W reconstruction level events. The given numbers show the ratio of the number of events in each bin to the total number of reconstructed event in the given mass bin. The diagonal of the upper panel gives the purity in the lower panel.

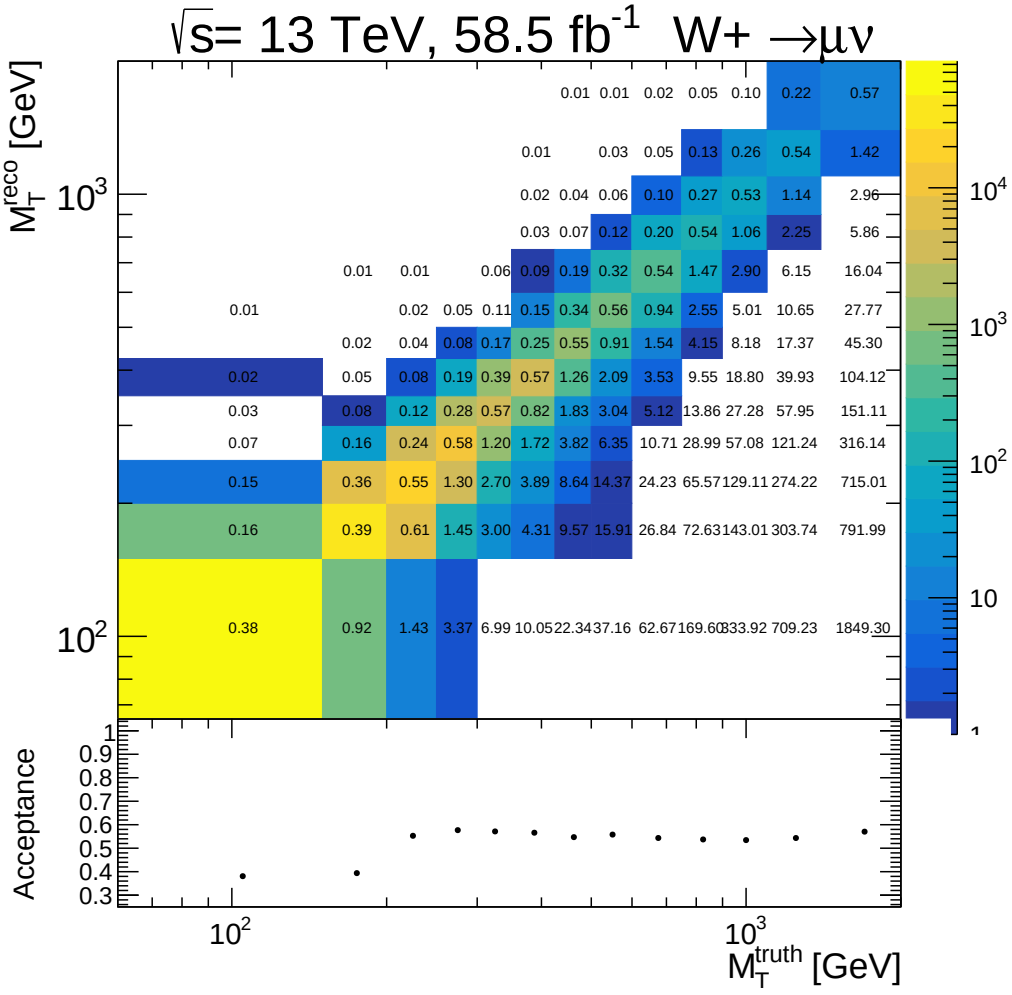

Figure F.15.: Acceptance for the $W^+ \to \mu^+\nu$ MC16e signal process. The upper panel shows the m_T^W truth level vs the m_T^W reconstruction level events. The given numbers show the ratio of the total number of truth events in each bin to the total number of reconstructed events in each bin. The diagonal of the upper panel gives the acceptance in the lower panel.

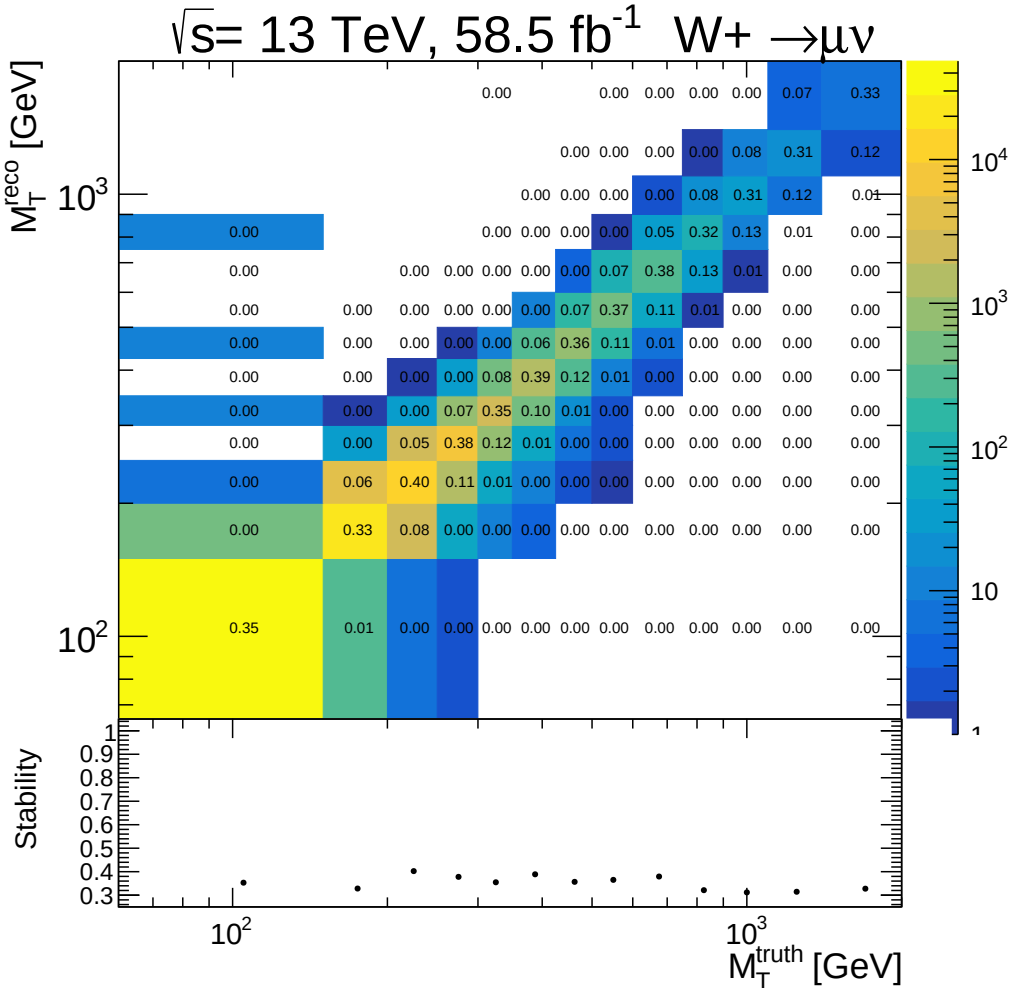

Figure F.16.: Stability for the $W^- \to \mu^- \bar{\nu}$ MC16e signal process. The upper panel shows the m_T^W truth level vs the m_T^W reconstruction level events. The given numbers show the ratio of the number of events in each bin to the total number of truth events in the given mass bin. The diagonal of the upper panel gives the stability in the lower panel.

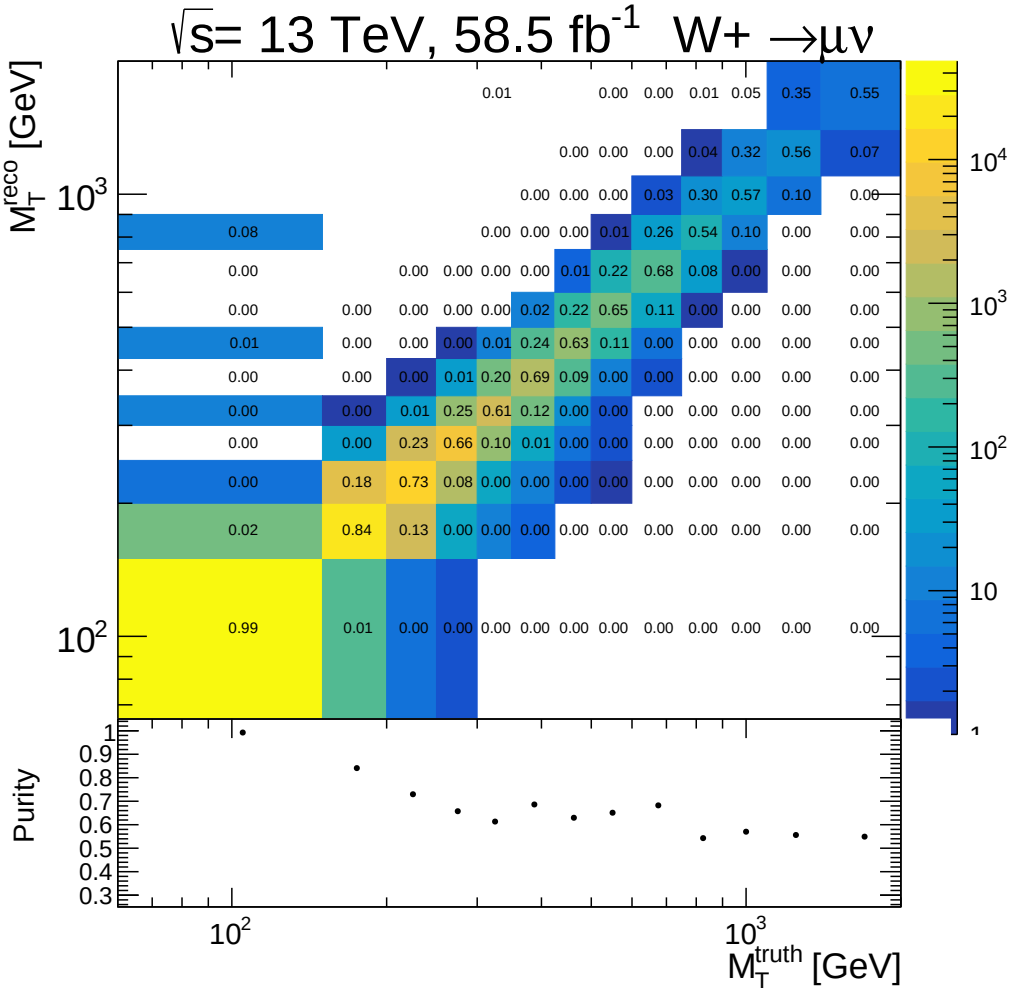

Figure F.17.: Purity for the $W^- \to \mu^- \bar{\nu}$ MC16e signal process. The upper panel shows the m_T^W truth level vs the m_T^W reconstruction level events. The given numbers show the ratio of the number of events in each bin to the total number of reconstructed event in the given mass bin. The diagonal of the upper panel gives the purity in the lower panel.

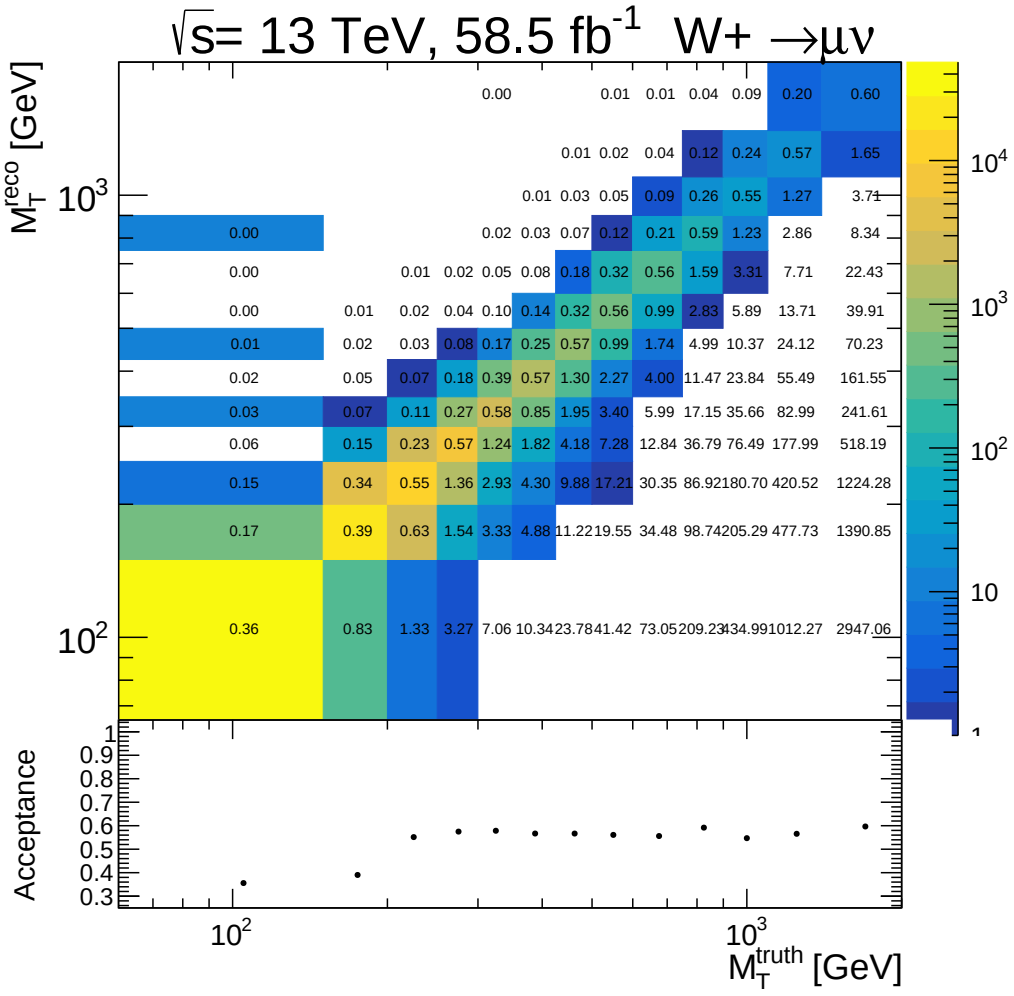

Figure F.18.: Acceptance for the $W^- \to \mu^- \bar{\nu}$ MC16e signal process. The upper panel shows the m_T^W truth level vs the m_T^W reconstruction level events. The given numbers show the ratio of the total number of truth events in each bin to the total number of reconstructed events in each bin. The diagonal of the upper panel gives the acceptance in the lower panel.

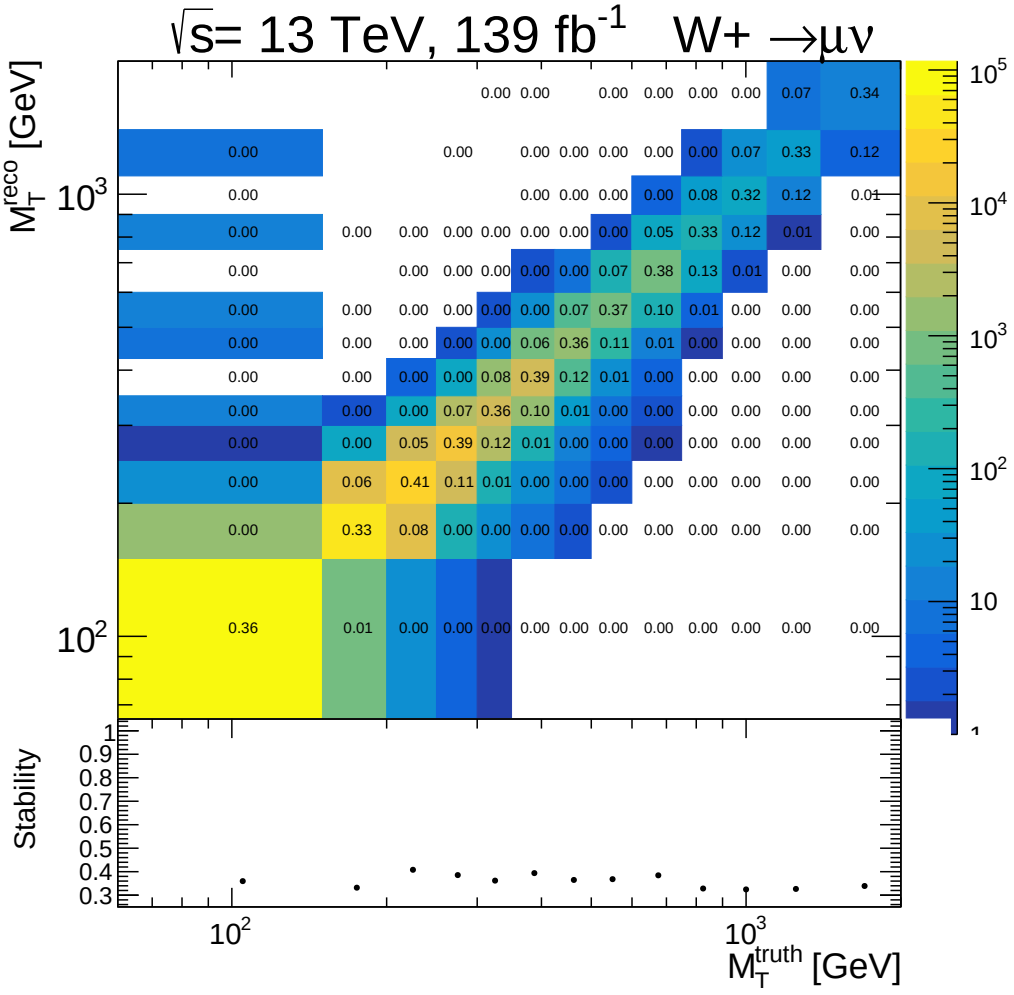

Figure F.19.: Stability for the $W^- \to \mu^- \bar{\nu}$ signal process. The upper panel shows the m_T^W truth level vs the m_T^W reconstruction level events. The given numbers show the ratio of the number of events in each bin to the total number of truth events in the given mass bin. The diagonal of the upper panel gives the stability in the lower panel.

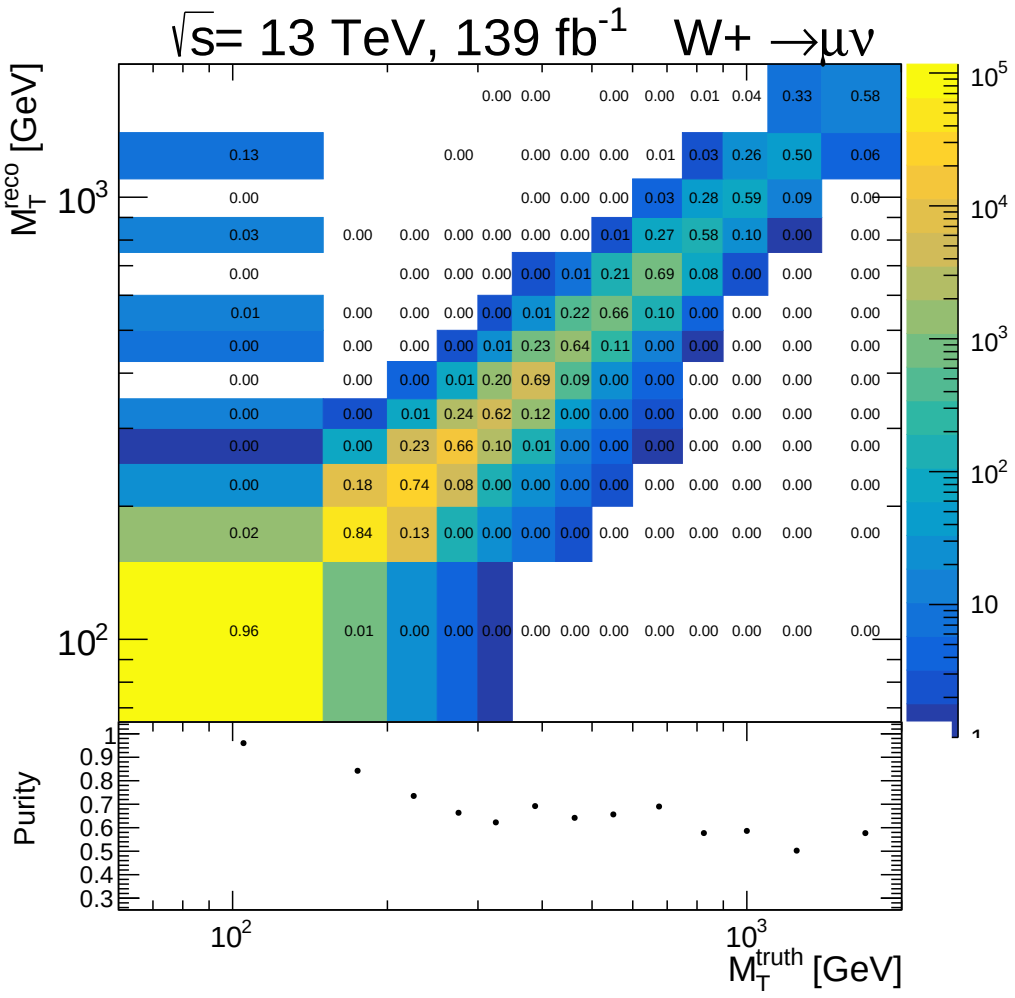

Figure F.20.: Purity for the $W^- \to \mu^- \bar{\nu}$ signal process. The upper panel shows the m_T^W truth level vs the m_T^W reconstruction level events. The given numbers show the ratio of the number of events in each bin to the total number of reconstructed event in the given mass bin. The diagonal of the upper panel gives the purity in the lower panel.

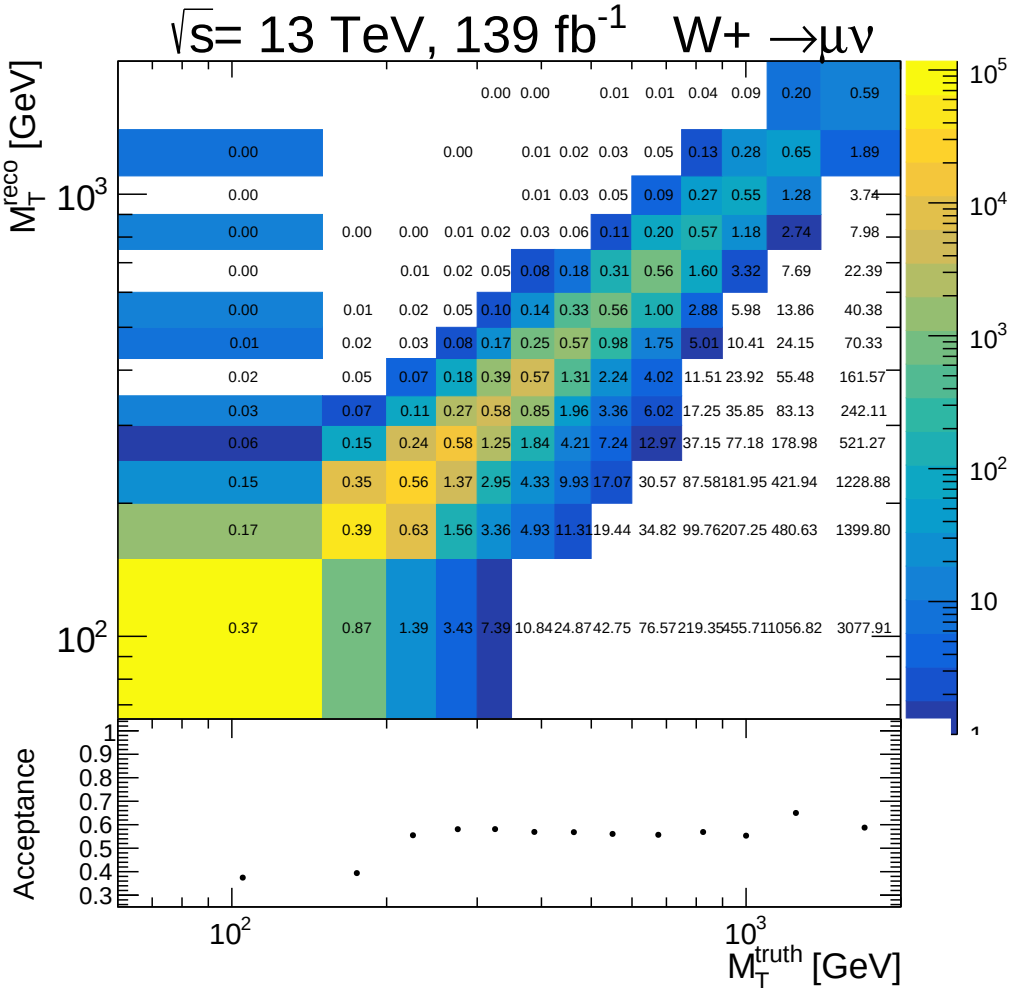

Figure F.21.: Acceptance for the $W^- \to \mu^- \bar{\nu}$ signal process. The upper panel shows the m_T^W truth level vs the m_T^W reconstruction level events. The given numbers show the ratio of the total number of truth events in each bin to the total number of reconstructed events in each bin. The diagonal of the upper panel gives the acceptance in the lower panel.

F.2. Migrations

The bin migration is discussed in Section 10.4.1 and is an important feature to consider in this measurement. The migration is an effect that should be well understood for it can be corrected for. Migration matrices as outlined in the section mentioned above have been created for each Monte Carlo campaign and presented individually in the following. As expected, the migrations are similar for each Monte Carlo campaign with W^- being few percent lower than the W^+.

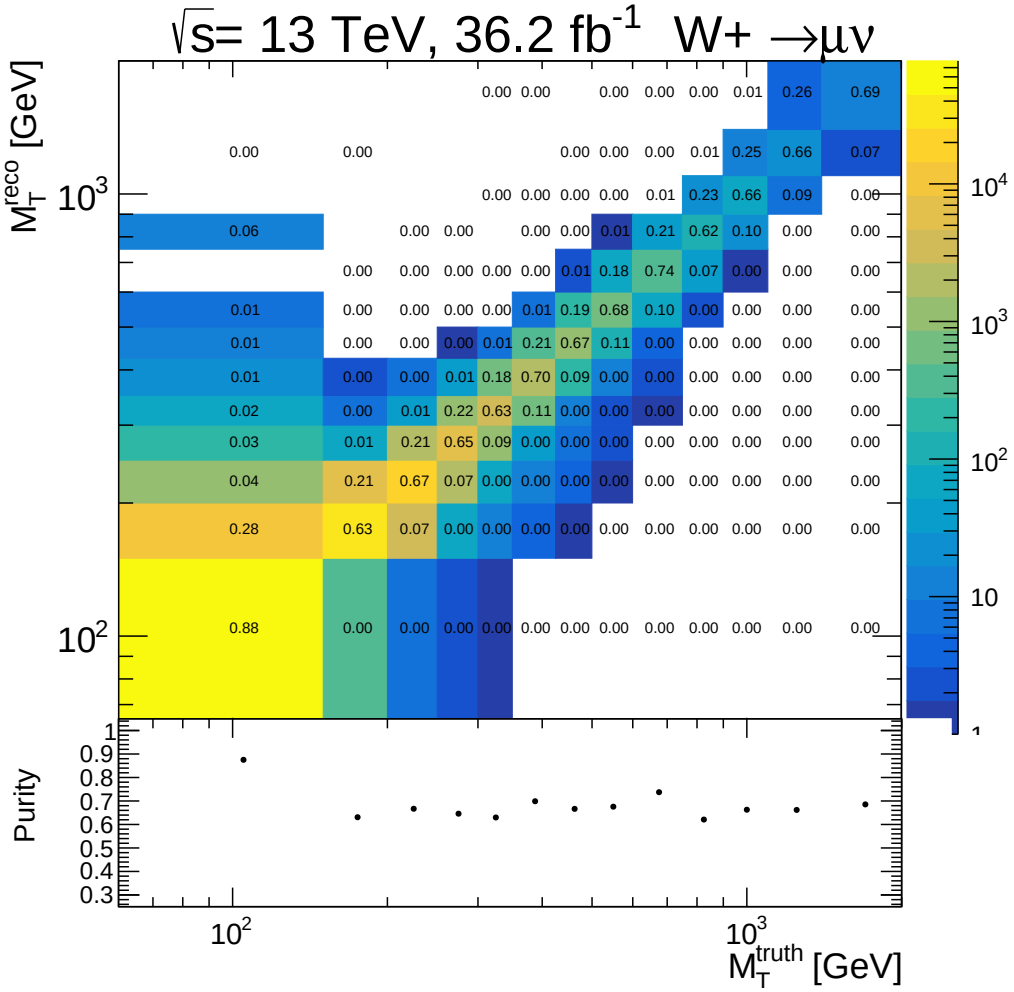

Figure F.22.: Migration matrix $M_{\text{reco,truth}}$ for the $W^+ \to \mu^+\nu$ MC16a signal process. The upper panel shows the m_T^W truth level vs the m_T^W reconstruction level events. The given numbers show the ratio of the number of events in each bin to the total number of reconstruced event in the given mass bin. The diagonal of the upper panel gives the purity in the lower panel.

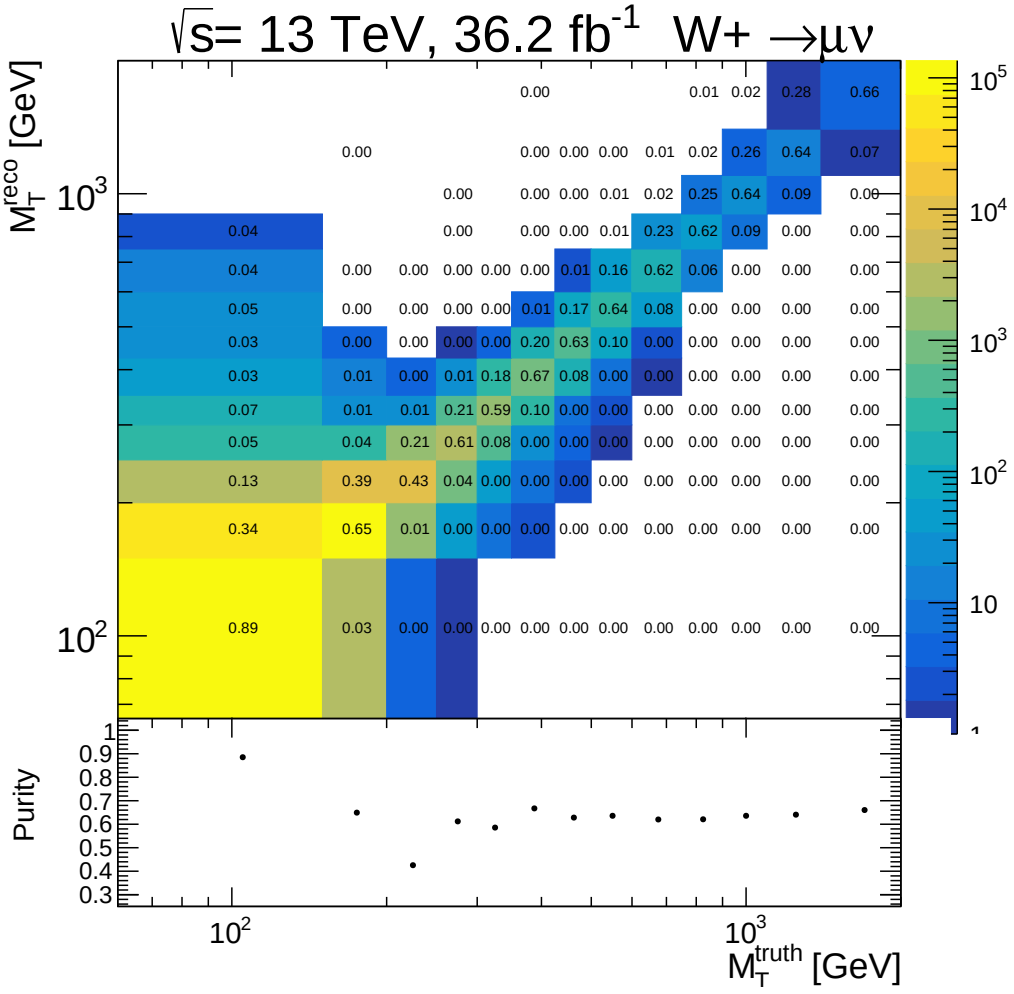

Figure F.23.: Migration matrix $M_{\text{reco,truth}}$ for the $W^- \to \mu^- \nu$ MC16a signal process. The upper panel shows the m_T^W truth level vs the m_T^W reconstruction level events. The given numbers show the ratio of the number of events in each bin to the total number of reconstruced event in the given mass bin. The diagonal of the upper panel gives the purity in the lower panel.

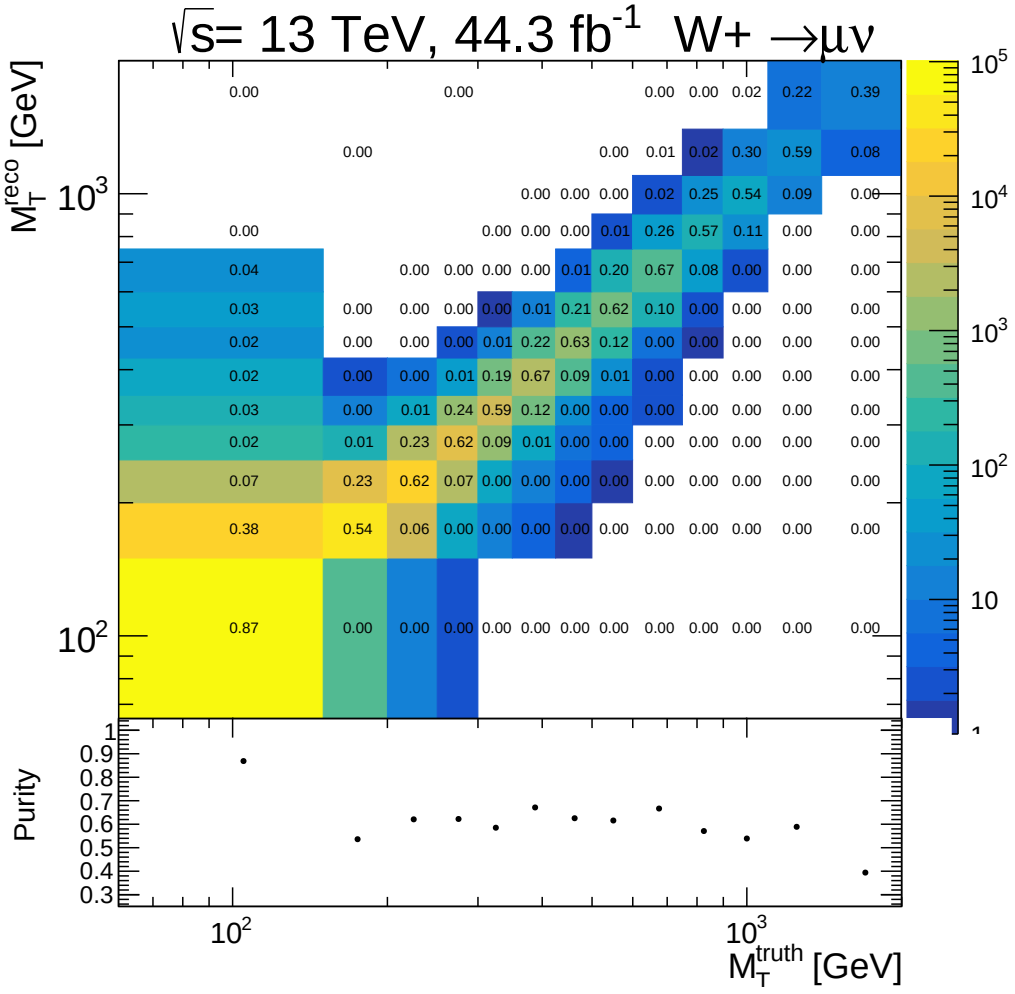

Figure F.24.: Migration matrix $M_{\text{reco,truth}}$ for the $W^+ \to \mu^+\nu$ MC16d signal process. The upper panel shows the m_T^W truth level vs the m_T^W reconstruction level events. The given numbers show the ratio of the number of events in each bin to the total number of reconstruced event in the given mass bin. The diagonal of the upper panel gives the purity in the lower panel.

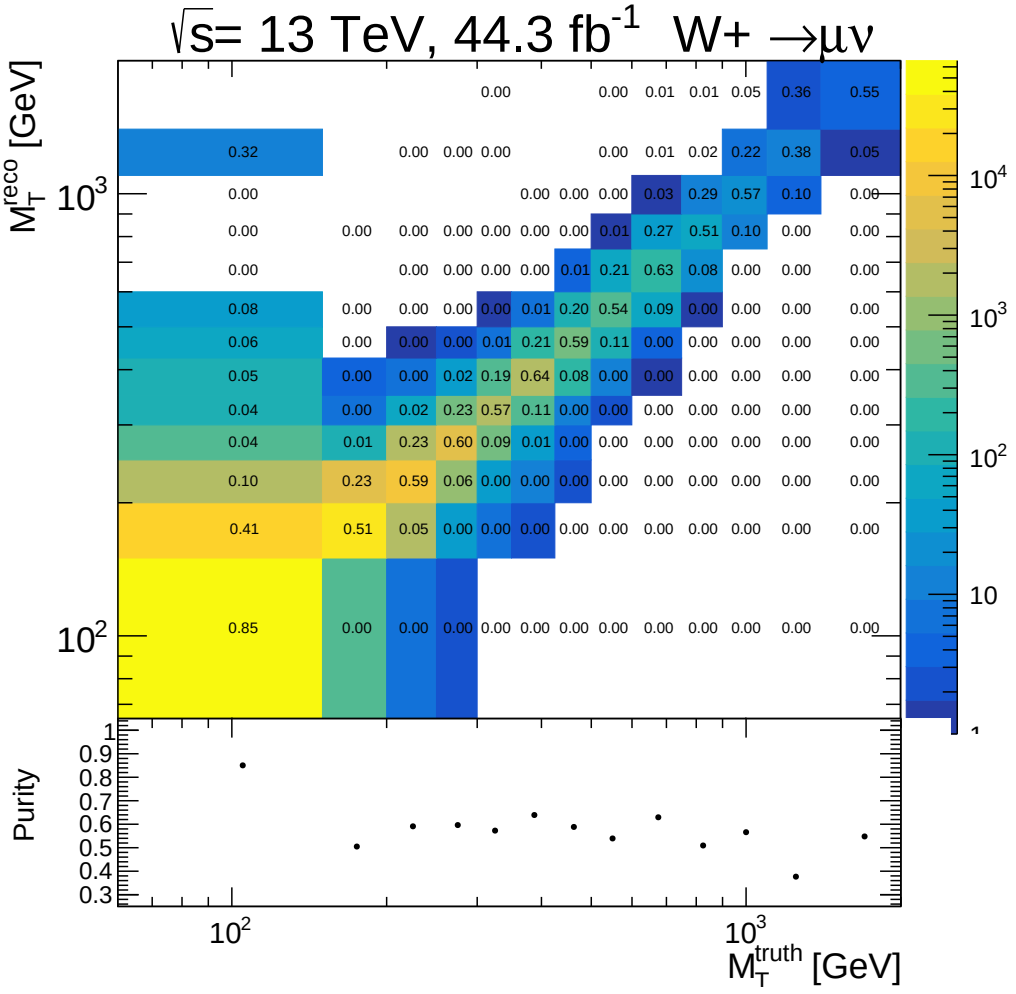

Figure F.25.: Migration matrix $M_{\text{reco,truth}}$ for the $W^- \to \mu^- \nu$ MC16d signal process. The upper panel shows the m_T^W truth level vs the m_T^W reconstruction level events. The given numbers show the ratio of the number of events in each bin to the total number of reconstruced event in the given mass bin. The diagonal of the upper panel gives the purity in the lower panel.

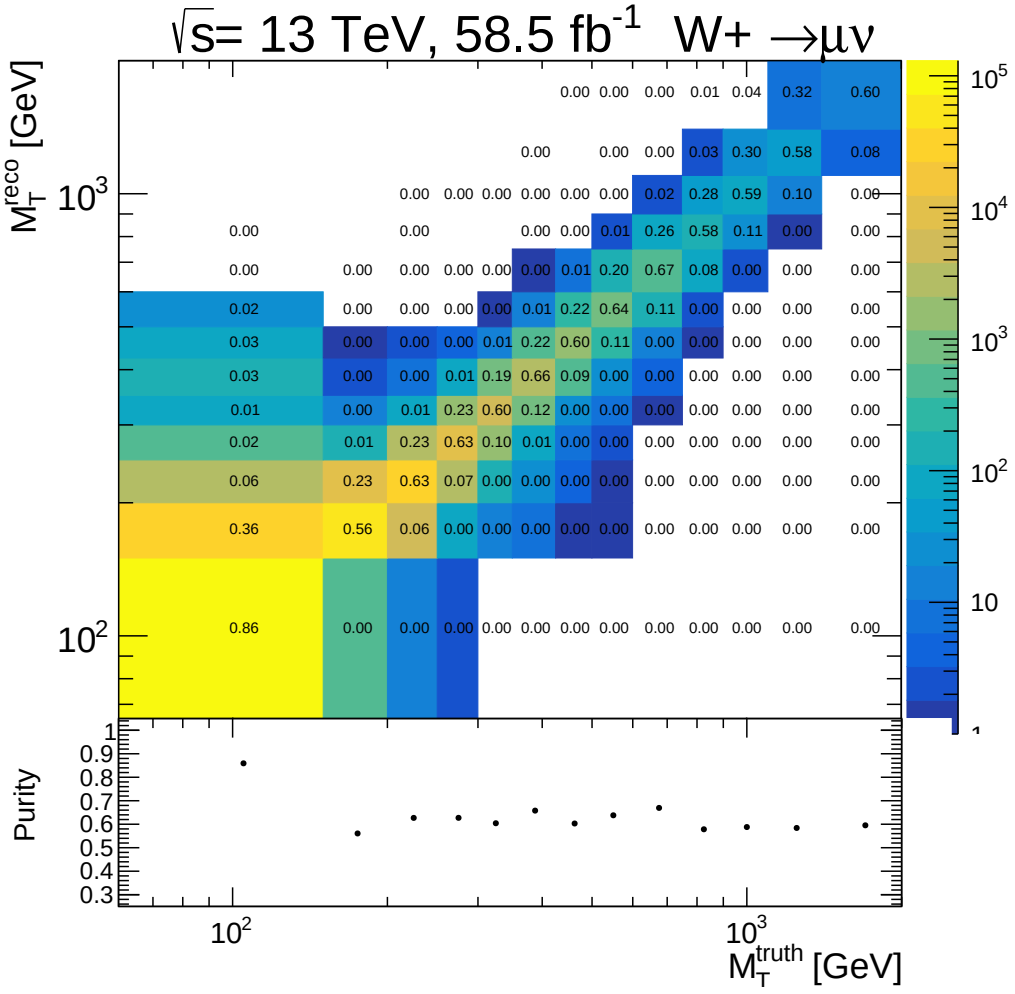

Figure F.26.: Migration matrix $M_{\text{reco,truth}}$ for the $W^+ \to \mu^+ \nu$ MC16e signal process. The upper panel shows the m_T^W truth level vs the m_T^W reconstruction level events. The given numbers show the ratio of the number of events in each bin to the total number of reconstruced event in the given mass bin. The diagonal of the upper panel gives the purity in the lower panel.

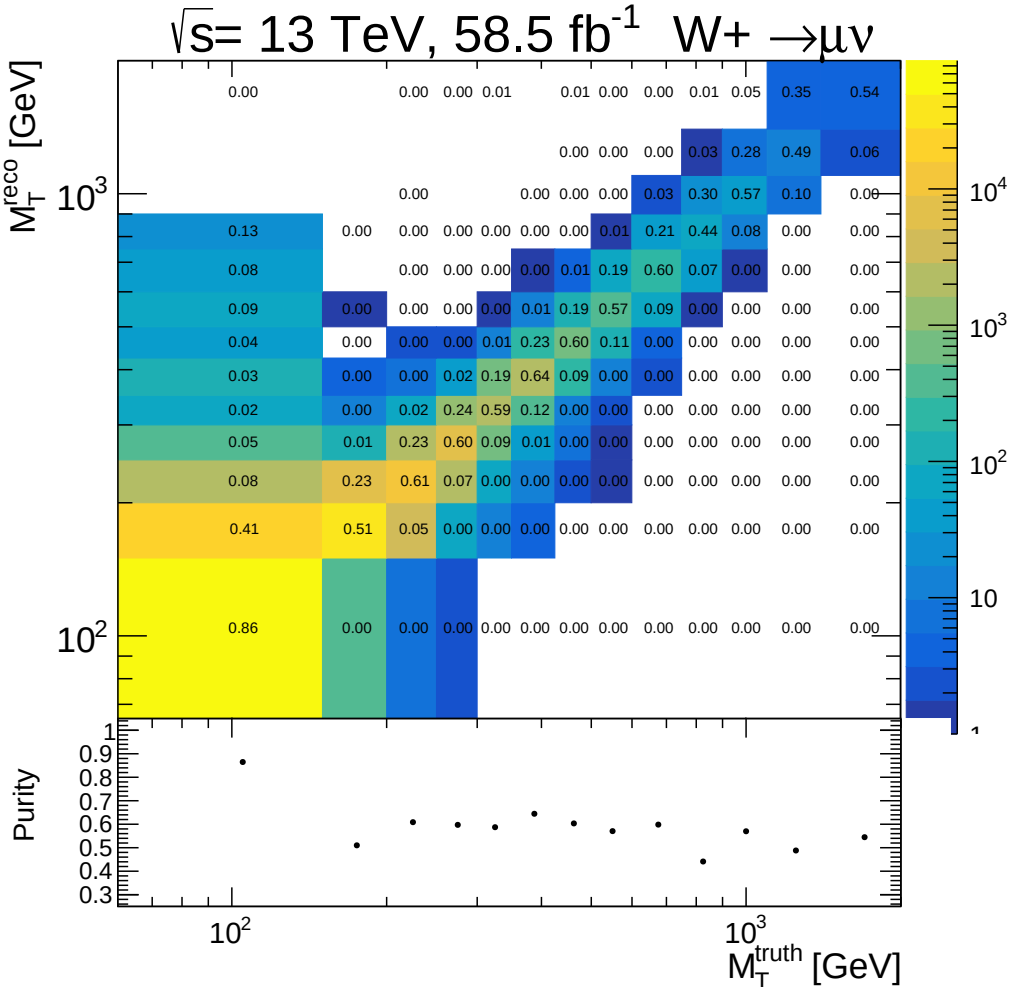

Figure F.27.: Migration matrix $M_{\text{reco,truth}}$ for the $W^- \to \mu^- \nu$ MC16e signal process. The upper panel shows the m_T^W truth level vs the m_T^W reconstruction level events. The given numbers show the ratio of the number of events in each bin to the total number of reconstruced event in the given mass bin. The diagonal of the upper panel gives the purity in the lower panel.

F.3. Results

The charge-current Drell-Yan cross-section and muon charge asymmetry measurements presented in Chapter 10 are shown for the full Run-2 statistics. This section contains the individual data and Monte Carlo contributions to the final results. The statistical and systematic uncertainties for each Monte Carlo campaign have been calculated separately following the procedure outlined in Chapter 8. The unfolded 1D cross-section for each data year show good agreement between the theory and prediction especially in the m_T^W region below 1 TeV. The charge asymmetry for each data year also has good agreement in lower m_T^W regions. Overall the data and prediction agreement for the charge asymmetry is good too although there some fluctuations that can be seen especially in 2017 data. This is due to a lack of statistics available and is not seen when the statistics are increased as seen by the combination of 2015-2018 data years as presented in the main body of this text.

F.3.1. Individual Systematic Uncertainty Tables

Each experimental systematic uncertainty calculated for the final measurement is explicitly listed in the following. Table F.1 and Table F.2 are for the positive and negative cross-sections respectively. The values have been calculated as outline by Chapter 8 and using Equation 10.1. Table F.3 explicitly lists the individual systematic uncertainties that contribute to the final uncertainty for the asymmetry. The values have been calculated as outline by Chapter 8 and using Equation 10.2. These tables show the breakdown of the value systematic in each m_T^W bin presented as percentages.

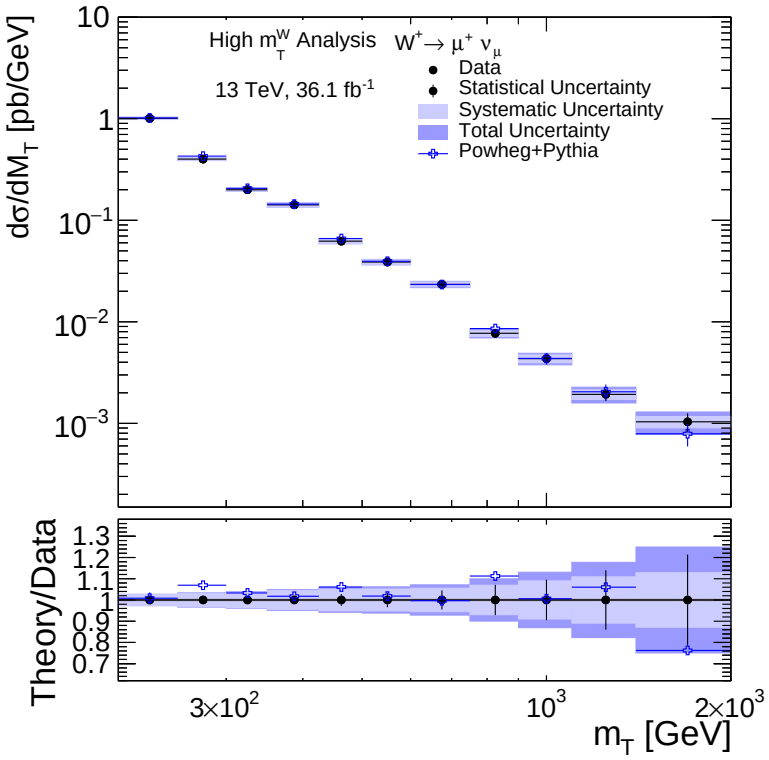

(a) W^+

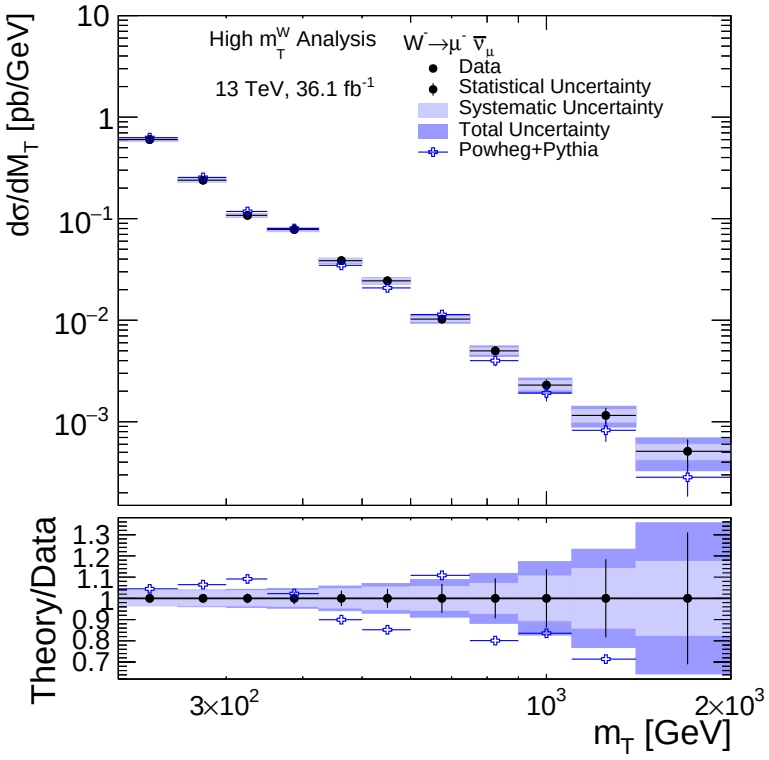

(b) W^-

Figure F.28.: Unfolded 1D cross sections binned in m_T^W for 2015/2016 data and MC16a calculated using Equation 10.1. Statistical and systematic uncertainties are included in the uncertainty band. The total uncertainty is shown by the dark blue band. The ratio is taken between the measured data and the truth (prediction) distributions.

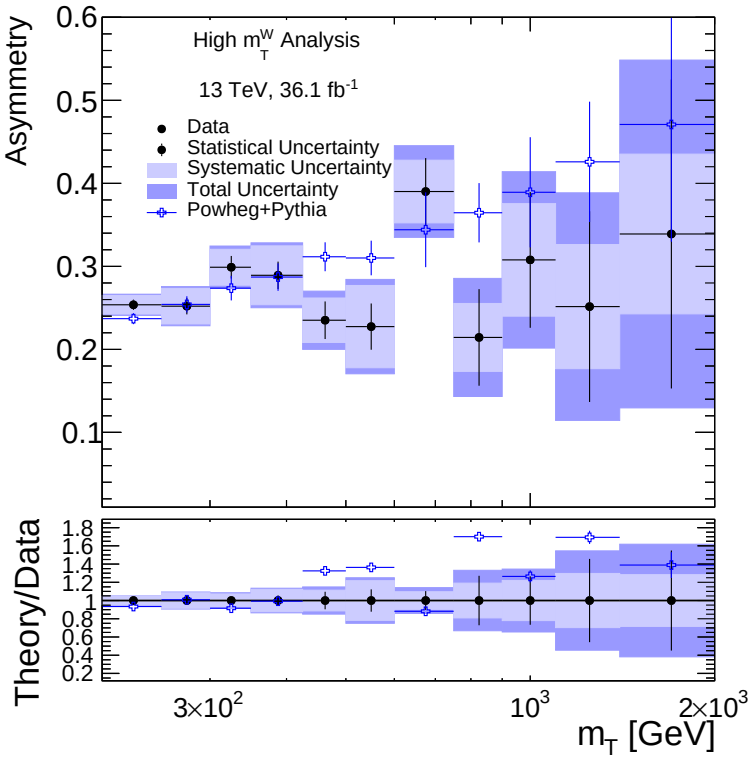

Figure F.29.: Muon charge aymmetry binned in m_T^W for 2015/2016 data and MC16a calculated using Equation 10.2. Statistical and systematic uncertainties are included in the uncertainty band. Statistical and systematic uncertainties are included in the uncertainty band. The total uncertainty is shown by the dark blue band. The ratio is taken between the measured data and the truth (prediction) distributions.

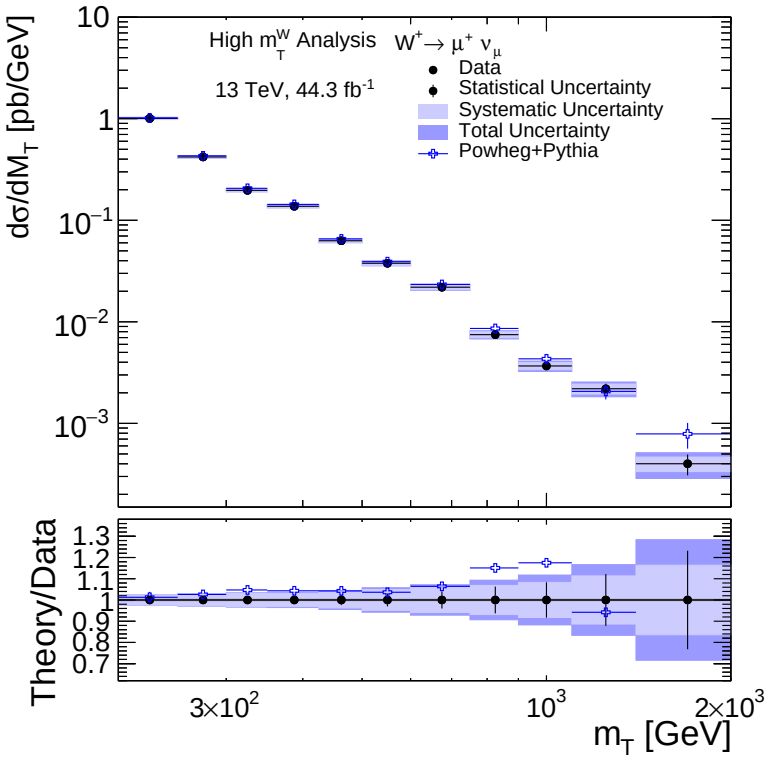

(a) W^+

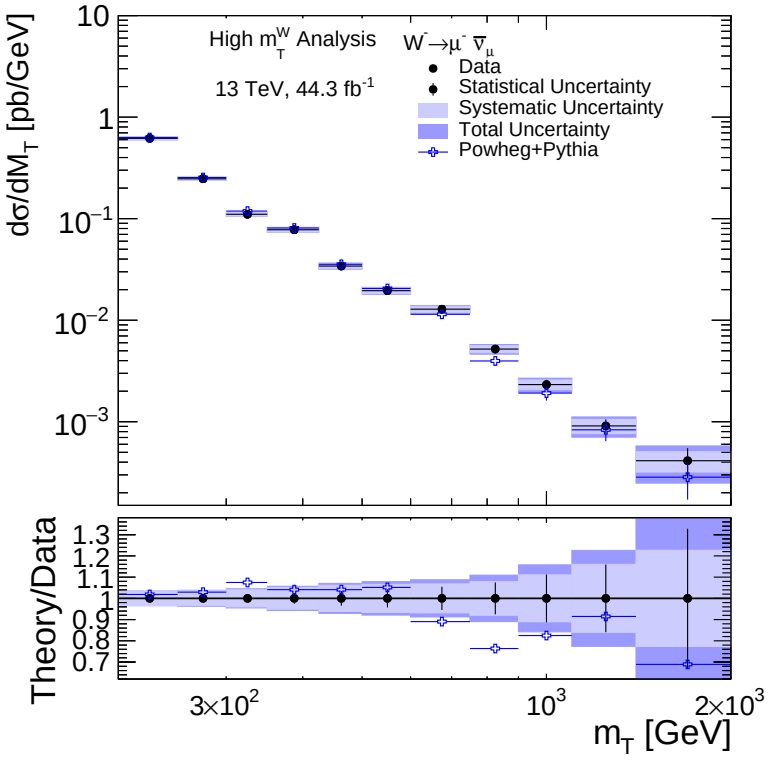

(b) W^-

Figure F.30.: Unfolded 1D cross sections binned in m_T^W for 2017 data and MC16d calculated using Equation 10.1. Statistical and systematic uncertainties are included in the uncertainty band. The total uncertainty is shown by the dark blue band. The ratio is taken between the measured data and the truth (prediction) distributions.

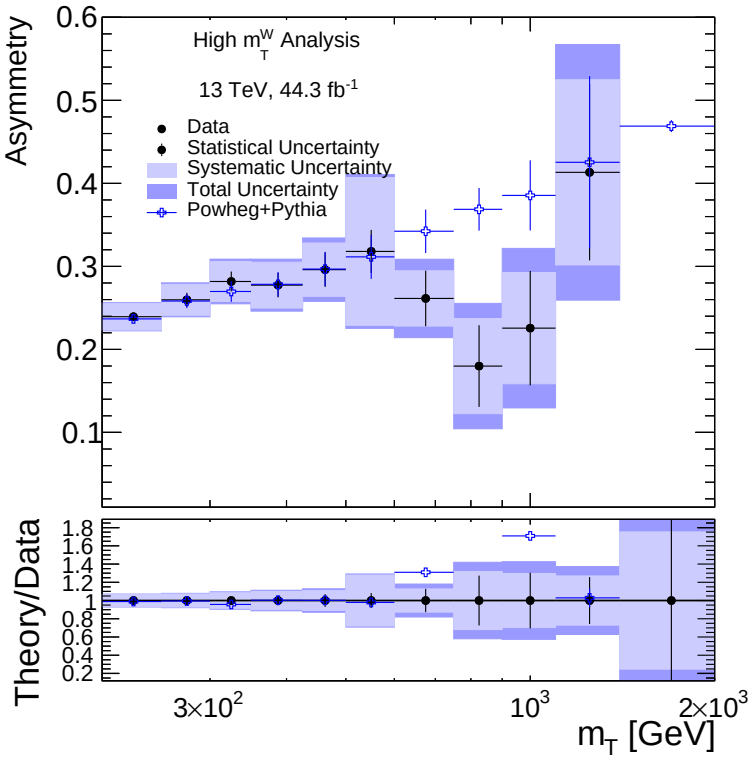

Figure F.31.: Muon charge aymmetry binned in m_T^W for 2017 data and MC16d calculated using Equation 10.2. Statistical and systematic uncertainties are included in the uncertainty band. Statistical and systematic uncertainties are included in the uncertainty band. The total uncertainty is shown by the dark blue band. The ratio is taken between the measured data and the truth (prediction) distributions.

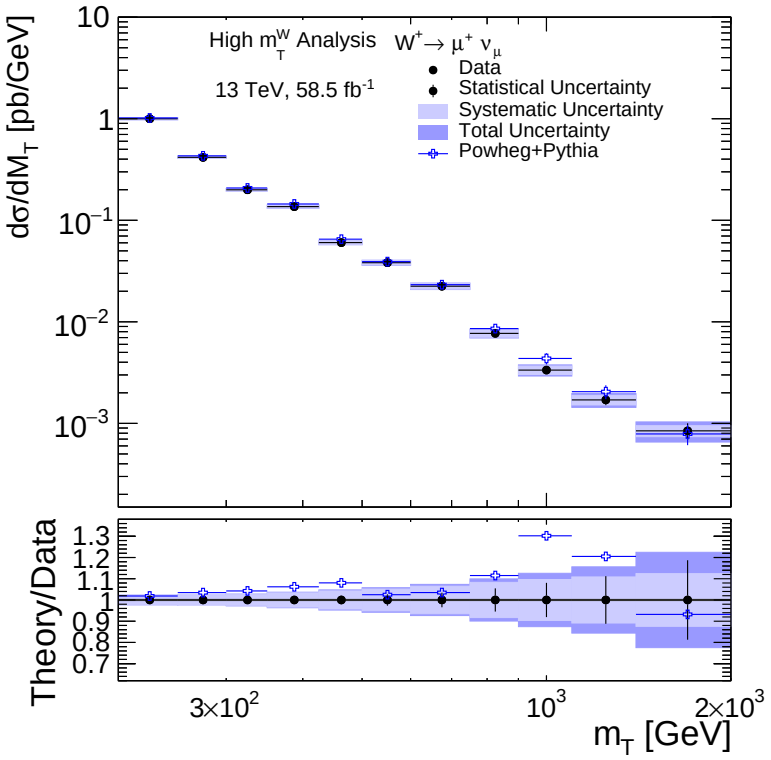

(a) W^+

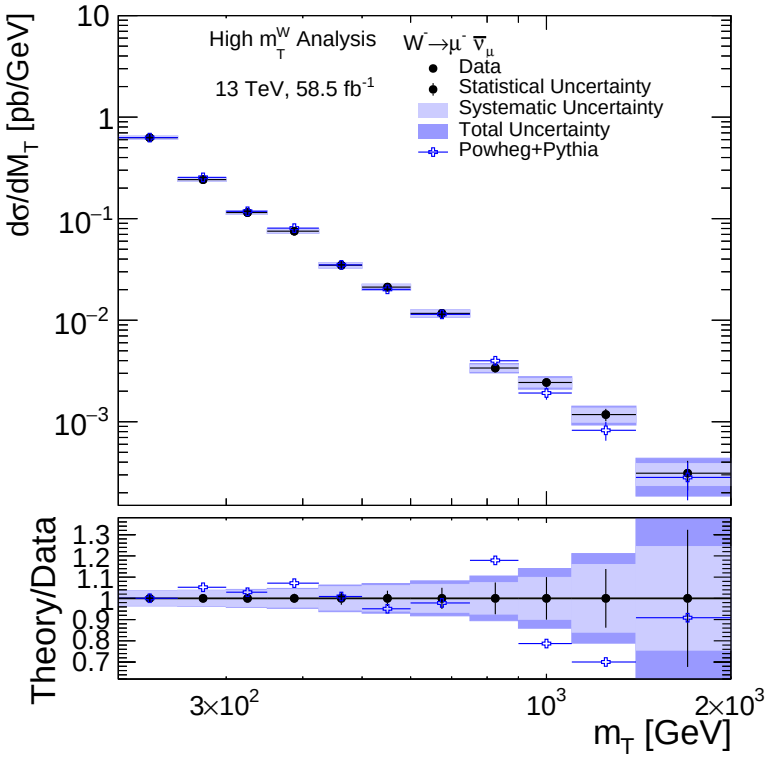

(b) W^-

Figure F.32.: Unfolded 1D cross sections binned in m_T^W for 2018 data and MC16e calculated using Equation 10.1. Statistical and systematic uncertainties are included in the uncertainty band. The total uncertainty is shown by the dark blue band. The ratio is taken between the measured data and the truth (prediction) distributions.

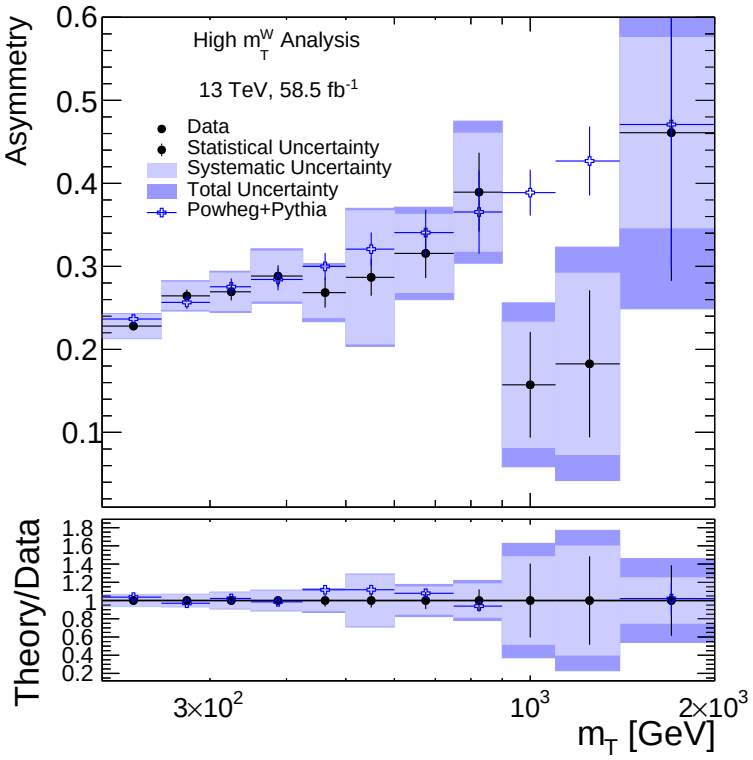

Figure F.33.: Muon charge aymmetry binned in m_T^W for 2018 data and MC16e calculated using Equation 10.2. Statistical and systematic uncertainties are included in the uncertainty band. Statistical and systematic uncertainties are included in the uncertainty band. The total uncertainty is shown by the dark blue band. The ratio is taken between the measured data and the truth (prediction) distributions.

Systematic	$200 \leq M_T < 250$	$250 \leq M_T < 300$	$300 \leq M_T < 350$	$350 \leq M_T < 425$	$425 \leq M_T < 500$	$500 \leq M_T < 600$	$600 \leq M_T < 750$	$750 \leq M_T < 900$	$900 \leq M_T < 1100$	$1100 \leq M_T < 1400$	$1400 \leq M_T < 2000$
MUON_MS	−0.07	−0.14	−0.24	−0.32	−0.36	−0.32	−0.22	−0.19	−0.29	−0.50	−0.78
	0.07	0.14	0.24	0.32	0.36	0.32	0.22	0.19	0.29	0.50	0.78
MUON_SCALE	−0.31	−0.33	−0.29	−0.25	−0.24	−0.24	−0.25	−0.26	−0.26	−0.26	−0.26
	0.31	0.33	0.29	0.25	0.24	0.24	0.25	0.26	0.26	0.26	0.26
IDSys	−0.50	−0.72	−0.85	−0.87	−0.84	−0.86	−0.95	−1.11	−1.37	−1.72	−2.03
	0.50	0.72	0.85	0.87	0.84	0.86	0.95	1.11	1.37	1.72	2.03
IsoSys	−0.11	−0.17	−0.28	−0.36	−0.40	−0.40	−0.38	−0.38	−0.38	−0.38	−0.38
	0.11	0.17	0.28	0.36	0.40	0.40	0.38	0.38	0.38	0.38	0.38
TrigSys	−0.45	−0.45	−0.45	−0.45	−0.44	−0.44	−0.44	−0.43	−0.43	−0.42	−0.41
	0.45	0.45	0.45	0.45	0.44	0.44	0.44	0.43	0.43	0.42	0.41
MUON_SAGITTA_RESBIAS	−0.94	−1.16	−1.48	−2.08	−2.76	−3.36	−4.16	−5.45	−6.50	−7.00	−7.45
	0.82	1.11	1.66	2.19	2.64	3.08	3.80	5.15	6.39	7.21	8.11
MET_SoftTrk_ResoPara	−0.35	−0.31	−0.19	−0.10	−0.05	−0.01	−0.01	−0.04	−0.07	−0.09	−0.09
MET_SoftTrk_ResoPerp	0.20	0.18	0.11	0.04	0.02	0.03	0.04	0.06	0.08	0.09	0.09
MET_SoftTrk_Scale	−0.38	−0.35	−0.25	−0.16	−0.09	−0.05	−0.04	−0.04	−0.05	−0.06	−0.06
	0.38	0.35	0.25	0.16	0.09	0.05	0.04	0.04	0.05	0.06	0.06
IDStat	−0.12	−0.12	−0.12	−0.12	−0.12	−0.12	−0.12	−0.12	−0.12	−0.12	−0.12
	0.12	0.12	0.12	0.12	0.12	0.12	0.12	0.12	0.12	0.12	0.12
IsoStat	−0.20	−0.24	−0.24	−0.21	−0.20	−0.20	−0.20	−0.20	−0.20	−0.20	−0.20
	0.20	0.24	0.24	0.21	0.20	0.20	0.20	0.20	0.20	0.20	0.20
PileUp	−0.12	−0.12	−0.12	−0.14	−0.16	−0.17	−0.17	−0.14	−0.09	−0.06	−0.06
	0.12	0.12	0.12	0.14	0.16	0.17	0.17	0.14	0.09	0.06	0.06
TrigStat	−0.09	−0.10	−0.10	−0.10	−0.10	−0.11	−0.11	−0.12	−0.12	−0.12	−0.13
	0.09	0.10	0.10	0.10	0.10	0.11	0.11	0.12	0.12	0.12	0.13
TTVAStat	−0.04	−0.04	−0.04	−0.04	−0.04	−0.04	−0.04	−0.04	−0.04	−0.04	−0.04
	0.04	0.04	0.04	0.04	0.04	0.04	0.04	0.04	0.04	0.04	0.04
TTVASys	−0.05	−0.05	−0.05	−0.05	−0.05	−0.05	−0.05	−0.05	−0.06	−0.06	−0.06
	0.05	0.05	0.05	0.05	0.05	0.05	0.05	0.05	0.06	0.06	0.06
MUON_SAGITTA_DATASTAT	0.11	0.12	0.15	0.17	0.20	0.23	0.32	0.50	0.59	0.62	0.67
	−0.13	−0.15	−0.17	−0.19	−0.22	−0.25	−0.29	−0.40	−0.52	−0.60	−0.65
MUON_ID	−0.05	−0.08	−0.10	−0.14	−0.16	−0.15	−0.12	−0.11	−0.11	−0.11	−0.11
	0.05	0.08	0.10	0.14	0.16	0.15	0.12	0.11	0.11	0.11	0.11
JET_BJES_Response	−0.01	−0.01	−0.00	−0.00	−0.00	−0.00	−0.00	−0.00	−0.00	−0.00	−0.00
	0.01	0.01	0.00	0.00	0.00	0.00	0.00	0.00	0.00	0.00	0.00
JET_EffectiveNP_Detector1	−0.01	−0.01	−0.01	−0.00	−0.01	−0.01	−0.01	−0.01	−0.01	−0.00	−0.00
	0.01	0.01	0.01	0.00	0.01	0.01	0.01	0.01	0.01	0.00	0.00
JET_EffectiveNP_Detector2	−0.00	−0.00	−0.00	−0.00	−0.00	−0.00	−0.00	−0.00	−0.00	−0.00	−0.00
	0.00	0.00	0.00	0.00	0.00	0.00	0.00	0.00	0.00	0.00	0.00
JET_EffectiveNP_Mixed1	−0.02	−0.04	−0.04	−0.04	−0.03	−0.02	−0.02	−0.02	−0.01	−0.01	−0.01
	0.02	0.04	0.04	0.04	0.03	0.02	0.02	0.02	0.01	0.01	0.01
JET_EffectiveNP_Mixed2	−0.03	−0.03	−0.02	−0.02	−0.01	−0.01	−0.01	−0.01	−0.01	−0.01	−0.01
	0.03	0.03	0.02	0.02	0.01	0.01	0.01	0.01	0.01	0.01	0.01
JET_EffectiveNP_Mixed3	−0.01	−0.01	−0.01	−0.00	−0.00	−0.00	−0.00	−0.00	−0.00	−0.00	−0.00
	0.01	0.01	0.01	0.00	0.00	0.00	0.00	0.00	0.00	0.00	0.00
JET_EffectiveNP_Modelling1	−0.10	−0.13	−0.16	−0.17	−0.13	−0.06	−0.03	−0.03	−0.02	−0.02	−0.01
	0.10	0.13	0.16	0.17	0.13	0.06	0.03	0.03	0.02	0.02	0.01
JET_EffectiveNP_Modelling2	−0.01	−0.01	−0.01	−0.01	−0.01	−0.01	−0.01	−0.01	−0.01	−0.00	−0.00
	0.01	0.01	0.01	0.01	0.01	0.01	0.01	0.01	0.01	0.00	0.00
JET_EffectiveNP_Modelling3	−0.01	−0.01	−0.01	−0.00	−0.00	−0.00	−0.00	−0.00	−0.00	−0.00	−0.00
	0.01	0.01	0.01	0.00	0.00	0.00	0.00	0.00	0.00	0.00	0.00
JET_EffectiveNP_Modelling4	−0.00	−0.00	−0.00	−0.00	−0.00	−0.00	−0.00	−0.00	−0.00	−0.00	−0.00
	0.00	0.00	0.00	0.00	0.00	0.00	0.00	0.00	0.00	0.00	0.00
JET_EffectiveNP_Statistical1	−0.00	−0.01	−0.01	−0.01	−0.01	−0.01	−0.01	−0.01	−0.00	−0.00	−0.00
	0.00	0.01	0.01	0.01	0.01	0.01	0.01	0.01	0.00	0.00	0.00
JET_EffectiveNP_Statistical2	−0.02	−0.02	−0.01	−0.01	−0.01	−0.01	−0.01	−0.01	−0.01	−0.00	−0.00
	0.02	0.02	0.01	0.01	0.01	0.01	0.01	0.01	0.01	0.00	0.00
JET_EffectiveNP_Statistical3	−0.00	−0.00	−0.01	−0.01	−0.01	−0.01	−0.00	−0.00	−0.00	−0.00	−0.00
	0.00	0.00	0.01	0.01	0.01	0.01	0.00	0.00	0.00	0.00	0.00

	$200 \leq M_T < 250$	$250 \leq M_T < 300$	$300 \leq M_T < 350$	$350 \leq M_T < 425$	$425 \leq M_T < 500$	$500 \leq M_T < 600$	$600 \leq M_T < 750$	$750 \leq M_T < 900$	$900 \leq M_T < 1100$	$1100 \leq M_T < 1400$	$1400 \leq M_T < 2000$
JET_EffectiveNP_Statistical4	−0.00 0.00	−0.01 0.01	−0.01 0.01	−0.00 0.00	−0.00 0.00	−0.00 0.00	−0.00 0.00	−0.00 0.00	−0.00 0.00	−0.00 0.00	−0.00 0.00
JET_EffectiveNP_Statistical5	−0.00 0.00	−0.00 0.00	−0.00 0.00	−0.00 0.00	−0.00 0.00	−0.00 0.00	−0.00 0.00	−0.00 0.00	−0.00 0.00	−0.00 0.00	−0.00 0.00
JET_EffectiveNP_Statistical6	−0.00 0.00	−0.00 0.00	−0.00 0.00	−0.00 0.00	−0.00 0.00	−0.00 0.00	−0.00 0.00	−0.00 0.00	−0.00 0.00	−0.00 0.00	−0.00 0.00
JET_EtaIntercalibration_NonClosure_2018data	−0.02 0.02	−0.03 0.03	−0.04 0.04	−0.04 0.04	−0.02 0.02	−0.01 0.01	−0.01 0.01	−0.01 0.01	−0.01 0.01	−0.01 0.01	−0.01 0.01
JET_EtaIntercalibration_NonClosure_negEta	−0.01 0.01	−0.01 0.01	−0.01 0.01	−0.01 0.01	−0.01 0.01	−0.01 0.01	−0.01 0.01	−0.00 0.00	−0.00 0.00	−0.00 0.00	−0.00 0.00
JET_EtaIntercalibration_NonClosure_posEta	−0.01 0.01	−0.01 0.01	−0.01 0.01	−0.00 0.00	−0.00 0.00	−0.00 0.00	−0.00 0.00	−0.00 0.00	−0.00 0.00	−0.00 0.00	−0.00 0.00
JET_EtaIntercalibration_TotalStat	−0.02 0.02	−0.02 0.02	−0.02 0.02	−0.01 0.01	−0.01 0.01	−0.01 0.01	−0.01 0.01	−0.01 0.01	−0.01 0.01	−0.01 0.01	−0.01 0.01
JET_Flavor_Composition	−0.22 0.22	−0.30 0.30	−0.31 0.31	−0.27 0.27	−0.22 0.22	−0.15 0.15	−0.10 0.10	−0.06 0.06	−0.04 0.04	−0.03 0.03	−0.02 0.02
JET_Flavor_Response	−0.15 0.15	−0.18 0.18	−0.21 0.21	−0.23 0.23	−0.21 0.21	−0.15 0.15	−0.06 0.06	−0.02 0.02	−0.02 0.02	−0.02 0.02	−0.02 0.02
JET_Pileup_OffsetMu	−0.18 0.18	−0.16 0.16	−0.09 0.09	−0.05 0.05	−0.04 0.04	−0.03 0.03	−0.03 0.03	−0.03 0.03	−0.02 0.02	−0.02 0.02	−0.01 0.01
JET_Pileup_OffsetNPV	−0.09 0.09	−0.08 0.08	−0.06 0.06	−0.05 0.05	−0.04 0.04	−0.03 0.03	−0.02 0.02	−0.02 0.02	−0.01 0.01	−0.01 0.01	−0.01 0.01
JET_Pileup_RhoTopology	−0.09 0.09	−0.11 0.11	−0.15 0.15	−0.17 0.17	−0.14 0.14	−0.09 0.09	−0.06 0.06	−0.05 0.05	−0.03 0.03	−0.01 0.01	−0.01 0.01
JET_EtaIntercalibration_Modelling	−0.06 0.06	−0.07 0.07	−0.08 0.08	−0.09 0.09	−0.07 0.07	−0.05 0.05	−0.04 0.04	−0.03 0.03	−0.02 0.02	−0.02 0.02	−0.02 0.02
JET_JER_EffectiveNP_1	−0.18 0.18	−0.19 0.19	−0.20 0.20	−0.21 0.21	−0.23 0.23	−0.23 0.23	−0.19 0.19	−0.12 0.12	−0.04 0.04	−0.01 0.01	−0.01 0.01
JET_JER_EffectiveNP_2	−0.10 0.10	−0.15 0.15	−0.27 0.27	−0.40 0.40	−0.44 0.44	−0.34 0.34	−0.21 0.21	−0.11 0.11	−0.04 0.04	−0.01 0.01	−0.01 0.01
JET_JER_EffectiveNP_3	−0.06 0.06	−0.04 0.04	−0.07 0.07	−0.17 0.17	−0.25 0.25	−0.22 0.22	−0.14 0.14	−0.08 0.08	−0.04 0.04	−0.03 0.03	−0.03 0.03
JET_JER_EffectiveNP_4	−0.02 0.02	−0.04 0.04	−0.11 0.11	−0.19 0.19	−0.28 0.28	−0.31 0.31	−0.25 0.25	−0.13 0.13	−0.04 0.04	−0.01 0.01	−0.01 0.01
JET_JER_EffectiveNP_5	−0.08 0.08	−0.08 0.08	−0.11 0.11	−0.14 0.14	−0.15 0.15	−0.13 0.13	−0.09 0.09	−0.06 0.06	−0.05 0.05	−0.04 0.04	−0.04 0.04
JET_JER_EffectiveNP_6	−0.09 0.09	−0.08 0.08	−0.09 0.09	−0.13 0.13	−0.15 0.15	−0.13 0.13	−0.08 0.08	−0.05 0.05	−0.04 0.04	−0.04 0.04	−0.04 0.04
JET_JER_EffectiveNP_7restTerm	−0.04 0.04	−0.05 0.05	−0.07 0.07	−0.13 0.13	−0.18 0.18	−0.17 0.17	−0.13 0.13	−0.07 0.07	−0.02 0.02	−0.00 0.00	−0.00 0.00
JET_JER_DataVsMC_MC16	−0.07 0.07	−0.07 0.07	−0.05 0.05	−0.03 0.03	−0.03 0.03	−0.05 0.05	−0.05 0.05	−0.03 0.03	−0.02 0.02	−0.01 0.01	−0.01 0.01
JET_Pileup_PtTerm	−0.05 0.05	−0.06 0.06	−0.05 0.05	−0.03 0.03	−0.02 0.02	−0.01 0.01	−0.01 0.01	−0.01 0.01	−0.01 0.01	−0.01 0.01	−0.00 0.00
JET_PunchThrough_MC16	0.00 −0.00	−0.00 −0.00	−0.00 0.00	0.00 −0.00	0.01 0.00	0.00 0.00	−0.00 −0.00	0.00 0.00	−0.00 0.00	0.00 0.00	0.00 $3.07 \cdot 10^{-5}$
MULTIJET_MET	−0.53 0.41	−0.72 0.54	−0.73 0.62	−0.68 0.61	−0.59 0.53	−0.42 0.39	−0.22 0.24	−0.12 0.14	−0.07 0.07	−0.01 0.01	0.08 −0.08
MULTIJET_PT	−0.68	−0.71	−0.59	−0.49	−0.44	−0.32	−0.17	−0.10	−0.06	−0.01	0.07
MULTIJET_JETPT	−1.15 0.11	−1.14 0.33	−0.88 0.47	−0.68 0.48	−0.57 0.45	−0.39 0.33	−0.20 0.17	−0.11 0.08	−0.06 0.05	−0.01 0.01	0.07 −0.06
MULTIJET_D0SIG	−0.60 0.27	−0.76 0.47	−0.75 0.58	−0.65 0.58	−0.55 0.49	−0.40 0.34	−0.20 0.16	−0.11 0.06	−0.08 0.02	−0.05 −0.01	0.02 −0.06

Table F.1.: This table contains the contribution of individual experimental systematic uncertainties in each bin for $W^+ \to \mu^+ \nu$. The systematics were computed with 10.1 and then summed in quadrature for the final result. The first column is the name of the systematic. All values are presented in percentages.

Systematic	$200 \le M_T < 250$	$250 \le M_T < 300$	$300 \le M_T < 350$	$350 \le M_T < 425$	$425 \le M_T < 500$	$500 \le M_T < 600$	$600 \le M_T < 750$	$750 \le M_T < 900$	$900 \le M_T < 1100$	$1100 \le M_T < 1400$	$1400 \le M_T < 2000$
MUON_MS	−0.02 0.02	−0.09 0.09	−0.28 0.28	−0.51 0.51	−0.64 0.64	−0.54 0.54	−0.28 0.28	−0.17 0.17	−0.41 0.41	−0.77 0.77	−0.98 0.98
MUON_SCALE	−0.31 0.31	−0.32 0.32	−0.27 0.27	−0.26 0.26	−0.28 0.28	−0.30 0.30	−0.29 0.29	−0.27 0.27	−0.27 0.27	−0.30 0.30	−0.35 0.35
IDSys	−0.50 0.50	−0.71 0.71	−0.85 0.85	−0.92 0.92	−0.95 0.95	−1.00 1.00	−1.03 1.03	−1.16 1.16	−1.63 1.63	−2.30 2.30	−2.86 2.86
IsoSys	−0.11 0.11	−0.18 0.18	−0.29 0.29	−0.38 0.38	−0.41 0.41	−0.40 0.40	−0.39 0.39	−0.38 0.38	−0.38 0.38	−0.38 0.38	−0.37 0.37
TrigSys	−0.45 0.45	−0.45 0.45	−0.45 0.45	−0.45 0.45	−0.45 0.45	−0.45 0.45	−0.44 0.44	−0.44 0.44	−0.44 0.44	−0.43 0.43	−0.43 0.43
MUON_SAGITTA_RESBIAS	1.10 −1.16	1.54 −1.56	2.04 −2.28	2.49 −2.77	2.81 −3.10	2.97 −3.68	3.48 −4.33	4.73 −5.08	6.73 −6.84	10.06 −10.38	14.73 −15.56
MET_SoftTrk_ResoPara	−0.25	−0.25	−0.20	−0.18	−0.16	−0.10	−0.04	−0.01	−0.01	−0.03	−0.04
MET_SoftTrk_ResoPerp	0.31	0.28	0.20	0.16	0.16	0.14	0.08	0.04	0.04	0.05	0.05
MET_SoftTrk_Scale	−0.22 0.22	−0.22 0.22	−0.22 0.22	−0.21 0.21	−0.19 0.19	−0.13 0.13	−0.06 0.06	−0.02 0.02	−0.03 0.03	−0.06 0.06	−0.07 0.07
IDStat	−0.13 0.13	−0.13 0.13	−0.12 0.12	−0.12 0.12	−0.12 0.12	−0.12 0.12	−0.12 0.12	−0.12 0.12	−0.12 0.12	−0.12 0.12	−0.12 0.12
IsoStat	−0.20 0.20	−0.24 0.24	−0.24 0.24	−0.21 0.21	−0.20 0.20	−0.20 0.20	−0.20 0.20	−0.20 0.20	−0.20 0.20	−0.20 0.20	−0.20 0.20
PileUp	−0.32 0.32	−0.27 0.27	−0.18 0.18	−0.17 0.17	−0.19 0.19	−0.19 0.19	−0.19 0.19	−0.19 0.19	−0.20 0.20	−0.23 0.23	−0.24 0.24
TrigStat	−0.09 0.09	−0.10 0.10	−0.10 0.10	−0.10 0.10	−0.10 0.10	−0.10 0.10	−0.10 0.10	−0.11 0.11	−0.11 0.11	−0.11 0.11	−0.12 0.12
TTVAStat	−0.04 0.04	−0.04 0.04	−0.04 0.04	−0.04 0.04	−0.04 0.04	−0.04 0.04	−0.04 0.04	−0.04 0.04	−0.04 0.04	−0.04 0.04	−0.04 0.04
TTVASys	−0.05 0.05	−0.05 0.05	−0.05 0.05	−0.05 0.05	−0.05 0.05	−0.05 0.05	−0.05 0.05	−0.05 0.05	−0.05 0.05	−0.05 0.05	−0.05 0.05
MUON_SAGITTA_DATASTAT	−0.10 0.12	−0.13 0.13	−0.20 0.13	−0.24 0.13	−0.25 0.13	−0.27 0.17	−0.30 0.28	−0.35 0.38	−0.45 0.47	−0.71 0.67	−1.11 0.99
MUON_ID	−0.05 0.05	−0.07 0.07	−0.08 0.08	−0.11 0.11	−0.13 0.13	−0.11 0.11	−0.07 0.07	−0.05 0.05	−0.06 0.06	−0.11 0.11	−0.16 0.16
JET_BJES_Response	−0.00 0.00	−0.00 0.00	−0.00 0.00	−0.00 0.00	−0.00 0.00	−0.00 0.00	−0.00 0.00	−0.00 0.00	−0.00 0.00	−0.00 0.00	−0.00 0.00
JET_EffectiveNP_Detector1	−0.01 0.01	−0.01 0.01	−0.02 0.02	−0.04 0.04	−0.05 0.05	−0.04 0.04	−0.02 0.02	−0.01 0.01	−0.01 0.01	−0.00 0.00	−0.00 0.00
JET_EffectiveNP_Detector2	−0.00 0.00	−0.00 0.00	−0.00 0.00	−0.00 0.00	−0.00 0.00	−0.00 0.00	−0.00 0.00	−0.00 0.00	−0.00 0.00	−0.00 0.00	−0.00 0.00
JET_EffectiveNP_Mixed1	−0.03 0.03	−0.05 0.05	−0.08 0.08	−0.14 0.14	−0.17 0.17	−0.14 0.14	−0.07 0.07	−0.04 0.04	−0.03 0.03	−0.02 0.02	−0.01 0.01
JET_EffectiveNP_Mixed2	−0.02 0.02	−0.03 0.03	−0.04 0.04	−0.04 0.04	−0.04 0.04	−0.04 0.04	−0.03 0.03	−0.02 0.02	−0.01 0.01	−0.01 0.01	−0.00 0.00
JET_EffectiveNP_Mixed3	−0.00 0.00	−0.00 0.00	−0.00 0.00	−0.00 0.00	−0.00 0.00	−0.00 0.00	−0.00 0.00	−0.00 0.00	−0.00 0.00	−0.00 0.00	−0.00 0.00
JET_EffectiveNP_Modelling1	−0.12 0.12	−0.16 0.16	−0.20 0.20	−0.25 0.25	−0.26 0.26	−0.18 0.18	−0.09 0.09	−0.04 0.04	−0.03 0.03	−0.02 0.02	−0.02 0.02
JET_EffectiveNP_Modelling2	−0.02 0.02	−0.03 0.03	−0.04 0.04	−0.06 0.06	−0.07 0.07	−0.06 0.06	−0.04 0.04	−0.02 0.02	−0.01 0.01	−0.01 0.01	−0.01 0.01
JET_EffectiveNP_Modelling3	−0.02 0.02	−0.03 0.03	−0.05 0.05	−0.06 0.06	−0.05 0.05	−0.04 0.04	−0.02 0.02	−0.01 0.01	−0.00 0.00	−0.00 0.00	−0.00 0.00
JET_EffectiveNP_Modelling4	−0.01 0.01	−0.01 0.01	−0.02 0.02	−0.03 0.03	−0.03 0.03	−0.03 0.03	−0.02 0.02	−0.01 0.01	−0.01 0.01	−0.01 0.01	−0.01 0.01
JET_EffectiveNP_Statistical1	−0.01 0.01	−0.01 0.01	−0.02 0.02	−0.03 0.03	−0.04 0.04	−0.03 0.03	−0.02 0.02	−0.01 0.01	−0.00 0.00	−0.00 0.00	−0.01 0.01
JET_EffectiveNP_Statistical2	−0.02 0.02	−0.02 0.02	−0.01 0.01	−0.01 0.01	−0.01 0.01	−0.01 0.01	−0.01 0.01	−0.01 0.01	−0.01 0.01	−0.00 0.00	−0.00 0.00
JET_EffectiveNP_Statistical3	−0.02 0.02	−0.02 0.02	−0.03 0.03	−0.04 0.04	−0.04 0.04	−0.03 0.03	−0.01 0.01	−0.00 0.00	−0.00 0.00	−0.00 0.00	−0.00 0.00

	$200 \leq M_T < 250$	$250 \leq M_T < 300$	$300 \leq M_T < 350$	$350 \leq M_T < 425$	$425 \leq M_T < 500$	$500 \leq M_T < 600$	$600 \leq M_T < 750$	$750 \leq M_T < 900$	$900 \leq M_T < 1100$	$1100 \leq M_T < 1400$	$1400 \leq M_T < 2000$
JET_EffectiveNP_Statistical4	−0.01 0.01	−0.02 0.02	−0.03 0.03	−0.04 0.04	−0.04 0.04	−0.03 0.03	−0.02 0.02	−0.01 0.01	−0.00 0.00	−0.00 0.00	−0.00 0.00
JET_EffectiveNP_Statistical5	−0.00 0.00	−0.00 0.00	−0.00 0.00	−0.00 0.00	−0.00 0.00	−0.00 0.00	−0.00 0.00	−0.00 0.00	−0.00 0.00	−0.00 0.00	−0.00 0.00
JET_EffectiveNP_Statistical6	−0.01 0.01	−0.01 0.01	−0.01 0.01	−0.00 0.00	−0.00 0.00	−0.00 0.00	−0.00 0.00	−0.00 0.00	−0.00 0.00	−0.00 0.00	−0.00 0.00
JET_EtaIntercalibration_NonClosure_2018data	−0.04 0.04	−0.05 0.05	−0.07 0.07	−0.11 0.11	−0.13 0.13	−0.10 0.10	−0.05 0.05	−0.03 0.03	−0.02 0.02	−0.01 0.01	−0.01 0.01
JET_EtaIntercalibration_NonClosure_negEta	−0.01 0.01	−0.01 0.01	−0.01 0.01	−0.01 0.01	−0.00 0.00	−0.00 0.00	−0.00 0.00	−0.00 0.00	−0.00 0.00	−0.00 0.00	−0.00 0.00
JET_EtaIntercalibration_NonClosure_posEta	−0.00 0.00	−0.00 0.00	−0.00 0.00	−0.00 0.00	−0.00 0.00	−0.01 0.01	−0.01 0.01	−0.00 0.00	−0.00 0.00	−0.00 0.00	−0.00 0.00
JET_EtaIntercalibration_TotalStat	−0.02 0.02	−0.02 0.02	−0.02 0.02	−0.02 0.02	−0.02 0.02	−0.02 0.02	−0.02 0.02	−0.01 0.01	−0.00 0.00	−0.00 0.00	−0.00 0.00
JET_Flavor_Composition	−0.20 0.20	−0.25 0.25	−0.25 0.25	−0.26 0.26	−0.28 0.28	−0.24 0.24	−0.12 0.12	−0.02 0.02	−0.01 0.01	−0.05 0.05	−0.09 0.09
JET_Flavor_Response	−0.31 0.31	−0.33 0.33	−0.33 0.33	−0.33 0.33	−0.33 0.33	−0.27 0.27	−0.13 0.13	−0.04 0.04	−0.02 0.02	−0.03 0.03	−0.06 0.06
JET_Pileup_OffsetMu	−0.13 0.13	−0.15 0.15	−0.16 0.16	−0.16 0.16	−0.16 0.16	−0.13 0.13	−0.07 0.07	−0.04 0.04	−0.03 0.03	−0.02 0.02	−0.02 0.02
JET_Pileup_OffsetNPV	−0.15 0.15	−0.15 0.15	−0.15 0.15	−0.15 0.15	−0.15 0.15	−0.12 0.12	−0.07 0.07	−0.05 0.05	−0.04 0.04	−0.04 0.04	−0.04 0.04
JET_Pileup_RhoTopology	−0.18 0.18	−0.20 0.20	−0.20 0.20	−0.22 0.22	−0.25 0.25	−0.22 0.22	−0.11 0.11	−0.03 0.03	−0.02 0.02	−0.03 0.03	−0.04 0.04
JET_EtaIntercalibration_Modelling	−0.11 0.11	−0.11 0.11	−0.11 0.11	−0.11 0.11	−0.10 0.10	−0.08 0.08	−0.05 0.05	−0.04 0.04	−0.04 0.04	−0.03 0.03	−0.02 0.02
JET_JER_EffectiveNP_1	−0.30 0.30	−0.30 0.30	−0.30 0.30	−0.30 0.30	−0.30 0.30	−0.28 0.28	−0.20 0.20	−0.09 0.09	−0.02 0.02	−0.03 0.03	−0.09 0.09
JET_JER_EffectiveNP_2	−0.44 0.44	−0.44 0.44	−0.44 0.44	−0.44 0.44	−0.44 0.44	−0.37 0.37	−0.18 0.18	−0.04 0.04	−0.01 0.01	−0.03 0.03	−0.10 0.10
JET_JER_EffectiveNP_3	−0.13 0.13	−0.14 0.14	−0.15 0.15	−0.15 0.15	−0.13 0.13	−0.08 0.08	−0.03 0.03	−0.00 0.00	−0.01 0.01	−0.03 0.03	−0.05 0.05
JET_JER_EffectiveNP_4	−0.16 0.16	−0.16 0.16	−0.16 0.16	−0.14 0.14	−0.10 0.10	−0.07 0.07	−0.05 0.05	−0.03 0.03	−0.04 0.04	−0.05 0.05	−0.07 0.07
JET_JER_EffectiveNP_5	−0.09 0.09	−0.14 0.14	−0.17 0.17	−0.17 0.17	−0.17 0.17	−0.14 0.14	−0.08 0.08	−0.03 0.03	−0.01 0.01	−0.00 0.00	−0.00 0.00
JET_JER_EffectiveNP_6	−0.19 0.19	−0.16 0.16	−0.10 0.10	−0.08 0.08	−0.07 0.07	−0.05 0.05	−0.02 0.02	−0.00 0.00	−0.00 0.00	−0.02 0.02	−0.05 0.05
JET_JER_EffectiveNP_7restTerm	−0.19 0.19	−0.16 0.16	−0.10 0.10	−0.08 0.08	−0.08 0.08	−0.08 0.08	−0.07 0.07	−0.04 0.04	−0.03 0.03	−0.03 0.03	−0.03 0.03
JET_JER_DataVsMC_MC16	−0.01 0.01	−0.03 0.03	−0.07 0.07	−0.11 0.11	−0.13 0.13	−0.14 0.14	−0.13 0.13	−0.07 0.07	−0.03 0.03	−0.03 0.03	−0.08 0.08
JET_Pileup_PtTerm	−0.07 0.07	−0.11 0.11	−0.15 0.15	−0.15 0.15	−0.10 0.10	−0.05 0.05	−0.02 0.02	−0.01 0.01	−0.01 0.01	−0.01 0.01	−0.01 0.01
JET_PunchThrough_MC16	−0.00 −0.00	0.00 −0.00	$-2.08 \cdot 10^{-5}$ −0.00	$-1.26 \cdot 10^{-5}$ 0.00	−0.00 −0.00	0.00 −0.00	−0.00 $-2.84 \cdot 10^{-5}$	0.00 −0.00	−0.00 0.00	$-1.95 \cdot 10^{-5}$ 0.00	0.00 −0.00
MULTIJET_MET	−0.84 0.70	−1.28 1.06	−1.41 1.26	−1.28 1.18	−0.99 0.90	−0.68 0.61	−0.42 0.45	−0.21 0.29	−0.03 0.08	0.11 −0.11	0.23 −0.27
MULTIJET_PT	−1.14	−1.18	−1.14	−1.02	−0.76	−0.44	−0.28	−0.20	−0.05	0.09	0.22
MULTIJET_JETPT	−1.88 0.21	−1.98 0.68	−1.79 0.99	−1.43 1.02	−0.99 0.88	−0.57 0.62	−0.35 0.39	−0.23 0.23	−0.06 0.07	0.10 −0.07	0.24 −0.19
MULTIJET_D0SIG	−1.00 0.46	−1.31 0.88	−1.35 1.12	−1.22 1.11	−0.95 0.89	−0.58 0.62	−0.33 0.41	−0.21 0.21	−0.07 0.03	0.08 −0.09	0.22 −0.21

Table F.2.: This table contains the contribution of individual experimental systematic uncertainties in each bin for $W^- \to \mu^- \bar{\nu}$. The systematics were computed with 10.1 and then summed in quadrature for the final result. The first column is the name of the systematic. All values are presented in percentages.

Systematic	$200 \leq M_T < 250$	$250 \leq M_T < 300$	$300 \leq M_T < 350$	$350 \leq M_T < 425$	$425 \leq M_T < 500$	$500 \leq M_T < 600$	$600 \leq M_T < 750$	$750 \leq M_T < 900$	$900 \leq M_T < 1100$	$1100 \leq M_T < 1400$	$1400 \leq M_T < 2000$
MUON_MS	−0.16	0.10	−1.05	−0.11	−0.37	−2.33	−0.03	−0.19	0.39	−1.24	−0.55
	−0.16	0.09	−0.16	−0.08	1.09	0.83	0.29	−0.09	−0.88	0.99	0.12
MUON_SCALE	−0.02	0.21	−0.35	0.26	0.21	0.09	−0.03	−0.31	−0.13	0.07	0.28
	−0.14	0.08	−0.05	0.37	0.02	−0.85	−0.15	0.10	0.02	−0.17	−0.20
IDSys	−0.03	−0.04	−0.04	−0.09	−0.31	−0.58	−0.13	−0.08	−0.75	−1.97	−1.54
	0.03	0.04	0.04	0.09	0.31	0.57	0.12	0.09	0.73	1.87	1.45
IsoSys	−0.00	−0.02	−0.03	−0.02	−0.02	−0.03	−0.01	$-1.54 \cdot 10^{-5}$	−0.01	0.01	0.00
	0.00	0.02	0.03	0.02	0.03	0.02	0.01	0.00	0.01	−0.01	−0.00
TrigSys	−0.00	−0.00	−0.01	0.02	0.02	0.01	0.00	0.02	0.03	0.03	0.03
	0.00	0.00	0.01	−0.02	−0.02	−0.01	−0.01	−0.02	−0.03	−0.03	−0.03
MUON_SAGITTA_RESBIAS	−3.91	−3.94	−6.15	−8.67	−6.74	−17.89	−11.91	−20.33	−29.61	−35.53	−33.38
	3.64	5.07	5.56	8.62	8.50	10.52	11.33	20.46	28.47	35.09	31.50
MET_SoftTrk_ResoPara	−0.48	0.82	−0.62	−0.18	−1.15	0.17	0.03	0.24	0.01	0.05	0.09
MET_SoftTrk_ResoPerp	−0.19	0.08	−0.47	0.34	−0.44	0.29	0.22	0.29	−0.14	−0.16	0.07
MET_SoftTrk_Scale	0.57	0.37	−0.38	0.28	0.42	−0.29	−0.19	−0.03	−0.12	0.06	0.06
	−0.75	0.21	−0.57	0.22	−0.44	0.41	0.02	0.07	0.03	−0.02	0.01
IDStat	0.00	0.00	0.00	0.00	0.01	−0.00	−0.01	−0.00	−0.01	−0.00	−0.00
	−0.00	−0.00	−0.00	−0.00	0.00	−0.00	−0.00	0.01	0.01	0.01	0.00
IsoStat	−0.01	−0.00	−0.00	$7.90 \cdot 10^{-6}$	0.01	−0.01	−0.01	0.00	0.00	0.01	0.00
	0.01	0.00	0.00	0.00	0.00	0.00	0.00	0.00	−0.00	−0.01	−0.00
PileUp	−0.91	−1.30	−0.26	−0.21	−1.72	−0.26	−0.38	−0.17	−0.33	−0.21	0.11
	−0.33	0.79	−0.48	−0.53	−0.75	−0.76	0.64	0.10	−0.56	−1.18	−0.25
TrigStat	−0.00	0.00	0.00	−0.00	0.02	0.01	0.02	0.03	0.03	0.03	0.02
	0.00	−0.00	−0.00	0.00	−0.01	−0.02	−0.02	−0.03	−0.03	−0.03	−0.02
TTVAStat	−0.00	−0.00	0.00	0.00	0.00	0.00	−0.00	0.01	0.01	0.01	0.01
	0.00	−0.00	−0.00	0.00	0.00	−0.01	−0.01	−0.00	−0.01	−0.01	−0.01
TTVASys	−0.00	−0.00	−0.00	−0.00	0.00	0.00	0.00	0.01	0.01	0.02	0.01
	0.00	0.00	0.00	−0.00	0.00	−0.01	−0.01	−0.01	−0.01	−0.02	−0.01
MUON_SAGITTA_DATASTAT	0.38	0.59	0.48	1.06	0.16	0.54	1.03	1.91	1.87	2.62	2.96
	−0.41	−0.28	−0.93	−0.64	−1.37	−0.64	−0.96	−1.83	−2.20	−2.57	−2.65
MUON_ID	−0.09	−0.01	0.01	−0.09	0.64	−1.05	−0.21	0.02	0.02	0.13	−0.24
	−0.03	0.36	−0.30	0.09	−0.16	−1.28	−0.24	0.39	−0.20	0.07	0.17
JET_BJES_Response	−0.04	0.00	0.01	0.01	−0.01	−0.00	−0.01	0.01	−0.01	0.00	−0.00
	−0.03	−0.06	−0.01	−0.01	0.02	0.01	−0.00	0.00	0.01	0.00	−0.00
JET_EffectiveNP_Detector1	−0.08	−0.04	−0.01	0.03	−0.02	0.01	−0.02	0.02	0.01	0.01	−0.00
	−0.02	0.06	0.04	0.17	−0.49	−0.11	0.04	0.05	−0.00	0.00	−0.00
JET_EffectiveNP_Detector2	−0.00	−0.03	−0.01	0.01	−0.02	0.01	0.00	0.00	0.01	0.00	0.00
	−0.00	0.01	0.00	−0.00	0.00	0.01	0.00	0.00	−0.00	0.00	0.00
JET_EffectiveNP_Mixed1	−0.10	0.05	−0.21	0.52	−0.55	−1.25	−0.11	0.08	0.16	0.11	0.03
	−0.08	0.19	−0.11	0.11	0.11	−1.36	−0.21	0.24	0.01	0.03	−0.04
JET_EffectiveNP_Mixed2	0.01	0.12	0.09	−0.02	−0.54	−0.13	0.03	0.06	0.02	0.03	−0.01
	−0.15	0.02	−0.11	0.30	0.02	−0.01	$6.91 \cdot 10^{-5}$	−0.11	−0.05	0.06	0.02
JET_EffectiveNP_Mixed3	−0.02	−0.03	−0.01	0.01	−0.01	−0.00	0.01	0.01	0.00	0.01	−0.01
	−0.00	0.07	0.00	0.01	−0.00	0.00	$4.91 \cdot 10^{-5}$	0.03	0.01	0.03	−0.01
JET_EffectiveNP_Modelling1	−0.23	0.57	0.09	0.16	0.58	1.02	0.10	−0.31	−0.30	0.09	0.11
	0.07	0.33	−0.22	0.05	−0.07	−0.11	−0.09	0.04	−0.18	−0.04	−0.00
JET_EffectiveNP_Modelling2	−0.02	0.10	0.01	−0.03	−0.47	0.68	0.07	−0.04	−0.00	0.03	0.00
	−0.07	−0.02	0.06	0.18	−0.50	−0.12	0.05	0.07	−0.05	0.01	−0.02
JET_EffectiveNP_Modelling3	−0.02	0.01	0.06	0.18	−0.50	−0.12	0.05	0.04	−0.02	0.02	−0.00
	−0.01	0.11	0.01	0.02	−0.01	−0.02	−0.01	0.03	−0.01	0.04	0.01
JET_EffectiveNP_Modelling4	−0.04	−0.03	−0.00	0.02	−0.03	0.01	0.00	0.00	−0.02	0.03	0.00
	−0.01	0.01	0.04	0.19	−0.50	−0.09	0.05	0.01	0.00	0.01	0.00
JET_EffectiveNP_Statistical1	−0.08	−0.04	0.00	0.04	−0.04	0.00	−0.03	−0.01	−0.00	0.02	0.01
	−0.01	0.00	0.04	0.19	−0.49	−0.09	0.03	0.02	−0.01	0.00	−0.02
JET_EffectiveNP_Statistical2	−0.05	0.06	−0.01	−0.01	0.06	−0.06	−0.01	0.07	0.00	0.03	0.01
	−0.08	−0.01	0.01	0.01	−0.01	−0.02	0.01	−0.04	−0.01	0.00	−0.01
JET_EffectiveNP_Statistical3	0.00	0.00	0.04	0.18	−0.50	−0.08	0.04	0.02	−0.01	−0.00	$-5.12 \cdot 10^{-5}$
	−0.07	0.04	0.02	0.03	−0.06	0.02	−0.03	−0.01	0.00	0.02	0.01

	$200 \leq M_T < 250$	$250 \leq M_T < 300$	$300 \leq M_T < 350$	$350 \leq M_T < 425$	$425 \leq M_T < 500$	$500 \leq M_T < 600$	$600 \leq M_T < 750$	$750 \leq M_T < 900$	$900 \leq M_T < 1100$	$1100 \leq M_T < 1400$	$1400 \leq M_T < 2000$
JET_EffectiveNP_Statistical4	−0.04	0.05	0.01	0.01	−0.01	0.00	−0.01	0.01	−0.01	0.01	0.01
	0.00	−0.01	0.04	0.19	−0.50	−0.09	0.06	0.02	−0.02	0.03	0.00
JET_EffectiveNP_Statistical5	−0.02	0.01	−0.01	0.01	−0.01	0.00	0.01	−0.00	−0.01	0.02	0.00
	−0.03	−0.04	−0.00	0.00	−0.03	−0.00	0.00	0.01	−0.00	0.01	0.01
JET_EffectiveNP_Statistical6	−0.04	−0.03	−0.01	0.02	−0.03	0.00	0.02	0.01	−0.02	0.02	−0.00
	−0.00	0.07	0.02	−0.00	−0.01	−0.00	0.02	0.01	−0.00	0.01	−0.01
JET_EtaIntercalibration_NonClosure_2018data	0.24	0.11	−0.25	0.07	−0.10	−1.01	−0.04	0.10	−0.07	0.08	0.01
	−0.02	−0.11	0.07	0.18	−0.47	−0.13	−0.02	0.14	−0.01	−0.02	0.01
JET_EtaIntercalibration_NonClosure_negEta	0.05	0.03	0.06	−0.01	−0.00	0.00	−0.01	0.02	−0.00	−0.02	0.01
	0.02	−0.03	−0.16	0.12	0.02	−0.02	0.02	0.00	0.01	0.01	−0.01
JET_EtaIntercalibration_NonClosure_posEta	0.03	−0.04	−0.03	0.01	0.00	−0.01	0.01	0.01	0.04	0.01	−0.01
	−0.04	0.03	0.01	0.01	0.01	−0.03	0.03	−0.01	−0.02	−0.00	0.00
JET_EtaIntercalibration_TotalStat	−0.13	−0.06	0.20	0.01	−0.03	0.00	0.04	−0.01	−0.02	0.01	0.02
	−0.04	0.04	0.08	0.21	0.10	−0.12	0.04	0.06	−0.02	0.06	−0.02
JET_Flavor_Composition	−0.62	0.47	−0.68	−0.10	1.37	−0.08	0.07	−0.23	−0.42	0.18	0.18
	−0.06	−0.29	−0.22	−0.16	−0.19	−1.16	0.25	−0.05	−0.35	−0.04	0.15
JET_Flavor_Response	−0.52	0.10	0.02	0.20	0.05	−1.13	−0.23	0.09	−0.13	−0.04	0.06
	0.09	0.95	−0.38	−0.51	0.99	−0.35	0.09	−0.10	−0.19	0.19	0.15
JET_Pileup_OffsetMu	−0.25	−0.60	0.48	−0.02	0.24	0.29	0.21	−0.05	−0.31	0.06	0.06
	0.70	0.19	−0.06	0.39	−0.55	−0.49	0.06	−0.20	−0.14	0.09	−0.02
JET_Pileup_OffsetNPV	−0.50	−0.10	−0.06	−0.07	0.76	0.24	−0.03	−0.17	−0.39	0.15	0.07
	−0.10	0.26	0.39	0.45	−0.91	−0.39	0.21	−0.09	−0.17	−0.05	−0.02
JET_Pileup_RhoTopology	−0.30	0.73	0.19	−0.22	1.06	0.98	0.07	0.04	−0.37	0.10	0.09
	−0.15	0.27	0.35	0.05	−0.63	−0.22	0.20	−0.01	−0.16	−0.02	0.06
JET_EtaIntercalibration_Modelling	−0.38	0.37	−0.30	−0.16	0.23	0.42	0.09	−0.14	−0.36	0.15	0.07
	0.47	0.11	0.57	−0.21	−0.71	−0.42	0.21	−0.09	−0.24	0.06	0.05
JET_JER_EffectiveNP_1	2.02	0.61	0.29	−0.08	0.83	−1.22	−0.03	−0.44	−0.05	−0.09	0.02
	2.02	0.61	0.29	−0.08	0.83	−1.22	−0.03	−0.44	−0.05	−0.09	0.02
JET_JER_EffectiveNP_2	1.33	0.66	0.32	−0.31	1.93	0.04	−0.00	−0.43	−0.06	−0.18	0.03
	1.33	0.66	0.32	−0.31	1.93	0.04	−0.00	−0.43	−0.06	−0.18	0.03
JET_JER_EffectiveNP_3	0.14	0.35	0.03	−0.23	0.27	1.38	0.30	−0.31	0.06	−0.15	−0.00
	0.14	0.35	0.03	−0.23	0.27	1.38	0.30	−0.31	0.06	−0.15	−0.00
JET_JER_EffectiveNP_4	0.55	0.47	−0.11	−0.45	−0.30	0.74	0.19	−0.43	−0.06	−0.12	0.08
	0.55	0.47	−0.11	−0.45	−0.30	0.74	0.19	−0.43	−0.06	−0.12	0.08
JET_JER_EffectiveNP_5	0.38	0.15	−0.22	0.33	0.05	−0.12	0.08	−0.34	0.15	−0.02	0.05
	0.38	0.15	−0.22	0.33	0.05	−0.12	0.08	−0.34	0.15	−0.02	0.05
JET_JER_EffectiveNP_6	0.35	0.26	−0.23	−0.31	−0.07	−0.73	0.07	−0.19	0.09	−0.01	0.05
	0.35	0.26	−0.23	−0.31	−0.07	−0.73	0.07	−0.19	0.09	−0.01	0.05
JET_JER_EffectiveNP_7restTerm	0.35	0.57	0.10	−0.35	0.05	1.32	0.24	−0.49	−0.05	−0.08	0.01
	0.35	0.57	0.10	−0.35	0.05	1.32	0.24	−0.49	−0.05	−0.08	0.01
JET_JER_DataVsMC_MC16	−0.19	0.09	0.57	−0.20	−0.12	−0.40	−0.18	−0.27	−0.13	−0.03	0.11
	−0.19	0.09	0.57	−0.20	−0.12	−0.40	−0.18	−0.27	−0.13	−0.03	0.11
JET_Pileup_PtTerm	0.27	0.42	−0.61	0.20	0.09	−0.07	0.05	0.03	−0.12	0.04	0.02
	−0.15	0.16	−0.94	−0.28	−0.40	−0.08	0.09	−0.05	0.03	−0.04	−0.02
JET_PunchThrough_MC16	0.00	0.00	0.00	−0.00	0.01	0.00	−0.00	0.00	−0.00	−0.00	0.00
	0.00	−0.00	−0.00	0.00	0.01	−0.00	−0.00	0.00	−0.00	0.01	−0.00
MULTIJET_MET	−0.47	−0.83	−1.06	−0.88	−0.63	−0.24	−0.69	0.28	−0.65	0.56	0.26
	−0.61	−1.02	−1.19	−0.96	−0.71	−0.35	−0.62	0.21	−0.35	0.63	0.19
MULTIJET_PT	−0.57	−0.95	−1.17	−0.93	−0.71	−0.28	−0.57	0.21	−0.54	0.40	0.21
MULTIJET_JETPT	−0.04	−0.64	−1.00	−0.85	−0.70	−0.41	−0.57	0.16	−0.50	0.35	0.18
	−1.29	−1.43	−1.39	−1.12	−0.73	−0.20	−0.57	0.26	−0.65	0.47	0.24
MULTIJET_D0SIG	−0.33	−0.78	−1.14	−0.73	−0.68	−0.33	−0.68	0.16	−0.45	0.56	0.21
	−0.73	−1.07	−1.21	−0.96	−0.73	−0.25	−0.67	0.21	−0.55	0.34	0.21

Table F.3.: This table contains the contribution of individual experimental systematic uncertainties in each bin for the charge asymmetry. The systematics were computed with 10.2 and then summed in quadrature for the final result. The first column is the name of the systematic. All values are presented in percentages.

References

[1] R. L. Workman and Others. "Review of Particle Physics". *PTEP* 2022 (2022), p. 083C01. doi: 10.1093/ptep/ptac097.

[2] Lyndon Evans and Philip Bryant. "LHC Machine". *Journal of Instrumentation* 3.08 (2008), S08001–S08001. doi: 10.1088/1748-0221/3/08/s08001. url: https://doi.org/10.1088/1748-0221/3/08/s08001.

[3] J. T. Boyd. *LHC Run-2 and Future Prospects*. 2020. doi: 10.48550/ARXIV.2001.04370. url: https://arxiv.org/abs/2001.04370.

[4] ATLAS Collaboration. "The ATLAS Experiment at the CERN Large Hadron Collider". *JINST* 3 (2008), S08003. doi: 10.1088/1748-0221/3/08/S08003.

[5] ATLAS Collaboration. "Measurement of the cross-section and charge asymmetry of W bosons produced in proton–proton collisions at 8 TeV with the ATLAS detector". *The European Physical Journal C* 79.9 (2019). doi: 10.1140/epjc/s10052-019-7199-0. url: https://doi.org/10.1140%2Fepjc%2Fs10052-019-7199-0.

[6] CMS Collaboration. "Measurements of the W boson rapidity, helicity, double-differential cross sections, and charge asymmetry in pp collisions at 13 TeV". *Physical Review D* 102.9 (2020). doi: 10.1103/physrevd.102.092012. url: https://doi.org/10.1103%2Fphysrevd.102.092012.

[7] *ATLAS Physics Modelling Group*. https://twiki.cern.ch/twiki/bin/view/AtlasProtected/PhysicsModellingGroup. Accessed: 08-03-2023.

[8] ATLAS. "AnalysisTop Software". 2023. url: https://twiki.cern.ch/twiki/bin/view/AtlasProtected/AnalysisTop21.

[9] R. Loll et al. *Quantum Gravity in 30 Questions*. 2022. doi: 10.48550/ARXIV.2206.06762. url: https://arxiv.org/abs/2206.06762.

[10] A. K. Halder, Andronikos Paliathanasis, and P. G. L. Leach. *Noether's Theorem and Symmetry*. 2018. doi: 10.48550/ARXIV.1812.03682. url: https://arxiv.org/abs/1812.03682.

[11] Max Bañ ados and Ignacio Reyes. "A short review on Noether's theorems, gauge symmetries and boundary terms". *International Journal of Modern Physics D* 25.10 (2016), p. 1630021. doi: 10.1142/s0218271816300214. url: https://doi.org/10.1142%2Fs0218271816300214.

[12] Rohini M. Godbole. “Field Theory and the Electro-Weak Standard Model” (2017). 61 pages and 34 figures, 1–61. 61 p. doi: 10.23730/CYRSP-2017-002.1. arXiv: 1703.04978. url: https://cds.cern.ch/record/2315320.

[13] Peter W. Higgs. “Broken Symmetries and the Masses of Gauge Bosons”. *Phys. Rev. Lett.* 13 (16 1964), pp. 508–509. doi: 10.1103/PhysRevLett.13.508. url: https://link.aps.org/doi/10.1103/PhysRevLett.13.508.

[14] F. Englert and R. Brout. “Broken Symmetry and the Mass of Gauge Vector Mesons”. *Phys. Rev. Lett.* 13 (9 1964), pp. 321–323. doi: 10.1103/PhysRevLett.13.321. url: https://link.aps.org/doi/10.1103/PhysRevLett.13.321.

[15] UA1 Collaboration. “Experimental observation of isolated large transverse energy electrons with associated missing energy at s=540 GeV”. *Physics Letters B* 122.1 (1983), pp. 103–116. issn: 0370-2693. doi: https://doi.org/10.1016/0370-2693(83)91177-2. url: https://www.sciencedirect.com/science/article/pii/0370269383911772.

[16] UA2 Collaboration. “Observation of single isolated electrons of high transverse momentum in events with missing transverse energy at the CERN pp collider”. *Physics Letters B* 122.5 (1983), pp. 476–485. issn: 0370-2693. doi: https://doi.org/10.1016/0370-2693(83)91605-2. url: https://www.sciencedirect.com/science/article/pii/0370269383916052.

[17] ATLAS Collaboration. “Observation of a new particle in the search for the Standard Model Higgs boson with the ATLAS detector at the LHC”. *Physics Letters B* 716.1 (Sept. 2012), 1–29. issn: 0370-2693. doi: 10.1016/j.physletb.2012.08.020. url: http://dx.doi.org/10.1016/j.physletb.2012.08.020.

[18] Alexandre Deur, Stanley J. Brodsky, and Guy F. de Téramond. “The QCD running coupling”. *Progress in Particle and Nuclear Physics* 90 (2016), pp. 1–74. doi: 10.1016/j.ppnp.2016.04.003. url: https://doi.org/10.1016%2Fj.ppnp.2016.04.003.

[19] P. A. Zyla et al. “Review of Particle Physics”. *PTEP* 2020.8 (2020), p. 083C01. doi: 10.1093/ptep/ptaa104.

[20] Henry W. Kendall. “Deep Inelastic Scattering: Experiments On The Proton and The Observation of Scaling”. 1990. url: https://www.nobelprize.org/uploads/2018/06/kendall-lecture-1.pdf.

[21] Ringaile Placakyte. “Parton Distribution Functions”. *Proceedings, 31st International Conference on Physics in collisions (PIC 2011): Vancouver, Canada, August 28-September 1, 2011*. 2011. arXiv: 1111.5452 [hep-ph].

[22] Tung-Mow Yan and Sidney D. Drell. “The parton model and its applications”. *International Journal of Modern Physics A* 29.30 (2014), p. 1430071. doi: 10.1142/s0217751x14300713. url: https://doi.org/10.1142%2Fs0217751x14300713.

[23] E. Perez and E. Rizvi. “The Quark and Gluon Structure of the Proton”. *Rept. Prog. Phys.* 76 (2013), p. 046201. doi: 10.1088/0034-4885/76/4/046201. arXiv: 1208.1178 [hep-ex].

[24] S. Bailey et al. “Parton distributions from LHC, HERA, Tevatron and fixed target data: MSHT20 PDFs”. *The European Physical Journal C* 81.4 (2021). doi: 10.1140/epjc/s10052-021-09057-0. url: https://doi.org/10.1140%2Fepjc%2Fs10052-021-09057-0.

[25] X. Ji. *Probing the Internal Structure of the Proton*. https://www.physics.umd.edu/courses/Phys741/xji/chapter4.pdf. Accessed: 28-08-2018.

[26] S. D. Drell and Tung-Mow Yan. “Massive Lepton Pair Production in Hadron-Hadron Collisions at High-Energies”. *Phys. Rev. Lett.* 25 (1970), pp. 316–320. doi: 10.1103/PhysRevLett.25.316,10.1103/PhysRevLett.25.902.2.

[27] Eram Rizvi. *PDF and BSM Effects in High Mass Tails*. Conference in Paris-Saclay, France, (Private Communication). https://indico.cern.ch/event/835066/contributions/3599445/attachments/1957337/3251839/UltimatePrecision-2019.pdf.

[28] Ryan Gavin et al. “FEWZ 2.0: A code for hadronic Z production at next-to-next-to-leading order”. *Computer Physics Communications* 182.11 (Nov. 2011), 2388–2403. issn: 0010-4655. doi: 10.1016/j.cpc.2011.06.008. url: http://dx.doi.org/10.1016/j.cpc.2011.06.008.

[29] Ryan Gavin et al. *W physics at the LHC with FEWZ 2.1*. 2012. arXiv: 1201.5896 [hep-ph].

[30] Ye Li and Frank Petriello. “Combining QCD and electroweak corrections to dilepton production in the framework of the FEWZ simulation code”. *Physical Review D* 86.9 (Nov. 2012). issn: 1550-2368. doi: 10.1103/physrevd.86.094034. url: http://dx.doi.org/10.1103/PhysRevD.86.094034.

[31] Stefano Catani and Massimiliano Grazzini. “Next-to-Next-to-Leading-Order Subtraction Formalism in Hadron Collisions and its Application to Higgs-Boson Production at the Large Hadron Collider”. *Physical Review Letters* 98.22 (May 2007). issn: 1079-7114. doi: 10.1103/physrevlett.98.222002. url: http://dx.doi.org/10.1103/PhysRevLett.98.222002.

[32] Stefano Catani et al. “Vector Boson Production at Hadron Colliders: A Fully Exclusive QCD Calculation at Next-to-Next-to-Leading Order”. *Physical Review Letters* 103.8 (Aug. 2009). issn: 1079-7114. doi: 10.1103/physrevlett.103.082001. url: http://dx.doi.org/10.1103/PhysRevLett.103.082001.

[33] R. Hamberg, W. L. van Neerven, and T. Matsuura. "A complete calculation of the order $\alpha - s^2$ correction to the Drell-Yan K factor". *Nucl. Phys. B* 359 (1991). [Erratum: Nucl.Phys.B 644, 403–404 (2002)], pp. 343–405. doi: 10.1016/0550-3213(91)90064-5.

[34] Charalampos Anastasiou et al. "High-precision QCD at hadron colliders: Electroweak gauge boson rapidity distributions at next-to-next-to leading order". *Physical Review D* 69.9 (May 2004). issn: 1550-2368. doi: 10.1103/physrevd.69.094008. url: http://dx.doi.org/10.1103/PhysRevD.69.094008.

[35] J. Butterworth et al. *Les Houches 2013: Physics at TeV Colliders: Standard Model Working Group Report*. 2014. arXiv: 1405.1067 [hep-ph].

[36] Marco Farina et al. "Energy helps accuracy: electroweak precision tests at hadron colliders". *Phys. Lett.* B772 (2017), pp. 210–215. doi: 10.1016/j.physletb.2017.06.043. arXiv: 1609.08157 [hep-ph].

[37] Stefano Carrazza et al. "Can New Physics hide inside the proton?" (2019). arXiv: 1905.05215 [hep-ph].

[38] James D. Wells and Zhengkang Zhang. "Effective theories of universal theories". *Journal of High Energy Physics* 2016.1 (2016). doi: 10.1007/jhep01(2016)123. url: https://doi.org/10.1007%2Fjhep01%282016%29123.

[39] CMS Collaboration. "The CMS Experiment at the CERN LHC". *JINST* 3 (2008), S08004. doi: 10.1088/1748-0221/3/08/S08004. arXiv: 0806.4949 [physics.ins-det].

[40] CERN. *CERN: Accelerating Science*. [Online; accessed 23-March-2023]. 2023. url: https://home.cern/.

[41] "LHC Guide". 2017. url: http://cds.cern.ch/record/2255762.

[42] Esma Mobs. "The CERN accelerator complex. Complexe des accélérateurs du CERN" (2016). General Photo. url: https://cds.cern.ch/record/2197559.

[43] V.A. Khoze et al. "Luminosity measuring processes at the LHC". *European Physical Journal C* 19 (Feb. 2001), pp. 313–322. doi: 10.1007/s100520100616.

[44] *Accelerators*. https://https://home.cern/science/accelerators. Accessed: 18-01-2022.

[45] *Luminosity determination in pp collisions at* $\sqrt{s} = 13$ *TeV using the ATLAS detector at the LHC*. Tech. rep. All figures including auxiliary figures are available at https://atlas.web.cern.ch/Atlas/GROUPS/PHYSICS/CONFNOTES/ATLAS-CONF-2019-021. Geneva: CERN, 2019. url: https://cds.cern.ch/record/2677054.

[46] Gregory Soyez. "Pileup mitigation at the LHC A theorist's view". *Physics Reports* 803 (Jan. 2018). doi: 10.1016/j.physrep.2019.01.007.

[47] ATLAS Outreach. “ATLAS Fact Sheet : To raise awareness of the ATLAS detector and collaboration on the LHC”. 2010. url: https://cds.cern.ch/record/1457044.

[48] Abraham Seiden. “Characteristics of the ATLAS and CMS detectors”. 370.1961 (2012), pp. 892–906. doi: 10.1098/rsta.2011.0461.

[49] Joao Pequenao. “Computer generated image of the whole ATLAS detector”. 2008. url: https://cds.cern.ch/record/1095924.

[50] The ATLAS Collaboration. “Performance of missing transverse momentum reconstruction with the ATLAS detector using proton–proton collisions at $\sqrt{s} = 13$ TeV”. *The European Physical Journal C* 78.11 (2018). doi: 10.1140/epjc/s10052-018-6288-9. url: https://doi.org/10.1140%2Fepjc%2Fs10052-018-6288-9.

[51] H.H.J. ten Kate. “The ATLAS superconducting magnet system at the Large Hadron Collider”. *Physica C: Superconductivity* 468.15 (2008). Proceedings of the 20th International Symposium on Superconductivity (ISS 2007), pp. 2137 –2142. issn: 0921-4534. doi: https://doi.org/10.1016/j.physc.2008.05.146. url: http://www.sciencedirect.com/science/article/pii/S0921453408004541.

[52] J. Goodson. *Magent Systems*. http://www.jetgoodson.com/images/thesisImages/magnetSystems.png. Accessed: 21-08-2018.

[53] *ATLAS inner detector: Technical Design Report, 1*. Technical Design Report ATLAS. Geneva: CERN, 1997. url: https://cds.cern.ch/record/331063.

[54] ATLAS Collaboration. “The ATLAS Inner Detector commissioning and calibration”. *Eur. Phys. J.* C70 (2010), pp. 787–821. doi: 10.1140/epjc/s10052-010-1366-7. arXiv: 1004.5293 [physics.ins-det].

[55] Joao Pequenao. “Computer generated image of the ATLAS inner detector”. 2008. url: https://cds.cern.ch/record/1095926.

[56] L. Taylor. *Silicon Pixels*. http://cms.web.cern.ch/news/silicon-pixels. Accessed: 22-08-2018.

[57] A Vogel. *ATLAS Transition Radiation Tracker (TRT): Straw Tube Gaseous Detectors at High Rates*. Tech. rep. ATL-INDET-PROC-2013-005. Geneva: CERN, 2013. url: https://cds.cern.ch/record/1537991.

[58] ATLAS Collaboration. “Performance of the ATLAS Transition Radiation Tracker in Run 1 of the LHC: tracker properties”. *Journal of Instrumentation* 12.05 (May 2017), P05002–P05002. issn: 1748-0221. doi: 10.1088/1748-0221/12/05/p05002. url: http://dx.doi.org/10.1088/1748-0221/12/05/P05002.

[59] M Capeans et al. *ATLAS Insertable B-Layer Technical Design Report*. Tech. rep. 2010. url: https://cds.cern.ch/record/1291633.

[60] Alessandro La Rosa. *The ATLAS Insertable B-Layer: from construction to operation*. 2016. arXiv: 1610.01994 [physics.ins-det].

[61] Yosuke Takubo. *ATLAS IBL operational experience*. Tech. rep. Geneva: CERN, 2017. doi: 10.22323/1.287.0004. url: https://cds.cern.ch/record/2235541.

[62] H. Pernegger. "The Pixel Detector of the ATLAS experiment for LHC Run-2". *Journal of Instrumentation* 10 (June 2015), pp. C06012–C06012. doi: 10.1088/1748-0221/10/06/C06012.

[63] Joao Pequenao. "Computer Generated image of the ATLAS calorimeter". 2008. url: https://cds.cern.ch/record/1095927.

[64] Dag Gillberg and (On behalf ofthe ATLAS Liquid Argon Calorimeter Group). "Performance of the ATLAS Forward Calorimeters in First LHC Data". *Journal of Physics: Conference Series* 293.1 (2011), p. 012041. doi: 10.1088/1742-6596/293/1/012041. url: https://dx.doi.org/10.1088/1742-6596/293/1/012041.

[65] *ATLAS muon spectrometer: Technical Design Report*. Technical Design Report ATLAS. Geneva: CERN, 1997. url: http://cds.cern.ch/record/331068.

[66] D G Drakoulakos et al. "The high-precision x-ray tomograph for quality control of the ATLAS MDT muon spectrometer" (Aug. 2018). url: https://www.researchgate.net/publication/41586323_The_high-precision_x-ray_tomograph_for_quality_control_of_the_ATLAS_MDT_muon_spectrometer.

[67] ATLAS collaboration. "Operation of the ATLAS trigger system in Run 2". *Journal of Instrumentation* 15.10 (Oct. 2020), P10004–P10004. issn: 1748-0221. doi: 10.1088/1748-0221/15/10/p10004. url: http://dx.doi.org/10.1088/1748-0221/15/10/P10004.

[68] A Ruiz Martínez and on behalf of the ATLAS Collaboration. "The Run-2 ATLAS Trigger System". *Journal of Physics: Conference Series* 762.1 (2016), p. 012003. doi: 10.1088/1742-6596/762/1/012003. url: https://dx.doi.org/10.1088/1742-6596/762/1/012003.

[69] *ATLAS Muon Combined Performance*. https://twiki.cern.ch/twiki/bin/view/AtlasProtected/MuonPerformance. Accessed: 09-03-2023.

[70] ATLAS Collaboration. "Muon reconstruction performance of the ATLAS detector in proton–proton collision data at $\sqrt{s}$ =13 TeV". *The European Physical Journal C* 76.5 (2016). issn: 1434-6052. doi: 10.1140/epjc/s10052-016-4120-y. url: http://dx.doi.org/10.1140/epjc/s10052-016-4120-y.

[71] ATLAS Collaboration. "Measurement of the muon reconstruction performance of the ATLAS detector using 2011 and 2012 LHC proton–proton collision data". *The European Physical Journal C* 74.11 (2014). issn: 1434-6052. doi: 10.1140/epjc/s10052-014-3130-x. url: http://dx.doi.org/10.1140/epjc/s10052-014-3130-x.

[72] *Tag and Probe*. Accessed: 09-03-2023. url: https://twiki.cern.ch/twiki/bin/view/Sandbox/TestTopic11111203.

[73] ATLAS Collaboration. "Muon reconstruction and identification efficiency in ATLAS using the full Run 2 pp collision data set at $\sqrt{s} = 13$ TeV". *Eur. Phys. J., C* 81 (2021), p. 578. doi: 10.1140/epjc/s10052-021-09233-2. arXiv: 2012.00578. url: https://cds.cern.ch/record/2746302.

[74] ATLAS Collaboration. "Electron reconstruction and identification in the ATLAS experiment using the 2015 and 2016 LHC proton-proton collision data at $\sqrt{s} = 13$ TeV". *Eur. Phys. J. C* 79.8 (2019), p. 639. doi: 10.1140/epjc/s10052-019-7140-6. arXiv: 1902.04655. url: https://cds.cern.ch/record/2657964.

[75] Matteo Cacciari, Gavin P Salam, and Gregory Soyez. "The anti-ktjet clustering algorithm". *Journal of High Energy Physics* 2008.04 (Apr. 2008), 063–063. issn: 1029-8479. doi: 10.1088/1126-6708/2008/04/063. url: http://dx.doi.org/10.1088/1126-6708/2008/04/063.

[76] Steven Schramm. *ATLAS Jet Reconstruction, Calibration, and Tagging of Lorentz-boosted Objects*. Tech. rep. Geneva: CERN, 2017. url: https://cds.cern.ch/record/2291608.

[77] *ATLAS Jet and Etmiss Combined Performance Group*. https://twiki.cern.ch/twiki/bin/view/AtlasProtected/JetEtMiss. Accessed: 11-01-2024.

[78] ATLAS Collaboration. *Technical Design Report for the Phase-I Upgrade of the ATLAS TDAQ System*. Tech. rep. CERN-LHCC-2013-018. ATLAS-TDR-023. Final version presented to December 2013 LHCC. 2013. url: https://cds.cern.ch/record/1602235.

[79] Reinhard Schwienhorst. *The Phase-1 Upgrade of the ATLAS First Level Calorimeter Trigger*. Tech. rep. ATL-DAQ-PROC-2015-047. 01. Geneva: CERN, 2015. doi: 10.1088/1748-0221/11/01/C01018. url: https://cds.cern.ch/record/2062021.

[80] W. Buttinger. "The ATLAS Level-1 Trigger System". *J.Phys* 1 (2012), pp. 1–14. doi: 10.1088/1742-6596/396/1/012010.

[81] Carlo Oleari. "The POWHEG-BOX". *Nucl. Phys. Proc. Suppl.* 205-206 (2010), pp. 36–41. doi: 10.1016/j.nuclphysbps.2010.08.016. arXiv: 1007.3893 [hep-ph].

[82] Torbjörn Sjöstrand, Stephen Mrenna, and Peter Skands. "A Brief Introduction to PYTHIA 8.1". English. *Computer Physics Communications* 178.11 (2008), pp. 852–867. issn: 0010-4655. doi: 10.1016/j.cpc.2008.01.036.

[83] M (CERN) Aleksa et al. *ATLAS Liquid Argon Calorimeter Phase-I Upgrade Technical Design Report*. Tech. rep. CERN-LHCC-2013-017. ATLAS-TDR-022. Final version presented to December 2013 LHCC. 2013. url: https://cds.cern.ch/record/1602230.

[84] *ROOT TGraphAsymmErrors*. Accessed: 08-03-2023. url: https://root.cern.ch/doc/master/classTGraphAsymmErrors.html.

[85] *Athena*. https://gitlab.cern.ch/atlas/athena. Accessed: 02-03-2021.

[86] *ATLAS Good Run Lists For Analysis Run2*. https://twiki.cern.ch/twiki/bin/viewauth/AtlasProtected/GoodRunListsForAnalysisRun2. Accessed: 02-03-2021.

[87] *Total Integrated Luminosity and Data Quality in 2015-2018*. https://twiki.cern.ch/twiki/bin/view/AtlasPublic/LuminosityPublicResultsRun2. Accessed: 15-08-2019.

[88] G. Cowan. *Statistical Data Analysis*. Oxford science publications. Clarendon Press, 1998. isbn: 9780198501565. url: https://books.google.co.uk/books?id=JhL2FiF3hO4C.

[89] P.A. Zyla et al. "Review of Particle Physics". *PTEP* 2020.8 (2020), p. 083C01. doi: 10.1093/ptep/ptaa104.

[90] Golonka, P. and Was, Z. "PHOTOS Monte Carlo: a precision tool for QED correctionsin Z and W decays". *Eur. Phys. J. C* 45.1 (2006), pp. 97–107. doi: 10.1140/epjc/s2005-02396-4. url: https://doi.org/10.1140/epjc/s2005-02396-4.

[91] Stefano Frixione, Paolo Nason, and Carlo Oleari. "Matching NLO QCD computations with parton shower simulations: the POWHEG method". *Journal of High Energy Physics* 2007.11 (2007), 070–070. issn: 1029-8479. doi: 10.1088/1126-6708/2007/11/070. url: http://dx.doi.org/10.1088/1126-6708/2007/11/070.

[92] Stefano Agostinelli. "Geant4 — a simulation toolkit". *Nucl. Instrum. Methods Phys. A* 506 (Jan. 2003).

[93] *Proposal for truth particle observable definitions in physics measurements*. Tech. rep. All figures including auxiliary figures are available at https://atlas.web.cern.ch/Atlas/GROUPS/PHYSICS/PUBNOTES/ATL-PHYS-PUB-2015-013. Geneva: CERN, 2015. url: https://cds.cern.ch/record/2022743.

[94] Andy Buckley. "ATLAS Monte Carlo generator tunes to LHC data" (2010), pp. 167–173. doi: 10.1109/NSSMIC.2010.5873738.

[95] Paolo Nason. "A New Method for Combining NLO QCD with Shower Monte Carlo Algorithms". *Journal of High Energy Physics* 2004.11 (2004), 040–040. issn: 1029-8479. doi: 10.1088/1126-6708/2004/11/040. url: http://dx.doi.org/10.1088/1126-6708/2004/11/040.

[96] *ATLAS Metadata Interface*. https://ami.in2p3.fr/. Accessed: 02-03-2021.

[97] *Scaling*. https://gitlab.cern.ch/atlas/athenahttps://danikam.github.io/2019-08-19-usatlas-recast-tutorial/09-scaling/index.html. Accessed: 09-03-2021.

[98] ATLAS. “LPXKfactorTool Software”. Accessed: 05-01-2024. 2023. url: https://twiki.cern.ch/twiki/bin/view/AtlasProtected/LPXKfactorTool.

[99] Andres Ramirez Morales. “Measurement of the cross section and muon charge asymmetry from charged current Drell-Yan process at 13 TeV centre of mass energy with the ATLAS detector”. 2018. url: https://cds.cern.ch/record/2717124.

[100] ATLAS Collaboration. “ATLAS data quality operations and performance for 2015 – 2018 data-taking”. *JINST* 15.04 (2020), P04003. doi: 10.1088/1748-0221/15/04/P04003. arXiv: 1911.04632 [physics.ins-det].

[101] Olivier Simard. “The monitoring and data quality assessment of the ATLAS liquid argon calorimeter”. *J. Phys. Conf. Ser.* 587.1 (2015), p. 012008. doi: 10.1088/1742-6596/587/1/012008.

[102] ATLAS Collaboration. “Reconstruction of primary vertices at the ATLAS experiment in Run 1 proton–proton collisions at the LHC”. *The European Physical Journal C* 77.5 (2017). issn: 1434-6052. doi: 10.1140/epjc/s10052-017-4887-5. url: http://dx.doi.org/10.1140/epjc/s10052-017-4887-5.

[103] S. Boutle et al. “Primary vertex reconstruction at the ATLAS experiment”. *J. Phys. Conf. Ser.* 898.4 (2017). Ed. by Richard Mount and Craig Tull, p. 042056. doi: 10.1088/1742-6596/898/4/042056.

[104] The ATLAS collaboration. “Operation of the ATLAS trigger system in Run 2”. *Journal of Instrumentation* 15.10 (2020), P10004–P10004. issn: 1748-0221. doi: 10.1088/1748-0221/15/10/p10004. url: http://dx.doi.org/10.1088/1748-0221/15/10/P10004.

[105] *Selection of jets produced in 13TeV proton-proton collisions with the ATLAS detector*. Tech. rep. All figures including auxiliary figures are available at https://atlas.web.cern.ch/Atlas/GROUPS/PHYSICS/CONFNOTES/ATLAS-CONF-2015-029. Geneva: CERN, 2015. url: https://cds.cern.ch/record/2037702.

[106] ATLAS Collaboration. “Measurement of the double-differential high-mass Drell-Yan cross section in pp collisions at $\sqrt{s} = 8$ TeV with the ATLAS detector”. *Journal of High Energy Physics* 2016.8 (2016). issn: 1029-8479. doi: 10.1007/jhep08(2016)009. url: http://dx.doi.org/10.1007/JHEP08(2016)009.

[107] ATLAS Collaboration. “Muon reconstruction performance of the ATLAS detector in proton–proton collision data at $\sqrt{s}$ =13 TeV”. *Eur. Phys. J. C* 76.5 (2016), p. 292. doi: 10.1140/epjc/s10052-016-4120-y. arXiv: 1603.05598 [hep-ex].

[108] *Flavor Tagging with Track Jets in Boosted Topologies with the ATLAS Detector*. Tech. rep. Geneva: CERN, 2014. url: https://cds.cern.ch/record/1750681.

[109] *ROOT Reference Guide: Smooth*. https://root.cern.ch/doc/master/classTH1.html#a0d08651c37b622f4bcc0e1a0affefb33. Accessed: 16-01-2024.

[110] J H Friedman. “Data analysis techniques for high energy particle physics” (1974). doi: 10.5170/CERN-1974-023.271. url: https://cds.cern.ch/record/695770.

[111] ATLAS Colalboration. “Measurement of the W charge asymmetry in the $W \to \mu\nu$ decay mode in pp collisions at $\sqrt{s} = 7$ TeV with the ATLAS detector.” *Phys. Lett. B* 701 (2013). 8 pages plus author list (23 pages total), 6 figure, 3 tables, submitted to Phys. Lett. B, pp. 31–49. doi: 10.1016/j.physletb.2011.05.024. arXiv: 1103.2929. url: https://cds.cern.ch/record/1336252.

[112] ATLAS Colalboration. “Electron reconstruction and identification in the ATLAS experiment using the 2015 and 2016 LHC proton–proton collision data at $\sqrt{s} =$ 13 TeV”. *The European Physical Journal C* 79.8 (2019). issn: 1434-6052. doi: 10.1140/epjc/s10052-019-7140-6. url: http://dx.doi.org/10.1140/epjc/s10052-019-7140-6.

[113] ATLAS Collaboration. “Jet energy scale measurements and their systematic uncertainties in proton-proton collisions at $\sqrt{s} = 13$ TeV with the ATLAS detector. Jet energy scale measurements and their systematic uncertainties in proton-proton collisions at $\sqrt{s} = 13$ TeV with the ATLAS detector”. *Phys. Rev. D* 96.7 (2017), p. 072002. doi: 10.1103/PhysRevD.96.072002. arXiv: 1703.09665. url: https://cds.cern.ch/record/2257300.

[114] ATLAS. “Extended Pileup Reweighting”. 2022. url: https://twiki.cern.ch/twiki/bin/viewauth/AtlasProtected/ExtendedPileupReweighting.

[115] G. Avoni et al. “The new LUCID-2 detector for luminosity measurement and monitoring in ATLAS”. *Journal of Instrumentation* 13.07 (2018), P07017. doi: 10.1088/1748-0221/13/07/P07017. url: https://dx.doi.org/10.1088/1748-0221/13/07/P07017.

[116] G. D’Agostini. “A multidimensional unfolding method based on Bayes’ theorem”. *Nuclear Instruments and Methods in Physics Research Section A: Accelerators, Spectrometers, Detectors and Associated Equipment* 362.2 (1995), pp. 487–498. issn: 0168-9002. doi: https://doi.org/10.1016/0168-9002(95)00274-X. url: https://www.sciencedirect.com/science/article/pii/016890029500274X.

[117] Frank Ellinghaus et al. *Charged-current Drell-Yan cross sections at high transverse masses in pp collisions at* $\sqrt{s} = 13$ *TeV*. Tech. rep. Geneva: CERN, 2020. url: https://cds.cern.ch/record/2711872.

[118] Tim Adye. “Unfolding algorithms and tests using RooUnfold” (2011). doi: 10.48550/ARXIV.1105.1160. url: https://arxiv.org/abs/1105.1160.